IntechOpen

The Transmission Electron Microscope

Theory and Applications

Edited by Khan Maaz

THE TRANSMISSION ELECTRON MICROSCOPE – THEORY AND APPLICATIONS

Edited by **Khan Maaz**

The Transmission Electron Microscope - Theory and Applications
http://dx.doi.org/10.5772/59457
Edited by Khan Maaz

Contributors

Masashi Nojima, Thomas Wagner, Josef Neumüller, Adolf Ellinger, Ying Li, Hideki Masuda, Marcelo Silva-Briano, Feng Xu, Yuping Ran, Masashi Arita, Kouichi Hamada, Yasuo Takahashi, Kazuhisa Sueoka, Tamaki Shibayama, Audrey Moores, Madhu Kaushik, Grégory Chauve, Carole Fraschini, Jean-Luc Putaux, Łukasz Mielańczyk, Natalia Matysiak, Olesya Klymenko, Romuald Wojnicz, Francisco Sola, Kelvii Wei Guo, Jian Wang, Nan Li, Marcia Helena Braga Catroxo

© **The Editor(s) and the Author(s) 2015**
The moral rights of the and the author(s) have been asserted.
All rights to the book as a whole are reserved by INTECH. The book as a whole (compilation) cannot be reproduced, distributed or used for commercial or non-commercial purposes without INTECH's written permission.
Enquiries concerning the use of the book should be directed to INTECH rights and permissions department (permissions@intechopen.com).
Violations are liable to prosecution under the governing Copyright Law.

Individual chapters of this publication are distributed under the terms of the Creative Commons Attribution 3.0 Unported License which permits commercial use, distribution and reproduction of the individual chapters, provided the original author(s) and source publication are appropriately acknowledged. If so indicated, certain images may not be included under the Creative Commons license. In such cases users will need to obtain permission from the license holder to reproduce the material. More details and guidelines concerning content reuse and adaptation can be foundat http://www.intechopen.com/copyright-policy.html.

Notice

Statements and opinions expressed in the chapters are these of the individual contributors and not necessarily those of the editors or publisher. No responsibility is accepted for the accuracy of information contained in the published chapters. The publisher assumes no responsibility for any damage or injury to persons or property arising out of the use of any materials, instructions, methods or ideas contained in the book.

First published in Croatia, 2015 by INTECH d.o.o.
eBook (PDF) Published by IN TECH d.o.o.
Place and year of publication of eBook (PDF): Rijeka, 2019.
IntechOpen is the global imprint of IN TECH d.o.o.
Printed in Croatia

Legal deposit, Croatia: National and University Library in Zagreb

Additional hard and PDF copies can be obtained from orders@intechopen.com

The Transmission Electron Microscope - Theory and Applications
Edited by Khan Maaz

p. cm.

ISBN 978-953-51-2150-3

eBook (PDF) ISBN 978-953-51-6384-8

We are IntechOpen, the world's leading publisher of Open Access books

Built by scientists, for scientists

3,800+
Open access books available

116,000+
International authors and editors

120M+
Downloads

Our authors are among the

151
Countries delivered to

Top 1%
most cited scientists

12.2%
Contributors from top 500 universities

WEB OF SCIENCE™

Selection of our books indexed in the Book Citation Index in Web of Science™ Core Collection (BKCI)

Interested in publishing with us?
Contact book.department@intechopen.com

Numbers displayed above are based on latest data collected.
For more information visit www.intechopen.com

Meet the editor

Dr. Maaz Khan is working as Foreign Scientist in the Chinese Academy of Sciences (CAS), Lanzhou, P.R. China. He obtained his PhD in Nanomagnetism from Qauid-i-Azam University, Islamabad, and post-doctorate from Sungkyunkwan University, Korea. His research interests include fabrication of nanomaterials by wet-chemical and electrodeposition techniques. He is working on structural, magnetic, optical, and electrical characterization of various materials. He has more than 40 research articles published in peer-reviewed journals and is the author and editor of the books. Moreover, Dr. Maaz is also working as editorial board member of World Journal of Condensed Matter Physics (WJCMP), International Journal of Nano-studies and Technology (IJNST), and International Journal of Materials Science and Applications (IJMSA).

Contents

Preface

Over the last few decades, remarkable developments have taken place in instrumentation and techniques for characterizing the microstructure and microcomposition of materials. The principal instruments include the scanning electron microscope, electron probe X-ray microanalyzer, and the analytical transmission electron microscope. Transmission electron microscopy (TEM) has developed into a sophisticated sub-nanometer resolution imaging technique. In this technique, the electron-beam is transmitted through an ultra-thin region, interacting with specimen as it passes through it. An image is formed from the interaction of the electrons transmitted through the specimen, which is then magnified and focused onto the imaging device, such as a fluorescent screen or a charge-coupled device (CCD) sensor. This technique has variety of applications in medical field, like cancer research and virology for diagnosis purposes, as well as in material science, nanotechnology, computer, and electronics industries for structural characterization. This book presents the background and implementation of techniques, which have allowed true imaging and chemical analysis at the atomic scale.

The book is structured in three parts. The first part introduces the basics of in-situ atomic-resolution electron microscopy imaging in TEM. This part also describes limits of in-situ microscopy for nanostructures, electronics, and dislocation interface interactions. The second part introduces fundamental electron microscopic concepts of sampling and characterization of nanomaterials including thin films and nanocrystals like carbon nanotubes. Based on the first and second parts of the book, the third part focuses on use of TEM for biological study; it describes the analysis of various samples, including clinical skin samples, plant cell wall, and three major groups of freshwater zooplankton. This part also provides information about veterinary diagnostic through atomic-resolution TEM imaging.

The topics in this book are developed to a level appropriate for most modern materials research using TEM. The content of this book provides the fundamental preparation needed for further study of advanced topics in microscopy. The book includes many practical details and examples for specimen preparation methods for TEM. Moreover, at the end of each chapter, proper references have been included that can lead the readers to the best sources in the literature and help them to go into more depth in electron microscopy. This second edition has been completely revised and updated in order to incorporate the very recent technological and scientific advancements in TEM that have been realized since the first edition appeared in 2012. This practically oriented book represents a clear and comprehensible introduction for all persons who want to use a transmission electron microscope in practice.

I am grateful to my doctorate student Ms. Adeela Nairan, who helped me in completing this project, and also to the entire InTech publishing team for making this project possible and to

all the authors who have contributed to this book. I am also thankful to the Publishing Process Managers Ms. Ana Pantar and Ms. Ivona Lovric for their cooperative attitudes during the publishing process. I hope that this book will help the readers in a more efficient way to characterize their materials and will provide them an opportunity to strengthen their research capabilities in the field of material science and nanotechnology.

Dr. Maaz Khan
Institute of Modern physics (IMP),
Chinese Academy of Sciences (CAS),
P.R. China

Section 1

In Situ Transmission Electron Microscopy

Chapter 1

Combined Transmission Electron Microscopy — *In situ* Measurements of Physical and Mechanical Properties of Nanometer-sized Single-phase Metallic structucre

Hideki Masuda

Additional information is available at the end of the chapter

http://dx.doi.org/10.5772/60750

Abstract

This chapter reviews the results of silver nanometer-sized contacts (Ag NCs). To realize fabrication, atomistic observation, and mechanical and electrical measurement of Ag NCs, an *in situ* method where a contact-retract test of atomic force microscopy and a current feedback function of scanning tunnelling microscopy have been combined with high-resolution transmission electron microscopy (HRTEM). By inserting these functions inside HRTEM, it has been enabled to observe atomistic structures, which can be formed at the final stage of a rapture process, and to measure a change of properties correlated to structural dynamics.

Keywords: Silver nanometer-sized contacts, atomic force microscopy, conductance quantization, Young's modulus

1. Introduction

Currently, miniaturisation of electronics has continued, and it started the device development at atomistic and molecular scale.[1] Devices included into this electronic circuit are nanometer-sized contacts (NCs), atomic-sized wires (ASWs), single molecular junctions (SMJs), and so on. [2] (Figure 1) SMJ is a system of a single molecule sandwiched by a pair of nanometer-sized metallic electrodes. SMJs enable single electronic operation, high-density integration, and electric power saving.[3-7] To engineer SMJs, we need to reveal structure of device configu-

INTECH
open science | open minds

© 2015 The Author(s). Licensee InTech. This chapter is distributed under the terms of the Creative Commons Attribution License (http://creativecommons.org/licenses/by/3.0), which permits unrestricted use, distribution, and reproduction in any medium, provided the original work is properly cited.

ration that includes interfaces between molecules and electrodes and mechanical and electrical properties. Metallic NCs and ASWs are fundamental materials that have potentials for device applications themselves as well as key factors of application for SMJs[8].

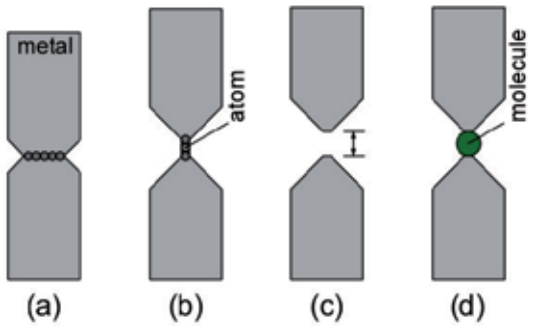

Figure 1. Schematics of atomistic scale devices. (a) NC, (b) ASW, (c) nano-gap structure, and (d) SMJ.

1.1. Electrical Property of NCs

Research in metallic NCs at 1988 by van Wees et al. started with conductance quantization in a point contact of two-dimensional electronic gas (2DEG) formed at interface of semiconductors. [9] When a negative bias is applied between gate electrodes placed on semiconductors, a depletion layer is formed in 2DEG under the electrodes. At a gap of this depletion layer, in which electrons cannot exist, a point contact of 2DEG forms. Energy of electrons passing through the contact is written as below, wherein W is the width of point contact.

$$E = \frac{\hbar^2 k_x{}^2}{2m} + \frac{\hbar^2}{2m}\left(\frac{\pi n_y}{W}\right)^2 \left(n_y = 1, 2, 3, \ldots\right) \tag{1}$$

Here, the first term is the kinetic energy along x direction, and the second term is the discrete energy level due to confinement along y direction. With n_y of the second term, one-dimensional sub-band is formed (Figure 2). The cross-point of sub-band and Fermi-level (E_F) correspond to one conductive channel. When you increase bias voltages applied to gate electrodes, the area of depletion layer becomes wider and the width of electrons passing through becomes narrower. The second term is inversely proportional to square of W; N decreases with decrement of W. In the experiment conducted by van Wees et al., the length of conductive channel was smaller than 0.3 μm, and because this is shorter than the mean free path of electrons in 2DEG (8 μm), electrons show ballistic conduction in this system. As a resultant, conductance of point contact is written as below (Landauer formula).

$$G = \frac{2e^2}{h}\sum T_n \tag{2}$$

http://dx.doi.org/10.5772/60750

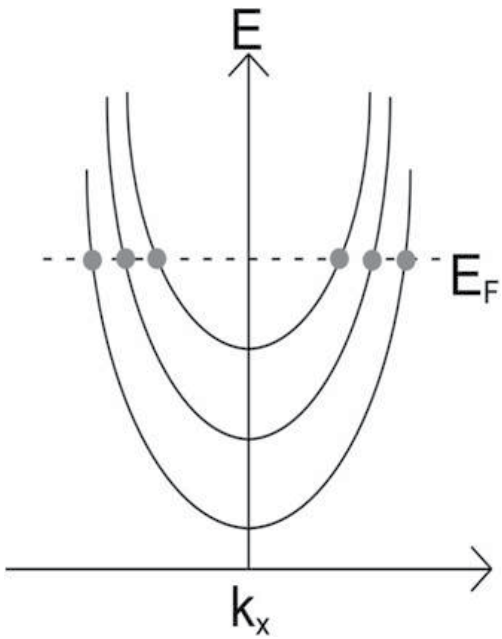

Figure 2. Schematic illustration of one-dimensional sub-band.

Here, T_n is the transmittance of an electron near the Fermi level (conductive channel), $2e^2/h$ (= G_0) is unit of quantization, e is charge of electron, and h is Plank's constant. Under assumption of ballistic conduction, transmittance of each conduction channel is $T_n = 1$; therefore, conductance of one conductive channel is $1\,G_0$. When the width of point contact (W) changes, the conductance varies with steps of integer multiples of G_0. That is, conductance quantization occurs when the length of electron conduction path becomes shorter than electron mean free path (ballistic conduction) and when the width of electron conduction path becomes narrow enough to count up the number of conductive channels. It is thought that this phenomenon also occurs in a system of metallic NCs, whose contact length is not so longer than electron mean free path.[10]

In early stage of metallic NCs, niobium (Nb) and nickel (Ni) NCs were researched. Just before the rapture of these NCs in tensile deformation process, the conductance of several G_0 is often observed.[11-15] This result triggered to relate the electrical conductance of metallic NCs to conductance quantization. Moreover, in gold (Au) or sodium (Na) NCs, a high probability of the conductance measured as integer multiples of G_0 is shown. [16-18] At that time, conductance of Au NCs varied in a staircase pattern (Figure 4). However, step height in this measurement is different from one time to another and not always corresponds to integer multiples of G_0. To analyse these result statistically, conductance histograms were made through the accumulation of considerable conductance variation traces (Figure 5). In the histograms for Au and Na NCs (Figure 6), peaks appeared at integer multiples of G_0.

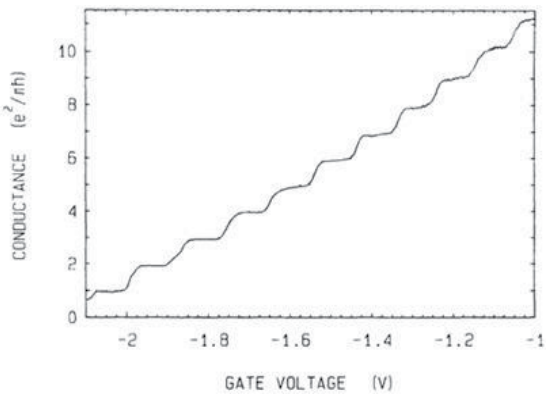

Figure 3. Conductance of 2DEG varies with gate voltage.[9]

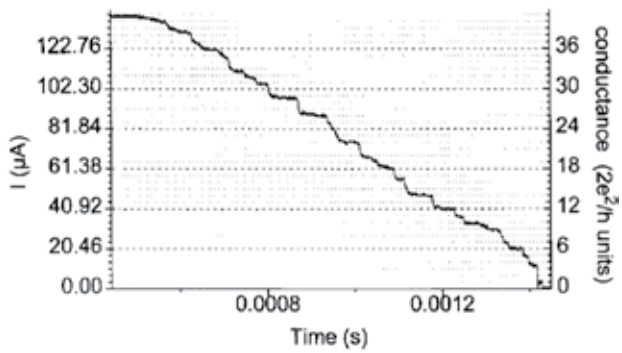

Figure 4. Time variation of conductance in tensile deformation process of Au NCs. [16]

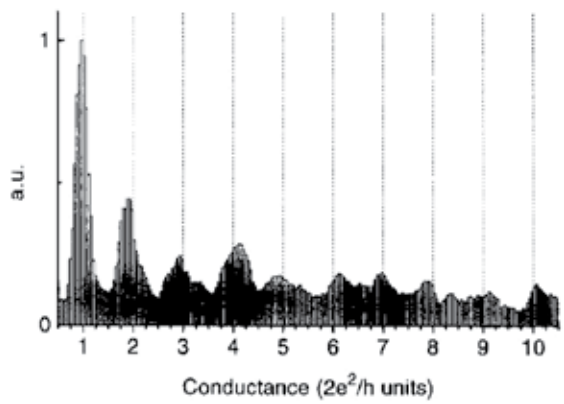

Figure 5. Conductance histogram of Au NCs. [16]

http://dx.doi.org/10.5772/60750

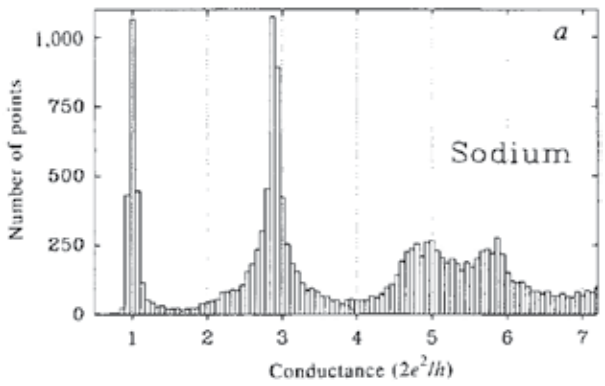

Figure 6. Conductance histogram of Na NCs. [16]

After the electrical conductance of NCs for other metallic species was researched, construable conductance of quantization was limited for monovalent metals, which are better suited for free electron approximation, such as Au[19, 20], silver (Ag) [19, 21-26], copper (Cu)[11, 19, 21, 27-35], and Na[18, 36, 37]. For the other metallic NCs, such as Nb[12, 13, 15, 21, 38], Ni[11, 14, 17, 22, 39-41], platinum (Pt) [11, 12, 17, 22, 28, 42-51], aluminium (Al), [13, 15, 28, 52, 53], paradium (Pd) [31, 44, 47, 49, 54, 55], iridium (Ir) [44, 46, 54], rhodium (Rh) [44, 54], zinc (Zn) [56, 57], and cobalt (Co)[47], the measured conductance is not construable for integer multiples of G_0. In other words, conductance of metallic NCs is categorized into two main types as quantization and anti-quantization.

1.2. Structure of NCs

To fabricate metallic NCs, mechanically controllable break junction (MCBJ) method [12, 38] and STM method [58]were mainly used. In these methods, however, one cannot observe the structure of NCs. Therefore, for quantization-type NCs, it is expected that the minimum cross-sectional area of NC, which shows the integer multiples of G_0, corresponds to the conductance using Landauer formula [59] and Sharvin's equation.[10, 60]

$$G_S = \frac{2e^2}{h}\left(\frac{k_F a}{2}\right)^2 \tag{3}$$

Here, k_F is Fermi wavelength of metals at room temperature, and a is the minimum cross-sectional radius. Objectively, the smallest structure that corresponds to the lowest step height of conductance staircase $(1\,G_0)$ is expected to be a single atom contact. Similarly, $2\,G_0$ to two atoms contact, $3\,G_0$ to three atoms contact, and so on; that is, a simple correspondence relation between the minimum cross-section area and the conductance of NCs is proposed. However, for Au NCs, direct observation using in situ HRTEM method show failure of this simple relationship.[61] For anti-quantization-type NCs, such relationship cannot be defined at all.

The structure should be directly observed to research a relationship between the structure and the conductance.

1.3. Mechanical property of NCs

Gimzewski et al. researched elastic and plastic deformation of NCs [62], but they could not discuss the mechanical properties of NCs by hitherto known MCBJ and STM methods. After that, Agraït et al. introduced the secondary STM tip on the backside of first tip to measure the displacement, and they also measured the conductance and force variation at the same time. [63] In 1996, Rubio et al. introduced an AFM cantilever to measure the force acting on NCs instead of STM tip.[64] The force value varied in a sawtooth pattern corresponding to the staircase pattern of conductance (Figure 7). It is supposed that the repetition of elastic and plastic regions appears in deformation process of Au NCs. In addition, force-displacement curve gives a spring constant of NCs.

In 2001, Kizuka et al. observed the deformation process of Au NCs using HRTEM-based *in situ* method with atomistic resolution. [65] They measured stress and strain quantitatively and started material mechanics research of metallic NCs. Using this method, mechanical properties of Cu[32], Ir[66], Pd[67], and Pt[51] NCs were researched. In 2005, Valkering et al. measured conductance and mechanical strength of Au and Pt NCs using developed tuning fork combined with MCBJ method. [68] As a result, force varied in a sawtooth pattern, which is similar to reference results. [63, 64].

1.4. Deformation of NCs

Sørensen et al. suggested three slip modes for deformation of NCs [69] (Figure 8). The tensile deformation axis is perpendicular to {111}. Deformation occurs with slipping on one, two, or three {111}, which are tilted from the tensile deformation axis (Figure 8).

To actually observe the deformation of NCs, two *in situ* HRTEM methods were developed; one is electron beam double holes drilling method. Electron beam drills two holes on material film with focused beam. A bridge that was formed between holes was gradually deformed using defocused electron beam.[70] The other method is the tip-sample contact method [65], and this fabricates and deforms NCs using piezo-driven tip. Kizuka and Tanaka observed Zn NCs using this method in HRTEM in 1994. [71] In 1997, Kizuka et al. directly observed the deformation process of Au NCs (Figure 9). [72] This is the first report that showed atomistic level observation of slip deformation process in crystals. After that, Ohnishi et al. fabricated Au NCs and observed deformation process from 5-atom width to 1-atom width in 1998. [73]

As Kizuka et al. further improved the *in situ* HRTEM method [74], they were able to observe the structural dynamics of NCs during tensile deformation process and research electrical and mechanical properties. [61] Until then, they were researched individually. They observed Au ASW at the final stage of tensile deformation process of Au NCs.

http://dx.doi.org/10.5772/60750

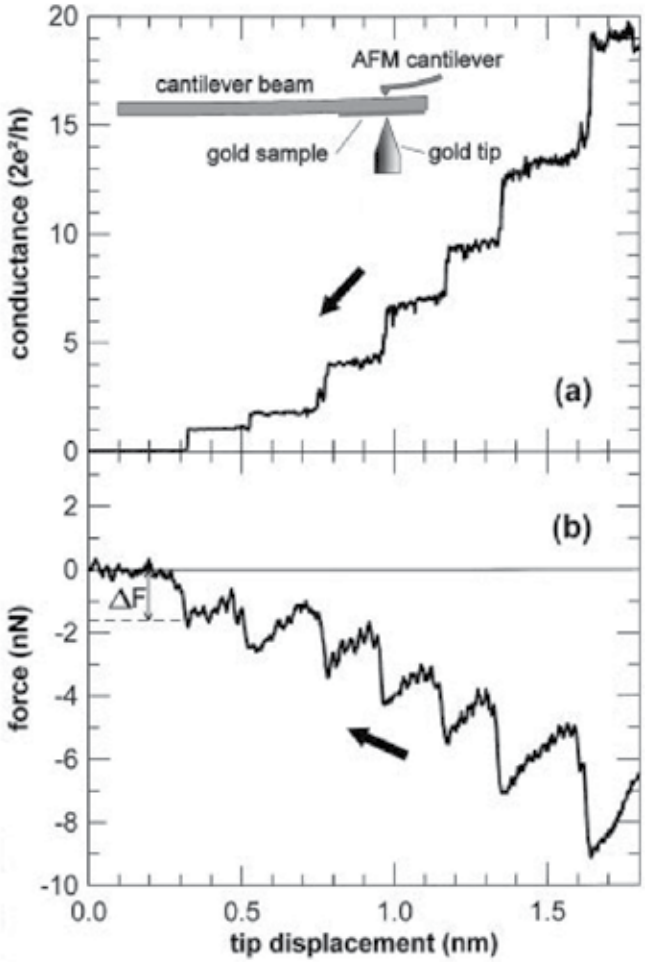

Figure 7. Conductance variation versus tip displacement in Au NCs measured by STM-AFM method.[64]

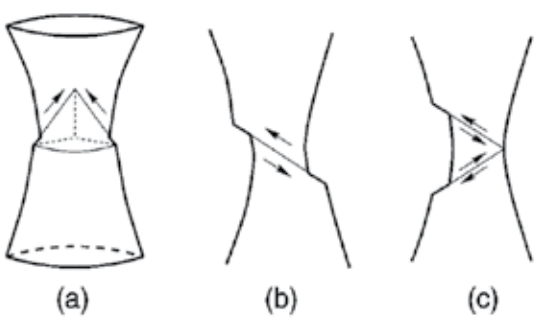

Figure 8. Deformation models of slip in Au NCs suggested by Sørensen et al.[69]

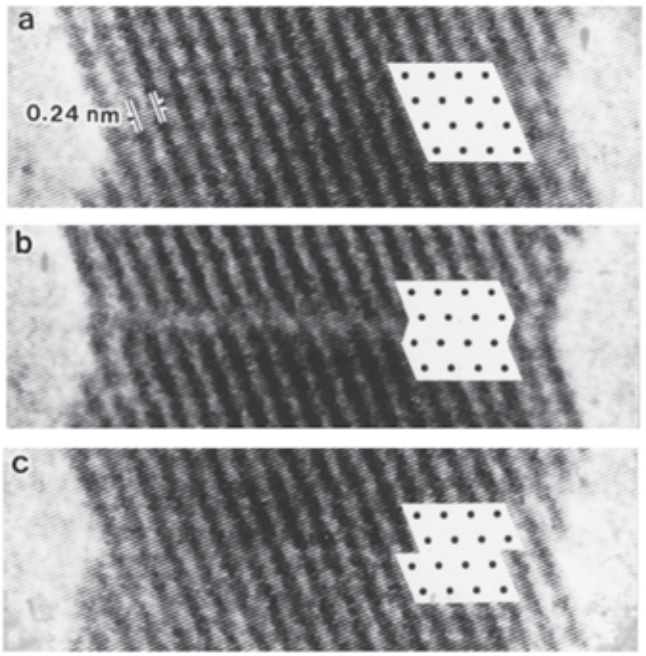

Figure 9. Time variation in elementary step of slip in shear deformation of Au NCs.[72]

The observed Au ASW has up to 10 atoms in length with an average interatomic distance of 0.27 nm (Figure 10). In tensile deformation process of ASWs, as tensile stress is concentrated on the contact region, interatomic distances of Au ASWs become longer up to 0.30 nm. At the same time, conductance of Au ASWs was measured. Resultant conductance greatly decreases when the number of atoms that is constructing ASWs exceed 4. Moreover, the force acting on the contact was measured. The tensile strength of this ASW was estimated to be from 8 to 17 GPa. This value is several times larger than that of Au NCs and much larger than bulk Au. At elastic deformation regions of stress-strain curves, Young's modulus of Au ASWs was estimated to be from 47 to 116 GPa. This value is remarkably comparable with that of single crystal Au.

The NCs and ASWs of other materials than Au have been also observed. The conductance quantization-type NCs, such as Au, Ag[26, 75] and Cu [34] ASWs, were also observed. On the other hand, those of anti-quantization-type NCs, such as Pt [47, 51], Pd[47, 76], Ir[66], and Co [47]ASWs, were also observed.

As described above, the problems in the research in metallic NCs commonly exist until now, among many materials as unrevealed below: 1) corresponding relationships between structure and electrical property of NCs, 2) phenomenon and mechanisms in the disappearance of conductance quantization, and 3) mechanical property of NCs. Especially, as research in NCs has been concentrated on Au, the structural dynamics of NCs is uncertain. Even some of the metallic NCs are already researched, only the structures that appeared in tensile deformation

http://dx.doi.org/10.5772/60750

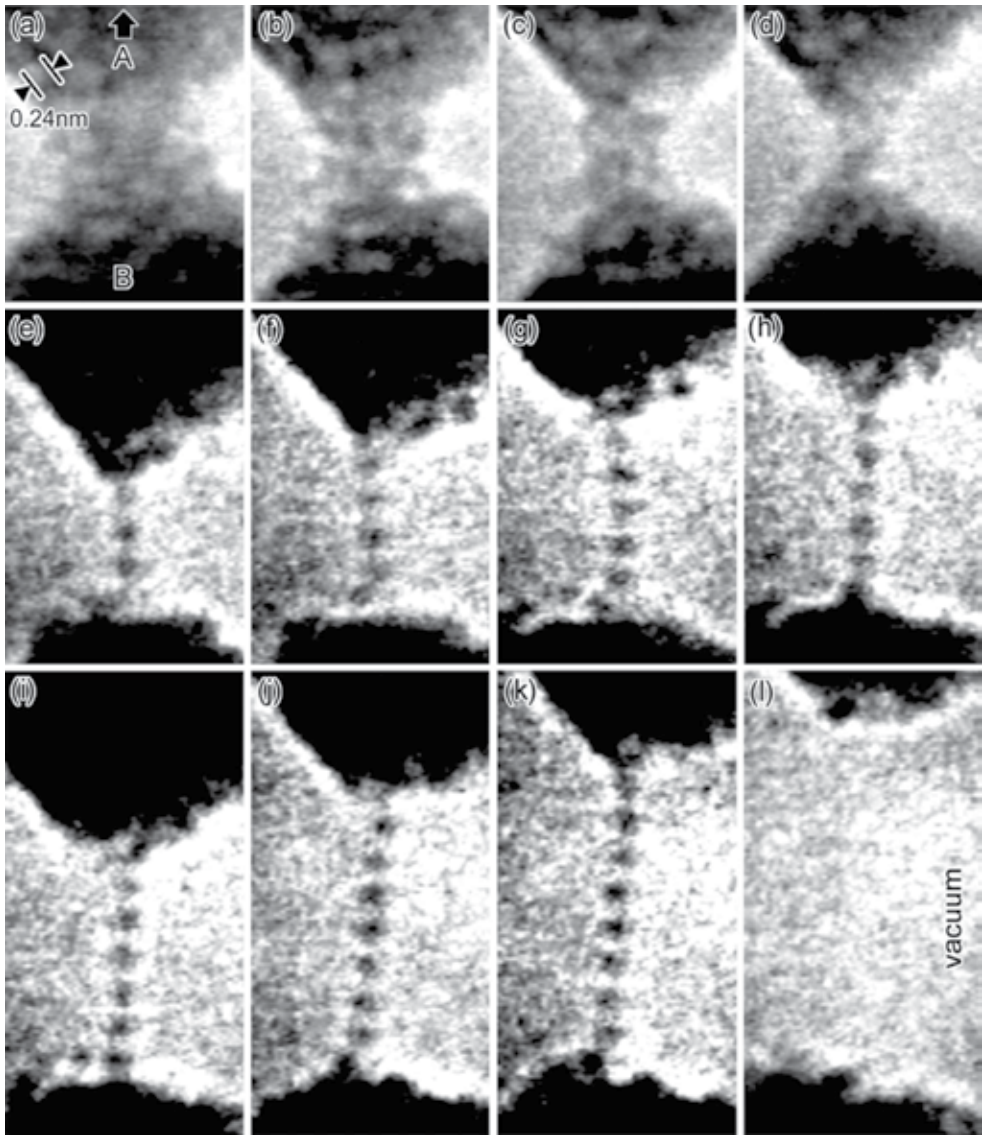

Figure 10. Time variation of Au ASW formation process observed by *in situ* HRTEM method.[61]

process have been observed. Therefore, the stable structure and electrical conductivity of the NCs are not yet revealed.

To guide the general rule of the phenomenon that appears in the metallic NCs, it is necessary to examine structural dynamics, electrical conductivity and mechanical properties, clarify the correspondence relationship between the structure and properties directly. The method used to observe structures and properties at the same time, which can analyse the correspondence, is limited *in situ* HRTEM method.

The purpose of this research is to clarify Ag NCs as a quantized metal using *in situ* HRTEM method. As Ag is expected to show the similar result as Au, statistical results are not observed.

2. *In situ* HRTEM

2.1. Experimental – *In situ* HRTEM -

In the observation of NCs, we used combined HRTEM with functions of STM and AFM (Figure 11) [61]. One can insert two specimen holders into the sample room of this microscopy. Each holder can be driven by a course mechanical goniometer that has ±1 mm with submicron resolution and a fine piezo that has picometer scale. That is, we can move the sample to make a contact or a deformation with atomistic level using eight degrees of freedom.

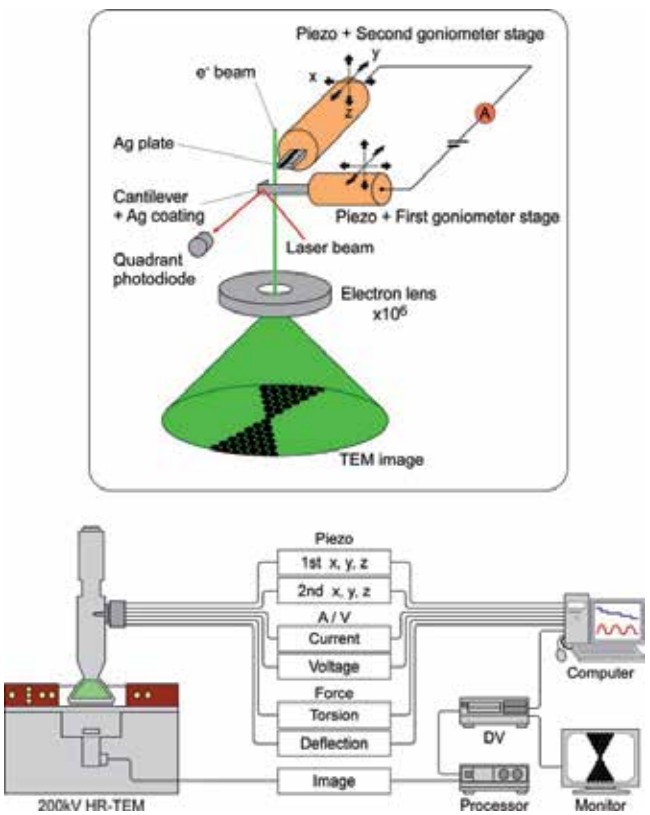

Figure 11. Schematic illustration of combined HRTEM.

When we measured the force acting on a contact, we attached a silicon cantilever used in AFM on one of the specimen holders. This cantilever was covered with metallic film that is 20-40 nm thick. The other one was mechanically polished and Ar-ion milled metallic thin plate.

http://dx.doi.org/10.5772/60750

HRTEM images were recorded with television camera. We applied bias voltages between samples. The current through the contact was measured by two-terminal method. The current signal was amplified 10^5 times and was then converted into voltage signal. Forces that are acting on a cantilever along deflection and torsion directions were detected using optical lever method used in AFM. When a laser is irradiated on the backside of cantilever, reflection angle of the laser varies with the cantilever deflection. We detected it as variation in relative strength of incident laser beam into quadrant photo-diode. These values were also amplified in the circuit. We recorded voltage signals corresponding to voltage, current, deflection, and torsion per 480 s, then we analysed these signals and observed images with time synchronizations.

Firstly, we set up two samples in a distance of 10 nm using course-moved mechanical goniometer with low magnification observation. After that, we made a contact using piezo drives. Then, we applied bias voltages of 13 mV and repeated to make a contact and tensile deformation. Each atomistic structure of NCs only appeared during several milliseconds in deformation process. This time is often shorter than the time resolution of the system of image recording for TEM (~17 ms / 1 frame). To observe specific structure longer, we used current to piezo drive feedback system.

3. Structure, conductance, and mechanical properties

3.1. Observation of tensile deformation process

In this section, we show the tensile deformation process of Ag NCs. Figure 12 is a time-sequence series of high-resolution images of the thinning process of Ag NC. The thinning was caused by the cantilever tip retraction from the plate with a speed of approximately 0.3 nm/s; the tip-plate distance was not controlled by the conductance feedback circuit in this observation. The tip and plate are observed with dark contrast in the upper and the lower regions of each frame, respectively. The NC is located at the centre of each image. The minimum cross section of the contacts is located in the middle of each frame between the tip and the plate in the vacuum. On the surfaces of both the tip and the plate, neither contamination nor an oxide layer is observed throughout Figs. 12(a)–12(f). The (111) lattice fringes with a 0.24 nm spacing are observed on the tip, the plate, and at their contact; the NC has a crystalline structure. The width of the minimum cross section in Fig. 12(a) is 2.2 nm. The width decreases as retraction proceeds, as shown in Figs. 12(b)–12(e). After this thinning, the width of the NC reaches 0.58 nm in Fig. 12(e), and finally, the NC breaks, as shown in Fig. 12(f).

Figure 13 is the time variation in strain, minimum cross-sectional area, current, current density, force, and stress of the Ag NC during the tip-plate retraction process shown in Fig. 12 as function of time. The time in Fig. 13 corresponds to the observation time in Fig. 12. As the tip-plate distance increases gradually, the minimum cross-sectional width decreases, as shown in Fig. 12(a) and 12(b). During this thinning process, rapid decreases in current and force are simultaneously observed. This shows that the thinning of the NC proceeds intermittently during tip retraction. Thus, slips occurred at these rapid decreases after elastic elongation, as indicated by the arrows above the force curve in Fig. 13. To calculate the current density and

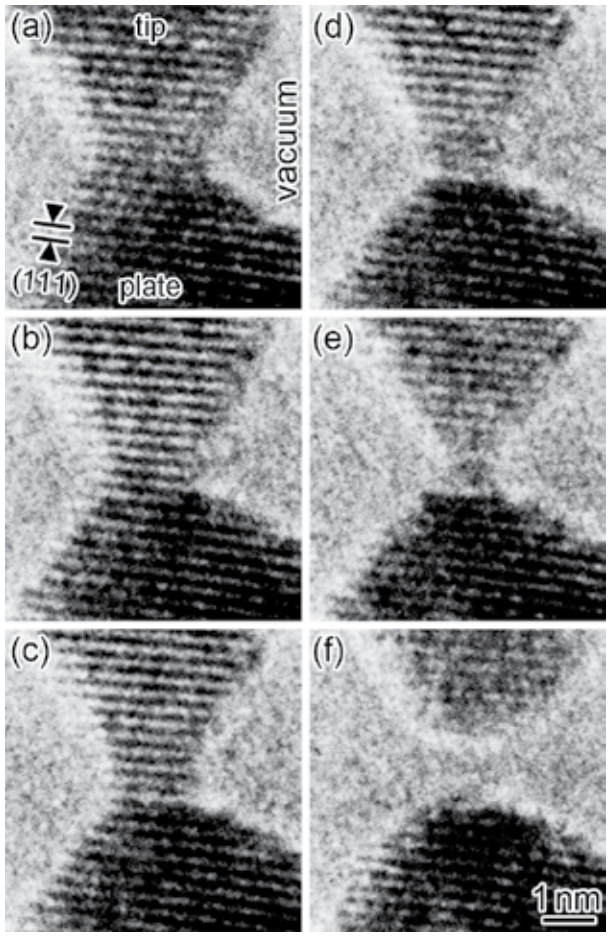

Figure 12. Time variation of HRTEM images in tensile deformation process of Ag NC. Bias voltage of 13 mV is applied. [77]

the stress of the NC, we assumed that the minimum cross section of the contact was circular. The minimum cross-sectional area was calculated using the observed width. In the time region from 0 to approximately 2.0 s, the stress increases as the cross-sectional area decreases.

The force at fracture is approximately 2 nN, which is similar to the values for Au single-atom contacts (approximately 1.5 nN).[64] The stress reaches approximately 3 GPa before fracture, which is 1/3 of the fracture strength previously observed for Au single-atom contacts(approximately 8 GPa)[61] and comparable to yield stress for Au NCs (1.7–4.2 GPa).[63] This shows that the critical shear stress of the Ag NC increases as the NC becomes thinner. The variation in stress against strain is represented in Fig. 14. A sawtooth curve, consisting of cycles of gradually increasing stress followed by a successive rapid decrease in stress is seen in Fig. 14. The regions of gradually increasing stress correspond to elastic elongation of the NC. The rapid decreases in the strain-stress curve correspond to slip events, due to the structural relaxation

http://dx.doi.org/10.5772/60750

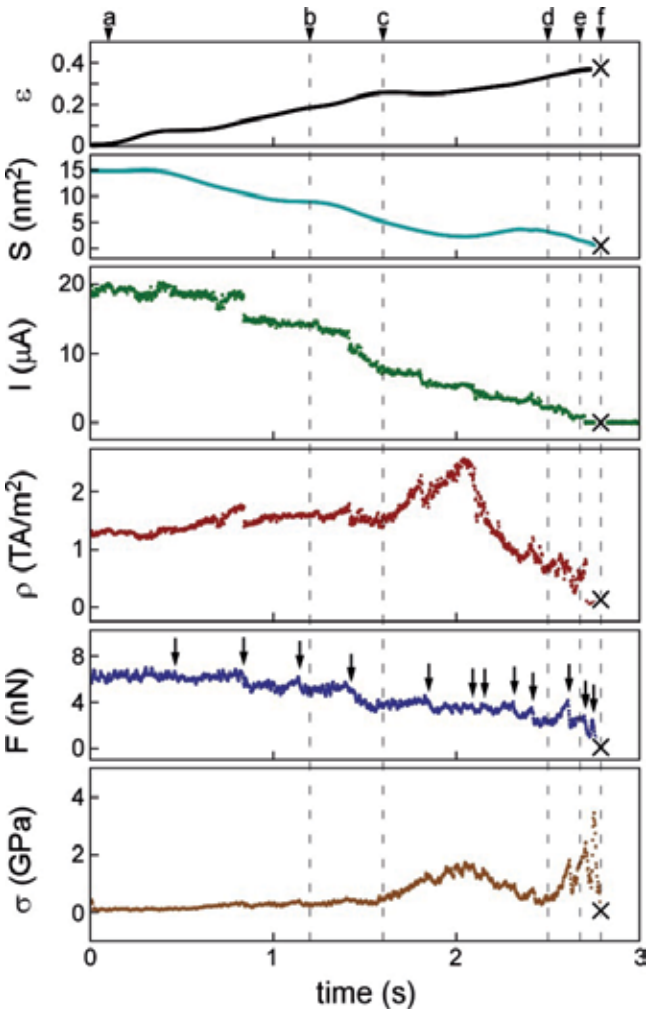

Figure 13. Time variation in strain, cross-sectional area, current, current density, force, and stress. Time is corresponding to Figure 12. Arrows corresponds to slip deformation of NC.[77]

of accumulated strain during elastic elongation. From the slope in each elastic elongation region, the plotted Young's modulus of the NC was estimated. Figure 15 shows the Young's modulus plotted against the minimum cross-sectional width. The slope changes at a width of approximately 1 nm.

3.2. Conductance histogram

Figure 16 shows the conductance of Ag NCs during the simple retraction of the tip. The histogram of the conductance values is integer multiples of G_0. Figure 17 shows histograms of conductance values observed during feedback control. When the feedback value is assigned to be $1\,G_0$, one main peak is observed at the assigned value. For feedback values of 2 and

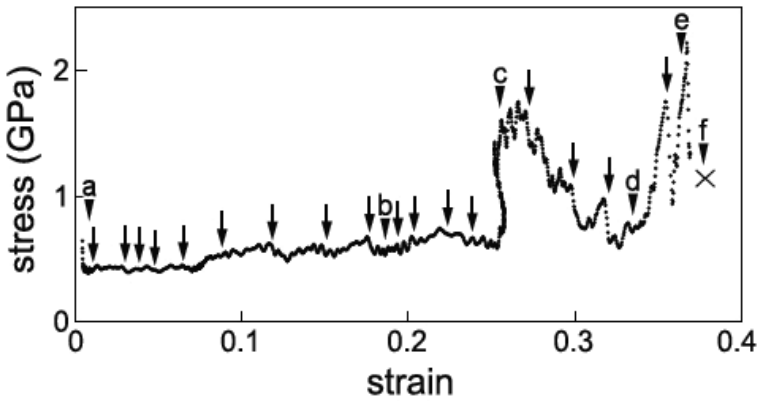

Figure 14. Stress-strain curve of Ag NC.[77]

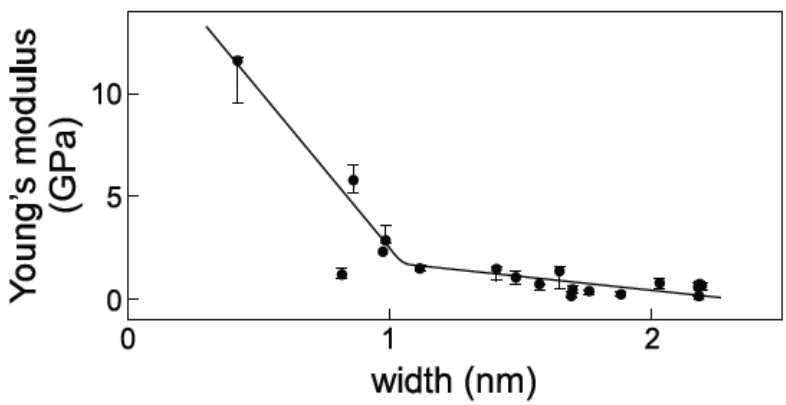

Figure 15. Young's modulus of Ag NC varied with width of contact.[77]

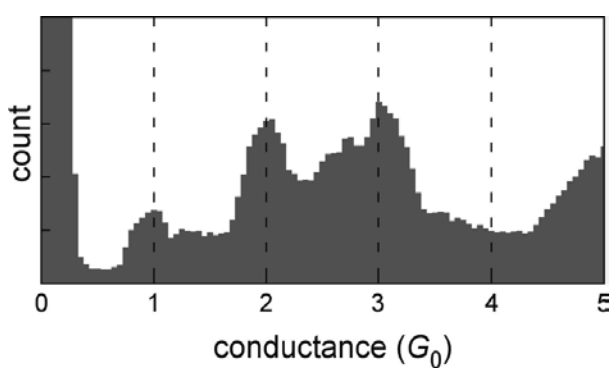

Figure 16. Conductance histograms accumulated from a plenty of tensile deformation process of Ag NCs.

http://dx.doi.org/10.5772/60750

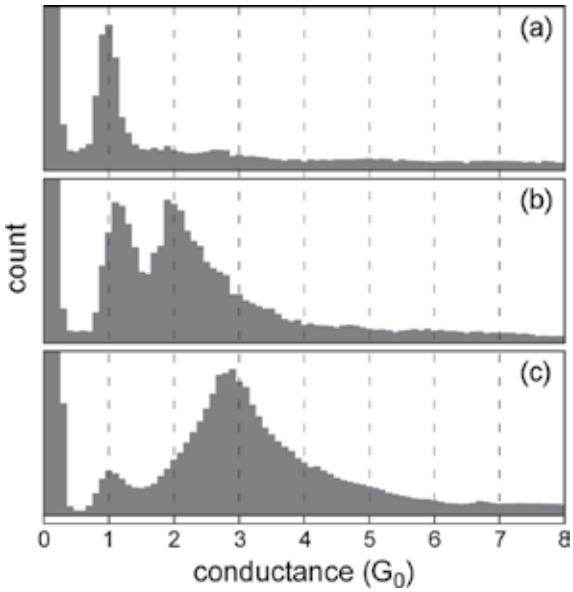

Figure 17. Conductance histograms of Ag NCs using current feedback system with bias voltage of 13 mV. Target conductance is (a) 1.0 G_0, (b) 2.0 G_0, and (c) 3.0 G_0.[77]

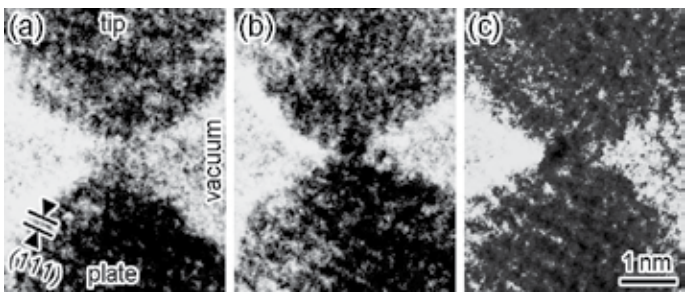

Figure 18. HRTEM images of Ag NCs using current feedback to 1 G_0 with 13 mV. Minimum cross-sectional width is (a) 1-, (b) 2-, and (c) 3-atom.[77]

3 G_0, in addition to the main peak corresponding to the assigned value, another peak is observed at 1 G_0.

Figure 18 shows high-resolution images of Ag contacts during conductance feedback control with an assigned value of 1 G_0. As described for the high-resolution images in Fig. 12, the contacts are seen between the tip in the upper and the plate in the lower regions of each frame. The minimum cross-sectional widths of the contacts presented in Figs. 18(a)–18(c) are one, two, and three atoms, respectively. Thus, although the conductance value was the same, three types of contacts were observed. The 1 – G_0 peaks in the conductance histograms arose from these types of contacts.

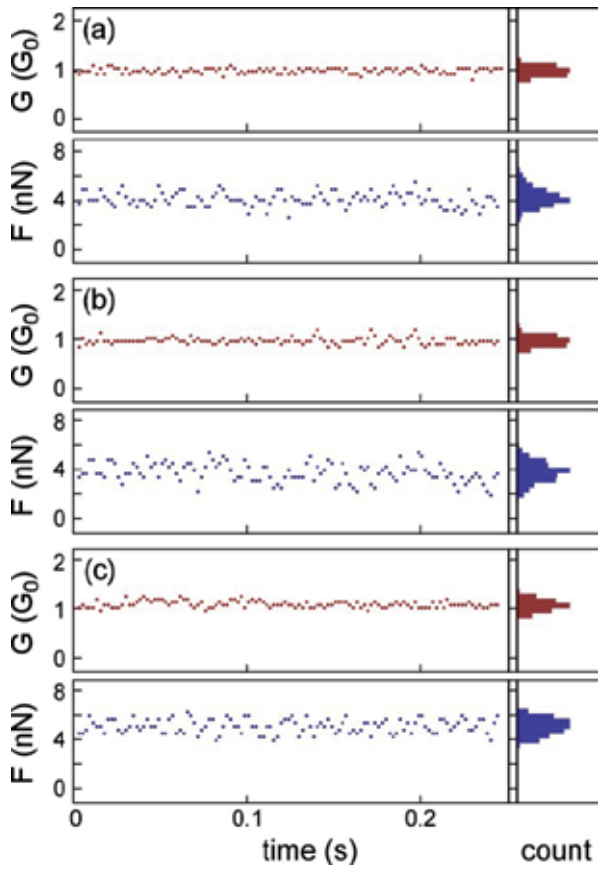

Figure 19. Conductance and force of Ag NCs under current feedback control.

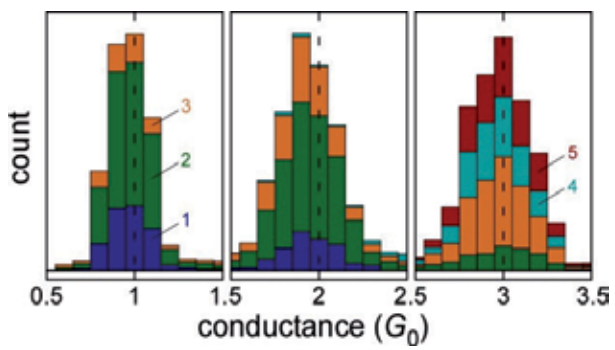

Figure 20. Conductance histograms of Ag NCs. Targets of current feedback system are 1 G_0, 2 G_0, and 3 G_0. Each bin is coloured by cross-sectional width of NCs.

The contrast in Fig. 18 is weaker than that of Au NCs because the electron-scattering intensity of Ag atoms is lower than that of Au atoms.[61] Figures 19(a)–19(c) show the conductance of

http://dx.doi.org/10.5772/60750

and the force acting on the Ag contacts presented in Figs. 18(a)–18(c) during the conductance feedback control, respectively. The observed conductance values converged to be assigned a value of $1G_0$. The tensile force acting on each contact is 4.1±1.0 nN for the single-atom contact [Fig. 19(a)], 4.0±1.5 nN for the NC with a width of two atoms [Fig. 8(b)], and 5.3±1.2 nN for the NC with a width of three atoms [Fig. 19(c)].

Figure 20 shows conductance histograms of the Ag contacts, along with their minimum cross-sectional width during feedback control with assigned values of conductance of 1, 2, and $3\,G_0$. The $1-G_0$ peak arose from contacts having widths of one, two, and three atoms with a counting ratio of 27%, 60%, and 13%, respectively. The $2-G_0$ and the $3-G_0$ peaks were generated by contacts having widths of one to four atoms and two to five atoms, respectively. For the $2\,G_0$ peak, the count ratio of the constituent contacts having width of one, two, three, and four atoms are 15%, 57%, 26%, and 3%, respectively. For the $3-G_0$ peak, the count ratio of the contacts having width of two, three, four, and five atoms are 12%, 36%, 26%, and 27%, respectively.

3.3. Mechanical properties of Ag NCs during thinning

The sawtooth curve was observed in the stress-strain relationship that is up to a strain of 0.25, as presented in Fig. 14. Thus, the tensile deformation of the NC initially proceeded through cycles of elastic elongation and subsequent slip up to this strain. The tensile stress at which the slips occurred was 0.5–0.6 GPa in the strain region of 0–0.25 in Fig. 3. The critical shear stress was calculated from the stress and the angle between the tensile and slip directions. The value calculated was 0.07 GPa, comparable to 1/10 of the theoretical shear stress (0.77 GPa) and the critical shear stress of Ag whiskers on {111} in <110> (0.71 GPa).[78] Thus, the slips in this strain region are inferred to be dislocation-mediated slips. After this slip process, a rapid increase in stress followed by a decrease is seen at a strain of 0.25. During the decrease, a sawtooth shape was observed: slip events continued after the rapid increase. The maximum stress in this region increased to 2 GPa. This stress corresponds to a critical shear stress of 0.2 GPa, comparable to 1/3 of the theoretical shear stress and whisker shear stress. It was also noted that for smaller contacts having widths of less than 1 nm, the slope of the Young's modulus-width relationship increased, and the modulus reached 10 GPa, as shown in Fig. 4. Thus, it is found that the elastic property of the NCs changes when their width decreases to less than 1 nm. These results reveal that a different type of deformation occurred for the smaller contacts. A molecular dynamics simulation by Sørensen et al. showed that in Au NCs, the crossover from a dislocation-mediated slip to a homogeneous slip occurs when their width decreases to less than 1.5±0.3 nm.[69] In the present observation, the minimum cross-sectional width of the Ag NCs was 1.5 nm when the critical shear stress was 0.2 GPa. Therefore, it is inferred that the deformation mechanism changes from dislocation-mediated slip to homogeneous slip when the width decreases to less than 1.5 nm. That is, changes, such as increase in the Young's modulus of nanoscaled materials, are caused by a simplification of deformation system to a direct atomistic materials mechanics rather than a slip system of macroscaled materials. In such cases, mechanical properties of the materials are subject to modulation by the size effect.

3.4. Stable contact with a certain conductance

When the feedback value was assigned to be $1\,G_0$, the observed conductance values converged to this assigned conductance, as shown in Fig. 6. On the other hand, when the feedback value was assigned to be other values, i.e., 2 and $3\,G_0$, a $1-G_0$ peak was observed in addition to the peak at each assigned value. In particular, when the assigned value was $2\,G_0$, which is closer to $1\,G_0$, the intensity of the $1-G_0$ peak was comparable to that of the peak at $2\,G_0$. This shows that the NCs exhibiting a conductance of $1\,G_0$ were observed preferentially although the feedback control was performed to form NCs having other conductance; the stability of the $1\,G_0$ NCs is higher than that of NCs exhibiting other conductance.

3.5. Structures of Ag NCs exhibiting a conductance of 1 G_0

During the feedback control with an assigned conductance of $1\,G_0$, three types of contacts, such as those with widths of one, two, and three atoms, were observed. In particular, we noted that in this feedback method, the contacts exhibiting a conductance of $1\,G_0$ are not wires of single-atom width but of zero-length contacts. Therefore, single-atom-width Ag wires are less stable than the zero-length single-atom-width contacts in which the tip and plate are connected with one atom when they exhibit a conductance of $1\,G_0$. It is pointed out, on the basis of theoretical analysis, tight binding, and free-electron calculations, that the conductance of metallic NCs and single-atom-width wires is sensitive to irregularities in the contact shape, a decrease in the convergent angle of electrodes, and small variation in the interatomic distance.[79-81] It was shown from a classical molecular dynamics simulation coupled with conductance calculations based on a tight binding model that the conductance of Ag NCs is sensitive to their atomic configuration and is not only determined by their width; for example, single-atom-width Ag contacts exhibit a conductance from 0.3 to $1.1\,G_0$.[82] Thus, the present observation reveals that although the widths of the three types of contacts are different, their conductance becomes the same value, $1\,G_0$, owing to this sensitivity. The force acting on the widest contacts, such as those with a width of three atoms, was larger than that acting on narrower contacts, such as NCs with width of one and two atoms. During feedback control, when the conductance of a NC was larger than the assigned value, the tip was manipulated to increase the tip-plate distance, resulting in the increase in force. It was reported that when tensile force acts on NCs during elastic elongation, the conductance decreases.[64] Thus, it is deduced that the conductance of the NC with a width of three atoms was decreased by the elongation due to the tensile force, and then the $1\,G_0$ state was realized under this strained condition.

In the present study, in addition to simple tensile deformation, we introduced a conductance feedback system into *in situ* HRTEM to continuously observe Ag NCs exhibiting a certain conductance; in particular, we observed the quantized conductance values. Simultaneously, we measured the force acting on the contacts to investigate the stress of the NCs. From the observed structure and strain-stress relationship, it was found that the Young's modulus, which is, the elastic property of the NCs, changes when their width decreases to less than 1 nm. From the estimation of the critical shear stress of NCs, it was also inferred that the

http://dx.doi.org/10.5772/60750

deformation mechanism of NCs during thinning by simple retraction changes from dislocation-mediated slips to homogeneous slips when the width of NCs decreases to less than 1.5 nm. Using the conductance feedback system, it was found that several types of contacts with different widths contribute to the formation of each peak at the assigned conductance at quantized levels ((1 G_0; 2G_0 and 3 G_0)) in the histogram. In particular, when the feedback conductance was assigned to be 1 G_0, the contacts were not single-atom-width wires but three types of contacts, i.e., zero-length contacts with widths of one, two, and three atoms. Thus, it is concluded that such zero-length Ag contacts are more stable than single-atom-width Ag wires when they exhibit a conductance of 1 G_0.

4. Current-voltage characteristics measurement

In this section, we show the current-voltage characteristics measurement of Ag NCs. Figure 21 is high-resolution images of the thinning process of Ag NC in a timeline. The NC is located at the centre of each image. The upper and the lower dark regions are the tip and the plate. The other brighter region is the vacuum. The continuous (111) lattice fringes of Ag (0.24 nm) are observed in the tip, the plate, and their contact region. It shows that the NC is a single crystalline structure. The width of the minimum cross section of the NC decreased from 6 atoms to 1 atom, and finally, the contact broke. Although the width of the contact region in Figs. 21(c) and 21(d) is the same, the contrast of the constricted region became brighter, implying that the thickness decreased. Figure 22 shows the high-resolution images and line profile of the constricted region of Figs. 21(d)–21(f). The intensity is classified into some levels; the intensities of the number of atom in thickness and the noise level in the vacuum. In Figs. 21(d) and 21(e), two and one large peaks are observed, indicating that their widths are 2 atoms and 1 atom, respectively. On the other hand, only the noise level is observed in the intensity in Fig. 21(f); the two tips are separated in the vacuum. From similar analysis, we constructed models of the atomic configurations of the Ag NC in Fig. 21, as shown in Fig. 22.

Figure 24 is the time-variation of the width, bias voltage, current, conductance, force, and stress during the thinning process of the Ag NC shown in Fig. 21, as a function of time. As the NC becomes thinner, the amplitude of the current and the conductance decrease stepwise. Similarly, the tensile force acting on the NC also decreases stepwise. The magnitude of the stress, which is calculated by dividing the force by the minimum cross-sectional area, is 1–6 GPa at times a–d and increases to 14 GPa before fracture at time e. Figure 25 shows the I–V curves measured for the NC presented in Fig. 21. The zero-bias conductance was estimated from the gradient of each curve to be 15 G_0, 11 G_0, 5 G_0, 3 G_0, and less than 0.1 G_0, for the NC presented in Fig. 21, respectively. As previously analysed by Nielsen et al.,[84]we fitted the curves with third-order polynomials,

$$I_{total} = G^{(1)}V + G^{(2)}V^2 + G^{(3)}V^3 \tag{4}$$

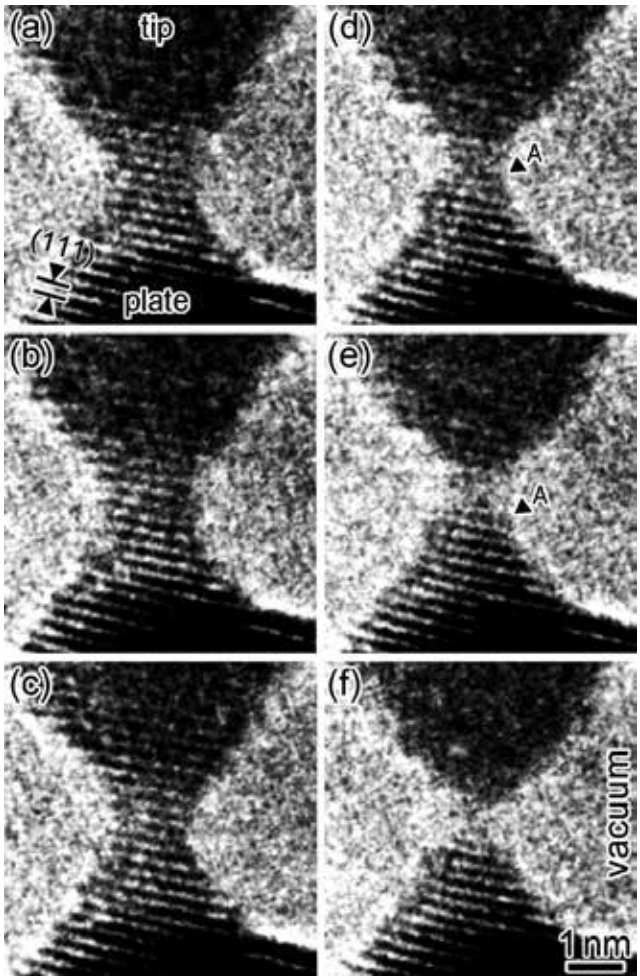

Figure 21. Time variation in HRTEM images of Ag NCs applying alternative current voltage of 13 mV.[83]

here, I_{total} is the current amount; V is the applied bias voltage; and $G^{(1)}V$, $G^{(2)}V^2$, and $G^{(3)}V^3$ are the coefficients of the first-, second-, and third-order-term that correspond to the conductance components – the lower bias voltages, the polarity dependence of the asymmetry of the contact structure, and the non-linearity, respectively. Figure 26 is the time variation of the non-linear parameter defined as $G^{(3)}/G^{(1)}$, and the ratio of the current of each term, $G^{(1)}V$, $G^{(2)}V^2$, and $G^{(3)}V^3$, to I_{total} as a function of conductance. The $G^{(1)}V$ component dominates the total current. For the NCs showing conductance larger than $10\,G_0$, both the $G^{(2)}V^2$ and $G^{(3)}V^3$ components show negative values; the total current is decreased from that in the case of linear I–V characteristics. For the NC of $3\,G_0$ (d in Fig. 26), the $G^{(2)}V^2$ component shows a positive value. The $G^{(3)}V^3$ component shows negative at states c and d in Fig. 26, whereas a positive value with an amount of 10% of the I_{total} was obtained at state e in Fig. 26. We compared

http://dx.doi.org/10.5772/60750

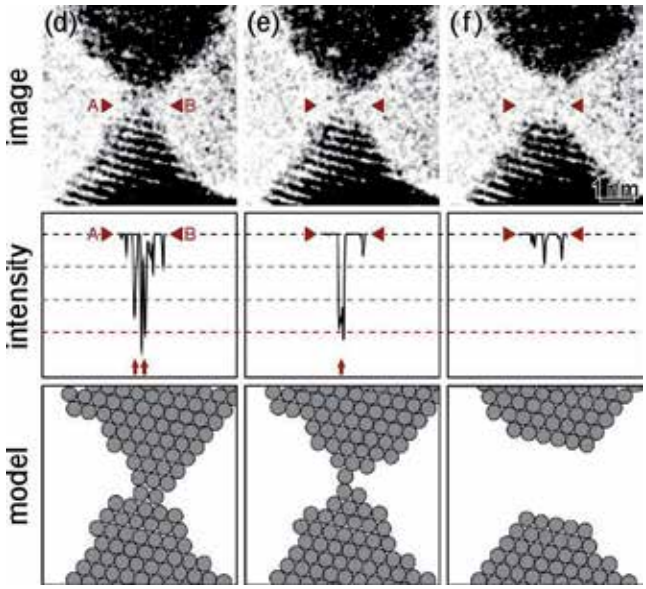

Figure 22. Atomistic configuration models of Ag NCs shown in Figure 21 (d-f).[83]

$G^{(3)}/G^{(1)}$ among those metallic NCs, i.e., Ag, Au, and Pt[51] NCs measured by the same method (Fig. 27).

4.1. Non-linearity of conductance and scattering of electrons in the Ag NC

The HRTEM images (shown in Fig. 21) were averaged over the time of 2 frames (over a period 67 ms,), which is similar to one cycle of alternating bias voltage that is 50 ms (Fig. 24). Thus, one of the I–V curves was corresponding to the averaged image over the 1 period. We confirmed that no discernible changes in image were observed between the 2-frame images used for averaging in the television system. We also noted that there was no identified hysteresis in any of the I–V curves, and no change was observed between the successive increases and decreases in voltage. Under these conditions, the variation in the non-linear parameter was observed. Therefore, even though a small invisible structural change might occur and affect each I–V curve, the variation in the non-linear parameter was observed, which we discuss next. As shown in Fig. 26, $G^{(3)}V^3$ is negative, and its absolute value increases as the NC width decreases to 2 atoms (in Fig. 23). Thus, $G^{(3)}/G^{(1)}$ is also negative. As a result, the I–V curve deviates from a linear slope on the lower side, implying that electron scattering occurs in the NC. In this study, we selected the amplitude of the bias voltage of 13 mV, and no change in structure was observed during this bias application. At room temperature, the thermal energy is approximately 25 meV which is larger than the bias window used in this experiment. This thermal effect causes fluctuation in the I–V curves. However, because a tendency in the I–V curves was observed as the size of the NC decreased, we suppose that the parameters $G^{(2)}V^2$ and $G^{(3)}V^3$ contain certain information regarding the conduction nature.

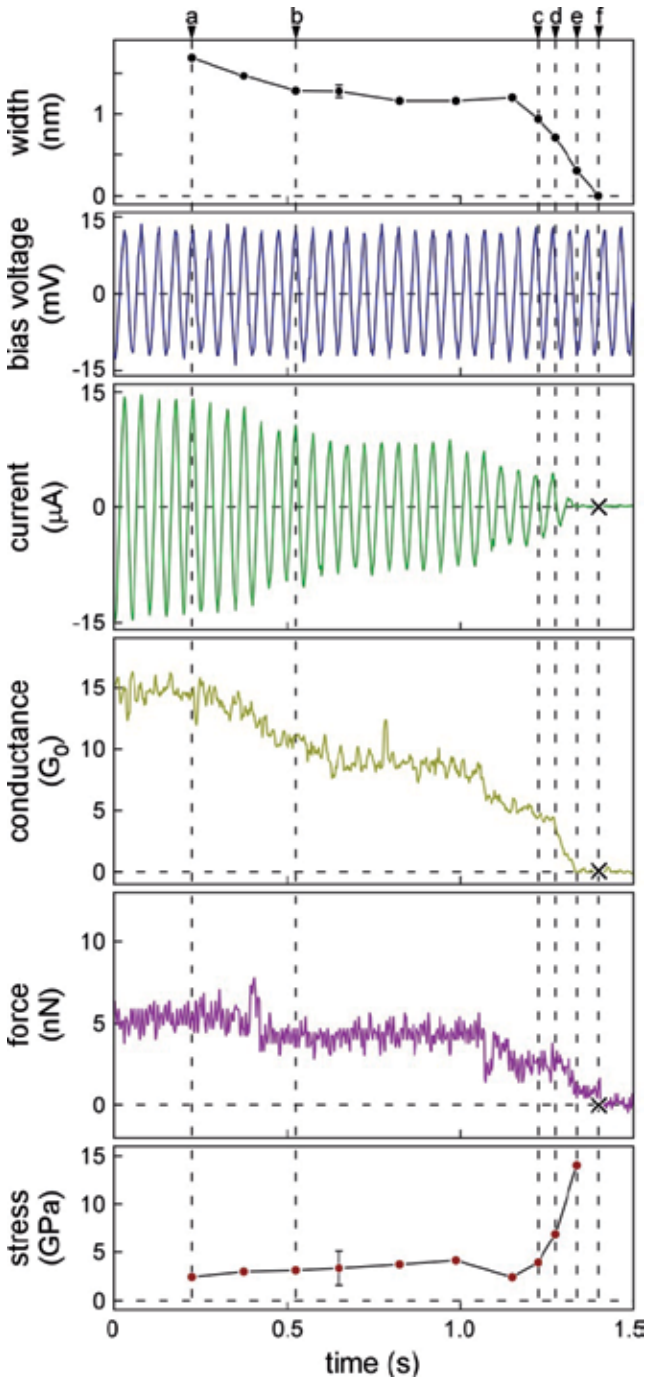

Figure 23. Time variation in width, applied bias, current, conductance, force, and stress of Ag NCs. Applied bias voltage is 20 Hz / 13 mV.

http://dx.doi.org/10.5772/60750

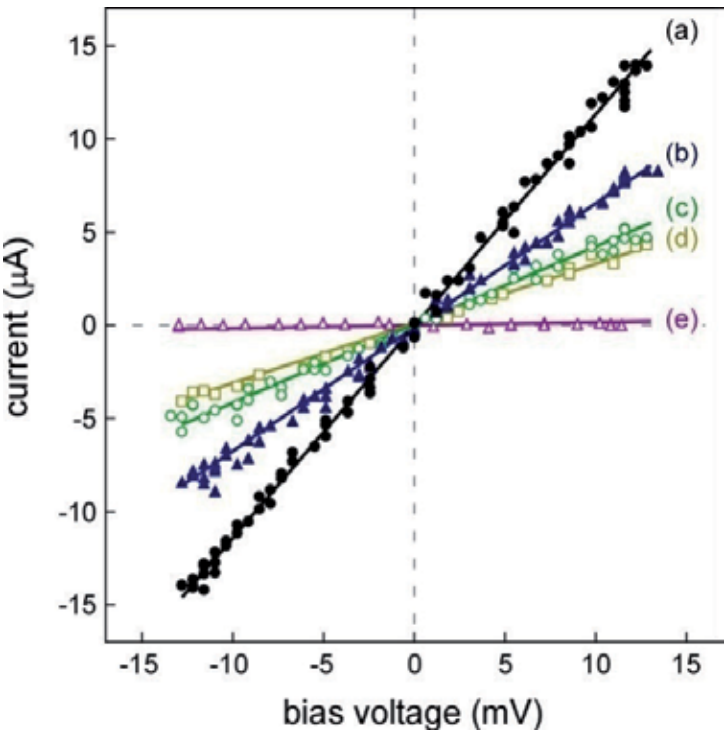

Figure 24. I-V curves of Ag NCs measured in Figure 21.

If we applied the bias voltage over 240 mV, the NCs of 5 nm size became unstable owing to electromigration; electron scattering increases enough to cause the atom migrations.[35] Such scattering contributes to the broadening of peaks in the conductance histograms of Ag NCs.[77]

As described above, electron scattering increases with decreasing contact width. During this thinning, the current density increased from 6 TA/m^2 (at time a) to 10 TA/m^2 (at time d). This current density was calculated by dividing the current value by the minimum cross-sectional area. On the other hand, when the contact transforms to the ASW, $G^{(3)}/G^{(1)}$ changes to positive. The current density of the ASW is 2 TA/m^2, which is a fifth of that of the 2-atom-width NC. These findings show that the density of states of the ASW differs from that of the NCs. As shown in Fig. 21, we could repeatedly observe the thinning of NCs to single-atom-contact. It was demonstrated that such contacts are sufficiently stable to analyse their I–V characteristics. However, we have confirmed that, in comparison with Au contacts, the stability of Ag contacts is lower. In particular, the formation probability of long ASWs in Ag is considerably lower. The smaller conductance of single-atom-width Ag contacts, observed in the present study, also shows the difference between Ag and Au single-atom-width contacts. Here, the result does not necessarily imply that the metal-insulator transition occurs in single-atom-width Ag contacts. This is because the current increases with the bias voltage even though the slope is lower than $0.1G_0$. At $0.1G_0$, the current corresponds to 100 nA at 13 mV, which is much larger than a tunnel current.

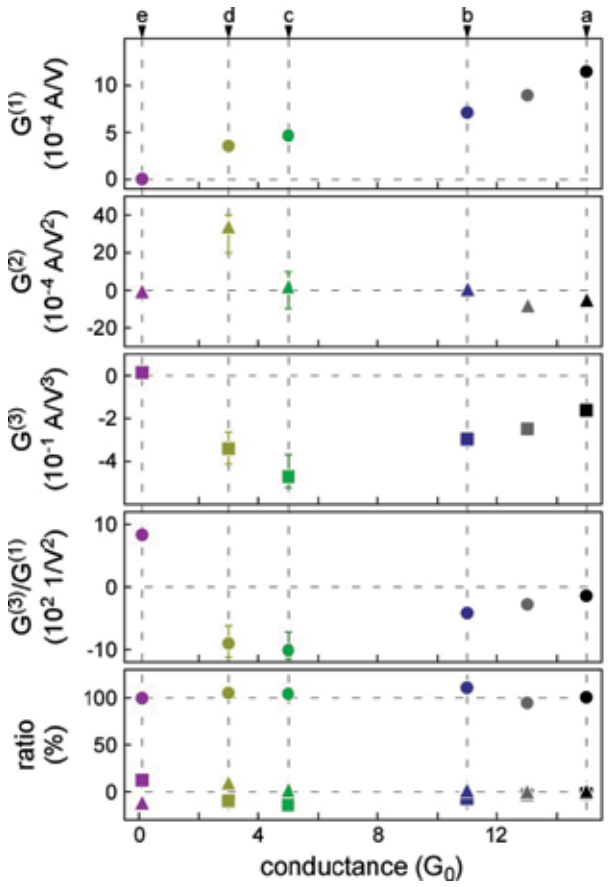

Figure 25. Fitting parameters of I-V curves.

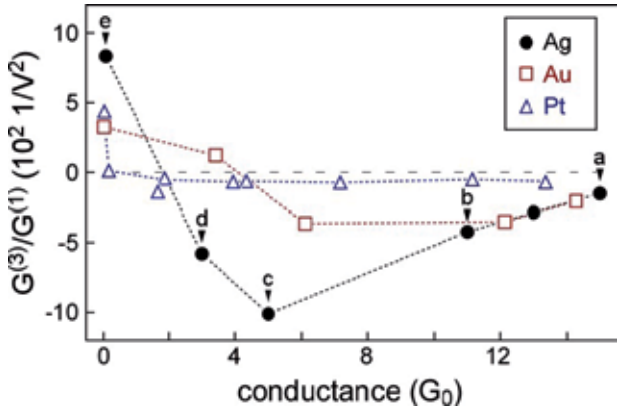

Figure 26. Non-linear parameter of metallic contacts.

http://dx.doi.org/10.5772/60750

4.2. Metal-specific differences

As shown in Fig. 26, $G^{(3)}/G^{(1)}$ in Ag and Au show similar variations; their $G^{(3)}/G^{(1)}$ values are negative and the absolute values increase with decreasing the width. The $G^{(3)}/G^{(1)}$ values of these ASWs have positive values. The $G^{(3)}/G^{(1)}$ values of Pt NCs are also negative: however, they are almost constant except for those of the ASW. This reflects that Ag and Au have s-like electronic structures, whereas Pt has a d-like electronic structure. Thus, the variation in the non-linear parameter $G^{(3)}/G^{(1)}$ depends on the valence electronic structure. We investigated the relationship between the structure andthe I–V characteristics of Ag NCs. It was found that the non-linearity of conductance in Ag NCs increased with decreasing contact width. This tendency changed when the contact transformed to ASWs; the non-linear component became positive. The variation in the non-linear parameter of Ag NCs against conductance was similar to that of Au NCs, whereas it differed from that of Pt NCs. This feature corresponds to a feature in the electronic configuration of these elements.

5. Conclusions

In this study, we focused on Ag NCs and investigated the atomic arrangement, electrical conductivity and mechanical properties. In addition to the simple tensile deformation, particularly to observe the Ag NCs representing the certain conductance value of the quantized conductance, feedback circuit was introduced into in situ electron microscopy. At the same time, the measured stress and force acting on the NCs were estimated. The observed image and the stress-strain relationship gave us the elastic constant such as Young's modulus. It was found that to reduce the contact width below 1 nm, Young's modulus should be increased. From the value of the critical shear stress of Ag NCs, it is suggested that deformation mechanism changes to isotropic slip from a dislocation slip when the contact width decreases below 1.5 nm.

From the observation using a conductance feedback circuit, several types of NCs structures with different widths were found to contribute to a peak, which correspond to the quantization level in the conductance histograms. In particular, when conductance is controlled to 1 G_0, the contact was 1-, 2-, and 3-atom width. From this fact, when the conductance indicates 1 G_0, it is considered that Ag single atom contacts of zero length are more stable than the ASW structure.

As a result of I-V measurement of Ag NCs, non-linearity of the conductance increase when the width of the contacts reduces. When NCs deformed ASWs, this trend changes; non-linear components became positive. Changes of the conductance in non-linear parameters of Ag NCs are similar to that of Au and different from that of Pt. This corresponds to the characteristics of the valence electron configuration of the elements.

As described above, in this study, I examined the structure and properties of Ag NCs using *in situ* HRTEM method. The results of this study give us basic structure and properties that are the engineering basis in expanding the atomistic and molecular electronics in the future.

Acknowledgements

This work was partly supported by Japan Society for the Promotion of Science Fellows (No. 221479).

Author details

Hideki Masuda*

Address all correspondence to: MASUDA.Hideki@nims.go.jp

Advanced Key Technologies Division, National Institute for Materials Science, Tsukuba, Japan

References

[1] Cuevas, JC, and Scheer, E: *Molecular electronics: an introduction to theory and experiment* (World Scientific, Singapore, 2010).

[2] Joachim, C, Gimzewski, JK, and Aviram, A: Electronics using hybrid-molecular and mono-molecular devices. 2000; 408: 541.Nature.

[3] Di Ventra, M, Pantelides, ST, and Lang, ND: First-principles calculation of transport properties of a molecular device. 2000; 84: 979.Physical Review Letters.

[4] Kubatkin, S *et al.*: Single-electron transistor of a single organic molecule with access to several redox states. 2003; 425: 698.Nature.

[5] Tao, NJ: Electron transport in molecular junctions. 2006; 1: 173.Nature Nanotechnology.

[6] Danilov, A *et al.*: Electronic transport in single molecule junctions: control of the molecule-electrode coupling through intramolecular tunneling barriers. 2007; 8: 1.Nano Letters. 10.1021/nl071228o.

[7] Kim, WY *et al.*: Application of quantum chemistry to nanotechnology: electron and spin transport in molecular devices. 2009; 38: 2319.Chemical Society Reviews.

[8] Masuda, H, and Kizuka, T: Distance control of electromigration-induced silver nanogaps. 2014; 14: 2436.Journal of Nanoscience and Nanotechnology. doi:10.1166/jnn.2014.8502.

[9] van Wees, BJ *et al.*: Quantized conductance of point contacts in a two-dimensional electron gas. 1988; 60: 848.Physical Review Letters.

[10] Agraït, N, Yeyati, AL, and van Ruitenbeek, JM: Quantum properties of atomic-sized conductors. 2003; 377: 81. Physics Reports.

[11] Olesen, L *et al.*: Quantized conductance in an atom-sized point contact. 1994; 72: 2251.Physical Review Letters.

[12] Muller, CJ, van Ruitenbeek, JM, and de Jongh, LJ: Conductance and supercurrent discontinuities in atomic-scale metallic constrictions of variable width. 1992; 69: 140.Physical Review Letters.

[13] Ludoph, B *et al.*: Multiple Andreev reflection in single-atom niobium junctions. 2000; 61: 8561.Physical Review B.

[14] Oshima, H, and Miyano, K: Spin-dependent conductance quantization in nickel point contacts. 1998; 73: 2203. Appl. Phys. Lett..

[15] Scheer, E *et al.*: The signature of chemical valence in the electrical conduction through a single-atom contact. 1998; 394: 154.Nature.

[16] Costa-Krämer, JL *et al.*: Nanowire formation in macroscopic metallic contacts: quantum mechanical conductance tapping a table top. 1995; 342: L1144. Surface Science.

[17] Costa-Krämer, JL: Conductance quantization at room temperature in magnetic and nonmagnetic metallic nanowires. 1997; 55: R4875. Physical Review B.

[18] Krans, JM *et al.*: The signature of conductance quantization in metallic point contacts. 1995; 375: 767.Nature.

[19] Fujii, A *et al.*: Break conductance of noble metal contacts. 2005; 72: 045407. Physical Review B.

[20] Rodrigues, V, Fuhrer, T, and Ugarte, D: Signature of atomic structure in the quantum conductance of gold nanowires. 2000; 85: 4124.Physical Review Letters.

[21] Ludoph, B, and van Ruitenbeek, JM: Conductance fluctuations as a tool for investigating the quantum modes in atomic-size metallic contacts. 2000; 61: 2273.Physical Review B.

[22] Untiedt, C *et al.*: Formation of a metallic contact: jump to contact revisited. 2007; 98: 206801.Physical Review Letters.

[23] Thijssen, WHA *et al.*: Oxygen-enhanced atomic chain formation. 2006; 96: 026806.Physical Review Letters.

[24] Mares, AI, and van Ruitenbeek, JM: Observation of shell effects in nanowires for the noble metals Cu, Ag, and Au. 2005; 72: 205402.Physical Review B.

[25] Liang, J *et al.*: Correlating conductance and structure of silver nano-contacts created by jump-to-contact STM break junction. 2013; 688: 257. Journal of Electroanalytical Chemistry.

[26] Rodrigues, V *et al.*: Quantum conductance in silver nanowires: Correlation between atomic structure and transport properties. 2002; 65: 153402.Physical Review B.

[27] Li, CZ, and Tao, NJ: Quantum transport in metallic nanowires fabricated by electrochemical deposition/dissolution. 1998; 72: 894.Applied Physics Letters.

[28] Krans, JM *et al.*: One-atom point contacts. 1993; 48: 14721.Physical Review B.

[29] Li, CZ *et al.*: Fabrication of stable metallic nanowires with quantized conductance. 1999; 10: 221.Nanotechnology.

[30] Bakker, DJ *et al.*: Effect of disorder on the conductance of a Cu atomic point contact. 2002; 65: 235416. Physical Review B.

[31] Li, J *et al.*: Metal-dependent conductance quantization of nanocontacts in solution. 2002; 81: 123.Applied Physics Letters.

[32] Fujisawa, S, Kikkawa, T, and Kizuka, T: Direct observation of electromigration and induced stress in Cu nanowire. 2003; 42: L1433. Japanese Journal of Applied Physics.

[33] Fujii, A *et al.*: High-bias conductance of atom-sized Cu contacts. 2004; 464-465: 251. Thin Solid Films.http://dx.doi.org/10.1016/j.tsf.2004.06.033.

[34] González, JC *et al.*: Indication of unusual pentagonal structures in atomic-size Cu nanowires. 2004; 93: 126103. Physical Review Letters.

[35] Kizuka, T, and Aoki, H: The dynamics of electromigration in copper nanocontacts. 2009; 2: 075003.Applied Physics Express.

[36] Yanson, AI, Yanson, IK, and van Ruitenbeek, JM: Observation of shell structure in sodium nanowires. 1999; 400: 144.Nature.

[37] Sim, HS, Lee, HW, and Chang, KJ: Even-odd behavior of conductance in monatomic sodium wires. 2001; 87: 096803.Physical Review Letters.

[38] Muller, CJ, van Ruitenbeek, JM, and de Jongh, LJ: Experimental observation of the transition from weak link to tunnel junction. 1992; 191: 485.Physica C: Superconductivity. http://dx.doi.org/10.1016/0921-4534(92)90947-B.

[39] Sirvent, C *et al.*: STM study of the atomic contact between metallic electrodes. 1996; 218: 238.Physica B: Condensed Matter.

[40] García, N, Muñoz, M, and Zhao, YW: Magnetoresistance in excess of 200% in ballistic Ni nanocontacts at room temperature and 100 Oe. 1999; 82: 2923.Physical Review Letters.

[41] Ono, T *et al.*: $2e^2/h$ to e^2/h switching of quantum conductance associated with a change in nanoscale ferromagnetic domain structure. 1999; 75: 1622.Applied Physics Letters.

[42] Sirvent, C *et al.*: Conductance step for a single-atom contact in the scanning tunneling microscope: Noble and transition metals. 1996; 53: 16086.Physical Review B.

[43] Yuki, K, Shu, K, and Akira, S: Quantized conductance in Pt nanocontacts. 2000; 39: 4593.Japanese Journal of Applied Physics.

[44] Yuki, K, Kurokawa, S, and Sakai, A: Conductance in breaking nanocontacts of some transition metals. 2001; 40: 803.Japanese Journal of Applied Physics.

[45] Smit, RHM *et al.*: 2002; 419: 906. Nature.

[46] Smit, RHM *et al.*: Observation of a parity oscillation in the conductance of atomic wires. 2003; 91: 076805.Physical Review Letters.

[47] Rodrigues, V *et al.*: Evidence for spontaneous spin-polarized transport in magnetic nanowires. 2003; 91: 096801.Physical Review Letters.

[48] Nielsen, SK *et al.*: Conductance of single-atom platinum contacts: Voltage dependence of the conductance histogram. 2003; 67: 245411. Physical Review B.

[49] Csonka, S *et al.*: Conductance of Pd-H Nanojunctions. 2004; 93: 016802. Physical Review Letters.

[50] Djukic, D *et al.*: Stretching dependence of the vibration modes of a single-molecule Pt-H[sub 2]-Pt bridge. 2005; 71: 161402.Physical Review B.

[51] Kizuka, T, and Monna, K: Atomic configuration, conductance, and tensile force of platinum wires of single-atom width. 2009; 80: 205406.Physical Review B.

[52] Yanson, AI, and van Ruitenbeek, JM: Do histograms constitute a proof for conductance quantization? 1997; 79: 2157.Physical Review Letters.

[53] Mizobata, J-i *et al.*: High-bias conductance of atom-sized Al contacts. 2003; 68: 155428.Physical Review B.

[54] Smit, RHM *et al.*: Common origin for surface reconstruction and the formation of chains of metal atoms. 2001; 87: 266102.Physical Review Letters.

[55] Minowa, T *et al.*: Conductance of Pd single-atom contacts. 2005; 241: 14.Applied Surface Science.http://dx.doi.org/10.1016/j.apsusc.2004.09.010.

[56] Suzuki, R *et al.*: Conductance of atom-Sized Zn contacts. 2006; 45: 7217.Japanese Journal of Applied Physics.

[57] Tsutsui, M, Kurokawa, S, and Sakai, A: Bias-induced local heating in atom-sized metal contacts at 77 K. 2007; 90: 133121. Applied Physics Letters.

[58] Post, N, and Ruitenbeek, JM: High stability STM made of a break junction. 1996; 46: 2853.Czechoslovak Journal of Physics.10.1007/bf02570413.

[59] Landauer, R: 1988; 32: 306. IBM Journal of Research and Development.

[60] Sharvin, YV: 1965; 48: 984. Zhurnal Eksperimental'noi i Teoreticheskoi Fiziki.

[61] Kizuka, T: Atomic configuration and mechanical and electrical properties of stable gold wires of single-atom width. 2008; 77: 155401.Physical Review B.

[62] Gimzewski, JK, and Möller, R: Transition from the tunneling regime to point contact studied using scanning tunneling microscopy. 1987; 36: 1284.Physical Review B.

[63] Agraït, N, Rubio, G, and Vieira, S: Plastic deformation of nanometer-scale gold connective necks. 1995; 74: 3995.Physical Review Letters.

[64] Rubio, G, Agraït, N, and Vieira, S: Atomic-sized metallic contacts: mechanical properties and electronic transport. 1996; 76: 2302.Physical Review Letters.

[65] Kizuka, T *et al.*: Simultaneous observation of millisecond dynamics in atomistic structure, force and conductance on the basis of transmission electron microscopy 2001; 40: L170. Japanese Journal of Applied Physics.

[66] Ryu, M, and Kizuka, T: Structure, conductance and strength of iridium wires of single atom Width 2006; 45: 8952. Japanese Journal of Applied Physics.

[67] Matsuda, T, and Kizuka, T: Structure of nanometer-sized palladium contacts and their mechanical and electrical properties 2007; 46: 4370. Japanese Journal of Applied Physics.

[68] Valkering, AMC *et al.*: A force sensor for atomic point contacts. 2005; 76: 103903. Review of Scientific Instruments.

[69] Sørensen, MR, Brandbyge, M, and Jacobsen, KW: Mechanical deformation of atomic-scale metallic contacts: Structure and mechanisms. 1998; 57: 3283.Physical Review B.

[70] Kondo, Y, and Takayanagi, K: Gold nanobridge stabilized by surface structure. 1997; 79: 3455.Physical Review Letters.

[71] Kizuka, T, and Tanaka, N: Dynamic high-resolution electron microscopy of diffusion bonding between zinc oxide nanocrystallites at ambient temperature 1994; 69: 135. Philosophical Magazine Letters.

[72] Kizuka, T: Atomistic visualization of deformation in gold. 1998; 57: 11158.Physical Review B.

[73] Ohnishi, H, Kondo, Y, and Takayanagi, K: Quantized conductance through individual rows of suspended gold atoms 1998; 395: 780. Nature.

[74] Kizuka, T, Umehara, S, and Fujisawa, S: Metal-insulator transition in stable one-dimensional arrangements of single gold atoms 2001; 40: L71. Japanese Journal of Applied Physics.

[75] Lagos, MJ *et al.*: Observation of the smallest metal nanotube with a square cross-section. 2009; 4: 149.Nature Nanotechnology.

http://dx.doi.org/10.5772/60750

[76] Matsuda, T, and Kizuka, T: Palladium wires of single atom width as mechanically controlled switching devices 2006; 45: L1337. Japanese Journal of Applied Physics.

[77] Masuda, H, and Kizuka, T: Structure, electrical, and mechanical properties of silver nanocontacts. 2010; 49: 045202. Japanese Journal of Applied Physics.

[78] Kelley, A, *Strong Solid* (Clarendon Press, Oxford, 1966).

[79] Bratkovsky, AM, Sutton, AP, and Todorov, TN: Conditions for conductance quantization in realistic models of atomic-scale metallic contacts. 1995; 52: 5036.Physical Review B.

[80] Scherbakov, AG, Bogachek, EN, and Landman, U: Quantum electronic transport through three-dimensional microconstrictions with variable shapes. 1996; 53: 4054.Physical Review B.

[81] Todorov, TN, and Sutton, AP: Jumps in electronic conductance due to mechanical instabilities. 1993; 70: 2138.Physical Review Letters.

[82] Pauly, F *et al.*: Theoretical analysis of the conductance histograms and structural properties of Ag, Pt, and Ni nanocontacts. 2006; 74: 235106. Physical Review B.

[83] Masuda, H, and Kizuka, T: Current-voltage characteristics of silver nanocontacts studied by *in situ* transmission electron microscopy. 2012; 81: 114707. Journal of Physical Society of Japan. 10.1143/JPSJ.81.114707.

[84] Nielsen, SK *et al.*: Current-voltage curves of atomic-sized transition metal contacts: an explanation of why Au is ohmic and Pt is not. 2002; 89: 066804.Physical Review Letters.

Chapter 2

In Situ Transmission Electron Microscopy for Electronics

Masashi Arita, Kouichi Hamada, Yasuo Takahashi,
Kazuhisa Sueoka and Tamaki Shibayama

Additional information is available at the end of the chapter

http://dx.doi.org/10.5772/60651

Abstract

Electronic devices are strongly influenced by their microstructures. *In situ* transmission electron microscopy (*in situ* TEM) with capability to measure electrical properties is an effective method to dynamically correlate electric properties with microstructures. We have developed tools and *in situ* TEM experimental procedures for measuring electronic devices, including TEM sample holders and sample preparation methods. The method was used to study metallic nanowire by electromigration, magnetoresistance of a ferromagnetic device, conductance quantization of a metallic nanowire, single electron tunnelling, and operation details of resistive random access memories (ReRAM).

Keywords: *In situ* TEM, TEM sample holder, electromigration, magnetoresistance, tunnel conduction, resistive RAM

1. Introduction

Transmission electron microscopy (TEM) has been efficiently used in a variety of research fields. It is possible to observe individual atoms by using up-to-date microscopes. In addition to conventional (static) TEM observation and microanalyses, dynamical observations and recording is possible under controlled conditions. While *in situ* TEM has already been utilized in early years [1, 2, 3], this method has attracted much attention in recent years because the atomic or nanoscale observations can be performed with simultaneous physical/chemical measurements. This type of investigation can be done without changing the TEM construction by using specially designed TEM holders such as TEM holder with a piezo actuator (even

INTECH
open science | open minds

© 2015 The Author(s). Licensee InTech. This chapter is distributed under the terms of the Creative Commons Attribution License (http://creativecommons.org/licenses/by/3.0), which permits unrestricted use, distribution, and reproduction in any medium, provided the original work is properly cited.

without the feedback system, it will be called the TEM/STM (scanning tunneling microscopy) holder in this report) [4, 5, 6, 7, 8].

In the research field of electronics, next-generation electronic devices are now under development from the perspective of power consumption, high integration as well as high functionality. The electronic properties of these devices have strong relationship with their crystallographic and/or magnetic microstructures which occasionally change during the device operation. Therefore, the importance of the *in situ* TEM is increasing to understand the operation mechanism in detail. Since the year of 2000, we have developed various types of TEM holders for *in situ* TEM of electronic devices. In this article, we will explain developed *in situ* TEM holders and present effectiveness of this method to magnetic RAM (MRAM) [9, 10], single-electron devices (SED) [11, 12], resistive RAM (ReRAM) [13, 14, 15], as well as electromigration [16, 17, 18, 19].

2. *In Situ* TEM system for electric measurements

There is a schematic of the *in situ* TEM system in Fig. 1(a), which is composed of a custom-made TEM holder, a holder control system if needed, an electric measurement system, and a charge-coupled device (CCD) camera system (30 ms/frame). All the image data including those from the personal computer (PC) display are superposed on one another when needed. The TEM instruments were JEM 2010 (200 kV, C_s = 0.5 mm) and JEM 200CX (200 kV) microscopes, whose vacuum was 10^{-4}–10^{-5} Pa. Figures 1(b) and 1(c) have control diagrams of the electromagnet holder and TEM/STM holder developed in this work. These systems have plural voltage/current sources controlled by a PC. Various types of electric measurements were carried out depending on the purpose. Conventional instruments such as an electric source, a digital multimeter, a source-measure-unit (SMU), and a digital oscilloscope were used. The system in Fig. 1(d) is for conventional 4-terminal measurements, that in Fig. 1(e) is for TEM/STM experiments with high-speed measurements, and that in Fig. 1(f) is for multipurpose usage using TEM/STM.

3. TEM holders developed for *in situ* electronic experiments

Three types of TEM holders were developed in this work. They were holders for current measurements of patterned media, a holder with electromagnets used for Lorentz TEM (LTEM), and TEM/STM holders. Their details are described in the following subsections.

3.1. Holders having four or multiple terminals to investigate patterned devices

There is a photograph of two custom-made single-tilt TEM holders with four electric terminals in Fig. 2(a). The samples are placed at position 1. Figures 2(b) and 2(c) are enlarged photographs. Samples of less than about 5 × 5 mm can be investigated. The sample electrodes were connected to two current terminals (I) and two voltage terminals (V). These terminals are

http://dx.doi.org/10.5772/60651

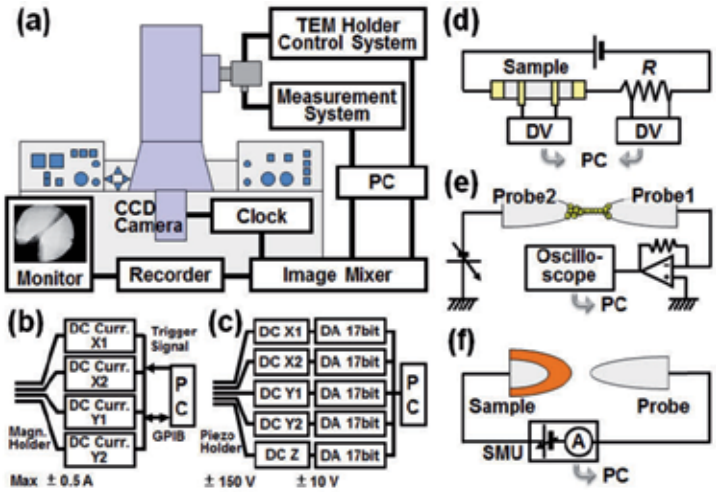

Figure 1. (a) Schematic of system. Diagrams of (b) electromagnet and (c) TEM/STM holders. Measurement systems for (d) four terminal method, (e) high-speed measurements, and (f) TEM/STM.

connected to four co-axial connectors (denoted as 2 in Fig. 2(a)). The shield lines of the cables are floated from the TEM holders, which are connected to the ground level (JEM200CX) or a certain voltage level (~2 V for JEM2010). Therefore, they can be used as the guard lines for low current measurements. These holders were mainly used for LTEM observations in this work. There are photographs of a double-tilt holder with 16 terminals in Figs. 2(d) and 2(e) [19]. The sample (turned upside down) was placed at the centre of the holder to face the terminals (Fig. 2(d)). When the cover is closed, the sample electrodes connect automatically with the terminals for electrical measurements (Fig. 2(e)). Multiple devices can be measured during one experiment by using this holder, which was used mainly to investigate electromigration.

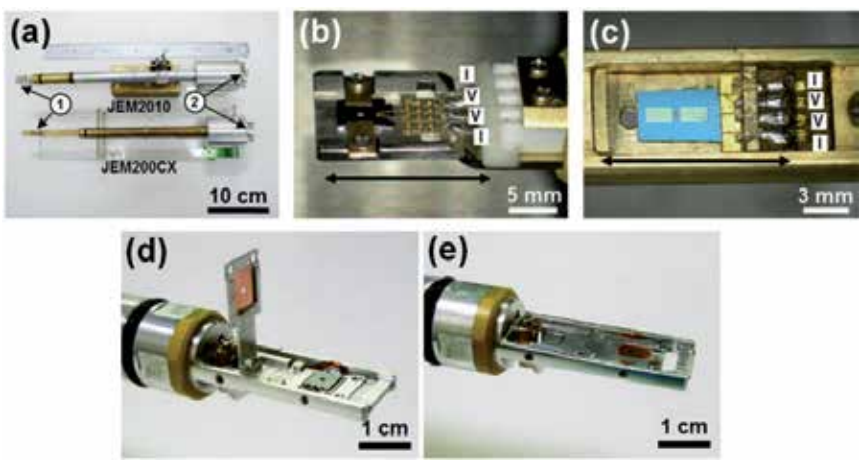

Figure 2. (a) TEM holders for four-terminal electrical measurements. Enlarged image of TEM holder head for (b) JEM2010 and (c) JEM200CX. (d) and (e) Double-tilt TEM holder having 16 electrodes.

3.2. Holder generating in-plane magnetic field

Magnetic devices are important in electronics. *In situ* observations of magnetic microstructures by LTEM should provide key information. The in-plane field of film devices can be varied by tilting the sample [20, 21, 22, 23] in the remanence field of the TEM objective lens (LowMag-mode). While this is quite simple, the field is single-axial, and the speed is slow. The installation of electromagnets effectively overcomes these problems, and speedy field control can be achieved. The TEM holder has coils on board in some cases [24, 25], which is an advantage for conventional TEM users. However, when coils generate a magnetizing field, the TEM electron beam is deflected, and the image is fatally shifted. Therefore, beam-deflection-back coils [2, 24, 25, 26, 27] should be installed. A TEM specimen holder with an electromagnet system needs to be developed, which generates a double-axial magnetic field and compensates beam deflection. This section presents a TEM holder with two miniaturized four-pole electromagnets [28]. *In situ* electrical measurements were made possible by using this holder with four terminals.

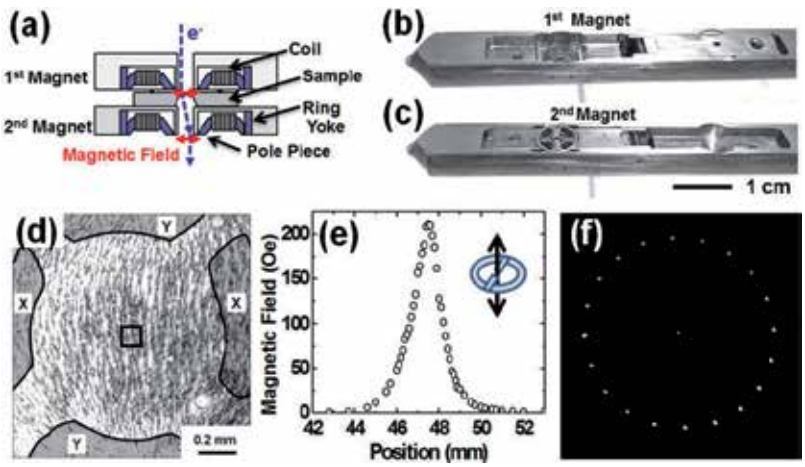

Figure 3. Electromagnet holder. (a) Cross-section of magnet system. Holder head (b) before and (c) after sample was placed. (d) Distribution of magnetic field. X and Y are pole pieces of electromagnet. Square at the centre is a region for observation. (e) Magnetic field in pole gap along arrow in schematic of magnet (inset). (f) Example of deflection of electron beam by electromagnet.

Figure 3(a) is a schematic cross section of the double-layer magnet system where a sample is sandwiched between two four-pole electromagnets. Each electromagnet is assembled from two perpendicularly oriented two-pole electromagnets with ring-shaped yokes (ϕ7 mm and gap of 1 mm). Two serially connected coils with ~30 turns are wound onto each two-pole magnet (maximum current: 500 mA). In-plane magnetic field can be applied to the sample along any direction. The first magnet was used to generate the magnetic field applied to the sample. Electron beam used for TEM observations were deflected by this field. The second magnet below the sample is used to compensate for this deflection. This prevented the TEM image from experiencing fatal deformation or movement. In addition, four electric terminals

http://dx.doi.org/10.5772/60651

were arranged in the chinks of the first magnet. Figures 3(b) and 3(c) are photographs of the TEM holder. This is a side entry holder designed for JEM-200CX. The sample is placed by facing it against the magnet. When it was fixed by closing the cover, the contact pads of the sample automatically made contact with the electrodes.

The maximum magnetic field between the pole pieces was measured to be 214 Oe at 500 mA by using a Hall probe. A software package was developed to compensate the hysteretic features of the magnet, and the generated field could be controlled with an accuracy of 1 Oe or better. The homogeneity of the field was checked by using Fe powder suspended in oil, as seen in Fig. 3(d), where only magnet Y was excited. The field within the LTEM observation window was homogeneous (square at the centre: 100 x 100 μm). The distribution of the magnetic field is shown in Fig. 3(e). The current through the coils was 500 mA. The magnetic field was ~7 Oe at 2.5 mm from the pole piece. Thus, there is almost no influence from the second magnet on the specimen: They were 2.5 mm apart from each other. One of the four-pole electromagnets was activated to generate a rotating field (38 Oe). The beam deflection with various magnetic fields was recorded in multi-exposed images (Fig. 3(e)). The beam spot was circularly moved. Excellent controllability of the field was achieved.

The LTEM image moved fatally due to beam deflection caused by the first electromagnet. There is an example in Fig. 4(a) where images with H_x = +9 Oe (along the right) and –9 Oe (along the left) are superposed on a wide-range image under 0 Oe. The image moved by about ±33 μm. The second electromagnet was simultaneously activated to compensate this image movement. The resulting images are compared in Fig. 4(b) where image movement decreased significantly.

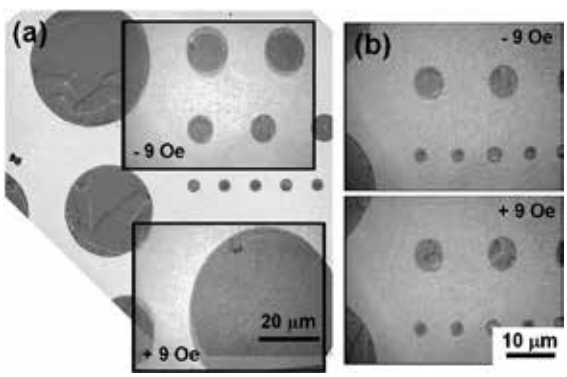

Figure 4. (a) Shift in CCD image (±9 Oe along right). Two CCD images are superposed on wide-range image. (b) CCD images taken with beam-deflection-back-system. Image movement was compensated for. LTEM images were taken using the Fresnel method in LowMag-mode.

3.3. TEM/STM holder

There is a schematic of a specimen holder fitted to a JEM 200CX microscope in Fig. 5(a) and photographs of this in Fig. 5(b) [8]. The probe was coarsely moved with three mechanical

micrometres (stroke: 0.2 × 0.2 × 10 mm). A piezo tube was placed at the left end of the column pole, with which the position of the probe was controlled at a rate of 400 nm/V (perpendicular to the column pole) and 30 nm/V (along the column pole). The maximum voltage was 100 or 150 V. Two probes could be attached to the piezo actuator. One of two electrodes placed at the piezo actuator could be selected without breaking the vacuum by rotating the column pole using a stepping motor. Figure 5(c) is a photograph of a holder designed for the JEM 2010 microscope [29]. Three electrodes could be placed in this TEM holder (two probes and one sample). The sample was directly connected to the voltage source using a coaxial cable, where the probes were connected to an in-column amplifier for nA measurements or an ammeter. While the basic design of the holders developed here may be the same as that of commercially available holders, additional functions such as multiple probing can be added through custom designing. It is quite important to design the piezo actuators and mechanism for coarse movement to enable the holder to be easily handled.

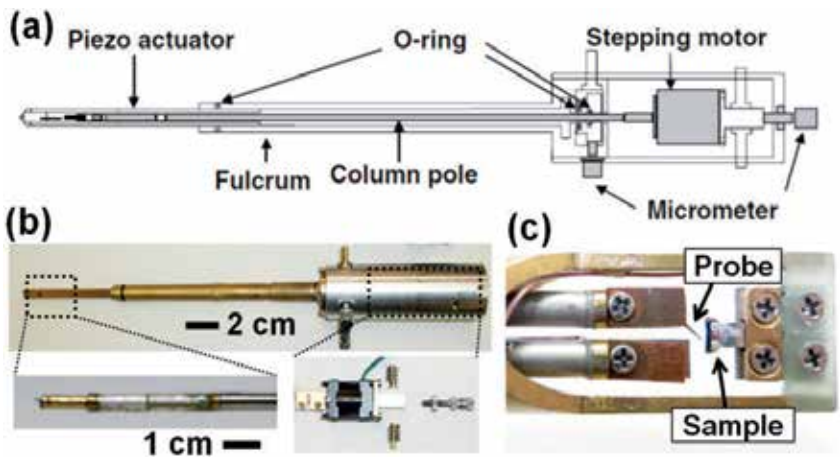

Figure 5. (a) Schematic and (b) photograph of TEM/STM holder for JEM200CX. Electrode and sample were placed inside. (c) Holder for JEM2010. Needle probe was moved to contact to fixed sample.

4. Sample preparation method

Our main purpose here is to develop *in situ* TEM that can be applied to electronic devices whose electrical properties have correlations with geometric and/or magnetic microstructures. Special sample preparation techniques were required to achieve this. One of them is the use of an Si_3N_4 membrane on which electronic devices are patterned. A method of fabricating TEM observation windows without inducing any electric leakage will be briefly described. Another method was used in the TEM/STM observations. The focused ion beam (FIB) method is widely utilized to observe electronic films and devices. However, it was time consuming and not cost effective because the samples are frequently destroyed during *in situ* experiments, for example,

ReRAM samples. This section describes also a method of preparing needle-shaped or wedge-shaped metallic (or Si) substrates for thin film deposition.

4.1. Patterned devices on SiN/Si substrate with observation window

Since the invention by Jacobs and Vehoeven [30], many electron microscopists focused their attention on the use of free-standing Si_3N_4 membranes as substrates [31]. These membranes are extremely flat and insulating and are now commercially available. However, it is important to prepare substrates and patterned devices on demand because we can design a variety of patterns by ourselves to carry *in situ* TEM observations on patterned electronic devices. The starting material was a Si_3N_4/Si wafer. The Si_3N_4 layer (25 or 35 nm thick) was formed on a 525-μm thick Si (001) wafer by chemical vapour deposition (CVD). The wafer was cut into pieces of 20 × 20 mm, and the sample preparation was done by combining the four processes (A-D) in the following text. There are some examples of the TEM samples in Fig. 6. While the samples in Figs. 6(a) and 6(b) [32] are for electric measurements, the one in Fig. 6(c) is only for TEM observation without electrodes.

(A) **Patterning of Si_3N_4 on backside of Si wafer**: This process involves the fabrication of the mask to chemically etch the Si wafer to form observation windows. We used photolithography followed by reactive ion etching (RIE, CF_4: O_2 = 4: 1) when high levels of accuracy were required. This process could be replaced by scratching with a diamond pencil if only rough positioning was required.

(B) **Patterning of devices**: Electrodes of $Au_{(30\ nm)}/Ti_{(10\ nm)}$ were formed on the front surface by using double layer photolithography of OFPR800/PMGI followed by lift-off. After this, the sample patterns such as Au or permalloy ($Ni_{81}Fe_{19}$, abbreviated as Py) were prepared by using the electron-beam lithography of ZEP/PMGI and lift-off or photolithography. Deposition by using a metal mask was used when rough positioning was required.

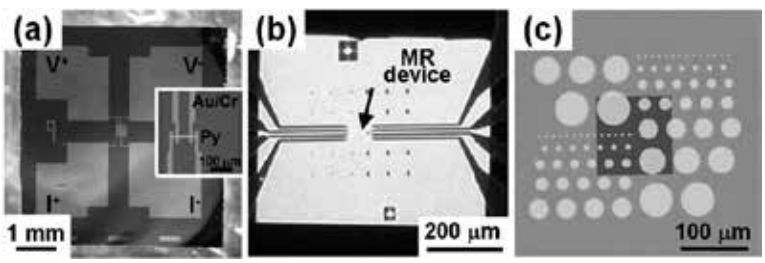

Figure 6. Py patterns prepared on Si_3N_4/Si substrates, (a) pattern for AMR measurements, (b) MR cantilever, and (c) disks to observe magnetic vortices. Square at centre in (a) or (c) is an observation window. Pads marked with V are voltage terminals, and those marked with I are current terminals.

(C) **Chemical etching to form windows**: To obtain a free-standing Si_3N_4 membrane, potassium hydroxide (KOH) etching at 80°C was done from the backside of the Si wafer. When patterning was carried out after this etching process, the substrate was simply dipped in the KOH aqueous solution. When the patterning was done before etching, a specially designed etching holder

made of Teflon was used to protect the pattern from the chemical. The window size was typically between 100 × 100 and 500 × 500 μm.

(D) **Cutting of the sample into small pieces**: TEM holders (Figs. 2 and 3) were developed for the sample size of 5 × 5 mm. Substrates with or without devices were cut into this size by cleaving the Si wafer.

4.2. Needle-shaped and wedge-shaped probes and substrates

The probes used in the TEM/STM experiments were prepared with methods based on ion milling. This is because very sharp probe apexes were required to select local areas to be measured. In addition, when the probe was used as the substrate for sample film deposition, its apex should be thin enough for high resolution TEM (HRTEM).

The ion-shadow method [33] was used for probe fabrication, which is a sputtering technique using powders (mask material) with low sputtering rate. After the probe material was mechanically sharpened into a cone, the mask particle (e.g., diamond or carbon: ϕ10 μm) was put on the top, and the Ar^+ ion sputtering was performed. During sputtering, the unmasked part of the tip material is etched, and the particle size was reduced. Finally, a fine cone was obtained when the powder was completely sputtered out within ~1 hour (Fig. 7(a)). While the underlying principles of this process are the same as that of ion-beam lithography, the use of the powder masks is essential in the ion-shadow method. There are examples in Figs. 7(b) and 7(c). The radius of curvature of the apex was usually ~20 nm or less.

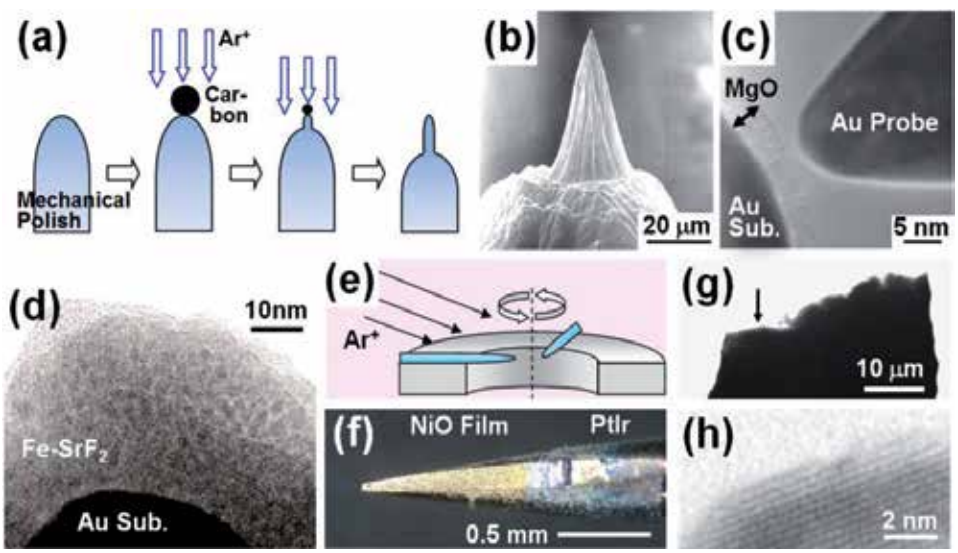

Figure 7. (a) Ion-shadow process forming cone-shaped probe. (b) Scanning electron microscopy (SEM) image of Au probe. (c) TEM image of Au probe approaching the MgO layer on Au substrate. (d) Fe-SrF_2 film on needle-shaped Au substrate. (e) Schematic of thinning process of substrate. (f) Optical micrograph of wedge-shaped PtIr substrate covered by NiO film. (g) TEM image of wedge-shaped PtIr substrate. Arrowed region is magnified in (g).

http://dx.doi.org/10.5772/60651

The probe can be used as the substrate for film deposition [8]. After the tip-shaped apex had been fabricated, the probe was washed with acetone and ethanol in an ultrasonic bath. It was annealed at 420 K for 30 min, and film deposition was done. One example can be seen in Fig. 7(c), where thin MgO was deposited on the "Au Sub." There is another example in Fig. 7(d), where a composite film of Fe–SrF_2 (~37 vol% Fe, 40 nm thick) was deposited at RT. The round grey contrast denotes Fe particles with sizes of ~2.7 nm.

Another method of fabricating very sharp probe is shown in Fig. 7(e). Commercially available STM tips or mechanically ground probes were sharpened using ion milling from backside with rotation. An apex of 10 nm or less was obtained. When the probe is used as a substrate, it is better to be wide to enable multiple investigations. For this purpose, the probe material was mechanically ground into a wedge and ion milled [34]. There is a micrograph of NiO on PtIr in Fig. 7(f), while TEM images are shown in Figs. 7(g) and 7(h). The substrate was about 50 μm wide and thin enough to observe lattice fringes.

4.3. Easy method to prepare miniaturized multilayer devices for *in situ* TEM

In situ investigation on multilayer devices is important for electronic devices, and FIB is one of the methods of fabricating these TEM samples. However, it is time consuming and costly, while devices can occasionally be easily destroyed. For example, current jump at resistive switching of ReRAMs induces overshoot current, and the samples are quite likely to be destroyed. We focused on the ion-shadow method and applied it to the sample preparation of multilayer films formed on Si wafers. A film on a substrate was cut into small pieces (e.g., 100 μm × 2.5 mm). Carbon spheres (10–30 μm) were used as the mask material. A drop of slurry was dripped onto a glass plate and dried, and the particles were transferred to the substrate by lightly scrubbing the glass surface. Next, a milling process (Ar^+, 5 kV, 1 mA) was carried out for 1 hour by using a milling apparatus for TEM. The ion beam was almost perpendicular to the substrate surface. As a result, a sample with needle-shaped projections would be prepared as shown in Fig. 8(a) [35].

Figure 8(b) has scanning electron micrographs (SEMs) over a wide area. Many needles can be identified on the Si surface. There are magnified images from two different regions in Figs. 8(c) and 8(d). A sharp needle 5 μm in length can be seen at around the beam centre (Fig. 8(d)). No carbon particle residuals can be identified at this magnification, and we can expect a small fragment of the film on the needle. On the other hand, the needle lengths are short, and large carbon residuals are identified in Fig. 8(c), which was away from the centre by 500 μm. The carbon residuals and the sample film on the apex should be completely etched out around the beam centre by increasing the milling time. However, the carbon residuals should become small at the neighbouring regions, and needles with adequate apex size should appear. There must be regions with needles suitable for *in situ* TEM somewhere on the substrate, independently of the milling time. Several needles with ReRAM fragments were obtained in one TEM sample. There is a top-view SEM micrograph in Fig. 8(e), where the needle had a symmetric cone shape. An example of the TEM image is in Fig. 8(f), which is a multilayer film ($Pt_{(100\ nm)}/Cu_{(30\ nm)}/MoO_{x\ (50\ nm)}$ on a TiN/Si substrate). The sample was ϕ230 nm and usable for

in situ TEM. No fatal current leakage appeared when the bias voltage was applied between Pt and Si.

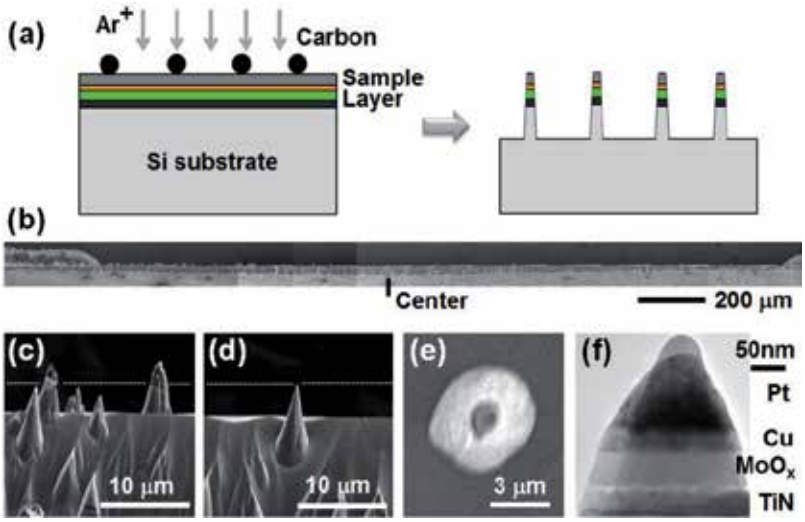

Figure 8. (a) Schematic of ion-shadow process. (b) SEM of needles formed at Si substrate. Magnified images (c) 500 μm left of beam centre and (d) at beam centre. Lines denote Si surface before milling. (e) Top view SEM of needles having regular shape. (f) TEM cross section of multilayer film.

5. Application of developed TEM holders

5.1. Electromigration

Electromigration (EM) is the term used for the electrically induced atom movement after momentum transfer from electrons. It causes failure in the wiring [36], and the researchers on LSI have tried to suppress it. However, EM has attracted a great deal of attention in creating metallic nanogaps used in SEDs as well as switching devices [37, 38]. Researchers in this field have developed methods of enhancing EM. It is important to achieve high levels of control for EM in both cases even though their purposes have differed. *In situ* TEM [17, 18, 39] can provide important information on this phenomenon. In this work, Au wire patterns were investigated with the current density of 10^9 A/cm^2 or more [19]. The operation system is in Figs. 1(a), 1(d) (using an SMU), and 2.

Atom transportation along the electron flow was identified in TEM images extracted from a video (Fig. 9). When a positive voltage was applied to the right of Fig. 9(a), narrowing occurred at the upstream side of the electron flow (left part of Fig. 9(b)). With polarity inversion, the left end of the wire gained area while the right end lost area (Fig. 6(c)). This morphological change during polarity inversion fits well with earlier reports [18]. Narrowing occurred at the upstream side, and widening on the downstream side, which was independent of the voltage

http://dx.doi.org/10.5772/60651

polarity. This suggested that Au atoms were transported along the same direction as that of the electron flow (i.e., opposite to current).

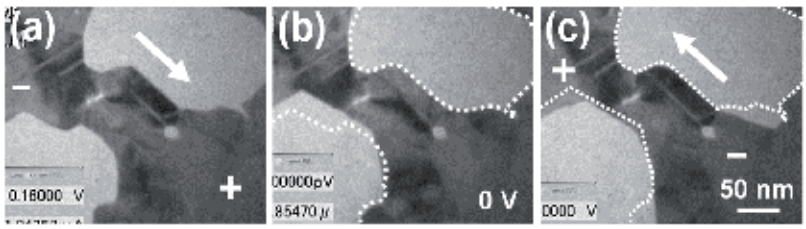

Figure 9. Sequential change in wire geometry during current reversion. Arrows are along electron flow. Broken lines in (b) and (c) correspond to edges in (a) and (b).

The metallic wire narrowed due to EM. The narrowing rate was not monotonous over time. The wire thinning occasionally started at a certain time, then stopped, and restarted. The wire thickened in some cases. There is an example in Fig. 10 where wire narrowing is evident near the surface step. The edge on the downstream side of the step (dotted line) retreated in Fig. 10(b) (5.25 seconds after Fig. 10(a)), while the edge on the upstream side (solid line) only retreated slightly. As a result, the step increased and cleared. The step started to collapse at the corner in Fig. 10(c). This collapse propagated to neighbouring regions in Fig. 10(d). The upstream side lost atoms in Figs. 10(e), and the downstream side gained atoms. Curve C on the upstream side has a sudden drop in wire width as can be seen in Fig. 10(g), while curve B on the downstream side has a gradual increase. Curve A apart from the step exhibits less change. The width at B reached maximum, and a new narrowing process. The wire narrowing accelerated when the step collapsed. Although only two examples have been presented in this report, contributions on wire narrowing and gap formation from various singularities such as grain boundaries and stacking faults can be investigated with the method used in this research.

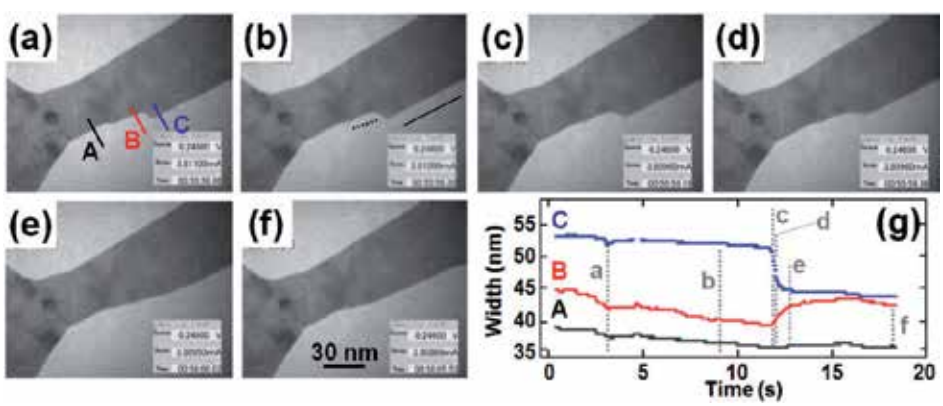

Figure 10. Collapse of surface step and wire narrowing. (a)-(f) Video images and (g) wire width at positions A to C. Electron flew from the right to the left (current: left to right).

5.2. Magnetic domains and magnetoresistance of ferromagnetic devices

Magnetic devices are one of the most important subjects in electronics. Their physical properties, such as magnetoresistance (MR) and magnetization reversal, are influenced by their magnetic microstructures. Therefore, the magnetic microstructures of tiny magnetic patterns have been investigated by using various techniques. *In situ* observations of magnetic microstructures when magnetic fields are applied should provide key information about these mechanisms. The LTEM explained in this section is one method that can clarify these operation mechanisms.

5.2.1. Experiments by using conventional current measurement holder

An $Ni_{79}Fe_{21}$ film (Py, 2 mm × 100 μm, 35 nm thick) was deposited by using a metal mask. Magnetic anisotropy was induced during the deposition by applying 300 Oe along the long axis of the pattern. It was composed of grains with a size of ~10 nm. The system is outlined in Figs. 1(a) and 1(d), and the holders are seen in Figs. 2(a)-(c). The effective magnetic field in the film plane was controlled by specimen tilt [20, 21, 22, 23]. The observations were carried out in the LowMag-mode, in which the TEM objective lens was switched off. While the residual field (43 Oe) of the objective lens was usually used, ~200 Oe was generated with external current through the lens coil if necessary. The in-plane field was $H = H_0 \sin\phi$, whereas H_0 is the field of the TEM lens and ϕ is the tilting angle. Because the film was thin, the influence from the out-of-plane component could be neglected. The magnification of the Lorentz images was usually × 600. The images were taken with the Fresnel method.

There are typical LTEM images in Figs. 11(a)-(c) with the simultaneously measured MR-curve, where magnetic field was applied downward in the image (perpendicular to the current) [40]. This was the transverse anisotropic magnetoresistance (AMR). The voltage electrodes are visible as dark parts on the left and right of the image. The fine image contrast in the shape of curves from the top to the bottom edges, called "ripple," reflects the spatial fluctuations in the magnetic moment in local areas. The averaged magnetic moment, *M*, in any local area is directed perpendicularly to the ripple (arrows). The resistance of the film varied between 35.68 and 35.94 Ω. The MR ratio defined as

$$MR(\%) = 100 \times (R_{max} - R) / R_{max} \tag{1}$$

was 0.7% at 25 Oe, where R_{max} and R were the maximum resistance and the resistance at a certain H. The ripple contrast was almost linear in a low field (Fig. 11(a)). The directions of local *M* at the top edge (A), the centre (B), and the bottom edge (C) were horizontal because of induced and shape anisotropy. Resistance was maximum. In Fig. 11(b) with 10 Oe, the resistance decreased and ripple contrast was bent (Fig. 11(b)). Local *M* rotated downward, but rotation angles θ (plus: clockwise) at both edges were smaller than those at the centre. The curvature of the ripple increased with field, and the resistance was further reduced. Strongly bent ripple contrasts were observed in areas 20 μm from the edges (Fig. 11(c)) when the field was beyond the inflection point of the MR-curve. On the other hand, the ripple in the innermost

part was almost linear, indicating almost downward M. The distribution of θ is summarized in Fig. 11(d) for various in-plane fields. The positions of 0, 50, and 100 μm correspond to A, B, and C in Fig. 11(a), respectively. The influence of the edges can clearly be identified.

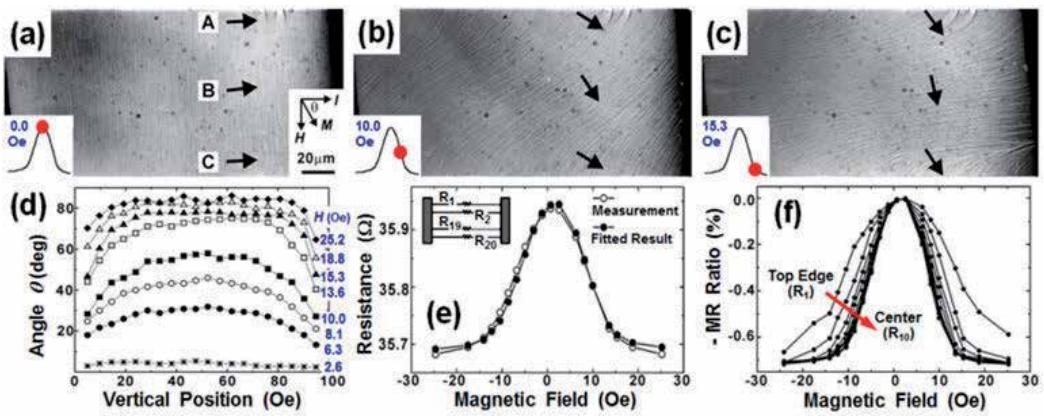

Figure 11. (a)-(c) LTEM images with MR-curves (inset). Relation between orientation of current I, H, and M is in (a). Distortion of images due to specimen tilt is corrected. Arrows are average directions of M at A, B, and C. (d) Angle θ as a function of vertical position from top (0) to bottom (100). (e) Fitted MR-curve using model (inset) compared with measured curve. (f) Estimated MR-curves at local areas between A and B.

Resistance R changes accordingly to

$$R = R_0 + \Delta R \cos^2\theta, \tag{2}$$

whereas R_0 is resistance when the magnetization is perpendicular to current, and ΔR is maximum change in resistance. Resistance and the MR-ratio change from place to place due to the inhomogeneity of M. Considering a model where the film is composed of 20 striped resistors parallel to the edges, the resistance was analysed as

$$1/R = \sum_{i=1}^{20} \left(1/R_i\right),\ R_i = 20\left(R_0 + \Delta R \cos^2\theta_i\right). \tag{3}$$

Here, R_i and θ_i are the resistance and angle θ of the i-th resistor. Least-square fitting was performed as seen in Fig. 11(e). The result from calculation agreed well with the measurements where R_0 = 35.69 Ω and ΔR = 0.26 Ω. The MR-curves at local areas were estimated by using these parameters and the observed θ_i, as shown in Fig. 11(f), where only the upper half of the pattern (R_1 to R_{10}) was evaluated. The MR-curve was broad at the edge (R_1). It became narrow near the central part of the film. We concluded on the basis of the results here that the main influence of the edges on the MR-curve extended ~20 μm.

Next, a Py stripe pattern was deposited at 500°C under a field of 300 Oe along the short axis to induce uniaxial magnetic anisotropy. *In situ* experiments with a field along the easy axis (perpendicular to the long axis) were carried out (Fig. 12). In this case, the AMR effect caused by changes in the ripple structure and appearance/disappearance of magnetic domain walls (DWs) could directly be investigated without any influence from the rotation of the magnetization [41]. H_0 was set to be 248 Oe by using external current to the TEM lens coil. The MR curve measured in the microscope is plotted in Fig. 12(a). The MR-ratio was 0.86% at 200 Oe. Separation in the MR curve was ±45 Oe. *In situ* TEM experiments were performed from +20 to +125 Oe (red curve in Fig. 12(a)). The micrographs in Fig. 12(b) correspond to A to D in Fig. 12(a). When the field is positive, it orients downward in these images. The black contrast on the right and left of the images denotes Au voltage terminals. Thus, all regions contributing to the MR effect in Fig. 12(a) can be seen.

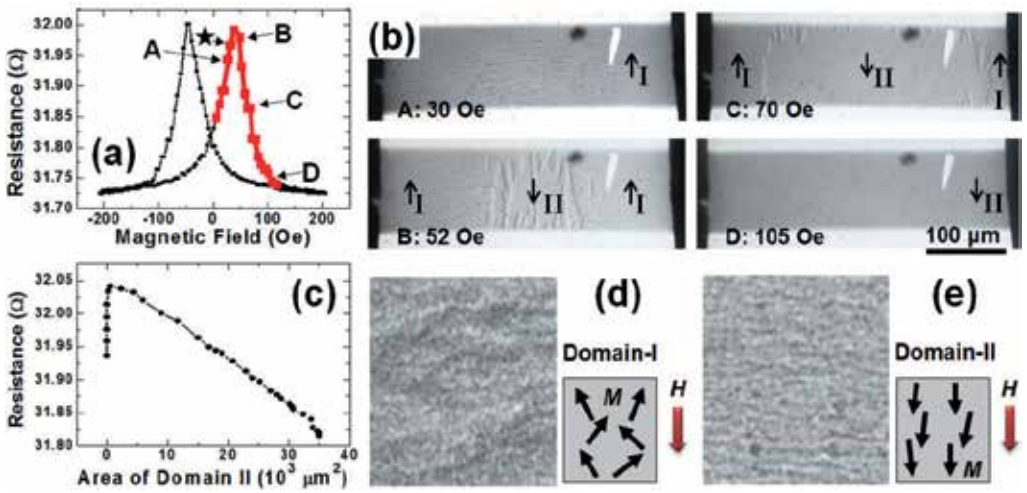

Figure 12. (a) MR curve measured with TEM. Domain wall appeared at point indicated by star. (b) LTEM at A-D in (a) (arrow: averaged direction of *M*). In-plane field *H* was downward in image. Dark regions on both ends of image are voltage terminals. (c) Resistance as a function of area of domain-II. Enlarged images in domains (d) I and (e) II with schematics of local moments (arrows).

The Py pattern was composed of a single domain (domain-I) in the state A (30 Oe), where the average magnetization is upward in the image. Resistance increased monotonically with the field. Domain-II having magnetization parallel to the field (downward) appeared at 43 Oe (state marked with a star in Fig. 12(a)). However, no remarkable changes in resistance could be identified. After this, the area of domain-II monotonically increased with the field. Resistance reached maximum at ~50 Oe, and then reduced monotonically (states B and C). At ~105 Oe (state-D), all regions were composed of domain-II with downward magnetization in the image. While decreased resistance continued after the disappearance of DWs, the rate of reduction was small. The resistance was plotted as a function of the area of domain-II (Fig. 12(c)) to investigate this change. It decreased linearly with this area. It is clear that resistances in domain-I (anti-parallel *M* and *H*) and domain-II (parallel *M* and *H*) differ.

By carefully observing the images in Fig. 12(b), we can identify fine stripe contrast, which is caused by magnetization ripple. This contrast was stronger in domain-I than that in domain-II (Figs. 12(d) and 12(e)). This indicates that the orientation dispersion of the local moment was strong in domain-I, and thus the moment inclined from a direction perpendicular to the current ($\theta < 90°$). However, this dispersion was weak in domain-II, and the moment was almost perpendicular to the sense current ($\theta \sim 90°$). The AMR effect is described as in Eq. 2. Thus, domain-II having weak dispersion should have lower resistance than domain-I. This is a possible explanation for the decrease in resistance in Fig. 12(c). A similar discussion can explain the increase in resistance in regions with small domain-II area. Magnetic domains with magnetization along the applied field have smaller resistance than domains with magnetization opposite to the field.

5.2.2. Experiments by using electromagnet holder

The experimental system is outlined in the schematics in Figs. 1(a), 1(b), 1(d), and Fig. 3. This subsection provides three examples using the electromagnet holder we developed.

5.2.2.1. Domain wall injection and movement in a wire pattern

The control of DWs in magnetic wires has been widely reported [42, 43]. A pad is usually attached to the wire to achieve stable injection of DWs into them [44]. There is a series of LTEM images of a Py wire pattern with a square pad with varying in-plane fields in Fig. 13. A field was applied horizontally. After 100 Oe was applied along the left to saturate magnetization, the field was gradually removed to zero (Fig. 13(a)). The wire was almost uniformly magnetized to the left. The contrast at the lower edge was dark while it was white at the upper edge. There was a clear structure of a solenoidal domain (with 90° and 180° DWs) inside the pad. The area of the domain around the pad's centre penetrated the wire under 6 Oe along the right in Fig. 13(b). A vortex DW (arrowhead) was injected in this case. The contrast of the wire edge changed from the left to the right. The DW moved to the right (Figs. 13(c)–(e)) by increasing the field along the right. The Py pattern was almost saturated in Fig. 13(f). Finally, it was fully saturated in Fig. 13(g) under 100 Oe. The wire edge contrast was reversed from that in Fig. 13(a). Increases and decreases as well as reversal of the magnetic field could be efficiently accomplished by using the system that we developed in this research.

5.2.2.2. Movement of vortex core by field rotation

Ferromagnetic patterns have attracted a great deal of attention in the development of miniaturized memories and logics. Disks with a vortex structure (Fig. 14(a)) represent one such pattern [45, 46]. Local magnetic moments form a clockwise or anti-clockwise loop, and that at the vortex core turns out-of-plane. The vortex core moves perpendicularly to the field when an in-plane field is applied. The direction of movement depends on the chirality of the vortex. There is a test pattern in Fig. 14(b), where Py disks with diameters of 5 and 10 μm can be seen. The arrow denotes an in-plane field of 11 Oe. The bright or dark spotty contrast near the centre of each disk corresponds to a vortex core. The LTEM contrast of the vortex core and disk edge alternates depending on the chirality of the vortex, as shown in Fig. 14(a). A series of LTEM

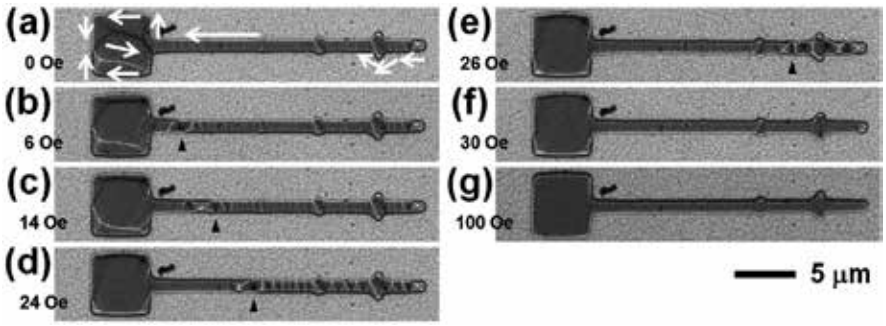

Figure 13. *In situ* LTEM images of Py wire with square pad by applying field along right. Injection of DW and its movement can be seen without large image deformation. White arrows in (a) denote local magnetization. Arrowheads in (b)-(e) indicate DW positions.

images with rotating magnetic fields is shown in Figs. 14(b)-(e). The vortex cores were displaced according to the respective fields to expand the area with magnetization nearly parallel to the field. The core positions moved gradually by rotating the field.

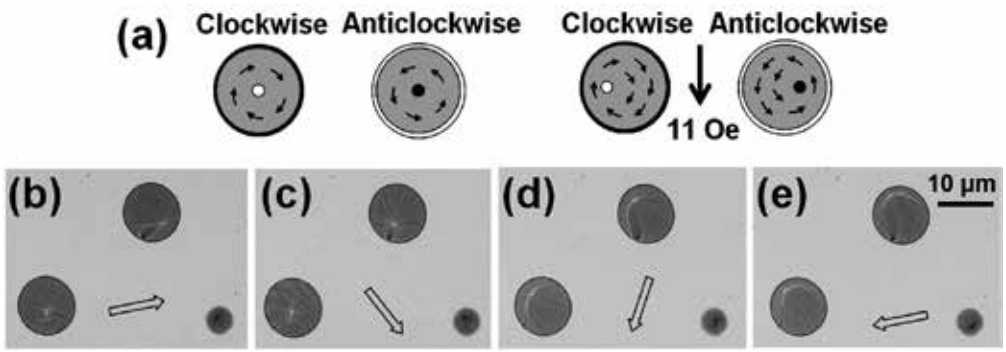

Figure 14. (a) LTEM of thin Py disc patterns with or without magnetic field. (b)-(d) Observed images with rotating in-plane field of 11 Oe. Thick arrows correspond to nominal field directions.

5.2.2.3. In-Situ LTEM observations and magnetoresistance measurements

The investigated MR effect was the longitudinal AMR where resistance was high with magnetization parallel or anti-parallel to the sense current. There is an example of an MR curve measured with TEM in Fig. 15(a), where the magnetic field was parallel to the sense current. Well-known positive MR was identified, where resistance was low around a zero magnetic field. *In situ* LTEM images are presented in Figs. 15(b)-(g), which corresponded to states (b)-(g) in Fig. 15(a). The directions of magnetization were roughly estimated by using faint ripple contrast as a guide (arrows). The region is composed of a single domain in Fig. 15(b) at +14 Oe (along the left) after saturation at +125 Oe. When the field was –21 and –28 Oe (along the right), cross-tie walls can be identified as black and white lines in Figs. 15(c) and 15(d) where resistance

was low. When DWs exited the region, resistance increased (Fig. 15(e)). After this, magnetization was saturated along the right, and the field was reversed. The DWs returned to this region at +22 Oe and resistance decreased (Fig. 15(f)). Resistance increased again when the DW exited from the region (Fig. 15(g)).

The pattern investigated in this work was large, and the DWs were expected to be thick [47]. Thus, the MR effect due to DWs themselves must be quite small. The MR effect identified here was caused by the change in the distribution of local magnetization. As seen in Figs. 15(c), 15(d), and 15(f), local magnetization tends to be parallel (or anti-parallel) to the DW, and its orientation inclines from the sense current. Therefore, the resistance is thought to be small. Another possibility influencing the MR effect is the strength of the magnetic ripple. A domain with anti-parallel magnetization to the applied field had clearer contrast than that with parallel magnetization to the field as was described in Subsection 5.2.1. This indicates that the former domain had larger fluctuations in the orientation of the magnetic moment, and thus the local moment was much more inclined from the sense current providing lower resistance. A similar phenomenon was expected, even though this difference in contrast was not clearly observed in this research because of weak contrast in the image.

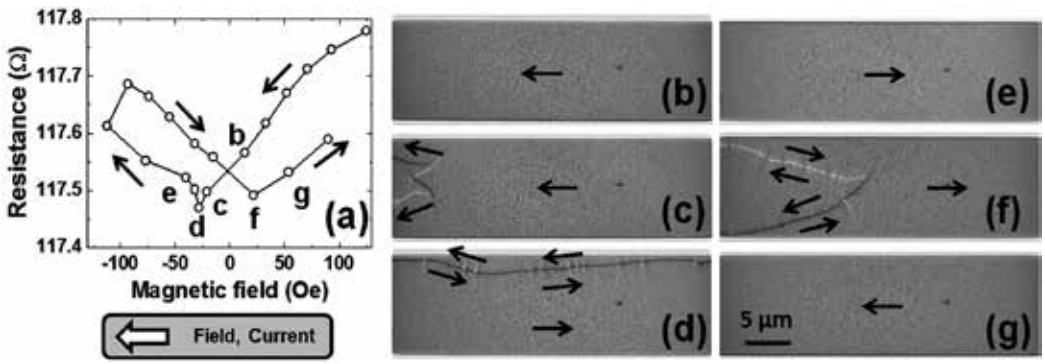

Figure 15. (a) Longitudinal AMR curve of Py pattern measured with TEM (arrow: measurement sequence). (b)-(g) LTEM images of whole area between voltage terminals corresponding to conditions (b) to (g) in (a) (arrow: local orientation of *M*). Magnetic field is positive when it is along left.

5.3. Quantum conductance of metallic nanowires

Metallic contacts and wires on the nanometre scale have been intensively studied [48]. These are expected to exhibit quantum effects at room temperature (RT). Several techniques have been adopted to produce nanowires [49, 50, 51, 52, 53]. Narrow wires with a width of one Fermi wavelength (~0.5 nm) have been the objects, and the energy split of electrons contributes to the conduction quantization.

The quantization unit of conduction in nonmagnetic materials is known to be $2e^2/h$ (= G_0: corresponding resistance is 12.9 kΩ), where e is the electron charge and h is Planck's constant. In ferromagnetic metals where the spin degeneracy is lifted, the quantization step is e^2/h (=

G_0/2). While the nonmagnetic wires such as Au and Cu have mostly exhibited G_0-quantization, a few reports have discussed the G_0/2-quantization [54, 55]. Some possibilities have been revealed to explain this phenomenon, including local atomic arrangement and gas adsorbates [55, 56, 57, 58]. This section explains the formation of Au wires with G_0/2-quantization, and the experimental factors that determined its appearance were investigated [59]. Two Au probes prepared with the method in Figs. 7(a)-(c) were placed inside a TEM, and Au nanowires were formed by touching and detaching these two Au probes. A TEM/STM holder (Fig. 5) was used for this treatment. The system is outlined in Figs. 1(a), 1(c), and 1(e). The TEM was JEM 200CX with a liquid nitrogen trap. The vacuum was 10^{-4}–10^{-5} Pa near the sample and 1–10^{-1} Pa in the pre-evacuation room. The influence of the electron beam was smaller than the current for measurements by two or three orders in magnitude. All measurements were performed at RT.

Three continuous video frames are presented in Figs. 16(a)-(c). The wire length was increased from 4 to 8 nm by stretching it from the state in Fig. 16(a) to that in Fig. 16(b). The wire widths changed from 2 to 1 nm. A further stretch to Fig. 16(c) broke the wire. The corresponding conductance curve is plotted in Fig. 16(d) with a bias voltage (V_b) of 258 mV. A stair-like change can be identified. This conductance quantization was also observed in a process where two probes touched each other. The time interval from $6G_0$ to breakage is ~3 ms, and this curve was obtained between Figs. 16(b) and 16(c). The quantization was observed for a wire having a width of 1 nm or less. Hundreds of curves were usually summarized as a (conductance) histogram. Figure 16(e) is an example using 270 curves having at least one conduction plateau. The experiment was performed with TEM in the Mag-mode (6.5 kOe). The G_0-quantization can clearly be identified. This histogram has also a weak peak at G_0/2. Two conductance with the G_0/2 plateau curves are presented in Figs. 16(f) and 16(g).

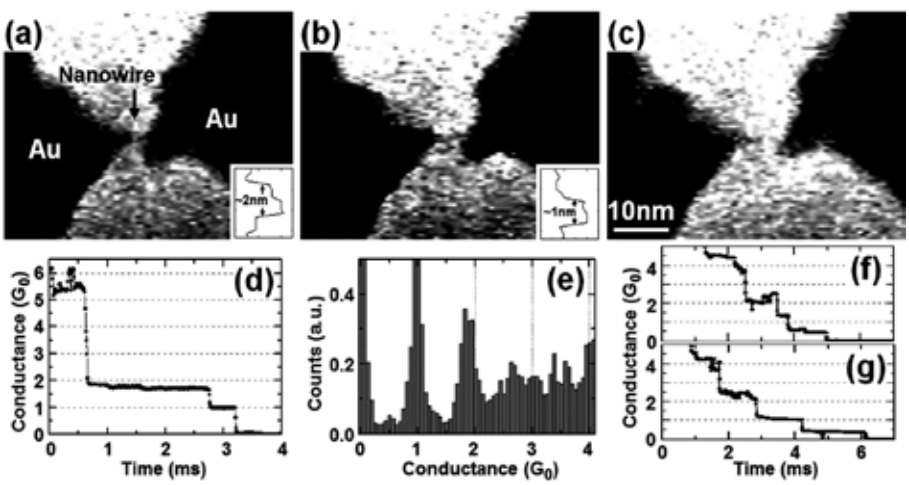

Figure 16. Conductance quantization of Au wires. (a)-(c) Continuous frames of TEM video (interval: 30 ms). Insets are density charts across wire (vertical: magnified vertical position, horizontal: brightness (right: dark)). (d) Conductance curve measured during (a)-(c). (e) Histogram using 270 conductance curves (V_b = 129 mV, H = 6.5 kOe). (f) and (g) Conductance curves having G_0/2 plateau.

Au nanowires were formed under various conditions with different values of H and V_b (Table 1) and the stretching speed (v), to clarify experimental factors influencing the G_0/2-quantization. First, three experiments were carried out at ~6.5 kOe (Mag-mode), ~40 Oe (LowMag-mode), or 0 Oe (samples placed in pre-evacuation room) with V_b = 258 mV. The probability of observing a G_0/2 plateau in the conductance curve was increased from 1% to 8% with increasing the magnetic field. Second, three bias voltages were investigated at ~ 6.5 kOe. The peaks of the conductance histogram broadened by increasing V_b, and the peaks of $2G_0$ and $3G_0$ were weak (data not shown) as in Ref. [50]. Third, a possible effect of the stretching speed (v = 5000, 500, and 5 nm/s) was checked with H = 0 Oe and V_b = 258 mV. The possibilities were 0% (5000 nm/s), 5% (500 nm/s), and 9% (5 nm/s). Previous report (without TEM) that have objected to the G_0/2-quantization revealed that it appeared due to gas adsorption [56, 57, 58]. The present work was carried out under a vacuum of 10^{-5} Pa or worse, and the influence of adsorbates could not be neglected. The following explanation is probable from this standpoint. Heat generation increases with large V_b, and gas molecules tend to desorb. Changes in stretching speed may vary the degree of adsorption. In the first stage of wire formation, Au probes moved against each other and formed the freshly clean wire surface. This wire surface has a chance to be covered with adsorbates during the stretching process. The probability may be high for a slow stretch. The present results, on the other hand, indicated that the probability of G_0/2-quantization increased with magnetic field. This cannot be explained by the direct influence of adsorption such as a partly open conduction channel accompanying any adsorbates or by a conduction circuit of several nano-contacts. One possible scenario that can explain the present results is that the atomic arrangement was modified due to gas adsorption, and that the magnetic properties of the wires were changed due to this modification. As described earlier, G_0/2 conductance is a characteristic of ferromagnetic nanowires where spin degeneracy is lifted. A conductance curve and a histogram of a Fe wire are presented in Fig. 17. Compared with Au wires, G_0/2-quantization can clearly be identified.

Magnetic field H (Oe)	**Bias voltage V_b (mV)**		
	- 26	**- 258**	**- 516**
6500	12%	8%	5%
40	----	3%	----
0	----	1%	----

Table 1. Probability to observe the G_0/2-quantization. The effects of the magnetic field and the bias voltage are summarized.

5.4. Single electron tunnelling of nanoparticle system

The conductance of nanostructures such as SED [11, 12] has been intensively investigated. The miniaturization of current paths plays a key role to observe the quantum effect at RT. An important area of research involves nanoparticle systems embedded in an insulator [60, 61,

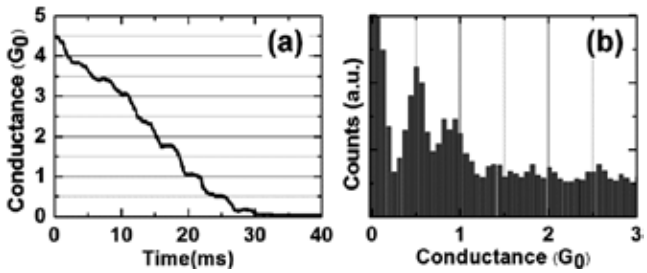

Figure 17. (a) Conductance curve and (b) histogram of Fe wires made from thin Fe layer on sharp Si needle. Measurements were done with TEM in Mag-mode.

62]. The tunnelling current is strongly influenced by their geometric arrangement, such as the particle size (i.e., area of the tunnelling junction) and inter-particle distance (i.e., thickness of the tunnelling barrier).

In this research, the TEM/STM was introduced to investigate the direct relation between the geometry and electrical characteristics of nanoparticle systems. The operation system is outlined in Figs. 1(a), 1(c), and 1(f). The samples were deposited on the needle-shaped Au substrate shown in Figs. 7(c) and 7(d). Two examples are presented, that is, tunnel conduction of a 2-nm thick MgO film and a 5-nm thick MgO/Fe/MgO tri-layer film [8, 29, 63, 64]. Nanoscale regions less than 10 nm^2 were selected using a movable probe. Current-voltage (*I-V*) measurements and TEM observations were performed.

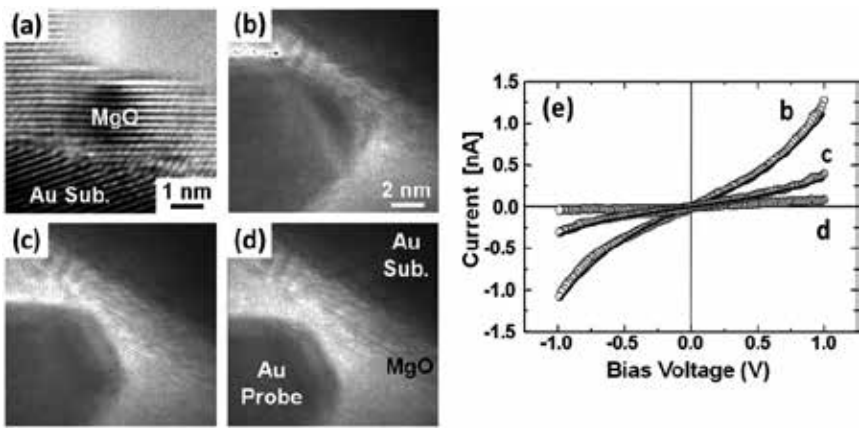

Figure 18. (a) HRTEM image of MgO/Au. (b)-(d) A series of CCD images and (e) corresponding *I-V* curves where solid curves are fitting results obtained by using the Simmons' equation.

There is a typical HRTEM image of MgO/Au with 200_{MgO} and 200_{Au} lattice fringes in Fig. 18(a). The MgO thickness was ~2 nm. Its barrier height for tunnel conduction was evaluated under the conditions in Figs. 18(b)-(d) using *I-V* curves (Fig. 18(e)). First, the probe made contact with the MgO surface. The contact area was ~10 nm^2 (Fig. 18(b)). The corresponding *I-*

http://dx.doi.org/10.5772/60651

V curve indicated nonlinear characteristics in Fig. 18(e). The current was 0.45 nA at V_b = 0.5 V. Next, the probe gradually moved from the sample, and the contact area was reduced. The contact in Fig. 18(c) was ~1.2 nm^2. The current at V_b = 0.5 V decreased to 0.2 nA. The probe was completely separated from the sample in Fig. 18(d), and the background current was measured. Simmons' equation [65] was used to analyse these *I-V* curves to evaluate the barrier height, while this assumption was not rigid because the contact area was not large compared with the MgO thickness.

$$I = \frac{S}{t} \cdot \left(\frac{e}{h}\right)^2 \cdot \sqrt{2m\phi} \cdot \exp\left(-D\sqrt{\phi}\right) \cdot \left\{V_b + \left(\frac{D^2e^2}{96\phi} - \frac{De^2}{32\phi\sqrt{\phi}}\right)V_b^{\,3}\right\} \tag{4}$$

and

$$D = 4\pi t \cdot \frac{\sqrt{2m}}{h}. \tag{5}$$

Here, *I* is the current, *S* is the contact area, *t* is the barrier width, ϕ is the barrier height, and V_b is the bias voltage. The constants *e*, *m*, and *h* correspond to the electron charge, the electron mass, and Planck's constant, respectively. Least-square fitting was performed by assuming contact areas described earlier. As a result, ϕ = 1.4 eV was obtained in both cases. This corresponds to the results using conventional tunnel junctions [10, 66].

The following is an example of $MgO_{(2\ nm)}/Fe_{(1\ nm)}/MgO_{(2\ nm)}$, where the Fe layer was composed of nanoparticles (Fig. 19(a)). The film formed a double tunnel junction. As the Fe particle size was on a nanometre scale, the Coulomb blockade (CB) effect was expected at RT. Here, the contact area must be small to detect the quantum effect. Therefore, the sample film was processed inside TEM. After the Au-probe lightly touched the film, 5 V or larger voltage was applied to the probe to exfoliate the sample layer. The narrow current paths were fabricated by repeating this process. Three Fe particles (diameters: 3.4, 3.2, and 2.9 nm) are seen in Fig. 19(b). The particle with a diameter of 2.9 nm was selected for the measurements. The distance between the film surface and the particle was estimated to be 2.4 nm from this image, and the distance between the particle and the Au-sub was 0.8 nm.

The results are presented in Figs. 19(c)-(e), where the tri-layer film can be identified as faint contrast on the Au-sub. The probe softly touched the sample in Fig. 19(c). The tunnelling current in the *I-V* curve was small because of the long probe-particle distance (2.4 nm). The probe was next moved along the white arrow by 1.3 nm to press the sample (Fig. 19(d)). The probe-particle distance was estimated as 1.1 nm by assuming that the Fe-particle positions did not change. This was almost the same as the substrate-particle distance (0.8 nm). The current increased markedly and the *I-V* curve revealed nonlinear characteristics. The current was small with low V_b, although the leakage current seemed to be superposed. This may have been due to the CB effect. The tip was shortly detached from the sample by 0.5 nm in Fig. 19(e). The

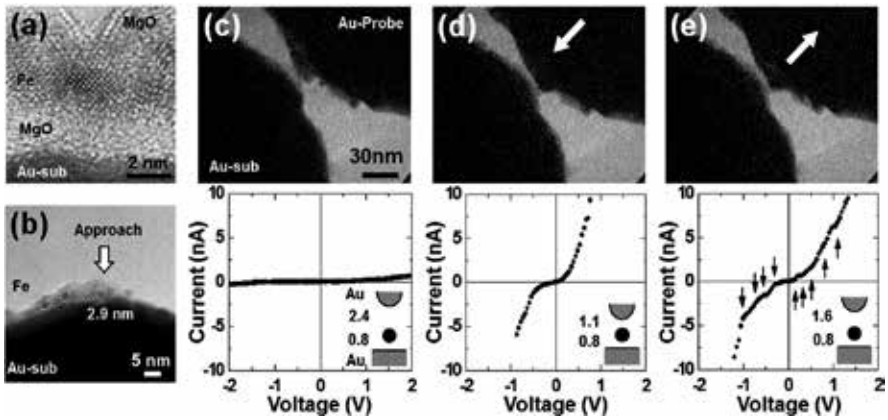

Figure 19. (a) Side view of MgO/Fe/MgO containing Fe particles. (b) Sample used for measurements. (c)-(e) Video images and *I-V* curves during deformation by moving Au probe along arrows (at RT). Steps (arrows) are recognized in *I-V* graph in (e). Insets are schematics of Fe particle (filled circle) sandwiched between Au probe and substrate. Numbers are distances in nm.

current was suppressed. There are weak steps at the positions indicated by the arrows in the *I-V* curve, which are thought to represent the Coulomb staircase (CS). Under this condition, the probe-particle distance was expected to be 1.6 nm while the particle-substrate distance was 0.8 nm (inset of Fig. 19(e)). Therefore, the probe-particle and particle-substrate tunnelling resistances must differ much. This corresponds to a well-known phenomenon that the CS appears only when the resistances of two junctions sandwiching the nanoparticle differ much [11, 12]. The step period was ~0.25 V. The Fe particle in this experiment was sandwiched between two large electrodes (i.e., the probe and substrate). The capacitance C in this nanostructure was assumed to be half the self-capacitance of particle $C_s = 4\pi\varepsilon_0\varepsilon_r r$, where ε_0 is the dielectric constant of the vacuum, ε_r is that of MgO, and r is the radius of the particle. The self-capacitance is $C_s = 1.3$ aF by using $2r = 2.9$ nm and $\varepsilon_r = 9.65$. The CS period is $e/C = 2e/C_s = 0.25$ V. This value approximately fits that obtained from the experimental result.

5.5. Resistance switching of the resistive random access memory

Resistive random access memory (ReRAM) has attracted a great deal of attention as a next-generation non-volatile memory [14, 15, 67, 68, 69, 70]. Its advantages include high-speed operation, low power consumption, etc. High integration is also expected due to its simple capacitor structure (Fig. 20(a)). Resistance switches between high and low resistance states (HRS and LRS) by applying voltage between top and bottom electrodes (TE and BE). The *I-V* curve exhibits hysteresis (Figs. 20(b)-(c)) that is useful in non-volatile ReRAMs. The resistance ratios of HRS/LRS are generally more than 100, and ReRAM devices are expected to be regulated in intermediate states to realize non-volatile analogue memories.

The pristine state is typically HRS and converts into LRS due to the first application of voltage. This process is called "forming". Subsequent voltage returns the resistance into HRS ("reset" process). Resistance again changes into LRS by another application of voltage ("set" process).

http://dx.doi.org/10.5772/60651

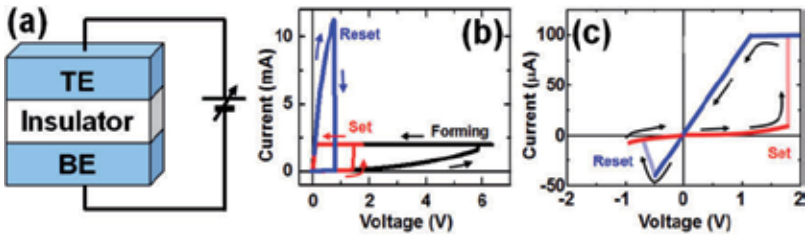

Figure 20. (a) Schematic of ReRAM. *I-V* switching curve of (b) unipolar and (c) bipolar ReRAMs (arrows: sequence of voltage sweep). Horizontal axis denotes setting voltage of SMU.

There are two types of switching. The same voltage polarity is used in "unipolar" switching (Fig. 20(b)), while polarity needs to be altered in "bipolar" switching (Fig. 20(c)). Current abruptly increases during forming or set, and ReRAMs are easily destroyed. To prevent this failure, current limitation (or compliance) of the electrical source is generally introduced. The horizontal line in the *I-V* curve is due to these limitations. Many materials have been applied to ReRAMs [14, 15], and various switching models have been reported. Of these, the "filament model" is believed to play a key role in many cases, where formation and erasure of conductive filaments of oxygen vacancies or Cu contribute to switching. However, their detailed behaviour is still obscure while finding the mechanism is quite important to develop ReRAM devices. *In situ* TEM was carried out in this report by using TEM /STM holders (Fig. 5). The system was that in Figs. 1(a), 1(c), and 1(f). ReRAMs of PtIr/NiO/PtIr [34, 71], PtIr/Cu-GeS/PtIr [72, 73], and Cu/MoO_x/TiN [74, 75, 76] will be explained.

5.5.1. Unipolar switching of PtIr/NiO/PtIr

A binary oxide NiO is one of the most widely investigated materials for ReRAMs and exhibits unipolar switching. The mechanism for this switching phenomenon may be one of the filament models based on soft-breakdown [68]. A conductive filament of oxygen vacancies connecting metal electrodes is formed during the forming. This forming process certainly plays a key role in achieving stable switching cycles. In this study, sharp PtIr probes (tip size: several tens of nanometres or less) to obtain *I-V* data from nano-regions were used, which were sharpened using the methods in Figs. 7(a) and 7(e). Wedge-shaped PtIr substrates (Figs. 7(f)-(h)) were used to deposit NiO. The Ni metal was deposited at RT onto this substrate, and oxidation was performed in air for 3 min typically at 200°C or 300°C. The NiO layer (40–50 nm in thickness) was polycrystalline with a grain size of 30–50 nm. The size of the apex of the probe was comparable to or less than this grain size, and thus the *I-V* characteristics could be obtained from individual grains. Because forming operation based on soft-breakdown is more or less violent, the films were permanently destroyed in many cases. Therefore, a resistor of 10 kΩ was inserted in series in the circuit to prevent this destruction.

The *I-V* curve is plotted in Fig. 21(a), and the corresponding TEM micrographs are in Figs. 21(b) and 21(c). The probe was moved along the arrow to make electrical connection with the NiO layer (Fig. 21(b)). The contact area was ~1200 nm^2 or less. The conducting properties were measured through this point. The voltage sweep sequence was typically from 0 to 3 V and

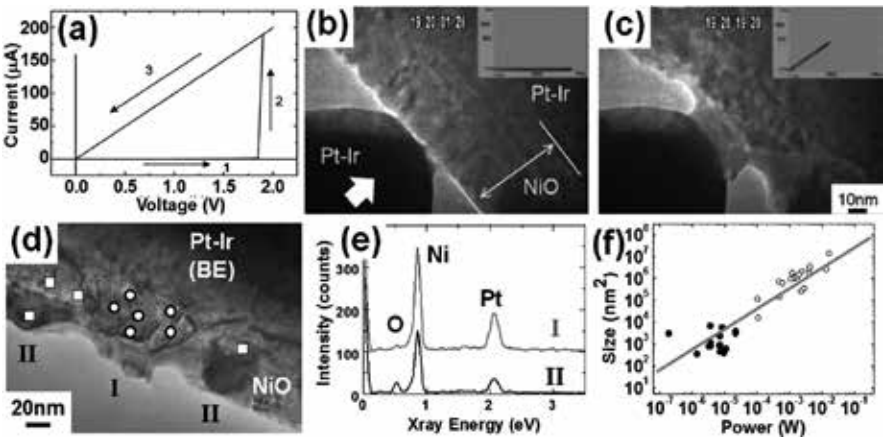

Figure 21. ReRAM switching of PtIr/NiO/PtIr in TEM. (a) *I-V* characteristics. Corresponding TEM micrographs (b) before and (c) after forming. (d) Image of filament in (c) after TE probe was detached. There is wreck of filament at centre (I, circles), which was surrounded by initial NiO (II, square). energy dispersive X-ray spectroscopy (EDX) was performed at these positions. (e) EDX spectra from regions I and II. (f) Filament size (filled circles) superposed on CS size (open circles). Line is extrapolation from CS data.

back to 0 V. The measurements were done within 18 seconds in which drift in the electrodes could be neglected. The current hardly passed in the first sequence (sequence 1), and the TEM image remained unchanged (Fig. 21(b)). Resistance (R) was ~1 MΩ. When voltage was increased to 1.7 V, the current suddenly increased (sequence 2) and the NiO film structure changed to have a bridge-like contrast (Fig. 4(b)). When the voltage was decreased to 0 V (sequence 3), resistance was almost that of the series resistor (10 kΩ). NiO changed to LRS (R <<10 kΩ). The PtIr electrode was then detached and touched again. R in region I of Fig. 21(d) (filament position) was still in LRS while adjacent region II remained insulating. The bridge region worked as a conductive filament. Regions I and II were analysed by using energy dispersive X-ray spectroscopy (EDX) at the positions with circles and squares in Fig. 21(d). Typical spectra are compared in Fig. 21(e). The oxygen peak was apparently weakened in region I. The estimated composition of Ni: O was 71: 29 for region I and 85: 15 for region II. This finding fits with the phenomenon in the filament model of binary oxides where the redox reaction contributes to switching. The forming power and the filament size are also important factors. Crater-shaped "conduction spots" (CS) have been observed using conventional ReRAM samples, and the CS area was proportional to the injection power [77]. The filament diameter measured from TEM images are summarized (filled circles) in Fig. 21(f) where the CS data are superposed as open circles. The bridge size was ~300 nm^2 (~20 nm diameter) at 10^{-6} W, and the size is expected to be less than 100 nm^2 (~ϕ12 nm diameter) at ~10^{-7} W. This indicates there is great potential in the scaling of resistive switching.

While the filament formation during the forming process could clearly be identified, reset operation was not found in TEM where the ambient was a vacuum. We fabricated NiO/Pt on a SiO_2/Si substrate which was not a TEM sample, to investigate the reason for this result. The *I-V* measurements (data are not provided here) were performed in air and in a vacuum by

http://dx.doi.org/10.5772/60651

using a PtIr probe as the TE. The switching sequence of the forming-reset-set was identified when the PtIr/NiO interface was exposed to air. However, there was no reset in the vacuum. After the vacuum was broken, reset-set operation recovered. Therefore, the phenomenon that appeared during *in situ* TEM experiments could be understood as follows. Oxygen in NiO diffused into the vacuum in the forming process, and did not remain in the vicinity of the PtIr/NiO interface. Therefore, the conductive filament could not be oxidized, and the reset process could not be achieved. Oxygen and/or water vapour played an important role in the ReRAM switching of NiO.

5.5.2. Bipolar switching of PtIr/Cu-GeS/PtIr

The ReRAMs of solid electrolytes are other examples (e.g., CuGeS and Ag_2S) [14, 67, 69]. This type of ReRAM is abbreviated as CBRAM (conductive bridging RAM) as well as PMC (programmable metallization cell). The operation is attributed to the conductive filament of Cu (or Ag). The cations (e.g., Cu^{2+}) generated at the anode are thought to migrate toward the cathode with bias voltage. The cations receive electrons at the cathode surface and become metal atoms. Metallic filament is formed by continuing this process, and it bridges the cathode and anode. An opposite bias voltage dissolves the metallic filaments into the solid electrolyte. This is the expected switching process. Real-space *in situ* observations are quite effective to elucidate this hypothesis and provide further detailed information. Cu-GeS thin films were deposited on the PtIr substrate. The films were 8–60 nm thick and were amorphous including Ge nanocrystals. The Cu ion source was the Cu-GeS layer itself. Although amorphous chalcogenides easily deteriorated during TEM observations, the influence of the electron beam was negligible (beam current densities lower than 170 fA/nm^2). A sharp PtIr probe was used as the TE. Since the substrate and the probe had different shapes, the structure of PtIr/Cu-GeS/PtIr was asymmetric while it was electrochemically symmetric.

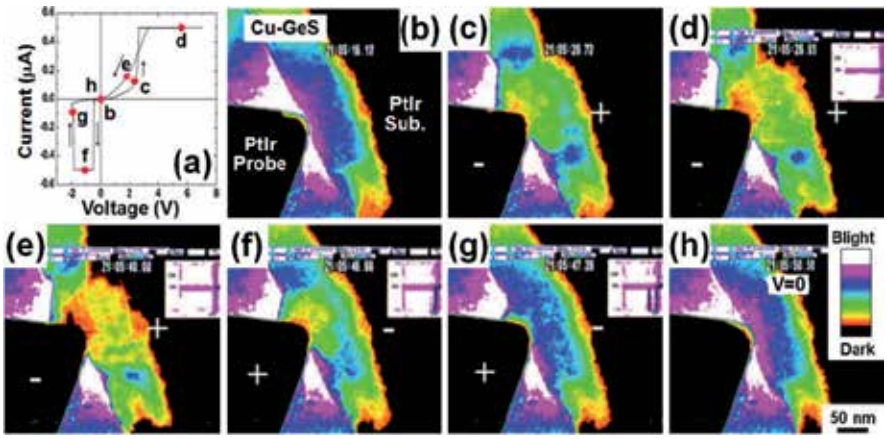

Figure 22. ReRAM switching of PtIr/Cu-GeS/PtIr in TEM. (a) *I-V* characteristics measured with TEM. (b)-(h) Series of images during application of voltage. Conductive filament in red and yellow appeared from the probe side (grounded) and disappeared during switching process.

The *I-V* curve during the *in-situ* TEM observations is plotted in Fig. 22(a), where the substrate was biased with the current compliance of 0.5 μA. The voltage was swept from 0 to 7 V, from 7 to –2 V, and back to 0 V, which indicates hysteresis. TEM images in pseudo-colours are presented in Figs. 22(b)-(h). The red and yellow parts correspond to dark contrast in the original images (Fig. 22(h)). There was no special contrast just after the probe contacted Cu-GeS (Fig. 22(b)). The resistance gradually changed at ~1 V, and this transfer was quickly completed at 2.6 V. This was the set operation. A small deposit (green, yellow, and red) gradually appeared in the same way (Fig. 22(c)). The size of the deposit was enlarged (Figs. 22(d)-(e)) and it contacted the substrate. The width of the filament-like red region was 10 nm. Although the details were altered by colouring conditions, this value may give some insights into the filament size. The *I-V* curve between (d) and (f) of Fig. 22(a) was abnormal compared with the curves of usual ReRAMs. Resistance suddenly increased at –0.5 V. This was caused by over accumulation of Cu around the TE (i.e., probe). This specially occurred for the sample without the Cu substrate and is not the set or the reset. The mechanism has been discussed in Ref. [73]. The deposit contracted as the application of negative voltage continued (Figs. 22(f)-(g)), and the sample resistance returned to HRS. This was reset switching. The deposit entirely disappeared in Fig. 22(h). The size of the deposit and the current value corresponded, and the deposit constituted a conducting path. The dependence on polarity may be attributed to the asymmetry of electric field caused by the difference in shape between the substrate and the probe. When positive voltage was applied to the substrate, Cu ions accumulated at the probe because of the concentrated electric field. However, when negative voltage was applied to the substrate, electric flux dispersed toward the substrate. Even though Cu was thought to accumulate at the substrate–film interface, its density was not high enough to form the filament connecting electrodes.

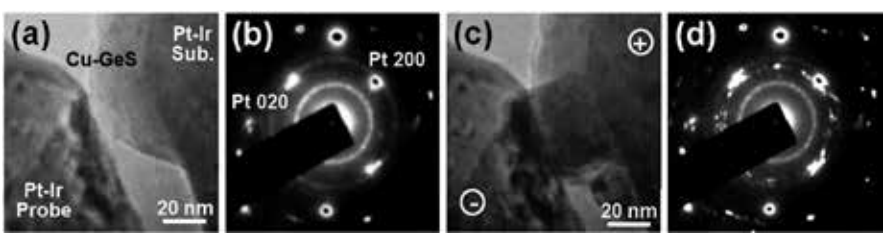

Figure 23. TEM micrograph and corresponding SAD pattern extracted from video (a) and (b) before and (c) and (d) during application of voltage (1 V).

The crystal structure of the deposit was studied by observing real-time selected area diffraction (SAD) patterns. The SAD pattern before voltage application was composed of a faint background and Debye rings (Figs. 23(a) and 23(b)), which indicated the film was amorphous with Ge nanocrystals. The clear spots were from PtIr. A deposit appeared by applying 1 V to the substrate (Fig. 23(c)), and sharp spots appeared in the SAD pattern. They continued to twinkle when voltage was applied. Well-crystallized nanocrystals grew, and their orientation frequently changed. We superposed 1152 frames of video images totalling 35 seconds of footage (Fig. 23(d)). Relatively sharp spots that formed rings corresponded to reflections of Cu. EDX

http://dx.doi.org/10.5772/60651

spectra were measured from the filament and other regions (but another sample). The intensity of the Cu peak greatly increased in the filament region. The composition of the deposit was Cu: Ge: S = 7: 2: 1 while it was 4: 4: 2 in the initial state by assuming thin foil approximation. Although this was a rough estimation, we can summarize that the deposit was an agglomeration of crystals with a large amount of Cu.

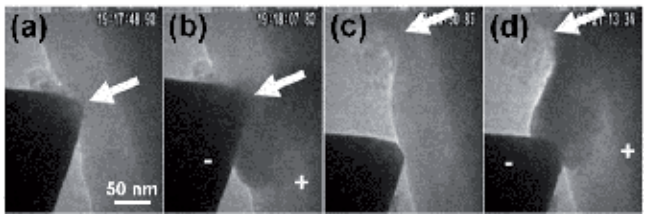

Figure 24. TEM images of (a) and (b) first, and (c) and (d) second switching from initial state (arrows: corresponding position). (a) and (c) are without voltage while (b) and (d) are with voltage of 5 V.

The sample after the voltage cycle differed from its initial state. Continuation of the *I-V* cycles reduced the set voltage. After a deposit appeared and was erased in the first voltage cycle (Figs. 24(a) and 24(b)), the contact position moved to a neighbouring region (Fig. 24(c)). A deposit appeared by applying positive voltage to the substrate (Fig. 24(d)). The deposit did not reach the substrate near the probe but elongated into the region where it had formed during the first cycle. The deposit appeared in the same place in iterative measurements. The regions where the deposit had been formed were thought to have priority in resistance switching. Extremely small metallic nanocrystals or clusters may have remained as residues, which could act as the nuclei of filaments and reduce the set voltage.

The phenomenon that occurred here can be explained in Fig. 25. An electric field is generated by applying positive voltage to the substrate, and the Cu ions dispersing in Ge-S move to the probe. Then, a small metallic deposit appears at the probe (Fig. 25(a)). The deposit expanded and finally touched the substrate (Figs. 25(b)-(c)). At this stage, the conductive filament bridges the probe and the substrate, and the resistance state is LRS. When further voltage is applied, several filaments increase even though the overall size of the conductive region does not expand (Fig. 25(d)). The Cu-based filaments dissolve and shrink toward the probe due to polarity change (Figs. 25(e)-(f)), and resistance reverts to HRS. There are some residues (nuclei of filaments) at the end of the cycle.

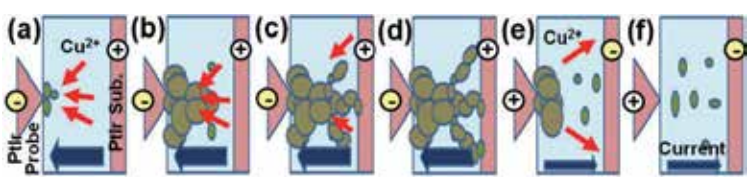

Figure 25. Schematic of resistance switching. Plus and minus signs indicate voltage polarity.

5.5.3. Formation and erasure of conductive filament in Cu/MoO$_x$/TiN

In situ TEM has successfully applied on ReRAM switching [34, 72, 78, 79, 80]. However, the sample was specially designed for TEM observations. For example, the TE was the movable probe. This structure was different from that of real ReRAM devices having multi-layered stacks. In addition, operation was quite slow, and the current was much less than a few μA. The ReRAM studied here was $Pt_{(100\ nm)}/Cu_{(30\ nm)}/MoO_{x\ (50\ nm)}$ on a TiN/Si substrate. The amorphous MoO_x (x ~ 3) acted as the switching layer [81, 82]. Samples were prepared using the ion-shadow method. Clear stacking images were obtained by using the double tilt TEM/STM holder (Fig. 8(f)). After the probe had been connected to the Pt layer, bias voltage was applied to Pt/Cu, and the substrate was grounded. The voltage was typically swept between ±3.0 V (rate: 0.7–0.8 V/s). The switching layer was nearly a disk with ϕ350 nm.

There is an example of the *I-V* curve (compliance current I_c = 400 μA) in Fig. 26(a). The current gradually increased and then abruptly jumped to I_c at 2.6 V (C, set) by increasing the positive voltage (Cu TE biased) from A to B. After positive voltage changed to D and E, it was reduced to zero. The polarity was reversed after 5 minutes. The resistance was LRS. The current exhibited two small jumps before G (reset to HRS). Negative current reached –400 μA with increasing the negative voltage to –3 V (G to H), and clear hysteresis characteristics were identified. The voltage was set to zero. This cycle denoted bipolar switching. The property of this *I-V* curve measured with TEM agreed well with that of ReRAM devices, and thus the vacuum environment and electron beam irradiation had no negative effects.

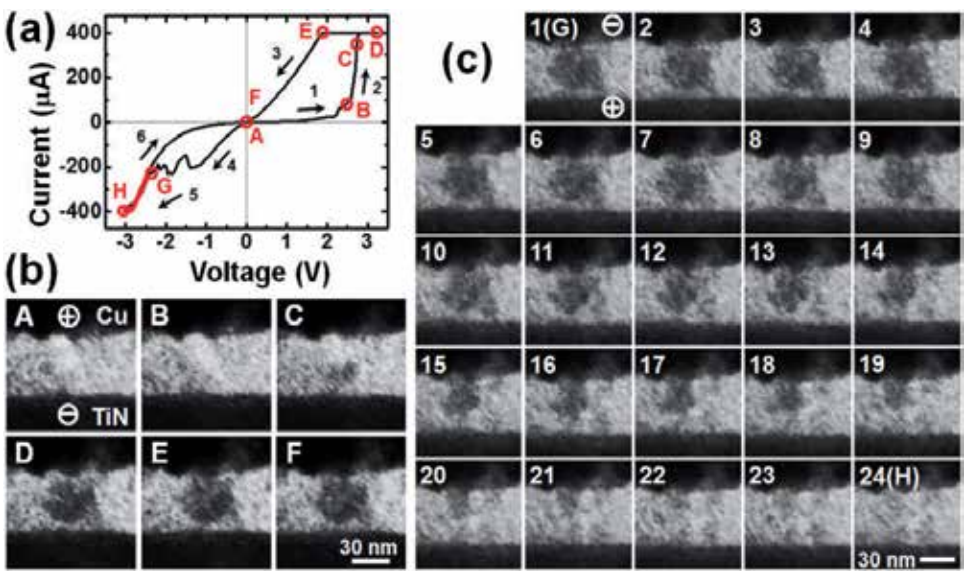

Figure 26. ReRAM switching of Cu/MoO$_x$/TiN multilayer where voltage was applied to Cu TE. (a) *I-V* curve during *in situ* observation. Alphabetical symbols correspond to images in (b) and (c). Magnified filament images in (b) set process and (c) reset process, which were extracted from the video. Numbers indicate the order of video frames counted from G (interval: 30 ms).

Filament-like dark contrast appeared in the set process and disappeared in the reset process. This indicates that this dark region behaved as a conductive filament. We analysed it (but in another sample) with EDX and found it contained more Cu than the other regions. Filament images extracted from the video of the set process (A to F) are summarized in Fig. 26(b). No drastic changes in the images can be identified between A and B (HRS). However, a small dark contrast appeared near TiN BE during abrupt set switching, which seemed to be the nucleus of the filament. Even though the current almost reached I_c at C, the filament did not connect to Cu TE. The current may be ionic that was contributed due to movements of dense Cu ions between the filament and TE. The filament grew toward Cu TE until D, and it thickened to be ~35 nm. After the nucleus appeared, the filament bridged two electrodes within 200 ms. This fits well with the electrochemical switching model [14, 69, 73].

The resistance change in the reset process was gradual. Even after the two-step weak reset, image G (frame #1) had similar contrast to F while resistance increased (Fig. 26(c)). The reset switching should occur very locally (e.g., at the ends of filaments). When we further increased the negative voltage to –2.6 V, negative current increased beyond –300 μA (#12), and the filament shrank toward Cu TE. When the current reached $-I_c$, the filament vanished although some residuals remained (H: #24). This filament erasure does not fit with reported models [83, 84]. This may be influenced by the surface oxidation of TiN BE. This region must have had higher resistance than other regions in the filament and generated Joule heat. This Joule heat must affect filament shrinkage, since it occurred at a relatively high current.

6. Summary and conclusion

We have shown various TEM holders developed in our group in the last 15 years. These holders can be used as accessories without changing the construction of the electron microscope. Thus, their principal design can be applied to any microscopes. In this paper, application of *in situ* TEM holders on magnetic and electronic devices was demonstrated, which are operated by voltage or current input. While some of these TEM holders have already been taken to the market, the designing and manufacturing of new TEM holders is still important for *in situ* TEM experiments for electronics because required functions of the holder depends on devices investigated.

Acknowledgements

This work was financially supported by KAKENHI, by the Ministry of Education, Culture, Sports, Science and Technology (MEXT) Japan, and by the Japan Society of the Promotion of Science (JSPS) (Nos. 13650708, 16206038, 17201029, 18560640, 19026001, 20035001, 21560681, 22240022, 24360128, 25420279, and 26630141). Part of this work was collaborated with the Semiconductor Technology Academic Research Center (STARC), as well as Prof. S. Takeda (Osaka Univ.) under the Cooperative Research Program of "Network Joint Research Center

for Materials and Devices". Support by the Nanotechnology Platform Program (Hokkaido Univ.) organized by MEXT, especially by Prof. N. Sakaguchi (Hokkaido Univ.), is grateful. We are thankful to Dr. T. Tesfamichael (Queensland Univ. Technol.) for critical reading of the manuscript. Finally, we are also grateful to our laboratory members for collaboration.

Author details

Masashi Arita[1*], Kouichi Hamada[1], Yasuo Takahashi[1], Kazuhisa Sueoka[2] and Tamaki Shibayama[3]

*Address all correspondence to: arita@nano.ist.hokudai.ac.jp

1 Laboratory of Nanomaterial Engineering, Graduate School of Information Science and Technology, Hokkaido University, Sapporo, Japan

2 Laboratory of Nanoelectronics, Graduate School of Information Science and Technology, Hokkaido University, Sapporo, Japan

3 Center for Advanced Research of Energy and Materials, Graduate School of Engineering, Hokkaido University, Sapporo, Japan

References

[1] Hirsch PB, Howie A, Nicholson, Pashley DW, Whelan MJ. Electron Microscopy of Thin Crystals. London: Butterworths; 1965.

[2] Fuchs VE, Liesk W. Optik. 1962; 19(6):307-310, in German.

[3] Blech IA, Meieran ES. J. Appl. Phys. 1969; 40(2):485-491.

[4] Iwatsuki M, Murooka K, Kitamura SI, Takayanagi K, Harada Y. J. Elect. Microsc. 1991; 40(1):48-53.

[5] Kizuka T, Yamada K, Deguchi S, Naruse M, Tanaka N. Phys. Rev. B. 1997; 55(12): R7398-R7401.

[6] Poncharal Ph, Frank St, Wang ZL, de Heer WA. Eur. Phys. J. D. 1999; 9(1):77-79.

[7] Svensson K, Jompol Y, Olin H, Olsson E. Rev. Sci. Instr. 2003; 74(11):4945-4947.

[8] Hirose R, Arita M, Hamada K, Takahashi Y, Subagyo A. Japn. J. Appl. Phys. 2005; 44(24):L790-L792.

[9] Miyazaki T, Yaoi T, Ishio S. J. Magn. Magn. Mater. 1991; 98(1):L7-L9.

[10] Yuasa S, Nagahama T, Fukushima A, Suzuki Y, Ando K. Nature Mater. 2004; 3(12): 868-871.

[11] Grabert H, Devoret MH, editors. Single Charge Tunneling. New York: Springer; 1992.

[12] Takahashi Y, Ono Y, Fujiwara A, Inokawa H. J. Phys. Cond. Matter. 2002; 267(14):R995-R1033.

[13] Liu SQ, Wu NJ, Ignatiev A. Appl. Phys. Lett. 2000; 76(19):2749-2851.

[14] Waser R, Aono M. Nat. Mater. 2007; 6(11):833-840.

[15] Akinaga H. Japn. J. Appl. Phys. 2013; 52(10R):100001.

[16] Park H, Lim AKL, Alivisatos AP, Park J, McEuen PL. Appl. Phys. Lett. 1999; 75(2): 301-303.

[17] Heersche HB, Lientschnig G, O'Neill K, van der Zant HSJ, Zandbergen HW. Appl. Phys. Lett. 2007; 91(7):072107.

[18] Strachan DR, Johnston DE, Guiton BS, Datta SS, Davies PK, Bonnell DA, Johnson ATC. Phys. Rev. Lett. 2008; 100(5):056805.

[19] Murakami Y. Real-time investigation of the electrically-induced metal atom migration by use of transmission electron microscopy [thesis]. Sapporo: Hokkaido Univ. 2015, in Japanese.

[20] Chapman JN, Scheifein MR. J. Magn. Magn. Mater. 1999; 200(1):729-740.

[21] Haug T, Vogl A, Zweck J, Back CH. Appl. Phys. Lett. 2006; 88(8):082506.

[22] Shindo D, Akase Z. Kenbikyo(Microscopy). 2009; 44(1):35-40, in Japanese.

[23] Hamada K, Chimura M, Arita M, Ishida I, Okada A. J. Elect. Microsc. 1999; 48(5): 595-600.

[24] Uhlig T, Heumann M, Zweck J. Ultramicros. 2003; 94(3-4):193-196.

[25] Inoue M, Tomita T, Naruse M, Akase Z, Murakami Y, Shindo D. J. Elect. Microsc. 2005; 54(6):509-513.

[26] Petford-Long AK, Bromwich T, Kohn A, Jackson V, Kasama T, Dunin-Borkowski R, Ross CA. Mater. Res. Soc. Symp. Proc. 2006: p. 907E, 0907-MM04-01.

[27] Yi G, Nicholson WAP, Lim CK, Chapman JN, McVitie S, Wilkinson CDW. Ultramicrosc. 2004; 99(1):65-72.

[28] Arita M, Tokuda R, Hamada K, Takahashi Y. Mater. Trans. 2014; 55(3):MD201310.

[29] Arita M, Okubo Y, Hamada K, Takahashi Y. Superlat. Microstr. 2008; 44(4-5):633-640.

[30] Jacobs JWM, Verhoeven JFCM. J. Microsc. 1986; 143(1):103-116.

[31] Khamsehpour B, Wilkinson CDW, Chapman JN, Johnston AB. J. Vac. Sci. Technol. B. 1996; 14(5):3361-3366.

[32] Takezaki T, Yagisawa D, Sueoka K. Japn. J. Appl. Phys. 2006; 45(3B):2251-2254.

[33] Hirose R, Arita M, Hamada K, Okada A. Mater. Sci. Eng. C. 2003; 23(6-8):927-930.

[34] Fujii T, Arita M, Hamada K, Kondo H, Kaji H, Takahashi Y, Moniwa M, Fujiwara I, Yamaguchi T, Aoki M, Maeno Y, Kobayashi T, Yoshimaru M. J. Appl. Phys. 2011; 109(5):053702.

[35] Kudo M, Arita M, Ohno Y, Fujii T, Hamada K, Takahashi Y. Thin Solid Films 2013; 533:48-53.

[36] Black JR. Proc. 6th Ann. Reliability Phys. Symp. 6-8 Nov. 1967 ; Los Angels, CA, USA. New York: IEEE; 1967. p. 148-159.

[37] Park J, Pasupathy AN, Goldsmith JI, Chang C, Yaish Y, Petta JR, Rinkoski M, Sethna JP, Abruna HD, McEuen PL, Ralph DC. Nature. 2002; 417(6890):722-725.

[38] Suga H, Horikawa M, Odaka S, Miyazaki H, Tsukagoshi K, Shimizu T, Naitoh Y. Appl. Phys. Lett. 2010; 97(7):073118.

[39] Chen LJ, Wu WW. Mater. Sci. Eng. R. 2010; 70(3-6):303-319.

[40] Arita M, Hamada K, Ono T, Okada A. Trans. Magn. Soc. Japn. 2004; 4(1):9-12.

[41] Michita N, Arita M, Hamada K, Takahashi Y. J. Magn. Soc. Japn. 2005; 29(2):128-131, in Japanese.

[42] Allwood DA, Xiong G, Faulkner CC, Atkinson D, Petit D, Cowburn RP. Science. 2005; 309(5741):1688-1692.

[43] Parkin SSP, Hayashi M, Thomas L. Science. 2008; 320(5873):190-194.

[44] Cowburn RP, Allwood DA, Xiong G, Cooke MD. J. Appl. Phys. 2002; 91(10): 6949-6951.

[45] Miramond C, Fermon C, Rousseaux F, Decanini D, Carcenac F. J. Magn. Magn. Mater. 1997; 165(1-3):500-503.

[46] Pigeau B, de Loubens G, Klein O, Riegler A, Lochner F, Schmidt G, Molenkamp LW, Tiberkevich VS, Slavin AN. Appl. Phys. Lett. 2010; 96(13):132506.

[47] Fuller HW, Hale ME. J. Appl. Phys. 1960; 31(2):238-248.

[48] Agraït N, Yeyati AL, van Ruitenbeek JM. Phys. Rept. 2003; 377(2-3):81-279.

[49] Pascual JI, Méndez J, Gómez-Herrero J, Baró AM, García N, Binh VT. Phys. Rev. Lett. 1993; 71(12):1852-1855.

[50] Yasuda H, Sakai A. Phys. Rev. B. 1997; 56(3):1069-1972.

[51] Shu C, Li CZ, He HX, Bogozi A, Bunch JS, Tao NJ. Phys. Rev. Lett. 2000; 84(22): 5196-5199.

[52] Ohnishi H, Kondo Y,Takayanagi K. Nature. 1998; 395(6704):780-783.

[53] Kizuka T, Umehara S, Fujisawa S. Japn. J. Appl. Phys. 2001; 40(1A/B): L71-L74.

[54] Ono T, Ooka Y, Miyajima H, Otani Y. Appl. Phys. Lett. 1999; 75(11):1622-1624.

[55] Gillingham DM, Linington I, Müller C, Bland JAC. J. Appl. Phys. 2003; 93(10): 7388-7389.

[56] Gillingham DM, Müller C, Bland JAC. J. Phys.: Cond. Matter. 2003; 15(19):L291-L296.

[57] Csonka Sz., Halbritter A, Mihály G, Jurdik E, Shklyarevskii OI, Speller S, van Kempen H. Phys. Rev. Lett. 2003; 90(11):116803.

[58] Untiedt C, Dekker DMT, Djukic D, van Ruitenbeek JM. Phys. Rev. B. 2004; 69:081401R.

[59] Arita M, Tajiri T, Hamada K, Miyagi H. J. Magn. Soc. Japn. 2005; 29(2):120-123, in Japanese.

[60] Ford EM, Dekker C, Schmid G. Appl. Phys. Lett. 1999; 75(3):421-423.

[61] Yakushiji K, Mitani S, Takanashi K, Takahashi S, Mekawa S, Imamura H, Fujimori H. Appl. Phys. Lett. 2001; 78(4):515-517.

[62] Hosoya H, Arita M, Hamada K, Takahashi Y, Higashi K, Oda K, Ueda M. J. Phys. D. 2006; 39(24):5103-5108.

[63] Arita M, Hirose R, Hamada K, Takahashi Y. Japn. J. Appl. Phys. 2006; 45(3B): 1946-1949.

[64] Arita M, Hirose R, Hamada K, Takahashi Y. Mater. Sci. Eng. C. 2006; 26(5-7):776-781.

[65] Simmons JG. J. Appl. Phys. 1963; 34(6):1793.

[66] Wulfhekel W, Klaua M, Ullmann D, Zavaliche F, Kirschner J, Urban R, Monchesky T, Heinrich B. Appl. Phys. Lett. 2001; 78(4):509-511.

[67] Kozicki MN, Park M, Mitkova M. IEEE Trans. Nanotechnol. 2005; 4(3):331-338.

[68] Sawa A. Mater. Today. 2008; 11(6):28-36.

[69] Chen A. Ionic Memory Technology. In: Kharton VV, editor. Solid State Electrochemistry II: Electrodes, Interfaces and Ceramic Membranes. 1st ed. Weinheim: Wiley-VCH; 2011.

[70] Kim KM, Hwang CS. Nanotechnol. 2011; 22(25):254002.

[71] Fujii T, Arita M, Hamada K, Takahashi Y, Sakaguch N. J. Appl. Phys. 2013; 113(8): 083701.

[72] Fujii T, Arita M, Takahashi Y, Fujiwara I. Appl. Phys. Lett. 2011; 98(21):212104.

[73] Fujii T, Arita M, Takahashi Y, Fujiwara I. J. Mater. Res. 2012; 27(6):886-896.

[74] Kudo M, Ohno Y, Hamada K, Arita M, Takahashi Y. ECS Trans. 2013; 58(5):19-25.

[75] Ohno Y, Hiroi T, Kudo M, Hamada K, Arita M, Takahashi Y. IEICE Tech. Rept ED. 2014; 113(449):89-94, in Japanese.

[76] Kudo M, Arita M, Ohno Y, Takahashi Y. Appl. Phys. Lett. 2014; 105(17):173504.

[77] Kondo H, Arita M, Fujii T, Kaji H, Moniwa M, Yamaguchi T, Fujiwara I, Yoshimaru M, Takahashi Y. Japn. J. Appl. Phys. 2011; 50(8):081101.

[78] Kwon DH, Kim KM, Jang JH, Jeon JM, Lee MH, Kim GH, Li XS, Park GS, Lee B, Han S, Kim M, Hwang CS. Nat. Nanotechnol. 2010; 5(2):148-153.

[79] Yang Y, Gao P, Gaba S, Chang T, Pan X, Lu W. Nat. Commun. 2012; 3:732.

[80] Liu Q, Sun J, Lv H, Long S, Yin K, Wan N, Li Y, Sun L, Liu M. Adv. Mater. 2012; 24(14): 1844-1849.

[81] Lee D, Seong D, Jo I, Xiang F, Dong R, Oh S, Hwang H. Appl. Phys. Lett. 2007; 90(12): 122104.

[82] Arita M, Kaji H, Fujii T, Takahashi Y. Thin Solid Films. 2012; 520(14):4762.

[83] Banno N, Sakamoto T, Iguchi N, Sunamura H, Terabe K, Hasegawa T, Aono M. IEEE Trans. Elect. Dev. 2008; 55(11):3283-3287.

[84] Bernard Y, Renard VT, Gonon P, Jousseaume V. Microelectr. Eng. 2011; 88(5):814-816.

Chapter 3

In-situ TEM Study of Dislocation-Interface Interactions

Nan Li and Jian Wang

Additional information is available at the end of the chapter

http://dx.doi.org/10.5772/60880

Abstract

In this chapter, we highlighted the in situ transmission electron microscope (TEM) observation of the interactions of dislocations with three types of interfaces: (i) twin boundaries in Cu; (ii) metallic interphase boundaries; and (iii) metal/ceramic interfaces. Interface structures, interface properties, and dislocation-interface interactions are characterized in a high-resolution TEM. These knowledge provided insights into the understanding of the physical properties of materials, developing materials modeling tools incorporating interface deformation physics, and designing materials with desired properties.

Keywords: Interfaces, dislocations, multilayers, TEM

1. Introduction

Extensive investigations over the past decade indicate that nanolayered composites have unprecedented levels of strength, ductility, and damage tolerance in extreme environments [1-10]. As the length-scale is reduced from micro- to nano-scales, interfaces become crucial in determining mechanical properties of nano-scale materials due to the change of deformation mechanisms from phase-dominated to interface-dominated [10]. Atomic-scale modeling is able to reveal unit processes (involving single or a few defects) occurring at interfaces during deformation with respect to kinetics and energetics, but is limited to time-scale (ns) and length-scale (nm) [11-21]. Current state-of-the-art micro-scale, meso-scale, and continuum scale modeling works well for micro-scale materials because of the dominated deformation processes by dislocation activities in phases. Due to the less dependence of deformation on interfaces, interfaces often are phenomenologically treated as boundaries without any

INTECH
open science | open minds

© 2015 The Author(s). Licensee InTech. This chapter is distributed under the terms of the Creative Commons Attribution License (http://creativecommons.org/licenses/by/3.0), which permits unrestricted use, distribution, and reproduction in any medium, provided the original work is properly cited.

structural characteristics [22-28]. For materials containing the high density of interfaces, it is still a challenge in incorporating interface physics, such as nucleation, motion, reactions, etc., in current models [29]. One of the bottlenecks is ascribed to the lack knowledge of interface-dominated deformation mechanisms because of the complexity of dislocation-interface interactions. To correlate the characteristics of interface with mechanical properties and behavior related to interfaces, it is essential to understand interfacial structure-property relationships at different scales and develop new materials modeling tools that incorporate interface physics and are able to address interface roles in terms of dislocation activity during mechanical deformation. Characterization of microstructures, defects, and defects interactions using ex situ and in situ microscopies has provided insights into understanding physical properties of materials, developing materials modeling tools incorporating interface deformation physics, and designing materials with desired properties [29].

In this chapter, we highlighted the in situ TEM observation of the interactions of dislocations with three types of interfaces: (i) twin boundaries in Cu; (ii) metallic interphase boundaries; and (iii) metal/ceramic interfaces. In situ nanoindentation tests were performed at room temperature in a Tecnai G(2) F30 microscope with a Nanofactory transmission electron microscopy-scanning tunneling microscopy (TEM-STM) platform. A Gatan CCD camera was used to capture the deformation of specimen during indentation with 3 frames/sec. The indenter tip made of W with a radius of 20 ~ 100 nm was pushed into the sample.

2. Twin boundaries in Cu

Metals with nanotwinned structure have received extremely high attention recently due to their unusual combination of properties of ultrahigh strength, high ductility, and high thermal stability, while still retaining the high electrical conductivity [30-42]. Twin boundaries surrounding a twin consist of coherent twin boundary and Σ3{112} incoherent twin boundaries (ITBs). Corresponding to crystallography of twins, the twinned and the matrix crystals have mirror symmetry across coherent twin boundary (CTB), causing the discontinuity of slip systems across CTBs. Thus, coherent twin boundaries can act as strong barriers for dislocation transmission, as demonstrated by both experiments and molecular dynamics (MD) simulations [41-47]. MD simulations have been used to explore the possible mechanisms for the transmission of a dislocation across a CTB with respect to the incoming dislocations and the stress states [48-54]. Using in situ TEM, ITBs have been observed to exert a crucial role over the mechanical deformation [55-61]. In this section, we characterized dislocation structure of Σ3{112} ITB in nanotwinned Cu, and investigated dislocation—CTB/ITB interactions using in situ TEM technique. Nanotwinned Cu is synthesized through physical vapor deposition on a 10% HF-etched Si (110) substrate at room temperature [34]. The chamber was evacuated to a base pressure of $\leq 5 \times 10^{-8}$ torr prior to deposition. The deposition rate was varied in the range of 0.6-4.0 nm s^{-1}.

2.1. Dislocation structure of Σ3 {112} ITB

Dislocation structure of Σ3{112} ITB was characterized according to the cross-sectional, high-resolution transmission electron microscope (HRTEM) image and dislocation theory. Figure

http://dx.doi.org/10.5772/60880

1a shows twin boundaries Σ3 {111} CTB oriented normal to the growth direction and Σ3 {112} ITB parallel to the growth direction. Along the Σ3 {112} ITB we observed a repeatable pattern with a unit involving three {111} atomic planes. Corresponding to crystallography of Σ3 twin, we constructed a schematic pattern of Σ3 {112} ITB as shown in Figure 1b. The {111} planes in the matrix crystal and in the twined crystal have a stacking sequence...ABCABC... and...ACBACB..., respectively. It is noticed that the stacking changing can be accomplished by the glide of any of the three Shockley partial dislocations, $\mathbf{b}_1$, $\mathbf{b}_2$, $\mathbf{b}_3$. They have Burgers vectors, ⅙, ⅙, and ⅙, respectively. By arranging the combination of these Shockley partial dislocations, ITB can be represented as different dislocation structures [59]. Molecular dynamics simulations and elastic analysis according to dislocation theory suggested a minimum energy interface that contains a repeatable sequence $\mathbf{b}_2$:$\mathbf{b}_1$:$\mathbf{b}_3$ on every {111} plane. The created ITB with such dislocations is consistent with the HRTEM observation [59]. In the absence of external stress, the compact ITB can spontaneously dissociate into two boundaries that are bonded with the 9R phase because of the reduction of dislocation core energy, i.e., one set of partials glide away from the initial compact ITB [62].

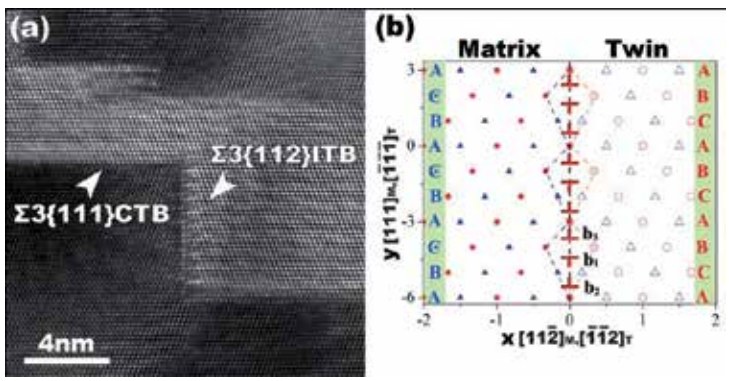

Figure 1. (a) HRTEM image showing atomic structures of both Σ3 {111} CTB and Σ3 {112} ITB. (b) A schematic illustration depicting the dislocation structure of Σ3 {112} ITB.

2.2. Migration of Σ3 {112} ITBs

By applying an in situ straining technique in a TEM, Σ3 {112} ITB migrates, corresponding to detwinning [60, 63]. Figure 2a shows the setup of a typical in situ nanoindentation experiment, where a nanotwinned Cu film is in contact with the W tip at the onset of an indentation test [60]. Three snapshots of the cross-sectional TEM (XTEM) micrographs, before indentation, at 33 seconds and at 55 seconds, show the migration of the two ITBs. The HRTEM micrograph in Figure 2e shows the migration unit, which is a 3-layer step and consistent with the unit of Σ3 {112} ITB.

The observed migration of Σ3 {112} ITBs thus can be explained from dislocation structure of the ITB. Atomistic simulations and topological model revealed that Σ3 {112} ITBs can be represented with a repeatable sequence $\mathbf{b}_2$:$\mathbf{b}_1$:$\mathbf{b}_3$ on every {111} plane that has net zero Burgers

vector [60, 63]. The attractive force between $\mathbf{b}_2$ and $\mathbf{b}_3$ groups them together to form paired partials. The partial dislocation $\mathbf{b}_1$ is easier to migrate than the paired partials because it experiences small Peierls barrier force [60, 63]. Under applied shear stress, the emitted partial dislocation $\mathbf{b}_1$ and the paired partials are subjected to the same magnitude but opposite-signed gliding force. Due to the high friction force on the paired partials, the dislocation $\mathbf{b}_1$ moves, meanwhile the interaction force drops. However, a load drop occurs around these dislocations due to the plastic strain associated with the motion of the dislocation $\mathbf{b}_1$, arresting the motion of the dislocation $\mathbf{b}_1$. The increasing stacking fault associated with the motion of dislocation $\mathbf{b}_1$ will pull the paired dislocations toward $\mathbf{b}_1$ until they again reach an equilibrium state.

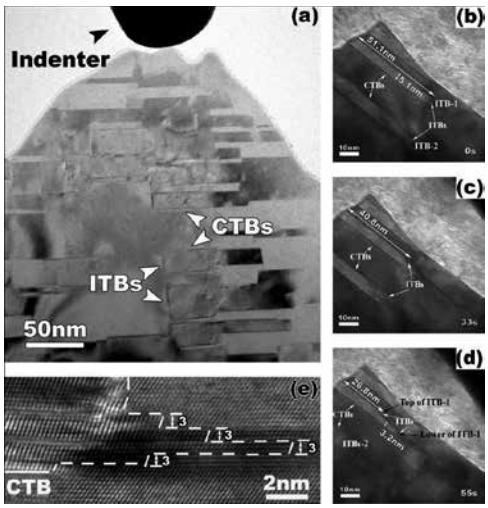

Figure 2. TEM images showing the migration of ITB in Cu. (a) Indentation tests, (b)-(d) three HRTEM images showing the position of Σ3 {112} ITB, and (e) the migration of Σ3 {112} ITB is accomplished via collective motion of three {111} atomic layers.

2.3. Dislocation-Σ3 {112} ITBs interactions

Figure 3 exhibits the dislocation-Σ3 {112} ITBs interaction and its influence on the migration of ITBs [61, 63]. In Figure 3a, we characterized an extended dislocation in the twin domain. After the dislocation entered into the ITB-1, we observed an emitted dislocation from the ITB-1 in the adjacent matrix (Figure 3b). Figure 3c shows the final structure of the ITB-1. Both its upper and lower sections have propagated towards the right, whereas the section that has a residual dislocation, $\mathbf{b}_r$, did not migrate. Using Burgers circuits we determine the Burgers vectors of incoming and emitted dislocations, respectively, while their line senses point into the paper. Figure 3d illustrates the dislocation-ITB interaction process. The incoming dislocation $\mathbf{b}_{in}$ glides on $\mathbf{B_TA_TC_T}$ (where T represents twin) and the Burgers vector could be either $\mathbf{B_TA_T}$ or $\mathbf{B_TC_T}$, since the screw component is invisible in the TEM image viewed along $\mathbf{A_TC_T}$. The emitted dislocation $\mathbf{b}_{out}$ glides on ACD plane and with the Burgers vector **AD** or **CD**. Assuming the incoming dislocation has Burgers vector $\mathbf{B_TA_T}$, the emitted dislocation should have Burgers vector **AD** or **CD**, minimizing the magnitude of the residual dislocation at the

http://dx.doi.org/10.5772/60880

ITB. The residual dislocation has the Burgers vector $\mathbf{b_r} = \mathbf{b_{in}} - \mathbf{b_{out}} = \mathbf{B_TA_T} - \mathbf{AD} = \mathbf{AB} - \mathbf{AD} = \mathbf{DB}$, which can be seen as $\mathbf{D\delta} + \mathbf{\delta B}$. As a result, the residual Frank dislocation is sessile and cannot glide on any {111} planes in either twin or matrix. Therefore, the migration of the ITB has been restrained.

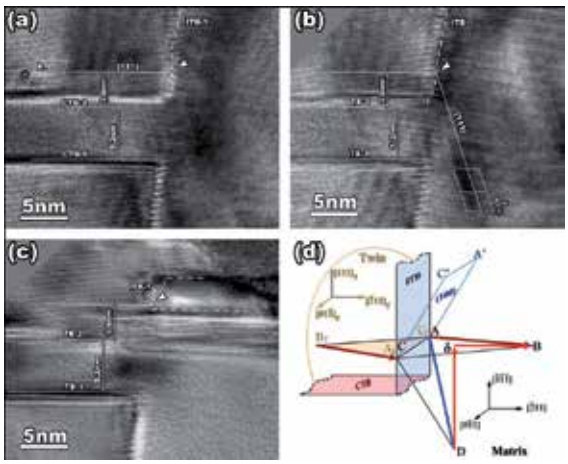

Figure 3. HRTEM images: (a) an extended dislocation in the twin domain and (b) an emitted dislocation in he matrix. The interaction position is indicated by the white arrow marks. $\mathbf{b_{in}}$, $\mathbf{b_{out}}$, and $\mathbf{b_r}$ are the incoming dislocation, the emitted dislocations, and the residual dislocation at ITB. (c) HRTEM image of the final stage of ITB-1 migration. The entire ITB has migrated except for the point at which slip transmission was observed. (d) Slip systems involved in slip transmission for a dislocation across ITBs.

2.4. Dislocation multiplication at coherent twin boundaries

Besides the well-known role of CTBs as barriers to block the movement of dislocations, in situ TEM experiments reveal a novel possibility that CTBs also facilitate the multiplication of Shockley partial dislocation [63, 64]. Figure 4 presents HRTEM snapshots of the interaction of a glide dislocation with a CTB, taken during dynamical loading. Figure 4a shows a HRTEM image—taken at 175.5s after the onset of the indentation experiment. Three dislocations close to the CTB are labeled as #1, #2, and #3. The stepped boundary suggests the formation of Shockley partial dislocations due to the interaction of glide dislocations with the CTB.

Corresponding to the configuration of the stepped coherent twin boundary, we labeled four segments as CTB-1, CTB-2, CTB-3, and CTB-4. During the observation period in the indentation experiment, we noticed that dislocations #1 and #2 and the segment CTB-1 did not move. For simplicity, CTB-1 is labeled as "0", corresponding to the reference position of the twin plane (Figure 4 a'). Under applied stress, we observed that the lattice dislocation #3 glides towards CTB-2, as identified in Figure 4 c. There is one extra {111} plane corresponding to the edge component of the dislocation normal to the CTB plane. During in situ TEM indentation test, the dislocation #3, a mixed 60° dislocation, glides towards the CTB. After 1 second, dislocation #3 entered the CTB-2. We observed one partial dislocation that is emitted into the adjacent matrix, and a sessile disconnection on the CTB (Figure 4b). Consequentially, we relabeled the CTB-2 with two segments separated by a sessile disconnection, the new segment is labeled as

CTB-2′. The most intriguing observation is that the CTB-2′ moves upward by three atomic planes (from -1 to +2), which implies that three Shockley partial dislocations nucleate and glide on the twin plane. Accompanying the migration of the CTB-2′, the CTB-3 also migrates upwards by five atomic planes (from -3 to +2), which is a result of the glide of the three newly nucleated Shockley partial dislocations. Figure 4d is one IFFT HRTEM snapshot, clearly showing a sharp step with the height of three {111} interplanar distances.

Corresponding to the change in the steps along the CTB, there are three possible mechanisms: (1) multiple transmission events of mixed dislocations, with each transmission producing one Shockley partial dislocation [65]; (2) nucleation of Shockley partial dislocations at the intersection of the CTB with the Σ3 {112} incoherent twin boundary (ITB) that runs almost vertically to the left of the HRTEM image in Figure 4a [60]; (3) multiple Shockley partial dislocations are generated due to the reaction of one lattice dislocation with the CTB. The first two mechanisms seem unlikely. First, TDs generated by multiple transmissions are unlikely to group together to form a sharp step due to their mutual repulsion [66, 67]. Secondly, if Shockley partial dislocations glide away from an adjoining ITB into the CTB, CTB-1 and CTB-2 would be displaced up or down by the same amount, more importantly, changing the positions of the dislocation #1 and #2 relative to the CTB-1.

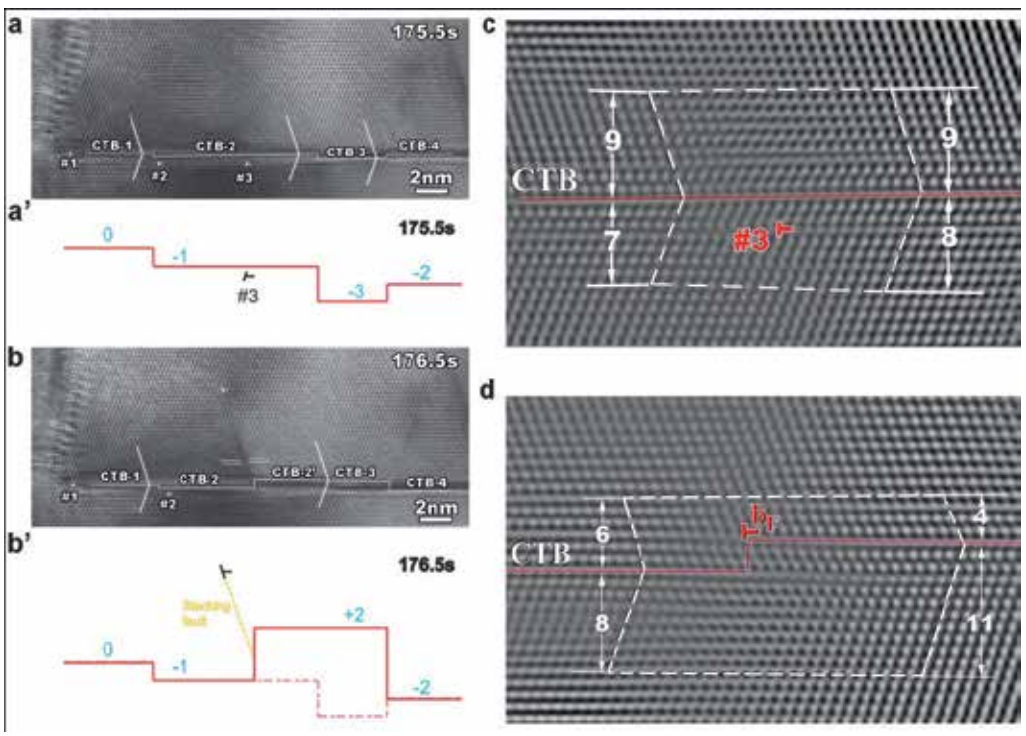

Figure 4. HRTEM images showing dislocation multiplication at a CTB. (a, a′) and (b, b′) illustrate the steps on the CTB before and after the dislocation-boundary reaction. Dislocation #1 and #2 did not move. The lattice dislocation #3 glides towards and enters CTB-2 after 1 second. (c) and (d) Magnified inverse fast Fourier transform (IFFT) HRTEM images showing dislocation #3 and a sharp step with the height of three {111} planes.

http://dx.doi.org/10.5772/60880

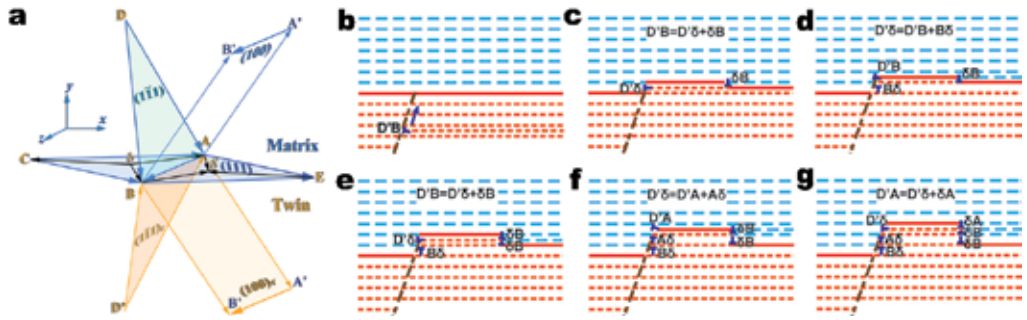

Figure 5. The orientation relation and several slip systems between twin and matrix. The CTB plane is defined as the (111) CBA plane with matrix above and twin below it. The *x*, *y*, and *z* directions are defined with respect to the matrix, along,, and, respectively. (b)-(g) Schematic illustration of the dislocation multiplication mechanism through the interaction of a mixed dislocation **D'B** with the twin boundary. A detailed description of the propagation process is given in the text.

The multiplication mechanism is schematically illustrated in Figure 5. The Thompson tetrahedron notation in Figure 5a shows the twin orientation relation and several slip systems that could be involved. The *x*, *y*, and *z* directions are defined with respect to the matrix, along,, and, respectively. Corresponding to the HRTEM image (Figure 4a), a full dislocation $\mathbf{b}_{in}$ with a ½<110> type Burgers vector (namely **D'B** in Figure 5a) on a {111} glide plane (namely in Figure 5a) glides towards the CTB (Figure 5b). Under compression due to the indentation, the suggested multiplication mechanism is presented as follows.

a. The lattice dislocation **D'B** glides towards the CTB (Figure 5b).

b. After the dislocation **D'B** encounters the CTB, it dissociates into a sessile Frank partial dislocation **D'δ** and a TD **δB**. The TD moves away from the intersection on the twin plane, resulting in the migration of the TB upwards by one atomic layer (Figure 5c). This initial dissociation had been confirmed in earlier MD simulations [34].

c. Once the partial **δB** moves away, the Frank partial **D'δ** could reassemble into a full dislocation accompanying the creation of a TD. This process is energetically un-favored. However, it could likely occur corresponding to plastic work and dislocation core reaction. Firstly, the dislocation core relaxes with a highly nonlinear energy change. The dissociation results new dislocations within a core dimension and the elastic energy is unchanged or slightly changed in the material. Secondly, the reassembly of a full dislocation from the Frank dislocation enables slip transmission, performing work. This reaction is very similar to that occurring at ratchet pole twinning generators and driven by the shear stress [68-71]. Correspondingly, the reaction is written as **D'δ = D'B + Bδ** or **D'δ = D'A+Aδ**. Once the dissociation is completed, the shear stress prevents the two partials **Bδ** and **δB** from annihilation, as shown in Figure 5 d.

d. The dislocation **D'B** then can experience a similar dissociation process as in (b) above. That is **D'B = D'δ + δB**. The shear stress causes the TD **δB** to move away, resulting in the migration of TB upward by one atomic layer (Figure 5e).

e. The residual dislocation **D'δ** can dissociate again as (c). However, with **Bδ** left by the 1st dissociation, the 2nd dissociation from **D'δ** to **D'A**+**Aδ** is favored energetically, as shown in Figure 5 f. The energy of the **Aδ/Bδ** pair, with a long-range energy equivalent to that of a single partial **δC** is much less than that of the pair 2**Bδ** that would result if the 2nd dissociation were D'δ to D'B+Bδ.

f. If the dislocation **D'A** dissociates into **D'δ** and **δA** again, and **δA** moves away under the shear stress, the twin boundary will migrate upward again by one atomic layer (Figure 5g). The left defect on the twin boundary is the sessile disconnection (**b** = **D'C**, h = height of three atomic layers), and **D'C** is the net of the three partials, **Bδ**, **Aδ**, and **D'δ**, respectively. The right defect on the twin boundary is the TD (**b** = **CB**, h = 3), and a net Burgers vector **CB** comprised of the partials δB, δB, and δA.

Accompanying with multiplication of Shockley partial dislocations at the CTB, the CTB will migrate upward and a stepped structure forms. The left comprises a step with an array of TDs in an alternating sequence **Bδ**: **Aδ**: **Bδ**: **Aδ**..., and one Frank partial **D'δ**. The right TD comprises a step with an array of TDs in a sequence of **δB**: **δB**: **δA**: **δB**: **δA**... on successive (111) planes. This mechanism provides a way to nucleate multiple TDs, causing the migration of CTBs. Of course, if the above operations are performed in the opposite sense, the twin boundary will migrate downward.

MD simulations were performed to further examine the multiplication mechanism proposed above. The simulation cell, shown in Figure 6a, contains about 24,000 Cu atoms with the coordinate systems of the x-axis along, the y-axis along, and the z-axis along. We initially disturb a group of atoms (10 atoms) with a displacement corresponding to half of a Shockley partial dislocation **δB** (Figure 6b). Figures 6c to 6e show several snapshots of nucleation and glide of two Shockley partial dislocations that form in accordance with the proposed mechanism. Accompanying the nucleation and glide of the dislocation **Bδ**, the Frank dislocation **D'δ** must locally shift upward as described previously, through a double-kink nucleation/core shuffle mechanism [65].

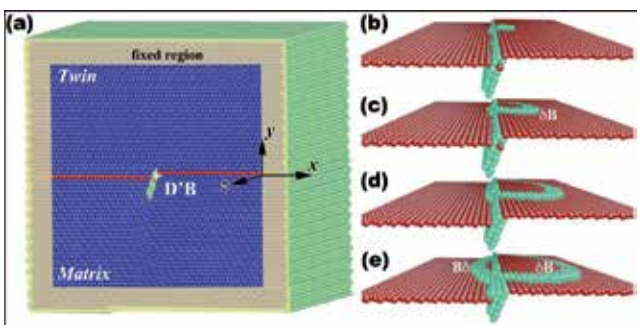

Figure 6. Molecular dynamics simulations: (a) Simulation cell, and four snapshots of the reaction mechanisms; (b) initial configuration (10 atoms are disturbed); (c) and (d) the nucleation and propagation of the TD δB; and (e) the glide of the other TD Bδ with the opposite sign in associated with the local climb of the dislocation D'B. Atoms are colored by common-neighbor-analysis. The red atoms represent stacking faults, relative to fcc.

http://dx.doi.org/10.5772/60880

3. Metallic interphase interfaces

Interfaces that act as sources, sinks, barriers, and storage sites for point and line defects strongly affect mechanical properties of materials [72-74]. Due to the controllability of dimensions and interface structures and properties, metallic multilayers that are synthesized using magnetic sputtering are good model systems to explore the effect of interfaces on the mechanical properties at different length scales ranging from nano- to micrometers [5, 10, 35, 75-89]. The strength of such metallic multilayers is significantly increased with decreasing layer thickness. Much of the mechanistic insights have been gained from computer simulations [13, 18, 90-93], but experimental measurements are limited to post mortem TEM of nano-indents, rolled, or fatigue samples [94-99]. Corresponding to the measured strength-layer thickness relation, the dominant deformation mechanisms in metallic multilayers have been postulated [5, 10] to vary with the layer thickness, from dislocation pile-up based Hall-Petch scaling law (layer thickness, $h \geq 50$ nm) to confined layer slip (CLS) (h around 5 ~ 50 nm), and ultimately to the interface resistance to single dislocation transmission ($h < 5$ nm). To elucidate the operation mechanisms of dislocations in multilayers at nanometer length scales, we performed in situ straining of Cu/Nb and Al/Nb multilayers in a TEM with the focus on interface structures, dislocation nucleation, dislocation climb, and interface shear resistance.

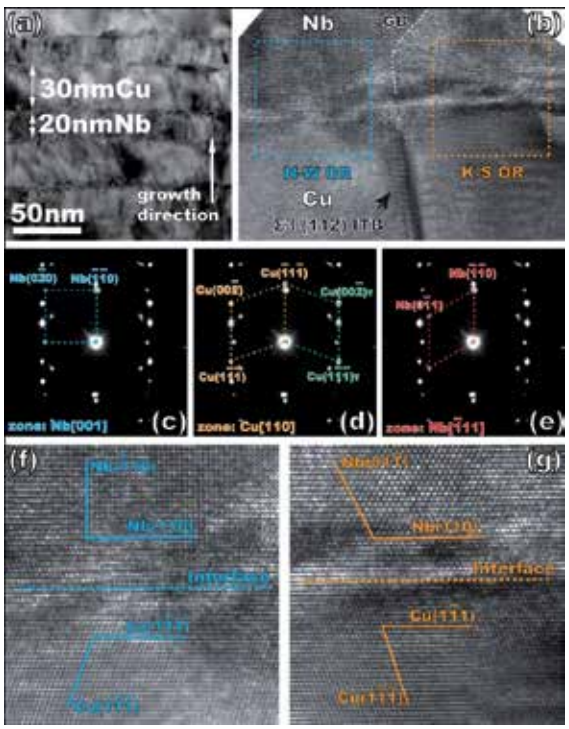

Figure 7. (a) Bright field TEM micrograph of Cu/Nb multilayer films with alternating layers of Cu (~30 nm) and Nb (~20 nm). (b) HRTEM image viewed from Cu [110], Nb [001] and Nb showing both K-S and N-W orientation relationships along Cu-Nb interface. (c)-(e) corresponding selected area diffraction pattern reveals Nb{110} || Cu{111} || Cu-Nb interface and twin orientation in Cu layer. (f) and (g) higher magnification images of N-W and K-S interface, respectively.

3.1. Interface structure

Bright field TEM micrograph of the cross-sectional view of the 20 nm Cu/Nb multilayers is shown in Figure 7 a. The interface is chemically sharp with no sign of intermixing. The dark shadow around interfaces is the strain contrast due to defects during the growth. The selected area diffraction patterns (SADP) shown in Figures 7 b-7dsuggest a quasi-single crystal film with a {110} Nb ||{111} Cu || interface plane. Diffraction pattern (DP) reveals that the Nb layers grow along <110> and the Cu layers grow along <111>. The DPs and the high-resolution TEM (HRTEM) images infer both Kurdjumov-Sacks (K-S, <001>Nb||<110>Cu) and Nishiyama-Wasserman (N-W, <111>Nb||<110>Cu) orientation relationships between Cu and Nb layers, as shown in Figures 7 f and 7g.

3.2. Dislocation nucleation

The in situ TEM has been performed at phase contrast imaging mode and explored the Shockley partial dislocations that nucleated at Cu/Nb interfaces. Figure 8a shows several stacking faults in Cu layers. With increasing strain, the stacking faults extend throughout the Cu layer as shown in Figures 8 b and 8c, and finally disappear, indicating that plastic deformation in Cu layers is carried over by full dislocations that nucleated from interfaces with the leading partial dislocation and trialing partial dislocation. Atomistic simulations have explored the nucleation mechanism of Shockley partial dislocations at interfaces, suggesting that the atomically flat KS interface can act as dislocation sources due to the presence of misfit dislocations [100]. In addition, during the indentation test, no deformation twins were observed even when the strain in some layers reaches ~50%, which is consistent with earlier post mortem TEM studies of rolled Cu-Nb multilayers [67, 101].

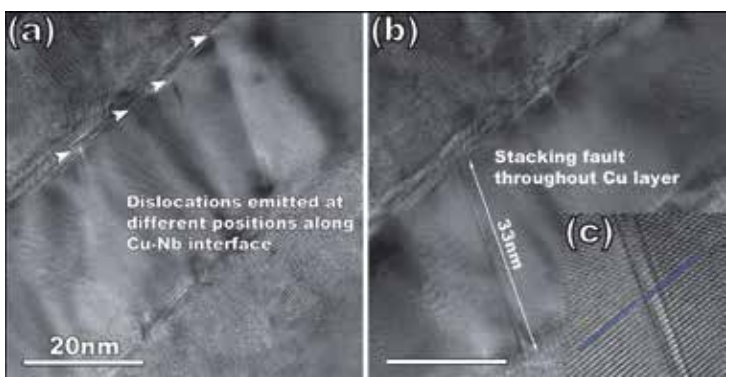

Figure 8. (a) HRTEM image shows several stacking faults generated in Cu, with the trailing partials trapped at Cu-Nb interface. (b) HRTEM image shows a stacking fault extending through the Cu layer. (c) Higher magnification image of the stacking fault in (b).

3.3. Confined layer slip

In situ nanoindentation is performed on the top surface of such multilayers under two-beam BF TEM mode, in which several threading dislocations with both ends pinned at the interfaces are seen as dark lines. However, images of loops gliding on the plane parallel to the electron

http://dx.doi.org/10.5772/60880

beam will not be visible. Figure 9 directly reveals the confined layer slip in both Cu and Nb layers. For simplicity, the discussion below is focused on observations made in the Cu layers. Two dislocations bow out under the applied stress as shown in Figure 9 a. With increasing stress, one new dislocation (marked as "III") nucleates and glides toward the same direction as the former two (Figure 9b) and two new dislocations (marked as "IV" and "V") nucleate and glide towards the opposite direction. With continuous compressive stress, the sixth dislocation (marked as "VI") nucleates. Four dislocations represented as blue dashed lines glide collectively towards the left, and the other two dislocations represented as yellow dashed lines glide towards the right. Since the TEM foil is under compressive stress, dislocations gliding to opposite directions should have opposite-signed Burgers vectors to each other. It is probable that two groups of dislocations glide on two different types of glide planes. As illustrated in Figure 9c', four dislocations with Burgers vector of **DB** glide to the left on a set of plane ABD, and the other two with opposite-signed Burgers vector glide towards the right on a set of plane BCD. Due to the frame rate limit of in situ TEM, there is another possible scenario regarding dislocations III and IV that belong to one loop expanding and then the threading arms moving in opposite directions but on the same plane.

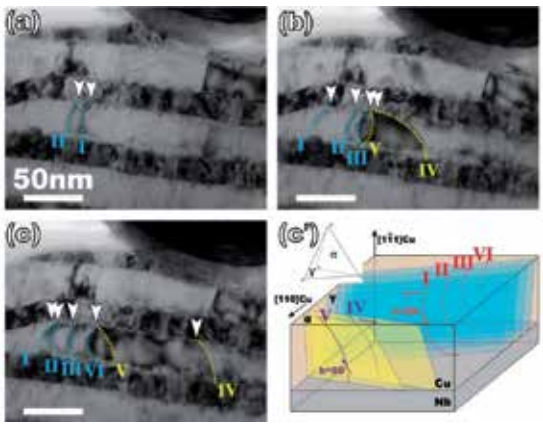

Figure 9. (a)-(c) A sequence of TEM movie images showing dislocation nucleation at Cu-Nb interfaces. Especially, two groups of dislocations glide in Cu layer towards opposite directions, which indicate they have opposite Burgers vector. (c') The corresponding schematic illustration shows the dislocations glide collectively on two sets of glide planes ABD and BCD.

3.4. Dislocations climb in interfaces

Figures 10a-d show a series of XTEM snapshots (processed by FFT) at different instants during a continuous loading process. Initially, two dislocations, labeled as $\mathbf{b_1}$ at the interface and $\mathbf{b_2}$ inside the Nb one atomic layer away from the interface, are separated by a distance, d_p, of 2.5 nm. d_p is measured along the direction parallel to the interface. After 2 seconds, d_p decreases to 1.7 nm as depicted in Figur 10b. The decrease in the separation distance via dislocation climb occurs at an average velocity of 0.4 nm/sec, two orders of magnitude larger than the climb velocity of dislocations in bulk Al lattice, ~0.001 nm/sec [102]. At 2.5 seconds, the two dislocations annihilate at the interface as shown in Fig. 10 c. The climb velocity is estimated to be 3.4 nm/sec, which is a lower bound estimation due to the big time step between frames. Finally, Figure 10d shows the annihilation of dislocations in the interface.

Dislocation climb involves mass transport via the absorption or emission of vacancies and/or interstitials [18, 103]. The climb rate depends on the concentration and diffusivity of point defects in the interface, in turn, depending on the formation energy of point defects [18, 90]. Figure 10e shows the mechanical work associated with the dislocation climb through the emission of one single vacancy as a function of the separation spacing d. When the vacancy formation energy is larger than the mechanical work (as discussed in Chapter 16 of *Theory of Dislocations*) [65], the dislocation climb is a thermal activated process [65]. Once the mechanical work is lower than the formation energy of vacancy, the climb becomes an athermal process with a sufficiently high rate. Corresponding to the formation energy of vacancy in bulk Al, 0.74 eV, we estimated the critical distance around 0.4 nm from the curve in Figure 10 e. However, the change of the climb velocity occurs at the distance of 1.7 nm (Figure 10b), suggesting that the athermal process begins below this critical distance. Correspondingly, we estimated the formation energy of vacancy from the curve (Figure 10e), 0.12 eV (a lower bound estimate). This energy is well in agreement with atomistic simulations [90].

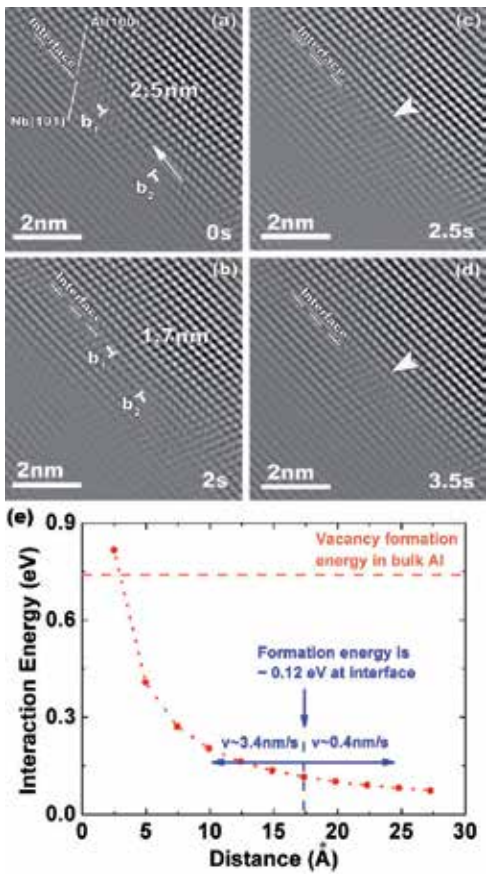

Figure 10. Dislocation annihilation process at Al/Nb interface. Two dislocations (a) with a separation of 2.4 nm at 0 second, (b) with a separation of 1.7 nm at 2 seconds, (c) annihilate each other at 2.5 seconds. (d) The interface becomes nearly perfect after dislocations annihilation At 3.5 seconds. (e) Mechanical work associated with the dislocation climb through the emission of one single vacancy from the dislocation as a function of the separation spacing d.

http://dx.doi.org/10.5772/60880

3.5. Interface shear strength

Using atomistic simulations, the critical stress corresponding to interfacial sliding is defined to be the interface shear strength [11, 104-107]. Molecular dynamics simulations have explored that Cu-Nb interface has a very low shear strength, significantly lower than the theoretical shear strengths of glide planes in perfect crystals of Cu and Nb [13, 108]. Using the push-out, full fragmentation and indentation tests in a SEM and TEM, people have measured interface strength (shearing and de-bonding) in experiments [5, 109-111]. However, the stress situation is rather complicated and thus many assumptions have to be made in interpreting experimental data.

Figure 11a shows the force versus displacement curve of an in situ compression test in TEM with compression axis at 25° off the pillar axis, while Figure 11b displays the starting microstructure. The sharp increase in load starting at the displacement of ~35 nm (Figure 11b) coincided with predominantly elastic behavior. At displacement of ~85 nm, load fluctuation was observed, indicative of the onset of dislocation activity. At this stage, the pre-existing dislocations might progressively glide out of the pillar and/or new dislocations might nucleate and glide from the interface and surfaces. At displacement of ~125 nm, the load steadily decreases. Comparing with the recorded video, we found that the steady decrease in force corresponds to the shearing of the pillar along the Cu-Nb interface. The microstructures immediately before and after failure are shown in Figure 11c and 11d.

We calculated the instantaneous shear stress at which the pillar failed, as shown in Fig. 11c'. The force is 63 uN and the Cu-Nb interface is 10° tilted away from the stage axis. The sheared Cu-Nb plane is approximately 224 nm in diameter. The critical shear strength of Cu-Nb interface is calculated to be 0.3 GPa. To ensure repeatability, several ex situ and in situ compression tests were performed, and the average shear strength of Cu-Nb interface is ~0.4 GPa among six tests, which is in good agreement with atomistic simulation [112] and evidences the concept of the easy nucleation and propagation of interfacial dislocations in a weak-shear interface [13, 113, 114].

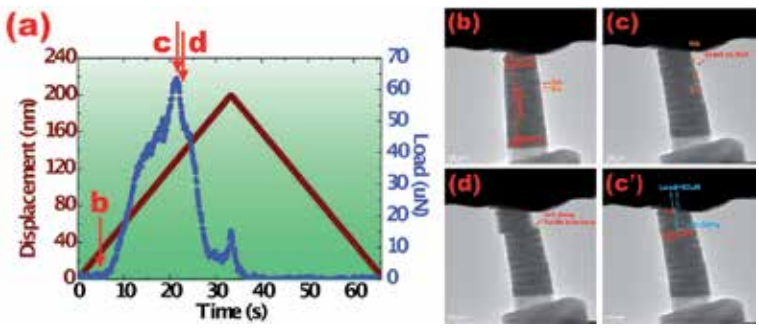

Figure 11. a) Force versus displacement curve of one typical pillar compression test. (b)-(d) Frames extracted from the video that correspond to the configuration of the pillar at the instances marked as b-d in (a), respectively. (c') displays the geometry relationship of compressed pillar with the indenter right before failure.

4. Metal/ceramic interfaces

Metal/ceramic multilayers with promising mechanical, physical, and chemical properties have been practically used in a wide range of temperatures, mechanical loadings, and environmental conditions [115-117]. One primary scientific interest stems partly from the large difference in strength and ductility between their constituent phases. By combining the two constitutes into a composite, the stronger constitute strengthens the composites while the ductile constitute make the composites ductile. In general, the mechanical properties of such composites have a low strength than the stronger constitute and a low ductility than the ductile constitute [118-132]. Ceramics are lacking in room temperature plasticity and fracture toughness [118, 119], although localized dislocation activity in ceramics at room temperature has been observed underneath the indenter [120-122]. However, for layered composites particularly with the individual layer thickness less than a few nanometers, both strength and ductility could be improved. Recent micro-pillar tests revealed plastic co-deformability in Al-TiN multilayers as the layer thickness less than 5 nm [133, 134]. In this section, we present our recent in situ TEM work on Al-TiN multilayers with various layer thicknesses, 50 nm, 5 nm and 2.7 nm, exploring the effect of reduced layer thickness on metal-ceramic plastic co-deformability [135].

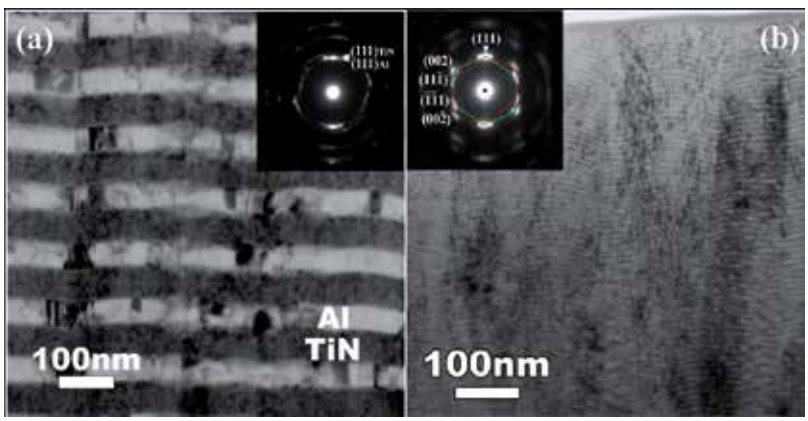

Figure 12. TEM images of the as-deposited films with the individual layer thickness (a) 50 nm and (b) 5 nm.

4.1. Interface structures

TEM images of the as-deposited films with the individual layer thickness 50 nm and 5 nm are shown in Figure 12. We characterized the orientation relation between the Al and TiN layers according to the diffraction patterns (DPs): (111)Al||(111)TiN||interface and <110>Al|| <110>TiN. The DPs indicate the epitaxial growth of Al and TiN within a column and the growth direction along <111>. The DP in Figure 2b also suggests that grains in a column may be misoriented with respect to each other by 60°, resulting in the formation of Σ3{112} incoherent twin boundaries (ITBs), as shown in Figure 13.

http://dx.doi.org/10.5772/60880

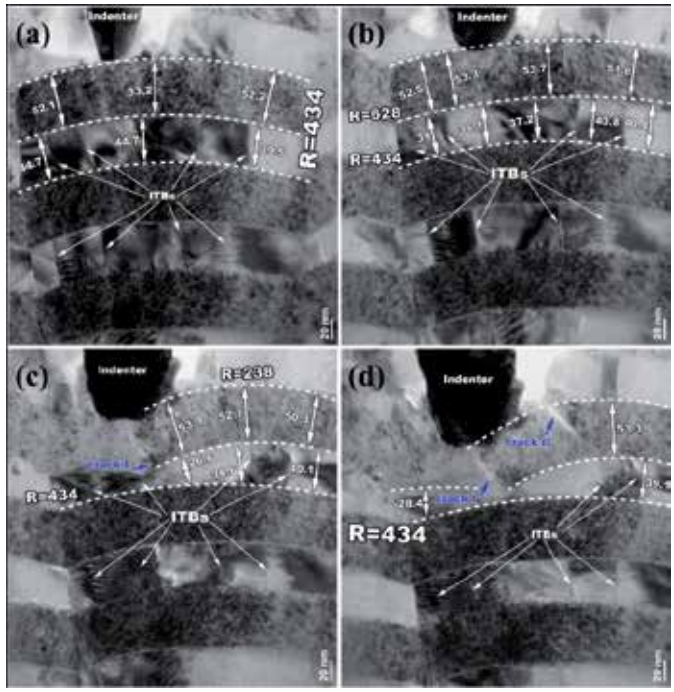

Figure 13. TEM images of the 50 nm Al-50 nm TiN multilayer during in situ indentation, showing the thickness reduction in the Al layers and cracks in the first TiN layer. Σ3{112} ITBs are present in the Al layers and migrate during indentation.

4.2. Deformation mechanism at large individual layer thickness (≥ 50 nm)

Four TEM images of the 50 nm Al-50 nm TiN multilayer during in situ indentation in Figure 13 show the thickness reduction in the Al layers and cracks in the first TiN layer and cracks in the first TiN layer. Being consistent with the DP in figure 12b, Σ3 {112} ITBs were identified in Al layers in one column (Figure 13a). During indentation testing, we observed that the thickness of the first Al layer beneath the indenter reduces from 45 nm to 37 nm to 27 nm (Figures 13a-c). Figures 14a and 14b show high-resolution TEM (HRTEM) images of Al-TiN interfaces before and after indentation. A low angle tilt boundary with the tilt angle of 9.4º was observed in the deformed Al-TiN interface, which is ascribed to the pileup of dislocations in the Al layer along the interface. However, the TiN layers are mainly subjected to elastic deformation and no detectable thickness reduction is measured in Figure 13. Consequently, we observed the first crack that is initiated in the TiN layer from the Al-TiN interface (Figures 13c and 14b) and the second crack that is initiated in the TiN layer from the top surface (Figures 13d and.14c). According to the crystallography of the TiN layer, the second crack surface is close to a {111} plane (Figure 14c). It is worthy of mentioning that the Al layer does not fracture associated with the opening of the crack (Figure 14d). Using finite element method we further studied the stress state associated with the crack initiation and found that both the cracks are initiated by the tensile stress (Figure 15).

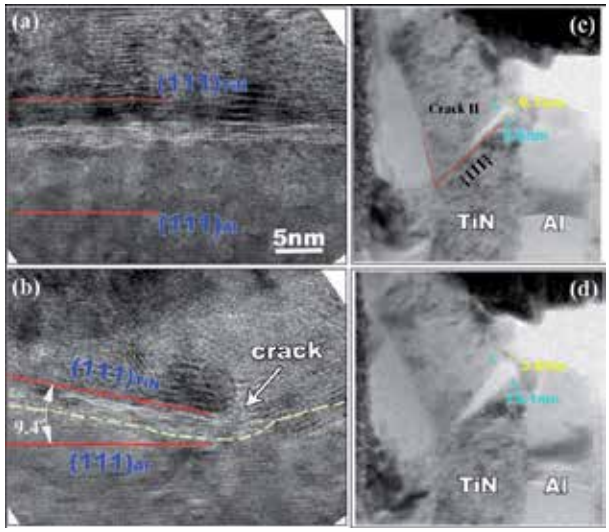

Figure 14. (a) and (b) HRTEM images of the Al-TiN interface before and after indentation. The red lines indicate the (111) plane. (c) and (d) Initiation and propagation of the crack II. The Al layer near the crack II does not fracture and the layer thickness reduces from 6.1 nm to 3.8 nm.

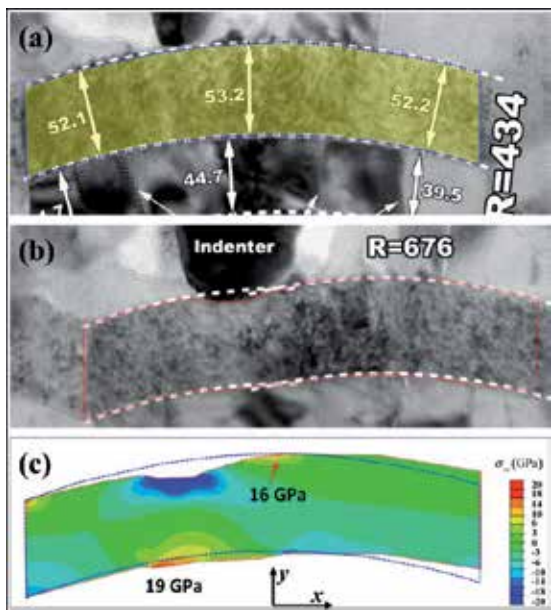

Figure 15. The change in the morphology of the first TiN layer during indentation, (a) the initial shape of the TiN layer before indentation and (b) the deformed TiN layer before cracking. The stress field was solved in the TiN layer with the displacement boundary condition, which is determined according to the morphology change from (a) to (b). The Young's modulus is 260 GPa and the Poisson's ratio is 0.30. Two high tensile stress regions are corresponding to the crack initiation.

http://dx.doi.org/10.5772/60880

4.3. Deformation mechanism when layer thickness is small (≤ 5 nm)

Plastic co-deformation was observed in the 5 nm Al-5 nm TiN multilayers and the 2.7 nm Al-2.7 nm TiN multilayer during in situ indentation. For the 5 nm Al-5 nm TiN multilayer, a significant plastic deformation beneath the indenter was measured in the first and second Al layers according to the change in layer thickness. Associated with the bending of the first TiN layer, the second Al layer reduces layer thickness from ~5.5 nm to ~1.9 (Figures 16a and 16b). The local radius of the first TiN layer beneath the indenter decreases from the initial infinity to the range of 102 ~ 156 nm (Figure 16b) and a slight reduction of the first TiN layer thickness is evidenced in the HRTEM images (Figures 16d and 16e) from 5.87 nm to 5.02 nm. Figure 16c shows the HRTEM image of a tilt boundary that is associated with the high density of dislocations in the Al layer and dislocation pile-up along the Al-TiN interface. Plastic deformation in TiN layers is achieved with the dislocations motion that is characterized in the TiN layer by the Burgers circuit (Figure 16f).

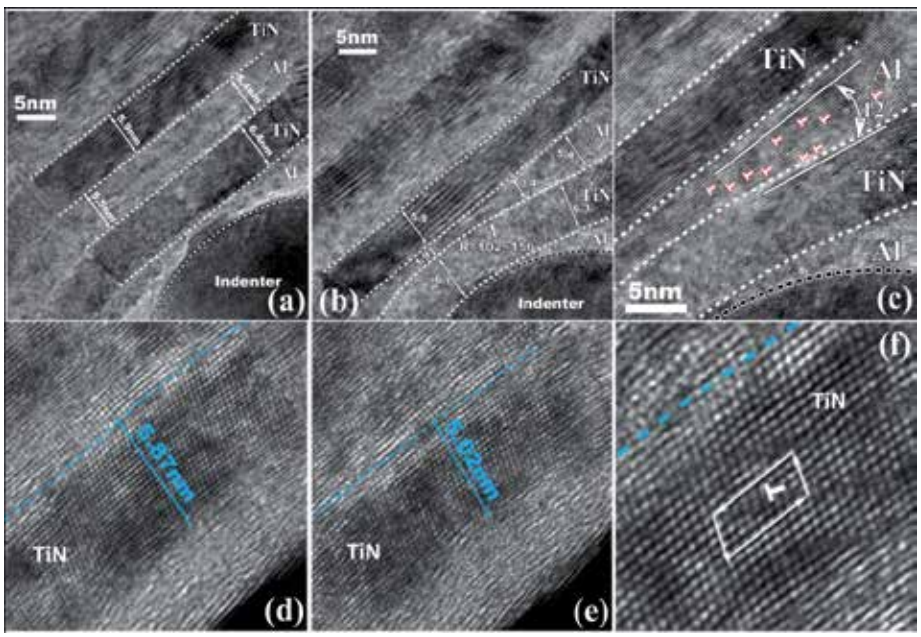

Figure 16. Plastic co-deformation in the 5 nm Al-5 nm TiN multilayers. (a) and (b) TEM images showing the reduction of thickness in the second Al layer. (c) A tilt boundary between the first TiN layer and the second Al layer, which is associated with the accumulation of dislocations in the Al layer and at the interface. Plastic deformation in the first TiN layer, (d) and (e) show the thickness reduction from 5.87 nm to 5.02 nm, and (f) a lattice dislocation identified by the Burgers circuit.

For the 2.7 nm Al-2.7 nm TiN multilayer, Figure 17c shows a highly coherent interface structure between the Al and TiN layers, this is due to the small lattice difference between Al and TiN and the fine layer thickness. During the film growth, Al atoms have a high diffusivity on Al (111) surface, facilitating the epitaxial growth of a flat Al layer. Consequently, the TiN layer will grow on a flat Al surface (111) and a sharp and flat Al-TiN interface forms. However, the

low diffusivity in the TiN layer may result in a relatively rough TiN (111) surface. The newly formed TiN-Al interface is relatively rough, reducing the contrast in terms of the coherent strain. Thus, the sharp Al-TiN interface benefits us to distinguish a bi-layer thickness (Figure 17c). A huge plastic deformation was measured according to the change in the first five bi-layers beneath the indenter, the thickness reduction in the first three bi-layers from 17.5 nm to 6.3 nm, corresponding to a strain of -64% (Figure 17d and 17e).

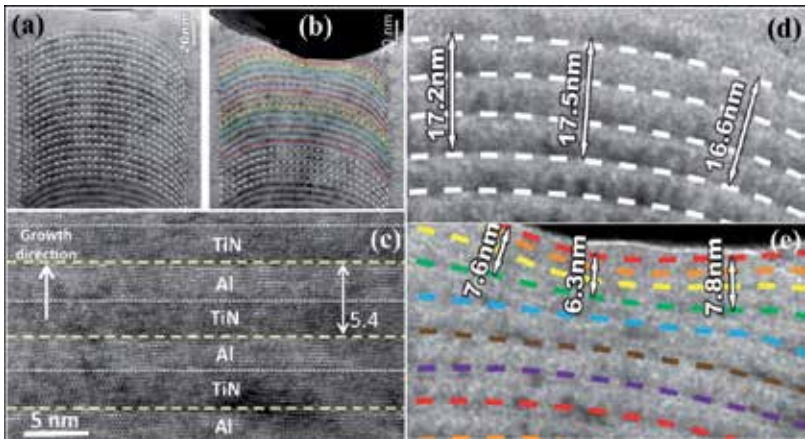

Figure 17. The 2.7 nm Al-2.7 nm TiN multilayer before (a) and during indentation (b). The bold dashed lines indicate the Al-TiN interfaces and the thin dashed indicate the TiN-Al interfaces. (d) and (e) Plastic deformation in first three bilayers corresponds to the thickness reduction from 17.5 nm to 6.3 nm.

5. Summary

Using in situ TEM, we studied the interactions of dislocations with three types of interfaces: (i) twin boundaries in Cu; (ii) metallic interphase boundaries; and (iii) metal/ceramic interfaces. For twin boundaries in face centered cubic structure, we characterized Σ3 {112} ITB with repeatable units of three Shockley partial dislocations. Such dislocation structure thus corresponds to detwinning of nanotwins, which is accomplished via stress-induced collective migration of Σ3 {112} ITB. When lattice gliding dislocations transmit across a Σ3 {112} ITB, we found that such transmission locally changes the dislocation structure of ITBs thereby pinning it against migration to higher levels of stress. More importantly, when a glide dislocation enters a Σ3 {111} CTB, Shockley partial dislocations can be multiplied via the dissociation of lattice dislocation. The fundamental understanding of the deformation behavior of metallic layered nanocomposites has been explored through in situ TEM observation: (1) the Cu-Nb interface acts as the preferred nucleation sites for glide dislocations and both Cu and Nb layers co-deform to large plastic strains without cracking via confined layer slip; (2) the Al/Nb interfaces can facilitate dislocation climb through vacancy diffusion, which result in the recovery of dislocation contents within interfaces, in agreement with the experimental observation in the

http://dx.doi.org/10.5772/60880

rolling of Cu/Nb multilayers; and (3) the Cu/Nb interface exhibits the low shear strength in the range of 0.3 to 0.55 GPa, and correspondingly, the plastic deformation may be localized along the interfaces when the shear stress on interface plane corresponding to any loading conditions reaches the interface shear strength. For metal-ceramics interface, a significant plastic co-deformation is only observed for the layer thickness in a few nanometers. For the layer thickness 5 nm and 2.7 nm, plastic deformation in TiN layer was measured according to the layer thickness reduction and plastic deformation mechanism was characterized with glide dislocations that have been identified in HRTEM images. For example in the 2.7 nm Al-2.7 nm TiN multilayer, the first five Al-TiN bi-layers beneath the indenter tip experience a significant elastic-plastic deformation of ~60% without detectable cracks, while retaining the interface plane orientation (111)Al||(111)TiN consistent with compatible plasticity between the Al and TiN layers.

Author details

Nan Li[1] and Jian Wang[1,2*]

*Address all correspondence to: wangj6@lanl.gov

1 Los Alamos National Laboratory, Los Alamos, NM, USA

2 Mechanical and Materials Engineering, University of Nebraska-Lincoln, Lincoln, NE, USA

References

[1] A. Misra, A. Gibala. Metall. Mater. Trans. A 30A, 991 (1999).

[2] R.G. Hoagland, T.E. Mitchell, J.P. Hirth, H. Kung. Philos. Mag. 82, 643 (2002).

[3] S.J. Zheng, I.J. Beyerlein, J.S. Carpenter, K. Kang, J. Wang, W.Z. Han, N.A. Mara. Nat. Commun. 4, 1696 (2013).

[4] I.J. Beyerlein, N.A. Mara, J.S. Carpenter, T. Nizolek, W.M. Mook, T.A. Wynn, R.J. McCabe, J.R. Mayeur, K. Kang, S.J. Zheng, J. Wang, M.P. Tresa. J. Mater. Res. 28, 1799 (2013).

[5] J. Wang, A. Misra. Curr. Opin. Solid State Mater. Sci. 15, 20 (2011).

[6] W.D. Sproul. Science 273, 889 (1996).

[7] B.M. Clemens, H. Kung, S.A. Barnett. MRS Bull. 24, 20 (1999).

[8] A. Misra, H. Kung. Adv. Eng. Mater. 3, 217 (2001).

[9] M.A. Phillips, B.M. Clemens, W.D. Nix. Acta Mater. 51, 3171 (2003).

[10] A. Misra, J.P. Hirth, R.G. Hoagland. Acta Mater. 53, 4817 (2005).

[11] J. Wang, R.G. Hoagland, J.P. Hirth, A. Misra. Acta Mater. 56, 5685 (2008).

[12] R.G. Hoagland, R.J. Kurtz, C.H. Jr Henager. Scr. Mater. 50, 775 (2004).

[13] J. Wang, R.G. Hoagland, A. Misra. Scr. Mater. 60, 1067 (2009).

[14] J. Wang, R.G. Hoagland, J.P. Hirth, A. Misra. Acta Mater. 56, 3109 (2008).

[15] M.J. Demkowicz, J. Wang, R.G. Hoagland, Dislocations in Solids, vol. 14, pp. 141-207 (chap.83). Editor: Hirth, J.P. Amsterdam: Elsevier North-Holland (2008).

[16] P.M. Derlet, P. Gumbsch, R.G. Hoagland, J. Li, D.L. McDowel, H. Van Swygenhoven, J. Wang. MRS Bull. 34, 184 (2009).

[17] X.Y. Liu, R.G. Hoagland, J. Wang, T.C. Germann, A. Misra. Acta Mater. 58, 4549 (2010).

[18] J. Wang, R.G. Hoagland, A. Misra. Appl. Phys. Lett. 94, 131910 (2009).

[19] J. Wang, A. Misra, R.G. Hoagland, J.P. Hirth. Acta Mater. 60, 1503 (2012).

[20] S. Shao, J. Wang, A. Misra, R.G. Hoagland. Sci. Rep. 3, 2448 (2013).

[21] I.J. Beyerlein, J. Wang, K. Kang, S.J. Zheng, N.A. Mara. Mater. Res. Lett. 1, 89 (2013).

[22] C.A. Bronkhorst, S.R. Kalidindi, L. Anand. Philos. Trans. R. Soc. Lond. A 341, 443 (1992).

[23] H.M. Mourad, K. Garikipati. Comput. Methods Appl. Mech. Eng. 196, 595 (2006).

[24] M.R. Tonks, J.F. Bingert, C.A. Bronkhorst, E.N. Harstad, D.A. Tortorelli. J. Mech. Phys. Solids 57, 1230 (2009).

[25] H. Wang, P.D. Wu, C.N. Tome, J. Wang. Mater. Sci. Eng. A 555, 93 (2012).

[26] H. Wang, P.D. Wu, J. Wang, C.N. Tome. Int. J. Plast. 49, 36 (2013).

[27] H. Wang, P.D. Wu, J. Wang. Int. J. Plast. 47, 49 (2013).

[28] H. Wang, P.D. Wu, C.N. Tome, J. Wang. Int. J. Solids Struct. 49, 2155 (2012).

[29] J. Wang. JOM 63 (9), 57 (2011).

[30] J.W. Christian, S. Mahajan. Prog. Mater. Sci., 39, 1 (1995).

[31] L. Lu, X. Chen, X. Huang, K. Lu. Science 323, 607 (2009).

[32] L. Lu, Y. Shen, X. Chen, L. Qian, K. Lu, Science 304, 422 (2004).

[33] E. Ma, M. Wang, Q.H. Lu, M.L. Sui, L. Lu, K. Lu. Appl. Phys. Lett. 85, 4932 (2004).

[34] X.Y. Li, Y.J. Wei, L. Lu, Ke Lu, H. J. Gao. Nature 464, 877 (2010).

[35] T. Zhu, Ju Li. Prog. Mater. Sci. 55, 710 (2010).

[36] X. Zhang, H. Wang, X.H. Chen, L. Lu, K. Lu, R.G. Hoagland, A. Misra. Appl. Phys. Lett. 88, 173116 (2006).

[37] O. Anderoglu, A. Misra, H. Wang, X. Zhang. J. Appl. Phys. 103, 094322 (2008).

[38] X. Zhang, A. Misra, H. Wang, J.G. Swadener, A.L. Lima, M.F. Hundley, R.G. Hoagland. Appl. Phys. Lett. 87, 233116 (2005).

[39] M. Dao, L. Lu, Y.F. Shen, S. Suresh. Acta Mater. 54, 5421 (2006).

[40] O. Anderoglu, A. Misra, H. Wang, F. Ronning, M.F.Hundley, X. Zhang. Appl. Phys. Lett. 93, 083108 (2008).

[41] X. Zhang, O. Anderoglu, R.G.Hoagland, A. Misra. JOM 60 (9), 75 (2008).

[42] C.J. Shute, B.D. Myers, S. Xie, S.-Y. Li, T.W. Barbee, Jr., A.M. Hodge, J.R. Weertman. Acta Mater. 59, 4569 (2011).

[43] V. Yamakov, D. Wolf, S. R. Phillpot, A. K. Mukherjee, H. Gleiter, Nature Mater. 3, 43 (2004).

[44] V. Yamakov, D. Wolf, S.R. Phillpot, H. Gleiter. Acta Mater. 50, 5005 (2002).

[45] K.S. KumarH. Van Swygenhoven, S. Suresh. Acta Mater. 51, 5743 (2003).

[46] H. van Swygenhoven, P.M. Derlet, A.G. Frøseth. Nature Mater. 3, 399 (2004).

[47] O. Anderoglu, A. Misra, J. Wang, R.G. Hoagland, J.P. Hirth, X. Zhang. Int. J. Plast. 26, 875 (2010).

[48] J. Wang, H. Huang. Appl. Phys. Lett. 88, 203112 (2006).

[49] T. Zhu, J. Li, A. Samanta, H.G. Kim, S. Suresh. Proc. Natl. Acad. Sci. U.S.A. 104, 3031 (2007).

[50] K.A. Afanasyev, F. Sansoz. Nano Lett. 7, 2056 (2007).

[51] Z.H. Jin, P. Gumbsch, K. Albe, E. Ma, K. Lu, H. Gleiter, H. Hahn. Acta Mater., 56, 1126 (2008).

[52] T.C. Lee, I.M. Robertson, H.K. Birnbaum. Philos. Mag. A 62, 131 (1990).

[53] T.C. Lee, I.M. Robertson, H.K. Birnbaum. Metall. Trans. A 21A, 2437 (1990).

[54] Y.B. Wang, M.L. Sui. Appl. Phys. Lett. 94, 021909 (2009).

[55] J.K. Rittner, D.N. Seidman, K.L. Merkle. Phys. Rev. B 53, R4241 (1996).

[56] G. Lucadamo, D.L. Medlin. Science 300, 1272 (2003).

[57] D.L. Medlin, G.H. Campbell, C.B. Carter. Acta Mater. 46, 5135 (1998).

[58] J.A. Brown, N.M. Ghoniem. Acta Mater. 57, 4454 (2009).

[59] J. Wang, O. Anderoglu, J.P. Hirth, A. Misra, X. Zhang. Appl. Phys. Lett. 95, 021908 (2009).

[60] J. Wang, N. Li, O. Anderoglu, X. Zhang, A. Misra, J.Y. Huang, J.P. Hirth. Acta Mater. 58, 2262 (2010).

[61] N. Li, J. Wang, J.Y. Huang, A. Misra, X. Zhang. Scr. Mater. 64, 149 (2011).

[62] J. Wang, A. Misra, J.P. Hirth. Phys. Rev. B 83, 064106 (2011).

[63] N. Li, J. Wang, X. Zhang, A. Misra. JOM 63(9), 62 (2011).

[64] N. Li, J. Wang, A. Misra, J.Y. Huang, J.P. Hirth. Acta Mater. 59, 5989 (2011).

[65] J. P. Hirth, J. Lothe, Theory of dislocations. New York: Wiley; 1982.

[66] C.H. Jr Henager, R.J. Kurtz, R. G. Hoagland. Philos. Mag. 84, 2277 (2004).

[67] A. Misra, J. P. Hirth, R. G. Hoagland, J. D. Embury, H. Kung. Acta Mater. 52, 2387 (2004).

[68] R. Priestner, W. C. Leslie. Philos. Mag. 11, 895 (1965).

[69] Z. S. Basinski, M. S. Szczerba J. D. Embury. In: Yoo MH, Wuttig M, editors. Twinning in advanced materials. Warrendaale, PA: TMS 1994.

[70] K.P. D. Lagerlof, J. Castaing, P. Pirouz, A. H. Heuer. Philos. Mag. 82A, 2841 (2002).

[71] Y.T. Zhu, X.L. Wu, X.Z. Liao, J. Narayan, L.J. Kecskes, S.N. Mathaudhu. Acta Mater. 59, 812 (2011).

[72] A.P. Suutton, R.W. Balluffi. *Interfaces in crystalline materials*. Oxford: Oxford University Press (1995).

[73] J.P. Hirth. Metall Trans 3, 3047 (1972).

[74] N. Li, J. Wang, A. Misra, J.Y. Huang. Microscopy and Microanalysis 18, 1155 (2012).

[75] A. Misra, M. Verdier, Y. C. Lu, H. Kung, T. E. Mitchell, M. Nastasi. Scr. Mater. 39, 555 (1998).

[76] P.M. Anderson, C. Li. Nanostruct Mater. 5, 349 (1995).

[77] P.M. Anderson, T. Foecke, P. M. Hazzledine. MRS Bull 24, 27 (1999).

[78] P.M. Anderson, J. S. Carpenter. Scr. Mater. 62, 325 (2010).

[79] L.H. Friedman, D.C. Chrzan. Phys. Rev. Lett. 81, 2715 (1998).

[80] C.S. Pande, R. A. Masumura, R.W. Armstrong. Nanostruct Mater. 2, 323 (1993).

[81] I.J. Beyerlein, J. Wang, R. Zhang. Acta Mater. 61, 7488 (2013).

[82] S.I. Rao, P.M. Hazzledine. Philos. Mag. A 80, 2011 (2000).

[83] C. H. Jr Henager, R. J. Kurtz, R.G. Hoagland. Philos. Mag. 84, 2277 (2004).

[84] J.P. Hirth, R.C. Pond, R.G. Hoagland, X.Y. Liu, J. Wang. Prog. Mater. Sci. 58, 749 (2013).

[85] I.J. Beyerlein, J. Wang, K. Kang, S.J. Zheng, N.A. Mara. Mater. Res. Lett. 1, 89 (2013).

[86] W.D. Nix. Metall Trans A 20A, 2217 (1989).

[87] J. Wang, R.F. Zhang, C.Z. Zhou, I.J. Beyerlein, A. Misra. Int. J Plast. 53, 40 (2014).

[88] N. Abdolrahim, I.N. Mastorakos, H.M. Zbib. Phys. Rev. B 81, 054117 (2010).

[89] N.R. Overman, C.T. Overman, H.M. Zbib, D.F. Bahr. J. Eng. Mater. Technol. 131, 041203 (2009).

[90] M.J. Demkowicz, R.G. Hoagland, J.P. Hirth. Phys. Rev. Lett. 100, 136102 (2008).

[91] R.G. Hoagland, J.P. Hirth, A. Misra, Philos. Mag. 86, 3537 (2006).

[92] S.S. Quek, Y. Xiang, Y. W. Zhang, D. J. Srolovitz, C. Lu. Acta Mater. 54, 2371 (2006).

[93] S.S. Quek, Y. W. Zhang, Y. Xiang, D. J. Srolovitz. Acta Mater. 58, 226 (2010).

[94] N.A. Mara, D. Bhattacharyya, P. Dickerson, R. G. Hoagland, A. Misra. Appl. Phys. Lett. 92, 231901 (2008).

[95] N.A. Mara, D. Bhattacharyya, J. P. Hirth, P. Dickerson, A. Misra. Appl. Phys. Lett. 97, 021909 (2010).

[96] I.J. Beyerlein, N. A. Mara, D. Bhattacharyya, D. J. Alexander, C. T. Necker. Int. J. Plast. 27, 121 (2010).

[97] P.M. Anderson, J.F. Bingert, A. Misra, J.P. Hirth. Acta Mater. 51, 6059 (2003).

[98] X. F. Zhu, B. Zhang, J. Gao, G. P. Zhang. Scr. Mater. 60, 178 (2009).

[99] Y. P. Li, G. P. Zhang. Acta Mater. 58, 3877 (2010).

[100] R. F. Zhang, J. Wang, I. J. Beyerlein, T. C. Germann. Scr. Mater. 65, 1022 (2011).

[101] A. Misra, X. Zhang, D. Hammon, R. G. Hoagland. Acta Mater. 53, 221 (2005).

[102] N. Li, J. Wang, J.Y. Huang, A. Misra, X. Zhang. Scr. Mater. 63, 363 (2010).

[103] E.G. Fu, N. Li, A. Misra, R.G. Hoagland, H. Wang, X. Zhang. Mater. Sci. Eng. A 493, 283 (2008).

[104] J. Wang, C. Zhou, I. J. Beyerlein, S. Shao. JOM 66(1), 102 (2014).

[105] F. Sansoz, J.F. Molinari. Scr. Mater. 50, 1283 (2004).

[106] S. Ogata, J. Li, S. Yip. Science 298, 807 (2002).

[107] S. Ogata, N. Hirosaki, C. Kocer, Y. Shibutani. J. Mater. Res. 18, 1168 (2003).

[108] N.I. Medvedeva, Y.N. Gornostyrev, O.Y. Kontsevoi, A.J. Freeman. Acta Mater. 52, 675 (2004).

[109] P.J. Withers, J.A. Bennett, M. Kuroda. Acta Mater. 58, 6090 (2010).

[110] T.E. Matikas. Adv. Compos. Mater. 17, 75 (2008).

[111] N. Li, N.A. Mara, J. Wang, P. Dickerson, J.Y. Huang, A. Misra. Scr. Mater. 67, 479 (2012).

[112] Z. Shen, R.H. Wagoner, W.A.T. Clark. Acta Metall. 36, 3231 (1988).

[113] N.I. Medvedeva, Y.N. Gornostyrev, O.Y. Kontsevoi, A.J. Freeman. Acta Mater. 52, 675 (2004).

[114] J.R. Greer, J.Th.M. De Hosson. Prog. Mater. Sci. 56, 654 (2011).

[115] G. Abadias, S. Dub, R. Shmegera. Surf. Coat. Technol. 200, 6538 (2006).

[116] I. Salehinia, S. Shao, J. Wang, H. M. Zbib. JOM 66(10), 2078 (2014).

[117] S. B. Sinnott, E. C. Dickey. Mater. Sci. Eng. R Rep. 43, 1 (2003).

[118] W. D. Kingery, H. K. Bowen, D. R. Uhlmann. *Introduction to Ceramics*, 2nd edn. Wiley (1975).

[119] L. E. Toth, *Transition Metal Carbides and Nitrides*. Academic Press (1971).

[120] M. Oden, H. Ljungcrantz, L. Hultman. J. Mater. Res.12, 2134 (1997).

[121] A. M. Minor, E. A. Stach, J. W. Morris, I. Petrov. J. Elec. Mater. 32, 1023 (2003).

[122] J. D. Embury, J. P. Hirth. Acta Metall. Mater. 42, 2051 (1994).

[123] D. R. P. Singh, N. Chawla, G. Tang, Y.L. Shen. Acta Mater. 58, 6628 (2010).

[124] X. Deng, N. Chawla, K. K. Chawla, M. Koopman, J. P. Chu. Adv. Eng. Mater. 7, 1099 (2005).

[125] W. M. Mook, R. Raghavan, J. Baldwin, D. Frey, J. Michler, N. A. Mara, A. Misra. Mater. Res. Lett. 1, 102 (2013).

[126] D. Bhattacharyya, N. A. Mara, P. Dickerson, R.G. Hoagland, A. Misra. Philos. Mag. 90, 1711 (2010)

[127] S. A. Barnett, A. Madan. Scr. Mater. 50, 739 (2004).

[128] I. Salehinia, J. Wang, D. F. Bahr, H. M. Zbib. Int. J. Plast. 59, 119 (2014).

[129] A. Duck, N. Gamer, W. Gesatzke, M. Griepentrog, W. Osterle, M. Sahre, I. Urban. Surf. Coat. Technol. 142-144, 579 (2001).

[130] X. Deng, C. Cleveland, N. Chawla, T. Karcher, M. Koopman, K. K. Chawla. J. Mater. Eng. Perform. 14, 417 (2005).

[131] P. L. Sun, J.P. Chu, T.Y. Lin, Y.L. Shen, N. Chawla. Mater. Sci. Eng. A 527, 2985 (2010).

[132] G. Tang, Y.L. Shen, D. R. P. Singh, N. Chawla. Acta Mater. 58, 2033 (2010).

[133] D. Bhattacharyya, N. A. Mara, P. Dickerson, R.G. Hoagland, A. Misra. Acta Mater. 59, 3804 (2011).

[134] J. Wang, A. Misra. Curr. Opin. Solid State Mater. Sci. 18, 19 (2014).

[135] N. Li, H. Wang, A. Misra, J. Wang. Sci. Rep. 4, 6633 (2014).

Chapter 4

Shave-Off Profiling for TEM Specimens

Masashi Nojima

Additional information is available at the end of the chapter

http://dx.doi.org/10.5772/60682

Abstract

This work aims to compare the results from the same specimens between shave-off profiling and TEM image. For the cross-check analysis, a specimen was picked up from a part was failed integrated chip (IC) package that may have suffered electrochemical migration. Critical disagreement between the results was found in the gradient curve of the shave-off profiling from the anode to the cathode. In each package, shave-off profiling revealed a faint gradient curve on migrated ions that could not be revealed from TEM image.

Keywords: shave-off profiling, cross-check with TEM, failure analysis

1. Introduction

In this study, we aimed to cross-check the same specimen, the same part and the same piece by using TEM imaging and shave-off profiling. The introduction of different analytical methods allows one specimen to be clarified from different and multiple angles. Agreement of the cross-check analysis provides reliability for each experimental result, whereas disagreement reveals the possibility that something has been overlooked in the other analytical results.

Cross-check analysis is usually carried out on the same specimen but at different points. For failure analysis, it is indispensable to cross-check the same specimen and the same point. We introduce two different analytical methods: TEM, which provides a projected image of the nanostructure with almost no damage, and shave-off profiling, which can reconstruct elemental distributions but the specimen completely disappeared. We have cross-checked the TEM specimens against the shave-off profiling specimens.

INTECH
open science | open minds

© 2015 The Author(s). Licensee InTech. This chapter is distributed under the terms of the Creative Commons Attribution License (http://creativecommons.org/licenses/by/3.0), which permits unrestricted use, distribution, and reproduction in any medium, provided the original work is properly cited.

2. Shave-off profiling

2.1. Shave-off depth profiling

Shave-off depth profiling has basically originated from shaving process with a focused ion beam (FIB) and secondary ion mass spectrometry (SIMS). The volume of the specimen for shave-off depth profiling is almost the same as that prepared for TEM. Both specimens are micromachined and picked up with the FIB microsampling technique. The only difference is the thickness of the microsampled specimen. A thickness of the order of submicrometers is suitable for TEM specimens, while shave-off profiling specimens are typically several micrometers thick [1].

Figure 1 shows the shave-off depth profiling procedures. At first, a piece is picked up from the surface of the specimen by the FIB lift-up technique (1, 2). The piece is then placed on another substrate, and the substrate and specimen are tilted so that they are parallel to the axis of focused beams (3). The FIB then shaves off the specimen layer by layer (4), generating secondary ions that are mass-separated and monitored as a function of depth. Shave-off depth profiling is able to be applied to almost all solid state materials, even for rough structures and heterointerfaces.

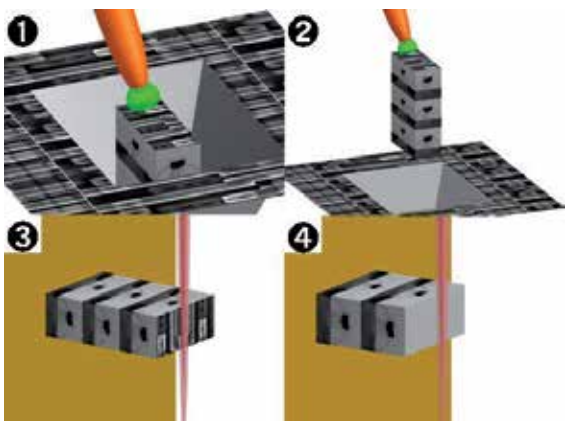

Figure 1. Schematic sequence of shave-off depth profiling

Detailed features of shave-off depth profiling have been noted in our previous paper [2]. The nanobeam SIMS system was significantly modified for shave-off depth profiling purposes [3].

2.2. Shave-off vector profiling

In respect to shave-off depth profiling, the "depth" only has meaning for the shave-off directions of specimen. The shave-off direction can be controlled by rotating the field of view, and the approach of "shave-off vector profiling" is a powerful technique for depth-profiled SIMS.

http://dx.doi.org/10.5772/60682

This study is focused on the lateral distribution of electrochemically migrated elements within a semiconductor package. All semiconductor packages are consisted of fillers, carbon black particles and resin. When the semiconductor packages are exposed to high-temperature, high-moisture conditions, metal elements on chip electrochemically migrate into the resin or onto the semiconductor chip board [4]. For failure analysis, the distribution of the migrated ions provides important information. Ion diffusion phenomena to the resin have been studied by using time-of-flight SIMS [5]; however, such depth profiling over a wide area dilutes true local information about failure points. Shave-off depth profiling has been used successfully to visualize the migration of Cu ions from electrodes into the resin within a point of failure [6]; the profile projected a distribution of migrated Cu ions to the depth direction.

The distribution of the migrated ions between the anode and cathode also provides important information about how electrochemical migration occurs between the electrodes. In this study, the shave-off direction was vectored to be that in the direction from the anode to the cathode.

3. Experiment

In the test semiconductor packages, chips are packed with silica fillers, carbon black particles and resin. The surfaces of test chips are mounted on Cu electrodes (10 μm line and space each reputational width) and Ti thin films (40 nm). Pairs of electrodes were biased in high-temperature, high-moisture conditions (10 V, 400 K, 85% relative humidity). Some semiconductor packages began to display unusual conductivities within 400 h. Electrochemical migration may have occurred in failed semiconductor packages. A piece including the electrodes, fillers, carbon black particles and resin was picked up in the FIB microsampling chamber (FB-2000; Hitachi High-Tech. Co. Ltd.). The piece had a thickness of 1 μm, which is slightly thick for TEM samples but sufficient for shave-off profiling. Figure 2 shows a scanning ion (SI) image of the piece. Fillers appear as dark contrast in the SI image. Rectangular regions of bright contrast indicate the Cu electrodes (left: anode; right: cathode), which are seated on the Si oxide (band of dark contrast) grown on the Si wafer. The Ti film plays the role of binding material between the electrodes and Si oxide layer.

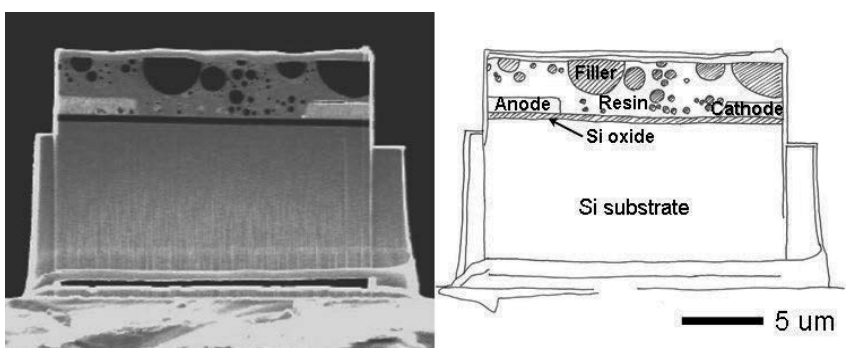

Figure 2. SI image (left) and sketch (right) of pick-up piece from failed semiconductor packages by FIB

The piece was manipulated in the TEM chamber (HD-2000 HITACHI High-Tech) and obtained secondary electron (SE) and TEM images. The specimen along with the substrate was then transferred to the nanobeam SIMS apparatus. The experimental conditions on shave-off profiling were as follows: an FIB potential and current of 24 kV and 35 pA, respectively, and total profiling time of 60 min for a 12 μm^2 area. Quick scanning started on the left (anodal region) and proceeded to the right (cathodal region) in the SI image.

4. Results and discussion

Figure 3 shows TEM bright-field image and SE image of the same piece picked up from a failed package. The TEM image reveals the whole volume of the piece. Comparing the SI and SE images reveals that the filler patterns are different. This difference arises from the different surfaces of the piece.

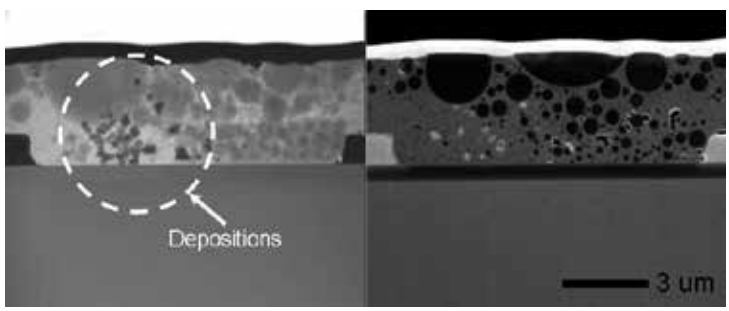

Figure 3. TEM bright-field image (left) and SE image (right) of the same specimen picked up from a failed package (both regions are the same)

In the STEM image, the rectangular regions indicating the anode (left) and cathode (right) appear in dark contrast, which is opposite to that in the SIM image. Small circular regions of dark contrast can also be observed in places between both electrodes. This dark contrast can indicate deposits from migrated material.

The spatial resolution of the shave-off profiling is estimated to be at most 40 nm for multilayers [7]. Electrochemical migration may occur in the field between the anode and cathode (10 μm width); the width of this field is wide compared to the spatial resolution. Figure 4 shows the shave-off vector profile of the as-prepared IC package. There are silent Cu^+ion signals between both electrodes. A faint tail, which could come from the memory effect, can also be observed; this point is discussed in another paper [8].

Figure 5 shows the shave-off vector profile and the corresponding TEM image of the same area. We see that the positions of the electrodes and depositions agree with the shape of the Cu^+profile and position of the dark contrast. Critical difference is found with the gradient curve of the shave-off vector profiling between the anodal region and cathodal region. The intensity of the gradient curve is high compared to the faint tail in Fig. 4 and may have its origin in

http://dx.doi.org/10.5772/60682

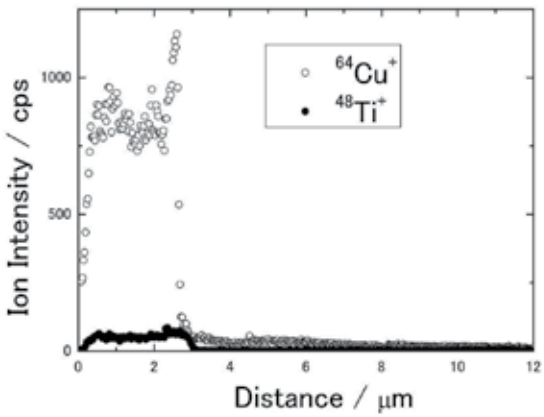

Figure 4. Shave-off profile of Cu electrode and Ti thin film in as-prepared IC package

electrochemical migration. Generally, the ionization probability of an oxide or complex is much higher than that of the elemental metal. It is possible that the high ionization probability of Cu^{+}ions amplifies the existence of electrochemical migration. In the same piece, shave-off profiling was able to visualize a migrated-ions distribution that could not be observed by TEM imaging. From these results, we emphasize that the advantage of shave-off profiling is the highly selective detection sensitivity especially for ions that have migrated into a package.

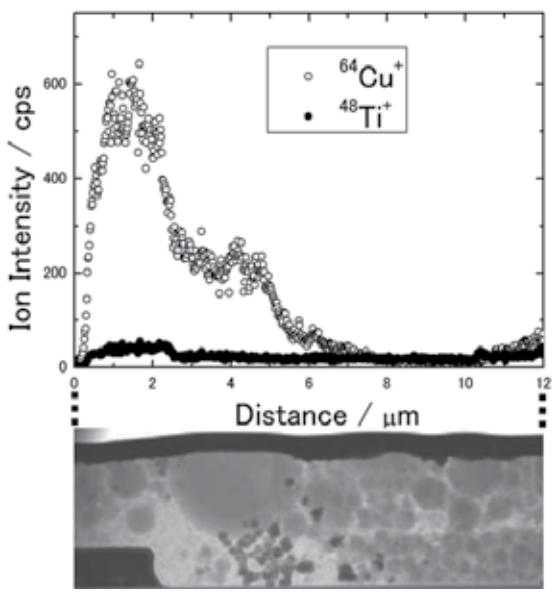

Figure 5. Cross-check analysis of semiconductor package that had undergone electrochemical migration (upper: shave-off profile; lower: TEM image)

5. Conclusions

We have cross-checked images of TEM specimens against shave-off profiling results and introduced a new approach to shave-off vector profiling. The results showed good agreement between the distribution of the electrodes and depositions. Critical difference was found with the gradient curve of the shave-off profiling from the anode to the cathode. In the same piece, shave-off profiling can be used to visualize a faint gradient of migrated-ions that could not be observed in TEM image.

Author details

Masashi Nojima*

Address all correspondence to: mnojima@rs.noda.tus.ac.jp

Res.Inst. for Sci. & Technology, Tokyo University of Science, 2541 Yamazaki Noda-shi Chiba, Japan

References

[1] B. Tomiyasu, S. Sakasegawa, T. Toba, M. Owari and Y. Nihei, *Secondary ion mass spectrometry SIMS XII*, eds. A. Benninghoven, P. Bertrand, H. N. Migeon and H. W. Werner, John Wiley & Sons (2000) pp.473-476

[2] M. Nojima, A. Maekawa, T. Yamamoto, B. Tomiyasu, T. Sakamoto, M. Owari and Y. Nihei, Appl. Surf. Sci., 252 (2006) 7293

[3] M. Nojima, M. Toi, A. Maekawa, B. Tomiyasu, T. Sakamoto, M. Owari and Y. Nihei, Appl.Surf. Sci., 231-232 (2004) 930

[4] S.-B. Lee, Y.-R. Yoo, J.-Y. Jung, Y.-B. Park, Y.-S. Kim and Y.-C. Joo, Thin Solid Films, 504 (2006) 294

[5] L. Lantz and M. G. Pecht, IEEE Trans. Compon. Packag. Technol., 26 (2003) 199

[6] T. Yamamoto, A. Maekawa, Y. Ishizaki, R. Tanaka, M. Owari, M. Nojima and Y. Nihei,Surf.Interface Anal., 38 (2006) 1662

[7] M. Toi, A. Maekawa, T. Yamamoto, B. Tomiyasu, T. Sakamoto, M. Owari, M. Nojima and Y.Nihei, J. Surf. Anal.,12 (2005) 170

[8] M. Nojima, M. Fujii,Y. Ishizaki, M. Owari and Y. Nihei, Bunseki Kagaku, 57 (2008) 67

Section 2

Transmission Electron Microscopy at Nanoscale

Chapter 5

Advanced Electron Microscopy Techniques in Nanomaterials Characterization at NASA Glenn Research Center

Francisco Solá

Additional information is available at the end of the chapter

http://dx.doi.org/10.5772/60532

Abstract

In this chapter, the author will review several advanced microscopy techniques developed at the NASA Glenn Research Center in the last 5 years. Topical areas include: unconventional approach to investigate the fine nanoporous structure of aerogels by scanning electron microscopy, new limits for transmission electron microscopy investigation of dispersion and chirality of single-walled carbon nanotubes within a polymer matrix, the importance of microstructure of porous tin dioxide nanostructure that lead to first time detection of methane at room temperature without doping or catalyst, in situ SEM methods to study the thermal stability of nanoparticles on Graphene/Cu based materials, electron beam irradiation effects on carbon nanotube yarns electrical properties, and nanoindentation work of multiphase thermoelectric material.

Keywords: Electron microscopy, Aerogels, CNT, SnO_2, Graphene/Cu, WSi_2/SiGe

1. Introduction

Nanomaterials can have a direct impact on NASA missions in areas of engineered materials and structures, devices, electronics, energy generation and storage, and sensors among others [1]. Nanomaterials can offer up to 50 percent weight savings, and thus cost [1]. This chapter will review several advanced microscopy techniques developed and applied to cutting-edge nanomaterials research at NASA Glenn Research Center (GRC) in the last 5 years [2]. The first

INTECH
open science | open minds

© 2015 The Author(s). Licensee InTech. This chapter is distributed under the terms of the Creative Commons Attribution License (http://creativecommons.org/licenses/by/3.0), which permits unrestricted use, distribution, and reproduction in any medium, provided the original work is properly cited.

topic investigates the examination of the nanoporous structure of aerogels with a scanning electron microscopy (SEM) technique. Aerogels are emerging materials with the promise of unusually high strength (for some cases), thermal insulation, and damping capability combined with very light weight. Because of these properties, aerogels have been used in several NASA missions to collect comet dust particles and provide thermal insulation of components in Mars rovers, for instance [3]. Other current applications include thermal insulation for inflatable reentry decelerators and extra-vehicular activity suits [4]. Many of the outstanding physical properties of aerogels depend on their porous structure. SEM is a commonly used technique to estimate the pore size in aerogels, but is hampered by charging, the accumulation of electrons on the surface of the sample. The common solution employed to minimize charging effects is to deposit a layer of a conducting material on the sample. However, this technique can drastically mask the intrinsic porous structure of the aerogel. Here it is shown that negative charging effects on aerogels can be dissipated using nitrogen gas [5-6].

The second subject will be carbon nanotube (CNT)/polymer nanocomposites, which have excellent promise for improved strength and light weight and are being actively researched in a number of NASA projects. Recently this type of material has been used in the Juno mission for electromagnetic charge dissipation and electromagnetic shielding; other applications include lightning strike protection of aircraft [7-8]. Transmission electron microscopy (TEM) is a technique used to characterize the dispersion of nanotubes in a polymeric matrix. However, imaging such CNTs is challenging because of both their small size and electron scattering by the polymer matrix affecting the image contrast. This effort determined new limits for TEM investigation of dispersion and chirality of nanotubes in polymer matrices. This work opened new possibilities for investigation of microstructure of polymer nanocomposites to further understand electrical, mechanical, and thermal properties [9-10].

The third area is related to microstructure investigation and in-situ heating experiments on copper-based nanoparticles embedded in a graphene matrix. This material was considered by us for lithium ion battery applications. Lithium-ion batteries have been used at NASA in human and robotic spacecraft, because of their high power density and the weight savings compared with traditional nickel based batteries [11]. In a few years one lithium-ion battery will replace two nickel-hydrogen batteries in the International Space Station. Lithium ion batteries formed with nanostructured materials can potentially increase battery efficiency because of high surface-to-volume ratio, while reducing weight and cost. Here we were looking for oxygen content, dispersion of nanoparticles in the graphene, possibilities to anneal agglomeration of nanoparticels by heating, as well as perform extreme heating experiments. The heating experiments are sustained with theoretical treatments of both the thermal stability of the particles, as well as the most energetically favorable orientation relationships between the atomic planes of the particles and the graphene. Evidence of neck evolution, coalescence, sublimation, and Ostwald ripening were observed [12].

The fourth topic is on TEM characterization of the detail in new porous tin dioxide (SnO_2) nanorods as the sensing material for room-temperature methane detection [13-14], which has applications in environmental and engine emissions monitoring. Particular emphasis will be on establishing bonding type and particle size of SnO_2 within the porous structure, as these has been shown to influence the sensitivity of SnO_2 materials. We were able to establish the

http://dx.doi.org/10.5772/60532

rutile structure of tin dioxide by high-angle annular dark field (HAADF) imaging with atomic resolution as well as electron diffraction (ED). The tin dioxide chemistry was also confirmed by electron energy-loss spectroscopy (EELS) fine structure using two methods: (1) the position of the peaks in the 530–540 eV range, which are fingerprints for tin oxide structure, and (2) estimation of the ratio of Sn-Sn and Sn-O bond lengths distances, by the so-called resonance peaks at higher energies.

The fifth area is on electron beam irradiation effects on the electrical resistivity of CNT yarns. Yarns are currently been investigated for structural applications and potential replacement of conventional carbon fiber in composite materials, as well for wiring applications. One specific example is composite overwrapped pressure vessel (COPV) tanks. These types of tanks are used to contain high-pressure fluids in propulsion, science experiments, and life support applications [15]. COPVs offer a 50% weight savings compared with metal tanks. One critical aspect of the project was to improve the mechanical properties of this material. One potential route to achieve the mechanical improvement is the cross-linking method induced by electron beam irradiation. The study of the electrical response of CNT yarns as a function of electron dose is one route to monitor possible cross-linking events. In this work, small segments of CNT yarns were exposed to e-beam irradiation in a TEM. The electrical resistivity as a function of e-beam irradiation was studied by the two probe method, using micromanipulators inside a SEM [16-17].

Finally, nanoindentation and microstructure investigation of thermoelectric (TE) composites consisting of silicon germanium (SiGe) combined with tungsten silicides will be presented [18-19]. SiGe alloys have been traditionally used for radioisotope thermoelectric generators (RTGs) in several spacecraft and NASA missions such as Apollo [12, 14-17], Cassini, Galileo, and recently Curiosity [20]. We have been working on ways to improve the thermoelectric figure of merit (ZT) of SiGe based TE alloys by incorporating WSi_2 phases in to the matrix. It is predicted that the incorporation of nano-size WSi_2 into a SiGe matrix will yield the lowest thermal conductivity (and therefore represents the best case to maximize the ZT) when compared with other types of silicides. Beyond traditional RTG applications, we are exploring other uses in the energy-harvesting arena. These include multifunctional structures that generate power while reducing weight, sensor systems to monitor performance of engines, hypersonic vehicles, and others. Considerable effort has been focused on microstructural engineering methods that lead to ZT improvement by microstructural optimization of TE materials.

Although critical for the previous mentioned applications, work pertinent to the mechanical integrity of this type of WSi_2/SiGe based TE materials is limited. Nanoindentation is a suitable technique to probe the local hardness (H) and modulus (E) of a multiphase material at micron and submicron dimensions. Probing the mechanical properties of the phases of a bulk multiphase material is of fundamental importance as this in principle can dictate the overall mechanical properties of the bulk, as well as provide insight to improving its mechanical properties. In more practical scenarios, TE materials can be exposed to several perturbations during service, such as mechanical and thermal loading, mechanical vibrations, and thermal gradients that can lead to the formation of cracks, which can potentially degrade the transport

properties (by reducing the electrical conductivity). In this regard it is therefore critical to study the mechanical properties of TE materials. We will examine the local mechanical properties and microstructure of WSi_2/Si_xGe_{1-x} multiphase thermoelectric material by nanoindentation, electron, and focused ion beam microscopy (FIB) methods.

2. Aerogels

Aerogels are nanoporous materials with high pore volume, frequently greater than 90%. The tortuosity of the pore structure and thinness of the solid struts render the aerogels exceptional insulators by decreasing both gaseous and solid conduction [21-22]. It is critical to find ways to characterize the porous structure of aerogels, as this dictates the thermal properties. Both TEM and SEM techniques are commonly used to explore the pore size in aerogels [23-25]; however, both techniques suffer from charging effects. Precaution must be exercised during TEM investigation of these materials at the nanoscale, as local high electric fields resulting from charge accumulation can cause surface mass migration of SiO_x species and may form local areas with collapsed porous structures [26-28].

The most common solution to reduce charging effects of nonconducting materials (like aerogels) is to deposit a conducting material at the surface of the sample. Yet this approach usually masks, and can change the inherent porous structure of, the aerogel [25]. We have developed a new procedure to reduce charging effects of aerogels during SEM imaging. The process involves the local recombination of the negative charges caused by electron beam irradiation during imaging with positive ions created by ionization events induced from inert gas injection near the surface of the sample. High-energy backscattered electrons (BSEs) are created by multiple elastic scattering events and have relative high energies, whereas low-energy secondary electrons (SE) are produced by inelastic scattering events. The SE yield is denoted by δ, whereas BSE yield is symbolized with η. In general, a sample can be charged positively or negatively or be in a neutralized state during SEM investigation [12]. The law of charge conservation describes the process analytically. Generally,

$$I_{PE}\left[1-\left(\delta+\eta\right)\right]-I_L=\frac{\partial Q}{\partial t} \tag{1}$$

where I_{PE} is the current added to the sample by primary beam of electrons (*PE*), I_L is the outflow current and $\partial Q/\partial t$ is the charge build–up rate [29]. Therefore negative charging effects will be fulfilled when I_{PE} is greater than the total emission/leakage current. Penalties of this negative charging are the production of image distortion and unbalanced white contrast features.

Figure 1a is a SEM image of an aluminosilicate aerogel in which charging effects are noticeable. These artifacts and image distortions are caused by negative charging, where a negative potential deflects the PE imaging beam. For clarity, some distorted lines are marked with white solid arrows in figure 1a. It is well known that charging is usually not a static problem and

http://dx.doi.org/10.5772/60532

may change under scanning events [30]. The defocused lines can be described by a capacitor model that takes into consideration charging and discharging events. For more details see references [5, 31]. To reduce these charging effects we proposed a nonconventional approach. The key is to neutralize/minimized negative charging by the recombination with local ions. For the formation ions, dry nitrogen (N_2) gas is inserted near the surface of the sample. Details of the process can be found in reference 5. Collisions of electron signals with the nitrogen gas ionizes the N_2 molecules forming positive ions (N_2^+) according to $N_2 + e^- \rightarrow N_2^+ + 2e^-$, where the ionization energy is near 15.6 eV [32].

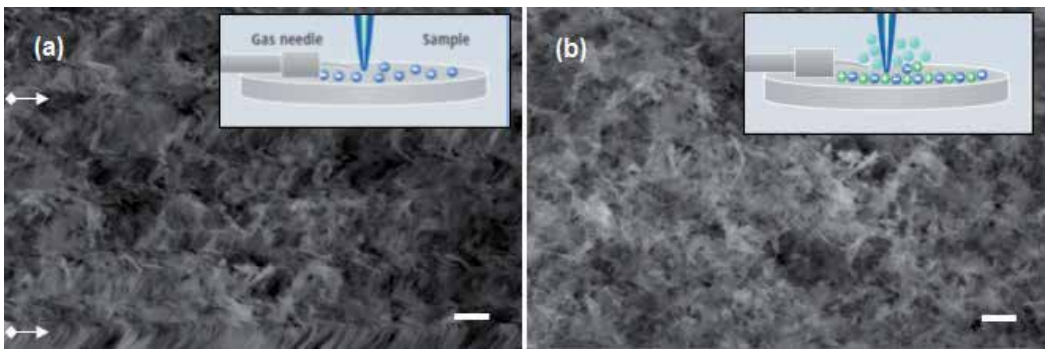

Figure 1. SEM images of aerogels with charging artifacts (gas needle off) (a) and when charge compensation device is working at 100% (b). Some artifact defocused lines are marked with solid arrows. Scale bar is 100 nm. Insets are the corresponding schematic representations of cases (a) and (b). Reproduced from reference 5 with permission from the Institute of Physics.

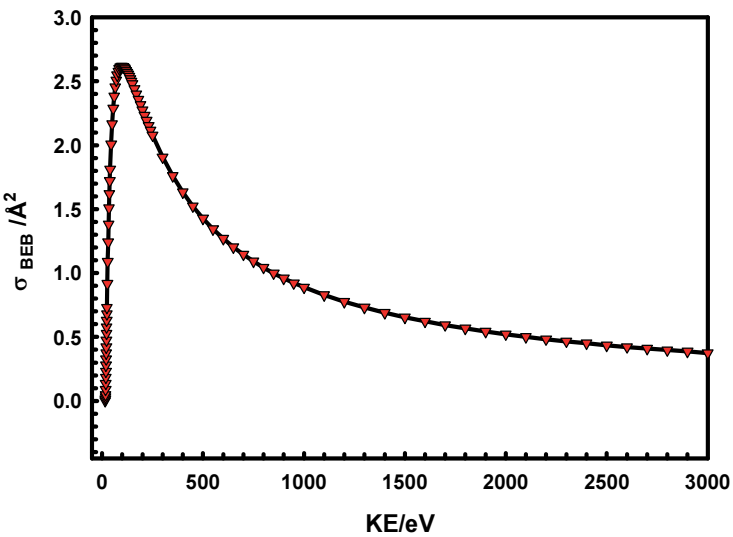

Figure 2. Predicted values for the N_2 ionization σ_{BEB} as a function of *KE* of electrons. Reproduced from reference 5 with permission from the Institute of Physics.

Consequently, N_2^+ ions are attracted to the sample surface by local electric fields, followed by recombination with negative charges and charge neutralization as pictured in the inset of figure 1b. Porous structure down to 3 nm where resolved. It is known that collisions with larger cross sections (σ) will produce more ions [33-34]. Figure 2 is the expected σ dependence of the kinetic energy (*KE*)for the electrons. The predicted values are based on the Binary-Encounter-Bethe (BEB) Model, which adds the Motts cross-section with the high *KE* factor and Bethe cross section [35]. The maximum value of σ_{BEB} (~ 2.62 Å^2) is produced with electrons with *KE* of ~100 eV, which corresponds to low energy BSE. For SE with energies of ~50 eV, σ_{BEB} is ~2.17 Å^2. However, if we consider the fact that most of the SE (~90%) have *KE* of 10 eV (or even less), which is below the ionization energy for N_2, ionization events by SE should be rare.

3. CNT/polymer nanocomposites

Numerous polymers have been used to synthesize CNT/polymer nanocomposites with the objective of achieving superior properties [36-40]. One key factor is the effective dispersion of fillers in the matrix. Still, dispersion is difficult as CNTs tends to agglomerate, causing weakening of the nanocomposite. The nature of the nanotube-polymer interface is particularly critical to the reinforcement of polymer matrices, where significant interfacial adhesion between the nanotube and surrounding polymer is essential. However, in the case of electrical properties and single-walled carbon nanotubes (SWCNTs), although the dispersion is important, the major control has to be focused in a reliable method to identify the abundance of metallic/semiconducting type of nanotubes through chirality [41]. Other important factors such as the CNTs alignment in the polymer matrix, as well as other common analyses involving distribution and quantification of nanotube dimensions can be explored by electron microscopy methods [10].

Although the resolution of a TEM can suffice to image SWCNTs, callenges do exist to image them in a polymer matrix and to explore its dispersion in an isolated form. Imaging individual SWCNTs in a polymer matrix is of great challenge because its small size and weak contrast signal typically is attenauted by the relatively strong polymer scattering signal. An example of this problem is shown in figure 3. It can be observed that while the SWCNT walls can be resolved in the hole (free standing) region, its contrast is lost in the polymer region.

New boundaries have been proposed to characterize SWCNTs within a polyethylene (PE)polymer matrix, by the assistance of modeling procedures [9]. A high-resolution TEM (HRTEM) image of a 25-Å nanocomposite of thickness (*t*) is presented in figure 4a. A HRTEM image of the same isolated SWCNT is included in the inset of figure 4a. Clearly the SWCNT walls can be resolved completely for the isolated case. However, even with a nanocomposite of t = 25 Å, a decrease in wall contrast signal as well as width is evident. In addition, the walls of the SWCNT totally vanish for a nanocomposite with t = 49 Å, as indicated in figure 4b. The interesting results are that ED analysis is less sensitive to these thickness problems. Figures 5a-c are ED patterns for isolated (5a), nanocomposite with thicknesses 25 Å (5b) and 49 Å (5c). Note that there are fingerprint reflection lines (D_i, i = 1, 2...4) in the isolated SWCNT that persist

http://dx.doi.org/10.5772/60532

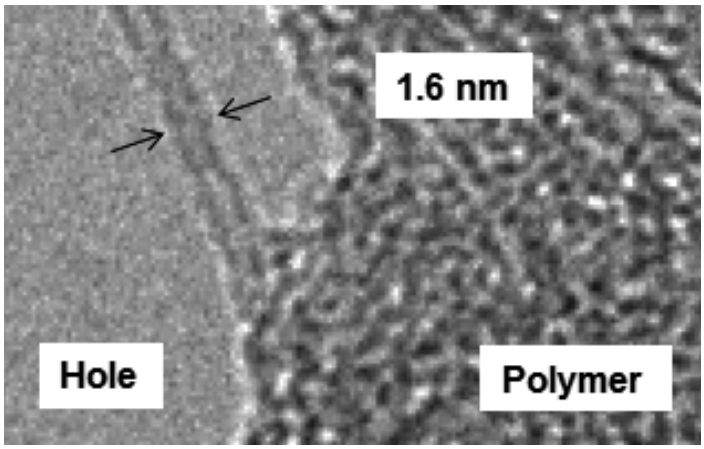

Figure 3. HRTEM of CNT in a polymer matrix. Reproduced from reference 10 with permission from Wiley/Scrivener.

for the nanocomposite cases in 5b and 5c. From these D_i distances both the diameter of the SWCNT and chirality can be estimated. This data can be used to understand the nanocomposite's electrical properties, by establishing the abundance of metallic and semiconducting nanotubes.

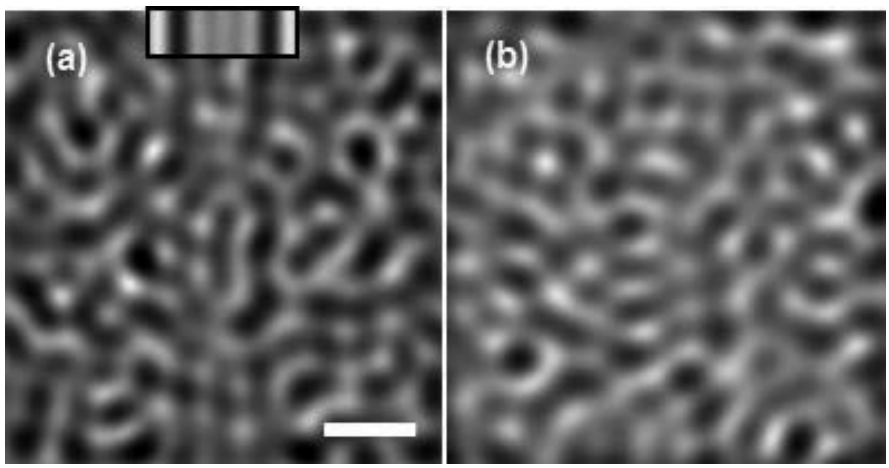

Figure 4. HRTEM simulations of SWCNT in PE matrix. Reproduced from reference 9 with permission from Wiley. Scale bar is 1 nm.

We also explored the case of nanotube walls oriented perpendicular to the electron beam and found that the nanotube can be resolved for a thicker nanocomposite, see reference 9. However, an apparent increase in nanotube diameter was evident event at optimum focus. As a result, estimating both chirality and diameter from HRTEM images will be erroneous in this case. Additionally, by combining results from data collected with the beam parallel and perpen-

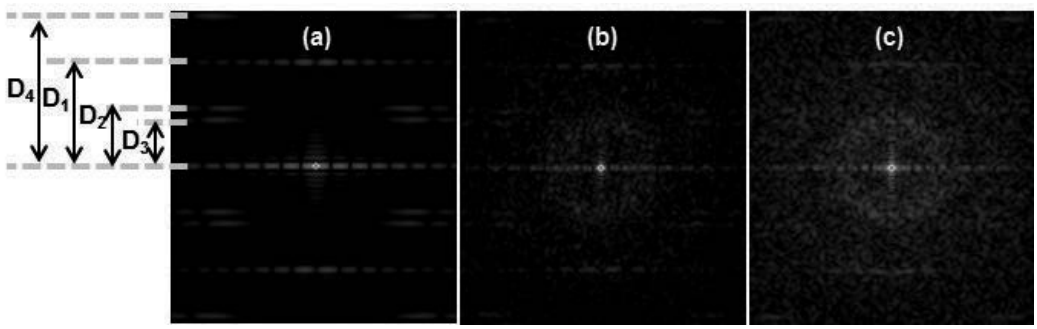

Figure 5. ED simulations of SWCNT in PE matrix. Reproduced from reference 9 with permission from Wiley.

dicular to the walls of the nanotube, it is possible to study dispersion of isolated SWCNT in a polymer matrix at the nanoscale level.

4. Graphene/Cu-based nanocomposites

Graphene materials have exceptional properties [44]. However, graphene/metal nanoparticle hybrids can have even superior properties than isolated or pure graphene material [45]. Applications in graphene/Cu-based hybrids include lithium ion batteries [46] and electronics [47, 48]. Electron microscopy, particularly in situ heating work, is a powerful technique to explore the stability of nanoparticle/graphene systems. In this section the stability of graphene/Cu-based hybrids is reported in a wide range of temperatures. Extensive microscopy analysis showed that the graphene material was decorated with Cu-based nanoparticles of different shapes and sizes. Identified nanoparticle shapes included: truncated nanocubes, octahedrons and its truncations, nanorods, triangular prisms, and decahedrons [49].

Figure 6 presents an energy-filtered TEM (EFTEM) EELS and selected area ED (SAED) analysis of the nanocomposite. Figure 6a is the zero-loss image, and figure 6b is the oxygen mapping [26]. We observed different degrees of oxidation, from partially oxidized (examples marked with dotted arrows) to fully oxidized nanoparticles. Likewise, some nanoparticles such as those marked with solid arrows in the figure were oxygen free. Based upon the results of figure 6 we were able to establish the presence of pure copper and copper oxide cubic phases [50]. Figures 7a to 7f present the low-magnification in situ SEM heating results where the whole composite could be observed. Evidence of coalescence (regions enclosed with solid circles), and Ostwald ripening (d regions enclosed with dotted circles) were observed [51-54]. The final individual nanoparticles transformed to spherical shapes in order to minimize the surface energy [55]. Numerical analysis of the neck formation between two nanoparticles was conducted to explore the initial steps of coalescence; the data is presented in figure 8. For two symmetrical spherical particles theory predicts that $D \sim t^b$, where t is time and $b \sim 0.143$ for surface diffusion or 0.167 for grain boundary diffusion [56]. The experimental value obtained for b was 0.518± 0.024. This higher value is in fact caused by faceting of the nanoparticles [57].

http://dx.doi.org/10.5772/60532

Molecular dynamics simulations were also conducted, taking into consideration facets of the nanoparticles that agreed with the experimental results [12]. In addition, MD results suggested that the growth rate of particle pairs on graphene was comparable to isolated pairs, which indicated that graphene had no significant effect on the coalescence. This effect may be consistent with a weak Cu-graphene interaction ("physisorption") as reported in other reports. We found that grain boundary energy was the main factor affecting the neck growth rate at the nanoscale. Sublimation experiments were also conducted, and it was observed that the {111} surfaces were more stable than {100}, which is consistent with predictions of Chatterjee's theory [58].

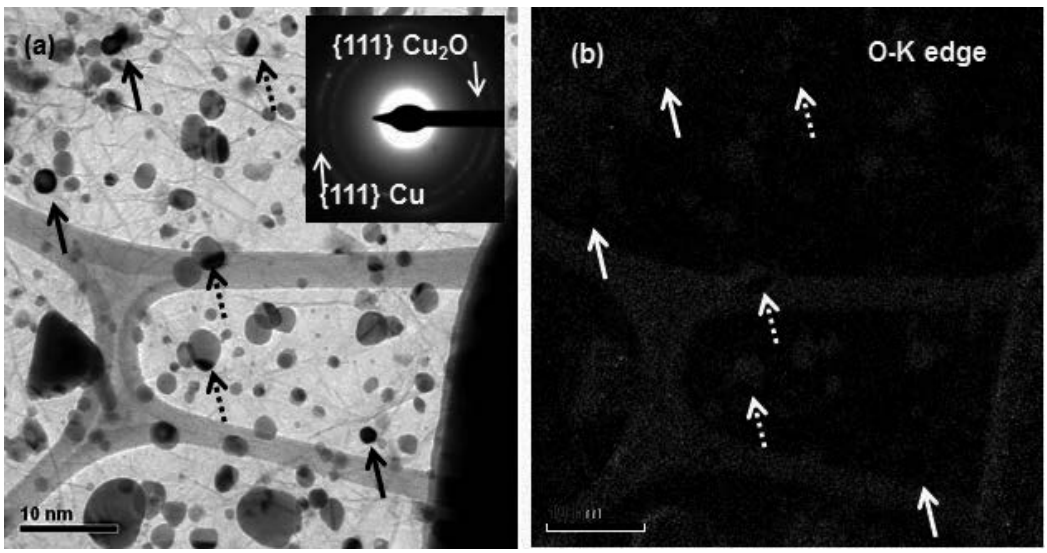

Figure 6. EFTEM and SAED analysis of the graphene/Cu-based nanocomposite. Reproduced from reference 12 with permission from the Institute of Physics.

5. Porous SnO_2 nanostructures

Semiconducting metal oxides like tin oxide (SnO_2) have been shown to respond to relevant chemical species such as oxygen (O_2), carbon monoxide (CO), ethanol (C_2H_5OH), nitric oxides (NO_x), propylene (C_3H_6), and hydrogen (H_2) [59-61]. Methane gas is highly volatile and when mixed with air can cause explosions at higher concentrations because it is readily flammable. Thus, the development of a reliable and cost-effective methane gas sensor is important. Room-temperature detection of methane is challenging and has been reported by others, but those lack the temperature range capability for realistic applications [62-69]. Recently NASA GRC developed porous SnO2 nanostructures for methane detection for a wide temperature range, including room temperature [13].

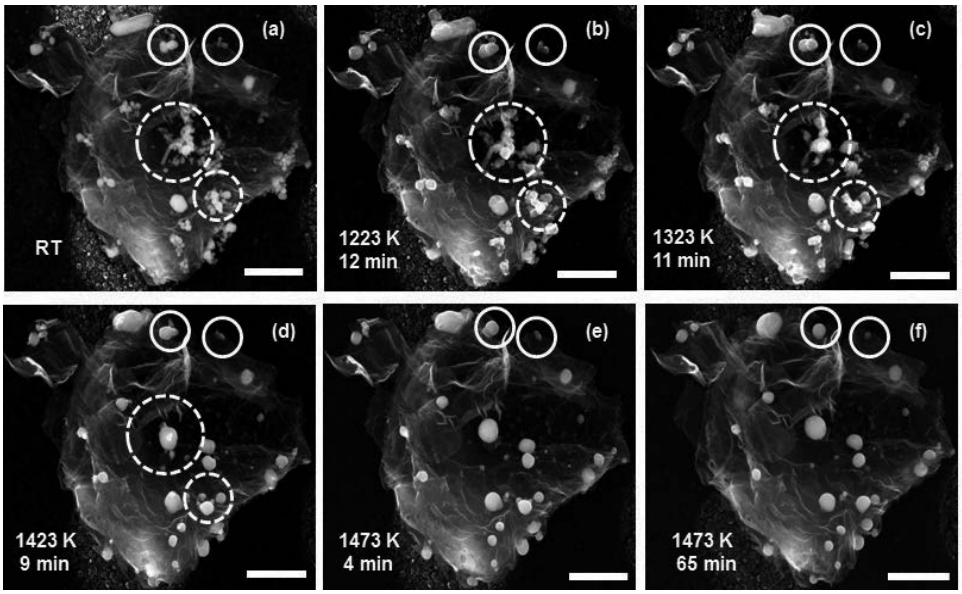

Figure 7. SEM images of microstructural evolution of a graphene sheet decorated with Cu nanoparticles in full view, as a function of temperature and time (a)–(f). Reproduced from reference 12 with permission from the Institute of Physics. Scale bar is 1μm.

The sensor was operated at room temperature and detection of 0.25% methane in air was demonstrated for the first time, without the use of any dopants or catalysts. Porous SnO_2 nanorods were synthesized using MWCNTs as templates, as indicated in figure 9. The process involves the decoration of MWCNTs with SnO2 nanoparticles (fig. 9a), followed by calcination of nanotubes at higher temperatures in air, the end product being a porous structures as pictured in figure 9b. The inset of figure 9b is the corresponding SAED pattern of the porous SnO_2 nanorods. Figure 9c is a HRTEM image of the nanocrystals in the porous SnO_2 nanorod. Both analyses indicated the rutile SnO_2 structure [13, 60].

Furthermore, EELS analysis confirmed the SnO_2 structure by two methods (see fig. 10): (1) determining the fingerprint of this rutile structure by the presence of unique peaks in the 530–540 eV energy range [70] and (2) estimating bond length (r), by the use of $\Delta E = k/r^2$, where k is a constant [71]. For example, for the peak at 543 eV, $\Delta E_1 = 10.9$ eV, and for the peak at 558.5 eV, $\Delta E_2 = 26.4$ eV. It follows that $r_1/r_2 = 1.556$, which agrees well with the ratio of bond length values of SnO_2 nanograins, for the second Sn-Sn (= 3.19 Å) and first Sn-O (= 2.05 Å) coordination shells [72]. The rutile structure of tin di-oxide was also resolved by HAADF imaging with atomic resolution as indicated in the inset image of figure 10.

6. CNT Yarns

NASA is exploring routes to replace conventional carbon fiber composites with CNT-based composite materials. This could traduce in approximately one-third reduction of unfueled

http://dx.doi.org/10.5772/60532

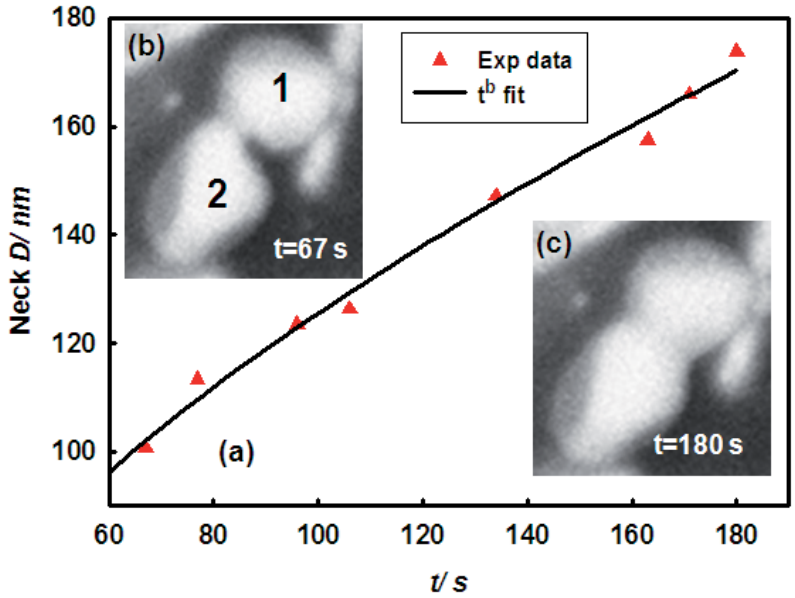

Figure 8. Quantitative neck evolution of two nanoparticles at 873 K shown graphically and with snapshots from a movie. Nanoparticle 1 had a diameter of ~ 250 nm, and nanoparticle 2 had a diameter of ~265 nm. (a) Plot of neck diameter, (b) and (c) are snapshots at 67 s and 180 s, respectively. Reproduced from reference 12 with permission from the Institute of Physics.

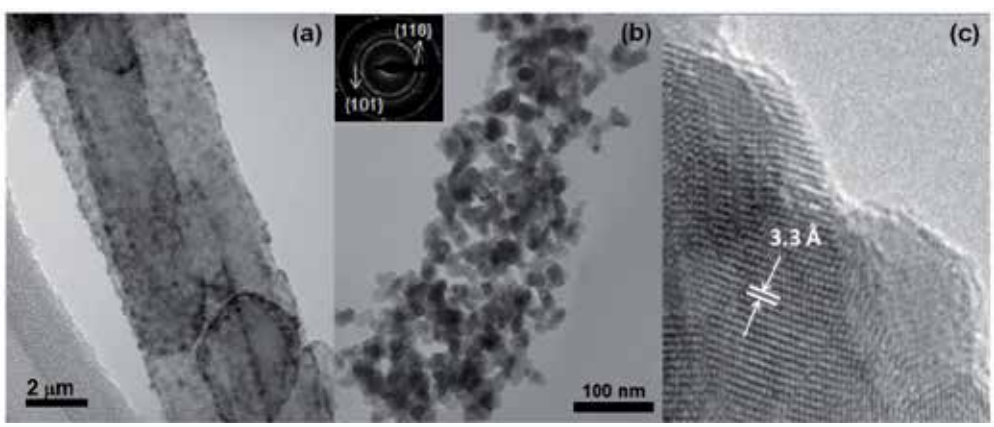

Figure 9. (a) TEM image of MWCNT covered with SnO_2 nanoparticles. (b) TEM image of a porous SnO_2 nanorod. Inset shows the ED pattern. (c) HRTEM image showing that the lattice spacing corresponds to the rutile structure of SnO_2. Reproduced from reference 13 with permission from the Institute of Physics.

weight of space vehicles and structures. To achieve this, commercially available CNT-based materials must have at least two times the strength of conventional carbon fibers. CNT yarns are currently the best commercially available CNT-based materials in terms of mechanical properties; however, their tensile strength is about half of conventional carbon fibers. This has

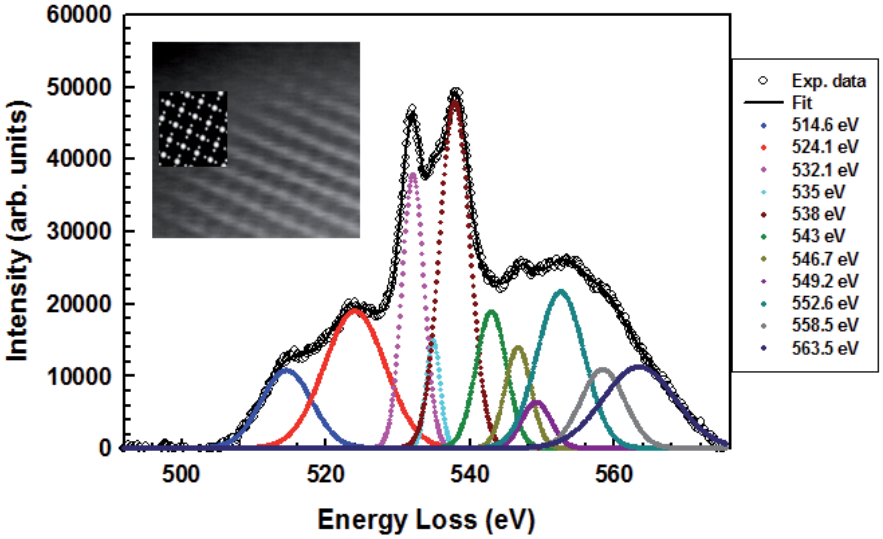

Figure 10. EELS spectrum of porous SnO_2 nanorods with its corresponding fit. Reproduced from reference 13 with permission from the Institute of Physics. The inset is atomic-resolution HAADF image.

to be with the weak shear interactions between carbon shells and bundles within a yarn [73-74]. Therefore, current efforts focus on developing protocols to improve mechanical properties of these materials.

One potential route to achieve mechanical improvement is the cross-linking method induced by electron beam irradiation. The weak shear interactions between adjacent carbon shells/CNT can be improved by the formation of sp^3 C-C bonds induced by e-beam irradiation [73]. This can occur at both the interwall sites of individual multiwall CNTs (MWCNTs) and between CNT neighbors, and both potentially will increase the mechanical response of CNT yarns [73, 76]. E-beam energies greater than 80 keV are needed to displace C atoms and to induce complex kinetics and recombination of lattice defects within the hexagonal carbon network, which eventually leads to cross-linking [77]. For one isolated MWCNT (and small bundles), energies at 100–200 keV are effective to cross-link [77]. Because CNT yarns are fibers composed of several MWCNTs, the question arises as to what extent energies in this range will still promote crosslinking effectively.

The study of the electrical response of CNT yarns as a function of electron dose can be a complementary route to monitor possible cross-linking events, and is important to establishing multifunctional properties of CNT yarns. Considerable effort has been focused in e-beam irradiation methods that lead to mechanical improvement. Although Mikó and coworkers reported the effects of e-beam irradiation on electrical resistivity of single-walled CNT (SWCNT) fibers systems [78-79], work on e-beam irradiation effects on electrical properties of CNT yarns is limited. Here, small segments of CNT yarns are exposed to e-beam irradiation in a TEM operated at 200 keV and different doses. The electrical resistivity as a function of e-beam irradiation is studied by the two-probe method, using micromanipulators inside a SEM.

http://dx.doi.org/10.5772/60532

The inset of figure 11 is a SEM image that illustrates the two-probe electrical characterization of CNT yarns. Typically the measurements were conducted to probe CNT yarns of ~450 μm in length and ~77–84 μm in diameter. The electrical resistivity as a function of e-beam irradiation is presented in figure 11. Irradiation times range from 10 to 60 min, which corresponds to dosages of ~$3x10^{15}$–$2x10^{16}$ e/cm^2. The average values of resistivity increased with irradiation time up to 30 min and decreased with further irradiation. Note that the maximum resistivity at 30 min of irradiation corresponds to an increase of ~1.5 times the resistivity of the pristine yarn, and that the resistivity at 60 min is just a slight decrease of the pristine resistivity. For comparison purposes, the resistivities of CNT yarns in the current study are about 10^2 times smaller than aerosol-like (nontwisted) yarns, but are ~10^3 times higher than other twisted yarns, though these values were estimated with a yarn segment length of 50 mm [80], and about 10 times higher than SWCNT fibers of 3–5 mm tested length [78, 79].

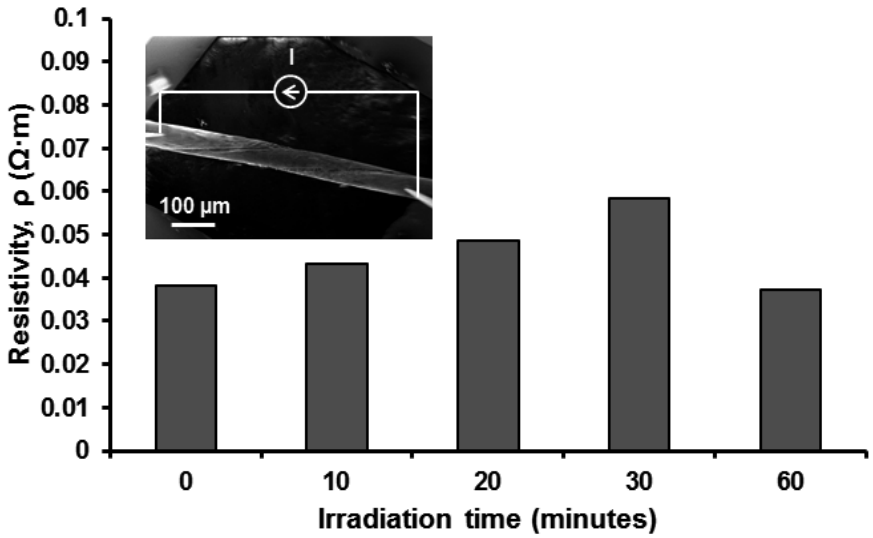

Figure 11. Effect of e-beam irradiation on CNT yarn resistivity. The inset is an SEM image of two tungsten probe electrical setup measurement. Reproduced from reference 16 with permission from OMICS Publishing Group.

To obtain possible explanations to the e-beam irradiation effects on resistivity, HRTEM analysis on the microstructure of CNT yarns were conducted. Figure 12 presents the HRTEM of CNT yarns of pristine (12a), e-beam irradiated with10 min (12b), 20 min (12c), 30 min (12d), and 60 min (12e). Figure 12f is a schematic that summarizes possible crosslinking sites (marked with red lines) of CNT constituents within the yarn at two different scales. The images were taken in thin areas located at the edges of the yarns so one can see the different planes of CNTs oriented in a given twisted direction. For the purpose of the following discussion, only areas of the images that are in focus are described. The area enclosed by a white circle in figure 12a shows that the CNTs of yarns are double walled, and the area enclosed by a black circle is consistent with a CNT bundle structure. The alternating black/white fringes correspond to the lattice planes of CNTs in the bundle, with each lattice plane built from a row of CNTs [81].

Crosslinking sites in CNTs can be monitored by these HRTEM images and typically correspond to areas were the fringes are less coherent but do not completely lose their structure to form an amorphous carbon (a-C) structure [75]. Cross-linking events can be observed at 10 min of irradiation (fig. 12b). Several types of microstructural changes of CNTs within the yarn are evident at 20 min of irradiation (fig. 12c). These includes cross-linked sites (area enclosed by a black box), pristine-non-cross-linked sites (yellow box), a-C structure sites (red box) [82-87], and sites with a mixture of a-C and cross-linked sites (white box). With further irradiation it can be noticed that both a-C and cross-linked sites grows; however, overall the crystallinity (fringes structure) of CNTs is preserved (in the sense that it is not totally lost).

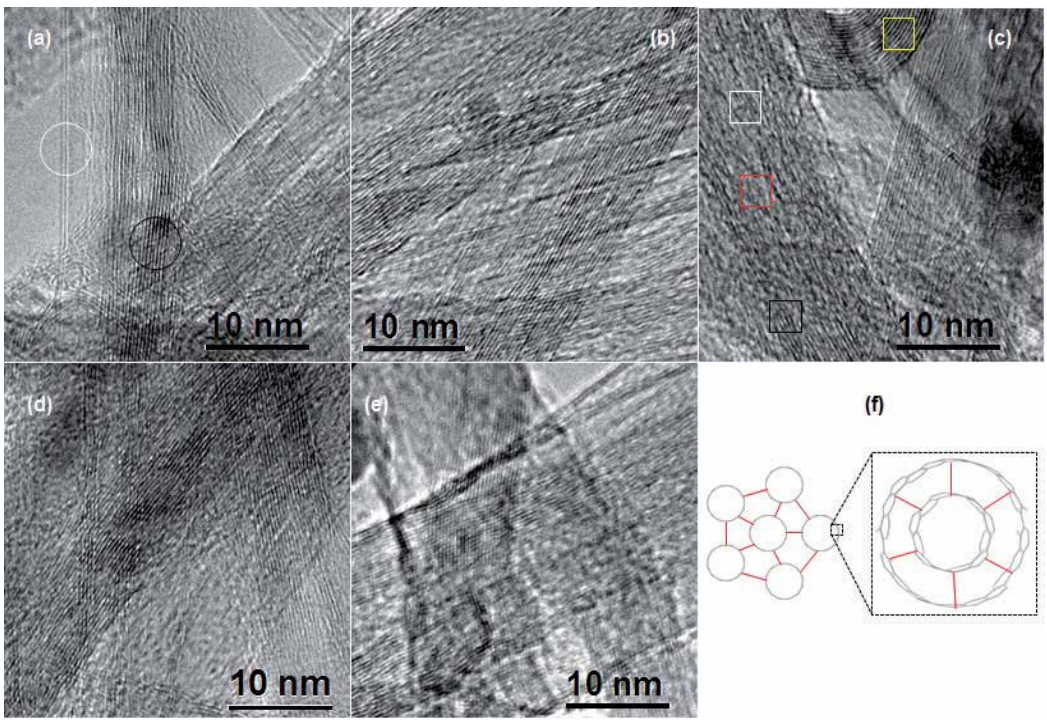

Figure 12. HRTEM of CNT yarns of pristine (a) and e-beam irradiated for10 min (b), 20 min (c), 30 min (d), and 60 min (e). (f) Schematic that explains possible crosslinking sites of CNT within the yarn, which are at bundle and isolated nanotube sites. Reproduced from reference 16 with permission from OMICS Publishing Group.

In order to understand these microstructural changes and how to correlate them with the corresponding resistivity results, a brief explanation on e-beam irradiation on CNT defect formation is needed. E-beam electrons can displace C atoms located at the hexagonal lattice network of CNTs only when critical minimum energy is used, known as the displacement threshold. However displacement threshold depends on the local arrangement of carbon atoms relative to the electron beam and type of CNT. This has to be with the direction of momentum transfer to C atoms distributed in the hexagonal lattice. For instance, displacement threshold energies of 82 keV have been reported for small CNTs oriented perpendicular to the

http://dx.doi.org/10.5772/60532

e-beam, and up to 240 keV for relative bulky CNTs oriented tangential to the e-beam [77]. For MWCNTs, displacement threshold energies correspond to 100 keV [77]. Once C atoms are displaced, lattice defect formation in the form of interstitials and vacancies will take place. Based on quantum mechanics calculations, defects on the form of divacancies, interstitials, and Frenkel pair (interstitial-vacancy pair) defects were shown to crosslink graphitic layers [88]. However, at the same time e-beam irradiation can lead to unwanted loss of lattice coherence, a processes known as amorphization. This has to be with the kinetics of defects (production rate, dynamics) on specific sites of the C lattice, and agglomeration of point defects that leads to larger defects. Dynamics of defects depends on temperature. E-beam irradiation at room temperature (as in this work) leads to the formation of vacancies and interstitials (for energies above the threshold energy), which remain relatively localized (immobile) at specific lattice sites. If they do not recombine to form cross-linking sites, high concentration and agglomeration of defects can occur as e-beam time increases, which eventually cause the lattice to lose its crystallinity at those sites. This model is consistent with the amorphous regions encountered in figure 12c–12e.

In terms of electrical results, the data can be explained in terms of a competitive process between cross-linking and amorphization. Cross-linking sites reduce the resistivity by reducing the CNT-to-CNT distance, while amorphization increases resistivity. Note that the reduction of resistivity by cross-linking events is not due to conduction of electrons through sp^3 C-C bonds. The increase in resistivity with10 min of e-beam irradiation can be explained by the formation of defects in the lattice that have not produced enough cross-linking sites to enhance conductivity. At irradiation times of 20–30 min, although cross-linking events are increasing, the resistivity is dominated by amorphization events. The reduction of resistivity at 60 min can only be explained by a significant increase in cross-linking population dominating the overall electrical conduction of electrons in the yarn. This is consistent with the microstructural data presented in figure 12.

7. WSi_2/SiGe composites

Figure 13a is a SEM image of the sample showing the typical sample microstructure of a WSi_2/SiGe composite. Note that there are micron-size as well as submicron-size grains within the microstructure. Standardless EDS point analysis in atomic percentage (at%) of region 1 marked with a black arrow indicated content of ~ 77 and ~23 at% for Si and Ge, respectively, whereas for region 2 ~91 at% (Si) and ~9 at% (Ge) were obtained. For simplicity regions of type 1 will be defined as Ge rich regions, and regions of type 2 will be referred to as Si rich. The local variations in Si and Ge content are caused by segregation during non-equilibrium solidification. These two regions contain grains of about 1–10 μm in size. Furthermore, the W:Si at% ratio of the region marked with the white arrow was ~1:2 consistent with a WSi_2 phase. We refer to the WSi_2 phase as those grains in the ~1–13 μm size range. The rest will be referred to as the matrix. The matrix actually comprises nanosized WSi_2 with grains down to ~3 nm, SiGe of uniform composition with sizes in the micron size range (upper value of ~15 um) and nanometer size range (lower value of ~120 nm), and some porosity.

Figure 13 presents SEM images showing examples of nanoindentation impressions (NI) for WSi_2 phase (13b), matrix (13c), WSi_2/matrix interface (13d), and Ge rich phase (13e). An example of WSi_2/matrix interface impression is included to show the level of positioning resolution of the diamond tip; however, no mechanical data related to interfaces will be included in this work. Figure 13f is an example of a SEM/FIB image cross section of a crack below the surface of a Ge-rich phase. Loads of 0.0012 N were used in NI on figures 13a–c, while 0.01 N was used in figures 13d and e. Note that the SEM image of figure 13f was taken with the sample oriented at an angle of 54 degrees relative to the electron beam and normal to the ion beam for the milling process. The inset of figure 13f is the surface view of the NI SEM image (also taken at 54 degrees), where the radial cracks can be noticed. As a final step, a protective material is deposited at the top of the NI area followed by the formation of two laterals and one front trench for cross section serial sectioning, as indicated in figure 13f.

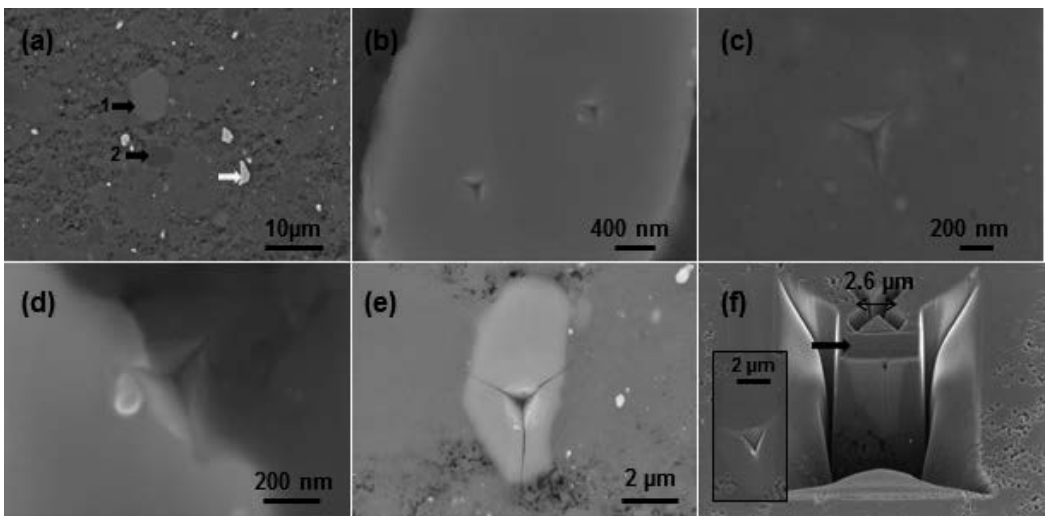

Figure 13. (a) SEM image showing the microstructure of the TE sample. SEM images showing examples of nanoindentation impressions for the WSi_2 phase (b), matrix (c), WSi_2/matrix interface (d), and Ge rich phase (e). (f) SEM/FIB image cross section of a crack below the surface of a Ge rich phase. Reproduced from reference 18 with permission from Elsevier.

Quantitative results for H and E for all phases can be found in figure 14a. For this analysis, a load of 0.0012 N was used. Average H (and E) values (in GPa) of 12.94 (464.95) for the WSi_2 phase, 19.49 (214.52) for the matrix, 14.95 (142.84) for the Si-rich phase, and 13.98 (138.56) for the Ge-rich phase. Figure 14b gives k_c for different phases, formed with data taken at a 0.02-N load for the WSi_2 and 0.01-N load for other phases, and average values of H and E. Fracture toughness was estimated using the relation $k_c = \alpha(E/H)^{0.5}P/c^{1.5}$, where P is the load, c is the total length of the radial crack, and $\alpha = 0.032$ for a cube-corner diamond tip [19]. Note that in order to estimate k_c, $c/a \geq 2.5$ must be true [24], where a is the diagonal length of the impression area. Average k_c values (in $MPa \bullet m^{0.5}$) were 1.37 for the WSi_2, 0.52 for the matrix, 0.36 for the Si rich phase, and 0.24 for the Ge-rich phase. Furthermore, cross-sectional TEM analyses of the

http://dx.doi.org/10.5772/60532

deformation zone showed evidence of crack formation, dislocations, shear fault formation, and crack-induced amorphization; while serial sectioning FIB/SEM showed evidence of median and lateral cracks. The complete set of data is reported elsewhere [18]. SEM images illustrating the lift-out method for TEM analysis for the WSi_2 phase are presented in figure 15. Again, note that the SEM images are oriented at an angle of 54 degrees relative to the electron beam and normal to the ion beam (see fig. 15 a-b). Figure 15c presents a low-magnification bright-field (BF) TEM image of the deformation zone enclosed by a black box. The corresponding dark-field (DF) TEM image of the region enclosed in figure 15c is presented in figure 15d, which shows a crack (white arrow), high density of dislocations around the nanoindentation area (as well as the by the area enclosed with the white circle), and shear faults lines (solid white arrows); the inset is a schematic of shear lines. A dotted white arrow points to a crack.

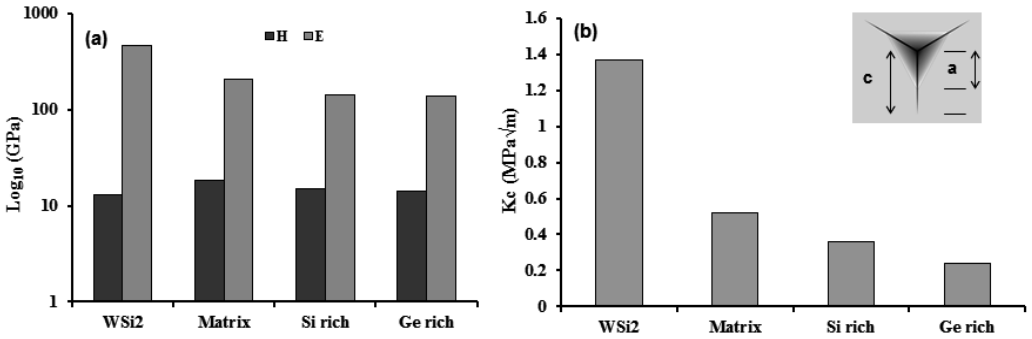

Figure 14. (a) Quantitative results for H and E for all phases. (b) k_c values for all phases. The inset is a schematic of radial crack formation induced by nanoindentation. Reproduced from reference 18 with permission from Elsevier.

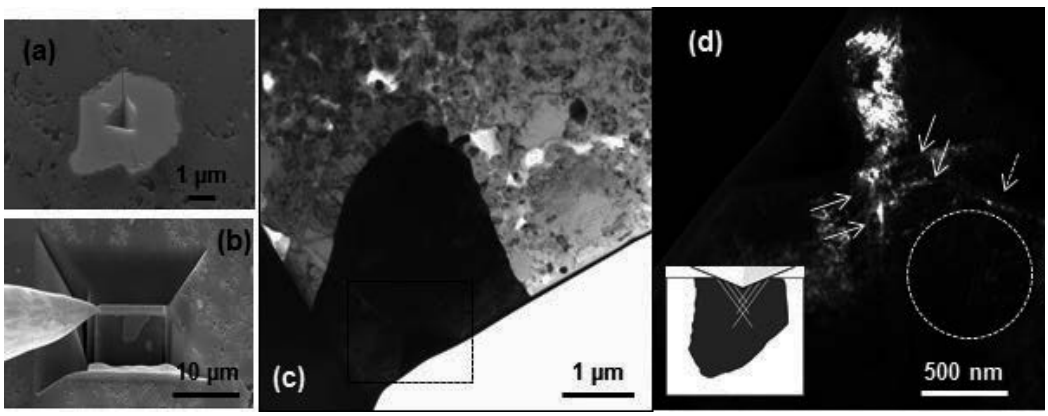

Figure 15. (a)-(b) SEM images illustrating the lift-out method for TEM analysis for the WSi_2 phase. BF-TEM (c) and DF-TEM (d) images showing the deformation zone. Reproduced from reference 18 with permission from Elsevier.

Based on the data obtained in this work, particularly on the superior hardness values and decent fracture toughness of the matrix (~45% upper value relative to pure WSi_2 phase) we proposed the following to obtain a robust TE WSi_2/SiGe material: (1) the segregation problem must be corrected, and (2) the porosity content needs to be minimized, as this will improve the mechanical properties as well as the electrical conductivity (and hence ZT). Higher population of nanosizes and less (or no) micron sized WSi_2 grains are needed. A higher population of nanosized WSi_2 will not only improve mechanical robustness, but can also improve ZT as well. Predictions by Mingo et al. [91] showed that WSi_2 nanoparticles below 30 nm in SiGe alloys will increase ZT considerably, with the optimum results being in the 2–10 nm range.

Acknowledgements

The author would like to acknowledge the collaborators who provided professional contributions to several topics covered in this book chapter. These include internal collaborators A. Biaggi-Labiosa (Sensor), F. Dynys (TE), F. Hurwitz (Aerogels), M. Meador (CNT/polymer), M. Lebrón (CNT/polymer); and external collaborators Z.H. Xia and J. Niu (CNT/polymer, Cu/G: U. North Texas), J. Yang (Aerogels: Carl Zeiss Microscopy). Technical support from J. Buehler, R. Rogers and M. Yoonessi is also acknowledged. This work was supported by the following projects: Hypersonic, Subsonic Fixed Wing, Vehicle Systems Safety Technologies, CNT Materials Development, and Advanced TE.

Author details

Francisco Solá

Address all correspondence to: francisco.sola-lopez@nasa.gov

Materials and Structures Division, NASA Glenn Research Center, Cleveland, OH, USA

References

[1] Meador MA, Files B, Li J, Manohara H, Powell D, Siochi EJ. NASA: Nanotechnology roadmap. http://www.nasa.gov/pdf/501325main_TA10-Nanotech-DRAFT-Nov2010-A.pdf (accessed 12 January 2015).

[2] Solá F. Latest developments in advanced electron microscopy techniques on nanomaterials at NASA Glenn Research Center. NTRS 2014; http://ntrs.nasa.gov/search.jsp?R=20140013326 (accessed 13 January 2015).

[3] National Aeronautics and Space Administration. NASA: STARDUST mission. http://stardust.jpl.nasa.gov/tech/aerogel.html (accessed 12 January 2015).

[4] National Aeronautics and Space Administration. NASA: Aerogels thinner, lighter, stronger. http://www.nasa.gov/topics/technology/features/aerogels.html (accessed 12 January 2015).

[5] Solá F, Hurwitz F, Yang J. New scanning electron microscopy approach to image aerogels at the nanoscale. Nanotechnology 2011; 22: 175704.

[6] Solá F, Hurwitz F, Yang J. New approach to image aerogels by scanning electron microscopy. APS March Meeting Abstracts 2011; 1: 1203.

[7] National Aeronautics and Space Administration. NASA: Mission Juno http://missionjuno.swri.edu/ (accessed 12 January 2015).

[8] Lebrón-Colón M, Meador M, Gaier JR, Solá F, Scheiman DA, McCorkle LS. Reinforced thermoplastic polyimide with dispersed functionalized single wall carbon nanotubes. ACS Applied Materials and Interfaces 2010; 2: 669.

[9] Solá F, Xia Z, Lebrón-Colón M, Meador MA. Transmission electron microscopy of single wall carbon nanotube/polymer nanocomposites: A first-principles study. Phys Status Solidi RRL 2012; 6: 349-351.

[10] Solá F. SEM and TEM characterization of polymer CNT nanocomposites. In: Mittal V (ed.) Polymer Nanotube Nanocomposite: Synthesis, Properties, and Applications. Wiley/Scrivener; 2014. p167-185.

[11] National Aeronautics and Space Administration. NASA: The heartbeat of the mars exploration rovers.https://solarsystem.nasa.gov/scitech/display.cfm?ST_ID=252 (accessed 13 January 2015).

[12] Solá F, Niu J, Xia Z. Heating induced microstructural changes in graphene/Cu nanocomposites. J Phys D: Appl Phys 2013; 46: 065309.

[13] Biaggi-Labiosa AM, Solá F, Lebrón-Colón M, Evans LJ, Xu, JC, Hunter GW, Berger G, González JM. A novel methane sensor based on porous SnO_2 nanorods: room temperature to high temperature detection. Nanotechnology 2012; 23: 455501.

[14] Biaggi-Labiosa A, Evans LJ, Xu JC, Hunter GW, Berger G, Solá F. Gas sensing properties of hybrid SnO2/carbon nanotubes. APS Meeting Abstracts 2011; 1, 21013.

[15] McLaughlan PB, Forth SC, Grimes-Ledesma LR. Composite overwrapped pressure vessels, a primer. NASA/SP 2011; 573: 1-20.

[16] Solá F. Electrical properties of pristine and electron irradiated CNT yarns at small length scales. Mod. Chem. and Appl. 2014; 2: 116.

[17] Solá F. Electrical properties of pristine and electron irradiated CNT yarns at small length scales: an electron microscopy study. Microscopy and Microanalysis 2013; 19 (S2): 518.

[18] Solá F, Dynys F. Probing the mechanical properties and microstructure of WSi_2/ Si_xGe_{1-x} multiphase thermoelectric material by nanoindentation, electron and focused ion beam microscopy methods. J. Alloys Comp. 2015; 633: 165.

[19] Solá F, Dynys F. Probing the mechanical properties and microstructure of WSi_2/ Si_xGe_{1-x} multiphase thermoelectric material by nanoindentation, electron and focused ion beam microscopy methods. Bulletin of the American Physical Society 60, 2015. http://absimage.aps.org/image/MAR15/MWS_MAR15-2014-000590.pdf (accessed 14 January 2015).

[20] Abelson RD. Space missions and applications. In: Rowe DM (ed.) Thermoelectrics handbook macro to nano. CRC press, Taylor & Francis Group; 2006. p874.

[21] Aegerter MA, Leventis N, Koebel MM. Aerogels handbook. Springer publishing; 2011. ISBN 978-1-4419-7477-8.

[22] Fricke J, Emmerling A. Aerogels. Adv. Mater. 1991; 3: 504.

[23] Stroud RM, Long JW, Pietron JJ, Rolison DR. A practical guide to transmission electron microscopy of aerogels. J. Non-Cryst. Solids 2004; 350: 277.

[24] Vacher R, Courtens E, Stoll E, Böffgen M, Rothuizen H. Pores in fractal aerogels and their incidence on scaling. J. Phys. Condens. Matter 1991; 3: 6531.

[25] Pajonk GM, Venkateswara-Rao A, Parvathy NN, Elaloui E. Microstructural characterization of silica aerogels using scanning electron microscopy. J. Mater. Sci. 1996; 31: 5683.

[26] Solá F, Resto O, Biaggi-Labiosa A, Fonseca LF. Electron beam induced growth of silica nanorods and heterostructures in porous silicon. Nanotechnology 2007; 18: 405308.

[27] Solá F, Resto O, Biaggi-Labiosa A, Fonseca LF. Electron-beam induced growth of silica nanowires and silica/carbon heterostructures. MRS Proceedings 2007; 1017: 1017-DD12-31.

[28] Betancourt J, Zypman F, Solá F, Resto O, Fonseca LF. The influence of roughness on the mechanical spectroscopy of SiO_2 nanorods grown by e-beam irradiation. Superlattices and Microstructures 2009; 45: 458-468.

[29] Cazaux J. Charging in scanning electron microscopy "from inside and outside". Scanning 2004; 26: 181.

[30] Reimer L. Scanning electron microscopy: physics of image formation and microanalysis, Springer series in optical sciences, 45, Ed: P.W. Hawkes (Springer-Verlag, Berlin, Germany), Ch. 3. ; 1998.

[31] Goldstein J, Newbury D, Joy D, Lyman C, Echlin P, Lifshin E, Sawyer L, Michael J. Scanning electron microscopy and X-ray microanalysis, 3 (Springer, New York, USA), Ch. 5; 2003.

[32] Moncrieff DA, Robinson VNE, Harris LB. Charge neutralisation of insulating surfaces in the SEM by gas ionization. J. Phys. D: Appl. Phys. 1978; 11: 2315.

[33] Toth M, Thiel BL, Donald AM. Interpretation of secondary electron images obtained using a low vacuum SEM. Ultramicroscopy 2003; 94: 71.

[34] Mohan A, Khanna N, Hwu J, Joy DC. Secondary electron imaging in the variable pressure scanning electron microscope. Scanning 1998; 20: 436.

[35] National Institute of Standards and Technology. NIST: Electron-impact cross sections for ionization and excitation. http://physics.nist.gov/PhysRefData/Ionization/ref.html (accessed 12 January 2015).

[36] Haggenmueller R, Gommans HH, Rinzler AG, Fischer JE, Winey KI. Aligned single-wall carbon nanotubes in composites by melt processing methods. Chem. Phys. Lett. 2000; 330: 219.

[37] Zhang X, Liu T, Sreekumar TV, Kumar S, Moore VC, Hauge RH, Smalley RE. Poly(vinyl alcohol)/SWNT composite film. Nano Lett. 2003; 3: 1285.

[38] Shaffer MSP, Windle AH. Fabrication and characterization of carbon nanotube/poly(vinyl alcohol) composites. Adv. Mater. 1999; 11: 937.

[39] Ajayan PM, Stephan O, Colliex C, Trauth D. Aligned carbon nanotubes arrays formed by cutting a polymer resin-nanotube composite. Science 1994; 265: 1212.

[40] Wagner HD, Lourie O, Feldman Y, Tenne R. Stress-induced fragmentation of multi-wall carbon nanotubes in a polymer matrix. Appl. Phys. Lett. 1998; 72 : 188.

[41] Chen Y, Malkovskiy A, Wang XQ, Lebrón-Colón M, Sokolov AP, Perry K, More K, Pang Y. Selection of single-walled carbon nanotube with narrow diameter distribution by using a PPE–PPV copolymer. ACS Macro Letters 2012; 1: 246.

[42] Solá F, Lebrón-Colón M, Ferreira F, Fonseca LF, Meador MA, Marín CJ. In-situ TEM-STM observations of SWCNT ropes/tubular transformations. MRS Proceedings 2009; 1204: 1204-K10-26.

[43] Qin LC. Determination of the chiral indices of carbon nanotubes by electron diffraction. Phys. Chem. Chem. Phys. 2007; 9, 31.

[44] Geim AK, Novoselov KS. The rise of graphene. Nat. Mater. 2007; 6: 183.

[45] Liang Y, Wang H, Sanchez-Casalongue H, Chen Z, Dai H. TiO_2 nanocrystals grown on graphene as advanced photocatalytic hybrid materials. Nano Res. 2010; 3: 701.

[46] Wang B, Wu XL, Shu CY, Guo YG, Wang CR. Synthesis of CuO/graphene nanocomposite as a high-performance anode material for lithium-ion batteries. J. Mater. Chem. 2010; 20: 10661.

[47] Torrisi F, Hasan T, Wu W, Sun Z, Lombardo A, Kulmala TS, Hsieh GW, Jung S, Bonaccorso F, Paul PJ, Chu D and Ferrari AC. Inkjet-printed graphene electronics 2012 ACS Nano 2012; 6: 2992.

[48] Hupalo M, Liu X, Wang C Z, Lu W C, Yao Y X, Ho K M and Tringides M C. Metal Nanostructure formation on Graphene: weak versus strong bonding. Adv. Mater. 2011; 23: 2082.

[49] Xia Y, Xiong Y, Lim B, Skrabalak SE. Shape-controlled synthesis of metal nanocrystals: simple chemistry meets complex physics?. Angew. Chem. Int. Ed. 2009; 48: 60.

[50] Cheng G, Hight Walker AR. Transmission electron microscopy characterization of colloidal copper nanoparticles and their chemical reactivity. Anal. Bioanal. Chem. 2010; 396: 1057.

[51] Kanda KK, Sahu SN, Behera SN. Liquid-drop model for the size-dependent melting of low-dimensional systems. Phys. Rev. A 2002; 66: 013208.

[52] José-Yacamán M, Gutierrez-Wing C, Miki M, Yang DD, Piyakis KN, Sacher E. Surface diffusion and coalescence of mobile metal nanoparticles. J. Phys. Chem. B 2005; 109: 9703.

[53] Tatchev D, Hoell A, Eichelbaum M, Rademann K. X-ray-assisted formation of gold nanoparticles in soda lime silicate glass: suppressed ostwald ripening. Phys. Rev. Lett. 2011; 106: 085702.

[54] Hawa T, Zachariah MR. Coalescence kinetics of unequal sized nanoparticles. J. Aerosol Sci. 2006; 37: 1.

[55] Tao AR, Habas S, Yang P. Shape control of colloidal metal nanocrystals. Small 2008; 4: 310.

[56] Lim TH, McCarthy D, Hendy SC, Stevens KJ, Brown SA, Tilley RD. Real-time TEM and kinetic monte carlo studies of the coalescence of decahedral gold nanoparticles. 2009 ACS Nano; 3: 3809.

[57] Khomyakov PA, Giovannetti G, Rusu PC, Brocks G, van den Brink J, Kelly PJ. First-principles study of the interaction and charge transfer between graphene and metals. Phys. Rev. B 2009; 79: 195425.

[58] Chatterjee B. Anisotropy of melting for cubic metals. Nature 1978; 275: 203.

[59] Shen G, Chen PC, Ryu K, Zhou C. Devices and chemical sensing applications of metal oxide nanowires. J. Mater. Chem. 2009; 19: 828.

[60] Gurlo A. Nanosensors: towards morphological control of gas sensing activity. SnO_2, In_2O_3, ZnO and WO_3 case studies. Nanoscale 2011; 3: 154.

[61] Hunter GW, Dweik RA. Applied breath analysis: an overview of the challenges and opportunities in developing and testing sensor technology for human health monitoring in aerospace and clinical applications. J. Breath Reas. 2008; 2: 037020.

[62] Choi YJ, Hwang IS, Park JG, Chpi KJ, Park JH, Lee JH. Novel fabrication of an SnO(2) nanowire gas sensor with high sensitivity. Nanotechnology 2008; 19: 095508.

[63] Batzill M, Diebold U. The surface and materials science of tin oxide. Prog. Surf. Sci. 2005; 79: 47.

[64] Tiemann M. Porous metal oxides as gas sensors. Chem. – Eur. J 2007; 13: 8376.

[65] Xia Y, Yang P, Sun Y, Wu Y, Mayers B, Gates B, Yin Y, Kim F, Yan H. One-dimensional nanostructures: synthesis, characterization, and applications. Adv. Mater. 2003; 15: 353.

[66] Choi KJ, Jang HW. One-dimensional oxide nanostructures as gas-sensing materials: review and issues. Sensors 2010; 10: 4083.

[67] Lu Y, Li J, Han J, Ng H T, Binder C, Partridge C and Meyyappan M. Room temperature methane detection using palladium loaded single-walled carbon nanotube sensors. Chem. Phys. Lett. 2004; 391: 344.

[68] Li Y, Wang H, Chen Y, Yang M. A multi-walled carbon nanotube/palladium nanocomposite prepared by a facile method for the detection of methane at room temperature. Sens.Act. B 2008; 132: 155.

[69] Lein G, Paquette S, Vadhavkar S, Fuller L, Santhanam KSV. Batron P-Si microsensor for methane and its derivatives. Sens. Act. B 2009; 142: 147.

[70] Moreno MS, Egerton RF, Midgley PA. Electronic structure of tin oxides by electron energy loss spectroscopy and real-space multiple scattering calculations. Phys. Rev. B 2005; 71: 035103.

[71] Kurata H, Lefêvre E, Colliex C, Brydson R. Electron-energy-loss near-edge structures in the oxygen *K*-edge spectra of transition-metal oxides. Phys. Rev. B 1993; 47: 13763.

[72] González GB. Investigating the defect structures in transparent conducting oxides using X-ray and neutron scattering techniques. Materials 2012; 5 : 818.

[73] Filleter T, Espinosa HD. Multi-scale mechanical improvement produced in carbon nanotube fibers by irradiation cross-linking. Carbon 2013; 56: 1-11.

[74] Miller SG, Williams TS, Baker JS, F Solá F, Lebron-Colon M, McCorkle LS, Wilmoth NG, Gaier J, Chen M, Meador MA. Increased tensile strength of carbon nanotube yarns and sheets through chemical modification and electron beam irradiation. ACS applied materials & interfaces 2014; 6: 6120.

[75] Kis A, Csányi G, Salvetat JP, Lee TN, Couteau E, Kulik AJ, Benoit W, Brugger, Forró L. Reinforcement of single-walled carbon nanotube bundles by intertube bridging. Nat Materials 2004; 3: 153 – 157.

[76] Xia ZH, Guduru P, Curtin WA. Enhancing mechanical properties of multi-wall carbon nanotubes via sp^3 inter-wall bridging. Phys Rev Lett 2007; 98: 245501.

[77] Krasheninnikov AV, Nordlund K. Ion and electron irradiation-induced effects in nanostructured materials. J Appl Phys 2010; 107: 071301.

[78] Mikó C, Milas M, Seo JW, Couteau E, Barišić N, Gaál R, Forró L. Effect of electron irradiation on the electrical properties of fibers of aligned single-walled carbon nanotubes. Appl Phys Lett 2003; 83: 4622-4624.

[79] Mikó C, Seo JW, Gaál R, Kulik A, Forró L. Effect of electron and ultraviolet irradiation on aligned carbon nanotube fibers. Phys Status Solidi b 2006; 243: 3351-3354.

[80] Miao M. Electrical conductivity of pure carbon nanotube yarns. Carbon 2011; 49: 3755-3761.

[81] Lambin Ph, Loiseau A, Culot C, Biró LP. Structure of carbon nanotubes probed by local and global probes. Carbon 2002; 40: 1635-1648.

[82] Solá F, Biaggi-Labiosa A, Fonseca LF, Resto O, Lebrón-Colón M, Meador MA. Field emission and radial distribution function studies of fractal-like amorphous carbon nanotips. Nanoscale Res Lett 2009; 4: 431-436.

[83] Solá F, Resto O, Biaggi-Labiosa A, Fonseca LF. Growth and characterization of branched carbon nanostructures arrays in nano-patterned surfaces from porous silicon substrates. Micron 2009; 40, 80-84.

[84] Li L, Solá F, Xia ZH, Yang YQ. Effect of amorphous carbon coatings on the mechanical behavior of silicon carbide nanowire. Journal of Applied Physics 2012; 111, 094306.

[85] St Dennis JE, Venkataraman P, He J, John VT, Obrey SJ, Currier RP, Lebrón-Colón M, Solá F, Meador MA. Rod-like carbon nanostructures produced by the direct pyrolysis of α-cyclodextrin. Carbon 2011; 49: 718-722.

[86] Fonseca LF, Resto O, Solá F. Branched nanostructures and method of synthesizing the same. US Patent 7, 528, 060; 2009.

[87] Solá F, Resto O, Biaggi-Labiosa A, Fonseca LF. Growth of branched carbon nanostructures in nanopatterned surfaces created by focused ion beam. MRS Proceedings 2007; 1059: 1059-KK04-12.

[88] Telling RH, Ewels CP, El-Barbary AA, Heggie MI. Wigner defects bridge the graphite gap. Nat Materials 2003; 2: 333 – 337.

http://dx.doi.org/10.5772/60532

[89] Kruzic JJ, Kimb DK, Koester KJ, Ritchie RO. Indentation techniques for evaluating the fracture toughness of biomaterials and hard tissues. Journal of the mechanical behavior of biomedical materials 2009; 2: 384-395.

[90] Frutos E, González-Carrasco JL. A method to assess the fracture toughness of intermetallic coatings by ultramicroindentation techniques: applicability to coated medical stainless steel. Acta Mater 2013; 61: 1886.

[91] Mingo N, Hauser D, Kobayashi NP, Plissonnier M, Shakouri A. "Nanoparticle-in-alloy" approach to efficient thermoelectrics: silicides in SiGe. Nano Lett 2009; 9:711.

Chapter 6

Transmission Electron Microscopy for the Characterization of Cellulose Nanocrystals

Madhu Kaushik, Carole Fraschini, Grégory Chauve, Jean-Luc Putaux and Audrey Moores

Additional information is available at the end of the chapter

http://dx.doi.org/10.5772/60985

Abstract

Cellulose nanocrystals (CNCs) are high aspect ratio nanomaterials readily obtained from cellulose microfibrils via strong acid hydrolysis. They feature unique properties stemming from their surface chemistry, their crystallinity, and their three-dimensional structure. CNCs have been exploited in a number of applications such as optically active coatings, nanocomposite materials, or aerogels. CNC size and shape determination is an important challenge and transmission electron microscopy (TEM) is one of the most powerful tools to achieve this goal. Because of the specifics of TEM imaging, CNCs require special attention. They have a low density, are highly susceptible to electron beam damage, and easily aggregate. Specific techniques for both imaging and sampling have been developed over the past decades. In this review, we describe the CNCs, their properties, their applications, and the need for a precise characterization of their morphology and size distribution. We also describe in detail the techniques used to record quality images of CNCs. Finally, we survey the literature to provide readers with specific examples of TEM images of CNCs.

Keywords: cellulose nanocrystals, transmission electron microscopy, particle size, characterization, size distribution, sample preparation

INTECH
open science | open minds

© 2015 The Author(s). Licensee InTech. This chapter is distributed under the terms of the Creative Commons Attribution License (http://creativecommons.org/licenses/by/3.0), which permits unrestricted use, distribution, and reproduction in any medium, provided the original work is properly cited.

1. Introduction

1.1. Native cellulose and the production of cellulose nanocrystals

Cellulose, the most abundant biopolymer on Earth, has been extensively used by man, in the form of macro- and microstructures, as a traditional resource in many aspects of daily life, notably to produce textiles and papers. This polymeric material is biosynthesized by a wide variety of living species such as plants, animals, bacteria, and some amoebas. Glucose is polymerized by enzymes in a continuous fashion. The resulting cellulose chains are homopolymers of β-1,4-linked anhydro-D-glucose units which associate to form microfibrils, further assembled into macrofibers and fibers. Crystalline and disordered regions alternate along the microfibrils (Figure 1a) [1-4].

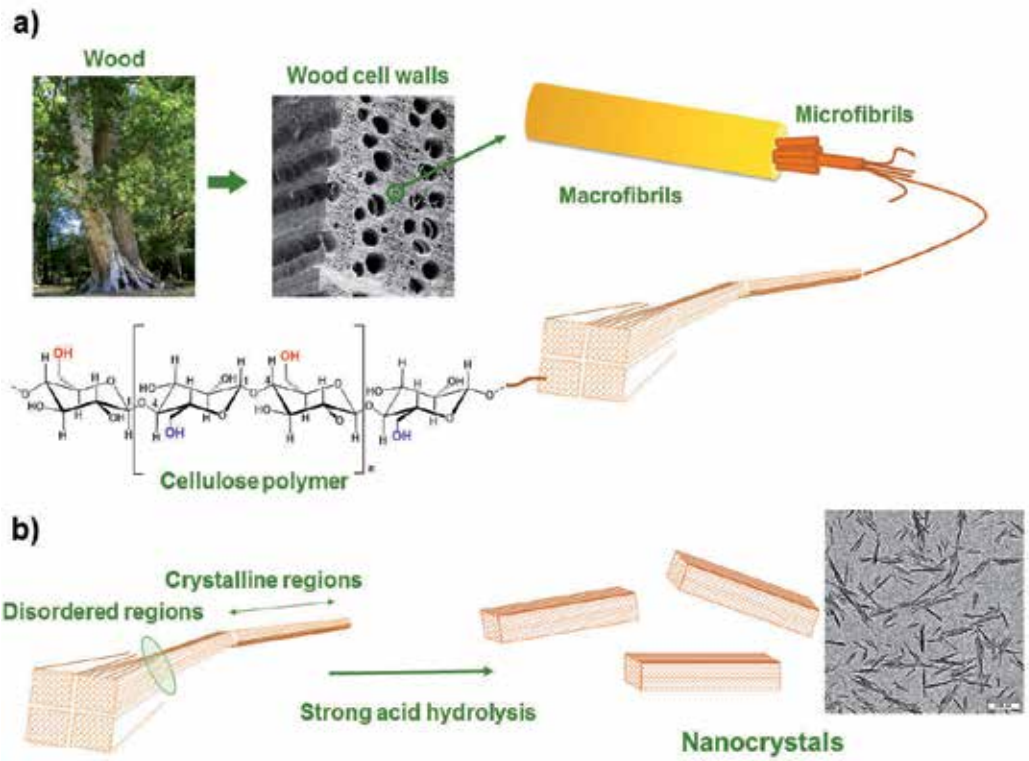

Figure 1. (a) Structural hierarchy of the cellulose fiber components from the tree to the anhydroglucose molecule (SEM image of wood cell structure: courtesy of D. Dupeyre, CERMAV); b) preparation of nanocrystals by selective acid hydrolysis of the disorganized regions of cellulose microfibrils (TEM image of cotton CNCs: courtesy of CERMAV).

In the late 1940s, cellulose crystallites were isolated for the first time by chemical treatment of a cotton substrate in hot concentrated sulfuric acid [5]. Soon after, Rånby showed that stable colloidal suspensions of negatively charged cellulose particles could be obtained [6, 7]. During

http://dx.doi.org/10.5772/60985

the extraction process, the cellulosic fibrous structure is broken down in the presence of concentrated sulfuric acid (other mineral acids can be used such as HCl). After diffusion of the acid within the substrate, the glycosidic linkages in disordered regions, more accessible and reactive, are preferentially broken. An additional mechanical or ultrasound treatment results in the release of rodlike cellulose crystallites, so-called cellulose nanocrystals or CNCs (Figure 1b). Consequently, as the hydrolysis proceeds, the degree of polymerization of the cellulose macrostructures decreases, while the crystallinity of the nonsoluble particles increases [8].

1.2. Cellulose nanocrystal properties

In the early 1950s, detailed characterizations of the shape and size of various CNCs (cotton, ramie [9], and bacterial cellulose [10]) were proposed from transmission electron microscopy (TEM) images. Since then, CNCs have been produced from a wide (and expanding) variety of sources [11] such as wood (Figure 2a), cotton (Figure 2b), bamboo (Figure 2c) [12], bacteria (Figure 2d) [13], algae (Figure 2e), tunicates (Figure 2f) [14], eucalyptus [12], spruce bark [15], corncob [16], etc. The CNCs are rodlike objects with a length typically ranging from 50 to 1000 nm and a width varying from 3 to 50 nm (Table 1). CNCs thus have high length-to-width (aspect) ratios (10-100) [17-22]. Their morphology depends on the cellulose source and the conditions of preparation (type and concentration of acid, acid-to-cellulose ratio, reaction time, and temperature) (Figure 2). The nanoscopic features of the resulting CNCs considerably influence their colloidal and macroscopic properties such as suspension rheology, phase separation concentration, liquid crystal behavior, orientation under electric or magnetic field, and mechanical reinforcement ability in nanocomposites [14, 16].

CNCs can be prepared in different forms. First, CNCs can be manipulated in the form of acidic aqueous suspensions resulting from the strong acid hydrolysis of microfibrils or as neutral suspensions after neutralization. Subsequent surface modifications can be achieved *via* chemical treatment [23, 24]. Alternatively, different drying methods may be used to afford a fluffy material, with the aspect of white sugar candy [25].

In 1959, Marchessault *et al.* revealed that the chemical reaction of sulfuric acid with hydroxyl groups at the surface of cellulose CNCs formed sulfate ester groups, resulting in electrostatic repulsions between the particles and ensuring colloidal stability. Moreover, the authors showed that CNCs could self-organize into liquid crystalline phases [26].

The sulfuric acid hydrolysis of cellulose has remained confined to academic research laboratories until a big step was made in the mid 1990s, when it was shown that CNCs were efficient reinforcing fillers in latex-based polymer matrices, opening a new potential market for this high-end material [14, 27]. Since then, CNCs have become intensively studied with an accelerating rate of publications released each year [17-22]. Beside mechanical properties, colloidal properties of CNCs in suspension generated a series of studies investigating their ability to form liquid-crystal phases. The colloidal suspensions of CNCs spontaneously organize into a chiral nematic phase above a certain critical concentration. As a consequence, CNCs have been used to produce iridescent and birefringent films [28-31], chiral mesoporous silica [32, 33] and carbon [34], gold nanoparticle films with chiral plasmonic properties [35], enantioselective amino acid hydrolysis catalysts [36], hydrogels [37], and aerogels [38].

Moreover, the high surface area and controllable surface chemistry of CNCs make them a unique support for metal nanoparticles (NPs) [39] CNC supported NPs, including Pd [40] and Au [41], were used as nanocatalysts. Pd NPs distributed onto CNCs were used for hydrogenation and carbon-carbon bond coupling reactions [40, 42-44], while the Au counterparts were used for 4-nitrophenol reduction [45]. Ag NPs were also deposited onto CNCs and the resulting material featured antibacterial activity [46].

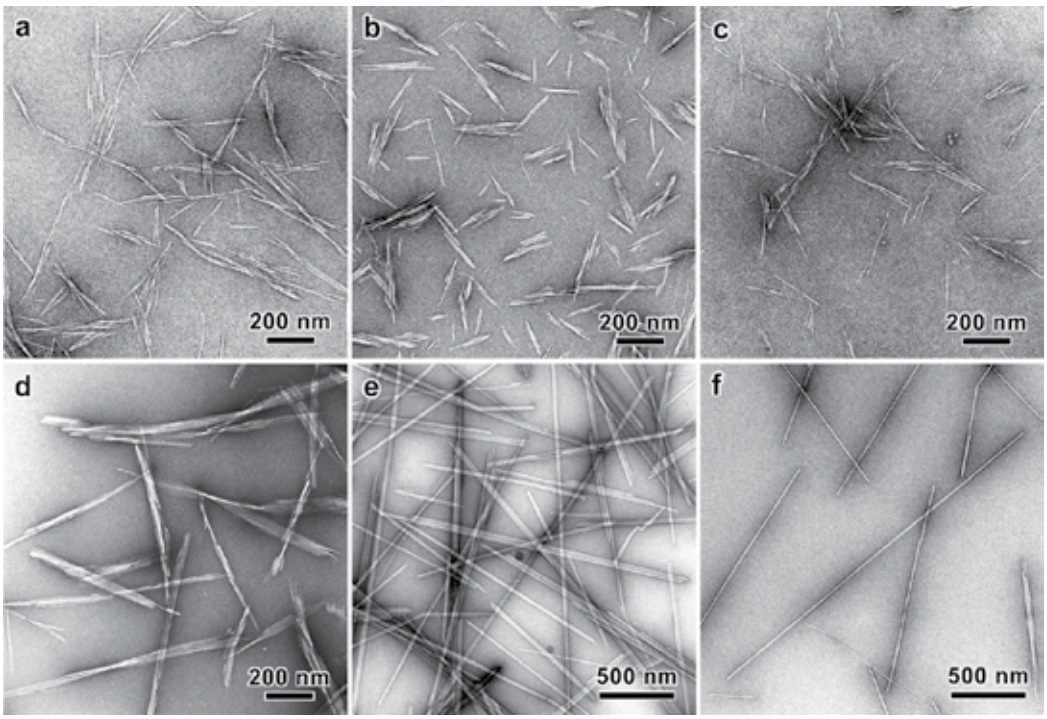

Figure 2. TEM images of negatively stained preparations of CNCs of various origins: a) wood (courtesy of G. Chauve, FPInnovations); b) cotton (courtesy of F. Azzam, CERMAV); c) bamboo (courtesy B. Jean, CERMAV; d) *Gluconacetobacter xylinus* (courtesy of H. Bizot, INRA); e) *Glaucocystis* (courtesy of Y. Nishiyama, CERMAV); f) *Halocynthia papillosa* (courtesy of A. Osorio-Madrazo, A. Ludwig University of Freiburg).

This large panel of high-end applications strongly encouraged industry to achieve large-scale production of CNCs. The forest-based industry in North America, Northern Europe, and Japan is currently looking into renewing and reinventing itself to extend its activities and guarantee its survival, while renewable materials are being increasingly appealing as fossil-based material replacement. In addition, CNCs are inherently safe, practically nontoxic materials [47]. Nanocellulose-based, value-added materials definitely constitute promising vectors to "turn wood into gold" and revive the forest-based industry. These combined factors led to the opening of the first commercial plant by CelluForce Inc. (Windsor, Québec, Canada), producing 1 ton of CNCs per day [48].

http://dx.doi.org/10.5772/60985

Several review articles and books have been published over the last few years which cover in detail the various aspects of the CNC features and applications [17, 18, 20, 21, 49].

1.3. Need for CNC characterization

CNCs possess appealing properties in direct relation with their three-dimensional (3D) structure, including well-defined shape, size, and aspect ratio. From an industrial perspective, it is essential to collect reliable data on CNCs, especially for quality control, toxicology assessment, R&D and applications.

1.3.1. Quality control

The large-scale production of CNCs became a reality when CelluForce Inc. started up its demonstration plant. Getting reliable, fast, and accurate measurement of the particle size is a key to guarantee a consistent production of high-quality CNCs. Several methods exist (*vide infra*) to determine the size, size distribution, and shape of CNCs. So far, they are typically used in academic studies and provide a fairly consistent understanding of the material structure. However, for the moment, no systematic and streamlined method exists for size determination and evaluation of polydispersity for anisometric nano-objects such as CNCs. This question is particularly acute for large-scale quality control, for instance, in pilot plant production and beyond.

1.3.2. Toxicology assessment

Manufactured nanomaterials have recently caused societal concerns about their possible adverse effects on health and safety. Properties of nanomaterials typically differ from those of their parent bulk materials because of their larger surface area, leading to a greater activity, their smaller size, resulting in their ability to cross natural barriers, and intrinsic effects caused by nanometric size, including electronic and plasmonic effects. Since such particles may have a negative effect on biological systems and ecosystems, their toxicological risks must be evaluated and an accurate description of the product in terms of dimensions, chemistry, and toxicity is required by the authorities. CNCs have extensively been evaluated using standard ecotoxicological and mammalian test protocols and have, to date, been shown to be practically nontoxic in each of the individual tests [47]. In addition, CNCs have recently obtained regulatory approval under Canada's New Substances Notification Regulations (NSNR) for unrestricted use in Canada and is the first organic nanomaterial to be added to Canada's domestic substance list.

1.3.3. R&D and applications

To maximize the reinforcing or liquid crystal behavior potential of CNCs, the particles have to be as well-dispersed as possible, especially in nanocomposite applications. An aspect that can lead to aggregation/agglomeration and then affect the further redispersion of the particles is mainly the final drying stage. Drying is a critical process for the large-scale industrial production of CNCs. Aqueous suspension leads to bacterial contamination and precludes

long-term storage. In addition, the cost associated to the transportation of suspensions containing up to 90% water is not economically viable. Various drying processes can be used such as freeze-drying, supercritical drying, spray-drying, oven drying, and air drying. Spray-drying methods are used in the industrial production of CNCs. The resulting solid, hornified macrostructure may be difficult to further redisperse, even in water. Neutralization of the acidic sulfate ester groups prior to drying helps with redispersion [25].

1.3.4. Challenges regarding CNC particle size measurement

The aspect ratio of CNCs dictates the percolation threshold, a key parameter to control mechanical properties in nanocomposites. Knowing the size and morphology of CNCs with precision plays a key role in the development of numerous applications where these features directly impact the properties of the final product. CNCs prepared by sulfuric acid hydrolysis of cellulose substrates are rigid, acicular-shaped and highly crystalline nanoparticles. The geometrical dimensions of these rodlike crystallites vary exceedingly with the source of cellulose (Table 1) and with the hydrolysis reaction conditions. For example, CNCs extracted from wood are 3-7 nm in width and 100-200 nm in length, while CNCs derived from tunicate are 10-20 nm in width and 500-2000 nm in length [14]. These values are indicative as different reaction conditions result in different sizes and size distributions. Indeed, size distributions were published as early as 1944 for ramie and cotton CNCs [50]. Lists of the different sizes of CNCs extracted from various sources can be found in recent reviews [17, 18, 20, 21] and in Table 1. The size distribution may have an impact on the properties and thus the applications of CNCs. For instance, it has been shown that polydispersity influenced the phase separation behavior of liquid crystalline suspensions [51, 52]. CNCs are usually obtained as colloidal aqueous suspensions and the production process induces batch-to-batch particle size variability. The rheological properties of the suspension and the state of individualization of the particles are strongly affected by external parameters such as nanoparticle concentration, pH, ionic strength, temperature, or the presence of an additional compound or impurities [53-55]. The stability of the suspension is due to the electrostatic repulsion forces created by the negatively charged sulfate ester groups located at the surface of the crystals. More generally, their propensity to agglomerate is driven by their surface chemistry. For example, the addition of electrolyte screens the surface charges of the particles, reducing the electrostatic repulsion that prevents CNCs from agglomerating, which results in either an increase or a decrease of the measured particle size by photon correlation spectroscopy (PCS) depending on the amount of electrolyte introduced. Since CNC particles do not undergo swelling or compaction upon the addition of electrolyte, this increase/decrease of the measured particle size is a pure artifact driven only by the laws of physics and thermodynamics. Consequently, for a given sample, particle size variability depends on the sample preparation conditions and the measurement techniques.

Particle size is a good indicator of the quality of the CNC dispersion but the direct observation of nanoparticles remains a challenge and high-resolution direct imaging or light scattering techniques are required.

http://dx.doi.org/10.5772/60985

1.4. Microscopy and spectroscopy techniques used for CNC characterization

As previously mentioned, CNCs come in a wide variety of length, width, and shape depending on the cellulose sources. The cross sections of CNCs also display a variety of shapes, e.g., square, rectangular, or parallelogram, that are dictated by the arrangements of enzymatic terminal complexes extruding cellulose chains during the biosynthesis. As shown in different cases, the edges of the crystals can be eroded during the acid hydrolysis yielding hexagonal or octagonal cross sections exposing small surface area of hydrophobic (200) planes [56].

Many instruments are commonly used for the determination of particle size distribution (PSD) and particle dimension(s), each instrument detecting size through its own physical principle. Numerous techniques based on microscopy, light interactions, electrical properties, sedimentation, sorting, and classification allow access to particle size. Depending on the technique, the results are more or less accurate and are related to the nanoparticle shape and its physicochemical features such as chemical composition, heterogeneity, topography, surface charge density, dispersing medium, viscosity, etc. The morphology of CNCs can be accurately revealed either by microscopic methods including transmission electron microscopy (TEM), cryo-TEM, atomic force microscopy (AFM), field emission gun scanning electron microscopy (FEG-SEM), or by scattering techniques such as polarized and depolarized light scattering (DLS and DDLS, respectively) and small- and wide-angle neutron or X-ray scattering (SANS, WANS, SAXS, and WAXS, respectively). Each of these techniques has its own advantages and limitations in their application to the study of CNCs. Consequently, care should be taken while comparing particle size data obtained from different techniques.

Light scattering techniques rely on the interaction of light with the hydrodynamic volume of a particle. With anisometric nanoparticles, the response varies as a function of the orientation of each individual particle. The collected data thus need to be mathematically processed to extract meaningful information. Typically, for acicular particles, such as CNCs, light scattering techniques have not been able to match the precision of microscopy. Microscopy, on the other hand, provides direct images of individual particles and allows characterization of its morphology and size (length, width and thickness). Microscopy techniques which have the nanometer scale resolution capabilities to image CNCs are electron microscopy and AFM. Electron microscopy enables the direct observation of the dimensions (*i.e.,* length and width) of a given particle. AFM provides information on morphology, surface topography, mechanical properties, and adhesion of CNCs under ambient conditions [15, 16, 57, 58]. While AFM provides reliable information on the thickness of the particles deposited on a flat substrate, the lateral resolution is limited by the convolution of the tip end, whose size and curvature are significantly larger than the dimensions of the nano-objects. However, this so-called tip-broadening effect can sometimes be deconvoluted [59]. On the contrary, TEM images provide good nanometric (and often subnanometric) lateral resolution, allowing to rapidly screen a large population of particles, thus avoiding major sampling issues. However, as TEM images are projections of the objects along the incident beam direction, it may be difficult to accurately measure the particle thickness. Moreover, the low density of CNCs calls for the use of staining methods. These limitations may be overcome by some of the recent developments described in the following sections, including low-dose microscopy and 3D imaging. When possible, the

combination of data from AFM and TEM images, and scattering analyses provides an optimal description of the particle morphology. For instance, a combination of imaging and scattering data was used by Elazzouzi-Hafraoui *et al.* [60] and Brito *et al.* [12] to precisely describe the morphology of CNCs extracted from a variety of sources.

It has to be noted that due to significant technical progress in instrumentation (low-voltage and beam-decelerated imaging, variable pressure) and detector variety and sensitivity, FEG-SEM imaging has become a perfectly valid approach to visualize the surface of CNC assemblies from dried systems [61] or fractured chiral nematic films [62]. CNC suspensions dried on TEM grids can be observed as well in an SEM equipped with a detector located below the specimen. With this so-called scanning transmission electron microscopy (STEM) mode, transmitted and scattered electrons can be collected to reconstitute an image of the specimen very similar to those obtained with a TEM. Although the accelerating voltage is lower (10-30 kV) than that used in a TEM (100-300 kV), the resolution is sufficient to see the fine details of CNCs [11].

This chapter focuses on TEM approaches. We describe several methods to prepare CNC specimens and emphasize the specific conditions to observe these highly beam-sensitive nanoparticles in order to provide images of CNC dispersions and determine reliable size distributions. A thorough description of sample preparation procedures and observation techniques is followed by a review of the literature on CNC imaging by TEM.

2. TEM techniques used for the observation of CNCs

2.1. Selected milestones in the characterization of nanocellulose by TEM

TEM imaging and electron diffraction played a significant role in the morphological and structural studies of cellulose microfibrils and nanocrystals, complementing data from spectroscopic (Fourier-transform infrared spectroscopy and solid-state NMR) and scattering (of X-rays or neutrons) analyses. Important information was obtained at a local scale, allowing to identify mechanisms at work during the biosynthesis and biodegradation of cellulose crystals and characterize some physical properties, with or without additional chemical modification, inside cell walls or, after extraction, in suspension or incorporated in nanocomposite materials.

In 1940, H. Ruska (brother of E. Ruska, inventor of the TEM) published what can be considered to be the first images of microfibrils obtained after HCl hydrolysis of cotton cellulose [63]. During the following two decades, the progress in TEM imaging of cellulose was mostly driven by the motivation to characterize the submicrometer structure of natural cellulose fibers. However, the identification of smaller constituting elements required the disintegration of cell walls and fibers using strong mechanical and/or chemical treatment [26, 64-68]. In particular, images of individual crystalline "fragments" (not yet called CNCs) were recorded after strong sulfuric acid hydrolysis of celluloses from various sources [9, 10, 69, 70].

In parallel to these morphological studies, important structural information was obtained using electron diffraction. Fiber diffraction patterns were collected from *Valonia* cell wall

http://dx.doi.org/10.5772/60985

fragments and microfibrils, at room [71] and low [72] temperature, confirming at a local scale the longitudinal orientation of the cellulose chains. The size and distribution of crystallites were determined in *Valonia* microfibrils using diffraction contrast imaging [73]. Later on, electron diffraction was notably used to validate the existence of separate regions of Iα and Iβ allomorphs of cellulose in microcrystals from *Microdictyon* cell wall fragments [74]. TEM imaging and diffraction methods were also combined to demonstrate that the biosynthesis of bacterial cellulose ribbons occurred by addition of the cellulose precursors at the nonreducing end of the chains [75]. A further striking demonstration of the molecular order in cellulose crystallites was provided when Sugiyama *et al.* successfully recorded the first high-resolution images directly showing longitudinal and axial projections of the crystal lattice of *Valonia* microfibrils [76, 77].

2.2. Sample preparation

The sample for TEM imaging has to be extremely thin in order to be transparent to electrons. Sample preparation is thus a crucial step. The limiting thickness depends on the atomic number and density of the observed material and on the energy of the incident electrons. Typically, for polymers, the thickness should remain well below 1 μm. For bulk materials, preparing such a thin specimen requires specific sectioning procedures. However, as the thickness of individual CNCs is well below this limit, the preparation of TEM specimens, for instance from dilute suspensions, is a lot easier.

2.2.1. Grids, supporting films and homogeneous distributions of nano-objects

In order to be observed by TEM, nanoparticle suspensions are deposited on 3.05-mm-large thin circular metallic grids with typical meshes around a few tens of micrometers, which will be placed in the sample holder for microscopy. There is a huge variety of TEM grids available and the selection of the right kind of grid is a crucial step for acquiring good images. Copper grids are the cheapest and the most widely used. However, when the pH of the suspension is low or high, copper can be degraded, resulting in the formation of artefactual crystallites or dendrites upon drying. In that case, gold or nickel grids have to be preferred. Carbon is by far the most commonly used supporting film. Carbon-coated grids are available commercially but carbon films can also be prepared in the laboratory by evaporating carbon on sacrificial collodion films or cleaved mica. The resulting films are then "fished" on copper grids. Carbon films have a typical thickness of 5-20 nm, depending on whether transparency or mechanical stability is favored. Formvar is also used as supporting film but it is less electron-transparent than carbon and can drift when heated by the electron beam at high magnification.

The main challenge in preparing a specimen suitable for TEM observation is to ensure a satisfying dispersion on the various objects. This is particularly critical when one wants to determine the size distribution of a population of CNCs. The supporting carbon film is initially rather hydrophobic, so the deposition of aqueous suspensions and subsequent air-drying generally result in locally accumulated material. Glow discharge is considered to be the easiest and most efficient pretreatment of carbon films before sample deposition. The TEM grids then are placed in the chamber of a glow discharge unit (*e.g.*, automated commercial systems like

easiGlow from Pelco or ELMO from Agar Scientific). A pumping system allows to reach a low pressure and the residual air is ionized. The grids are submitted to this mild plasma cleaning during a few seconds, which results in a hydrophilic carbon surface (at least during several minutes) onto which aqueous suspensions easily spread. As charges are also generated on carbon during the treatment, the nano-objects tend to adsorb on the surface. The excess of liquid can thus be gently blotted out without waiting for complete drying and the objects should be homogenously distributed on the grid. An example of a distribution of cotton CNCs prepared after glow discharge of the carbon film is shown in Figure 3a. The factory settings of the commercial systems generally promote negative charges and hydrophilic surfaces but, depending on the applications and systems, positive charges and/or hydrophobic surfaces can be produced using additional agents.

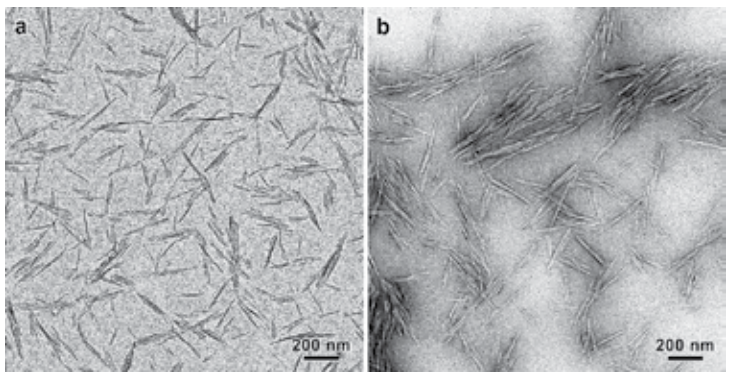

Figure 3. Comparison of images of unstained (a) and negatively stained (b) preparations of cotton CNCs. In both cases, the suspensions have been deposited on freshly glow-discharged carbon-coated grids.

Different materials have been tested as supporting films. While hydrophobic formvar promoted aggregation (Figure 4a), satisfactory dispersions of individual CNCs were achieved on hydrophilic silicon monoxide (Figure 4b) [78]. Silica (SiO_2) and silicon nitride (Si_3N_4) films, with or without additional functionalization, are also commercially available (NanoGrids from Dune Sciences).

In addition to the choice of supporting film and the use of an additional pretreatment, the use of very dilute suspensions is recommended, typically 0.001-0.01 % (w/v) for CNC suspensions. The nanocrystals will adsorb more efficiently onto hydrophilic films and particularly those that have been glow-discharged and this effect can be compensated by a higher dilution.

2.2.2. Impact of the CNC suspension on the TEM observation

After acid hydrolysis, CNCs occur in the form of suspensions that generally require further purification steps to remove the residual acid and salts. Indeed, residual soluble salts will likely crystallize upon drying on the supporting film of the TEM grid, resulting in the formation of artifactual dendrites. The suspensions are dialyzed against water to reach a pH around 2.5-3. Then CNCs may be used as such – *i.e.*, in the form of an acidic aqueous suspension – or may

http://dx.doi.org/10.5772/60985

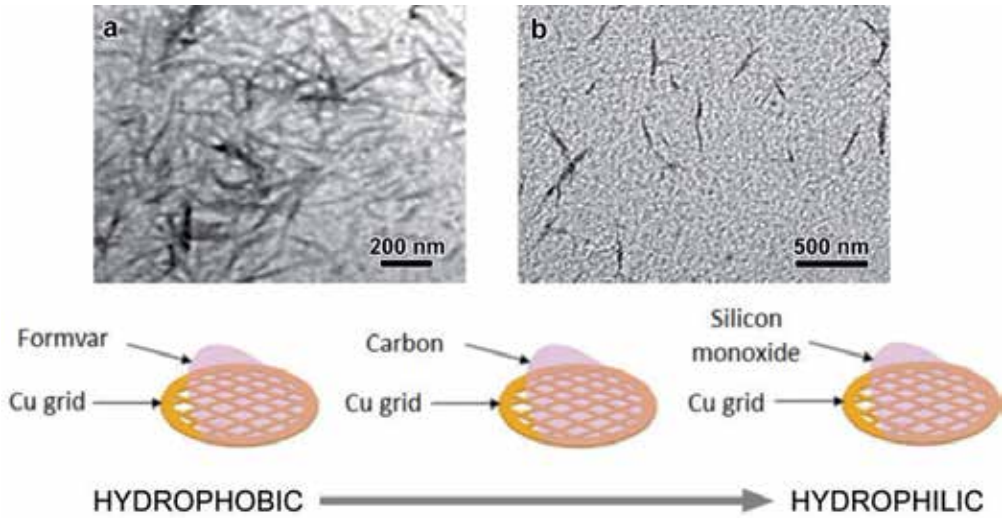

Figure 4. Comparison of never-dried CNCs at pH 5-6 on different types of supporting films: a) formvar; b) silicon monoxide (reproduced from [78] by permission of the KTH Royal Institute of Technology).

be neutralized with NaOH to reach pH~7, and be used in the form of neutral aqueous suspension [25]. The drying step of an acidic CNC suspension prevents the CNCs to be later redispersed in water because CNC aggregates are created by hydrogen bonds *via* a phenomenon called hornification. Adjusting the suspension to a neutral pH prior to drying allows the dried CNCs to be spontaneously redispersed in water, while the specimens dried from acid pH suspensions cannot be properly resuspended [25].

The impact of the drying step of the CNCs prior to resuspension has been demonstrated by comparing three TEM specimens: 1) "never-dried" CNCs – CNC suspensions resulting directly from cellulose hydrolysis, 2) "freeze-dried" CNCs – CNC suspensions made from dispersing pH-neutralized freeze-dried CNCs, and 3) "spay-dried" CNCs – CNCs suspension made from dispersing pH-neutralized spray-dried CNCs [78]. For all three specimens, the pH of the redispersed suspension was adjusted to 5-6 and the suspensions were deposited on carbon-coated grids. As seen in Figure 5, dispersions from spray-dried samples featured more CNC aggregates than those prepared from freeze-dried and never-dried samples. More single rods were observed in the latter than in any of the other two. On Figure 5a, the typical width of the observed bundles in the three samples is marked and is indicative of the degree of aggregation. This conclusion is actually consistent with the fact that spray-dried CNCs are more difficult to disperse than freeze-dried or never-dried counterparts [25]. In addition, a mushroom-like morphology has been exclusively reported for the spray-dried CNCs, which look like patches, with a size ranging from 100 to 200 nm, with a much higher contrast than the rods [79, 80]. However, this morphology was proved to be an artifact from improper dispersion of the sample on the TEM grid [78]. Additionally, the suspensions of previously dried CNCs could be briefly sonicated to promote greater dispersion before preparing TEM grids.

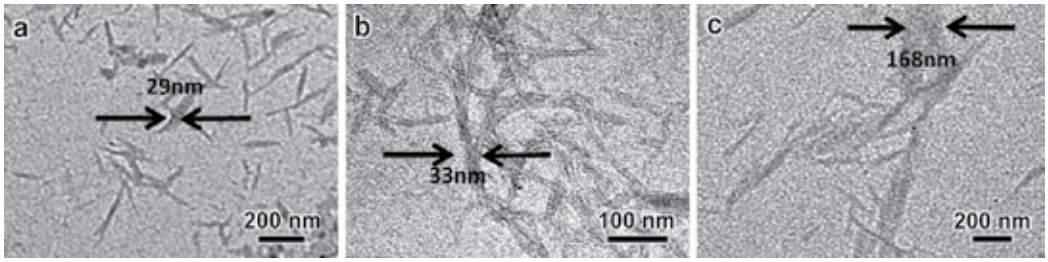

Figure 5. TEM images of unstained wood pulp CNCs: a) from a suspension of never-dried CNCs; b) from a freeze-dried suspension of redispersed CNCs; c) from a spray-dried suspension. All suspensions were adjusted to pH 5-6 before deposition onto carbon-coated copper grids (reproduced from [78] by permission of the KTH Royal Institute of Technology).

The pH of CNC suspensions before TEM sample preparation has a clear influence on the CNC dispersion on the grid. When CNCs are redispersed in dionized water, the pH is around 5-6. If never-dried CNCs are observed at this pH, on carbon-coated TEM grids, the images show both individual and aggregated CNCs (Figure 6). Theimproved CNC dispersion on the grid is obtained at pH 3.5. Indeed, at pH below 4-5, CNCs are more negatively charged as the half-sulfate ester groups are in their acidic form.

The particle morphology and aggregation state observed by TEM depends on how the dried CNC sample has been redispersed in water (use of sonication to promote de-agglomeration), which in turn depends upon the drying history of the CNCs (*i.e.*, the pH of the suspension before drying). The optimal conditions to image CNCs is to prepare a TEM specimen from a suspension of never-dried CNCs or a pH-neutralized suspension.

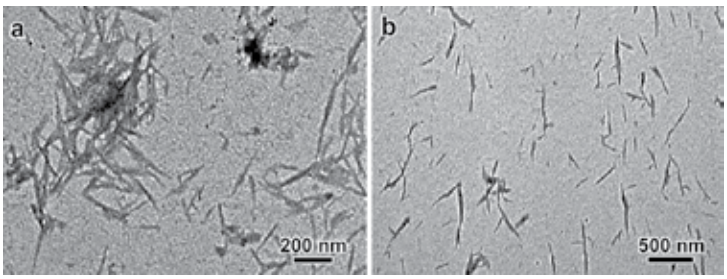

Figure 6. Influence of the pH of the CNC suspension on the dispersion on carbon films: a) pH 5-6; b) pH 3.5 (reproduced from [78] by permission of the KTH Royal Institute of Technology).

2.2.3. Contrast enhancement techniques

2.2.3.1. Negative staining

Since the contrast of cellulose specimens is rather low, and since using high magnification to see more details will result in a rapid degradation of the particles (hence a loss of contrast),

http://dx.doi.org/10.5772/60985

several techniques may be used to enhance the contrast in the images. The most widely used is commonly called negative staining. A drop of an aqueous solution of heavy atom salts is deposited on the specimen. Upon drying, a thin layer of heavy atoms concentrate around the nanoparticles, creating an electron dense outline [81]. The CNCs thus appear as clear objects on a dark background, hence the negative effect on the image. The preparations can be observed at a higher magnification as, although cellulose is indeed damaged by the electron beam, the heavy atom "imprint" is resistant, revealing fine details of the surface topography. So far, 2% (w/v) uranyl acetate solutions have been the most commonly used stain but phototungstic acid or ammonium molybdate are sometimes used as well. Uranyl acetate will likely disappear from the catalogues as recent regulations have been enforced regarding the handling of radioactive products, resulting in a significant price increase. Consequently, new commercial ready-to-use stain solutions have been recently proposed, such as Uranyless (that contains lanthanides, from Delta Microscopies) or NanoVan (methylamine vanadate, from Nanoprobes). Practically, a homogenous negative staining of CNCs will be achieved under two conditions: i) the supporting carbon film has to be glow-discharged before the nanoparticles and the stain are deposited; ii) the negative stain has to be deposited on the specimen before drying. After a few minutes, the stain in excess can be blotted away with filter paper and the residual thin stain film allowed to dry. It has to be noted that negative staining can partly promote the local flocculation of the CNCs on the supporting film, as can be seen in Figure 3b.

2.2.3.2. Metal shadowing

The technique has been used very early on to observe nanocellulose. Indeed, in the 1950s, Rånby published images of metal-shadowed preparations of wood and cotton microfibrils [10], as well as tunicate [70] and bacterial CNCs [10]. Images of ramie and cotton CNCs can also be found in Mukherjee and Woods' paper [9]. Metal (generally gold/palladium or platinum) is vaporized on the sample with a given incidence angle. It thus accumulates on one side of the nanoparticles (electron-dense region) and is absent on the other side (electron-transparent region). This results in a shadow-and-light effect that enhances the topography details of the specimen with a very high contrast. Again, it is the metallic layer that is observed even if the cellulose particles are damaged by the incident electron beam. The resolution is limited by the granularity and thickness of the metal film that increases the apparent width of the particles.

In the specific case of concentrated CNC suspensions, freeze-fracture can be used. A drop of the suspension is fast frozen and, under vacuum, a sharp knife breaks the frozen specimen into two fragments. The resulting surfaces are then directionally shadowed with a thin layer of evaporated metal, consolidated with an additional layer of carbon. The specimen is then warmed up and the metallic replica washed, deposited on a carbon-coated grid, and observed in the TEM, providing a high-contrast image of the topography of the fractured surface. An example of freeze-fracture replica of a concentrated suspension of cotton CNCs is shown in Figure 7a.

2.2.4. Cryo-TEM

Cryo-TEM consists in observing nanoparticles embedded in a thin film of transparent vitreous ice, thus avoiding the detrimental effects of drying and/or staining (degradation, deformation, aggregation, agglomeration, coalescence, uniplanar orientation, buffer salt crystallization, etc.). This technique is particularly helpful with dilute suspensions of nano-objects that are soft or liquid at room temperature and whose morphology or structure may be affected by air-drying (deformation due to capillary forces, decrystallization). Droplets of suspensions are typically deposited on holey or lacey (*e.g.*, NetMesh from Pelco) carbon films supported by TEM copper grids. Perforated support foils with predefined hole size and arrangements (*e.g.*, Quantifoil from Quantifoil Micro Tools or C-flat from Protochips) can also be used. The liquid in excess is blotted with filter paper and the thin remaining film is quench-frozen in liquid ethane [81]. The frozen specimen is mounted in a cryo-specimen holder precooled with liquid nitrogen, transferred in the microscope, and maintained at low temperature during TEM observation. Temperature- and humidity-controlled chambers with automated plungers are commercially available (Vitrobot from FEI, EM-GP from Leica or Cryoplunge from Gatan), ensuring a higher reproducibility of the fast-freezing procedure. Cryo-TEM is not limited to aqueous suspensions and organic solvents can also be used, provided that they can be properly vitrified and that they are not dissolved in liquid ethane.

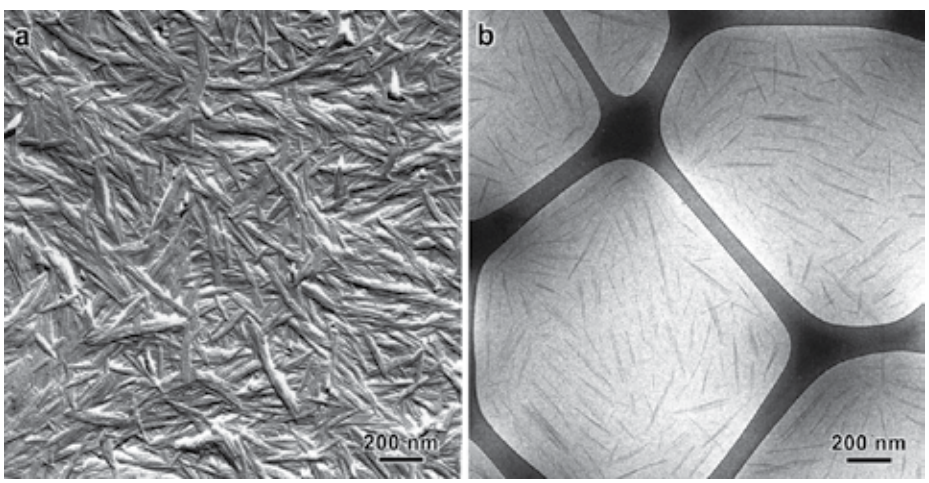

Figure 7. Alternative methods to observe cotton CNC dispersions: a) Pt/C replica of a freeze-fractured concentrated suspension; b) cryo-TEM preparation of a dilute suspension. The CNCs are embedded in a thin film of vitreous ice (courtesy of S. Elazzouzi-Hafraoui, CERMAV).

In the case of CNCs which are rigid crystalline nanoparticles, using cryo-TEM is helpful to prevent the aggregation that may happen upon drying, resulting in unwanted particle superimposition. Indeed, cryo-TEM has only been used in a small number of cases, to observe unstained nonflocculating cotton CNCs (Figure 7b) [60, 82] and characterize by electron tomography (see § 2.3.3) the 3D shape of CNCs wrapped with dendronized-polymers [62] or covered with Pd patches [44].

http://dx.doi.org/10.5772/60985

2.2.5. Ultramicrotomy

This preparation technique should be used for bulk materials like plant tissues, cell wall fragments, nanocomposite materials, fibers, etc. When the specimen is affected by air-drying, it has to be first fixed in paraformaldehyde/glutaraldehyde, post-fixed with osmium tetroxide, dehydrated by exchange with ethanol and embedded in hardening resins (Epon, LR White, Spurr, etc.) [83]. In the case of nanocomposite materials incorporating cellulose microfibrils (CMFs) or CNCs as reinforcing fillers, small fragments can be used without resin-embedding, provided that the material is sufficiently hard. Ultrathin (50-150 nm) sections of the specimens are then cut at room temperature with a diamond knife in an ultramicrotome [84]. The sections are collected on bare or carbon-coated TEM grids and, if necessary, in order to enhance contrast, may be post-stained with uranyl acetate/lead citrate. When the sample is soft at room temperature, ultrasectioning has to be performed in cryogenic conditions with a dedicated unit.

2.3. Observation techniques

Beside the constraints directly related to sample preparation (drying, staining, etc.), the TEM observation of CMFs and CNCs should result in the recording of images with a good signal-to-noise ratio and showing enough fine details of the objects. The various contrasts observed in the images are generated by physical interactions of the incident electrons with the material [85] and these contrasts have to be properly recorded by a sensitive "detector." Although for many years, micrographs were recorded on films, those have been progressively replaced by digital cameras typically equipped with a 1k×1k, 2k×2k or 4k×4k pixel-large CCD or CMOS detector. These cameras have wide dynamics, good linearity, and are very sensitive, allowing to record images with short exposure times and low electron doses. In addition, the software that pilots the camera can process the signal in real time, allowing, for instance, to calculate Fourier transform and correct some aberrations.

2.3.1. Contrast

Three main phenomena contribute to the overall contrast of CNCs in an image. Mass/thickness contrast (also called amplitude or diffusion contrast) is generally low for polymer particles as they are mostly composed of light elements that weakly scatter electrons. The proportion of electrons transmitted and scattered by the specimen depends on its density and thickness. By inserting an aperture located in the back focal plane of the objective lens, the operator blocks a certain amount of scattered electrons and form an image with the transmitted (or weakly scattered) electrons. In this so-called bright field image, the dark regions thus correspond to the ones scattering electrons the most. As CMFs and CNCs are generally very thin, they generate a low amplitude contrast which, as described in § 2.2.3, can be significantly enhanced by using specific staining techniques involving heavy atoms. However, for unstained preparations, large differences in contrast can be observed in hybrid organic-inorganic systems, allowing, for instance, to locate metallic or oxide nanoclusters distributed along cellulose nanoparticles [40].

Diffraction contrast occurs when the specimen is crystalline or semicrystalline, independently of its chemical nature (light or heavy atoms). Depending on the orientation of the crystal with respect to the incident beam, the electrons will be diffracted away from the optical axis. The set of discrete diffraction angles is defined by the unit cell of the crystal and can be determined using Bragg's relation [85]. When a diffracted beam is stopped by the objective lens aperture, in images with negative defocus, the regions of the particle from which the diffracted beam originates are very dark against the clear amorphous carbon background. This effect is thus important to visualize CNCs in bright field mode as it compensates somewhat the low amplitude contrast. It depends on the crystallinity index of cellulose (low for wood and high for tunicate CNCs, for instance). However, as cellulose is highly sensitive to beam damage, the diffraction contrast lasts for a limited time and disappears as soon as the material becomes amorphous.

Phase contrast is crucial in the case of electron-transparent nano-objects. It results from sharp differences in scattering properties between regions of the specimen. This is the case for CNCs spread on a carbon film (particles in vacuum), and CNC suspensions observed by cryo-TEM (particles embedded in vitreous ice). Phase contrast generates interference Fresnel fringes whose amplitude and distribution depend on the defocus of the objective lens [85]. The effect of phase contrast on the image of unstained CNCs is illustrated in Figure 8a and 8c. High defocus values (positive or negative) increase contrast but also generate larger Fresnel fringes and increase the apparent size of the nanoparticles. Note the complete reverse of contrast between underfocused and overfocused images. In overfocused images, the CNCs are clear with a dark outline which reminds the aspect they would have after negative staining. Close to zero defocus, the contrast is minimal and the specimen is hardly visible. Paradoxically, the operator will be satisfied by images recorded with some defocus as the contrast is higher and as the Fresnel fringes around the particles create an impression of "sharpness." However, this effect is associated with a loss of details. A satisfactory image is thus obtained by balancing the opposing requirements of contrast and ultrastructural details. By convention, the images are recorded in underfocused conditions, the amount of applied defocus increasing with decreasing magnification (typically about -5 µm at 3000x and -1 µm at 10000x). The importance of using underfocused conditions is clear in the case of negatively stained specimens, as seen in Figure 8b.

In the routine observation of unstained CNCs, three types of contrast contribute: a weak amplitude contrast due to the small size and organic nature of the particles; a significant diffraction contrast that depends on the crystallinity index of cellulose and orientation of the particles with respect to the incident electron beam; a phase contrast that generate Fresnel fringes along the CNCs controlled by the amount of defocus. As detailed in the following section, all these contributions will be affected by radiation damage.

2.3.2. Radiation damage

The most important limitation to observe crystalline polymers by TEM is the significant damage created by the electron beam which rapidly affects the resolution and decreases the

http://dx.doi.org/10.5772/60985

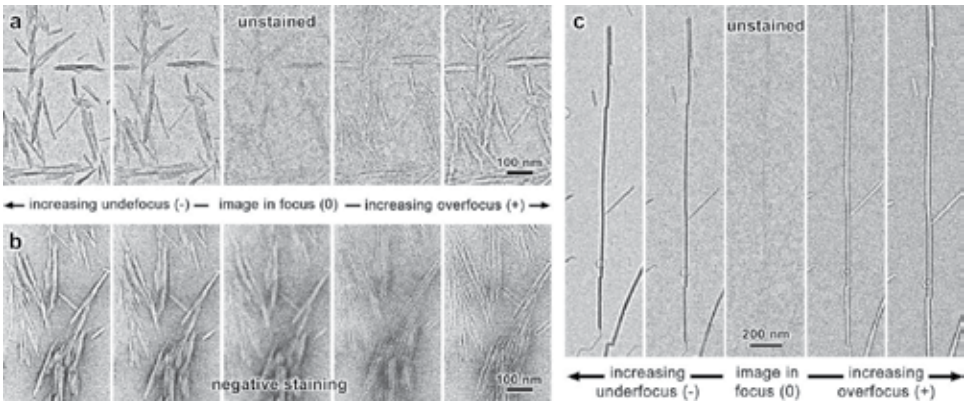

Figure 8. Influence of the defocus on the contrast of cotton (a,b) and tunicate (c) CNCs. The preparations are unstained (a,c) and negatively stained with uranyl acetate (b).

contrast of the objects. In such low-density materials, the inelastic scattering of the electrons generates molecular excitations and ionization phenomena, resulting in local heating of the material, breaking of covalent bonds, diffusion of free radicals, and emission of volatile species [86]. The consequences can be mass loss, fusion, vaporization, loss of crystallinity, all resulting in a significant decrease of amplitude, diffraction, and Fresnel contrasts. For crystalline materials, one can define a "lethal" or "total end point" dose by monitoring the disappearance of the electron diffraction pattern and calculating the electron dose at which crystallinity is irreversibly lost.

Even if the selected microscope has the ability to visualize details down to a resolution of 0.1-0.2 nm, the sample itself imposes drastic constraints. Several solutions exist to limit the detrimental effects of beam damage during the observation and image recording. First, contrary to what is done with materials made of heavy atoms, increasing the accelerating voltage of the electrons decreases the interactions with the polymer and thus increases the lethal dose (typically about a factor of 2 between 100 and 200 kV). However, the consequence of a higher accelerating voltage is a decrease in contrast. For instance, individual CNCs observed at 200 kV or a higher voltage tend to become transparent.

Second, the operator has to work with electron doses much lower than the lethal dose, which requires both to use low magnifications and significantly decrease the illumination (*e.g.*, by changing the "spot size" and spreading the surface of illumination). The observation of unstained cellulose specimens thus requires for the operator to make a compromise between image magnification (to see fine details with a sufficient contrast) and electron dose (to have a sufficient signal-to-noise ratio for the detector recording the image). Chanzy has quantified the lethal dose of cellulose by submitting *Valonia* CMFs to increasing electron doses at various accelerating voltages and monitoring the decay of diffracted beam intensity [87]. The average value for the lethal dose was about 4 electrons.$Å^{-2}$, which illustrates the extreme sensitivity of polysaccharides.

Third, the radiation damage can be significantly slowed down (but not suppressed) when the diffusion of free radicals is reduced by maintaining the specimen at low temperature, using a specific specimen holder cooled down with liquid nitrogen. In that case, an increase of the lethal dose by a factor of 3 has been reported in the literature.

The images in Figure 9 qualitatively illustrate the cumulative effect of beam damage during the observation of CNCs. Cotton and tunicate CNCs (Figures 9a and 9b, respectively) have been submitted to increasing electron doses. The three contributions to contrast previously mentioned are affected: diffraction contrast by disruption of the crystallinity; amplitude contrast by mass loss; and phase contrast by thinning of the particle and surface damage. The CNCs become transparent and their shape less well-defined. These effects are very fast and irreversible, in particular if the specimen is readily observed at magnifications above 10000x or the beam is inadvertently focused into a smaller disk (Figure 9c).

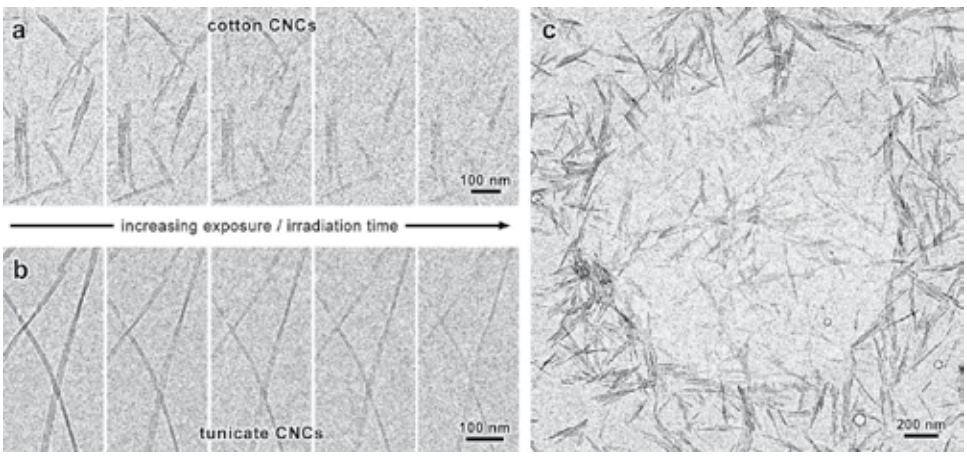

Figure 9. Influence of the radiation damage on the contrast of unstained cotton (a) and tunicate (b) CNCs. In (c), the electron beam has been briefly condensed into a smaller disk resulting in a marked damage on a distribution of unstained cotton CNCs.

2.3.3. 3D imaging

TEM images are two-dimensional (2D) projections of the 3D objects along the beam direction. Information along this direction is thus lost. One 2D image is generally not enough for the viewer to have a clear idea of the 3D shapes and several images, recorded at different tilt angles of the specimen, are necessary to make a reliable morphological analysis. Electron tomography (ET) can be performed in modern microscopes, thanks to the use of digital cameras and software that can precisely control the specimen orientation and image acquisition. Briefly, series of 2D images containing the data for mass-density distribution in the specimen are automatically recorded with small angular increments over a large angular range (usually from +70° to -70°). Using specific software, the collected images are aligned with respect to one another and a back-projection is carried out to obtain a 3D reconstruction of the specimen

volume [88-90]. While this technique is now widely used to study the morphology and structure of biological systems (proteins, viruses, membranes, etc.), So far, only two cases of CNC analysis can be found in the literature and will be described in § 3.4 [44, 62]. As explained in § 2.3.2, unstained cellulose is highly sensitive to beam damage and will be rapidly degraded. The amplitude contrast will thus decrease during the recording of the tilt series. This necessitates working at low magnification, with extremely low electron doses and a sensitive digital camera. In addition, due to the crystalline nature of CNCs, the contribution of diffraction contrast may fluctuate depending on the tilt angle of the particles.

3. Review of cellulose nanocrystal imaging and size analysis

3.1. TEM images and size distributions of CNCs

Although AFM is still often used to perform size measurements of CNC populations [15, 16, 57-59], TEM has been a method of choice to visualize the shape and structure of individual or bundled CNCs [16, 60, 91, 92]. The images are consistent and show that CNCs are rodlike and have a high aspect ratio. Some authors have observed spherical CNC particles [79] but these have been shown to be aggregation-induced artifacts [78]. As seen in Figure 2, the CNC aspect ratio and structure greatly vary with the cellulose source. CNCs obtained from plant sources like cotton [60, 93, 94], rice [95, 96], ramie [97-99], sisal [99, 100], or sugar beet [94] have smaller aspect ratios than those of bacterial cellulose [101, 102], microcrystalline cellulose (MCC) [51, 98, 103-106] and tunicin [98] (Table 1). The significant heterogeneity of the length and width distributions of CNCs, for a given source of cellulose, can be attributed to the method of preparation: type and concentration of the acid, reaction time, temperature, sonication, method of drying, etc.

Source of Cellulose		Length (nm)	Width (nm)	References*
Plants	Cotton	50–300	5–10	[60, 94]
	Rice	50–300	10–15	[95, 96]
	Ramie	50–250	5–10	[97-99]
	Sisal	100–200	3–7	[100, 107]
Microcrystalline cellulose (MCC) from wood		50–500	5–50	[103, 104, 106, 108]
Tunicates		100–3000	10–50	[60, 94, 109, 110]
Bacteria		200–3000	10–75	[101, 102, 105]

*Proposed references are representative examples and do not constitute an exhaustive list.

Table 1. Size distribution of CNCs from various sources of cellulose.

To a first approximation, the size measurement of CNCs should not be particularly difficult, provided that the objects are fairly well individualized on the supporting films, not severely

damaged by the electron beam (§ 2.3.2), and that a reasonable underfocus was used to record the image (§ 2.3.1). Their length and width can be measured from general views recorded at intermediate magnifications (typically 5000 to 10000×) by using a software like ImageJ [111]. Automated procedures are generally difficult to implement with TEM micrographs as the preliminary binarization of the images requires to clearly distinguish the CNCs from a continuous background. As seen in many images presented in this article, this is rarely the case. Thus, one directly uses the measurement tools of the software or outlines each CNC so that a semiautomatic measurement routine can be run. In addition, a review of the literature shows that the number of counted particles greatly varies (typically from 100 to 1000), mostly depending on the number of individual particles in the images and the patience of the operator. Of course, the number of objects taken into account will influence the reliability of the population statistics.

When higher magnifications are used (typically, 10000 to 50000×), keeping in mind the potential beam damage of unstained specimens, a better resolution is achieved and more details are revealed, particularly after negative staining. As confirmed by many images found in the literature, the majority of CNCs prepared from various sources are not single crystallites. They are often composed of a few laterally joined rodlike crystallites, as illustrated by Figure 10 in the case of cotton CNCs. The same feature has been reported for tunicate [60], Avicel [60], or bamboo [12] CNCs, to give just a few examples. The images in Figure 10 clearly show that cotton CNCs have a high variability in shape and dimensions. They are all different in size and structure, being composed of different numbers of unit crystallites, joined in a different fashion. This association inside individual particles does not result from artifactual flocculation but rather from the fact that the hydrolysis was performed on dry cellulosic substrates in which microfibrils are strongly linked by hydrogen bonds. Neither acid hydrolysis nor sonication (nor any high-shearing device) could fully separate the constituting crystallites.

The composite nature of most CNCs, which was validated by a combination of imaging and scattering techniques [12, 60], will thus influence the measurement of the lateral dimensions which depend on the cross-sectional shape and its regularity along the whole particle, the existence of a longitudinal twist, and the specimen preparation method. Considering the acicular morphology of CNCs, their distribution on a supporting film or inside thin vitreous ice favors their planar orientation, allowing to easily measure the length of the rodlike nanoparticles. However, while the particle thickness can be accurately measured from tapping mode AFM images, a choice has to be made regarding the definition of the width in TEM micrographs. As many types of CNCs exhibit a spindle-like shape, the width is generally defined as the largest dimension perpendicular to the particle long axis. Moreover, when the CNCs are ribbon-like, because of the rectangular cross section of individual crystallites (tunicate CNCs, for instance) or the lateral association of crystallites (cotton CNCs), the drying on a supporting film will generate a strong uniplanarity, the particles tending to lie on their widest face. This propensity to uniplanarity, which brings very useful information of the crystallite orientation in the CNCs, can be easily evaluated by performing complementary WAXS analysis on air-dried films [12, 60]. In addition, some CNCs are longitudinally twisted, which can be detected in TEM images by variations in contrast or stain distribution along the

http://dx.doi.org/10.5772/60985

particle (an example on tunicate CNCs can be seen in Figure 9b). Therefore, the apparent width of the particle will vary, making the choice of a relevant region to measure more difficult.

Cryo-TEM has been shown to be helpful in preventing particle aggregation/agglomeration due to drying [60, 82]. If the suspension concentration has been chosen with care, and considering the fact that CNCs have charges on their surface, they are conveniently individualized in the embedding film of vitreous ice. As their lateral dimensions are smaller than the typical thickness of the liquid film prior to fast-freezing, they could freely rotate around their long axis. Consequently, the measured width indeed corresponds to the projection of the CNC in a given orientation. Therefore, the width distribution of the population from a cryo-TEM image provides a rotational average of the lateral dimension of the particle and can thus be different from the distribution that is obtained from a specimen prepared by air-drying on a supporting film. The effect will be more pronounced for flat particles, such as cotton CNCs, as shown in Figure 10. Using a simple model, Elazzouzi-Hafraoui *et al.* have described the relation that can be made between the distributions obtained with both preparation techniques [60].

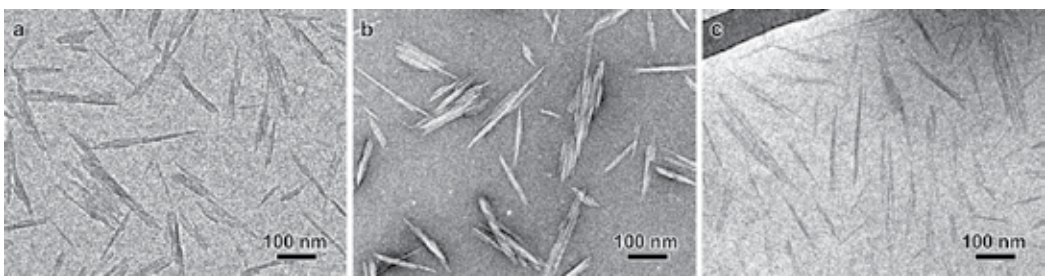

Figure 10. TEM images illustrating the diversity of shapes and structures of CNCs prepared by acid hydrolysis of cotton linters: a) dry specimen; b) negative staining (courtesy of F. Azzam, CERMAV); c) cryo-TEM (courtesy of S. Elazzouzi-Hafraoui, CERMAV).

Determining a size distribution from TEM images thus implies clearly stating the choices that were made in relation with the particle morphology. In addition, length and width distribution can be determined independently (Figure 11a) [78, 82] or assuming that there is a correlation between longitudinal and lateral dimensions of the CNCs. In that case, length and width are tabulated for each particle, resulting in a 2D size distribution histogram (Figure 11b) which validates (or not) the correlation [60].

The relevance of the size distribution of a given population of CNCs depends on several factors in relation with the problem that is addressed or the specific property that is investigated. For acicular (and possibly ribbon-like) CNCs, the influence of the statistical errors on the measurements will differ depending on the considered dimension (smaller for the length and larger for the width and thickness). Moreover, the size distributions are always wide, with large standard deviations and asymmetrical shapes (Figure 11) [16, 82, 91, 92]. Average lengths, widths, and thicknesses provide a cylindrical average view of the particles that can be useful to build a preliminary model. However, it is likely that a more complete description of the population, made by fitting the data with suitable functions, will be more relevant for

comparisons with X-ray or neutron scattering results [60], or, for example, to understand the percolation behavior of CNCs inside nanocomposite materials.

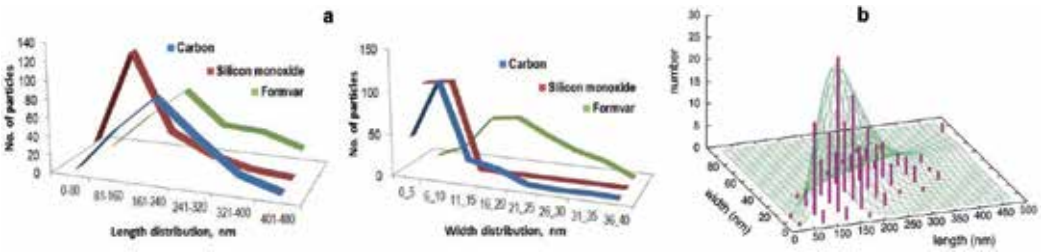

Figure 11. Length and width distributions histograms of various CNC systems determined from TEM images: a) never-dried CNCs at pH 3.5 deposited on different types of grids and observed unstained [78]; b) 2D histogram from negatively stained cotton CNCs (reprinted with permission from [60]. Copyright 2008 American Chemical Society).

3.2. TEM of CNC-hybrid composites

Hybrid composites of CNC with metal nanoparticles (NPs) such as Ag [39, 46, 112], Au [39, 41], Cu [39], Pd [40, 44, 113], Pt [39, 114], or Se [115] have been reported. TEM, along with its analytical tools, was used to characterize such composites (Figure 12). Due to their high atomic number and possible crystallinity, the metal NPs appear as dark spots in underfocused images. The difficulty to observe such hybrid organic-inorganic systems comes from the fact that CNCs and metal NPs have very different sensitivity to beam damage. While metallic NPs are very stable, cellulose is rapidly damaged, resulting in a significant loss of contrast and recognizable morphology. Consequently, to have a better visibility, a large defocus is usually applied which causes an overestimation in the size of metal NPs [78]. Additional negative staining can be effective to outline the CNCs more precisely but care must be taken to prevent the layer of stain from overshadowing the contrast of the metallic nanoclusters. Indeed, if the metallic NPs are smaller than 3-4 nm, they will not be distinguished from the granularity of the dry stain. As shown in Figure 12f, for larger NPs, CNCs can benefit from the negative staining while the metallic clusters still appears as dark spots. Finally, recent results demonstrated that highly sensitive direct detection device (DDD) cameras, associated with phase plates, allowed to observe simultaneously CNCs and subnanometer-thick palladium plates at their surface (Figure 13) [44]. In this experiment, the organic and inorganic phases were observed together at near-focus conditions.

Alongside visualization of metal NPs, it is very important to validate the chemical nature of the NPs seen in the images. This analysis can be done in a TEM by using energy-dispersive X-ray spectroscopy (EDX) which allows for quantitative measurement of the chemical composition [40].

http://dx.doi.org/10.5772/60985

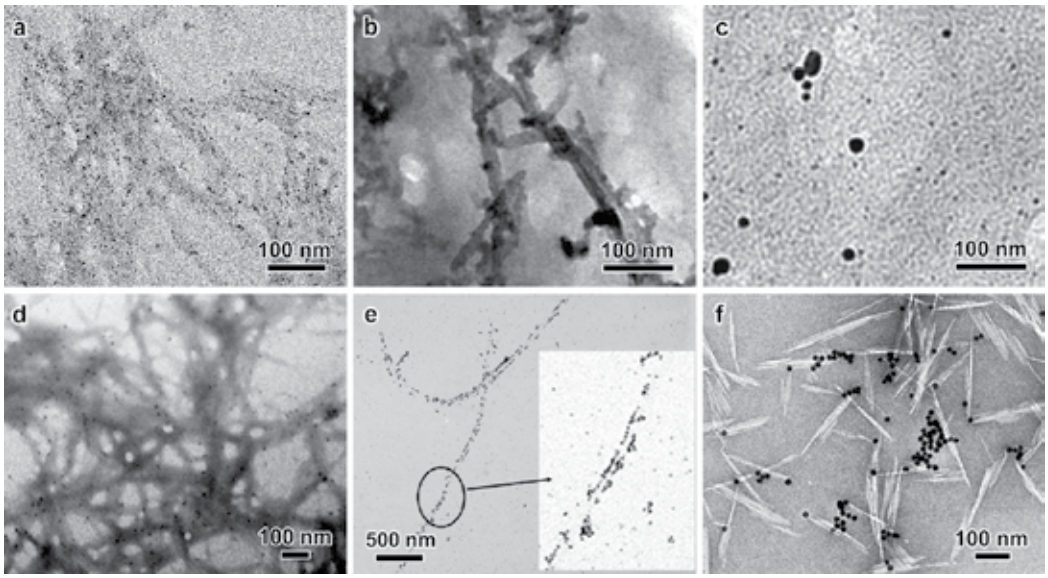

Figure 12. Hybrid systems with metallic nanoparticles supported by CNCs: a) Pd on wood pulp CNCs (reproduced from [40] by permission of The Royal Society of Chemistry); b) Pt on cotton CNCs (reproduced from [114] by permission of The Royal Society of Chemistry); c) Ag on cotton CNCs (reprinted with permission from [112]. Copyright 2014 American Chemical Society); d) Au on wood pulp CNCs (reproduced from [41] by permission of The Royal Society of Chemistry); e) Cu on tunicate CNCs (reprinted with permission from [39]. Copyright 2010 American Chemical Society); f) colloidal gold nanoparticles in interaction with cotton CNCs (negative staining) (courtesy of B. Jean, CERMAV – unpublished results).

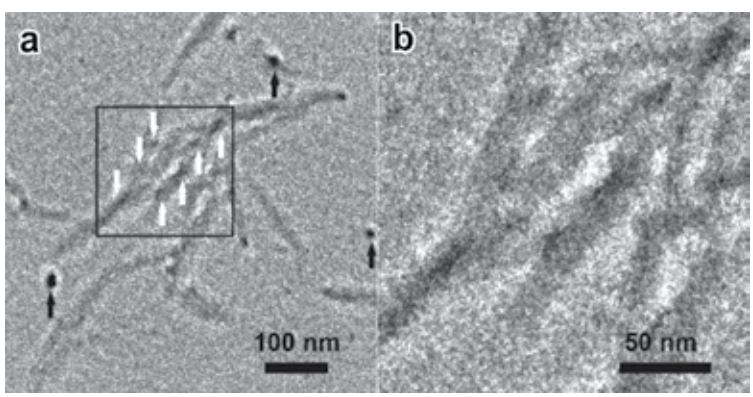

Figure 13. TEM images of patches of Pd onto CNCs recorded using a DDD camera: a) the white arrows point at Pd plates located on the surface of isolated CNCs. The black arrows point at larger and darker NPs that are not physically linked to CNCs; b) close-up view of the area indicated by the box on the left and revealing Pd patches (reprinted with permission from [44]. Copyright 2015 American Chemical Society).

3.3. TEM of CNC-polymer nanocomposites

Due to their nanoscale dimensions, high surface area, low density, and high mechanical strength, CNCs have been incorporated as reinforcing component into various polymer matrices: styrene-butyl acrylate [14, 27] polylactic acid [116, 117], poly(vinylalcohol) [118], polyurethane [119, 120], epoxy [121], and polyvinylacetate [100, 122]. In order to explain the variation in mechanical properties, these bulk materials have often been characterized by SEM after fracturing, allowing to visualize the distribution of CNCs that emerge at the fracture surface. However, SEM remained limited to the characterization of the topography of the fracture surfaces. TEM was also used to visualize the CNCs inside the material *via* preparation by ultramicrotomy of ultrathin sections of the composites. Figure 14 shows examples of images of nanocomposites of CNCs in matrices of styrene-butyl acrylate [14] and polyurethane [120]. CNCs can be visualized using their intrinsic diffraction contrast [14] but, as they are very sensitive to beam damage, their contrast rapidly decreases to the point where they become hardly visible with the polymer matrix due to the lack of density difference. Additional staining of the matrix can be used, for instance with OsO_4, creating a negative staining effect revealing the embedded CNCs [121].

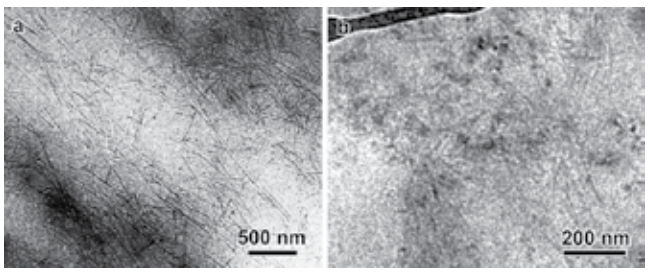

Figure 14. TEM images of ultrathin sections of nanocomposite materials incorporating CNCs as reinforcing component: a) tunicate CNCs in a matrix of styrene-butyl acrylate – diffraction contrast in bright field mode (reprinted with permission from [14]. Copyright 1995 American Chemical Society); b) thin cryosection of a cotton CNC/polyurethane composite observed under cryo-TEM conditions (reprinted with permission from [120]. Copyright 2011 American Chemical Society)

3.4. 3D imaging of CNCs and polymer-wrapped CNCs

Electron tomography (described in § 2.3.3) has only very recently begun to be used to characterize cellulose-based architectures or individual particles. Ciesielski *et al.* have recently published ET reconstructions of treated plant cell walls, allowing to get 3D information on the microfibril morphology [123]. Majoinen *et al.* studied the morphology of individual CNCs embedded in vitreous ice. Using cryo-TEM conditions, they recorded tilt series and reconstructed tomograms from pristine CNCs (Figure 15a) and from CNCs wrapped up with dendronized polymers (Figure 15b). This 3D visualization of the CNCs revealed the presence of an helicoidal twist along the rodlike particles. These twists have been proposed to be significant in explaining the cholesteric liquid crystalline assembly [18, 19] and their use in chiral templating [32, 33]. More recently, tomograms of ice-embed-

http://dx.doi.org/10.5772/60985

ded Pd modified CNCs were also useful to gain insight into the nature of the material under close-to-catalysis conditions [44].

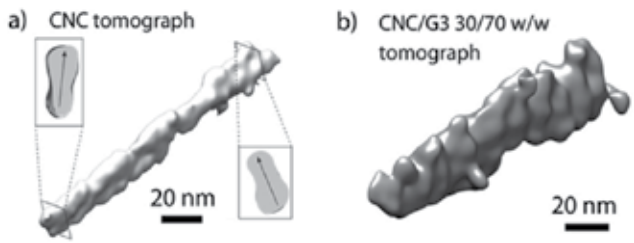

Figure 15. Electron tomography reconstitution of initial (a) and dendronized (b) polymer-wrapped cotton CNCs (reprinted with permission from [62]. Copyright 2014 American Chemical Society).

4. Conclusion and perspectives: Challenges and solutions in imaging CNCs

CNCs have been extensively studied and many reports can be found in the literature. The particle shape and size vary as a function of the cellulose source and the methodology used to produce the CNCs. In all cases, the CNC populations are polydisperse, featuring wide and asymmetrical size distributions. An accurate knowledge of the CNC dimensions and size distribution is crucial to characterize the properties of individual particles and their assemblies in suspension, in dry films or after incorporation into matrices. For instance, morphology and size will influence the phase separation behavior and the formation of liquid crystalline organizations or the percolation properties in nanocomposites. The development of chemical modifications strategies also requires a good knowledge of the accessible surface. In addition, CNCs have recently become a new type of industrial nanomaterial with numerous exciting properties, and an accurate characterization is important to optimize processes and control their reproducibility.

TEM is a key imaging technique to achieve this goal, thanks to the development of specific techniques to observe beam-sensitive polymers. Cellulose is without doubt one of the most beam-sensitive materials that can be observed by TEM. Consequently, special care must be taken to record reliable images of CNCs (low dose, low temperature, additional staining). In this article, we have described several sample preparation procedures and observation techniques adapted to the recording of images of CNC populations and have carried out reliable size distribution analyses. New approaches have recently been proposed, taking advantage of technical improvements of the microscopes, such as a better control of the stage movements, the use of highly sensitive digital cameras, and automatized corrections of several optical aberrations, allowing to record electron tomography image series and reconstruct the volume of the specimens. Although these sophisticated approaches are not routinely used yet

in the field of cellulose science, they will certainly rapidly develop. In addition, at a time when the research on CNCs is booming and the range of commercial applications is expanding, TEM imaging will continue to play a central role. Automated particle measurement procedures using TEM image analysis software will be needed to streamline quality control.

Acknowledgements

The TEM images in Figures 3, 8, and 9 were specifically recorded for this chapter by J.-L. Putaux on a Philips CM200 microscope operating at an accelerating voltage of 200 kV and equipped with a TVIPS TemCam F216 camera. We thank the Electron Microscopy Platform of Institut de Chimie Moléculaire de Grenoble for granting access to this equipment.

Author details

Madhu Kaushik[1], Carole Fraschini[2], Grégory Chauve[2], Jean-Luc Putaux[3,4*] and Audrey Moores[1*]

*Address all correspondence to: audrey.moores@mcgill.ca, putaux@cermav.cnrs.fr

1 Centre for Green Chemistry and Catalysis, Department of Chemistry, McGill University, Montréal, QC, Canada

2 FPInnovations, Pointe-Claire (Québec), Canada

3 Université Grenoble Alpes, Centre de Recherches sur les Macromolécules Végétales (CERMAV), Grenoble, France

4 CNRS, CERMAV, Grenoble, France

Disclaimer: Mention of trademarks or commercial products in this article is solely for the purpose of providing examples of sample preparation materials and methods and does not imply any affiliation from the authors with the mentioned companies.

References

[1] Chinga-Carrasco G. Cellulose fibres, nanofibrils and microfibrils: the morphological sequence of MFC components from a plant physiology and fibre technology point of view. *Nanoscale Res Lett*. 2011; 6 (1): 1-7.

[2] Nishiyama Y. Structure and properties of the cellulose microfibril. *J Wood Sci*. 2009; 55 (4): 241-9.

[3] Klemm D, Philipp B, Heinze T, Heinze U, Wagenknecht W. *Comprehensive Cellulose Chemistry 1. Fundamentals And Analytical Methods*. Weinheim: Wiley-VCH; 1998.

[4] Klemm D, Heublein B, Fink HP, Bohn A. Cellulose: fascinating biopolymer and sustainable raw material. *Angew Chem Int Ed*. 2005; 44 (22): 3358-93.

[5] Nickerson RF, Habrle JA. Cellulose intercrystalline structure. *Ind Eng Chem*. 1947; 39 (11): 1507-12.

[6] Rånby BG. Aqueous colloidal solutions of cellulose micelles. *Acta Chem Scand*. 1949; 3 (1): 649-50.

[7] Rånby BG. Fibrous macromolecular systems. Cellulose and muscle. The colloidal properties of cellulose micelles. *Discuss Faraday Soc*. 1951; 11: 158-64.

[8] Revol J-F, Bradford H, Giasson J, Marchessault RH, Gray DG. Helicoidal self-ordering of cellulose microfibrils in aqueous suspension. *Int J Biol Macromol*. 1992; 14 (3): 170-2.

[9] Mukherjee SM, Woods HJ. X-ray and electron microscope studies of the degradation of cellulose by sulphuric acid. *Biochim Biophys Acta*. 1953; 10: 499-511.

[10] Rånby B. Physico-chemical investigations on bacterial cellulose. *Arkiv for Kemi*. 1952; 4 (3): 249.

[11] Fraschini C, Chauve G, Berre J-FL, Ellis S, Méthot M, O'Connor B, et al. Critical discussion of light scattering and microscopy techniques for CNC particle sizing. *Nord Pulp Pap Res J*. 2014; 29 (1): 31-40.

[12] Brito BS, Pereira FV, Putaux J-L, Jean B. Preparation, morphology and structure of cellulose nanocrystals from bamboo fibers. *Cellulose*. 2012; 19 (5): 1527-36.

[13] Lopez M, Bizot H, Chambat G, Marais M-F, Zykwinska A, Ralet M-C, et al. Enthalpic studies of xyloglucan–cellulose interactions. *Biomacromolecules*. 2010; 11 (6): 1417-28.

[14] Favier V, Chanzy H, Cavaillé J-Y. Polymer nanocomposites reinforced by cellulose whiskers. *Macromolecules*. 1995; 28 (18): 6365-7.

[15] Le Normand M, Moriana R, Ek M. Isolation and characterization of cellulose nanocrystals from spruce bark in a biorefinery perspective. *Carbohydr Polym*. 2014; 111: 979-87.

[16] Silvério HA, Neto WPF, Dantas NO, Pasquini D. Extraction and characterization of cellulose nanocrystals from corncob for application as reinforcing agent in nanocomposites. *Ind Crops Prod*. 2013; 44: 427-36.

[17] Eichhorn SJ, Dufresne A, Aranguren M, Marcovich NE, Capadona JR, Rowan SJ, et al. Review: current international research into cellulose nanofibres and nanocomposites. *J Mater Sci*. 2010; 45 (1): 1-33.

[18] Habibi Y, Lucia LA, Rojas OJ. Cellulose nanocrystals: chemistry, self-assembly, and applications. *Chem Rev*. 2010; 110 (6): 3479-500.

[19] Klemm D, Kramer F, Moritz S, Lindström T, Ankerfors M, Gray D, et al. Nanocelluloses: a new family of nature-based materials. *Angew Chem Int Ed*. 2011; 50 (24): 5438-66.

[20] Moon RJ, Martini A, Nairn J, Simonsen J, Youngblood J. Cellulose nanomaterials review: structure, properties and nanocomposites. *Chem Soc Rev*. 2011; 40 (7): 3941-94.

[21] Lin N, Huang J, Dufresne A. Preparation, properties and applications of polysaccharide nanocrystals in advanced functional nanomaterials: a review. *Nanoscale*. 2012; 4 (11): 3274-94.

[22] Salas C, Nypelö T, Rodriguez-Abreu C, Carrillo C, Rojas OJ. Nanocellulose properties and applications in colloids and interfaces. *Curr Opin Colloid Interface Sci*. 2014; 19 (5): 383-96.

[23] Azzam F, Heux L, Putaux J-L, Jean B. Preparation by grafting onto, characterization, and properties of thermally responsive polymer-decorated cellulose nanocrystals. *Biomacromolecules*. 2010; 11 (12): 3652-9.

[24] Lam E, Male KB, Chong JH, Leung ACW, Luong JHT. Applications of functionalized and nanoparticle-modified nanocrystalline cellulose. *Trends Biotechnol*. 2012; 30 (5): 283-90.

[25] Beck S, Bouchard J, Berry R. Dispersibility in water of dried nanocrystalline cellulose. *Biomacromolecules*. 2012; 13 (5): 1486-94.

[26] Marchessault RH, Morehead FF, Walter NM. Liquid crystal systems from fibrillar polysaccharides. *Nature*. 1959; 184 (4686): 632-3.

[27] Favier V, Canova G, Cavaillé J-Y, Chanzy H, Dufresne A, Gauthier C. Nanocomposite materials from latex and cellulose whiskers. *Polym Adv Technol*. 1995; 6 (5): 351-5.

[28] Revol J-F, Godbout L, Dong X-M, Gray DG, Chanzy H, Maret G. Chiral nematic suspensions of cellulose crystallites; phase separation and magnetic field orientation. *Liq Cryst*. 1994; 16 (1): 127-34.

[29] Picard G, Simon D, Kadiri Y, LeBreux J, Ghozayel F. Cellulose nanocrystal iridescence: a new model. *Langmuir*. 2012; 28 (41): 14799-807.

[30] Liu D, Wang S, Ma Z, Tian D, Gu M, Lin F. Structure–color mechanism of iridescent cellulose nanocrystal films. *RSC Adv*. 2014; 4 (74): 39322-31.

[31] Chen Q, Liu P, Nan F, Zhou L, Zhang J. Tuning the iridescence of chiral nematic cellulose nanocrystal films with a vacuum-assisted self-assembly technique. *Biomacromolecules*. 2014; 15 (11): 4343-50.

[32] Shopsowitz KE, Qi H, Hamad WY, MacLachlan MJ. Free-standing mesoporous silica films with tunable chiral nematic structures. *Nature*. 2010; 468 (7322): 422-5.

[33] Shopsowitz KE, Kelly JA, Hamad WY, MacLachlan MJ. Biopolymer templated glass with a twist: controlling the chirality, porosity, and photonic properties of silica with cellulose nanocrystals. *Adv Funct Mater*. 2014; 24 (3): 327-38.

[34] Shopsowitz KE, Hamad WY, MacLachlan MJ. Chiral nematic mesoporous carbon derived from nanocrystalline cellulose. *Angew Chem Int Ed*. 2011; 50 (46): 10991-5.

[35] Querejeta-Fernández A, Chauve G, Methot M, Bouchard J, Kumacheva E. Chiral plasmonic films formed by gold nanorods and cellulose nanocrystals. *J Am Chem Soc*. 2014; 136 (12): 4788-93.

[36] Serizawa T, Sawada T, Wada M. Chirality-specific hydrolysis of amino acid substrates by cellulose nanofibers. *Chem Commun*. 2013; 49 (78): 8827-9.

[37] Yang J, Han C-R, Duan J-F, Ma M-G, Zhang X-M, Xu F, et al. Studies on the properties and formation mechanism of flexible nanocomposite hydrogels from cellulose nanocrystals and poly (acrylic acid). *J Mater Chem*. 2012; 22 (42): 22467-80.

[38] Yang X, Cranston ED. Chemically cross-linked cellulose nanocrystal aerogels with shape recovery and superabsorbent properties. *Chem Mater*. 2014; 26 (20): 6016-25.

[39] Padalkar S, Capadona JR, Rowan SJ, Weder C, Won Y-H, Stanciu LA, et al. Natural biopolymers: novel templates for the synthesis of nanostructures. *Langmuir*. 2010; 26 (11): 8497-502.

[40] Cirtiu CM, Dunlop-Brière AF, Moores A. Cellulose nanocrystallites as an efficient support for nanoparticles of palladium: application for catalytic hydrogenation and Heck coupling under mild conditions. *Green Chem*. 2011; 13 (2): 288.

[41] Lam E, Hrapovic S, Majid E, Chong JH, Luong JHT. Catalysis using gold nanoparticles decorated on nanocrystalline cellulose. *Nanoscale*. 2012; 4 (3): 997-1002.

[42] Zhou P, Wang H, Yang J, Tang J, Sun D, Tang W. Bacteria cellulose nanofibers supported palladium(0) nanocomposite and its catalysis evaluation in Heck reaction. *Ind Eng Chem Res*. 2012; 51 (16): 5743-8.

[43] Rezayat M, Blundell RK, Camp JE, Walsh DA, Thielemans W. Green one-step synthesis of catalytically active palladium nanoparticles supported on cellulose nanocrystals. *ACS Sustain Chem Eng*. 2014; 2 (5): 1241-50.

[44] Kaushik M, Basu K, Benoit C, Cirtiu CM, Vali H, Moores A. Cellulose nanocrystals as chiral inducers: enantioselective catalysis and transmission electron microscopy 3D characterization. *J Am Chem Soc*. 2015; 137 (19): 6124-7.

[45] Wu X, Lu C, Zhou Z, Yuan G, Xiong R, Zhang X. Green synthesis and formation mechanism of cellulose nanocrystal-supported gold nanoparticles with enhanced catalytic performance. *Environ Sci Nano*. 2014; 1 (1): 71-9.

[46] Xiong R, Lu C, Zhang W, Zhou Z, Zhang X. Facile synthesis of tunable silver nanostructures for antibacterial application using cellulose nanocrystals. *Carbohydr Polym*. 2013; 95 (1): 214-9.

[47] Kovacs T, Naish V, O'Connor B, Blaise C, Gagné F, Hall L, et al. An ecotoxicological characterization of nanocrystalline cellulose (NCC). *Nanotoxicology*. 2010; 4 (3): 255-70.

[48] Celluforce [cited 2015 29 March 2015]. Available from: http://celluforce.com/en/.

[49] Charreau H, L Foresti M, Vazquez A. Nanocellulose patents trends: a comprehensive review on patents on cellulose nanocrystals, microfibrillated and bacterial cellulose. *Recent Pat Nanotech*. 2013; 7 (1): 56-80.

[50] Husemann E CA. Über die Lagerung der Lockerstellen yon Cellulosemolekülen in der Faser. *Naturwissenschaften*. 1944; 32: 79-80.

[51] Dong XM, Kimura T, Revol J-F, Gray DG. Effects of ionic strength on the isotropic −chiral nematic phase transition of suspensions of cellulose crystallites. *Langmuir*. 1996; 12 (8): 2076-82.

[52] Elazzouzi-Hafraoui S, Putaux J-L, Heux L. Self-assembling and chiral nematic properties of organophilic cellulose nanocrystals. *J Phys Chem B*. 2009; 113 (32): 11069-75.

[53] Shafiei-Sabet S, Hamad WY, Hatzikiriakos SG. Rheology of nanocrystalline cellulose aqueous suspensions. *Langmuir*. 2012; 28 (49): 17124-33.

[54] Shafiei-Sabet S, Hamad W, Hatzikiriakos S. Ionic strength effects on the microstructure and shear rheology of cellulose nanocrystal suspensions. *Cellulose*. 2014; 21 (5): 3347-59.

[55] Derakhshandeh B, Petekidis G, Sabet SS, Hamad WY, Hatzikiriakos SG. Ageing, yielding, and rheology of nanocrystalline cellulose suspensions. *J Rheol*. 2013; 57 (1): 131-48.

[56] Helbert W, Nishiyama Y, Okano T, Sugiyama J. Molecular Imaging of Halocynthia papillosa Cellulose. *J Struct Biol*. 1998; 124 (1): 42-50.

[57] dos Santos RM, Neto WPF, Silvério HA, Martins DF, Dantas NO, Pasquini D. Cellulose nanocrystals from pineapple leaf, a new approach for the reuse of this agro-waste. *Ind Crops Prod*. 2013; 50: 707-14.

[58] Sacui IA, Nieuwendaal RC, Burnett DJ, Stranick SJ, Jorfi M, Weder C, et al. Comparison of the properties of cellulose nanocrystals and cellulose nanofibrils isolated from bacteria, tunicate, and wood processed using acid, enzymatic, mechanical, and oxidative methods. *ACS Appl Mater Inter*. 2014; 6 (9): 6127-38.

[59] Urena-Benavides EE, Brown PJ, Kitchens CL. Effect of jet stretch and particle load on cellulose nanocrystal− alginate nanocomposite fibers. *Langmuir*. 2010; 26 (17): 14263-70.

[60] Elazzouzi-Hafraoui S, Nishiyama Y, Putaux J-L, Heux L, Dubreuil F, Rochas C. The shape and size distribution of crystalline nanoparticles prepared by acid hydrolysis of native cellulose. *Biomacromolecules*. 2008; 9 (1): 57-65.

[61] Kalashnikova I, Bizot H, Bertoncini P, Cathala B, Capron I. Cellulosic nanorods of various aspect ratios for oil in water pickering emulsions. *Soft Matter*. 2013; 9 (3): 952-9.

[62] Majoinen J, Haataja JS, Appelhans D, Lederer A, Olszewska A, Seitsonen J, et al. Supracolloidal multivalent interactions and wrapping of dendronized glycopolymers on native cellulose nanocrystals. *J Am Chem Soc*. 2014; 136 (3): 866-9.

[63] Ruska H. Structure of cellulose fibers. *Kolloid-Z*. 1940; 92: 276-85.

[64] Eisenhut O, Kuhn E. Lichtmikroskopische und übermikroskopische Untersuchungen an natürlichen und künstlichen Cellulosefasern. *Angew Chem*. 1942; 55 (25-26): 198-206.

[65] Hambraeus G, Rånby B. Electron microscopic investigation of precipitates of cellulose nitrates. *Nature*. 1945; 155 (3929): 200-1.

[66] Husemann E CA. Elektronenmikroskopische Untersuchungen über submikroskopische Fibrillen aus Kunstfasern. *Makromol Chem*. 1947; 1: 158-63.

[67] Kinsinger WG, Hock CW. Electron microscopical studies of natural cellulose fibers. *Ind Eng Chem*. 1948; 40: 1711-6.

[68] Hock CW. Degradation of cellulose as revealed microscopically. *Text Res J*. 1950; 20 (3): 141-51.

[69] Rånby B, Ribi E. Über den feinbau der zellulose. *Experientia*. 1950; 6 (1): 12-4.

[70] Rånby B. Physico-chemical investigations on animal cellulose (Tunicin). *Arkiv for Kemi*. 1952; 4 (3): 241.

[71] Preston R, Ripley G. Electron diffraction diagrams of cellulose micro-fibrils in Valonia. *Nature*. 1954; 174: 76-7.

[72] Honjo G, Watanabe M. Examination of cellulose fibre by the low-temperature specimen method of electron diffraction and electron microscopy. *Nature*. 1958; 181: 326-8.

[73] Bourret A, Chanzy H, Lazaro R. Crystallite features of Valonia cellulose by electron diffraction and dark-field electron microscopy. *Biopolymers*. 1972; 11 (4): 893-8.

[74] Sugiyama J, Vuong R, Chanzy H. Electron diffraction study on the two crystalline phases occurring in native cellulose from an algal cell wall. *Macromolecules*. 1991; 24 (14): 4168-75.

[75] Koyama M, Helbert W, Imai T, Sugiyama J, Henrissat B. Parallel-up structure evidences the molecular directionality during biosynthesis of bacterial cellulose. *Proc Natl Acad Sci*. 1997; 94 (17): 9091-5.

[76] Sugiyama J, Harada H, Fujiyoshi Y, Uyeda N. Observations of cellulose microfibrils in Valonia macrophysa by high resolution electron microscopy. *J Jpn Wood Res Soc*. 1985; 31: 61-7.

[77] Sugiyama J, Harada H, Fujiyoshi Y, Uyeda N. Lattice images from ultrathin sections of cellulose microfibrils in the cell wall of Valonia macrophysa Kütz. *Planta*. 1985; 166 (2): 161-8.

[78] Kaushik M, Chen WC, van de Ven TGM, Moores A. An improved methodology for imaging cellulose nanocrystals by transmission electron microscopy. *Nord Pulp Pap Res J*. 2014; 29 (1): 77-84.

[79] Peng Y, Han Y, Gardner DJ. Spray-drying cellulose nanofibrils: effect of drying process parameters on particle morphology and size distribution. *Wood Fiber Sci*. 2012; 44 (4): 448-61.

[80] Peng Y, Gardner DJ, Han Y, Kiziltas A, Cai Z, Tshabalala MA. Influence of drying method on the material properties of nanocellulose I: thermostability and crystallinity. *Cellulose*. 2013; 20 (5): 2379-92.

[81] Harris JR. *Negative Staining and Cryoelectron Microscopy: The Thin Film Techniques. RMS Microscopy Handbook*. Oxford: BIOS Scientific Publishers; 1997.

[82] Abitbol T, Kloser E, Gray D. Estimation of the surface sulfur content of cellulose nanocrystals prepared by sulfuric acid hydrolysis. *Cellulose*. 2013; 20 (2): 785-94.

[83] Glauert AM. *Fixation, Dehydration and Embedding of Biological Specimens*. North-Holland/American: Elsevier; 1975.

[84] Reid N. *Practical Methods in Electron Microscopy: Ultramicrotomy*. North-Holland/American: Elsevier; 1975.

[85] Watt IM. *The Principles and Practice of Electron Microscopy*. Cambridge University Press; 1997.

[86] Grubb D. Radiation damage and electron microscopy of organic polymers. *J Mater Sci*. 1974; 9 (10): 1715-36.

[87] Chanzy H. Irradiation de la cellulose de Valonia au microscope à 1 MV. *BIST Commissariat à l'énergie Atomique*. 1975: 55-7.

[88] Fridman K, Mader A, Zwerger M, Elia N, Medalia O. Advances in tomography: probing the molecular architecture of cells. *Nat Rev Mol Cell Biol*. 2012; 13 (11): 736-42.

[89] Kremer JR, Mastronarde DN, McIntosh JR. Computer visualization of three-dimensional image data using IMOD. *J Struct Biol*. 1996; 116 (1): 71-6.

[90] Frank J. *Electron Tomography: Methods for Three-Dimensional Visualization of Structures in the Cell*. Springer Science & Business Media; 2008.

[91] Dong XM, Revol J-F, Gray DG. Effect of microcrystallite preparation conditions on the formation of colloid crystals of cellulose. *Cellulose*. 1998; 5 (1): 19-32.

[92] Henrique MA, Silvério HA, Neto WPF, Pasquini D. Valorization of an agro-industrial waste, mango seed, by the extraction and characterization of its cellulose nanocrystals. *J Environ Manage*. 2013; 121: 202-9.

[93] Rosa M, Medeiros E, Malmonge J, Gregorski K, Wood D, Mattoso L, et al. Cellulose nanowhiskers from coconut husk fibers: effect of preparation conditions on their thermal and morphological behavior. *Carbohydr Polym*. 2010; 81 (1): 83-92.

[94] Heux L, Chauve G, Bonini C. Nonflocculating and chiral-nematic self-ordering of cellulose microcrystals suspensions in nonpolar solvents. *Compos Interfaces*. 2000; 16 (21): 8210-2.

[95] Lu P, Hsieh Y-L. Preparation and characterization of cellulose nanocrystals from rice straw. *Carbohydr Polym*. 2012; 87 (1): 564-73.

[96] Johar N, Ahmad I, Dufresne A. Extraction, preparation and characterization of cellulose fibres and nanocrystals from rice husk. *Ind Crops Prod*. 2012; 37 (1): 93-9.

[97] Peresin MS, Habibi Y, Zoppe JO, Pawlak JJ, Rojas OJ. Nanofiber composites of polyvinyl alcohol and cellulose nanocrystals: manufacture and characterization. *Biomacromolecules*. 2010; 11 (3): 674-81.

[98] Habibi Y, Goffin A-L, Schiltz N, Duquesne E, Dubois P, Dufresne A. Bionanocomposites based on poly (ε-caprolactone)-grafted cellulose nanocrystals by ring-opening polymerization. *J Mater Chem*. 2008; 18 (41): 5002-10.

[99] Junior de Menezes A, Siqueira G, Curvelo AAS, Dufresne A. Extrusion and characterization of functionalized cellulose whiskers reinforced polyethylene nanocomposites. *Polymer*. 2009; 50 (19): 4552-63.

[100] Garcia de Rodriguez NL, Thielemans W, Dufresne A. Sisal cellulose whiskers reinforced polyvinyl acetate nanocomposites. *Cellulose*. 2006; 13 (3): 261-70.

[101] Roman M, Winter WT. Effect of sulfate groups from sulfuric acid hydrolysis on the thermal degradation behavior of bacterial cellulose. *Biomacromolecules*. 2004; 5 (5): 1671-7.

[102] Grunert M, Winter WT. Nanocomposites of cellulose acetate butyrate reinforced with cellulose nanocrystals. *J Polym Environ*. 2002; 10 (1-2): 27-30.

[103] Bondeson D, Mathew A, Oksman K. Optimization of the isolation of nanocrystals from microcrystalline cellulose by acid hydrolysis. *Cellulose*. 2006; 13 (2): 171-80.

[104] Capadona JR, Shanmuganathan K, Trittschuh S, Seidel S, Rowan SJ, Weder C. Polymer nanocomposites with nanowhiskers isolated from microcrystalline cellulose. *Biomacromolecules*. 2009; 10 (4): 712-6.

[105] Araki J, Kuga S. Effect of trace electrolyte on liquid crystal type of cellulose microcrystals. *Langmuir*. 2001; 17 (15): 4493-6.

[106] Araki J, Wada M, Kuga S, Okano T. Influence of surface charge on viscosity behavior of cellulose microcrystal suspension. *J Wood Sci*. 1999; 45 (3): 258-61.

[107] Siqueira G, Bras J, Dufresne A. Cellulose whiskers versus microfibrils: influence of the nature of the nanoparticle and its surface functionalization on the thermal and mechanical properties of nanocomposites. *Biomacromolecules*. 2008; 10 (2): 425-32.

[108] Araki J, Wada M, Kuga S, Okano T. Flow properties of microcrystalline cellulose suspension prepared by acid treatment of native cellulose. *Colloids Surf A*. 1998; 142 (1): 75-82.

[109] Anglès MN, Dufresne A. Plasticized starch/tunicin whiskers nanocomposites. 1. Structural analysis. *Macromolecules*. 2000; 33 (22): 8344-53.

[110] Kimura F, Kimura T, Tamura M, Hirai A, Ikuno M, Horii F. Magnetic alignment of the chiral nematic phase of a cellulose microfibril suspension. *Langmuir*. 2005; 21 (5): 2034-7.

[111] ImageJ. Available from: http://imagej.nih.gov/ij/.

[112] Lokanathan AR, Uddin KMA, Rojas OJ, Laine J. Cellulose nanocrystal-mediated synthesis of silver nanoparticles: role of sulfate groups in nucleation phenomena. *Biomacromolecules*. 2014; 15 (1): 373-9.

[113] Wu X, Lu C, Zhang W, Yuan G, Xiong R, Zhang X. A novel reagentless approach for synthesizing cellulose nanocrystal-supported palladium nanoparticles with enhanced catalytic performance. *J Mater Chem A*. 2013; 1 (30): 8645-52.

[114] Benaissi K, Johnson L, Walsh DA, Thielemans W. Synthesis of platinum nanoparticles using cellulosic reducing agents. *Green Chem*. 2010; 12 (2): 220-2.

[115] Shin Y, Blackwood JM, Bae I-T, Arey BW, Exarhos GJ. Synthesis and stabilization of selenium nanoparticles on cellulose nanocrystal. *Mater Lett*. 2007; 61 (21): 4297-300.

[116] Bondeson D, Oksman K. Dispersion and characteristics of surfactant modified cellulose whiskers nanocomposites. *Compos Interfaces*. 2007; 14 (7-9): 617-30.

[117] Petersson L, Kvien I, Oksman K. Structure and thermal properties of poly(lactic acid)/cellulose whiskers nanocomposite materials. *Compos Sci Technol*. 2007; 67 (11–12): 2535-44.

[118] Paralikar SA, Simonsen J, Lombardi J. Poly(vinyl alcohol)/cellulose nanocrystal barrier membranes. *J Membr Sci*. 2008; 320 (1-2): 248-58.

[119] Marcovich NE, Auad ML, Bellesi NE, Nutt SR, Aranguren MI. Cellulose micro/nanocrystals reinforced polyurethane. *J Mater Res*. 2006; 21 (04): 870-81.

[120] Pei A, Malho J-M, Ruokolainen J, Zhou Q, Berglund LA. Strong nanocomposite reinforcement effects in polyurethane elastomer with low volume fraction of cellulose nanocrystals. *Macromolecules*. 2011; 44 (11): 4422-7.

[121] Matos Ruiz M, Cavaillé J-Y, Dufresne A, Gérard J-F, Graillat C. Processing and characterization of new thermoset nanocomposites based on cellulose whiskers. *Compos Interfaces*. 2000; 7 (2): 117-31.

[122] Roohani M, Habibi Y, Belgacem NM, Ebrahim G, Karimi AN, Dufresne A. Cellulose whiskers reinforced polyvinyl alcohol copolymers nanocomposites. *Eur Polym J*. 2008; 44 (8): 2489-98.

[123] Ciesielski PN, Matthews JF, Tucker MP, Beckham GT, Crowley MF, Himmel ME, et al. 3D electron tomography of pretreated biomass informs atomic modeling of cellulose microfibrils. *ACS Nano.* 2013; 7 (9): 8011-9.

Chapter 7

TEM Morphology of Carbon Nanotubes (CNTs) and its Effect on the Life of Micropunch

Kelvii Wei Guo and Hon-Yuen Tam

Additional information is available at the end of the chapter

Abstract

Carbon nanotubes (CNTs) coated on the WC/Co micropunch, with diameter of 150 μm, for prolonging the life of micropunch were investigated. Carbon nanotubes were synthesized by homemade method. Through scanning electron microscopy (SEM) and transmission electron microscopy (TEM), the morphology and structure of CNTs were expressed. After the punching test, wherein Ti was used as substrate, the effect of CNTs in prolonging the life of micropunch on the wear loss and the surface morphology of micropunch had been studied through confocal laser, SEM, digital balance, *etc*. Results show that the wear of CNT-coated micropunch obviously decreased; and that even in the severe wear period, the wear loss is lesser than that of non-CNT-coated micropunch. Compared with the micropunch without CNTs coating, the promising results are due to the formation of a transfer film at the contact region by rubbing of the CNT forest. CNTs produced adhered to the micropunch surface, thereby avoiding direct contact during the punching period and providing lubricant properties to the interface due to their graphitic nature. Moreover, the relevant mechanism was primarily illustrated by movable cellular automaton.

Keywords: Carbon nanotubes, Micropunch, Wear characteristic, WC/Co

INTECH
open science | open minds

© 2015 The Author(s). Licensee InTech. This chapter is distributed under the terms of the Creative Commons Attribution License (http://creativecommons.org/licenses/by/3.0), which permits unrestricted use, distribution, and reproduction in any medium, provided the original work is properly cited.

1. Introduction

Carbon nanotubes (CNTs) [1, 2] are unique nanosystems with extraordinary mechanical and electronic properties due to their unusual molecular structure. CNTs with wall thickness of one carbon sheet are named as single-walled carbon nanotubes (SWCNTs). SWCNTs can be considered as the building blocks of multi-walled carbon nanotubes (MWCNTs), which consist of a coaxial array of SWCNTs with increasing diameter that is from two to several tens of nanometers, thus providing very high aspect ratio structures [2].

In the last decade, an enormous amount of work has been devoted to reveal the unique, structural, electrical, mechanical, and chemical properties of carbon nanotubes and to explore what might be their most interesting applications [3-10]. CNTs showing unique properties, such as high tensile and flexural strengths, high elastic modulus, and high aspect ratio, have also been considered as attractive contenders for tribological applications. In this sense, interesting results have been reported with significant improvements in friction and wear rates for nanotubes-polymers [11, 12], ceramics [13, 14], and metal composites [15, 16]. According to theoretical considerations [17, 18, 19], friction coefficients between the walls of multi-walled carbon nanotubes should be extremely low.

Due to wear of the WC/Co micropunch, the quality of the punched holes significantly deteriorates after about 1,000 punching shots [20]. Furthermore, the cost of the punches is high; therefore, it is desirable to prolong the life of the micropunches.

As mentioned above, CNTs are high in strength and low in friction coefficient. CNTs coated on the surface of micropunches may greatly prolong the tool life by reducing wear loss during punching and by enhancing the wear resistance of the punches.

Consequently, to prolong the life of serving tools in microfabrication, the effects of CNTs coated on WC/Co micropunches on wear resistance improvement were investigated in this research. In the long run, this research can lead to the improvement of wear resistance properties of such tools made of WC/Co and other engineering materials.

2. Experimental material and procedures

2.1. Experimental material

Micropunch (made by Ultrahardness tools company, Japan) with 75% volume fraction WC particle and 25% volume fraction Co particle of 50 μm mean size, 150 μm in diameter was delivered with precisely grinding by experimental requirements. Figure 1 shows the surface texture of micropunch for CNTs coating. Pure titanium sheet with 200 μm in thickness was used as the substrate. Alcohol with a normal purity of 95% was purchased from Sigma Aldrich.

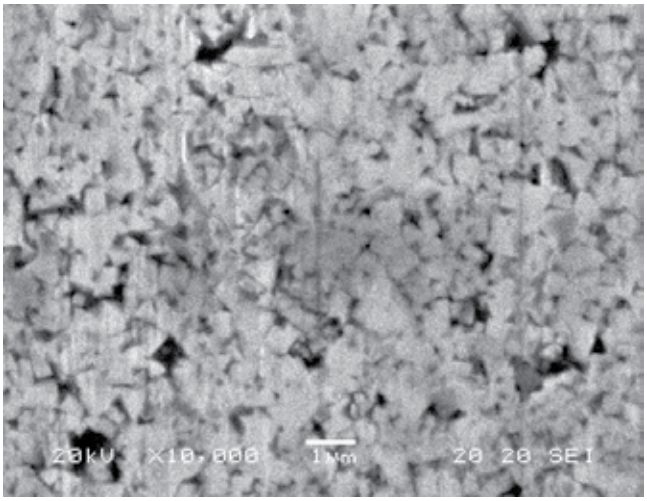

Figure 1. Surface texture of micropunch

2.2. Experimental procedures

2.2.1. CNTs synthesis

The micropunches were cleaned using acetone and pure ethyl alcohol to remove any possible contaminant and were carefully put into the vacuum chamber prior coating.

For CNTs coating on micropunch, first of all, the catalyst (Fe) was deposited on the micropunch working section by electron cyclotron resonance (ECR) (made by Elionix, Japan), and the related processing parameters are listed in Table 1. At the same time, remains of the micropunch were covered with Al foil to avoid the effect of Co distributed in micropunch because pure Ni, Co, or Fe, and their alloys or compounds are widely acceptable catalysts for the growth of CNTs [21-22].

Substrate	**WC/Co micropunch**
Catalyst	Fe
Irradiation time	60 s
Accelerated voltage	2,500 V
Ion current density	12.0 mA/cm^2
Gas	Ar
Gas flow rate	0.6 SCCM
Vacuum	1.5×10^{-4} Pa

Table 1. ECR processing parameters for Fe deposition

After catalyst deposition, CNTs were synthesized by homemade method. The schematic diagram of the self-designed equipment for CNTs synthesis with alcohol chemical vapor deposition (CVD) is shown in Fig. 2. The sizes of vacuum chamber and the heater are Φ100×150 mm and 50×30 mm, respectively. The electrical resistance is taken as the heating resource. The alcohol in a ceramic container was placed under the heater, and the specimen was placed on the heater in the vacuum (1×10^{-2} Pa) under 38~40 A.

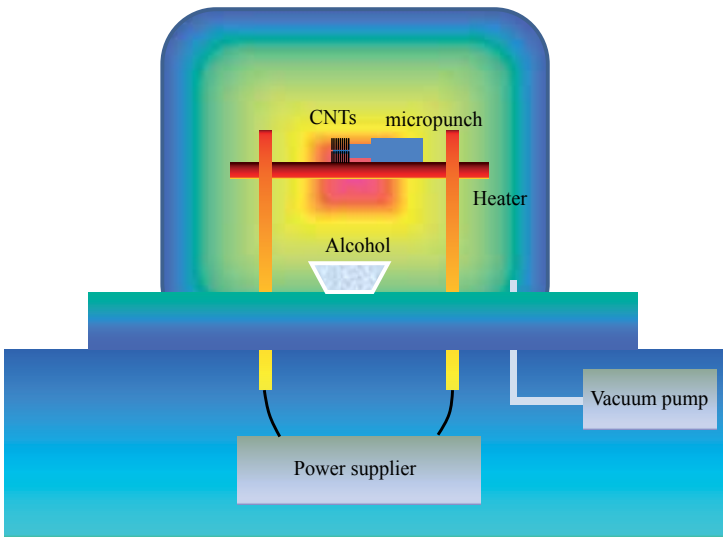

Figure 2. Equipment for CNTs synthesis

2.2.2. Micropunching

The prepared pure titanium sheet was properly cleaned with acetone and pure ethyl alcohol to remove any possible contaminant, and it was carefully put into the microdie. Thereafter, specimens were punched by the microprocessing machine MP50 (made in Japan), with 20 pulses per minute and feedrate of 2 mm.

The effects of CNTs on the wear loss and the surface morphology of micropunch were investigated through confocal laser, scanning electron microscopy (SEM), digital balance, *etc*.

3. Results and discussion

3.1. SEM and TEM morphology of CNTs coated on micropunch

The synthesized CNTs are shown in Fig. 3. It demonstrates that the length of CNTs is about 15 μm. Moreover, CNTs are tightly compacted, which resulted in curve aligning. The relevant

TEM image is shown in Fig. 4, which shows that CNTs are multi-walled nanotubes and that the diameter of the synthesized MWCNT was about 3~5 nm.

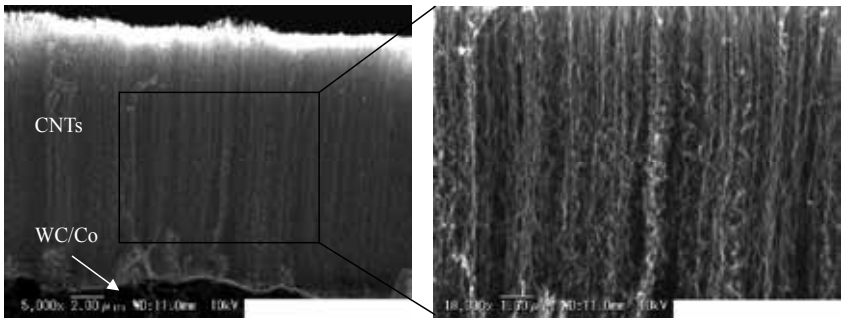

Figure 3. Synthesized CNTs coated on micropunch

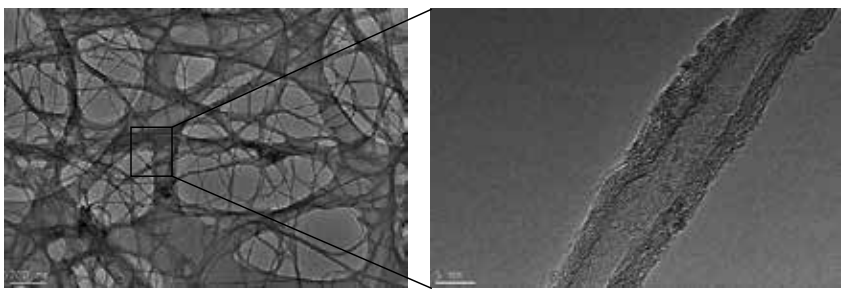

Figure 4. TEM image of synthesized CNTs

3.2. Wear loss of micropunches

The wear loss of non-CNT- and CNT-coated micropunches is shown in Fig. 5. It illustrates that the weight of both kinds of micropunches (each for 5 times) decreases with the increment in punching number in the initial stage, which means that the wear of both micropunches in the initial stage was significantly increased and that the effect of CNTs on the wear loss was not remarkable.

With the punching in progress, the wear of non-coated/coated micropunches is in the quasi-stable period with a little wear loss as shown in Fig. 5, especially for punching number from 500 to 1,200 for non-coated micropunches and from 450 to 1,400 for CNTs coated micropunches. In this period, the effect of CNTs on the wear loss of micropunch is obviously sound.

During the severe wear period, with the punching numbers increasing further, such as over 1,200 for non-coated micropunch and over 1,400 for CNTs coated micropunch, the wear of micropunch was increased distinctly (Fig. 5). At the same time, the effect of CNTs on the wear loss decreased.

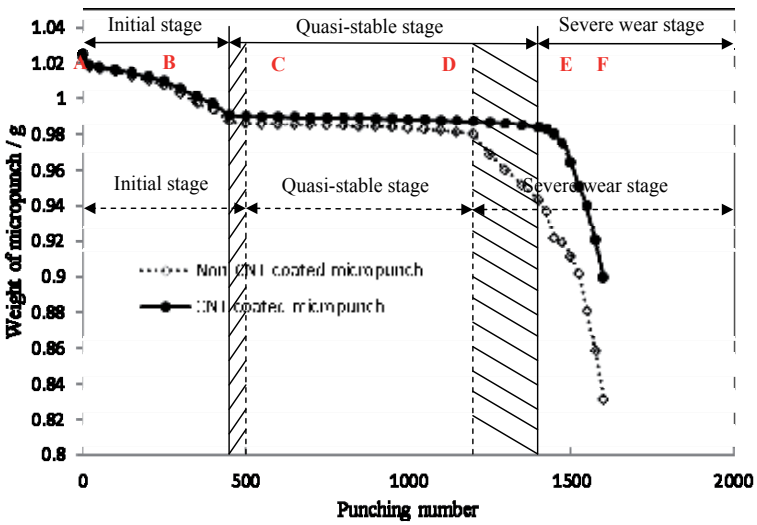

Figure 5. Relationship between wear loss and punching numbers

Also, due to CNTs coated on micropunches, the start of quasi-stable period was advanced. On the contrary, the end of quasi-stable period was postponed, as shown in Fig. 5. It elucidates that the effective quasi-stable period is longer than that of non-coated micropunches. For CNT-coated micropunches, it is 1,400 – 450 = 950. By comparison, for non-coated micropunches, it is 1,200 – 500 = 700. Furthermore, the total wear loss of CNT-coated micropunches was lesser than that of non-coated micropunches. It demonstrates that the life of micropunch was improved or prolonged evidently.

3.3. Surface texture of CNT-coated micropunch

Figure 6 shows the surface textures of CNT-coated micropunches during various punching periods. Figure 6a shows the initial surface texture of CNT-coated micropunch (see point A in Fig. 5). Carbon nanotubes forest was synthesized and distributed successfully on the surface of micropunch and tangled mutually.

With the punching being in progress in the initial stage, the distribution of CNTs is shown in Fig. 6b (Point B in Fig. 5). It shows that CNTs distributed on the surface non-uniformly and that a bulk of CNTs attached on the surface by the punching rubbing effect. When the punching is in the quasi-stable period, the surface texture of micropunch is shown in Figs. 6c and 6d (See point C and D in Fig. 5). It illustrates that CNTs uniformly distributed on the micropunch surface where a transfer film was formed between micropunch and substrate (Ti foil) during the punching process. It is due to the formation of this transfer film at the contact region by rubbing of the CNT forest that CNTs or debris produced adhered to the micropunch surface (or the mating surfaces), thereby avoiding direct contact during the punching period and providing lubricant properties to the interface due to their graphitic nature. The results presented are in accordance with the results shown in Fig. 5, and they are promising for prolonging the life of micropunches.

With the increment in punching number, the surface texture of micropunch is shown in Figs. 6e and 6f (See point E and F in Fig. 5). It shows that CNTs distributed sparsely and disappeared finally (Fig. 6f). It is noted that the promising effect of CNTs was lost, which resulted in severe wear of the micropunch.

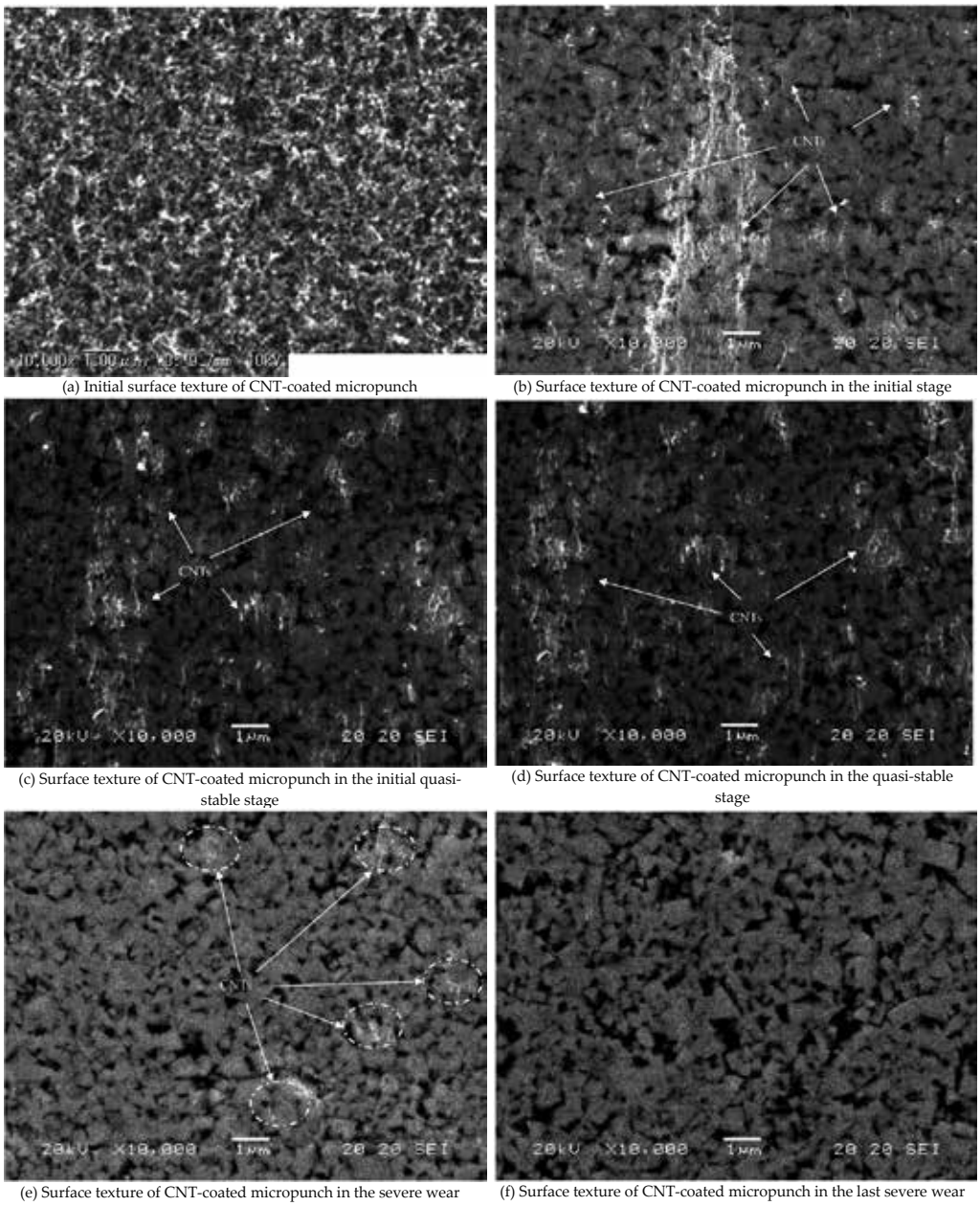

(a) Initial surface texture of CNT-coated micropunch

(b) Surface texture of CNT-coated micropunch in the initial stage

(c) Surface texture of CNT-coated micropunch in the initial quasi-stable stage

(d) Surface texture of CNT-coated micropunch in the quasi-stable stage

(e) Surface texture of CNT-coated micropunch in the severe wear stage

(f) Surface texture of CNT-coated micropunch in the last severe wear stage

Figure 6. Surface texture of micropunch in various conditions

3.4. Profile of punched microholes

The diameter of the punched microhole by non-CNT-coated and CNT-coated micropunches was measured by LEXT confocal laser-OLS3000, as shown in Fig. 7. The relevant results (each for 5 times) are shown in Fig. 8. Compared with Figs. 5 and 6, it illustrates that for both cases (non-CNT-coated and CNT-coated micropunches), in the different wear conditions, the diameter of the punched microhole changed correspondingly. In the initial condition, the diameter obviously decreased with the increment in punching number.

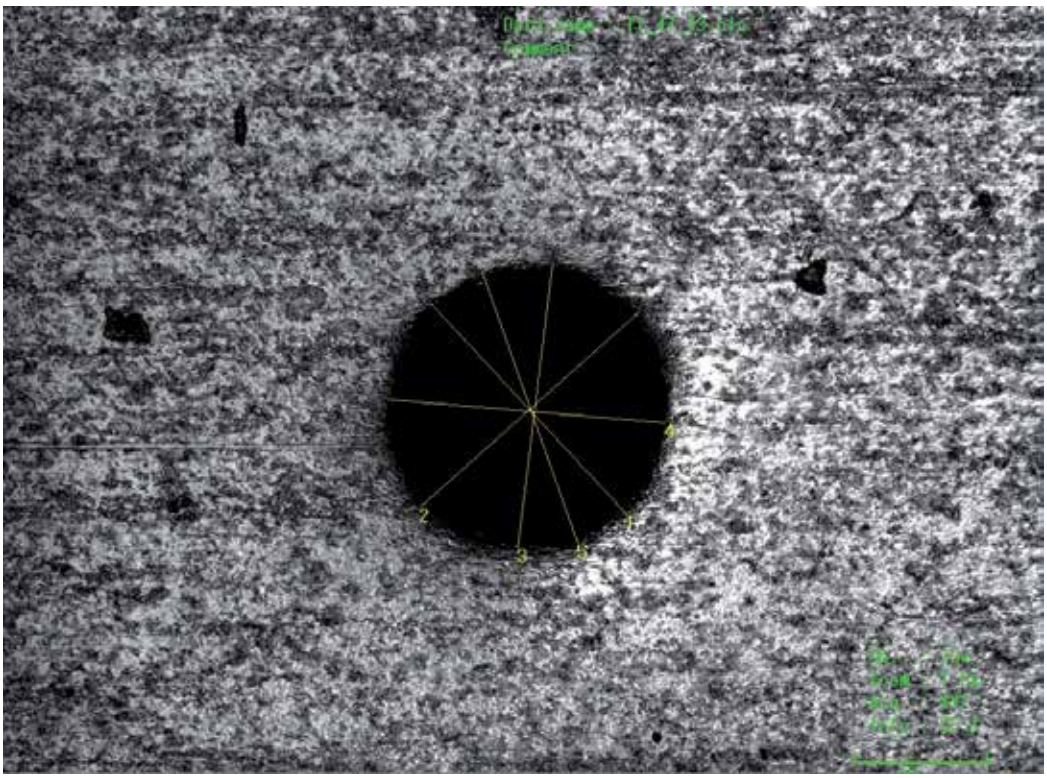

Figure 7. Profile of punched microhole measured by OLS3000

When the punching process is in the quasi-stable period, the diameter of the punched microholes was kept relatively stable. With the punching number increasing further, the diameter was decreased remarkably. For CNT-coated micropunch, due to the lack of attached CNTs on the micropunch, the relevant wear characteristic is same as that of non-CNT-coated micropunch. Therefore, the serious wear of the micropunch appeared during the micropunching in the severe wear condition. Consequently, the diameter of the punched microholes decreased seriously.

Moreover, the results shown in Fig. 8 well agreed with the wear loss of micropunches in the punching period, as shown in Fig. 5.

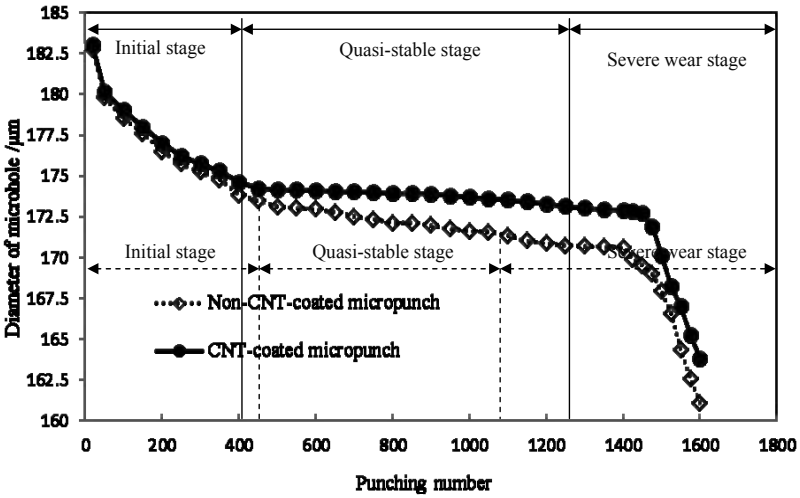

Figure 8. Relationship between diameter of punched microhole and punching number

3.5. Benefit of micropunching

Microtechnology encompasses the technological approach, directed to the miniaturization of components and systems, down to micrometer scale. The major goals are integration and increase in functionality of systems and devices while keeping the dimensions small. Microtechnological components, such as distributed holes, bear the potential to provide further functionality, for instance, in sensor technologies and in biomedical applications. One prominent example is the lab-on-chip technology wherein the analytical functionality of the chip is given by specific functionalized surfaces. Microsystems are going to play an important and critical role in application domains. The development of highly integrated microsystems necessitates the advancement of compatible assembly and joining techniques. Existing macrolevel techniques are adapted for downsizing the assembly of hybrid microsystems. The ever increasing demands for smaller, higher-quality, and lower-priced products from almost all fields of industry, household equipment, and entertainment electronics require the optimization of existing techniques and the development of new methods for the customized manufacture of microsystems with higher precision.

However, current microdevices are mainly made of silicone or glass and are fabricated using photo-resist techniques and/ or micro-machining and micro-molding techniques. It is well known that with these conventional technologies the mechanical properties of substrate will be seriously affected. During the processing, when the source energy is input into the substrate, the substrate suffers heating, melting, vaporizing, and solidifying. Consequently, the properties of substrate will be changed obviously, which cannot meet requirements of application afterwards. Meanwhile, chemicals taken in microfabrication are harmful to environments. In the eco-friendly viewpoint, the minimization of potential environmental and human health risks associated with the manufacture is crucial and urgent. The highlighted key issue is the exploration of new methods to lower the cost and produce large quantities that are more

environmentally friendly. As an attractive promising technique, micropunch overcomes the above-mentioned drawbacks of the traditional technologies successfully. HAZ (heat-affected zone) is avoided, and chemicals are not employed. Meanwhile, the efficiency of microhole forming is remarkably improved. Moreover, the debris formed in the process of micropunching can be recycled. According to principles of green engineering, such as to ensure that all material and energy inputs and outputs are as inherently safe and benign as possible; to minimize depletion of natural resources; to strive to prevent waste; to create engineering solutions beyond current or dominant technologies; improve, innovate, and to invent (technologies) to achieve sustainability, micropunching with CNTs is not only beneficial to microfabrication but also encourages the replacement of existing technologies with new methods that are more environmentally friendly throughout their life cycles.

4. Mechanism of CNTs' effect

The effect of coated CNTs on the micropunches was simulated by movable cellular automaton. The results are shown in Fig. 9. It demonstrates that at the beginning of micropunching, because CNTs adhesion to micropunch is relatively low, the coated CNTs are easily detached from the surface of micropunch as shown in Fig. 9b (green circle with dash line).

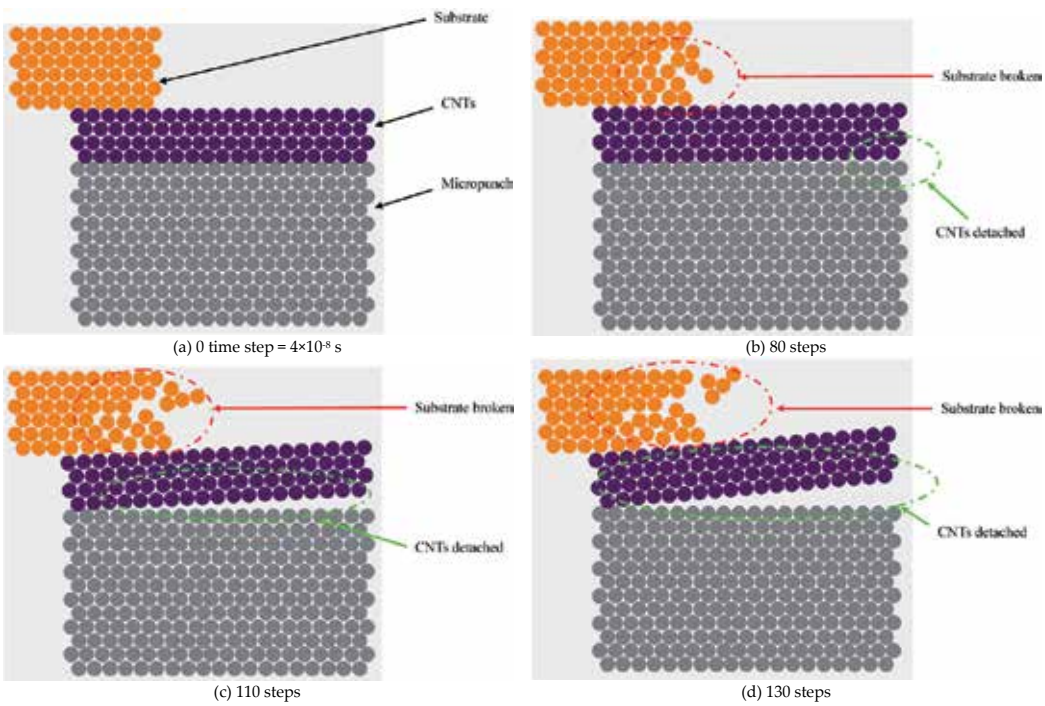

(a) 0 time step = 4×10^{-8} s

(b) 80 steps

(c) 110 steps

(d) 130 steps

Figure 9. MCA simulation of micropunching with CNTs coating

With the micropunching processed further, the coated CNTs are detached from the surface with larger areas as shown in Figs. 9c and 9d. Consequently, only a small fraction of micropunch surface can remain with CNTs under the effect of friction between the substrate and the surface of micropunch. It soundly agrees with the results as shown in Fig. 6. Therefore, the ability of CNTs' adhesion to the surface of the micropunch is crucial to the longevity of the micropunch. CNTs with higher adhesion to the micropunch surface are hardly detached from the surface. During micropunching, the CNTs attached that are uniformly distributed on the surface of micropunch are the ideal media between the substrate and micropunch to lower the friction coefficient. As a result, the wear of micropunch was decreased significantly and the life of micropunch was prolonged remarkably. Meanwhile, the CNT-coated micropunch with higher adhesion will be more promising for the microfabrication.

5. Conclusion

Carbon nanotubes (CNTs) coated on the WC/Co micropunch and its effect on its wear characteristic were studied. It shows that due to the formation of this transfer film at the contact region by rubbing of the CNT forest, the CNTs produced adhered to the micropunch surface (or the mating surfaces), thereby avoiding direct contact during the punching period and providing lubricant properties to the interface due to their graphitic nature. For CNT-coated micropunches, the punching number in the quasi-stable period is 950. By comparison, for non-coated micropunches, it is 700. In addition, the total wear loss of CNT-coated micropunches is lesser than that of non-coated micropunches. As a result, CNT-coated micropunch is evidently promising to improve or prolong the life of micropunch.

Acknowledgements

The work was fully supported by a grant from City University of Hong Kong (Project No. 7004246).

Author details

Kelvii Wei Guo* and Hon-Yuen Tam

*Address all correspondence to: guoweichinese@yahoo.com

Department of Mechanical and Biomedical Engineering, City University of Hong Kong, Kowloon Tong, Kowloon, Hong Kong, China

References

[1] Iijima S. Single-shell carbon nanotubes of 1-nm diameter. Nature 1993; 363: 603-605.

[2] Iijima S. Helical microtubules of graphitic carbon. Nature 1991; 354: 56-58

[3] Boncel S, Müller KH, Skepper JN, Walczak KZ, Koziol KKK. Tunable chemistry and morphology of multi-wall carbon nanotubes as a route to non-toxic, theranostic systems. Biomaterials 2011; 32: 7677-7686.

[4] Gutierrez F, Rubianes MD, Rivas GA. Dispersion of multi-wall carbon nanotubes in glucose oxidase: Characterization and analytical applications for glucose biosensing. Sensors and Actuators B 2012; 161: 191-197.

[5] Tofighy MA, Mohammadi T. Adsorption of divalent heavy metal ions from water using carbon nanotube sheets. Journal of Hazardous Materials 2011; 185: 140-147.

[6] Upadhyayula VKK, Gadhamshetty V. Appreciating the role of carbon nanotube composites in preventing biofouling and promoting biofilms on material surfaces in environmental engineering: A review. Biotechnology Advances 2010; 28: 802-816.

[7] Tiusanen J, Vlasveld D, Vuorinen J. Review on the effects of injection moulding parameters on the electrical resistivity of carbon nanotube filled polymer parts. Composites Science and Technology 2012; 72: 1741-1752.

[8] Alig I, Pötschke P, Lellinger D, Skipa T, Pegel S, Kasaliwal GR, Villmow T. Establishment, morphology and properties of carbon nanotube networks in polymer melts. Polymer 2012; 53: 4-28.

[9] Bhattacharya M, Hong S, Lee D, Cui T, Goyal SM. Carbon nanotube based sensors for the detection of viruses. Sensors and Actuators B 2011; 155: 67-74.

[10] Kasel D, Bradford SA, Šimůnek J, Heggen M, Vereecken H, Klumpp E. Transport and retention of multi-walled carbon nanotubes in saturated porous media: Effects of input concentration and grain size. Water Research 2012; 1-12.

[11] Pöllänen M, Pirinen S, Suvanto M, Pakkanen TT. Influence of carbon nanotube–polymeric compatibilizer masterbatches on morphological, thermal, mechanical, and tribological properties of polyethylene. Composites Science and Technology 2011; 71: 1353-1360.

[12] Green MJ, Behabtu N, Pasquali M, Adams WW. Nanotubes as polymers. Polymer 2009; 50: 4979-4997.

[13] Zhan GD, Kuntz JD, Wan JL, Mukherjee AK. Single-wall carbon nanotubes as attractive toughening agents in alumina-based nanocomposites. Nature Materials 2003; 2(1): 38-42.

[14] Hvizdoš P, Puchý V, Duszová A, Dusza J, Balázsi C. Tribological and electrical properties of ceramic matrix composites with carbon nanotubes. Ceramics International 2012; 38: 5669-5676.

[15] Guiderdoni CH, Pavlenko E, Turq V, Weibel A, Puech P, Estournés C, Peigney A, Bacsa W, Laurent CH. The preparation of carbon nanotube (CNT)/copper composites and the effect of the number of CNTwalls on their hardness, friction and wear properties. Carbon 2013; 58: 185-197.

[16] Bakshi SR, Keshri AK, Agarwal A. A comparison of mechanical and wear properties of plasma sprayed carbon nanotube reinforced aluminum composites at nano and macro scale. Materials Science and Engineering A 2011; 528: 3375-3384.

[17] Damnjanović M, Vuković T, Milosević I. Super-slippery carbon nanotubes: symmetry breaking breaks friction. European Physical Journal 2002; B 25: 131-134.

[18] Dickrell PL, Sinnott SB, Hahn DW, Raravikar NR, Schadler LS, Ajayan PM, Sawyer WG. Frictional anisotropy of oriented carbon nanotube surfaces. Tribology Letters 2005; 18(1): 59-62. DOI: 10.1007/s11249-004-1752-0.

[19] Dickrell PL, Pal SK, Bourne GR, Muratore C, Voevodin AA, Ajayan PM, Schadler LS, Sawyer WG. Tunable friction behavior of oriented carbon nanotube films. Tribology Letters 2006; 24(1): 85-90. DOI: 10.1007/s11249-006-9162-0.

[20] Guo W, Tam HY. Effects of extended punching on wear of the WC/Co micropunch and the punched microholes. The International Journal of Advanced Manufacturing Technology 2011; 59: 955-960. DOI 10.1007/s00170-011-3567-0.

[21] Esconjauregui S, Whelan CM, Maex K. The reasons why metals catalyze the nucleation and growth of carbon nanotubes and other carbon nanomorphologies. Carbon 2009; 47: 659-669.

[22] Dupuis AC. The catalyst in the CCVD of carbon nanotubes—a review. Progress in Materials Science 2005; 50: 929-961.

Chapter 8

HRTEM Study on Resistive Switching ZrO_2 Thin Films and Their Micro-Fabricated Thin Films

Ying Li, Gaoyang Zhao, Zhibo Kou, Long Jin and Yajing Wang

Additional information is available at the end of the chapter

http://dx.doi.org/10.5772/60973

Abstract

For the next-generation nonvolatile memory material, the most promising candidate is resistive random access memory (RRAM) which is nonvolatile memory with high density, high speed, and low power consumption. Resistive switching (RS) behavior had been reported in various films including transition metal oxides, perovskite, and chalcogenide. For further application, it is still a challenge to fabricate nanostructures of RS material. Micro-fabrication method involves traditional lithography, chemical etching, electron beam direct writing, nano-imprint, and so on. However, the procedure and the cost of these methods are relatively complex and high for semiconductors process. In this chapter, we demonstrate a method for fabricating sub-micro ZrO_2 lattice by using sol-gel method combined with laser interference lithography and micro-analysis with high-resolution transmission electron microscopy (HRTEM).

Researchers used all kinds of techniques to investigate the mechanism such as conductive atomic force microscopy, HRTEM, and scanning electrical microscopy. Despite the extensive research, much of the underlying mechanism is still unclear and controversial. This task can be accomplished only with advanced measurement and technique such as in HRTEM, local conductive atomic force microscopy, and so on. HRTEM sample preparation method for array dots is also discussed. In our research, the bipolar RS behavior can be observed successfully in this structure. And HRTEM observation was used to study the interface between the layers. RRAM unit consists of a conductive atomic force microscope tip as an anode, a ZrO_2 lattice dot as RS material, and a copper electrode as a cathode.

Keywords: Resistive switching, HRTEM, Sample preparation

INTECH
open science | open minds

© 2015 The Author(s). Licensee InTech. This chapter is distributed under the terms of the Creative Commons Attribution License (http://creativecommons.org/licenses/by/3.0), which permits unrestricted use, distribution, and reproduction in any medium, provided the original work is properly cited.

1. Introduction

The development of information technology has brought rapid changes to people's life. Resistive random access memory (RRAM), because of its fast response, high stability, low power consumption, with the traditional advantages of the semiconductor technology, has good compatibility, and according to scientists, is expected to become one of the next generations of memory [1-5]. In this chapter, by using shadow lithography and laser interference lithography, two kinds of methods to micro-fabricate the RS oxide film, it is suggested that the oxide film is suitable for micromachining process than using atomic force microscopy (AFM) in situ electrical measurement technique for fine-patterned films after the oxide film was studied by means of in situ micro area electrical performance. In this chapter, we used sol-gel method and chemical modification method for the preparation of a variety of ZrO_2 sol, and optimizing the good comprehensive properties of oxide RS material, through the analysis of the HRTEM studies of the oxide film [6-10].

2. Experiment

2.1. ZrO_2 thin films preparation

Photosensitive ZrO_2 films were fabricated with the metal alkoxide zirconium tetran-butoxide [$Zr(OC_4H_9)_4$], benzoylacetone (BzAcH), and ethanol (EtOH) in the molar ratio of Zr:BzAcH:EtOH at 1:1:40. After being mixed and refluxed for 2 to 3 hours, the photosensitive ZrO_2 solution was obtained. Then using dip-coating process, ZrO_2 organic films were formed on copper substrate. The copper substrates were fabricated by magnetic sputtering.

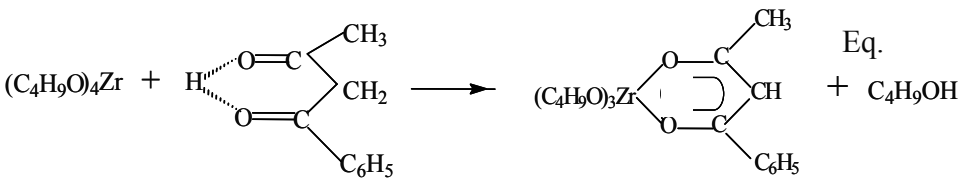

2.2. ZrO_2 lattice preparation

ZrO_2 lattice was fabricated by double exposures of two-beam laser interference through 90° rotation of the sample in its own plane between twice exposures with 350 nm Krypton ion laser. After laser exposure, the exposed part of ZrO_2 film is not soluble in leaching solution while the un-exposed part is still soluble. Therefore, ZrO_2 lattice can be obtained [11-14].

The UV–visible absorption spectra were measured and these spectra of the ZrO_2 films were dip-coated on quartz glass substrate. It was known that an absorption peak of BzAcH at 308 nm was due to the π-to-π* transition. These peaks shift to 338 nm in the spectra of the ZrO_2 gel films. This red shift indicates the chelation between Zr^{4+} and BzAcH, and the reaction re-

http://dx.doi.org/10.5772/60973

sults in the partial replacement of the alkoxy group by β-diketone ligand [see Eq. (1)]. Fig. 1 also shows the AFM image of ZrO_2 films irradiated by a UV Krypton ion laser. The intensity of absorption peaks at around 338 nm decreases step by step with increasing irradiation time from 0 second to 400 seconds. These decreasing spectra showed that the chelate rings were dissociated by UV irradiation.

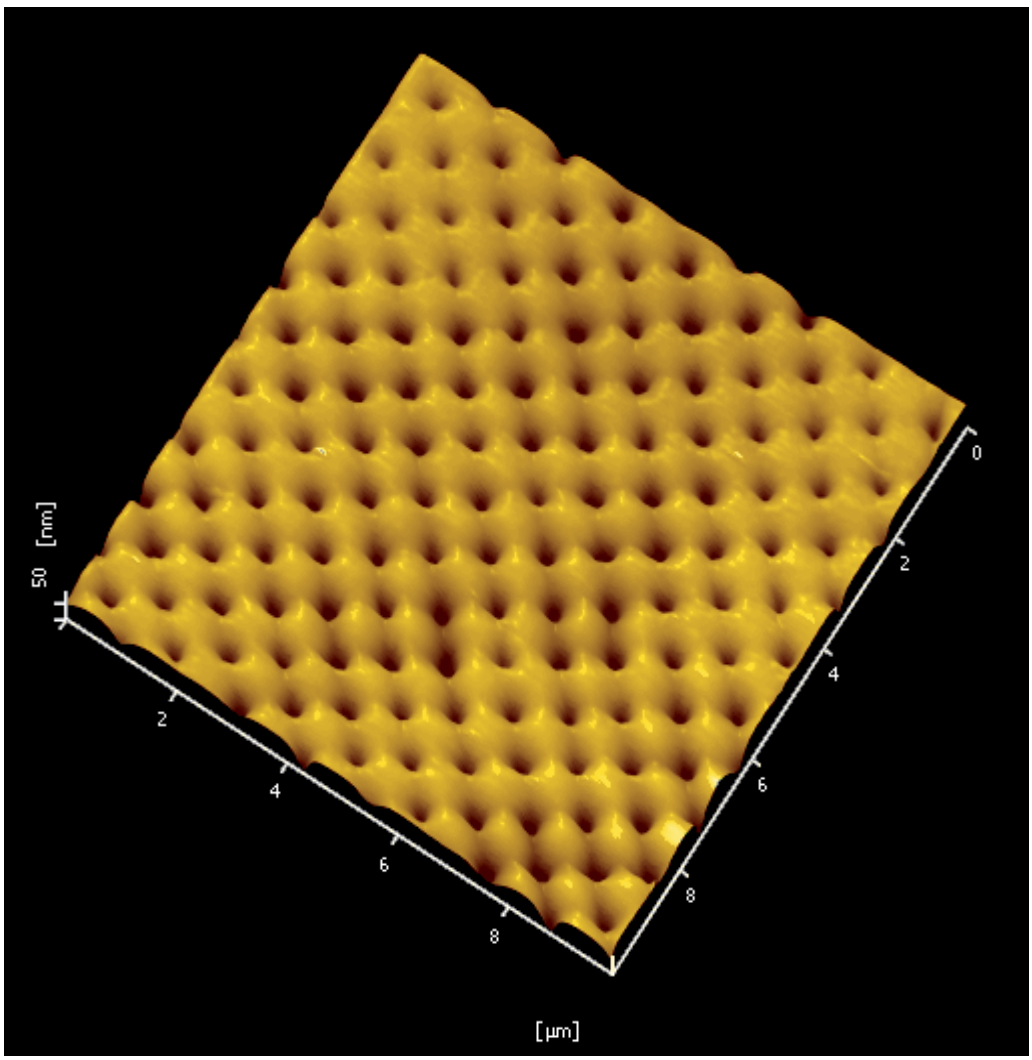

Figure 1. Observation of ZrO_2 lattice dot by AFM measurement systems.

2.3. I-V measurement with ZrO_2 thin films

Before the local conductive AFM (LC-AFM) measurement of the ZrO_2 lattice dots, a traditional I-V probe station measurement was carried out with the normal ZrO_2 thin film which

is made of the photosensitive ZrO_2 solution. This RS structure is formed with platinum (top electrode), ZrO_2 photosensitive film (RS layer), and copper (bottom electrode). The platinum top electrode is made by sputtering with shadow mask. The pattern of the shadow mask is periodic lattice dot with a diameter of 2 mm.

2.4. I-V measurement with ZrO_2 lattice

This LC-AFM measurement system consists an atomic force microscope (AFM, Seiko Instruments Inc, SPI3800N/SPA-400) with a resolution of 0.1 nm in x–y directions and 0.01 nm in the z direction and a Keithly 2400 I-V source meter (Keithly, USA.). The silicon tips (PPP-CONT, Nanosensors) were coated by sputtering deposition with a 25 nm thick double layer of chromium and platinum/Iridium (Pt/Ir) with an initial 20 nm radius. In our LC-AFM measurement study, RRAM unit consists of a conductive atomic force microscope tip as an anode, a ZrO_2 lattice dot as RS material, and a copper electrode as a cathode. In order to identify the RS properties of ZrO_2 array dot, the Pt/Ir conductive atomic force microscope tip is tightly positioned at the center of one of the dots. During the LC-AFM measurement, Pt/Ir conductive probe and the base of the LC-AFM are connected to Keithly 2400 meter to apply the excitation signal and record voltage and current response of the RS array dots. When the voltages from Keithly 2400 meter are applied to the Pt/Ir conductive AFM tip and the bottom electrode of the sample, the current flow occurs through the cantilever and goes back to the Keithly 2400 meter. Then a local I-V curve can be obtained.

In order to solve the influence from huge contact resistance between the Pt/Ir conductive atomic force microscope tip and a single ZrO_2 array dot, a platinum layer was spread on the whole ZrO_2 lattice by sputtering. In this way, the contact can be improved.

2.5. HRTEM sample preparation

The HRTEM observation was carried out by HRTEM (JEOL 3010, Japan). The diagram of sample preparation process is shown in Fig. 2. In Fig. 2(a), we cut some tiny part from the platinum-covered sample which can achieve I-V curves by LC-AFM systems for HRTEM observations.

Two tiny parts were pasted by AB glue face-to-face. AB glue should be used as less as possible because the more AB glue used the worse ion milling would be. And this unit was milled by hand in x direction as smooth as possible. When the thickness in z direction decreases down to less than 1 μm, this unit can be pasted to nickel (Ni) grid. This will be ready for Argon ions milling. A cross-section sample of Pt/ZrO_2 lattice dot/Cu unit was milled by the low-angle Argon milling machine (Gatan, USA). The milling angle was less than 8°. Microstructural analysis was done on the basis of HRTEM observations. It is well known that the preparation of good specimens for high-resolution transmission microscopy is a very important process. The milling angle of Argon ions was less than 8° for the reasons of the damage from Argon ions. The transparent area to electrons can be widened if the Argon ions milling angle was small. However, it cannot mill if the milling angle was less than 3°. The ideal milling angle of Argon ions was between 4° and 8°.

http://dx.doi.org/10.5772/60973

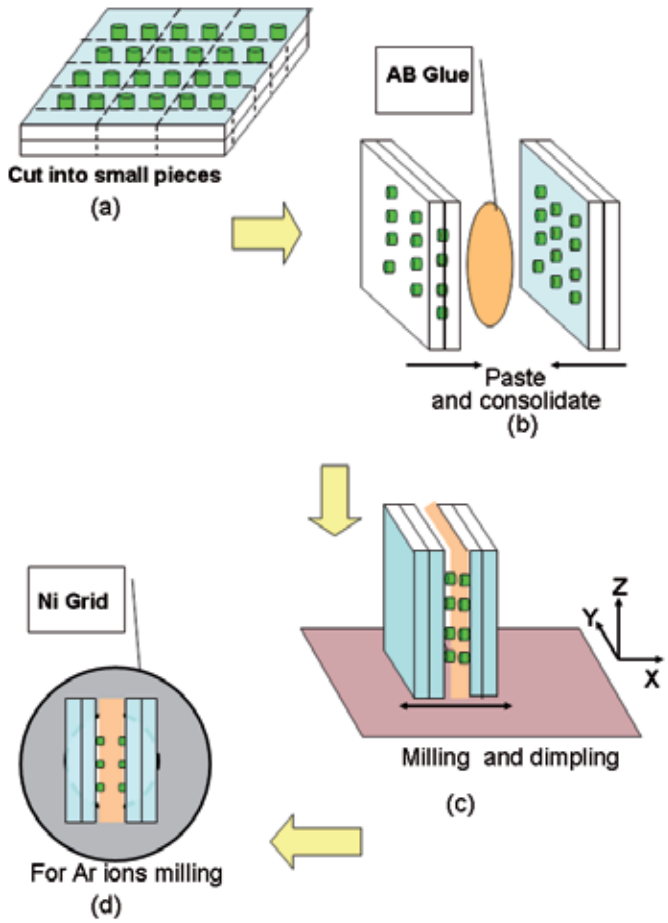

Figure 2. Illustration of HRTEM samples preparation process.

3. Discussion and results

3.1. Normal probe station I-V curves

For the electrical measurements, probes contact top electrode (Cu) and bottom electrode SnO_2:Sb (ATO), respectively. The bottom electrode was grounded. In Fig. 3, it shows the I-V characteristics of the Cu/ZrO_2/ATO structure after fifty times of I-V measurements cycles. The current compliance (CC) is applied to 10 mA during I-V sweep. When the voltage goes to 0.5 V, the current increases rapidly which means the OFF state switches to the ON state. During the I-V sweep at negative side, when the voltage goes to -1.4 V, the current decreases rapidly which means the ON state switches to the OFF state. This behavior can be repeated more than fifty times.

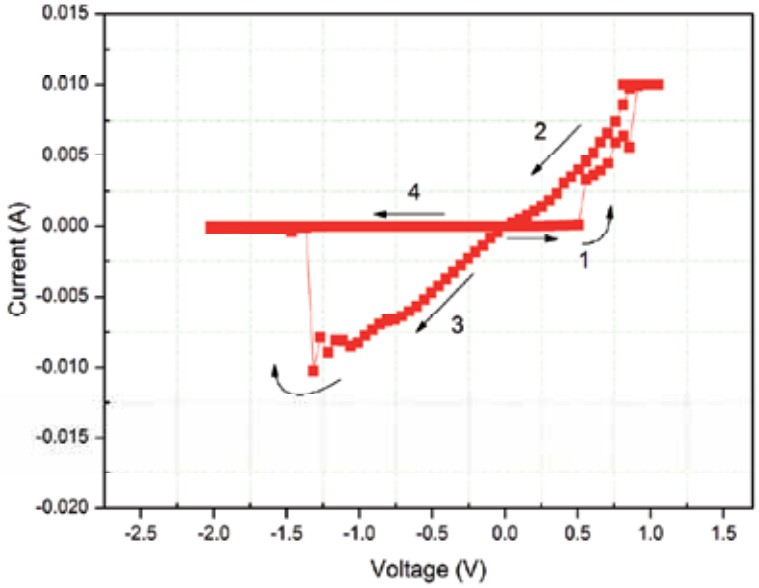

Figure 3. I-V curve of the Cu/ZrO_2/ATO structure after fifty cycles.

Bipolar RS characterization was stable for ZrO_2 thin film in the structure unit. Normally, the voltage sweeps start from 0 V and go to the positive side (1 V) and goes back to 0 V. Resistance switches from high resistance state (R_H) to low resistance state (R_L) and it is called SET process. And then the voltage sweeps from 0 V to the negative side (-2 V) and goes back to 0 V. Resistance switches from R_L to R_H and it is called RESET process. When the voltage swept at -0.5 V, R_L was 70 Ω and R_H was 100 KΩ. This behavior can be repeated hundreds of times. The CC is applied with 10 mA. The highest ratio of R_H:R_L can reach to 10^4.

During the RESET operation, the interesting thing we found is that R_H varied when we changed the RESET voltage. R_H decreased when the RESET voltage value decreased. For I-V curve in Fig. 3, voltage sweep started from 0 V to the -2 V and then from -2 V to 0 V during the RESET process. When the voltage swept at -0.5 V, R_L was 100 Ω and R_H was 250 KΩ. This behavior can be repeated more than several times. The CC is applied with 10 mA. The highest ratio of R_H:R_L can reach to 10^4.

3.2. Local I-V curves by LC-AFM measurement systems

During the LC-AFM measurement, the parameters of I Gain and P Gain should be adjusted. The value of P Gain should be set as one-third of I Gain value. The Pt/Ir conductive coating could be switched off when the value of Force Reference is too small. This value should be set from -1 nm to -4 nm. The sweep voltage can be set from -25 V to 25 V. The height of array dot A (ΔZ) is about 61 nm and dot B (ΔZ) is about 58 nm. The diameter of dot A is about 1.2 μm and that of dot B is about 1.1 μm. Local I-V curves are measured while the LC-AFM image was scanning. The CC is applied to 100 μA during I-V sweep. When the voltage goes to

http://dx.doi.org/10.5772/60973

18 V, the current increases rapidly which means the OFF state switches to the ON state. During the I-V sweep at negative side, when the voltage goes to -5.0 V, the current decreases rapidly which means the ON state switches to the OFF state. In order to make sure that the array dot is not shifted during the LC-AFM measurement, an AFM image scan is very necessary after the local I-V measurement is finished.

A platinum film of 30 nm thickness was sputtered on ZrO_2 lattice dot. Fig. 4 is a local I-V curve which is also measured while the LC-AFM image was scanning. The CC is applied to 100 μA during I-V sweep. When the voltage goes to 0.8 V, the current increases rapidly which means the OFF state switches to the ON state. During the I-V sweep at negative side, when the voltage goes to -2.2 V, the current decreases rapidly which means the ON state switches to the OFF state.

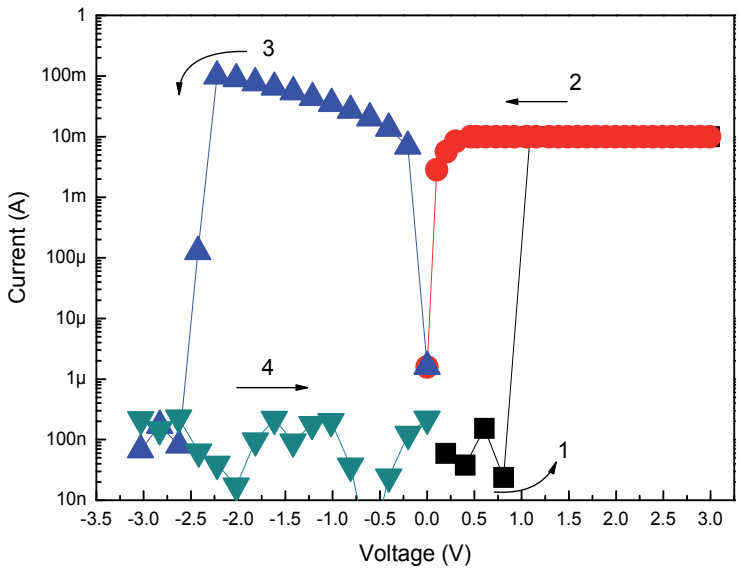

Figure 4. A local I-V curve which is measured while the LC-AFM image was scanning.

3.3. HRTEM observations

We took one unit of samples for TEM observations in which the ZrO_2 thin film in the structure was annealed at 300°C. Microstructural analysis has been done on the basis of TEM observations. Fig. 5 shows the interface image of Cu/ZrO_2/ATO structure in which the ZrO_2 thin film was annealed at 300°C. The bottom electrode (BE) is ATO film and the thickness is about 400 nm. The ZrO_2 work layer is about 200 nm thick and it is amorphous according to the selected area diffraction pattern. In Fig. 5, it is shown that copper ions are penetrated into the ZrO_2 layer. It can be proved by the Fast Fourier Transform patterns. According to the filament formation mechanism, resistance reduction in the devices is due to the existing

copper to form conducting copper-rich pathways. An opposite bias takes the existing copper back to the copper electrode to its high resistance state [15-19].

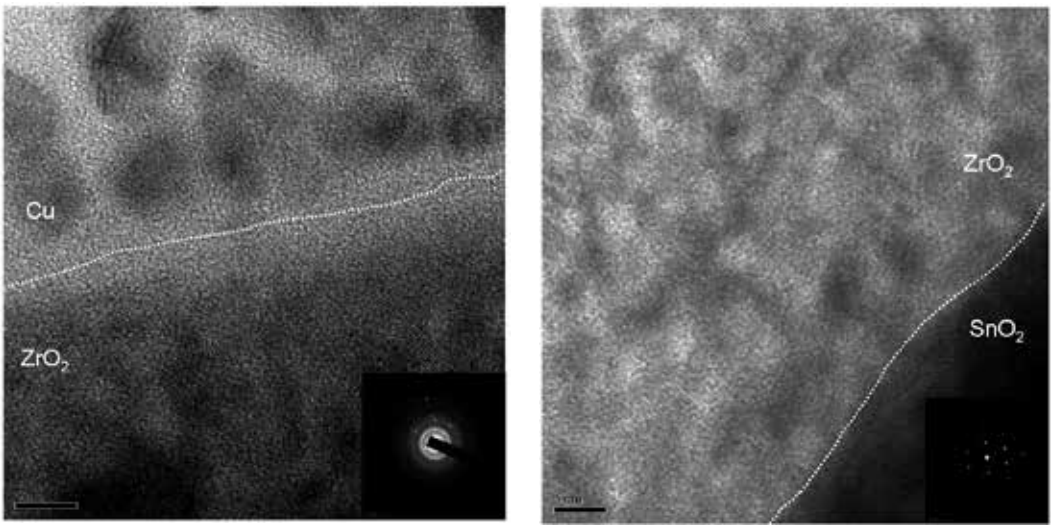

Figure 5. HRTEM image of $Cu/ZrO_2/ATO$ structure.

Fig. 6(a) shows the interface image of Pt/ZrO_2 lattice dot/Cu sandwiched structure. Two lattice dots were seen in this figure, which are labeled as A and B. These two dots were not similar in size. This phenomenon was also seen in the rest of the HRTEM sample observations. The diameter of dot A is around 800 nm while that of dot B is around 700 nm. This is not agreeing with the LC-AFM image results. Through LC-AFM image observation, it is shown that the ZrO_2 array dots are even and in the same diameter range of about 1 μm. This is because when the HRTEM sample was milling manually in the first stage, it was difficult to keep the milling plane vertical to the ZrO_2 array plane. This is shown in Fig. 7(a) as the ideal case. It was always tilted a little bit which was perhaps due to the milling stage, sandpaper, or movement by hands. This is shown in Fig. 7(b) which is the practical case. For the conventional TEM specimen preparation techniques such as polished milling, the milling direction is controlled only by hands. Therefore, in the future HRTEM observation, an automatic monitor for sample milling system is necessary.

This HRTEM image is accepted for interface analysis. In inset of Fig. 6(a), it shows the selected area diffraction pattern of platinum, ZrO_2, and copper which are corresponding to polycrystalline, amorphous, and polycrystalline behaviors, respectively. Fig. 6(a) shows the HRTEM image of copper layer and Fig. 6(c) shows the interface between ZrO_2 array dot and platinum layer. In HRETM images, copper ions filaments were not found in the amorphous ZrO_2 array dot. Therefore, it is possible that the Redox process could have happened in the interface between copper layer and ZrO_2 array dot.

http://dx.doi.org/10.5772/60973

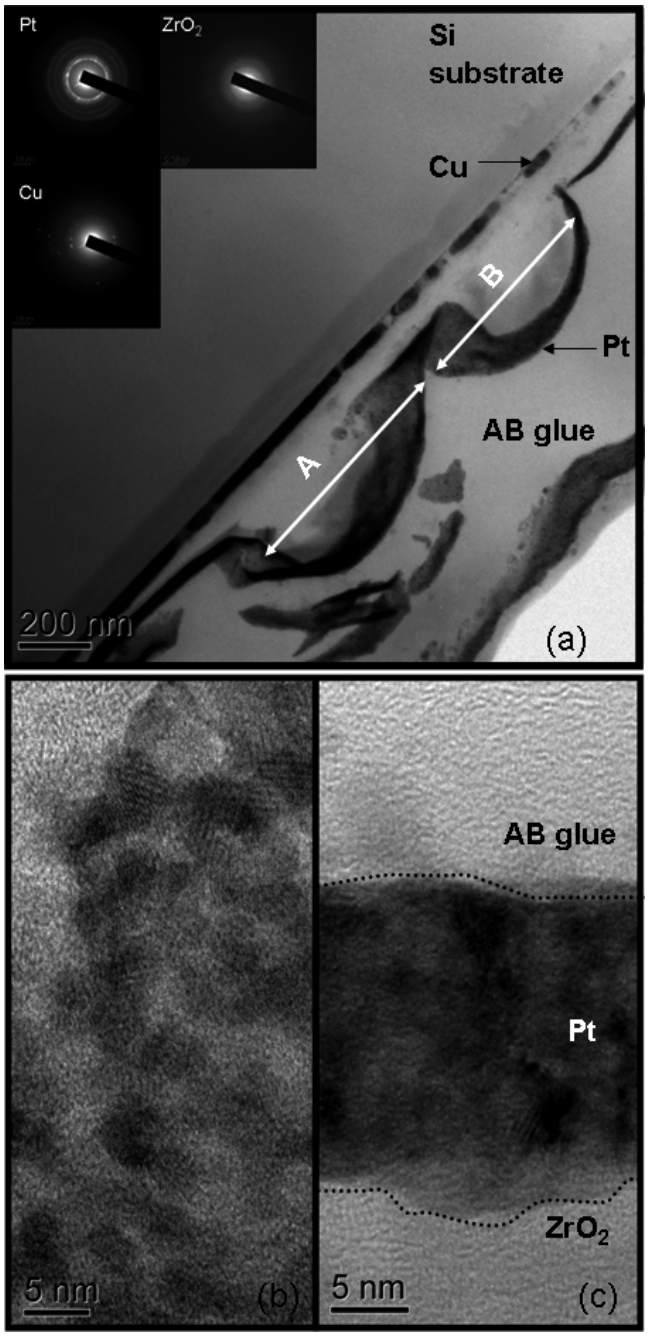

Figure 6. HRTEM interface image of Pt/ZrO_2 lattice dot/Cu structure.

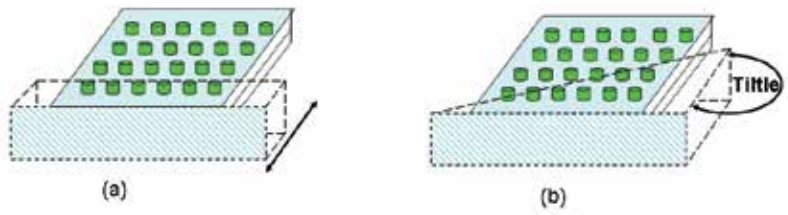

Figure 7. HRTEM sample milling diagrams.

4. Conclusion

We fabricated ZrO_2 thin films after annealing at 300°C through sol-gel deposition. Reproducible I-V curves can be obtained with these samples at room temperature (300 K). The ZrO_2 thin film annealed at 300°C in Cu/ZrO_2/ATO device can also be operated in RS sweeps cycles. In summary, we fabricated TiO_2 thin films by sol-gel deposition. Successful Cu/ZrO_2/ATO structure device in which ZrO_2 thin film was calcined at 300°C can be obtained. The bipolar RS behavior was observed and the ratio of R_{off}:R_{on} can be reached to 10^4. We also investigated the switching device of Pt/ZrO_2 lattice dot/Cu sandwiched structure by HRTEM.

Acknowledgements

This work is supported by the National Natural Science Foundation of China (No. 51372198). The authors also thank the Foundation of Excellent Doctoral Dissertation of Xian University of Technology and the Scientific Research Projects of Shaanxi Education Department (No. 101-211111).

Author details

Ying Li[1*], Gaoyang Zhao[2], Zhibo Kou[3], Long Jin[2] and Yajing Wang[2]

*Address all correspondence to: liying@xaut.edu.cn

1 Advanced Material Analysis Center, Xi'an University of Technology, Xi'an, Shaanxi, China

2 Material Science and Engineering School, Xi'an University of Technology, Xi'an, Shaanxi, China

3 Northwest Electric Power Design Institute of China Power Engineering Consulting Group, Xi'an, Shaanxi, China

http://dx.doi.org/10.5772/60973

References

[1] B.J. Choi, D.S. Jeong, S.K. Kim, et al. Temperature influence and reset voltage study of bipolar resistive switching behaviour in ZrO_2 thin films. *J Appl Phys*. 98 (2005), 037715-037725.

[2] H. Shima, Y. Tamai. Top electrode effects on resistive switching behavior in CuO thin films. *Microelectron J*. 40 (2009), 628-632.

[3] M.J. Rozenberg, I.H. Inoue, M.J. Sanchez. Nonvolatile memory with multilevel switching: A basic model. *Phys Rev Lett*. 92 (17) (2004), 178302-178306.

[4] X. Guo, C. Schindler, S. Menzel, R. Waser. Understanding the switching-off mechanism in Ag+ migration based resistively switching model systems. *Appl Phys Lett*. 91 (13) (2007), 133513-133516.

[5] R. Waser. Resistive non-volatile memory devices. *Microelectron Eng*. 86 (2009), 1925-1928.

[6] Y. Li, G. Zhao, J. Su, E. Shen, Y. Ren. Top electrode effects on 6 resistive switching behavior in CuO thin films. *Appl Phys A*. 104 (2011), 1069-1073.

[7] C. Gopalan, M.N. Kozicki, S. Bhagat. *J Non-Crystal Solids*. 353 (2007), 1844-1848.

[8] X. Zhi, G. Zhao, T. Zhu, Y. Li. The morphological, optical and electrical properties of SnO_2:F thin films prepared by spray pyrolysis. *Surf Interface Anal*. 40 (2008), 67-70.

[9] S. Pulston, P.M. Parlett, P. Stones, M. Bowker. Surface Oxidation and Reduction of CuO and Cu_2O Studied Using XPS and XAES. *Sur Interface Anal*. 24 (1996), 811-820.

[10] M.C. Lopez, B. Galiana, C. Algora, I. Rey-Stolle, M. Gabas, J.R. Ramos-Barrado. Chemical characterization by XPS of Cu/Ge ohmic contacts to n-GaAs, *Applied Surface Science*, 253 (2007), 5062-5066.

[11] C.D. Wagner,W.M. Riggs, L. E. Davis, J.F. Moulder, G. E. Muilenberg. Handbook of X-ray Photoelectron Spectroscopy. Perkin-Elmer, Minnesota, 1979.

[12] X. Wu, P. Zhou, J. Li, et al. Reproducible unipolar resistance switching in stoichiometric ZrO_2 films.*Appl Phys Lett*. 90 (2007), 183507-183511.

[13] D.Lee. Resistance switching of copper doped MoO*x* films for nonvolatile memory applications. Appl Phys Lett. 90 (2007), 122104.

[14] C.C. Lin, B.C. Tu. Resistive switching mechanisms of V-doped $SrZrO_3$ memory films. *IEEE Electron Device Lett*, 27 (2006), 725–727.

[15] D.S. Jeong, C.S. Hwang. Reasons for obtaining an optical dielectric constant from the Poole–Frenkel conduction behavior of atomic-layer-deposited HfO2 films. *Appl Phys Lett*. 86 (2005), 072903.

[16] C. Schindler, S.C.P. Thermadam, R. Waser, M.N. Kozicki. Bipolar and unipolar resistive switching in Cu-doped SiO_2. *IEEE Trans Electr Dev*. 30 (1) (2007), 2762.

[17] A. Sawa, T. Fujii, M. Kawasaki. Interface resistance switching at a few nanometer thick perovskite manganite active layers. *Appl Phys Lett*. 88 (2006),1-3.

[18] K.M. Kim, B.J. Choi, Y.C. Shin, S. Choi, C.S. Hwang. Anode-interface localized filamentary mechanism in resistive switching of TiO_2 thin films. *Appl Phys Lett*. 91 (2007), 012907.

[19] C. Kügeler, R. Rosezin, E. Linn, R. Bruchhaus, R. Waser. Materials, technologies, and circuit concepts for nanocrossbar-based bipolar RRAM. *App*l Phys A. 102 (2011), 791-809.

Section 3

Transmission Electron Microscopy for Biological Samples

Chapter 9

Transmission Electron Microscopy of Biological Samples

Łukasz Mielańczyk, Natalia Matysiak,
Olesya Klymenko and Romuald Wojnicz

Additional information is available at the end of the chapter

Abstract

During the last 70 years, transmission electron microscopy (TEM) has developed our knowledge about ultrastructure of the cells and tissues. Another aim is the determination of molecular structure, interactions and processes including structure-function relationships at cellular level using a variety of TEM techniques with resolution in atomic to nanometre range. Even with the best transmission electron microscope, it is impossible to obtain real results without optimal sample preparation, respecting both the structure and the antigenicity preservation. Preparation techniques for high-resolution study of both macromolecular complex and organelles within cellular complex are based on fast cryoimmobilisation process, where the sample is in the most native, hydrated state. Next, thin samples are directly visualised under cryo-transmission electron microscopy (cryo-TEM), while thicker samples require a thinning step via cryo-electron microscopy of vitreous sections (CEMOVIS) or cryo-focused ion beam (cryo-FIB) before visualisation. Alternatively, vitrified samples are freeze substituted and embedded in chosen resin for room temperature ultramicrotomy. This preparation technique is suitable for morphological study, 3D analysis of cellular interior and immunoelectron microscopy. A different route for immunolocalisation study is cryosectioning according to the Tokuyasu technique that is a choice for rare or methacrylate-sensitive antigens. Most recently, new hybrid techniques have been developed for difficult-to-fix organisms and antigens or labile and anoxia-sensitive tissues. Another preparation technique is, the oldest but still important, conventional chemical fixation dedicated in a wide range of research interest, involving morphological and immunolocalisation study. In this chapter, we present different sample preparation approaches for transmission electron microscopy of biological samples, including its methodological basis and applications.

INTECH
open science | open minds

© 2015 The Author(s). Licensee InTech. This chapter is distributed under the terms of the Creative Commons Attribution License (http://creativecommons.org/licenses/by/3.0), which permits unrestricted use, distribution, and reproduction in any medium, provided the original work is properly cited.

Keywords: conventional TEM, cryo-TEM, cryofixation, CEMOVIS, freeze substitution, Tokuyasu technique, hybrid techniques, water

1. Introduction

The first transmission electron microscope was constructed in the early 1930s by Ernst Ruska and Max Knoll [1]. Roughly a decade later, the first electron microscope picture of eukaryotic cells was taken by Keith Porter [2]. Since then TEM made it possible to study cells and tissue structure and function at nanoscale. This technique is placed between high-resolution methods like X-ray crystallography or nuclear magnetic resonance and lower-resolution light/fluorescence microscopy techniques. Although fluorescence techniques allow for imaging dynamic process in living cells and modern fluorescence microscopes overcoming the diffraction limits that makes it possible to zoom in on cellular structure with resolution under 100 nm [3], TEM remains the main technique which makes it possible to study biological systems owing to its near-atomic-level resolution [4]. Moreover, TEM gives opportunities to visualise an interesting target with surrounding structure, when unlabelled surroundings still remain hidden at fluorescence sample [5]. Additionally, TEM comprises different branches: electron crystallography and single-particle analysis are dedicated to study proteins and macromolecular complexes, (cryo-)electron tomography and CEMOVIS for cellular organelles and molecular architectures and conventional TEM for gross morphology. Such a wide range of electron microscope techniques gives opportunity to find the relation between different macromolecules, their supramolecular complexes and organelles assembled into an intricate network of cellular compartments. Knowledge of the cellular ultrastructure can contribute to an understanding of how cells and tissues function in both normal physiological and pathological state.

Since the invention of the first TEM, the aim has been to image liquid samples at higher resolution but as easily as with light microscopy. At the beginning, it was impossible to accomplish due to low technological knowledge and lack of appropriate tools. Thus, scientists have introduced sample preparation techniques for observing soft and frail living matter in the inhospitable environment of an electron microscope. The TEM column is under ultrahigh vacuum, where electrons as a coherent beam are directed on the sample. From a biological point of view, living matter consists of up to 80% water; therefore, without appropriate sample preparation, the high vacuum literally sucks out every trace of liquid. Moreover, biological matter compose mainly of light elements (e.g. carbon, hydrogen, oxygen, nitrogen, sulphur, etc.) and for that reason, electrons which travel at a fraction of the speed of light, do not interact strongly with these atoms. Consequently, native biological materials are of extremely low contrast. On the other hand, the two aforementioned factors oriented sample preparation strategies. Due to the electron's scattering phenomena within the sample, only small objects can be observed directly. Larger samples need to be sectioned for analysis, but cells and tissues are too soft to be sectioned thinly enough without earlier sample preparation. Many laboratories have been ingenious in designing and implementing different preparation techniques over the years, and as a result, scientists have found at least a partial remedy to these problems.

Therefore, a biological sample can be prepared either by removing or by freezing water. The oldest method is conventional sample preparation which uses chemical fixation, sample dehydration at room temperature and embedding with chosen resin. In the 1970s, Tokuyasu introduced an alternative to conventional sample preparation dedicated for immunocytochemistry. An alternative method to chemical fixation is cryofixation via vitrification process. Taking into consideration the size of the sample, electron microscopists have a wide range of freezing techniques at their disposal. Small or thin sample after plunge freezing can be directly observed at low temperature under cryo-transmission electron microscope (cryo-TEM). Thicker samples are first vitrified by using high-pressure freezing (HPF) or self-pressurised rapid freezing (SPRF) technique and then proceed to thinning process at liquid nitrogen temperature by CEMOVIS procedure or cryo-FIB milling. Finally, thin frozen-hydrated samples are directly observed under cryo-TEM. Another option is freeze substitution (FS) which bridges the gap between vitreous states and room temperature ultramicrotomy. Lastly, different combinations of mentioned techniques offer a new research possibility, especially for difficult-to-fix organisms or antigens. In a particular situation, chemical pre-fixation step is a prerequisite for successful sample vitrification, although it seems to be contradicted.

Biological systems are very complex; thus, it is impossible to understand structure-function relationship outside the surrounding context. These days, dynamic developing of correlative light and electron microscopy (CLEM) approach can be observed. This approach relies on two steps. Firstly, the object of interest is located and imaged with fluorescence microscopy (FM), and then the sample is imaged in TEM. This technique is highly demanding according to cell biologists because high-resolution data can be fitted in the cellular context. However, new possibilities introduce new challenges in the preparative stage, and protocols for TEM and FM often are incompatible. Therefore, it is worth to mention that technological progress stimulates new sample preparation design, but often existing preparation schemes initiate new ideas.

In this chapter, we present different specialised preparation techniques dedicated to cells and tissues; but at the beginning, we would like to impress the importance of water in life on readers, because for a long time, its role in living organisms was neglected. Another point is that for a long time, water was treated as a foe by electron microscopists. Nevertheless, readers should bear in mind that selection of an appropriate technique strongly depends on the material and aims of the study. Thus, a general rule of thumb is that the higher the resolution is important, the closer to the native state sample preparation is desired. Moreover, the higher the resolution, the thinner sample should be, but at the same time, less information is achievable. During morphological study, more important is the sample size; hence, the preparation technique based on resin-embedded sample is an adequate choice. However, for immunolabelling research, compromise between antigens and ultrastructure preservation is the major challenge. Although the main aim of this chapter is to present different preparation techniques of biological specimens for TEM, we would like to also point out that the preparation step is important for correlative approach.

We strongly encourage further reading of proposed positions where the reader can find practical insights of the presented subject, e.g. chosen volumes from *Methods in Molecular Biology* [6–8] and *Methods in Enzymology* [9–11], and with practical application in different model systems, positions from the Methods in Cell Biology series [12–14]. Many important hints in sample preparation for TEM are also connected with CLEM field [15,16] and immu-

noelectron microscopy [17]. In our opinion, a complete library should also include the *Handbook of Cryo-Preparation Methods for Electron Microscopy* because this position is strongly oriented to the practical side of sample preparation art [18]. It is also important to know what was done so far and thus where we should go. Among many old books, but with still-current knowledge, *Cryotechniques in Biological Electron Microscopy* [19] captured our attention. The last but not the least position is the *Principles and Techniques of Electron Microscopy: Biological Applications* [20].

2. Water and its vital role in life

Organisms consist in major part of liquid water which is the medium in which life takes place. Hence, life on our planet and its probability elsewhere in the universe cannot have evolved or continue without water. In view of the abundant presence of water in living organisms, this substance cannot be perceived as an inert diluent. Water performs many functions: it transports, reacts, lubricates and structures and is used in signalling. Water is also a metabolite and a temperature buffer. The physical properties of water, which result from its structure, play a key role in the orchestration of the cell machinery. Biological molecules and water should be thought as equal partners where one is required and structured by the other.

From a chemical point of view, a water molecule contains one oxygen atom covalently bounded with two hydrogen atoms. Due to positively charged hydrogen atoms and a negatively charged oxygen atom, where negative charge comes from two lone electron pairs, water is a dipole. Water as a dipole has the most important property: water molecules are able to form multiple hydrogen bonds between each other. A hydrogen bond occurs when a partially positively charged hydrogen atom lies between partially negatively charged oxygen of H_2O molecules. A hydrogen bond is naturally formed from a complex combination of different interactions: an electrostatic, a polarisation and a covalent attraction, and a dispersive attractive interactions, an electron repulsion and a nuclear quantum effects. In theory, one water molecule can interact with four other water molecules, thereby forming a tetrahedron configuration. In practice, hydrogen bonds are very dynamic and heterogeneous structures, both on energetic and structural levels, and a single water molecule can form two or four hydrogen bonds. As a result, in liquid water, hydrogen bonds behave in cooperative and anticooperative manner [21]. At the higher level of organisation, water molecules in liquid state tend to create tetrahedral pentameric clusters, which are linked to other water molecules and clusters to form a complex network or liquid phases [22]. Such a network of hydrogen bonds is dynamic and ordered in a nanometre range structure.

From a biological point of view, a cell's interior consists of membranes and cytoskeleton together with proteins, carbohydrates and nucleic acids which are strongly and inseparable dependent on water molecules. The dipolar nature of water enables to arrange molecules of water into an ordered, very constrained manner on the surface of biological molecules. Depending on the chemical nature of surface domains, hydrophobic or hydrophilic, water order is different. Water molecules are strongly attracted by ionised and hydrophilic domains than by apolar domains, where H_2O molecules arrange themselves into clathrate-like struc-

tures [23]. They form a hydration shell, called also interfacial water, built from several water layers. Hydration shells are critical for solubility of molecules and prevent them from aggregating. When two particles meet, they do not stick together, but separate [24]. Moreover, protein folding is mediated and guided by aqueous solvation, and protein structure is stabilised by water clusters and their hydrogen bonding capabilities. Water also gives proteins flexibility during conformational changes, and its molecules mediated protein-ligand interaction. Another interesting example of water role in the cellular world is nucleic acid-water interactions. Firstly, water molecules stabilise structure of double helix. Secondly, water hydrates both the major and the minor grooves of DNA. The hydration shells have a characteristic pattern reliant on bases and their sequences and thus create a 'hydration fingerprint' for a given DNA sequence. The specific arrangement of interfacial water governs protein binding to the DNA. The enumerated examples are further discussed in detail in [25]. Water inside the cell, which is not bound in hydration shell, is unaffected by the biomolecules. Additionally, cellular unbounded water behaves differently from water outside, e.g. intracellular water has higher viscosity. The cytoplasm has a sol-gel nature. The local parts of the cytoplasm may manifest itself as a more highly viscous and stiff environment, likened to a gel-state, or as a low-viscosity sol-state solution [21]. In the former case, water molecules form more strongly hydrogen-bounded water clusters. This reduces local fluctuations in the nearby macromolecules and slows down metabolite and ion migration [23]. An additional function of strong hydrogen-bonded network existence is transmission of information about solutes and surfaces at distances of several nanometres. In this way, biomolecules 'sense' each other, thereby changing their solubility and activity. In the latter case, proteins can release a significant amount of water, changing the fluidity and activity of the intracellular 'sol'-state environment. The state of the water is thus essential for the biological activity of the cell, and the state of metabolites controls water structure. Thus, water is defined as an engine of life [26].

From the physical point of view, water is usually perceived as an ordinary substance because people interact with it all the time in their everyday lives. Very often, people think that other liquids have similar properties to this liquid; however, nothing could be further from the truth. Water is the only liquid that exists in all three states on Earth: liquid, solid and gas. Although some researchers believe that intracellular water is the fourth phase of water [27]. Some properties of water, such as large heat capacity and high thermal conductivity, allow the control of body temperature. The high latent heat of evaporation is a protection from dehydration and considerable evaporative cooling [21]. To sum up, water is essential for life existence at different levels: from molecular to cellular and organisms to whole-planet level. All properties of this substance are not yet known; therefore, new discoveries in this field will have an interesting impact in understanding how life works.

3. Conventional TEM

As the vital role of water was outlined in the last paragraph, it must be borne in mind that the knowledge about water and its role in living organisms has evolved over decades. Recently, however, the role of water in cell and molecular biology has become clearer and much more

important than in the past. At the beginning of the sample preparation, biologists carefully eliminate every trace of water. Conventional specimen preparation is the most commonly used method for TEM. The major advances in conventional specimen preparation technique are summarised at the end of the section.

The first step in this procedure is chemical fixation to preserve the biological sample with minimal alteration of volume and morphology from the native state. Chemical fixation can be carried out in various fixatives which are used separately or in combination, i.e. glutaraldehyde (GA), paraformaldehyde, osmium tetroxide, uranyl acetate (UA) and tannic acid solution are usually used. Glutaraldehyde, as a dialdehyde, preserves ultrastructure well but penetrates slower than the monoaldehyde, i.e. paraformaldehyde. Glutaraldehyde is used alone for small pieces of material, but a mixture of the two aldehydes may be used for fixation of larger items. The most popular fixation strategy in conventional preparation is double fixation with GA and osmium tetroxide. The aldehydes preserve mainly proteins, but reaction with lipids is limited. Therefore, to stabilise the lipid part of the sample, the post-fixation with osmium tetroxide is required [28]. Furthermore, osmication enhances contrast which is important during the analysis in the TEM, but it is important to remember that prolonged process can destroy proteins; as a consequence, the biological material becomes brittle. It should also be noted that the common practice in conventional electron microscopy is en bloc fixation/staining with UA and tannic acid. The first fixative decreases protein and phospholipid extraction; the second one reveals ultrastructure of microtubules.

The chemical fixation depending on its sample type and size can be performed in four various ways: by in situ fixation (applied to cell cultures), by immersion (small pieces of tissues are carefully excised and immersed in fixative as soon as possible), by vascular perfusion (the fixative is pumped through the vascular system of deeply sedated animals) or by vapours (the small delicate specimens, such as membranes, are suspended over a solution of osmium tetroxide). Usually, in standard conditions, fixation is carried out by immersion method. After fixation with buffered fixatives, the sample is dehydrated in increasing concentration of a solvent (a combination of either alcohol or acetone with propylene oxide) to enable infiltration with a liquid resin. An epoxy resin is most commonly used in conventional TEM. Finally, supersaturated and surrounded by resin, the sample is polymerised by applying gentle heat. Cured resin block containing biological material is thinly sectioned (40–150 nm), and subsequently post-stained with heavy metal salts, such as uranyl, and lead in order to introduce contrast inside the sample.

Previous reports revealed that chemical fixation, dehydration, heavy metal staining and plastic embedding can introduce various artefacts. Fixation with GA prior to dehydration results in cross-linking, causing aggregation of proteins, collapse of highly hydrated glycans and loss of lipids. Heavy metals can cause additional artefacts in the form of precipitation [24,29,30]. To sum up, artefacts introduced during conventional sample preparation limit the resolution of biological samples to about 2 nm [20]. Further, modern transmission electron microscopes with a field emission gun can obtain sub-angstrom resolution; thus, the resolution is mainly limited by the properties of the sample [31]. Therefore, the improvement of biological sample preparation technique has become the challenge for many scientists, and nowadays, some interesting alternatives are available.

On the other side, it should be stressed that TEM with conventional preparation is still an essential tool in many fields of tissue and cell biology, as well as in medicine. Where the approach is quality control method or gold standard to complement, support or confirm the results of specific histopathological diagnosis (neoplastic, renal, neuromuscular, infectious, hereditary and metabolic diseases) [32,33]. Therefore, the advantages of the conventional sample preparation should be emphasised, starting from simplicity of this fixation technique. There is no requirement for any specialised equipment; indeed, simple vessels with fixatives are sufficient. At the same time, numerous 1-mm^3-in-volume blocks of tissue can be fixed; thus, large areas of sample are accessible to analysis. When the tissue autolyses quickly, organs are too large or dissecting is difficult, chemical fixation is carried out by perfusion. Appropriate optimisation of fixation parameters, i.e. fixative concentration, buffer pH, temperature of fixative and time fixation, results in optimal ultrastructure preservation. Therefore, the unique advantage of conventional fixation is its ability to fix human tissue biopsies and study different animal organs without biopsy need.

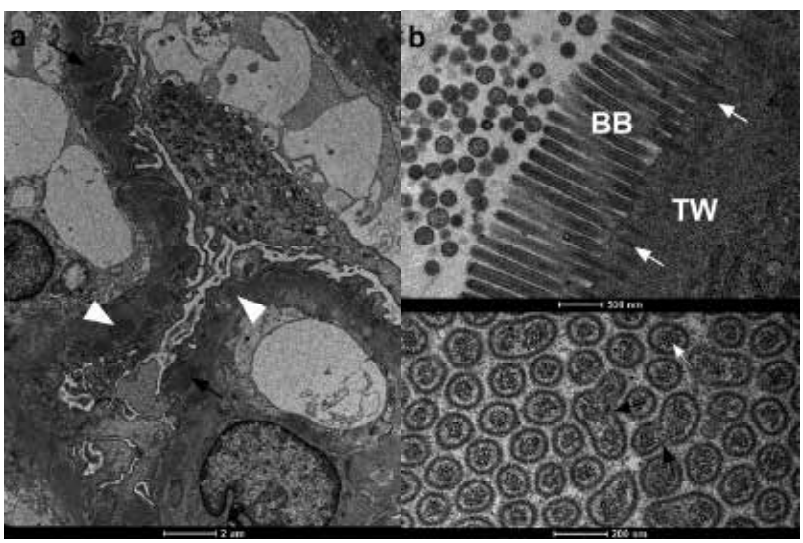

Figure 1. (a) Example of membranous glomerulopathy. Electron photomicrograph shows large amounts of electron-dense deposits in the glomerular basement membrane (black arrows); the sub-epithelial deposits are covered by a bridge of newly formed glomerular base membrane (white arrowheads). The foot processes of the epithelial cells are obliterated. In the cytoplasm of the epithelial and endothelial cells are numerous organelles and vacuoles. **(b)** Electron micrograph chemically fixed and an Epon-embedded rat's small intestine. Ultrastructure of the brush border (BB) and terminal web (TW) region of an enterocyte. Notice the actin filaments (white arrows) that descend from each microvillus deep into the underlying terminal web; below, organelles are visible. Lower part: transverse section through brush border showing numerous microvilli containing actin filaments (white arrow) and fusion of microvilli (black arrows).

In particular cases, pre-fixation with aldehydes is a prerequisite for further sample processing (see Sect. 8). Another advantage of chemical fixation is the possibility to perform sample preparation in different locations, e.g. in an operating room, in a laboratory other than EM lab and in the natural environment.

Adding to this knowledge about artefacts that are introduced during sample preparation, these advantages constitute strong position of conventional TEM in modern science. To prove this statement, some examples are presented. The conventional sample preparation in ultrastructural pathology is often irreplaceable (Figure 1a), as evidenced by different books [32,34]. A human biopsy from a patient with mitochondrial cardiomyopathy may serve as another example, where pathogenic giant mitochondria probably are formed to compensate effects caused by mutation of mitochondrial DNA [35]. Also, some interesting discoveries at scientific ground are contributed by conventional TEM. Among examples, electron microscopic analysis of a spherical structure of mitochondria is quite interesting [36]. Conventional sample preparation combined with ET revealed that mitochondria under oxidative stress were able to undergo a structural transformation in spheroid form. This novel mitochondrial dynamic process is probably involved in some pathological conditions; however, further study is needed.

Key events in the history of conventional TEM in the life science	
1932	Ruska and Knoll built the first transmission electron microscope
1932–1934	The first images of unfixed biological material were obtained (the wings and legs of a housefly)
1939	Ruska obtained the first bacterium and virus TEM pictures
1943	Sjöstrand built the first ultramicrotome and developed a method of producing ultrathin tissue samples which were used to study the skeletal muscle. Rapid development of ultramicrotomy since 1948
1945	Porter, Claude and Fullam imaged whole eukaryotic cells that were fixed in osmium vapour and then dried
1949	Newman et al. introduced methacrylates which became the first embedding media of quality for TEM samples
1950	Latta and Hartmann used glass knife in ultramicrotomy
1952	Palade recommended buffered osmium fixative for the preservation of cell ultrastructure
1956	Fernandez-Moran used for ultrathin sectioning a diamond knife
	Potassium permanganate fixation was introduced by Luft
1956–1982	Introduction of new resins for electron microscopy: Araldite (1958), epoxy resin (1961) and Lowicryl media (1982)
1958	Kellenberger used UA to stabilise viral and bacterial DNA
1959	Singer employed ferritin coupled with immunoglobulins to recognise the location of the antigen of interest
1963	David D. Sabatini introduced the aldehyde fixation; previously used fixatives were replaced by double fixation with glutaraldehyde and osmium tetroxide. This fixation strategy revolutionised the field of biological electron microscopy, and it is still the method of choice for many laboratories nowadays
1963	Reynolds used lead citrate as electron-dens stain in TEM
1966	Graham and Karnovsky developed a cytochemical method for horseradish peroxidise localisation
1971	Faulk and Taylor introduced colloidal gold labelling technique for ultrathin sections

Telocytes are a new type of interstitial cells characterised by the presence of telopodes, visible only by TEM [37]. These cells can be found in most organs, including the heart. The recent study showed the new type of extracellular vesicles released by heart telocytes that probably are an essential component in the paracrine secretion and may be involved in the heart physiology and regeneration process [38]. The combination of classical TEM and cell culture is an unbiased approach to identify unrecognised pathogen, provide the first clue about investigated pathogen and guide further laboratory study and epidemiology [39]. Another example is ultrastructure of the glomerular filtration barrier in the kidney [40]. ET in combination with scanning electron microscopy (SEM) confirmed suggestions that the glomerular filtration barrier comprises five layers instead of three. This discovery should allow for deeper understanding of kidney physiology and diseases.

Although conventional TEM is also appropriate for immunogold labelling, we leave this approach out. For more information about immunogold labelling on resin section, refer to Chapter **X**.

4. The Tokuyasu technique

Cryosectioning according to Tokuyasu is one of the most reliable and sensitive immunolocalisation techniques for different types of sample. It was introduced in the 1970s by Tokuyasu, using a cryo-ultramicrotome developed by A. Christensen [41], although the first attempts at cryosectioning were pioneered by Fernandez-Moran in 1952 [42] and further developed by Bernhard and Leduc [43]. Similarly to the conventional specimen preparation techniques, the biological material is first chemically fixed with aldehydes at low concentration. Instead of dehydration with organic solvent and resin embedding, the fixed material is infiltrated with sucrose, subsequently frozen in liquid nitrogen and sectioned with a dry knife at low temperature. What is interesting is in the past, it was suggested that wet sectioning based on water mixtures with sucrose, dimethyl sulfoxide or glycerol may resemble conventional resin ultramicrotomy. This idea dies a natural death because of limited temperature range for optimisation of the cryosectioning and chemical properties of proposed mixtures [44]. Obtained cryosections are retrieved from the knife surface, thawed and placed either onto microscope slides for light microscopy applications or electron microscopy formvar-carbon-coated grids. Such prepared cryosections are ready to perform immunolocalisation step on both fluorescence microscopy [45] and EM level [46]. For the latter, immunolabelled cryosections are stained with UA, embedded in methylcellulose to prevent drying and cell organelle irregular shrinkage artefacts and examined in the TEM [41,47]. The final step for fluorescence microscopy is mounting the coverslip with immunolabelled material on a slide with a drop of mounting medium before examination.

At a recent time, a new and improved contrasting procedure called 2+Staining was introduced for Tokuyasu cryosections for correlative approach [48]. 2+Staining consists of contrasting immunolabelled sections with 1% osmium tetroxide, 2% UA and lead citrate and followed by embedding in 1.8% methylcellulose. In comparison with the Griffith method, where membrane

contrast is excellent but fluorescence signal on the section is strongly reduced or lost altogether [49], the introduced procedure yielded a positive contrast of the cellular organelles and membranes, as in the contrast obtained from stained resin-embedded sections. The 2+Staining procedure shows little to no effect on the signal of the fluorescence labelling on the sections.

In comparison with conventional technique, the sucrose infiltration step dehydrates chemically fixed specimen in lesser degree. Thus, the advantage of thawed cryosection labelling over resin sections stems from the preservation of a natural hydrophilic environment. Moreover, resin sections are created with a polymeric cross-linked matrix; thus, antigen accessibility is lower and mainly restricted to the resin surface. In consequence, thawed cryosections enable better access to the antigens, particularly rare ones, for the probes and high detection sensitivity [50]. Over the years, the technique has been further improved by Tokuyasu and his colleagues [51–54]. These improvements become basis for the future research on various biological organisms and hybrid technique developments [48,55–59] including correlative approach [4,48].

5. Vitrification as an alternative to conventional fixation

An alternative way to deal with water is keep it inside the biological specimen by cryofixation. Cryofixation is based on vitrification that is not fixation per se, because vitrification is a physical process of the solidification of a liquid into noncrystalline or amorphous solid known as glass, usually induced by rapid cooling [60]. Water molecules do not have time to start to crystallise because heat is extracted from the system with high efficiency. Accordingly, term fixation cannot be understood in a chemical sense, where covalent bond is created. In the case of water, its vitreous state can be seen as liquid water with extremely high viscosity. Hence, cryofixation of biological matter allows instantaneous immobilisation of all cell constituents in their current positions which translates to obtain a true snapshot of the cell at the moment of ultrarapid freezing [61]. To précis, diffusible ions and molecular components are not shifted or extracted from the cell [62–64]; ultrastructural morphology is preserved close to the nature state, and rapid physiological processes can be characterised in a precise point in time.

When cooling rate is not sufficient, the formation of crystalline water destroys cellular ultrastructure. Another anomalous property of water is its increasing volume during crystallisation. Water freezing is not the reverse process of ice melting [65]. The freezing process is complex and influenced by nucleation centre, crystal growth and cooling rate. Slow cooling rate at ambient pressure results in hexagonal ice, whereas cubic ice forms under faster cooling rate, especially in the presence of nucleation centre. However, liquid water below its melting point is supercooled water. Liquid water is easily supercooled down to about -25 ºC and in 9-μm-diameter tiny droplet, down to about -46 ºC [66] and -92 ºC at 204,8 MPa [60]. Below these temperatures, crystal formation rapidly takes place as supercooled water has to go through the nucleation process by itself, generating nucleation centre distributed uniformly over the phase. In the end, ice crystals are formed. In the context of biological matter, cellular interior is a complex solution of different soluble materials, such as ions, proteins and sugars that

interact with the water molecules, thus changing water freezing behaviour. The presence of salts and hydrophilic solutes increase the extent of supercooling by lowering the freezing point of the solution. Furthermore, increasing solution concentration increases the temperature at which water becomes vitreous. In general, there is lack of heterogeneous nucleation centres inside the cell, and cellular solution concentration is usually higher compared to the surrounding medium. For these reasons, freezing starts somewhere in the external medium or on the surface where cells or tissues are placed. Growing ice crystals outside the cell are avid for any water molecules, including intracellular water, resulting in osmotic pressure changes and eventually bursting of the membrane [67]. Finally, biological matter after freezing consists of ice crystals and dehydrated solution between ice ramifications. Therefore, the water in the cell and around it should always be vitrified to avoid deleterious effects of ice formation. The mentioned issue underlies the success of the Tokuyasu method, where cryoprotected chemically fixed sample is vitrified by dropping it into liquid nitrogen. Nevertheless, the time when vitrification becomes more understandable and easier to perform had yet to come.

The preparation of biological samples by vitrification process is relatively a new technique. Until 1980, it was thought that water cannot be vitrified because of its thermodynamic properties. However, the big breakthrough came in 1980 when Mayer and Bruggeler had used X-ray diffraction to prove that small water droplets can be vitrified [68]. One year later, Dubochet and McDowall published an article where they demonstrated that small droplets of water or aqueous solution can be vitrified on electron microscopic grids [69]. These discoveries marked a turning point in biology, especially structural biology, and changed the point of view on water in electron microscopy from being the foe to being the best friend of electron microscopists [70]. The vitrification process depends on biological and physical factors such as the thermal diffusivity, the thickness and solute concentration of the sample as well as the cooling rate and the pressure applied. Nonetheless, the cooling rate seems to be the most important factor and decides which technique should be used [60]. Different preparation techniques are available for different sample sizes and the microscopy approach.

5.1. Plunge freezing

The simplest way to obtain a vitrified sample is through the so-called bare grid method [71] or plunge freezing (PF). Typically, vitrification is done by an immersion of small biological objects within a thin water film into properly chosen cryogen. After vitrification, the sample is directly imaged in a frozen state under a cryo-electron microscope. Under atmospheric pressure, cooling rate as high as 10^8 K/s is possible, at least in theory [72]. The successful vitrification obtained by PF is strongly dependent on properties of the grid, the temperature and nature of cryogen and the environment of the sample. The cryogen of choice is ethane, cooled to their freezing points by thermal contact with liquid nitrogen [71]. However, the usage of the mixture composed of propane and ethane has two advantages over pure ethane. Firstly, pure alkane is solid at 77 K, whereas the above mixture remains as a liquid at this temperature. For that reason, ethane-propane mixture does not require repeated cooling and warming cycles in order to ensure proper vitrification conditions. Secondly, the mixture produces less damage to carbon layer on the grids and to specimens mounted on C-flat holey carbon grids [73]. In

addition, the surrounding environment has an influence on the success of the final vitrification. In the case of thin films, usually 100 nm thick, prepared before plunging, sample is subjected to evaporation and heat transfer processes. In consequence, sample is exposed to risk of concentration, pH, ionic strength and temperature changes. Therefore, a new method was devised by Bellare et al. [74] and further improved by Frederik [75], who has constructed a new robot for sample vitrification by this technique. Plunge freezing can be applied to viruses [76], bacteria [77,78], isolated protein complexes [79,80] and whole cells [81,82], however, only 10 μm thick. In the last case, the flat thin periphery of cells [81] or whole thin cells, e.g. *Ostreococcus* [83] and *Plasmodium* sporozoites [84], is directly observed.

Although high cooling rate values are obtained during vitrification by PF, this technique is suitable for samples as thick as few micrometres. The reason is poor heat conduction properties of water because even an infinitely high cooling rate applied at the sample surface rapidly decays within the sample. Thicker-sample vitrification is only possible when cooling rate is reduced under particular conditions [60,85].

5.2. High-pressure freezing

The high-pressure freezing (HPF) technique was developed in the 1960s by Moor and Riehle [86], but as a routine laboratory technique, it became available from the mid-1980s. This freezing technique is based on Le Chatelier's principle and on the fact that physical properties of water can be manipulated in some range. Water during crystallisation expands its volume and forms crystal. According to Le Chatelier's principle, the increase in ice volume can be hindered by external high pressure which suppresses ice nucleation and ice crystal growth. Hence, high pressure is physical cryoprotectant which additionally changes the physical behaviour of water. High pressure lowers both the melting point and the freezing point, with the effect that at 2,048 bar, the melting point of water reaches its minimum of -22 ºC. At the same time, the possibility for supercooling is expanded, and the freezing point is shifted to -92 ºC [87]. Consequently, less heat is produced by crystallisation and less heat has to be extracted from the sample during freezing. In practice, it means that only several 1,000 K/s are required to vitrify biological matter at 2,048 bar [85]; thus, the sample thickness that can be vitrified increases tenfold, up to 200 μm [88]. Vitrification process during high-pressure freezing is obtained by pressurising the sample at 2,048 bar and subsequent rapid cooling at -196 ºC using liquid nitrogen jets within tens of milliseconds [72]. However, in very special cases, if the concentration of intrinsic cryoprotectants is high, samples even as thick as 600 μm can be vitrified [89,90]. Usually, the space around samples during vitrification has to be filled with appropriate filler. The role of the filler is to effectively transfer heat across the sample as well as cryoprotection during cooling process. Therefore, an important issue is physiological compatibility with the cells or tissues [67].

Except that HPF technique enables vitrification of thick samples, this technique has evident limitations. Firstly, gaseous compartments collapse at a high pressure. To counteract this phenomenon, intracellular air-filled spaces (e.g. lung tissue, plant leaves) need to be filled with a chemically inert solvent not mixable with water [91,92]. Secondly, high pressure solidifies the lipid bilayers and leads to a change in biological membrane structure [93]. Similarly, cholesteric liquid crystal of DNA cannot be retained by using HPF [94]. The

variety of samples prepared by HPF is enormous, and in the literature, there can be found numerous articles about the advantage of cryoimmobilisation over chemical fixation. Naturally, some exceptions to this rule exist. The HPF technique is less successful for labile tissue, such as brain or nerve tissue, where excision of tissue can last for quite some time, which results in anoxia and osmotic effects [95]. The inner ear tissue is another example of difficult to preserve sample by HPF [96]. In the case of stereocilia, which are mechanosensing organelles of hair cells, the actin core had a distorted appearance after freezing, described as 'tangled'. Fortunately, a hybrid technique resolves this problem and amplify the strength of HPF as cryopreparation technique (see Sect. 8).

The handling time during sample preparation is crucial because short time enables to obtain sample quality close to the native state. This requirement has brought several interesting solutions for sample preparation step prior HPF. While whole organisms (e.g. *Caenorhabditis elegans*, *Drosophila* [67], zebrafish embryos [97]) or human and animal cell culture is quite easy to load into the carrier, tissue sampling is more demanding. In the former case, cells are either directly loaded into the carriers or first cultured on chosen substrates (e.g. sapphire coverslips [98], Aclar disc [99] or gold grids [100]) and subsequently transferred to the live carriers and vitrified. For different tissues, short handling times can be reduced by using a rapid microbiopsy system. The microbiopsy system allows to accomplish the excision of a small sample and freeze it in less than 30 s [101]. Another solution for improving both the fast sample transfer and freezing reproducibility process is the rapid transfer system [102]. The principal advantage of this tool is the ability to correlate light microscopy and HPF with about 5 s time resolution [103]; thus, a catching of dynamic processes at known point and rare event localisation is possible. For faster cellular events, such as ultrafast endocytosis, flash-and-freeze approach was designed [104]. Flash-and-freeze electron microscopy combines optogenetics with HPF; viz. a brief single light stimulus is applied to the sample with subsequent freezing step. This tool can capture cellular dynamics with millisecond temporal resolution and nanometre spatial resolution.

5.3. Self-pressurised rapid freezing

Self-pressurised rapid freezing (SPRF) has been introduced in 2007 as a novel and low-cost cryofixation method. Sample is loaded inside the copper tube which is then clamp sealed at both ends and plunged directly into the cryogen [105]. The essence of vitrification by SPRF is isochoric freezing process. This technique is based on the fact that water expands upon freezing, and formed crystal ice builds pressure inside the confined volume of the tube. Thus, formation of internal pressure by hexagonal ice and/or supercooled water expansion supports the vitrification of the sample, at least in parts of the tube. Additionally, growing ice crystals close to the tube wall might concentrate the cryoprotectant in the centre and support vitrification [106]. Another factor that influence cryofixation is higher heat diffusion coefficient of crystalline ice, and this means a faster cooling system [107]. Although this explanation is still only hypothetical, the fact is that for vitrification by SPRF, lower concentration of dextran is required in comparison with HPF, thereby causing less osmotic changes [108]. The ultrastructural quality of vitrified specimens by SPRF and HPF is comparable, although on average, only 50% of the

structures will be vitrified and 50% will be in crystalline form. To prove the concept of self-pressurised vitrification, different organisms were used including bacterial strains, yeast cells, eukaryotic cell culture and *C. elegans* nematodes. In the case of eukaryotic cell culture, it was noted that the copper tubes are poisonous, even in a typical time range (30–60 s) during sample preparation prior vitrification. Thus, the physiological or 'close-to-native' state is definitely lost [106]. An aluminium container was proposed as a substitute for poisonous copper tubes, although authors suggested developments of new biocompatible coatings of the copper tube's internal surface. The reason was a slightly higher degree of crystalline ice volume in aluminium tubes. The necessity to prepare cell culture as a suspension is a different obstacle; therefore, although SPRF technique is cheaper and less laborious in comparison with HPF, this technique cannot be used in morphological research where cell adhesion is of critical point. More recently, SPRF was used to vitrify *Arabidopsis* inflorescence stems with subsequent cryosectioning in order to obtain architecture information about plant cell walls. This knowledge is another step to improve understating of biofuel plant material and to rationalise reengineering of second-generation lignocellulosic biofuel crops [109].

6. Post-freezing processing

After vitrification, water within the samples is amorphous as long as samples are stored below devitrification temperature (<-136 ºC). Further processing of the sample depends on its size and aims of the study. The electron beam penetration limit in TEM is about 1 μm. Therefore, many different small-enough samples, such as macromolecular complexes, viruses or bacteria as well as subcellular structures at a periphery of the cell, can be imaged directly under cryo-TEM. Water inside a column of TEM evaporates, unless a special cold stage holder is used at temperature close to that of liquid nitrogen. At this temperature, water evaporation rate is almost negligible and vitrified material can be observed without loss of image quality [110]. However, thicker samples require distinct follow-up procedures – specimen sectioning is the basic need. Vitrified material can be sliced at a temperature below devitrification point into ultrathin sections and subsequently analysed under cryo-microscope (CEMOVIS). As another option, the focused ion beam technology is adequate for the purpose of thinning vitreously frozen biological material. Besides application of pure cryotechniques, specimens can be prepared by cryo-to-room temperature techniques.

6.1. CEMOVIS

In principle, cryo-electron microscopy of vitreous sections (CEMOVIS) technique is as simple as possible. The first step is vitrification of biological material; then vitrified material is sectioned in a cryo-ultramicrotome. Frozen sections are transferred to a grid, and subsequently the grid is imaged in a cryo-TEM under low-dose condition [111]. Critical issue leading to final success is hidden in performing all these manipulations below devitrification temperature. In spite of the fact that CEMOVIS seems to be a simple technique, the modern state of this approach was strongly connected with indispensable laboratory work and technological development of electron microscopy field.

In the first cryosectioning-based studies [42,43], samples were freeze-dried before analysis under electron microscope. Another important development was sectioning of unfixed biological material at -150 ºC [112], together with transfer and observation of frozen-hydrated specimens in the transmission electron microscope [113]. Similar to the previous studies, also in these works, obtained sections were not analysed as vitreous specimens.

However, the first successful trails in cryosectioning of vitreous material were built on precursors' work and existing cryo-microtomes and took place in the eighties of the last century [111,114]. Obtained good results were not reproduced each time, and they were difficult to extend to other specimens [70]. It took another 20 years, where new vitrification techniques were established, and scientists obtained better knowledge of the vitreous state of water and cryosectioning method was optimised. Although promising results have been obtained at the beginning of this century, 2004 was a pivotal year because CEMOVIS has reached maturity. Since then, CEMOVIS is regarded as a routine laboratory technique, at least by some researchers, and reveals the native state of cells and tissues with remarkable quality and resolution [115].

Frozen-hydrated sections are prepared without any additional purification, fixation, dehydration and staining steps. As a result, all cellular components are immobilised inside vitrified water, with preservation to the atomic level [116]. During vitrification process, using HPF or SPRF, usually a 20% solution of a high-molecular-mass dextran is used. Addition of dextran to the sample mimics the vitrification properties of typical cells. Consequently, surrounding environment of the cells is vitrified and thus eliminates possibility of crystalline ice formation. Hexagonal or cubic ices make the sample brittle for sectioning. From another point of view, addition of dextran polymer ensures better sectioning of the sample [117]. In spite of the fact that observed specimen remains fully hydrated, unstained and close to the native state, it is not absolutely free of artefacts.

Vitreous water is a liquid with very high viscosity. This viscous nature of water entails difficulties during cryosectioning process and results in cutting-induced deformation. Resin-embedded and vitrified materials differ in cutting properties. During the cutting process of resin-embedded material, obtained thin sections from diamond knife are subsequently straightened during floating on the water surface through a high surface tension [118]. The required liquid for CEMOVIS techniques probably does not exist [117]. Therefore, a dry diamond knife is dedicated for cryosectioning of vitreous samples. The absence of liquid to float vitreous sections results in increasing interaction between the forming section and the knife [118]. These factors results in the formation of cutting artefacts such as chatter, compression, knife marks and crevasses [119]. In fact, sectioning of vitreous biological samples is technically difficult, but what is more important is some of the artefacts can be eliminated to some extent [119,120]. For example, knife marks are reduced through the use of undamaged diamond knife and through elimination of frost and debris at the edge of the knife [121]. The humidity inside the chamber of the cryo-ultramicrotome can be reduced to below 1% by using a protective glove box surrounding the cryo-ultramicrotome. It ensures that cryo-tools remain clean from frost contamination during vitreous sectioning [122]. The forming section flows during cutting process, thus applied force yields in different deformations. Crevasses are

fractures on the surface of the section and they are more severe in thick sections and high cutting speed [115,119]. To minimise this artefact, sections should be thick but less than 70 nm. Chatter is defined as a periodic variation in section thickness along the cutting direction and depends on the gliding properties of the knife surface. It can be minimised by increasing cutting speed [117,123]. Chatter is associated with irregular compression which is considered as the most prominent cutting artefact. Compression is formed due to irregular friction of the knife surface, and it makes the section shorter along cutting direction compared to the length of sample's block face. The main problem associated with compression is its heterogeneous nature which is discerned at cellular and molecular level [119,124–127]. Microtubule may serve as an example [124,125]: very often microtubules were observed as noncircular-shaped structures in case when long axes of these structures were not perpendicular to the cutting direction. What is more interesting, microtubules that were close to each other did not always display the same degree of deformation. A more detailed explanation can be found in [125]. Compression is reduced either through the use of low-angle knives [128] or through increasing the cutting thickness. Each sample is different, and different combinations of artefacts are possible. For that reason, it is important to find appropriate sectioning conditions to obtain optimal results [126]. Another solution is application of an oscillating knife to reduce cutting-induced artefacts of vitreous sections [120].

Probably the most difficult step during cryo-ultramicrotomy is transfer of vitreous ribbon of sections onto the carbon grid. To accomplish this step successfully, different approaches have been developed. One of the solutions is micromanipulator to hold and control the vitreous cryosections by eyelash when they come off from the knife edge. During the entire process, the ribbon is under constant tension as it grows longer, thereby keeping the ribbon as straight as possible. When the appropriate length is obtained, the ribbon is attached to the grid surface by lowering the micromanipulator and holding it in optimal position while a second eyelash is used to affix the other end of the ribbon to the grid surface from the knife edge. It is possible to affix a few ribbons to a single grid. However, the discussed solution is time consuming and prone to ice contamination [129]. The ribbons on the grid can be flattened by pressing with tools. The aim of this step is to reduce the probability of losing the sections during storage and transfer the grid, as well as improve the stability of section under electron beam [117]. Another solution is electrostatic charging for attaching the sectioned ribbon to the grid [122]. In comparison with micromanipulator solution, this method increases the successful attachment of frozen-hydrated sections to the carbon film, albeit both methods cannot guarantee uniform attachment of cryosections to the carbon film. This results in higher sensitivity of the section to the beam exposure and section movement during image acquisition, especially during electron tomography [123]. Recently, a new tool based on an aforementioned solution was presented [130]. One of the micromanipulator is used to manipulate the section ribbon by electrically conductive fibre; the second one positions the grid beneath the newly formed ribbon, and with the help of an ioniser, the ribbon is attached to the grid. This tool greatly facilitates manipulations, but sectioning artefacts remain. In summary, although much is known about CEMOVIS procedure and its artefacts, there is no remedy so far for discussed limitations. For this reason, CEMOVIS is still far from a routine application and general use.

6.2. Focused ion beam milling of vitreous samples

Focused ion beam (FIB) is an alternative method for sample thinning, free of artefact characteristic for CEMOVIS. This technique is widely used in material science; however, Marko et al. [131] proved that FIB milling can be applied in preparing biological material. FIB milling of vitreous samples is conducted using a dual-beam microscope. The dual-beam microscope is a combination of FIB system and scanning electron microscope. During FIB milling of vitreous sample, a finely focused beam of ions, usually gallium, is used to ablate the surface of the specimen through sputtering process. The whole procedure is under visual control of the SEM to ensure optimal procedure of sample preparation [132]. However, direct interaction between the ion beam and vitreous material must be taken into consideration due to possible sample damage. The application of a gallium ion beam with current of 10 pA and 30 kV acceleration does not cause sample devitrification [131]. Moreover, interaction of FIB with vitreous sample results in implantation of an ion layer, as thick as 5–20 nm into the FIB milling surface [133]. Indeed, the thickness of implanted gallium layer is almost negligible in a vitreous specimen with a thickness of 100–300 nm. Furthermore, the ion layer is much thinner in comparison with crevasses found in vitreous sections.

Cryo-FIB micromachining is a relatively new technique and remains in its early stages. Nevertheless, few sample preparation strategies have been introduced in the last 10 years. To date, bacteria and small eukaryotic cells, like *Mycobacterium smegmatis, Saccharomyces cerevisiae* and *Dictyostelium discoideum* [134,135], *Escherichia coli*, HeLa cells [136,137], BHK-21 cells [138] and *Aspergillus niger* [139], are deposited for culturing on the TEM grids and vitrified by plunge freezing technique. Next, vitrified material is transferred into the dual-beam microscope for a thinning process with a precision in the 10–100 nm range. At this stage, different FIB milling strategies for vitrified cellular samples are possible. The optimal geometry for small prokaryotic cells is wedge shaped, where frozen material is sputtered away at an oblique angle (~10º) with respect to the plane of the grid. Consequently, wedge-shaped vitreous material can be imaged with up to 3 μm transparency length and a thickness gradient less than 400 nm [134]. Eukaryotic and other cells similar in shape and size are milled in a thin self-supported membrane. During this process, a specific region of interest is localised and then rectangular sector below and above the selected volume is sputtered away, leaving behind a thin membrane, commonly referred to as a lamella, supported by the surrounding unmilled cells and ice [135]. Another option to obtain lamellas is a traditional FIB lift-out method, although it was deemed impossible because of the difficulty in obtaining platinum deposition at cryogenic temperatures [139,140]. Shortly, after vitrification, the feature of interest is defined through SEM; next the sample is cryo-coated with platinum (Pt) and two trenches are milled on each side of the lamella to be extracted. In the next steps, the sides and bottom of the lamella are sputtered away, and by using cold nanomanipulator, lamella is then lifted out from the sample and finally attached to the TEM grid by cryo-Pt deposition. During the last step, the attached lamella is thinned enough to be transparent to electron beam. The lamella-based sample preparation has an advantage over the wedge-shaped strategy, because the simple ablation geometry would not permit to easily find and target structures of interests embedded deeply

in cellular volume [135,136]. Thick samples and suspension of cells, e.g. *S. cerrevisiae* [140,141] and muscle tissue [142,143], are vitrified in copper tube or dedicated carriers via high-pressure freezing. After that, material hidden inside both the tube and the carrier is exposed during pretrimming step inside the cryo-ultramicrotome. Subsequently, vitreous sample is transferred to the dual-beam microscope and milled according to H-bar strategy, ultimately resulting in lamellas with the required thickness and surface area. Finally, prepared sample is transferred to the cryo-TEM in order to perform visualisation under low-dose mode. Critical point is when each of the described steps must be carried under devitrification temperature and minimising frost or warming during transfer steps implicates customised transfer device introduction. For samples vitrified by plunge freezing, different cryo-FIB transfer stations and cryo-FIB shuttles were introduced [135–137], while high-pressure frozen samples require sophisticated and complex transfer systems like cryo-nano-bench system [140] or an intermediate specimen holder [142,143].

The cryo-FIB technique provides controlled access to specific supramolecular structures buried inside the cell. Moreover, many macromolecular complexes that are present in low copy numbers may be studied in their native cellular environment because homogenously thick lamellas with more than 100 μm^2 areas can be prepared in a controlled and targeted manner. However, this preparation technique is low throughput due to several factors. As it was mentioned, an incidence of the ion beam should be as low as possible because a smaller milling angle produces a larger viewing area for analysis and minimises the deposition effect of milled material. The latter factor is not interrelated with milling currents or other parameters during sample thinning as such [135,137]. Inhomogeneous and varied composition of the vitreous samples is the main cause for curtaining effect which finally results in strong inhomogeneous lamella thickness [134,142]. These effect is reduced by deposition of organometallic platinum with a gas injection system without electron or ion beam radiation, prior to lamella preparation [144]. Another issue is the amount of information obtained from prepared samples during cryo-electron tomography. During cryo-FIB milling process, part of the vitreous specimen is physically destroyed along all axes [134]. In contrary, after vitreous sectioning, a series of cryosections is obtained, and information along these axes is partly remained, especially along *z*-axis. A further problem is the time needed to prepare sample prior to visualisation. Due to the large size of eukaryotic cells, longer milling time is required in comparison with the prokaryotic samples [135–137]. Other challenges related to the increased size of eukaryotic cells are identifying and targeting specific sites for processing. Small organisms, such as *E. coli*, are readily distinguished from the vitreous ice. Inversely, eukaryotic cells are surrounded by thick ice, thus identifying the area of interest is not simple. A method to overcome this limitation is either milling of many adjacent places to find features of interest or application of correlative light and electron microscopy techniques. Cells are cultured on EM finder grids and optical images are recorded before vitrification. Appropriate regions are selected for subsequent cryo-FIB milling based on light microscopy photos [136,145]. Alternatively, the frozen-hydrated sample is imaged under cryo-fluorescence microscopy before sample preparation by cryo-FIB for further analysis. The second approach allows direct correlation of the prepared vitreous sample between the two imaging modalities [134,138,146]. Moreover, localisation of smaller molecules or structures that exist in low copy number is simplified because targeting is based

on clonable labels, such as green fluorescent protein [134]. The new idea presented recently is to localise structure of interest by fluorescent labels using cryo-light microscopy and then use it for coordinate transformation-based approach in the FIB-SEM system for milling [138].

At present, cryo-FIB milling of vitreous samples remains cumbersome and far from routine [143]. Much effort is required to improve the efficiency and repeatability of cryo-FIB milling process, such as reproducibility of lamella quality, i.e. overall thickness and thickness homogeneity, localisation feature of interests or better avoidance of frost during cryo-transfer steps. Therefore, the main issue in the presented articles is improving sample preparation protocols. Nevertheless, some interesting results have been achieved. For example, ten nuclear pore complexes in *D. discoideum* cells were identified in situ in one tomogram. Subtomogram averaging process yields the structure of nuclear pore with resolution of 7.9 nm. To achieve 6 nm resolution, 4,182 protomers are required from isolated nuclei using the same type of analysis [135]. Another result comes from bacterial cells, where membrane invaginations into both the cytoplasmic and periplasmic spaces of *E. coli* were found [136]. This technique will greatly facilitate high-resolution imaging of dynamic process, such as HIV particles travelling into the deep side of the host cell at different stages of infection, especially when viral capsid interacts with nuclear pore complex components [136]. By using FIB milling process, ryanodine receptors in toadfish swimbladder muscle were determined. Obtained results agreed remarkably well with those described previously, albeit further study will be required to understand structural features of ryanodine receptor connected to the T-tubule [143]. Cryo-FIB is also a promising thinning tool for describing new bacterial cytoplasmic structures termed as a stack. Stacks were defined as piles of oval disc subunits which are surrounded by a membrane-like structure. These structures are localised in the cell cytoplasm and are presented separately or grouped together in variable number within each cell. One can only speculate about stacks' function, but it is suggested that they could be related to the bacterial cell replication process. Due to compression created during CEMOVIS and visualisation limitations arising from plunged frozen samples, cryo-FIB technique could provide new insight into macromolecular assembly of membrane-enclosed discs [147].

6.3. Nature of vitreous material

The sample in native state is very different from what has been seen before with conventional microscopy. Vitrified material is as close as possible to the native state because during sample preparation, neither chemical fixation, staining nor dehydration is used. Therefore, the final images represent the real distribution of the immobilised biological material within vitrified water. With frozen-hydrated samples, the contrast is proportional to the density and distribution of molecular inhabitants within the thickness of the sections. Moreover, structures in vitreous material are equally visible over the entire thickness, thus the native-state inherent low contrast due to low signal-to-noise ratio. In contrary to stained material, imaging of native biological material relies on phase contrast, which strongly depends on focus [71]. An additional issue is plethora of overlapping information for the reason that the typical fine details are much smaller than the section thickness. The solution overcoming this limitation is both

preparation of thin sections or lamellas and electron tomography to obtain a three-dimensional model of the material distribution in the vitreous material. Frozen-hydrated specimens behave differently under electron beam in comparison with plastic sections. A characteristic phenomenon that may be developed is bubbling. Bubbling is a result of gas accumulation produced by electron beam decomposition of biological matter. What is the most interesting is that different substances have different electron radioresistance. Another problem is beam-induced deformations which are seen twofold. Vitreous material can be considered as high-viscosity liquid and can be rearranged by the electrons. On the one hand, sharp irregularities, such as crevasses and knife marks, under electron beam are removed from the vitreous section due to increasing the flow of the section. On the other hand, some biological structures, i.e. chromatin, aggregate under the effect of beam producing locally apparent higher-density area [148].

The main disadvantage of frozen-hydrated specimens is its uselessness to perform post-immunolocalisation of studied target. Antibodies require proper conditions for working, that is, ambient conditions and water solution. Accordingly, some researchers have developed a specific label for the identification of molecules for cryo-electron microscopy. These labelling techniques are base either on a clonable ferritin FtnA protein [149] or a biotin-streptavidin complex [150], called STAMP approach [151] and SNAP-tag technology [152]. However, ligand labelling for cryo-EM is still an emerging field; hence, another preparation technique is dedicated for immunogold labelling and structural studies, namely, freeze substitution. Indeed, vitreous and freeze-substituted materials are very complementary [123]. The latter preparation solution should be considered as the method of choice when high-resolution study is not the major aim. Resin-embedded material is easier to obtain and is less sensitive to electron beam in comparison with vitreous material, and for this reason, analysis of larger sample area is possible. Additionally, plastic sections can be thicker than vitreous ones, and thus, the former enable studying a larger volume. The other advantage of resin sections is the possibility of immunogold labelling.

6.4. Freeze substitution

Freeze substitution (FS) is a hybrid method that bridges the gap between vitrified material and room temperature ultramicrotomy of resin-embedded material. Biological material after vitrification process is gradually dehydrated in the presence of chemical fixatives at low temperature. Later, the whole process is gradually warmed, and finally, the sample is embedded in resin. This technique was first introduced in 1941, as a preparative technique for light microscopy samples [153]. The potential of FS at electron microscopy filed was explored by Fernandez-Moran [154] and was further developed by others [155–158].

Freeze substitution process consists of dehydration and chemical fixation step followed by either low- or room-temperature embedding in chosen resin. Dehydration process usually starts at -90 ºC in an organic substitution medium containing chemical fixatives. The key point is that sample must be kept below devitrification temperature. In case of biological material, this temperature remains well below -100 ºC. What happens during water substitution at low temperatures is not fully understood. Nevertheless, vitrified water turns into cubic ice, and then transition takes place into hexagonal ice. Cubic ice is a metastable state, thermodynami-

cally more stable form of water. The second transition process, from cubic to hexagonal form, occurs at around -80 ºC. The most important event during these transitions is that water molecules probably rearrange by rotation with only small transitional displacement which leads to embedding the biological structure by ice without any segregation. Then the result is that the structural preservation is excellent down to molecular dimension. In reality, FS process deals with cubic and sometimes with hexagonal ice but never with vitreous water [60]. This would imply that cubic ice has no significant influence on the observed morphology at the level of resolution of biological samples during FS process under controlled conditions. Besides these theoretical bases, other aspects must be considered.

From the biophysical side, low temperature influences on ultrastructure preservation through hydration shell preservation and infiltration of chemical fixatives. FS process preserves the hydration shell at least partially, although less hydrophilic organic solvents are used, e.g. acetone or methanol. It is well known that organic solvents cause protein aggregation, and chemical fixatives react relatively slowly; therefore, it cannot preserve all the cellular components simultaneously. The consequences of chemical fixation are seen as osmotic changes and redistribution or extraction different molecules, i.e. lipids and ions [85,157,159,160]. The reason for the superior structural preservation is infiltration of stabilising or fixative compounds together with the dehydrating agents. After raising the temperature, fixatives react in situ, between -90 ºC and -30 ºC, avoiding penetration and diffusion artefacts [157]. Many different substitution media compositions were developed. The main fixatives are GA, osmium tetroxide and UA used in different combinations and at different percentages in acetone, methanol or ethanol [67,161–164]. Acetone is the most commonly used dehydrating agent because it substitutes at a slower rate than methanol, thus resulting in better structural preservation [165, 166]. The most-used fixatives are OsO_4 with or without UA in acetone for morphological study and low concentrated GA in acetone for immunolabelling detection [167–169]. The interesting observation concerning reactivity of used fixatives was made. Osmium tetroxide at low temperature does not react as protease, but begins cross-linking, via cis-diol covalent bonding to unsaturated lipid chains at -70 ºC [170]. Uranyl acetate binds to proteins and phospholipids at an even lower temperature. Glutaraldehyde starts cross-linking at -50 ºC, but it acts readily only at or above -30 ºC [161]. For some immunolabelling study, pure solvent preserves well both the antigenicity and the ultrastructure of the cells [159,171]. A distinct feature of well-vitrified samples, without visible ice segregation artefact, is a 'reverse contrast' seen as pale membrane against a more electron dense background [172,173]. In order to improve the membrane contrast and preservation of cultured cells, a few different substitution media were introduced. The most interesting substitution medium contains 5% water in acetone [173]. It has been proved that substitution cocktails can include up to 20% of water without deleterious ice damage or extending dehydration time [174]. These protocols totally contradict the long-standing theory that a low amount of water as 1% in acetone extends freeze-substitution process four times [161]. A disadvantage of a medium containing water is antigen loss by extraction. Similar results were observed for pure solvents; thus, low concentration of glutaraldehyde can be generally used [175], but the exact substitution protocol requires an individual approach. Alternatively, membrane contrast can be enhanced by using tannic acid-mediated osmium impregnation method [176], tannic acid in acetone during FS [95,177] or different combina-

tions of glutaraldehyde, UA and OsO_4 [178,179]. An attractive protocol omitting osmium tetroxide is based on 20% Araldite/Epon in acetone as fixative in the first step and subsequent embedding in pure epoxide resin. Epoxide compounds react with proteins and lipids and provide interesting results which may become an important tool in getting information about influence of different reagents and protocols on ultrastructure preservation [180]. Current FS procedures are measured in wide time range from less than 24 h for cell culture [162,172,174,181] to longer period of time such as four days for plant material [182,183]. However, other tissues are usually substituted during 2–4 days, e.g. rat liver [184], mouse skin [185] or *C. elegans* [186]. On the one hand, such a wide range of different fixative cocktails gives opportunity to study different structures of interests in both structural and immunolocalisation research. On the other hand, the variety of possibilities become a challenging task for optimisation of FS process because each sample is unique [67].

The last step during sample preparation for the room-temperature ultramicrotomy is sample embedding. Epoxide-based polymers are dedicated for morphological analysis including electron tomography by virtue of a larger stability in the electron beam and ease of sectioning. In contrast to epoxide resins, methacrylates do not bind covalently to cellular structures; hence, the antigens of interests remain unaltered and section surface has higher roughness, thereby higher access to antigens. Another advantage of methacrylic resins is low-temperature embedding and polymerisation by UV light (Figures 2 and 3); thus, harmful heat effects on epitopes is avoided [157,165]. However, this division is not a rule, because Epon sections were used to identify the subcellular localisation of proteins [187], lipids [188] or carbohydrates [189]. Special attention should be directed to McDonald's FS protocols [168,190]. Super-Quick FS takes only about 6 h from freezing process to resin blocks preparation ready to section. Substitution process from -90 ºC to 0 ºC is performed during 2,5 h; then rapid infiltration in LR White or Epon resin takes another two hours followed by polymerisation at 100 ºC for 1,5–2 h. For this protocol, organisms considered as difficult to fix were chosen. As a result, presented ultrastructure preservation was comparable to standard FS protocols, and high-temperature polymerisation does not affect antigen preservation.

7. Sample examples prepared by cryotechniques

High-resolution study requires superior sample preparation via vitrification process. Sample such as protein, protein complexes, viruses, bacteria or organelles in vitro and in situ within whole organisms or single cell are prepared by plunge freezing. Moreover, in modern structural biology, the main goal is in situ structure determination within unperturbed cells because purified objects are disintegrated during sample purification. Thus, for structural biology at cellular and tissue level, thicker samples are prepared by CEMOVIS (30–200 nm) or cryo-FIB (100–300 nm) techniques. The visualisation of frozen-hydrated biological samples is performed by single-particle analysis or cryo-electron tomography. The former technique enables to achieve near-atomic resolution and is applied to purified viruses, macromolecular complexes and single proteins [80,191,192]. On the other hand, cryo-ET bridges the gap between cellular ultrastructure and the structural analysis of macromolecular complexes

within the cell with resolution in the sub-nanometre [193] to 10 nm range [194–196]. Electron tomography of plastic sections is another technique dedicated for cellular structural biology, where the more important aim is to reveal functional-morphological relationships than macromolecular details. Sample is prepared by cryoimmobilisation followed by freeze-substitution process. Next, polymerised specimen is sectioned in 100–400 nm range and analysed [194]. Combination of subsequent section tomograms extended the depth of analysed volume to several micrometres. These advantages led to large-scale imaging where both detail and overview are necessary. Another worth-noting point for ET study is a scanning transmission electron microscopy (STEM) mode. Due to lack of inelastic scattering of electrons and chromatic aberration in a STEM mode, resin sections as thick as 1 μm can be analysed [197–200]. Besides three-dimensional analysis, both frozen-hydrated and plastic sections are also analysed at lower resolution at 2D morphological level.

CEMOVIS has already provided unusual views of different structures with a molecular resolution in native cellular context including microtubules, mitochondria, Golgi apparatus [194] or desmosomes [116]. Combination of CEMOVIS with electron tomography, called TOVIS [201], becomes a powerful tool in virology [76], microbiology, cellular biology and tissues. The reader is referred to review articles that cover mentioned topics with further references [79,202–205] due to limited space. However, two examples of CEMOVIS application will be pointed out. Cryo-EM of vitreous sections gives opportunity to study different tissues, including skin biopsies. The unravelling of molecular organisation of the skin lipids will significantly improve molecular understanding of the tissue. Until recently, six theoretical models for the molecular arrangement of the extracellular lipid matrix have been proposed. Nevertheless, combination of TOVIS, molecular modelling and EM simulations has revealed a new model of lipid organisation, which rationalises the skin nature and functions [206]. These results will influence dermatology field and thereby further translates in technological developments of new, transdermal drug delivery systems, the development of noninvasive diagnostic sensors and dealing with toxicity from topical exposure to chemicals. Without CEMOVIS, it would be impossible to perform the simultaneous quantification of water and elements in the native state [63]. In combination with fluorescence microscopy, it was showed that the induction of nucleolar stress in cancer cells resulted in both an increase in water content and a decrease in the element content in all cell compartments. The presented study opens new way to understand cell functions, and future research could extend our knowledge about cell activities, depending on actual concentration of ions and the hydration status.

The classical examples of superiority of the cryopreparation techniques, based on HPF followed by FS process, over conventional TEM were showed on the method-dependent bacterial mesosomes [55] and articular cartilage [85], although in the former, further investigation led to revisiting the mesosome as a site of hydrogen accumulation [208] using quick-freezing preparation of TEM. Among the advantages of plastic sections, one is the section thickness; thus, comparatively large cellular volume can be analysed that was exemplified by microtubule cytoskeleton architecture in yeast [209], organellar relationship in the Golgi region of the pancreatic cells [210] or architecture of the caveolar system [211]. Besides, the reader can find many articles where either different techniques were compared [55,91,96,212–216] or examples were collected in reviews [194,217].

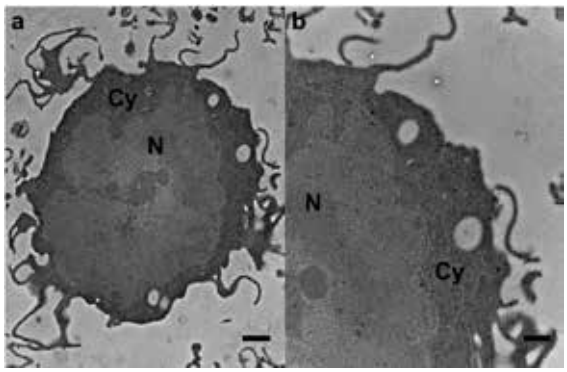

Figure 2. Ultrastructural demonstration of immunogold labelling of visfatin particles or small clusters consisting of number gold particles were demonstrated in the subcellular compartments of human colorectal HCT-116 mononucleated cells which were cultured in log phase of growth (Cy cytoplasm, N nucleus, Scale bars: a) 1 μm, b) 500 nm). Cells were chemically fixed, dehydrated and embedded in LR White resin [207]. Visfatin is an enzyme which overexpression is correlated with poor prognosis in cancer patients. In this study, we tried to explore the association between visfatin distribution in subcellular compartments and increased apoptosis in cells treated with cytochalasin B. For further study, our aim is to optimise of HPF-FS protocols for cytoskeleton ultrastructure. Figure and legend adapted and changed from [207] under terms of the CC BY 3.0 license.

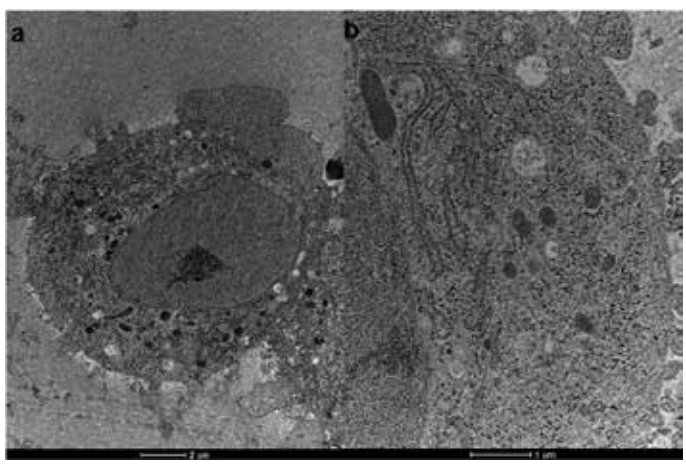

Figure 3. Human colorectal HCT-116 were vitrified by HPF followed by FS and embedding in LR White resin. During FS process, cells were fixed with only 0,25 % GA. In comparison with cells prepared by conventional method (Figure 2), vitrified and freeze-substituted material show outstanding ultrastructure preservation. Even without OsO_4 fixation, membranes are clearly visible, mainly rough endoplasmic reticulum and nuclear membranes. Nevertheless, further protocol optimisation is required.

8. Unity is strength: The hybrid techniques

Immunoelectron microscopy bridges the information gap between molecular biology and ultrastructural studies providing information regarding the function of the internal structures

of the cell. The main requirements to obtain valuable results are suitable fixation protocol and functional antibody conjugated with an appropriate nanoparticle to be detected. For many years different protocols were developed for structure localisation study [167] based mainly on Tokuyasu technique, HPF followed by FS and low-temperature embedding [169] or conventional chemical fixation [207,218] together with progressive-lowering temperature technique. Nevertheless, this field is still amenable to new solutions, especially for difficult-to-fix samples and difficult-to-fix antigens. The hybrid techniques combine advantages of different cryopreparation techniques in order to eliminate the particular step limitations of each one, at least in part.

Cryosectioning according to Tokuyasu is one of the most reliable and efficient immunolocalisation techniques for different types of sample. An inherent limitation of Tokuyasu cryosectioning is mild chemical fixation at the beginning of the sample preparation. Thus, small molecules, including molecules of interests, may be dislocated or extracted during chemical fixation. Besides, it should be mentioned that process of chemical fixation is selective and results in pH-related and osmotic changes in the different organelles [58]. Another restriction is intractability of samples, which contain a hydrophobic cuticle or a rigid wall, such as *C. elegans*, *Drosophila* or plants. Cryoimmobilisation should be used to overcome difficulties arising from chemical fixation during sample fixation. In spite of the all above-mentioned issues, one more should be considered – the nature of the antigen. Some antigens are sensitive on chemical fixation at room temperature or resin components and solvents and thus cannot be immunolabelled either in thawed cryosections or after cryoimmobilisation, freeze substitution and resin embedding. Therefore, the main aim was to introduce hybrid methods that combine the high-efficiency Tokuyasu cryosectioning labelling technique with an initial cryoimmobilisation step. Different approaches have been introduced with different results. The first attempts were taken by the group of Slot and Geuze [53,56] by combination of a frozen-hydrated cryosections with subsequent material fixation during thawing and after transfer to a grid. This method turned out to be unsuitable to routine use because, besides technical requirements and lack of reproducibility, only a small area of obtained sections has got desired morphological quality [56].

Another strategy to improve the antigenicity and ultrastructure preservation is rehydration method (RHM) based on cryofixation, freeze substitution and rehydration process before entering Tokuyasu cryosectioning and immunolabelling [56]. Sample after vitrification is dehydrated at low temperature with a substitution medium containing UA, glutaraldehyde and/or OsO_4 and water to improve membrane contrast. After freeze substitution step, a rehydration process is carried out on ice. Rehydration step is necessary to enter the Tokuyasu procedure, i.e. sample embedding in gelatine, infiltration with high concentrated sucrose and freezing in liquid nitrogen. During dehydration step, additional chemical fixation is performed because fixation during FS step turns out to be insufficient. This approach resulted in excellent preservation of HepG2 cells, primary chondrocytes, cartilage and exocrine pancreases and immunolabelling efficiency comparable to Tokuyasu method. In the case of tested samples, authors suggested using the standard Tokuyasu technique because it is much easier, faster and allows the preparation of larger samples. The real power of the RHM methods was showed on *Arabidopsis* tissues, anthers containing pollen grains, *D. melanogaster* embryos and young

adult nematodes. For these organisms, the RHM method was slightly modified [58,59] on dehydration step which was started at subzero temperatures. Obtained results were similar to the Van Donselaar et al. study: 1) water addition to FS cocktail appeared to be necessary for improved visibility of the membrane's bilayer structure and 2) sample fixation with osmium tetroxide, UA and glutaraldehyde during FS and post-fixation with glutaraldehyde at 0 ºC did not influence immunolabelling. Moreover, fixation-sensitive antigens were not inactivated, despite of using high concentration of fixatives. An additional benefit is usefulness of the hybrid techniques for fluorescence microscopy and CLEM due to the optimised ultrastructure preservation. Green fluorescent protein signal could be observed even after OsO_4 treatment [58]. High lateral and axial fluorescence resolution can be obtained using thin cryosections; thereby, blurred signals are eliminated. Fluorescence-tagged antibody is much more sensitive than gold markers; thus, if fluorescence signal is not detected, then immunogold labelling is not worth to perform [59].

Hybrid techniques provide an alternative for worthlessness of vitrified cryosections in immunogold labelling. Recently, a novel hybrid technique called VIS2FIX was presented. First, vitrified material is cut into vitreous sections (VIS) and adhered to the EM grid. Next, the sections on the grid are fixed and brought to room temperature by means of FS and immunolabelling. Vitreous sections are fixed (FIX) either by $VIS2FIX_{FS}$ method using a high-speed FS procedure with subsequent rehydration procedure or by $VIS2FIX_{H}$ approach based on water-based frozen fixation, hence 'H' for hydrated [219]. Different combinations of fixatives were tested, including osmium tetroxide, glutaraldehyde, formaldehyde, acrolein and UA. The variety of mentioned fixatives and short time needed for sample preparation give huge possibilities in protocol optimisation for different antibodies and samples. The unique feature of $VIS2FIX_{H}$ method is fixation of lipids droplets, offering an interesting application in the lipidomics field. Although vitreous section is open structure and thus fixatives can penetrate it in high extent, the lack of embedding medium does not cause the material extraction. The high accessibility for the fixatives results in outstanding preservation of vesicles, particularly in the Golgi area and organelles. Further superiority over other techniques was proved through immunolabelling of both resin and aldehyde-sensitive antigens. As another option for making the impossible possible is vitrification of Tokuyasu-style immunolabelled sections, in brief VOS (vitrification of sections) technique. This approach was first time presented nearly a quarter of century ago by Sabanay et al. [220], and further afresh used in reconstruction of adhesion structures in tissues by cryo-ET [221]. In contrary to the described hybrid approach, in VOS technique, the first step is based on Tokuyasu sample preparation. The common steps are mild chemical fixation and cryoprotection in sucrose followed by immunogold labelling. After that, sample is re-vitrified in liquid ethane instead of treatment with methylcellulose and air-drying steps, as in the Tokuyasu technique [220]. The interesting thing is that the refrozen cryosections are free from cutting artefacts related with CEMOVIS procedure. Therefore, VOS technique provides meaningful 3D information on 300-400 nm thick sections. This method was used for 3D reconstruction of desmosomal adhesions in stratified epithelium and membrane-dense plaques and flanking caveolae in smooth muscle tissue [221]. The VOS technique is a valuable tool in fluorescence-based CLEM study, but together with Cryo-ET, its possibility to gain localisation of the targeted object in three-dimensional context is unique [222]. The

advantage of VOS technique over standard Tokuyasu cryosectioning is that re-frozen cryosections are visualised by phase contrast results in more native sample preservation and overall better resolution. Moreover, structures invisible in Tokuyasu cryosections, i.e. cytoskeleton and ribosomes, should be possible to reveal with VOS.

In some conditions, chemical pre-fixation is an essential step prior vitrification process. This is true when safety consideration must be fulfilled, especially when pathogen organisms are the aims of the study. An aldehyde fixation step was introduced before vitrification of *Bacillus anthracis* spores [223]. Chemical pre-fixation step (CAF) followed by CEMOVIS made it possible to describe two new structures present in the spore. In some cases, chemical fixation is the only alternative for sample preservation. Biopsy specimen is particular situation, considering the place of sample collection where immediate processing of samples by HPF is rarely possible, i.e. a hospital or external laboratory. Thus, even sample is prolonged and stored in fixatives, subsequent processing by HPF followed by FS and polymer embedding results in better ultrastructure preservation compared to the conventional methods [224]. Some tissues are challenging specimen for ultrastructural preservation due to varied morphologies across its entity. Brain tissue integrity is degraded due to anoxia, unless chemical pretreatment is applied after the excision. The utility of this hybrid technique was demonstrated for variety of nervous system tissues. Aldehyde fixation prior to cryoimmobilisation and tailored FS protocol provides ultrastructural preservation superior to that obtained by conventional preparation and close to that obtained by HPF-FS protocol for tested samples [95]. Another challenging structure to preserve by HPF are stereocilia on the apical part of epithelial cells inside the inner ear. Preservation of the inner ear tissue using HPF is a challenging task, because the overall preservation of the sample was generally very good except for stereocilia. The explanation for this observation is unusual freezing properties of stereocilia actin bundles [96]. Authors considered different factors that could account for these properties, such as structure of the stereociliary actin bundles, high pressure during vitrification process and the treatment of the sample after freezing. Based on their research, authors were not able to unambiguously explain this phenomenon due to further study is required. Most importantly, chemical pre-fixation before cryoimmobilisation step resulted in preservation of cellular structure close to that prepared by HPF alone, and stereocilia actin bundle was preserved in a consistent manner.

9. Conclusions and outlook

The resolving power of TEM made it possible to visualise different objects at various resolution level ranging from angstroms for macromolecular complexes to nanometre scale for subcellular complexes and cells to micrometres for tissue gross morphology. Thus, electron micrographs have contributed significant understating of cellular structure and functions in physiological state as well as disease process. The sample preparation methods, however, still pose the main issue in biological TEM. It is important to realise that there is no single preparation technique that could be applied universally. Appropriate choice of the preparation technique is determined by different factors:

1. A model organism. Vitrification should be method of choice for formidable to fix organisms such as plants or *C. elegans* where a hydrophobic cuticle, thick wall or starch granules slow down chemical fixatives and thereby induce artefactual morphological changes.
2. When the time matters. Significant advantage of cryoimmobilisation over chemical fixation is the possibility to catch a dynamic cellular process at a known point and localisation of a rare event and structures, e.g. endomembrane transport in tissue culture cells, syncytial mitoses in early *Drosophila* embryos, nuclear division in *C. elegans* [103,225] or viral dynamics in cell [203].
3. The aim of the study and the object size.

The first aim is structural analysis. Sample architecture should be changed as less as possible for high-resolution analysis; therefore, cryoimmobilisation-based techniques are the best choice. Sample in near to native state can be prepared as follows:

- By plunge freezing, dedicated to proteins, macromolecular complexes and viruses suspension, for atomic or near-to-atomic resolution study
- By high-pressure freezing or self-pressurised rapid freezing for CEMOVIS or cryo-FIB, dedicated to samples thicker than 10 μm and by plunge freezing dedicated to small organisms, for analysis in sub-nanometre to nanometres range of macromolecular complexes and organelles within the cells

For morphological and cellular structural biology studies, sample is prepared as follows:

- By conventional sample preparation, dedicated for different samples, especially human tissue biopsies and whole organs of different animals. In some instances, this technique is more preferred, especially when the final contrast after cryoimmobilisation followed by FS is insufficient for further analysis. Good examples of this are synaptic vesicles in nerve cells and thylakoid chloroplasts [190]. If the extractions and/or distortions of the cytoplasm do not influence on data analysis then conventional TEM is a good choice.
- By HPF/SPRF followed by FS combination; thereby, structural artefacts are limited. Resin sections give opportunities to obtain large-scale imaging at nanometre resolution.

The second aim of TEM is the immunocytochemical localisation of biochemically defined antigens within the cell landscape. Pure frozen-hydrated samples are useless for this task; thus, vitrified material is resin embedded after FS. Also specimen chemically fixed can be embedded in methacrylic resins for immunolocalisation study. Cryosectioning according to Tokuyasu is an alternative for both rare and sensitive to ethanol or methacrylates antigens. Tokuyasu technique excels in membrane contrast; hence, it is best suited for locating antigens in correlation to cellular compartments. On the other hand, resin sections have a larger area to analysis and better contrast that can be optimised for specific task. As it was mentioned in previous sections, hybrid techniques can offer a solution to antigens and samples difficult to fix for various reasons.

Another problem where preparation techniques pose the main issue is element distribution within analysed organism. Indeed, it is critical point to avoid and prevent diffusion of water

and ions between cell compartments and outside the cell. To study element distribution within the cells and tissue, the best choice is CEMOVIS where sample remains at native state [62,63], at least in theory. Distribution of elements in resin sections obtained after vitrification and freeze substitution process are closer to natural state [64,226] in comparison with conventionally prepared sample. Nevertheless, a conventional TEM is also used for analysis of ions in biological study [227,228].

Last but not the least is technical level of difficulty and equipment requirements. Cryotechniques are generally more technically demanding, including skills (e.g. cryosectioning of vitreous samples) and devices (e.g. cryo-ultramicrotome, cryo-EM, vitrification machines) in comparison with conventional TEM.

On the whole, the wide variety of available preparation techniques for biological samples enables to answer specific questions dependent on the study aims, model organisms and required resolution.

Considering the technological advances at EM field during the last decade, it is nearly impossible to predict future developments. Currently, some interesting solutions in both imaging and sample preparation at different level are under development, and presented ideas may significantly improve the ability to investigate and understand the world around us. Continuous software development for images acquisition, 3D reconstruction and further image processing and interpretation during electron tomography pushes the resolution limit down [229]. Another factor for improving resolution is new direct detection system with better quantum detection efficiency and high speed that allows corrections of beam-induced movements [230]. Further reduction of image distortions can be achieved by applying a holey carbon grid modified with graphene sheets [231]. An alternative way to improve final image of vitrified specimen is introduction of Zernike phase plate. This modification permits to record higher contrasted images with better resolution [232]. On the other side of scale of resolution, correlative light and electron microscopy has its own place. This modern approach is strongly explored in cell biology at various levels of resolution, and further progress is driven by scientific needs. Most recently, an integrated system for live microscopy and vitrification (MAVIS) was presented [233]. MAVIS combines a light microscope with a plunger to vitrify the specimen, and in this time lapse, imaging in a few second time resolution could be performed without the need for transfer step. An elegant solution called integrated light and electron microscope (ILEM) joins light and electron microscopes within one set-up and in this way greatly simplifies sample handling and navigation between the two modalities, therefore increasing final success of image correlation of both plastic sections and vitrified material [48,234]. Fluorescence signal during sample observation inside the column of ILEM is detected at dry environment; thereby, fluorescence marker should be picked carefully. Additionally, to avoid quenching and loss of signal, the en bloc staining, for example, via FS process, is a prerequisite for resin sections post-labelled with fluorescent dyes [48]. The ultimate goal of every microscopy technique which contribute to biology is visualisation of working life in as close to the native state as possible. Incompatibility of a liquid sample with the vacuum needed for electron microscopy seems to be apparent since electron microscopy of specimens in liquid is possible [235]. Another dream of electron microscopists has come true, but even so, appropriate sample preparation is still a basic need.

The last decades have seen exponential technological progress that improves electron microscopes. Nevertheless, even if modern TEM will reach the electrons resolution limits, the sample preparation step remains a critical issue, limiting final achievements. Arguably, the optimisation of sample preparation is key issue for the integration different microscopy techniques and joining data acquired at different-length scale into one view.

Acknowledgements

The experiments were performed in the Department of Histology and Embryology in Zabrze, Silesian Medical University in Katowice using equipment financed by the Silesian Biofarma with infrastructure supported by POIG.02.03.01-24-099/13 grant: GCONiI – Upper-Silesian Center for Scientific Computation.

Author details

Łukasz Mielańczyk*, Natalia Matysiak, Olesya Klymenko and Romuald Wojnicz

*Address all correspondence to: mieluk@gmail.com

School of Medicine with the Division of Dentistry in Zabrze, Medical University of Silesia, Department of Histology and Embryology, Zabrze, Poland

References

[1] Knoll M, Ruska E. Das Elektronenmikroskop. Zeitschrift fur Phys. 1932;78:318–39.

[2] Porter KR. A study of tissue culture cells by electron microscopy. J Exp Med. 1945;81:233–46.

[3] Lidke DS, Lidke KA. Advances in high-resolution imaging – Techniques for three-dimensional imaging of cellular structures. J Cell Sci. 2012;125:2571–80.

[4] Cortese K, Diaspro A, Tacchetti C. Advanced correlative light/electron microscopy: Current methods and new developments using Tokuyasu cryosections. J Histochem Cytochem. 2009;57:1103–12.

[5] Knott G, Genoud C. Is EM dead? J Cell Sci. 2013;126:4545–52.

[6] Hajibagheri MAN, editor. Methods in Molecular Biology, Volume 117: Electron Microscopy. 1st ed. Totowa: Humana Press; 1999.

[7] Kuo J, editor. Methods in Molecular Biology, Volume 369: Electron Microscopy. 2nd ed. Totowa: Humana Press; 2007.

[8] Kuo J, editor. Methods in Molecular Biology, Volume 1117: Electron Microscopy. 3rd ed. New York: Humana Press; 2014.

[9] Jensen GJ, editor. Methods in Enzymology, Volume 481: Cryo-EM Part A: Sample Preparation. San Diego: Academic Press; 2010.

[10] Jensen GJ, editor. Methods in Enzymology, Volume 482: Cryo-EM Part B: 3D Reconstruction. San Diego: Academic Press; 2010.

[11] Jensen GJ, editor. Methods in Enzymology, Volume 483: Cryo-EM Part C: Analyses, Interpretation, and Case Studies. San Diego: Academic Press; 2010.

[12] McIntosh JR, editor. Methods in Cell Biology, Volume 79: Cellular Electron Microscopy. San Diego: Academic Press; 2007.

[13] Allen TD, editor. Methods in Cell Biology, Volume 88: Introduction to Electron Microscopy for Biologists. San Diego: Academic Press; 2008.

[14] Muller-Reichert T, editor. Methods in Cell Biology, Volume 96: Electron Microscopy of Model Systems. San Diego: Academic Press; 2010.

[15] Muller-Reichert T, Verkade P, editors. Methods in Cell Biology, Volume 111: Correlative Light and Electron Microscopy. San Diego: Academic Press; 2012.

[16] Muller-Reichert T, Verkade P, editors. Methods in Cell Biology, Volume 124: Correlative Light and Electron Microscopy II. San Diego: Academic Press; 2014.

[17] Schwartzbach SD, Osafune T, editors. Methods in Molecular Biology, Volume 657. New York: Humana Press; 2010.

[18] Cavalier A, Spehner D, Humbel BM, editors. Handbook of Cryo-preparation Methods for Electron Microscopy. Boca Raton: CRC Press; 2009.

[19] Steinbrecht RA, Zierold K, editors. Cryotechniques in Biological Electron Microscopy. Berlin/Heidelberg/New York: Springer Verlag; 1987.

[20] Hayat MA, editor. Principles and Techniques of Electron Microscopy: Biological Application. 4th ed. Cambridge: Cambridge University Press; 2000.

[21] Chaplin M. The Water Molecule, Liquid Water, Hydrogen Bonds and Water Networks. Water: The Forgotten Biological Molecule. Singapore: Pan Stanford Publishing; 2010. pp. 3–19.

[22] Giovambattista N, Mazza MG, Buldyrev SV, Starr FW, Stanley HE. Dynamic Heterogeneities in Supercooled Water. J Phys Chem B. 2004 May;108:6655–62.

[23] Mentré P. Water in the orchestration of the cell machinery. Some misunderstandings: A short review. J Biol Phys. 2012;38:13–26.

[24] Kellenberger E. The response of biological macromolecules and supramolecular structures to the physics of specimen cryopreparation. In: Steinbrecht RA, Zierold K, editors. Cryotechniques in Biological Electron Microscopy. Berlin/Heidelberg: Springer; 1987. pp. 35–63.

[25] Chaplin M. Do we underestimate the importance of water in cell biology? Nat Rev Mol Cell Biol. 2006;7:861–6.

[26] Ho M-W. Liquid crystalline water, quantum molecular machines & the living tate. Contemp Mater. 2010;1:117–23.

[27] Pollack G. The Fourth Phase of Water – Beyond Solid, Liquid, and Vapour. Seattle WA, USA: Ebner and Sons Publishers; 2014.

[28] Wineya M, Meehla JB, O'Toole ET, Giddings TH. Conventional transmission electron microscopy. Mol Biol Cell. 2014;25:319–23.

[29] Dubochet J, Sartori Blanc N. The cell in absence of aggregation artifacts. Micron. 2001;32:91–9.

[30] Lucić V, Förster F, Baumeister W. Structural studies by electron tomography: From cells to molecules. Annu Rev Biochem. 2005;74:833–65.

[31] Massover WH. New and unconventional approaches for advancing resolution in biological transmission electron microscopy by improving macromolecular specimen preparation and preservation. Micron. 2011;42:141–51.

[32] Stirling JW, Curry A, Eyden B, editors. Diagnostic Electron Microscopy – A Practical Guide to Interpretation and Technique. Chichester: John Wiley & Sons, Ltd; 2012.

[33] Wągrowska-Danilewicz M, Danilewicz M. Current position of electron microscopy in the diagnosis of glomerular diseases. Polish J Pathol. 2007;58:87–92.

[34] Cheville NF, editor. Ultrastructural Pathology: The Comparative Cellular Basis of Disease. 2nd ed. Ames: Wiley-Blackwell; 2009.

[35] Kanzaki Y, Terasaki F, Okabe M, Otsuka K, Katashima T, Fujita S, et al. Giant mitochondria in the myocardium of a patient with mitochondrial cardiomyopathy: Transmission and 3-dimensional scanning electron microscopy. Circulation. 2010;121:831–2.

[36] Ding W-X, Li M, Biazik JM, Morgan DG, Guo F, Ni H-M, et al. Electron microscopic analysis of a spherical mitochondrial structure. J Biol Chem. 2012;287:42373–8.

[37] Popescu LM, Faussone-Pellegrini MS. TELOCYTES – A case of serendipity: The winding way from Interstitial Cells of Cajal (ICC), via Interstitial Cajal-Like Cells (ICLC) to TELOCYTES. J Cell Mol Med. 2010;14:729–40.

[38] Fertig ET, Gherghiceanu M, Popescu LM. Extracellular vesicles release by cardiac telocytes: Electron microscopy and electron tomography. J Cell Mol Med. 2014;18:1938–43.

[39] Goldsmith CS, Ksiazek TG, Rollin PE, Comer JA, Nicholson WL, Peret TCT, et al. Cell culture and electron microscopy for identifying viruses in diseases of unknown cause. Emerg Infect Dis. 2013;19:886–91.

[40] Arkill KP, Qvortrup K, Starborg T, Mantell JM, Knupp C, Michel CC, et al. Resolution of the three dimensional structure of components of the glomerular filtration barrier. BMC Nephrol. 2014;15:24.

[41] Tokuyasu KT. A study of positive staining of ultrathin frozen sections. J Ultrastruct Res. 1978;63:287–307.

[42] Fernandez-Moran H. Application of the ultrathin freezing sectioning technique to the study of cell structures with the electron microscope. Ark Fys. 1952;4:471–91.

[43] Bernhard W, Leduc EH. Ultrathin frozen sections. I. Methods and ultrastructural preservation. J Cell Biol. 1967;34:757–71.

[44] Leunissen JLM, Verkleij AJ. Chapter 6 cryo-ultramicrotomy and immuno-gold labeling. In: Verkleij AJ, Leunissen JLM, editors. Immuno-gold Labeling in Cell Biology. Boca Raton: CRC Press; 1989. pp. 95–114.

[45] Slot JW, Geuze HJ. Cryosectioning and immunolabeling. Nat Protoc. 2007;2:2480–91.

[46] Slot JW, Geuze HJ. Sizing of protein A-colloidal gold probes for immunoelectron microscopy. J Cell Biol. 1981;90:533–6.

[47] Griffiths G, Brands R, Burke B, Louvard D, Warren G. Viral membrane proteins acquire galactose in trans Golgi cisternae during intracellular transport. J Cell Biol. 1982;95:781–92.

[48] Karreman MA, Agronskaia AV, van Donselaar EG, Vocking K, Fereidouni F, Humbel BM, et al. Optimizing immuno-labeling for correlative fluorescence and electron microscopy on a single specimen. J Struct Biol. 2012;180:382–6.

[49] Karreman MA, Agronskaia AV, Verkleij AJ, Cremers FFM, Gerritsen, HC, Humbel BM. Discovery of a new RNA-containing nuclear structure in UVC-induced apoptotic cells by integrated laser electron microscopy. Biol Cell. 2009;101:287–99.

[50] Humbel BM, Stierhof YD. Cryo-sectioning according to Tokuyasu. In: Cavalier A, Spehner D, Humbel BM, editors. Handbook of Cryo-preparation Methods for Electron Microscopy. Boca Raton: CRC Press; 2009. pp. 467–98.

[51] Geuze HJ, Slot JW. Disproportional immunostaining patterns of two secretory proteins in guinea pig and rat exocrine pancreatic cells. An immunoferritin and fluorescence study. Eur J Cell Biol. 1980;21:93–100.

[52] Tokuyasu KT. Use of poly(vinylpyrrolidone) and poly(vinyl alcohol) for cryoultramicrotomy. Histochem J. 1989;21:163–71.

[53] Liou W, Geuze HJ, Slot JW. Improving structural integrity of cryosections for immunogold labeling. Histochem Cell Biol. 1996;106:41–58.

[54] Griffith JM, Posthuma G. A reliable and convenient method to store ultrathin thawed cryosections prior to immunolabeling. J Histochem Cytochem. 2002;50:57–62.

[55] Bleck C, Merz A, Gutierrez MG, Walther P, Dubochet J, Zuber B, et al. Comparison of different methods for thin section EM analysis of Mycobacterium smegmatis. J Microsc. 2010;237:23–38.

[56] Van Donselaar E, Posthuma G, Zeuschner D, Humbel BM, Slot JW. Immunogold labeling of cryosections from high-pressure frozen cells. Traffic. 2007;8:471–85.

[57] Griffith J, Mari M, De Mazie A, Reggiori F. A cryosectioning procedure for the ultrastructural analysis and the immunogold labelling of yeast Saccharomyces cerevisiae. Traffic. 2008;9:1060–72.

[58] Ripper D, Schwarz H, Stierhof Y. Cryo-section immunolabelling of difficult to preserve specimens: Advantages of cryofixation, freeze-substitution and rehydration. Biol Cell. 2008;100:109–23.

[59] Stierhof YD, El Kasmi F. Strategies to improve the antigenicity, ultrastructure preservation and visibility of trafficking compartments in Arabidopsis tissue. Eur J Cell Biol. 2010;89:285–97.

[60] Dubochet J. The physics of rapid cooling and its implications for cryoimmobilization of cells. In: Allen TD, editor. Methods in Cell Biology, Volume 79. San Diego: Academic Press; 2007. pp. 7–21.

[61] McDonald KL, Auer M. High-pressure freezing, cellular tomography, and structural cell biology. Biotechniques. 2006;41:137–43.

[62] Zierold K, Michel J, Terryn C, Balossier G. The distribution of light elements in biological cells measured by electron probe X-ray microanalysis of cryosections. Microsc Microanal. 2005;11:138–45.

[63] Nolin F, Michel J, Wortham L, Tchelidze P, Balossier G, Banchet V, et al. Changes to cellular water and element content induced by nucleolar stress: Investigation by a cryo-correlative nano-imaging approach. Cell Mol Life Sci. 2013;70:2383–94.

[64] Volland S, Lütz C, Michalke B, Lütz-Meindl U. Intracellular chromium localization and cell physiological response in the unicellular alga Micrasterias. Aquat Toxicol. 2012;109:59–69.

[65] Moura Ramos JJ, Diogo HP. Are crystallization and melting the reverse transformation of each other? J Chem Educ. 2006;83:1389.

[66] Sellberg JA, Huang C, McQueen TA, Loh ND, Laksmono H, Schlesinger D, et al. Ultrafast X-ray probing of water structure below the homogeneous ice nucleation temperature. Nature. 2014;509:381–4.

[67] McDonald K. Cryopreparation methods for electron microscopy of selected model systems. In: McIntosh JR, editor. Methods in Cell Biology, Volume 79. San Diego: Academic Press; 2007. pp. 23–56.

[68] Bruggeller P, Mayer E. Complete vitrifcation in pure liquid water and dilute aqueous solutions. Nature. 1980;288:569–71.

[69] Dubochet J, McDowall AW. Vitrification of pure water for electron microscopy. J Microsc. 1981;124:3–4.

[70] Dubochet J. Cryo-EM-the first thirty years. J Microsc. 2012;245:221–4.

[71] Dubochet J, Adrian M, Chang JJ, Homo JC, Lepault J, McDowall AW, et al. Cryo-electron microscopy of vitrified specimens. Q Rev Biophys. 1988;21:129–228.

[72] Studer D, Humbel BM, Chiquet M. Electron microscopy of high pressure frozen samples: Bridging the gap between cellular ultrastructure and atomic resolution. Histochem Cell Biol. 2008;130:877–89.

[73] Tivol WF, Briegel A, Jensen GJ. An improved cryogen for plunge freezing. Microsc Microanal. 2008;14:375–9.

[74] Bellare JR, Davis HT, Scriven LE, Talmon Y. Controlled environment vitrification system: An improved sample preparation technique. J Electron Microsc Tech. 1988;10:87–111.

[75] Frederik PM, Hubert DHW. Cryoelectron microscopy of liposomes. In: Duzgunes N, editor. Methods in Enzymology. San Diego: Academic Press; 2005. pp. 431–48.

[76] Zeev-Ben-Mordehai T, Hagen C, Grünewald K. A cool hybrid approach to the herpesvirus “life” cycle. Curr Opin Virol. 2014;5:42–9.

[77] Milne JLS, Subramaniam S. Cryo-electron tomography of bacteria: Progress, challenges and future prospects. Nat Rev Microbiol. 2009;7:666–75.

[78] Luef B, Frischkorn KR, Wrighton KC, Holman H-YN, Birarda G, Thomas BC, et al. Diverse uncultivated ultra-small bacterial cells in groundwater. Nat Commun. 2015;6:6372.

[79] Harapin J, Eibauer M, Medalia O. Structural analysis of supramolecular assemblies by cryo-electron tomography. Structure. 2013;21:1522–30.

[80] Zhou ZH. Atomic resolution cryo electron microscopy of macromolecular complexes. Adv Protein Chem Struct Biol. 2011;82:1–35.

[81] Koning RI, Zovko S, Bárcena M, Oostergetel GT, Koerten HK, Galjart N, et al. Cryo electron tomography of vitrified fibroblasts: Microtubule plus ends in situ. J Struct Biol. 2008;161:459–68.

[82] Medalia O, Weber I, Frangakis AS, Nicastro D, Gerisch G, Baumeister W. Macromolecular architecture in eukaryotic cells visualized by cryoelectron tomography. Science. 2002;298:1209–13.

[83] Henderson GP, Gan L, Jensen GJ. 3-D ultrastructure of O. tauri: Electron cryotomography of an entire eukaryotic cell. PLoS One. 2007;2:e749.

[84] Kudryashev M, Lepper S, Stanway R, Bohn S, Baumeister W, Cyrklaff M, et al. Positioning of large organelles by a membrane-associated cytoskeleton in Plasmodium sporozoites. Cell Microbiol. 2010;12:362–71.

[85] Studer D, Michel M, Wohlwend M, Hunziker EB, Buschmann MD. Vitrification of articular cartilage by high-pressure freezing. J Microsc. 1995;179:321–32.

[86] Moor H, Riehle U. Snap-freezing under high pressure: A new fixation technique for freeze-etching. Proc 4th Eur Reg Conf Electron Microsc. 1968;2:33–4.

[87] Kanno H, Speedy RJ, Angell CA. Supercooling of water to −92°C under pressure. Science. 1975;189:880–1.

[88] Sartori N, Richter K, Dubochet J. Vitrification depth can be increased more than 10-fold by high-pressure freezing. J Microsc. 1993;172:55–61.

[89] Moor H, Bellin G. Cell and tissue: The influence of high pressure freezing on mammalian nerve tissue. Cell Tissue Res. 1980;216:201–16.

[90] Hunziker EB, Herrmann W, Schenk RK, Mueller M, Moor H. Cartilage ultrastructure after high-pressure freezing, freeze substitution, and low-temperature embedding.I. Chondrocyte ultrastructure – implications for the theories of mineralization and vascular invasion. J Cell Biol. 1984;98:267–76.

[91] Vanhecke D, Herrmann G, Graber W, Hillmann-Marti T, Mühlfeld C, Studer D, et al. Lamellar body ultrastructure revisited: high-pressure freezing and cryo-electron microscopy of vitreous sections. Histochem Cell Biol. 2010;134:319–26.

[92] Van Belleghem F, Cuypers A, Semane B, Smeets K, Vangronsveld J, D'Haen J, et al. Subcellular localization of cadmium in roots and leaves of Arabidopsis thaliana. New Phytol. 2007;173:495–508.

[93] Semmler K, Wunderlich J, Richter W, Meyer HW. High-pressure freezing causes structural alterations in phospholipid model membranes. J Microsc. 1998;190:317–27.

[94] Leforestier A, Richter K, Livolant F, Dubochet J. Comparison of slam-freezing and high-pressure freezing effects on the DNA cholesteric liquid crystalline structure. J Microsc. 1996;184:4–13.

[95] Sosinsky GE, Crum J, Jones YZ, Lanman J, Smarr B, Terada M, et al. The combination of chemical fixation procedures with high pressure freezing and freeze substitution preserves highly labile tissue ultrastructure for electron tomography applications. J Struct Biol. 2008;161:359–71.

[96] Bullen A, Taylor RR, Kachar B, Moores C, Fleck RA, Forge A. Inner ear tissue preservation by rapid freezing: Improving fixation by high-pressure freezing and hybrid methods. Hear Res. 2014;315:49–60.

[97] Nixon SJ, Webb RI, Floetenmeyer M, Schieber N, Lo HP, Parton RG. A single method for cryofixation and correlative light, electron microscopy and tomography of zebrafish embryos. Traffic. 2009;10:131–6.

[98] Reipert S, Fischer I, Wiche G. High-pressure freezing of epithelial cells on sapphire coverslips. J Microsc. 2004;213:81–5.

[99] Jiménez N, Humbel BM, Van Donselaar E, Verkleij AJ, Burger KNJ. Aclar discs: A versatile substrate for routine high-pressure freezing of mammalian cell monolayers. J Microsc. 2006;221:216–23.

[100] Mesman RJ. A novel method for high-pressure freezing of adherent cells for frozen hydrated sectioning and CEMOVIS. J Struct Biol. 2013;183:527–30.

[101] Vanhecke D, Graber W, Herrmann G, Al-Amoudi A, Eggli P, Studer D. A rapid microbiopsy system to improve the preservation of biological samples prior to high-pressure freezing. J Microsc. 2003;212:3–12.

[102] Verkade P. Moving EM: The rapid transfer system as a new tool for correlative light and electron microscopy and high throughput for high-pressure freezing. J Microsc. 2008;230:317–28.

[103] McDonald KL. A review of high-pressure freezing preparation techniques for correlative light and electron microscopy of the same cells and tissues. J Microsc. 2009;235:273–81.

[104] Watanabe S, Rost BR, Camacho-Pérez M, Davis MW, Söhl-Kielczynski B, Rosenmund C, et al. Ultrafast endocytosis at mouse hippocampal synapses. Nature. 2013;504:242–7.

[105] Leunissen JLM, Yi H. Self-pressurized rapid freezing (SPRF): a novel cryofixation method for specimen preparation in electron microscopy. J Microsc. 2009;235:25–35.

[106] Han H-M, Huebinger J, Grabenbauer M. Self-pressurized rapid freezing (SPRF) as a simple fixation method for cryo-electron microscopy of vitreous sections. J Struct Biol. 2012;178:84–7.

[107] Yakovlev S, Downing KH. Crystalline ice as a cryoprotectant: Theoretical calculation of cooling speed in capillary tubes. J Microsc. 2011;243:8–14.

[108] Yakovlev S, Downing KH. Freezing in sealed capillaries for preparation of frozen hydrated sections. J Microsc. 2011;244:235–47.

[109] Sarkar P, Bosneaga E, Yap EG, Das J, Tsai W-T, Cabal A, et al. Electron tomography of cryo-immobilized plant tissue: a novel approach to studying 3D macromolecular architecture of mature plant cell walls in situ. PLoS One. 2014;9:e106928.

[110] Dubochet J, Lepault J, Freeman R, Berriman JA, Homo J-C. Electron microscopy of frozen water and aqueous solutions. J Microsc. 1982;128:219–37.

[111] McDowall AW, Chang JJ, Freeman R, Lepault J, Walter CA, Dubochet J. Electron microscopy of frozen hydrated sections of vitreous ice and vitrified biological samples. J Microsc. 1983;131:1–9.

[112] Hodson S, Marshall J. Ultracryotomy: A technique for cutting ultrathin sections of unfixed frozen biological tissues for electron microscopy. J Microsc. 1970;91:105–17.

[113] Hutchinson TE, Johnson DE, MacKenzie AP. Instrumentation for direct observation of frozen hydrated specimens in the electron microscope. Ultramicroscopy. 1978;3:315–24.

[114] Chang J-J, McDowall AW, Lepault J, Freeman R, Walter CA, Dubochet J. Freezing, sectioning and observation artefacts of frozen hydrated sections for electron microscopy. J Microsc. 1983;132:109–23.

[115] Al-Amoudi A, Norlen L, Dubochet J. Cryo-electron microscopy of vitreous sections of native biological cells and tissues. J Struct Biol. 2004;148:131–5.

[116] Al-Amoudi A, Díez DC, Betts MJ, Frangakis AS. The molecular architecture of cadherins in native epidermal desmosomes. Nature. 2007;450:832–7.

[117] Bouchet-Marquis C, Dubochet J, Al-Amoudi A, Zuber B, Eltsov M. Cemovis cryo-electron microscopy of vitreous sections. In: Cavalier A, Spehner D, Humbel BM, editors. Handbook of Cryo-preparation Methods for Electron Microscopy. Boca Raton: CRC Press; 2008. pp. 259–89.

[118] Griffiths G, McDowall A, Back R, Dubochet J. On the preparation of cryosections for immunocytochemistry. J Ultrastruct Res. 1984;89:65–78.

[119] Al-Amoudi A, Studer D, Dubochet J. Cutting artefacts and cutting process in vitreous sections for cryo-electron microscopy. J Struct Biol. 2005;150:109–21.

[120] Al-Amoudi A, Dubochet J, Gnaegi H, Lüthi W, Studer D. An oscillating cryo-knife reduces cutting-induced deformation of vitreous ultrathin sections. J Microsc. 2003;212:26–33.

[121] Michel M, Gnagi H, Muller M. Diamonds are a thief ' s best friend. J Microsc. 1992;166:43–56.

[122] Pierson J, Fernández JJ, Bos E, Amini S, Gnaegi H, Vos M, et al. Improving the technique of vitreous cryo-sectioning for cryo-electron tomography: Electrostatic charging

for section attachment and implementation of an anti-contamination glove box. J Struct Biol. 2010;169:219–25.

[123] Bouchet-Marquis C, Hoenger A. Cryo-electron tomography on vitrified sections: A critical analysis of benefits and limitations for structural cell biology. Micron. 2011;42:152–62.

[124] Zuber B, Nikonenko I, Klauser P, Muller D, Dubochet J. The mammalian central nervous synaptic cleft contains a high density of periodically organized complexes. Proc Natl Acad Sci USA. 2005;102:19192–7.

[125] Bouchet-Marquis C, Zuber B, Glynn A-M, Eltsov M, Grabenbauer M, Goldie KN, et al. Visualization of cell microtubules in their native state. Biol cell. 2007;99:45–53.

[126] Han HM, Zuber B, Dubochet J. Compression and crevasses in vitreous sections under different cutting conditions. J Microsc. 2008;230:167–71.

[127] Bouchet-Marquis C, Dubochet J, Fakan S. Cryoelectron microscopy of vitrified sections: a new challenge for the analysis of functional nuclear architecture. Histochem Cell Biol. 2006;125:43–51.

[128] Studer D, Gnaegi H. Minimal compression of ultrathin sections with use of an oscillating diamond knife. J Microsc. 2000;197:94–100.

[129] Ladinsky MS, Pierson JM, McIntosh JR. Vitreous cryo-sectioning of cells facilitated by a micromanipulator. J Microsc. 2006;224:129–34.

[130] Studer D, Klein A, Iacovache I, Gnaegi H, Zuber B. A new tool based on two micromanipulators facilitates the handling of ultrathin cryosection ribbons. J Struct Biol. 2014;185:125–8.

[131] Marko M, Hsieh C, Moberlychan W, Mannella CA, Frank J. Focused ion beam milling of vitreous water: Prospects for an alternative to cryo-ultramicrotomy of frozen-hydrated biological samples. J Microsc. 2006;222:42–7.

[132] Villa E, Schaffer M, Plitzko JM, Baumeister W. Opening windows into the cell: Focused-ion-beam milling for cryo-electron tomography. Curr Opin Struct Biol. 2013;23:771–7.

[133] Matteson TL, Schwarz SW, Houge EC, Kempshall BW, Giannuzzi LA. Electron backscattering diffraction investigation of focused ion beam surfaces. J Electron Mater. 2002;31:33–9.

[134] Rigort A, Bäuerlein FJB, Leis A, Gruska M, Hoffmann C, Laugks T, et al. Micromachining tools and correlative approaches for cellular cryo-electron tomography. J Struct Biol. 2010;172:169–79.

[135] Rigort A, Bäuerlein FJB, Villa E, Eibauer M, Laugks T, Baumeister W, et al. Focused ion beam micromachining of eukaryotic cells for cryoelectron tomography. Proc Natl Acad Sci USA. 2012;109:4449–54.

[136] Wang K, Strunk K, Zhao G, Gray JL, Zhang P. 3D structure determination of native mammalian cells using cryo-FIB and cryo-electron tomography. J Struct Biol. 2012;180:318–26.

[137] Strunk KM, Wang K, Ke D, Gray JL, Zhang P. Thinning of large mammalian cells for cryo-TEM characterization by cryo-FIB milling. J Microsc. 2012;247:220–7.

[138] Fukuda Y, Schrod N, Schaffer M, Feng LR, Baumeister W, Lucic V. Coordinate transformation based cryo-correlative methods for electron tomography and focused ion beam milling. Ultramicroscopy. 2014;143:15–23.

[139] Rubino S, Akhtar S, Melin P, Searle A, Spellward P, Leifer K. A site-specific focused-ion-beam lift-out method for cryo transmission electron microscopy. J Struct Biol. 2012;180:572–6.

[140] Hayles MF, de Winter DAM, Schneijdenberg CTWM, Meeldijk JD, Luecken U, Persoon H, et al. The making of frozen-hydrated, vitreous lamellas from cells for cryo-electron microscopy. J Struct Biol. 2010;172:180–90.

[141] De Winter DAM, Mesman RJ, Hayles MF, Schneijdenberg CTWM, Mathisen C, Post JA. In-situ integrity control of frozen-hydrated, vitreous lamellas prepared by the cryo-focused ion beam-scanning electron microscope. J Struct Biol. 2013;183:11–8.

[142] Hsieh C, Schmelzer T, Kishchenko G, Wagenknecht T, Marko M. Practical workflow for cryo focused-ion-beam milling of tissues and cells for cryo-TEM tomography. J Struct Biol. 2014;185:32–41.

[143] Wagenknecht T, Hsieh C, Marko M. Skeletal muscle triad junction ultrastructure by focused-ion-beam milling of muscle and cryo-electron tomography. Eur J Transl Myol. 2015;25:49–56.

[144] Hayles MF, Stokes DJ, Phifer D, Findlay KC. A technique for improved focused ion beam milling of cryo-prepared life science specimens. J Microsc. 2007;226:263–9.

[145] Jun S, Ke D, Debiec K, Zhao G, Meng X, Ambrose Z, et al. Direct visualization of HIV-1 with correlative live-cell microscopy and cryo-electron tomography. Structure. 2011;19:1573–81.

[146] Schwartz CL, Sarbash VI, Ataullakhanov FI, Mcintosh JR, Nicastro D. Cryo-fluorescence microscopy facilitates correlations between light and cryo-electron microscopy and reduces the rate of photobleaching. J Microsc. 2007;227:98–109.

[147] Delgado L, Martínez G, López-Iglesias C, Mercadé E. Cryo-electron tomography of plunge-frozen whole bacteria and vitreous sections to analyze the recently described bacterial cytoplasmic structure, the Stack. J Struct Biol. 2015;189:220–9.

[148] Sartori Blanc N, Studer D, Ruhl K, Dubochet J. Electron beam-induced changes in vitreous sections of biological samples. J Microsc. 1998;192:194–201.

[149] Wang Q, Mercogliano CP, Löwe J. A ferritin-based label for cellular electron cryotomography. Structure. 2011;19:147–54.

[150] Oda T, Kikkawa M. Novel structural labeling method using cryo-electron tomography and biotin-streptavidin system. J Struct Biol. 2013;183:305–11.

[151] Gold V a M, Ieva R, Walter A, Pfanner N, van der Laan M, Kühlbrandt W. Visualizing active membrane protein complexes by electron cryotomography. Nat Commun. 2014;5:4129–38.

[152] Song K, Awata J, Tritschler D, Bower R, Witman GB, Porter ME, et al. In situ localization of N- and C-termini of subunits of the flagellar nexin-dynein regulatory complex (N-DRC) using SNAP-tag and cryo-electron tomography. J Biol Chem. 2015;290:5341–53.

[153] Simpson WL. An experimental analysis of the Altmann technic of freezing-drying. Anat Rec. 1941;80:173–89.

[154] Fernandez-Moran H. Low-temperature preparation techniques for electron microscopy of biological specimens based on rapid freezing with liquid Helium II. Ann N Y Acad Sci. 1960;13:689–713.

[155] Bullivant S. The staining of thin sections of mouse pancreas prepared by the Fernandez-Moran helium II freeze-substitution method. J Biophys Biochem Cytol. 1960;8:639–47.

[156] Van Harreveld A, Crowell J. Electron microscopy after rapid freezing on a metal surface and substitution fixation. Anat Rec. 1964;149:381–5.

[157] Humbel BM, Schwarz H. Freeze-substitution for immunocytochemistry. In: Verkleij AJ, Leunissen JLM, editors. Immuno-gold Labeling in Cell Biology. Boca Raton: CRC Press; 1989. pp. 114–34.

[158] Shiurba R. Freeze-substitution: origins and applications. Int Rev Cytol. 2001;206:45–96.

[159] Kellenberger E. The potential of cryofixation and freeze substitution: Observations and theoretical considerations. J Microsc. 1991;161:183–203.

[160] Studer D, Hennecke H, Müller M. High-pressure freezing of soybean nodules leads to an improved preservation of ultrastructure. Planta. 1992;188:155–63.

[161] Hess MW. Cryopreparation methodology for plant cell biology. In: McIntosh JR, editor. Methods in Cell Biology, Volume 79. San Diego: Academic Press; 2007. pp. 57–100.

[162] Hess MW. Of plants and other pets: practical aspects of freeze-substitution and resin embedding. J Microsc. 2003;212:44–52.

[163] Tomova C, Humbel BM, Geerts WJC, Entzeroth R, Holthuis JCM, Verkleij AJ. Membrane contact sites between apicoplast and ER in Toxoplasma gondii revealed by electron tomography. Traffic. 2009;10:1471–80.

[164] Humbel B. Freeze-substitution. In: Cavalier A, Spehner D, Humbel BM, editors. Handbook of Cryo-preparation Methods for Electron Microscopy. Boca Raton: CRC Press; 2008. pp. 319–41.

[165] Monaghan P, Perusinghe N, Müller M. High-pressure freezing for immunocytochemistry. J Microsc. 1998;192:248–58.

[166] Steinbrecht R, Müller M. Freeze-substitution and freeze-drying. In: Steinbrecht R, Zierold K, editors. Cryotechniques in Biological Electron Microscopy. Berlin/Heidelberg/New York: Springer Verlag; 1987. pp. 149–72.

[167] Möbius W. Cryopreparation of biological specimens for immunoelectron microscopy. Ann Anat. 2009;191:231–47.

[168] McDonald KL. Rapid embedding methods into epoxy and LR White resins for morphological and immunological analysis of cryofixed biological specimens. Microsc Microanal. 2014;20:152–63.

[169] Sobol M, Philimonenko VV, Hozak P. Comparison of methods of high-pressure freezing and automated freeze-substitution of suspension cells combined with LR White embedding. Histochem Cell Biol. 2010;134:631–41.

[170] White DL, Andrews SB, Faller JW, Barrnett RJ. The chemical nature of osmium tetroxide fixation and staining of membranes by x-ray photoelectron spectroscopy. Biochim Biophys Acta. 1976;436:577–92.

[171] Bohrmann B, Kellenberger E. Cryosubstitution of frozen biological specimens in electron microscopy: use and application as an alternative to chemical fixation. Micron. 2001;32:11–9.

[172] Hawes P, Netherton CL, Mueller M, Wileman T, Monaghan P. Rapid freeze-substitution preserves membranes in high-pressure frozen tissue culture cells. J Microsc. 2007;226:182–9.

[173] Walther P, Ziegler A. Freeze substitution of high-pressure frozen samples: The visibility of biological membranes is improved when the substitution medium contains water. J Microsc. 2002;208:3–10.

[174] Buser C, Walther P. Freeze-substitution: the addition of water to polar solvents enhances the retention of structure and acts at temperatures around −60°C. J Microsc. 2008;230:268–77.

[175] Sobol MA, Philimonenko VV, Philimonenko AA, Hozák P. Quantitative evaluation of freeze-substitution effects on preservation of nuclear antigens during preparation

of biological samples for immunoelectron microscopy. Histochem Cell Biol. 2012;138:167–77.

[176] Jiménez N, Vocking K, van Donselaar EG, Humbel BM, Post JA, Verkleij AJ. Tannic acid-mediated osmium impregnation after freeze-substitution: A strategy to enhance membrane contrast for electron tomography. J Struct Biol. 2009;166:103–6.

[177] Siksou L, Rostaing P, Lechaire J-P, Boudier T, Ohtsuka T, Fejtová A, et al. Three-dimensional architecture of presynaptic terminal cytomatrix. J Neurosci. 2007;27:6868–77.

[178] Giddings TH. Freeze-substitution protocols for improved visualization of membranes in high-pressure frozen samples. J Microsc. 2003;212:53–61.

[179] Wild P, Schraner EM, Adler H, Humbel BM. Enhanced resolution of membranes in cultured cells by cryoimmobilization and freeze-substitution. Microsc Res Tech. 2001;53:313–21.

[180] Matsko N, Mueller M. Epoxy resin as fixative during freeze-substitution. J Struct Biol. 2005;152:92–103.

[181] Walther P, Ziegler A. Freeze substitution of high-pressure frozen samples: the visibility of biological membranes is improved when the substitution medium contains water. J Microsc. 2002;208:3–10.

[182] Zechmann B, Müller M, Zellnig G. Membrane associated qualitative differences in cell ultrastructure of chemically and high pressure cryofixed plant cells. J Struct Biol. 2007;158:370–7.

[183] Austin JR, Staehelin LA. Three-dimensional architecture of grana and stroma thylakoids of higher plants as determined by electron tomography. Plant Physiol. 2011;155:1601–11.

[184] Hsieh CE, Leith A, Mannella CA, Frank J, Marko M. Towards high-resolution three-dimensional imaging of native mammalian tissue: electron tomography of frozen-hydrated rat liver sections. J Struct Biol. 2006;153:1–13.

[185] Reipert S, Fischer I, Wiche G. High-pressure cryoimmobilization of murine skin reveals novel structural features and prevents extraction artifacts. Exp Dermatol. 2004;13:419–25.

[186] Müller-Reichert T, Hohenberg H, O'Toole ET, Mcdonald K. Cryoimmobilization and three-dimensional visualization of C. elegans ultrastructure. J Microsc. 2003;212:71–80.

[187] Burghardt T, Näther DJ, Junglas B, Huber H, Rachel R. The dominating outer membrane protein of the hyperthermophilic Archaeum Ignicoccus hospitalis: a novel pore-forming complex. Mol Microbiol. 2007;63:166–76.

[188] Kirschning E, Rutter G, Hohenberg H. High-pressure freezing and freeze-substitution of native rat brain: suitability for preservation and immunoelectron microscopic localization of myelin glycolipids. J Neurosci Res. 1998;53:465–74.

[189] Peschke M, Moog D, Klingl A, Maier UG, Hempel F. Evidence for glycoprotein transport into complex plastids. Proc Natl Acad Sci USA. 2013;110:10860–5.

[190] McDonald KL. Out with the old and in with the new: rapid specimen preparation procedures for electron microscopy of sectioned biological material. Protoplasma. 2014;251:429–48.

[191] Durand A, Papai G, Schultz P. Structure, assembly and dynamics of macromolecular complexes by single particle cryo-electron microscopy. J Nanobiotechnology. BioMed Central Ltd; 2013;11 Suppl 1:S4.

[192] Bartesaghi A, Matthies D, Banerjee S, Merk A, Subramaniam S. Structure of -galactosidase at 3.2-A resolution obtained by cryo-electron microscopy. Proc Natl Acad Sci. 2014;111:11709–14.

[193] Schur FKM, Hagen WJH, De Marco A, Briggs J a G. Determination of protein structure at 8.5Å resolution using cryo-electron tomography and sub-tomogram averaging. J Struct Biol. 2013;184:394–400.

[194] Bárcena M, Koster AJ. Electron tomography in life science. Semin Cell Dev Biol. 2009 Oct;20:920–30.

[195] Ben-Harush K, Maimon T, Patla I, Villa E, Medalia O. Visualizing cellular processes at the molecular level by cryo-electron tomography. J Cell Sci. 2010;123:7–12.

[196] Ortiz JO, Brandt F, Matias VRF, Sennels L, Rappsilber J, Scheres SHW, et al. Structure of hibernating ribosomes studied by cryoelectron tomography in vitro and in situ. J Cell Biol. 2010;190:613–21.

[197] Hohmann-Marriott MF, Sousa AA, Azari AA, Glushakova S, Zhang G, Zimmerberg J, et al. Nanoscale 3D cellular imaging by axial scanning transmission electron tomography. Nat Methods. 2009;6:729–31.

[198] De Jonge N, Sougrat R, Northan BM, Pennycook SJ. Three-dimensional scanning transmission electron microscopy of biological specimens. Microsc Microanal. 2010;16:54–63.

[199] Sousa AA, Azari AA, Zhang G, Leapman RD. Dual-axis electron tomography of biological specimens: extending the limits of specimen thickness with bright-field STEM imaging. J Struct Biol. 2011;174:107–14.

[200] Wu JS, Kim AM, Bleher R, Myers BD, Marvin RG, Inada H, et al. Imaging and elemental mapping of biological specimens with a dual-EDS dedicated scanning transmission electron microscope. Ultramicroscopy. 2013;128:24–31.

[201] Norlén L, Oktem O, Skoglund U. Molecular cryo-electron tomography of vitreous tissue sections: Current challenges. J Microsc. 2009;235:293–307.

[202] Lučič V, Rigort A, Baumeister W. Cryo-electron tomography: The challenge of doing structural biology in situ. J Cell Biol. 2013;202:407–19.

[203] Zhang P. Correlative cryo-electron tomography and optical microscopy of cells. Curr Opin Struct Biol. 2013;23:763–70.

[204] Koning RI, Koster AJ. Cryo-electron tomography in biology and medicine. Ann Anat. 2009;191:427–45.

[205] Hoenger A. High-resolution cryo-electron microscopy on macromolecular complexes and cell organelles. Protoplasma. 2014;251:417–27.

[206] Bułdak R, Skonieczna M, Bułdak Ł, Matysiak N, Mielańczyk Ł, Wyrobiec G, et al. Changes in subcellular localization of visfatin in human colorectal HCT-116 carcinoma cell line after cytochalasin B treatment. Eur J Histochem. 2014;58:239–46.

[207] Iwai I, Han H, Hollander L den, Svensson S, Öfverstedt L-G, Anwar J, et al. The human skin barrier is organized as stacked bilayers of fully extended ceramides with cholesterol molecules associated with the ceramide sphingoid moiety. J Invest Dermatol. 2012;132:2215–25.

[208] Xin L, Lipeng Y, Jiaju Q. Revisiting the mesosome as a novel site of hydrogen peroxide accumulation in Escherichia coli. Curr Microbiol. 2014;69:549–53.

[209] Höög JL, Antony C. Whole-cell investigation of microtubule cytoskeleton architecture by electron tomography. Methods Cell Biol. Academic Press. 2007;79:145–67.

[210] Marsh BJ, Mastronarde DN, Buttle KF, Howell KE, McIntosh JR. Organellar relationships in the Golgi region of the pancreatic beta cell line, HIT-T15, visualized by high resolution electron tomography. Proc Natl Acad Sci USA. 2001;98:2399–406.

[211] Lebbink MN, Jiménez N, Vocking K, Hekking LH, Verkleij AJ, Post JA. Spiral coating of the endothelial caveolar membranes as revealed by electron tomography and template matching. Traffic. 2010;11:138–50.

[212] Eltsov M, Sosnovski S, Olins AL, Olins DE. ELCS in ice: cryo-electron microscopy of nuclear envelope-limited chromatin sheets. Chromosoma. 2014;123:303–12.

[213] Hudoklin S, Jezernik K, Neumüller J, Pavelka M, Romih R. Electron tomography of fusiform vesicles and their organization in urothelial cells. PLoS One. 2012;7:1–8.

[214] Royer SM, Kinnamon JC. Comparison of high-pressure freezing/freeze substitution and chemical fixation of catfish barbel taste buds. Microsc Res Tech. 1996;35:385–412.

[215] Henrich P, Kilian N, Lanzer M, Cyrklaff M. 3-D analysis of the Plasmodium falciparum Maurer's clefts using different electron tomographic approaches. Biotechnol J. 2009;4:888–94.

[216] Chlanda P, Carbajal MA, Cyrklaff M, Griffiths G, Krijnse-Locker J. Membrane rupture generates single open membrane sheets during vaccinia virus assembly. Cell Host Microbe. 2009;6:81–90.

[217] Gan L, Jensen GJ. Electron tomography of cells. Q Rev Biophys. 2012;45:27–56.

[218] Sendrowski K, Sobaniec W, Sobaniec P, Sobaniec-Lotowska ME. Ultrastructural study of hippocampal cortex neurons in an experimental model of valproate encephalopathy. Folia Histochem Cytobiol. 2013;51:31–7.

[219] Karreman MA, van Donselaar EG, Gerritsen HC, Verrips CT, Verkleij AJ. VIS2FIX: A high-speed fixation method for immuno-electron microscopy. Traffic. 2011;12:806–14.

[220] Sabanay I, Arad T, Weiner S, Geiger B. Study of vitrified, unstained frozen tissue sections by cryoimmunoelectron microscopy. J Cell Sci. 1991 Sep;100:227–36.

[221] Bokstad M, Sabanay H, Dahan I, Geiger B, Medalia O. Reconstructing adhesion structures in tissues by cryo-electron tomography of vitrified frozen sections. J Struct Biol. 2012;178:76–83.

[222] Bos E, Hussaarts L, van Weering JRT, Ellisman MH, de Wit H, Koster AJ. Vitrification of Tokuyasu-style immuno-labelled sections for correlative cryo light microscopy and cryo electron tomography. J Struct Biol. 2014;186:273–82.

[223] Couture-Tosi E, Ranck J-L, Haustant G, Pehau-Arnaudet G, Sachse M. CEMOVIS on a pathogen: Analysis of Bacillus anthracis spores. Biol Cell. 2010;102:609–19.

[224] Venter C, van der Merwe CF, Oberholzer HM, Bester MJ, Taute H. Feasibility of high pressure freezing with freeze substitution after long-term storage in chemical fixatives. Microsc Res Tech. 2013;76:942–6.

[225] Caplan J, Niethammer M, Taylor RM, Czymmek KJ. The power of correlative microscopy: multi-modal, multi-scale, multi-dimensional. Curr Opin Struct Biol. Elsevier Ltd; 2011;21:686–93.

[226] Boonrungsiman S, Gentleman E, Carzaniga R, Evans ND, McComb DW, Porter AE, et al. The role of intracellular calcium phosphate in osteoblast-mediated bone apatite formation. Proc Natl Acad Sci USA. 2012;109:14170–5.

[227] Cloyd KL, El-Hamamsy I, Boonrungsiman S, Hedegaard M, Gentleman E, Sarathchandra P, et al. Characterization of porcine aortic valvular interstitial cell "calcified" nodules. PLoS One. 2012;7:1–9.

[228] Bertazzo S, Gentleman E, Cloyd KL, Chester AH, Yacoub MH, Stevens MM. Nanoanalytical electron microscopy reveals fundamental insights into human cardiovascular tissue calcification. Nat Mater. 2013;12:576–83.

[229] Vanhecke D, Asano S, Kochovski Z, Fernandez-Busnadiego R, Schrod N, Baumeister W, et al. Cryo-electron tomography: methodology, developments and biological applications. J Microsc. 2011;242:221–7.

[230] Grigorieff N. Direct detection pays off for electron cryo-microscopy. Elife. 2013;2013:2–4.

[231] Sader K, Stopps M, Calder LJ, Rosenthal PB. Cryomicroscopy of radiation sensitive specimens on unmodified graphene sheets: reduction of electron-optical effects of charging. J Struct Biol. 2013;183:531–6.

[232] Murata K, Liu X, Danev R, Jakana J, Schmid MF, King J, et al. Zernike phase contrast cryo-electron microscopy and tomography for structure determination at nanometer and subnanometer resolutions. Structure. 2010;18:903–12.

[233] Koning RI, Faas FG, Boonekamp M, de Visser B, Janse J, Wiegant JC, et al. MAVIS: an integrated system for live microscopy and vitrification. Ultramicroscopy. 2014;143:67–76.

[234] Faas FGA, Bárcena M, Agronskaia AV, Gerritsen HC, Moscicka KB, Diebolder CA, et al. Localization of fluorescently labeled structures in frozen-hydrated samples using integrated light electron microscopy. J Struct Biol. 2013;181:283–90.

[235] De Jonge N, Ross FM. Electron microscopy of specimens in liquid. Nat Nanotechnol. 2011;6:695–704.

Chapter 10

Observation of Viruses, Bacteria, and Fungi in Clinical Skin Samples under Transmission Electron Microscopy

Yuping Ran, Wengying Hu, Kaiwen Zhuang, Mao Lu, Jinghong Huang, Fengni Xu, Xiaoxi Xu, Xia Hua, Jebina Lama, Xin Ran, Yalin Dai and Song Lei

Additional information is available at the end of the chapter

http://dx.doi.org/10.5772/60957

Abstract

The highlight of this chapter is the description of the clinical manifestation and its pathogen and the host tissue damage observed under the transmission electron microscopy, which helps the clinician understand the pathogen's ultrastructure, the change of host sub-cell structure, and helps the laboratory workers understand the pathogen-induced human skin lesions' clinical characteristics, to establish a two-way learning exchange database with vivid images.

Keywords: Viruses, bacteria, fungi, clinical skin samples, TEM

1. Introduction

In the Dermatovenereology department, skin infections by bacteria, viruses, and fungi are very common in routine clinical practice. Discrimination and identification of these pathogens is a huge challenge and very important for patient's disease diagnosis and treatment. Transmission electron microscopy (TEM) is a very strong tool for detection and observation of the pathogen from the clinical samples that help us obtain the direct proof of presence of the pathogen inside the skin samples of the lesion. Based on the detailed morphologic image, we can recognize the ultrastructures of the pathogen and understand the pathogenesis of the infectious skin diseases. During recent years, we collected several pathogenic microorganisms' photographs which were taken by TEM; these pathogens included viruses (*Herpes simplex virus, Varicella-*

INTECH
open science | open minds

© 2015 The Author(s). Licensee InTech. This chapter is distributed under the terms of the Creative Commons Attribution License (http://creativecommons.org/licenses/by/3.0), which permits unrestricted use, distribution, and reproduction in any medium, provided the original work is properly cited.

zoster virus, Molluscum contagiosum virus), bacteria (*Mycobacterium leprae*), and fungi (*Trichophyton violaceum, T. tonsurans, T. mentagrophytes, Trichosporon inkin, Penicillium marneffei*). The diagnosis and clinical manifestation, the source of sample, and the image of the pathogen are summarized in Table 1.

Diagnosis	Clinical manifestation	Sample	Image of pathogen by TEM
Herpes simplex	Painful grouped vesicles, pustular, ulcer, crust usually on the skin; oral, labial, and ocular mucosa.	Blister wall	Virus (*Herpes simplex virus*)
Herpes zoster	Erythema, papule, vesicles, or bullous distributed unilaterally within the peripheral nerves.	Blister wall	Virus (*Varicella-zoster virus*)
Molluscum contagiosum	Dome-shaped papules of 3-5 mm in diameter with a waxy appearance on the surface and a white curd-like core.	Papule	Virus (*Molluscum contagiosum virus*)
Leprosy	Erythematous patches or papules, alopecia, leproma; thickening of peripheral nerves, neurological disorders.	Skin tissue	Bacteria (*Mycobacterium leprae*)
Tinea capitis	Erythema, papules, scales, and pustule on the scalp; broken hair, and hair loss.	Infected hair	Fungus (*Trichophyton violaceum; T. tonsurans*)
Trichomycosis nodularis	White or brown nodules surround the pubic or armpit hair shaft, the nodule is soft.	Infected hair	Fungus (*Trichosporon inkin*)
Penicilliosis marneffei	Fever, anima, superficial lymphadenopathy, hepatosplenomegaly, polymorphic skin lesions on face, torso, and extremities.	Skin tissue	Fungus *(Penicillium marneffei)*

Table 1. The summary of diagnosis and clinical manifestation, kinds of sample, and the image of the pathogen observed by TEM

2. Methods

All samples for TEM were taken from clinical patients. These samples include blister wall, papule, infected hair, scales, and biopsy tissue. The samples were double-fixed in 2% glutaraldehyde and 2% osmium tetroxide for 3h at the room temperature, dehydrated in series of grade ethanol solutions and propylene oxide, then embedded in resin. Ultrathin longitudinal sections of infected hair were cut with an ultramicrotome and a diamond knife. Observation was carried out by TEM (Hitachi H-7650 microscope), which was operated at 120 kV and equipped with a LaB6 source.

3. Results

3.1. Herpes simplex

Herpes simplex is a viral dermatosis caused by *Herpes simplex virus* (HSV) infection, and characterized by painful grouped vesicles on the skin or mucous membranes, mainly on the

http://dx.doi.org/10.5772/60957

mucocutaneous junction. It is self-limiting, but tends to recur frequently. HSV, a member of alpha subfamily of the *Human herpes virus*, is a double-stranded DNA virus that affects humans only. It is sub-classified as type 1 and type 2 according to the differences in its transmission modes and clinical features. One of the important biological properties of alpha herpes virus is its ability to establish latent infections in neurons. When HSV encounters broken skin or a mucosal surface, viral replication occurs first at the point of entry, initiating a primary infection. The virus then invades in local nerve endings, where, latency is established. In the latent stage, the virus resides in infected ganglia in a nonreplicating state and persists for the lifetime of the host. Several provocative stimuli can reactivate virus from the latent stage: transient immunosuppressive states of the host induced by fever, gastrointestinal disturbance, menstruation, or stress. During the reactivation, the latent virus returns to the peripheral sites of the skin or mucous membranes and replicates to produce an outbreak of recurrent herpes simplex. The aim of herpes simplex treatment is to shorten the current outbreak, to prevent secondary bacterial infections, and to avoid or postpone recurrence [1, 2]. The frequency and severity of recurrent outbreaks vary greatly among people. Some individuals' outbreaks can be quite debilitating, with large, painful lesions persisting for several weeks, while others may experience only minor itching or burning for a few days. Immunity to the virus is built over time. Most infected individuals experience fewer outbreaks and outbreak symptoms often become less severe. After several years, some people become perpetually asymptomatic and no longer experience outbreaks, though they may still be contagious to others. Immunocompromised individuals may experience longer, more frequent and severer episodes. Antiviral medication has been proven to shorten the frequency and duration of outbreaks [3].

We describe a case of herpes simplex. A seven-year-old girl presented at our clinic with the complaint of painful blisters and erosions on right eyelid and lower left eyelid for five days (Fig. 1a). Sample was taken from the blister's wall for TEM observation. A large number of electron empty, particle, and dense cores were discovered, which were the characteristics of *Herpes simplex virus* (Fig. 1b). The patient was diagnosed with bilateral eyelid herpes simplex and was cured by anti-virus therapy.

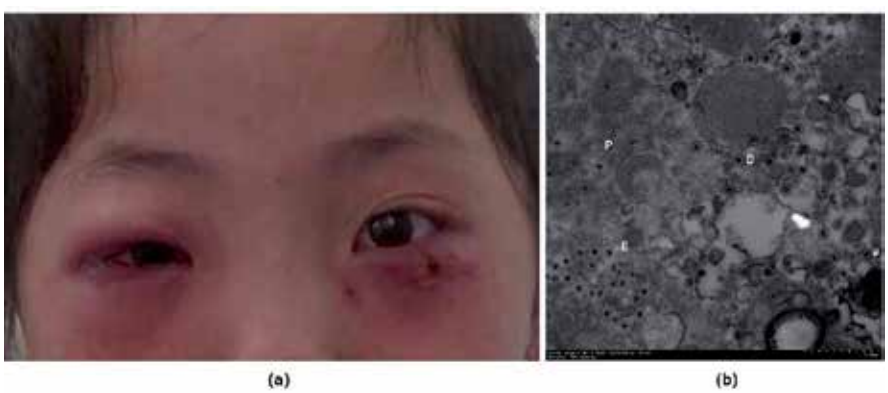

Figure 1. a. A 7-year-old girl presented at our clinic with the complainant of painful blisters and erosions on right eyelid and lower left eyelid for five days. The patient's eyelids were swollen significantly, white-like substance was observed on the right corner, the left lower eyelid was covered with brown crust. b. TEM revealed that the cellus membrane dissolved the mitochondria and the nucleus was swollen.

3.2. Herpes zoster

Herpes zoster is a viral disease characterized by a painful skin rash with erythema, papule, vesicles, or bullous in a limited area (often in a stripe) on one side of the body (left or right) [4]. The initial infection with *Varicella-zoster virus* (VZV) causes the chickenpox which generally occurs in children and young adults. The virus is then transported by retrograde axonal flow to the dorsal root ganglia, where, after further replication, latency is established. If the VZV is not eliminated from the body, it can go on to cause herpes zoster. Typical clinical manifestations and laboratory tests (VZV-specific IgM antibody, VZV DNA, electron microscopy for virus particles, etc.) can diagnose herpes zoster. Antiviral agents, analgesics, or even steroids can be used for the treatment. Rash and acute neuritis are the most common clinical manifestations of herpes zoster. Herpes zoster usually starts as erythema and papule, which change to vesicles or bullous quickly and may occasionally change to pustular or hemorrhagic in few days. Pain is the most common symptom which feels like burning, throbbing, or stabbing. The sensation can be prodromal or simultaneous. When the patient gets facial paralysis, ear pain, and vesicles in the auditory canal and auricle, it is called Ramsay Hunt syndrome. Postherpetic neuralgia is the most commonly found sequela. Severe or recurrent zoster usually happens in immunocompromised host such as patients with HIV infections or AIDS. Timely treatment can relieve symptoms and shorten the course of disease.

We describe a case of herpes zoster. The patient was a 36-year-old man who had suffered for painful vesicles for four days (Fig. 2a) on his left back and chest. The diagnosis of herpes zoster was established by the typical clinical manifestations and the numerous viruses under TEM (Fig. 2b). He was cured after taking brivudine tablet 125 mg per day for a week.

Figure 2. a. The patient was a 36-year-old man who had suffered from painful vesicles for four days on his left back and chest. b. TEM revealed that the cellus membrane dissolved. A large number of electron empty (E) and dense (D) of VZV nucleocapsids in the nucleus and these nucleocapsids were generally 100 nm in diameter.

http://dx.doi.org/10.5772/60957

3.3. Molluscum contagiosum

Molluscum contagiosum (MC) is a viral infection of the skin or occasionally of the mucous membranes, which is caused by *Molluscum contagiosum virus* (MCV, a double-stranded DNA poxvirus) [5]. Skin lesions classically present as flesh-colored papules of 3 to 5 mm in diameter with central umbilication and a white curd-like core [6]. It has a higher incidence in children, sexually active adults, and those who are immunodeficient, and the infection is most common in children aged one to ten years [7]. Various regions of the body are usually affected, plantar localization of MC is uncommon and can cause pain on walking. Secondary bacterial infection can occur, particularly if patients are scratching their lesions. Inflammatory reaction to MCV is called molluscum dermatitis, inflamed MC lesions, which can lead to reactions like Gianotti-Crosti syndrome [8]. Typical clinical appearance or laboratory tests (histology, electron microscopy, etc.) can make diagnosis definite. A vaccine for this infection is not available. Removal by curettage then topical use antiviral is widely used and effective.

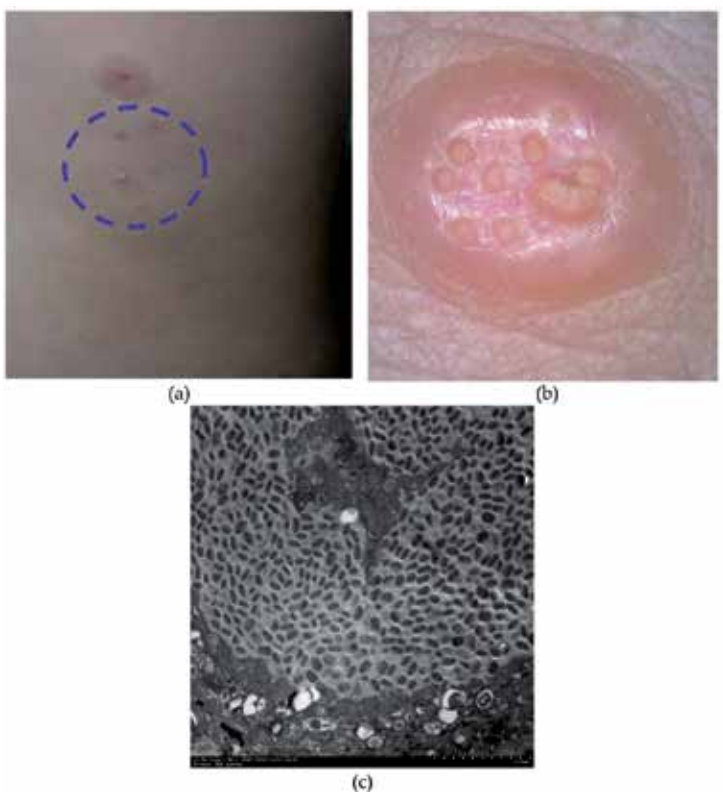

Figure 3. a. A 10-year-old boy presented at our clinic who wanted to know what the cuticolor papule on his chest was, which appeared one year before. Also, he did not feel pruritus or pain or anything else about the papule. b. Under the dermoscopy, the hemispheric papule was shiny and waxy, with several molluscum bodies on the top, just like cheese. c. TEM revealed that the cytoplasm was full of MCV nucleocapsids which were of the same size as 200 to 300 nm.

We describe a case of MC on chest. The patient was a 10-year-old boy who presented at our clinic to know what the cuticular papule on his chest was, which appeared one year before, also he did not feel pruritus or pain or anything else about the papule (Fig. 3a). Under the dermoscopy, the hemispheric papule was shiny and waxy, with several molluscum bodies on the top, just like cheese (Fig. 3b). In the TEM, the cytoplasm was full of nucleocapsids which were of the size 200 to 300 nm (Fig. 3c). The boy was cured after scraping the skin lesions and topically using 2% tincture of iodine.

3.4. Genital molluscum contagiosum

We describe a case of genital MC. The patient was a woman aged 31 years who had suffered for light pruritus papules on her vulva for nearly a week (Fig. 4a), the proximal skin of her left thigh suffered from tinea cruris. The diagnosis of genital MC was established by clinical manifestations and the numerous MCV under TEM (Fig. 4b). She was cured after removal by curettage per week and topical imiquimod cream three times a week for two weeks.

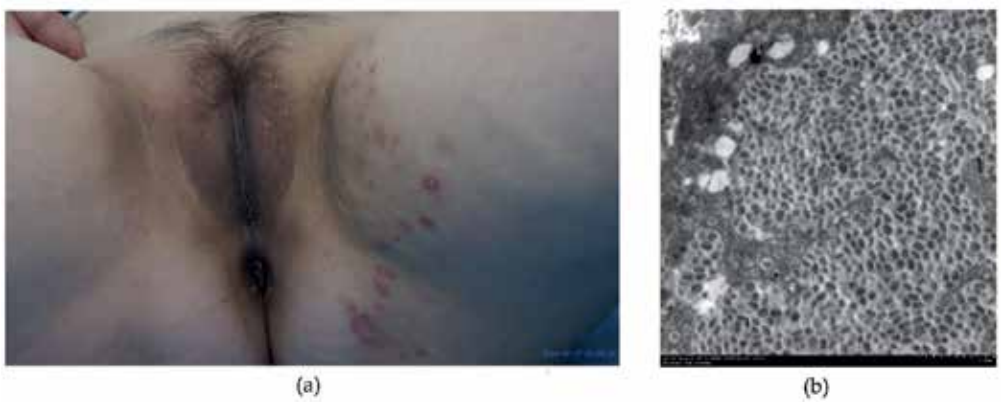

Figure 4. a. A female patient of 31 years old presented at our clinic whose vulva and pubic area had developed pruritus papules for nearly a week. Physical examination revealed the papules of 3 to 5 mm in diameter with a waxy appearance on the surface, some of which had atypical central umbilication and a white curd-like core. The proximal skin of her left thigh suffered from tinea cruris with target-like erythema and scales. b. TEM of the central waxy core revealed the strands of cytoplasmic material separating pockets of mature MCV which were generally 300 nm in length and 100 nm in height.

3.5. Leprosy

Leprosy, formerly known as Hansen's disease, is a chronic infection caused by *Mycobacterium leprae*, and mainly involves the skin and peripheral nerves. It is classified as tuberculoid (TT), borderline tuberculoid (BT), mid-borderline or borderline (BB), borderline lepromatous (BL), and lepromatous (LL), according to the cellular immunity against *M. leprae* [9]. In TT, there are few erythemas, a small number of papules, and slightly reduced sensory perception. In LL, *M. leprae* proliferate in the entire body to form lepromas, multidrug therapy including dapsone is the main treatment. The mechanism of infection has not been fully clarified. Because

http://dx.doi.org/10.5772/60957

the pathogenicity of *M. leprae* is extremely low, the natural immune response normally eliminates the infection. The incubation period is about 3 to 5 years. This makes the early diagnosis of the disease difficult. Leprosy occurs worldwide, with half of the world's (approximately 12 million) cases occurring in Asia and Africa. Skin lesions of leprosy can be single or multiple, usually hypopigmented, although occasionally reddish or copper-colored. The lesions may be macules (flat), papules (raised), or nodular. Thickened nerves are associated with leprosy and can be accompanied by loss of sensation or muscle weakness. People with leprosy often encounter discrimination. Depending on the level of disfigurement, a patient with leprosy receives varying stigma and ostracism [10].

Figure 5. a. A 64-year-old woman consulted of the lesion developed over her whole body for 2 years. Physical examination showed the facial visible invasive dark red plaques, eyebrows lose off. Dark red macules and subcutaneous nodules could be seen scattered on her trunk, limbs. b. Close look of dark red macules and subcutaneous nodules on the arms of the patient. c. A part of biopsy tissue from left waist lesion was processed for TEM studies. The arrows point to bacteria of *Mycobacterium leprae* inside the Langerhans cell. The length of the bacilli was about 2000 to 6000 nm, the width was 200 to 600 nm.

We describe a case of leprosy. A 64-year-old woman presented at our clinic with the complaint of dark red macules and subcutaneous nodule on whole body for 2 years (Figs. 5a, 5b). A part of biopsy tissue from her arm was processed for TEM studies (Fig. 5c). The patient was diagnosed with leprosy and cured with anti-leprosy therapy.

3.6. Tinea capitis

Tinea capitis is a common superficial fungal infection of scalp hair follicles, hair shaft, and, surrounding skin. It often affects children while rarely adults. Its pathogens are dermatophytes, usually species of the genera *Microsporum* and *Trichophyton,* such as *Microsporum canis*, *Trichophyton tonsurans*, *T. violaceum*, and *T. mentagraphytes* [11]. The clinical manifestation of tinea capitis is highly variable, depending on the causative organism, type of hair invasion, and degree of host inflammatory response. Common features are patchy hair loss with varying degrees of scaling and erythema. In kerion, the lesions were characterized by pustules in different sizes, which can lead to scarring alopecia. However, the clinical signs may be subtle and diagnosis can be challenging. A number of clinical patterns exist [12]. The accurate diagnosis of tinea capitis usually depends on the laboratory investigation, mainly including direct microscopic examination (DME) with 10% to 30% potassium hydroxide, and fungal culture. It can confirm the diagnosis to detect or isolate the causal organism either by these two methods. Tinea capitis always requires systemic antifungal treatment. Topical treatment is only used as adjuvant therapy to systemic antifungal agents, as topical antifungal agents do not penetrate the hair follicle. Recommended drug in systemic treatment include itraconazole, terbinafine, and griseofulvin.

We describe two cases of tinea capitis due to *T. violaceum* [13] and *T. tonsurans*. Both species of dermatophytes invade only the inner area of the hair shaft, called "endothrix." The patient suffering from tinea capitis caused by *T. violaceum* was a 9-year-old boy, weighing 25 kg presented to our clinic because of multiple, slightly itching, and patchy areas of gray scales on the scalp associated with hair loss (Fig. 6a). The diagnosis of tinea capitis caused by *T. violaceum* was established by DME, culture, and slide-culture. Under the TEM, the transected section of infected hairs revealed abundant fungus within the hair shaft (Figs. 6b, 6c). The boy was cured after receiving 4 weeks of systemic treatment with itraconazole 125 mg per day and topical treatment with 1% naftifine-0.25% ketaconazole cream once a day. Another patient was a 2-year-old girl, with scalp erythema, scaling for 2 months, and previously healthy. Dermatologic examination was as follows: several erythema, scales were visible on scalp, did not see obvious papules, pustule, and hair loss (Fig. 7a). Laboratory examination results were as follows: Hyphae were seen by DME with 10% KOH of the scales from hair. Fungal culture of hair revealed white villiform colonies which were identified as *T. tonsurans* by ITS1/4-PCR, sequence-based molecular validation. When examined through TEM, it showed many fungal spores inside the infected hair shaft (Fig. 7b). The patient was diagnosed with tinea capitis caused by *T. tonsurans*. She was prescribed itraconazole capsule 50 mg per day for 4 weeks and her clinical condition was improved.

http://dx.doi.org/10.5772/60957

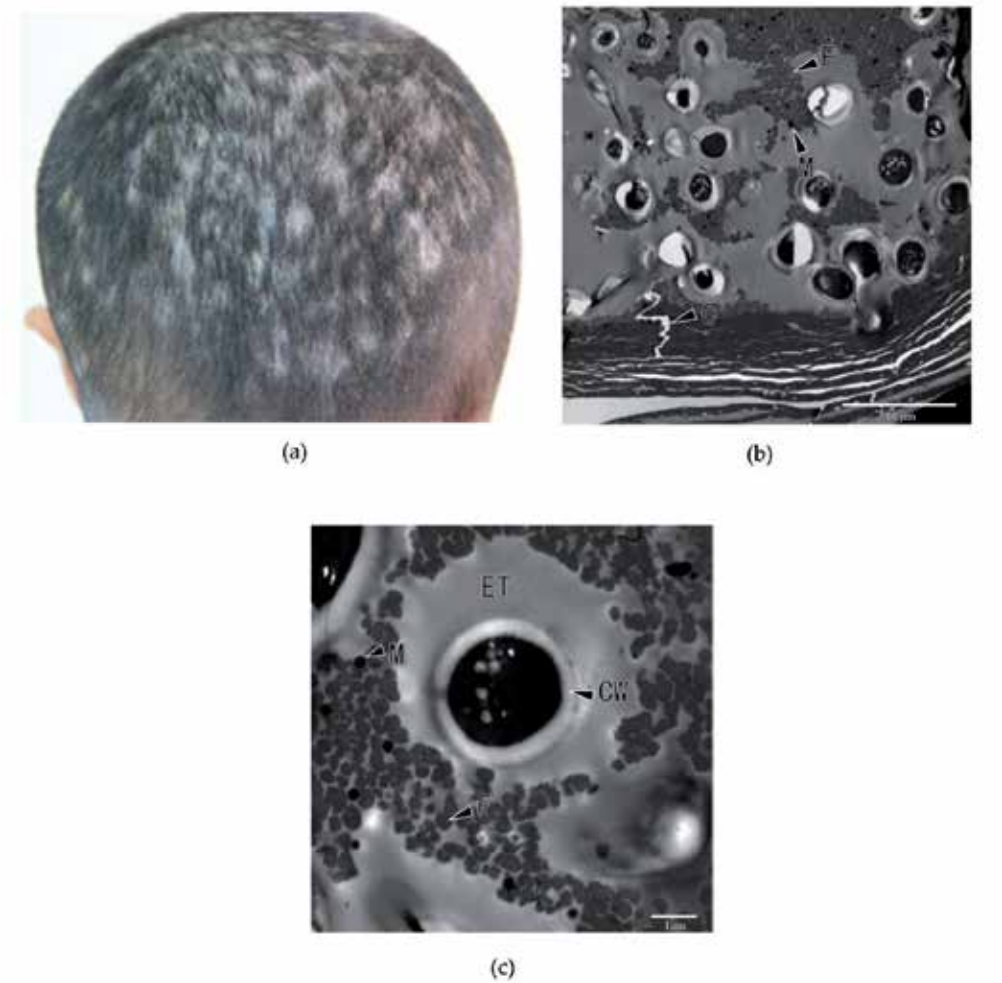

Figure 6. a. A patient with tinea capitis caused by *T. violaceum* is a 9-year-old boy, weighing 25 kg presented to our clinic because of multiple, slightly itching, and patchy areas of gray scales on the scalp associated with hair loss. b. Cross-section of the affected hairs showing abundant arthroconidias and residual keratinized fibrils (F) in which menalosomes (M) scattered, a crack (C) in the separated cuticle layer. c. High magnification of cross-section of cortex of the affected hairs: the endothrix arthrospore with cell wall (CW), electron-transparent zone (ET), residual hair-macrofibril bundles (F), and the melanin pigment particles (M).

3.7. Trichomycosis nodularis

Trichomycosis nodularis, so called as piedra, is a fungal infection of the hair shaft, which has been subclassified into white piedra (WP) and black piedra, caused by *Piedraia hortae*. WP is often caused by the *Trichosporon* genus including *T. cutaneum*, *T. asahii*, *T. mucoides*, *T. ovoides*, *T. asteroides*, and *T. inkin*, all of which belong to the class of *Basidiomycetes* [14] and can be the

Figure 7. a. A 2-year-old girl presented with erythema and scaling on her scalp for 2 months. Several erythema, scales were visible on scalp, did not see obvious papules, pustule, and hair loss. b. Cross-section of the infected hair. It shows the cortex of the affected hairs (A), the damaged fragment of hair medulla (B), and endothrix fungal spores (C).

resources of systematic infection especially to immunodeficient patients. This condition predominantly occurs in tropical and subtropical regions. Humidity, hyperhidrosis, and poor personal hygiene are important predisposing factors. The clinical appearance of WP is characterized by concretions or soft, whitish nodules on hair shaft. WP can be found in a variety of hairy areas including the scalp, beard, moustache, genitals, axilla, and even eyebrows and eyelashes [15]. The scalp lesions of white piedra are usually asymptomatic and can be misdiagnosed as pediculosis. DEM of infected hair and culture can confirm the diagnosis. In treatment, shaving off the infected hairs and topical use of antifungal agents are the paramount regime [16].

We describe a case of white piedra due to *T. inkin*. The patient was a 30-year-old African man. The dermoscopy reveals discrete yellowish concretions randomly distributed on the curly shafts of his pubic hairs (Fig. 8a). The diagnosis of WP caused by *T. inkin* was established by DME, culture, and molecular study. Under the TEM, the longitudinal section of the infected pubic hair revealed that the yellowish nodule was full of many spores. Spores were closely attached with each other with intercellular materials of cell wall, lower electronic dense vacuole, and nuclear inside the spores were noted (Fig. 8b). The patient was cured after complete shaving, clearance of pubic hairs, oral itraconazole, and topical treatment with 2% ketaconazole shampoo once a day.

3.8. Penicilliosis marneffei

Penicillium marneffei is the only dimorphic pathogenic species in the genus, making penicilliosis marneffei mainly epidemic in the Southeast Asia, which includes southern China. The patients

http://dx.doi.org/10.5772/60957

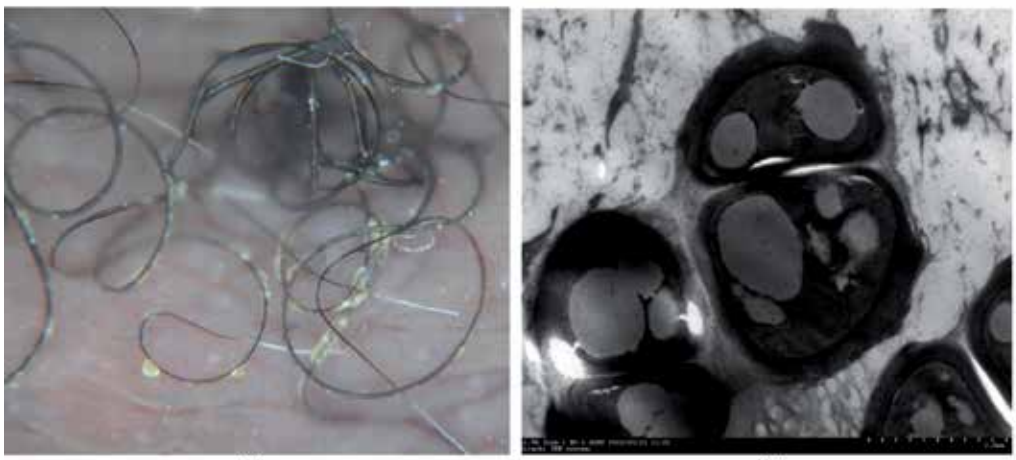

Figure 8. a. The patient is a 30-year-old African man, having uneasiness in his pubic hairs, having some dirty materials attached to them. Under the dermoscopy, some yellowish nodules attached to the shaft of pubic hairs. b. TEM revealed the internal structure of those attachments, which were full of many spores. Closely attached with each other with intercellular materials of cell wall, lower electronic dense vacuole, and nuclear inside the spores were noted.

infected with HIV/AIDS are the most common susceptible population of *P. marneffei* infection, which is the marker of screening the HIV/AIDS patients. *P. marneffei* appear at 25°C for mycelial form, and at 37°C for yeast form. The former in the culture medium can form the wine-like pigment, the latter does not. Only yeast form can be seen inside the infectious tissue. *P. marneffei* violate mononuclear phagocyte system and the main clinical manifestations were fever, anima, superficial lymphadenopathy, and hepatosplenomegaly. *P. marneffei* in host macrophages is always mostly round or oval shape, about 3 μm in diameter. The yeast cells of *P. marneffei* with septate formed during binary fission. Sometimes we can find macrophages phagocytosing yeast cells [17]. A few lymphocytes or other inflammatory cells are formed in the macrophages. When macrophages were destroyed, yeast was temporarily free from cells [18]. Drug sensitivity test *in vitro* showed that *P. marneffei* is highly sensitive to itraconazole and ketoconazole. The prognosis of patients with *P. marneffei* infection is poor. Although the use of antifungal drugs can improve the prognosis, the mortality rate has reached 20%. Research shows that, although the effect is good, there are still about 50% of patients in the initial treatment of relapse six months after remission.

We describe a case of penicillinosis marneffei. The patient was a 39-year-old man who presented at our clinic with the chief complaint of swelling in left side of the cheek for four months duration (Fig. 9a). Under the TEM, six oval-shaped phagocytosed yeast cells, within distended histocytes, were observed (Fig. 9b). Among them, the highlight for differentiating *P. marneffei* yeast from other organisms was the characteristic septum of cell (Fig. 9c). The patient was cured with taking itraconazole for 3 months.

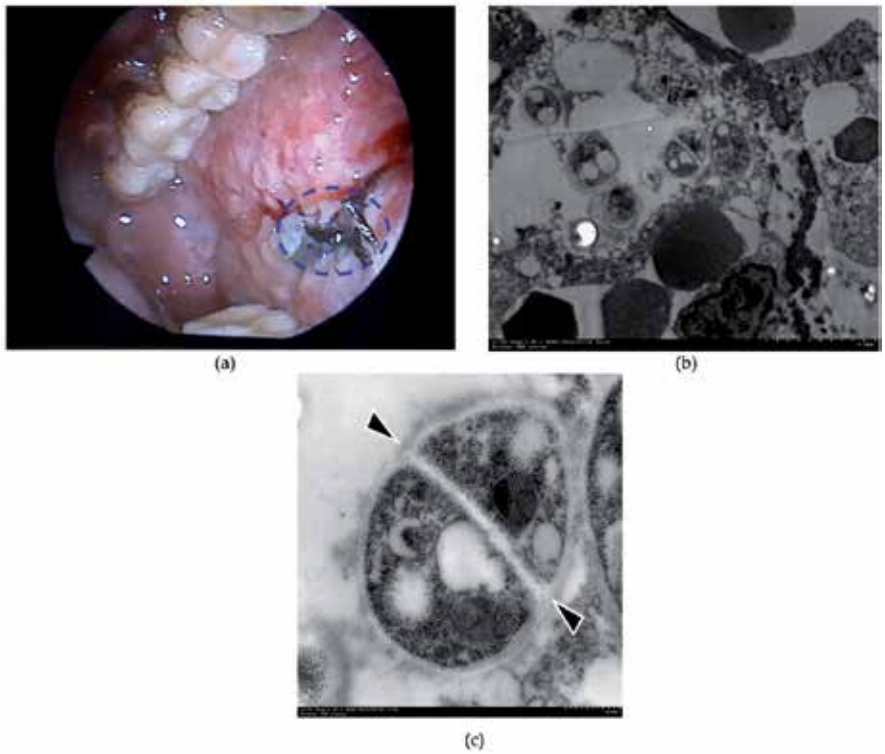

Figure 9. a. A 39-year-old man who presented at our clinic with the chief complaint of swelling in left side of the cheek for 4 months duration. Physical examination revealed a granuloma of about 3 × 4 cm^2 size on left side of oral cavity mucosa. b. TEM revealed six oval-shaped phagocytosed yeast cells within distended histocytes. c. A typical septum (arrow pointed) in the organism, which was the characteristic structure of *P. marrneffei*.

Author details

Yuping Ran[1*], Wengying Hu[1], Kaiwen Zhuang[1], Mao Lu[1], Jinghong Huang[1], Fengni Xu[1], Xiaoxi Xu[1], Xia Hua[1], Jebina Lama[1], Xin Ran[1], Yalin Dai[2] and Song Lei[3]

*Address all correspondence to: ranyuping@vip.sina.com

1 Departments of Dermatovenereology, West China Hospital, Sichuan University, Chengdu, China

2 Departments of Medical Laboratory, West China Hospital, Sichuan University, Chengdu, China

3 Departments of Pathology, West China Hospital, Sichuan University, Chengdu, China

http://dx.doi.org/10.5772/60957

References

[1] Liesegang TJ. *Herpes simplex virus* epidemiology and ocular importance. Cornea. 2001;20:1-13.

[2] Roizman B, Sears AE. *Herpes simplex viruses* and their replication. Fields Virol. 2001;2:2399-2459.

[3] Martinez V, Caumes E, Chosidow O. Treatment to prevent recurrent genital herpes. Curr Opin Infect Dis. 2008;21(1):42-48.

[4] Herpes zoster. Available at: http://en.wikipedia.org/wiki/herpes_zoster. Last updated March 9, 2015.

[5] Postlethwaite R. Molluscum contagiosum: A review. Arch Environ Health. 1970;21(3):432-452.

[6] Hanson D, Diven DG. Molluscum contagiosum. [electronic resource] Dermatol Online J. 2003;9(2).

[7] Rown J, Janniger CK, Schwartz RA, Silverberg NB. Childhood molluscum contagiosum. Int J Dermatol. 2006;45(2):93-99.

[8] Basta-Juzbašić A, Čeović R. Chancroid, lymphogranuloma venereum, granuloma inguinale, genital herpes simplex infection, and molluscum contagiosum. Clin Dermatol. 2014;32(2):290-298.

[9] Pardillo FE, Fajardo TT, Abalos RM, Scollard D, Gelber RH. Methods for the classification of leprosy for treatment purposes. Clin Infect Dis. 2007;44:1096.

[10] Leprosy. Available at: http://en.wikipedia.org/wiki/leprosy. Last updated April 9, 2015.

[11] Ellabib MS, Agaj M, Khalifa Z, Kavanagh K. *Trichophyton violaceum* is the dominant cause of tinea capitis in children in Tripoli, Libya: Results of a two year survey. Mycopathologia. 2001;153:145-147.

[12] Yu J, Li R, Bulmer G. Current topics of tinea capitis in China. Jpn J Med Mycol 2005;46:61-66.

[13] Zhuang K, Ran X, Lei S, et al. Scanning and transmission electron microscopic observation of the parasitic form of *Trichophyton violaceum* in the infected hair from tinea capitis. Scanning. 2014;36:465-470.

[14] Schwartz RA. Superficial fungal infections. Lancet. 2004;364:1173-1182.

[15] Shivaprakash MR, Singh G, Gupta P, et al. Extensive white piedra of the scalp caused by *Trichosporon inkin*: A case report and review of literature. Mycopathologia. 2011;172(6):481-486.

[16] Kiken DA, Sekaran A, Antaya RJ, et al. White piedra in children. J Am Acda Dermatol. 2006;55:956-961.

[17] Khongkunthian P, Isaratanan W, Samaranayake LP, Gelderblom HR, Reichart PA. Case Report. Oro-facial manifestations of *Penicillium marneffei* infection in a Thai patient with AIDS. Mycoses. 2002;45(9-10):411-414.

[18] Hua X, Zhang R, Yang H, Lei S, Zhang Y, Ran Y. Primary oral *Penicillium marneffei* infection diagnosed by PCR-based molecular identification and transmission electron microscopic observation from formalin-fixed paraffin-embedded tissues. Med Mycol Case Rep. 2013;2:15-18.

Chapter 11

Transmission Electron Microscopy of Platelets FROM Apheresis and Buffy-Coat-Derived Platelet Concentrates

Josef Neumüller, Adolf Ellinger and
Thomas Wagner

Additional information is available at the end of the chapter

http://dx.doi.org/10.5772/60673

Abstract

Platelet concentrates are produced in order to treat bleeding disorders. They can be provided by apheresis machines or by pooling of buffy coats from four blood donations. During their manufacturing and storage, morphological alterations of platelets occur which can be demonstrated by transmission electron microscopy. Alterations range from slight and reversible changes, such as formation of small cell protrusions and swelling of the surface-connected open canalicular system, to severe structural changes, where platelets undergo transitions from discoid to ameboid shapes as a consequence of platelet activation. These alterations end in delivery of the contents of platelet granules as well as platelet involution caused by apoptosis and necrosis processes denoted as the platelet release reaction. Hereby, the involvement of the network of the open canalicular system, helping to deliver the contents of platelet granules into the surrounding milieu via pores, is distinctly shown by electron tomography. As a consequence of platelet activation, a delivery of differently sized microparticles takes place which is thought to play an important role in the adverse reactions in some recipients of platelet concentrates. In this article, the formation and delivery of platelet microparticles is illustrated by electron tomography. Above all, the ultrastructural features of platelets and megakaryocytes are discussed in the context of the molecular characteristics of the plasma membrane and organelles including the different granules and the expression of receptors engaged in signaling during platelet activation. Starting from the knowledge of the ultrastructure of resting and activated platelets, a score classification is presented, allowing the evaluation of different activation stages in a reproducible manner. Examples of evaluations of platelet concentrates using electron microscopy are briefly reviewed. In the last part,

INTECH
open science | open minds

© 2015 The Author(s). Licensee InTech. This chapter is distributed under the terms of the Creative Commons Attribution License (http://creativecommons.org/licenses/by/3.0), which permits unrestricted use, distribution, and reproduction in any medium, provided the original work is properly cited.

experiments showing the interaction of platelets with bacteria are presented. Using the tracer ruthenium red, for staining of the plasma membrane and the open canalicular system of platelets as well as the bacterial wall, the ability of platelets to adhere and sequestrate bacteria by formation of small aggregates, but also to incorporate them into compartments of the open canalicular system which are separated from the surrounding milieu, was shown. In conclusion, electron microscopy is an appropriate tool for the investigation of the quality of platelet concentrates. It can efficiently support results on the functional state of platelets obtained by other methods such as flow cytometry and aggregometry.

Keywords: Platelet concentrates, Quality control, Platelet ultrastructure, Platelet activation, Platelet microparticles, Uptake of bacteria

1. Introduction

Platelet concentrates (PCs) are indispensable biopharmaceuticals for treatment of bleeding disorders. Indications for PC transfusions are either prophylactic, to prevent hemorrhage in oncohematology, or therapeutic, using limited platelet (PLT) transfusion to actual bleeding episodes. They are also applied to treat hematologic patients undergoing surgery and invasive procedures and disorders of PLT function, such as Glanzmann's thrombasthenia, Bernard–Soulier syndrome, Gray and White platelet syndrome, Storage Pool disease, Scott syndrome, and Disseminated Intravascular Coagulation [1]. Above all, massive PLT transfusions are indicated for treatment of Refractory Autoimmune Thrombocytopenias [2]. The short storage period of five days, where PC can be used for transfusion, reflects the high sensitivity of these cell fragments. This sensitivity is related to the high reactivity of PLTs in respect to their activation potential but also to their fragility. PCs can be produced by a variety of manufacturing processes which affect more or less the viability and reactivity of PLTs. Several publications report on this subject [3–15].

The reactivity of PLTs in the recipient of a PC can only be estimated through the recovery of the hemostatic balance. To date, no function test is adequate to reliably predict PLT behavior in vivo following transfusion [16]. A few laboratory tests available provide insufficient or conflicting results [17]. Therefore, it is obligatory in blood banking to determine the quality of the PC itself. Nevertheless, it can be assumed that irreversible PLT activation during processing would impair PLT functionality in vivo. It has been shown that activated PLTs stored for 3 days can provoke activation of T cells, B cells, and monocytes of the recipient [18]. During storage of PC, activation and release of inflammatory mediators may occur, leading to adverse effects in transfused patients after cardiac surgery [19]. Above all, the formation of platelet membrane microparticles (PMPs) contributes to the induction of adverse transfusion reactions by facilitating cell–cell interactions with cells of the recipient including signal transduction and even receptor transfer [20]. PMPs could also play a role in anaphylactic transfusion reactions [21].

http://dx.doi.org/10.5772/60673

Electron microscopy has been used to investigate the complex and highly dynamic structure of the PLT cytoplasm, including their specific organelles that are primarily formed in the megakaryocyte (MK) from which they originate.

The ultrastructure of platelets and MKs as well as highlights of their discovery are presented in Chapter 1 in the form of a historical overview. In Chapter 2, we describe the ultrastructure of MKs, PLTs in resting and activated forms, as well as PMPs using conventional fixation methods and advanced methods such as high-pressure fixation, cryosectioning, and cryosubstitution representing state-of-the-art EM techniques. In Chapter 3, we discuss where EM can efficiently support commonly used routine methods for quality assessment of PCs such as the flow cytometry and light microscopic methods or aggregometry in respect to the viability and activation of their particular PLT. In Chapter 4, results on the interaction of bacteria with platelets are presented. We discuss whether PLT are able to phagocytize bacteria or only sequestrate them by uptake into the surface-connected open canalicular system or by the formation of aggregates.

2. Ultrastructure of platelets and megakaryocytes

2.1. Historical overview

Most of the EM reports about PLT were published in the last four decades of the twentieth century starting from the early 1970s. A remarkable number of reports were published by James G. White (University of Minnesota, Minneapolis, USA), who focused in his oeuvre on the ultrastructural investigation of platelets in healthy condition [22–40] but also in several PLT-associated disorders [41–49]. Marcel Bessis (Centre Nationale de Transfusion Sanguine, Paris, France) was one of the first who investigated megakaryocytes and PLT among other blood cells ultrastructurally [50, 51]. In the following years, fine structural features of PLT have been described, such as the microtubular coil (MTC) providing the discoid shape of non-activated PLT [40, 52–60], the microfilamentous network providing their contractile apparatus [29, 53, 55, 61, 62], and the surface-connected open canalicular system (OCS). The latter represents an invagination of the plasma membrane providing a connection with the outer milieu via pores at the surface and a two-way channel for uptake of particles and the delivery of granular contents during activation and degranulation [24, 34, 35, 63–65]. Furthermore, the dense tubular system (DTS), originating from the endoplasmic reticulum of MKs [66–76] and small Golgi systems [47, 77–80], has been described. Three types of PLT granules have been identified morphologically and by histochemical and immunohistochemical methods: dense granules [22, 80], α-granules [28, 30, 58, 82–85], and lysosomes [72, 78]. Immunogold labeling allowed the identification of PLT receptors at the plasma membrane and along the invaginations of the OCS. In this way, Stenberg et al. identified the CD62P receptor (GMP-140) in unstimulated and in thrombin-activated PLTs [79]. Lewis et al. [80] showed contact sites leading to aggregated PLTs involving fibrinogen and its receptor GPIIb/IIIa via immunogold labeling of whole-mount PLT preparations and high-voltage transmission electron microscopy. In these preparations, granulomeres could be easily distinguished from hyalomeres, separated by a filamentous network. GPIIb/IIIa-positive regions could be identified at cell contacts, in the surroundings of the granulomere, as well as inside the OCS.

2.2. Megakaryocytes and the formation of platelets

For understanding the fine structural features in the function of PLTs, dynamic processes with respect to the rearrangement of organelles, above all of the membranous components, are important (Figure 1).

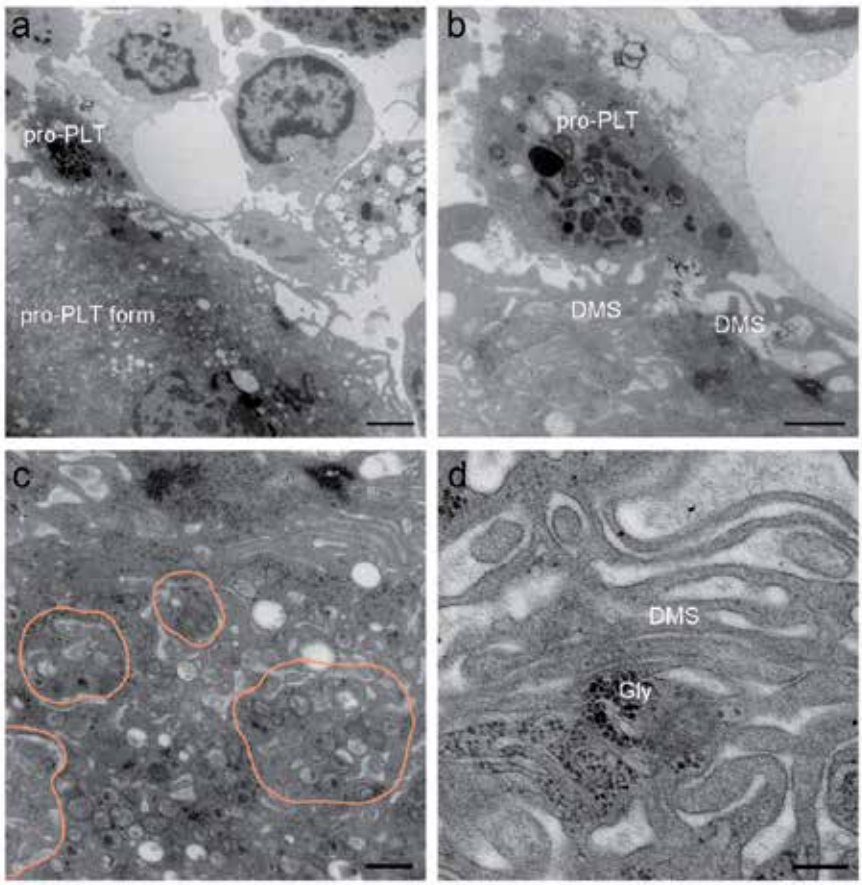

Figure 1. Aspects of an MK. In Figure 1a, the delivery of a pro-PLT is shown. The region where pro-PLT (pro-PLT form) surrounded by the DMS are formed is visible. Note the huge lobulated nucleus (N). Figure 1b: Same aspect at higher magnification. The delivered pro-PLT is still connected with a network, formed by the DMS. Figure 1c: The assembly of organelles of newly formed pro-PLTs is indicated by colored contours. Figure 1d: Pleomorphous regions of the DMS surrounding granules and glycogen aggregates (Gly). Size bars: 2 μm in Figure 1a, 1 μm in Figure 1b, 500 nm in Figure 1c,d. The samples were routinely prepared by chemical fixation, dehydration, and embedding in Epon, and 70 nm ultrathin sections were viewed under a Tecnai 20 (FEI Co.) at 80 KV acceleration voltage. Digital images were acquired using an Eagle 4k bottom-mount camera (FEI Co.).

Recently, Machlus and Italiano Jr. reviewed the development of PLTs, starting from MK development to PLT formation [81]. MKs are the rarest but also the largest cells (50–100 μm in diameter) of the bone marrow. They mature at the hematopoietic niche (osteoblastic niche) and travel to the bone marrow sinusoids (vascular niche) in order to deliver 10–20 pro-PLTs

http://dx.doi.org/10.5772/60673

into the bloodstream. The maturation process, starting from hematopoietic stem cells, is driven by thrombopoietin which binds to the MK-specific receptor MP-1 [82–84]. Under the influence of thrombopoietin, the nuclei of MKs enlarge by endomitosis, increasing their DNA content of 4n, 8n, 16n, 32n, 64n, and even 128n. Obviously, the reason for the augmentation of DNA in a single nucleus is to provide a sufficient amount of m-RNA in order to form the equipment for newly formed pro-PLTs while maintaining full functionality of the whole cell [85]. Between the lobules of the polyploid nucleus, the DMS is formed from the plasma membrane. Required membranes are provided by the Golgi apparatus via the trans-Golgi network but also by the endoplasmic reticulum [86]. Using laser confocal microscopy, electron tomography, and focused ion beam scanning electron microscopy, these authors could show that at all developmental stages of MKs, the DMS was in continuity with the PM and that the number of these connections correlated with nuclear lobulation. They propose that at early MK development stages, a PM invagination process takes place that resembles cleavage furrow formation. During MK maturation, the DMS enlarges to a conspicuous network of tubules and cisternae distributed throughout the whole cytoplasm. The DMS needs support from the cytoskeleton provided mainly by spectrin; it is essential for the formation of the PM of pro-PLTs [87].

In the terminal maturation process of MKs, long cell extensions, composed of pro-PLTs, extend into the sinusoidal vessels of the bone marrow, a process also guided by the cytoskeleton. The pro-PLT elongation is provided mainly by β1-tubulin [88]. In a later publication, this author described also a new stage of PLT formation; the pre-PLT which can convert into a barbell-like pro-PLT form, subsequently dividing into two newly formed PLTs [89].

The question how pro-PLTs can pass the wall of the bone marrow sinusoids has been elucidated by the detection of podosomes which represent micrometer-sized, highly dynamic circular protrusions of the PM of MK and other cells such as osteoclasts, macrophages, dendritic cells, and endothelial cells [90, 91]. Podosomes are adhesion domains consisting of F-actin-rich cores with integrin-associated ring structures. Typical core proteins include Arp2/3 complex, WASp, and cortactin, whereas integrins, vinculin, talin, paxillin, and myosin IIA localize to the ring structure [92]. The authors could also demonstrate that MK podosomes are able to degrade extracellular matrix using matrix metalloproteinases. EM contributed significantly to visualization and understanding of podosomes. Former publications demonstrated the actin filament arrangement in core and network [93, 94]. In more recent works, podosomes have been investigated in 3D environments [95–98] using super-resolution light microscopic techniques such as STED (stimulated emission depletion), dSTORM (direct stochastic optical reconstruction microscopy), and PALM (photoactivated localization microscopy) that complement electron microscopic capabilities.

2.3. The ultrastructure of platelets

PLTs are the smallest cellular blood components (Figure 2). They are discoid cell fragments with a remarkable equipment of dynamic organelles but lacking a nucleus. Their diameter varies between 2 and 3 μm, but their thickness is only less than 1 μm. In human peripheral blood, the absolute number of PLT ranges from 150,000 to 450,000 per ml. The average lifetime in the circulation is 5 to 11 days. After this time, they become degraded in the spleen but also in the liver and in the lung.

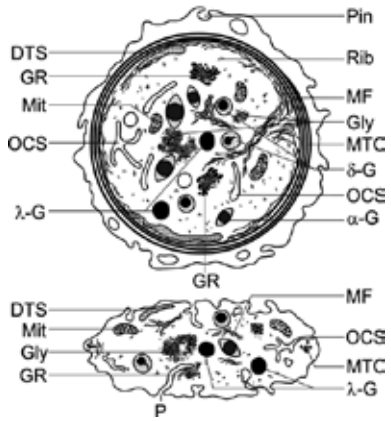

Figure 2. A scheme of a PLT in the equatorial plane (upper image) and in cross section (image at the bottom). Abbreviations: DTS *dense tubular system*, Gly *glycogen*, α *α-granules*, δ *δ-granules or dense bodies*, λ *λ-granules or lysosomes*, GR *Golgi remnants*, MF *microfilaments*, Mit *Mitochondria*, OCS *open canalicular system*, P *pores of the OCS*, Rib *ribosomes*.

PLTs circulate under normal health conditions in a quiescent discoid stage that is maintained by the anti-homeostatic properties of the endothelium that lines the inner wall of the entire vasculature. After vessels are injured due to trauma or pathological conditions such as atherosclerosis and diabetes, where a degeneration of endothelium takes place, PLTs become activated and change their shape dramatically acquiring an ameboid form due to the rearrangement of organelles, triggered by microtubules and microfilaments.

An ongoing activation takes place if PLTs adhere to a glass surface. After a few minutes, a characteristic compartmentalization in a dense central granulomere and a peripheral lucent hyalomere can be seen already under the light microscope (Figure 3).

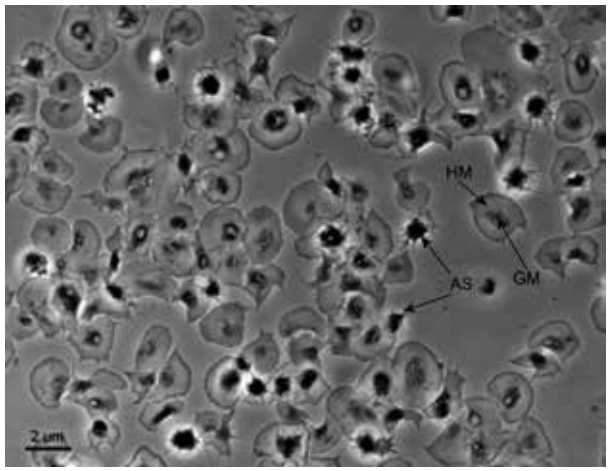

Figure 3. Light microscopic picture of glass-adherent PLTs, incubated for 15 min in phosphate buffered saline. Hyalomere (HM) and granulomere (GM) are clearly visible. Some adherent PLTs show an ameboid shape (AS) as a sign of activation.

http://dx.doi.org/10.5772/60673

In TEM, the granulomere is surrounded by a contractile ring of cytoskeleton elements. The granulomere contains not only different species of granules but also parts of the surface-connected OCS, mitochondria, and glycogen. Parts of the DTS line the marginal cytoskeletal ring (Figure 4b). Resting discoid PLTs contain a peripheral stabilizing microtubular ring built up of β-tubulin (Figure 4a). This ring represents a circumferential MTC consisting of one microtubule wound 8–12 times stabilizing the PLT shape. During PLT activation, the MTC is primary contracted and then fragmented and dislocated to the newly formed filopodia.

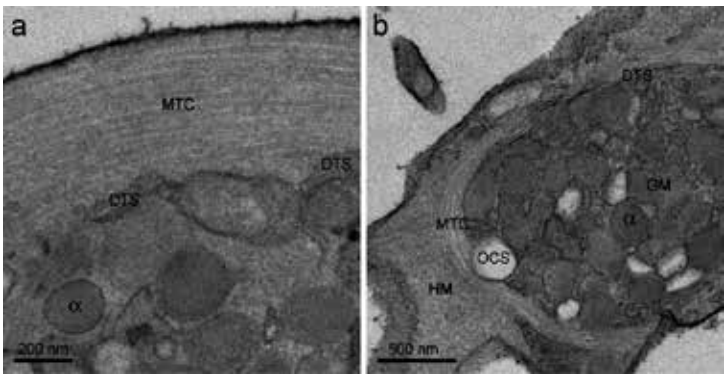

Figure 4. TEM of glass-adherent PLTs, fixed for 5 min (a) and 15 min (b) after incubation. Figure 4a shows the MTC and in close vicinity the DTS. In Figure 4b, hyalomere and granulomere appear separated by the MTC and can be clearly distinguished. Abbreviations as in Figure 2.

The DTS triggers the resting stage as well as the transition into the activation process of PLTs. It originates from the rough endoplasmic reticulum of MK. It has an irregular form, and in resting PLTs, it is located close to the MTC. Its peroxidase content allows to contrast it via a diaminobenzidine reaction. In contrast to the OCS, it contains slightly electron-dense amorphous material. Lipid-modifying enzymes such as cyclooxygenase and thromboxane synthetase catalyze downstream metabolites of the arachidonic acid degradation pathway and the delivery of thromboxane into the extracellular milieu. The PLT activation is regulated by the maintenance of calcium storage which is controlled by the action of a membrane-associated pump (sarcoplasmic reticulum Ca^{2+} ATPase) and by the action of the second messenger cAMP that initiates the delivery of Ca^{++} into the cytosol inducing PLT activation.

As mentioned above, PLTs are interlaminated by the OCS originating from the DMS of MKs and are connected as well with the outer milieu via pores (Figure 5).

The cytoplasm contains α-, δ-, and λ-granules and the dense tubular system which derives from the endoplasmic reticulum of MKs. Ribosomes and polyribosomes as well as few mitochondria are also present as equipment remaining from MKs. PLTs also contain often a high number of accumulated glycogen granules.

alpha-granules contain proteoglycans, hemostasis factors and cofactors (fibrinogen, factors V, VII, XI, and XIII, kininogens, protein S, and plasminogen), adhesive matrix proteins (fibronectin (FN), vitronectin (VN), thrombospondin (TSP), von Willebrand factor (vWF), adhesion

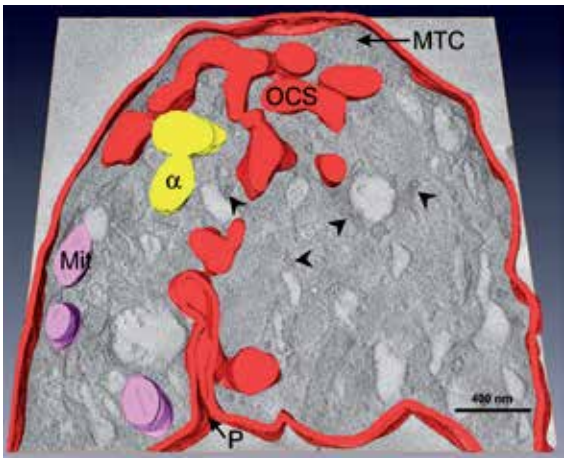

Figure 5. Electron tomographic 3D model of the OCS showing a pore (P) connecting it with the surrounding milieu. The DTS is indicated by arrowheads. One virtual slice is shown in background. The electron tomographic acquisition was performed on a Tecnai 20 (FEI Co., Eindhoven, The Netherlands). Using 200 nm semithin sections, tilt series were started from –65 ° to +65 ° with 1 ° increment by the help of the Xplore3D software (FEI Co.). Reconstruction of the tilt series was performed with the IMOD software (Boulder Laboratories, University of Colorado). The model was drawn using the Amira 4.1 software (Mercury Computer Systems, Merignac, Cedex, France). For abbreviations, see Figure 2.

molecules such as GP140 (CD62P), cytokines and chemokines like RANTES and interleukin 8, as well as several growth factors: TGF-β (transforming growth factor-β), PDGF (platelet-derived growth factor), ECGF (platelet-derived endothelial growth factor), VEGF (vascular endothelial growth factor), bFGF (basic fibroblast growth factor), EGF (epidermal growth factor), and IGF (insulin-like growth factor). In addition, protease inhibitors, albumin and immunoglobulins are stored in α-granules.

Dense granules (δ-granules) are the smallest ones with a diameter of about 150 nm. Their name is related to their strongly electron-dense core, surrounded by a clear space enclosed by a single membrane. These organelles develop in early MKs where they look primarily empty, acquiring their dense core by incorporation of adenine nucleotides and serotonin during maturation. They contain a metabolic inert adenine nucleotide pool and store serotonin at concentrations of about 65 mM. In addition, they contain a high amount of bivalent cations—predominantly calcium—that is not mobilized in the course of PLT activation.

Lysosomes (λ-granules) exhibit a lower electron density than δ-granules. They contain lysosomal enzymes playing a role in clot formation but also in antibacterial defense such as acid proteases and glycoproteases. The lysosomal membrane contains the integral membrane protein LIMP (CD63) which is transferred to the plasma membrane during PLT activation as well as the two membrane-associated glycoproteins LAMP-1 and LAMP-2. CD63 is used as a PLT activation marker and can be routinely demonstrated by flow cytometry using fluorolabeled monoclonal antibodies.

The ultrastructure of PLTs as well as the release reaction of granule contents during PLT activation has been summarized in an excellent review [72].

http://dx.doi.org/10.5772/60673

In the past two decades, new methodical and technical developments, such as cryofixation combined with freeze substitution, were applied for the investigation of PLT morphology, avoiding the problems of chemical fixation-dependent artifacts. In addition, the implementation of electron tomography allowed a better understanding of the three-dimensional architecture of PLT organelles. In this respect, many views about cytoskeleton and the internal structure of granules had to be revised [99]. It could be impressively demonstrated that the OCS and the DTS are highly intertwined, forming close associations in specialized membrane regions. These authors discerned three subtypes of α-granules based on morphological features: first, spherical granules with an electron-dense and electron-lucent zone containing microtubules built up of vWF multimerin elements and a diameter of 12 nm; a second type containing a multitude of luminal vesicles, 50 nm wide tubular organelles; and a third population with 18.4 nm crystalline cross striations. Using electron tomography, the authors could impressively reveal the spatial arrangement of these organelles.

The plasma membrane is the site where a multitude of receptors is present that can interact with soluble ligands, with cellular counter receptors on other PLTs, on leucocytes, or on endothelial cells, with molecules of the extracellular matrix but also with pathogens. These receptors play an important role in inside–outside signaling in the course of PLT activation and the release reaction. As outlined in a review by Rivera et al. in 2009 [100], many types of mobile transmembrane receptors are present at the PLT membrane, including many integrins (αIIbβ3, α2β1, α5β1, α6β1, αVβ3), leucine-rich repeat (LRR) receptors (glycoprotein [GP] Ib/IX/V, toll-like receptors), G-protein coupled seven-transmembrane receptors (GPCR) (PAR-1 and PAR-4, thrombin receptors, P2Y1 and P2Y12 ADP receptors, TPα and TPβ (TxA2 receptors), proteins belonging to the immunoglobulin superfamily (GP VI, FcγRIIA), C-type lectin receptors (P-selectin), tyrosine kinase receptors (thrombopoietin receptor, Gas-6, ephrins, and Eph kinases), and a miscellaneous of other types (CD63, CD36, P-selectin glycoprotein ligand 1, TNF receptor type, etc.). Many of these receptors have been characterized using immune electron microscopy [30, 33, 73, 74, 79, 80].

New methods have been developed allowing to share the results from biochemistry, laser confocal microscopy, and EM to explain the different steps in PLT activation starting from Ca^{++} mobilization of the dense tubular system, the degranulation process of dense granules followed by the delivery of the contents of α-granules and lysosomes via docking and fusion of the membranes of granules with the membrane of the OCS using the SNARE machinery [101].

2.4. Platelet activation and the release reaction

By EM, PLT changes and signs of activation due to preparatory influences can precisely be determined and classified. Canizares and coworkers [61] showed the different steps of PLT activation in detail. Their classifications include six stages: (1) the unaltered discoid form; (2) the pseudotubular form (very slight activation) when the peripheral MTC disappears, a pseudotubular membranous structure occurs, and the OCS increases; (3) the membranous form (slight activation) characterized by pseudomyelinic structures; (4) the saccular stage (moderate activation) showing an ameboid PLT shape and saccular–tubular reorganizations

of the OCS and the onset of degranulation; (5) the pseudopodical stage (strong activation) showing numerous cell projections containing prominent microfibrils present mainly in the periphery of PLTs. In this stage, the degranulation is already completed; (6) the hyaline stage refers to the end of the activation process, where shadows of granules and "obscure fibrillar" structures are visible.

Former concepts describing the dynamics of the MTC have to be revised. It can be demonstrated that after exposure of PLTs to agonists, the MTC remains intact. In the course of activation, the MTC becomes constricted into tight rings around centrally concentrated granules. During the process of irreversible aggregation and clot retraction, the MTC disintegrate, and groups of individual polymers appear in pseudopods or are oriented in the long axis of the PLTs. It has been shown that the MTC consists of a single polymer that is wound in 8–12 coils in the periphery of the cytoplasm [63, 64]. However, three-dimensional cryoelectron tomographic reconstructions of individually traced microtubules showed that some circumferential microtubules end at OCS invaginations. They are sometimes incomplete and occasionally reveal interconnections [65]. The release reaction implicates the fusion of granules with the OCS where they disintegrate. The fusion event is not easily followed by TEM. In our image (Figure 6), such a fusion could be demonstrated using rapid cryofixation followed by cryosubstitution.

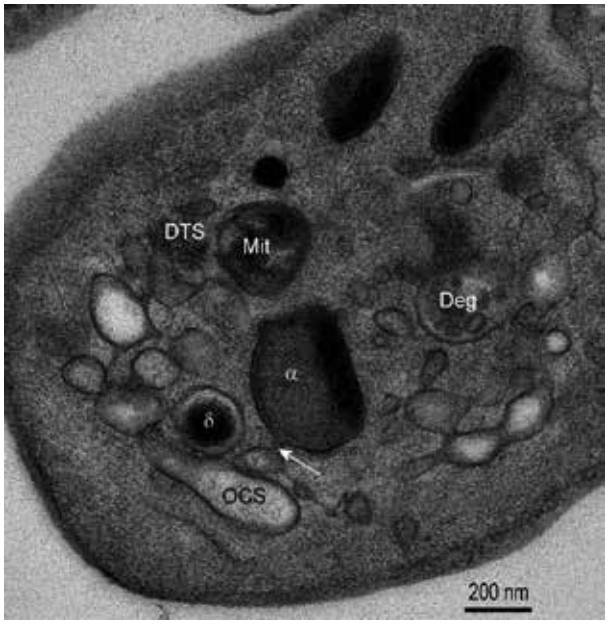

Figure 6. PLT showing the delivery of α-granules content into the OCS. Preparation by high-pressure fixation and cryosubstitution into Epon. PLTs from an apheresis PC were sucked into cellulose tubes that were closed at both ends and subjected to high-pressure fixation. 70 nm ultrathin sections were viewed under a Tecnai 20 electron microscope, and digital images were acquired using an Eagle 4k bottom-mount camera (FEI Co.). The connection between an α-granule and the OCS is indicated by the arrow. Abbreviations as in Figure 2.

http://dx.doi.org/10.5772/60673

2.5. Platelet Microparticles (PMP)

Among other cells such as endothelial and immune cells, PLTs are able to form PMPs which play a pivotal role in immunology and vascular biology. These particles are thought to be of significant clinical relevance as they can bind to and interact with macrophages, neutrophil granulocytes, and endothelial cells [102, 103]. They were first described already in 1967 by Wolf et al. [104]. PLTs form two types of PMPs differing in size and molecular composition [105]. One type is relatively large with diameters ranging from 100 nm to 1 μm expressing $GP\alpha_{IIb}$-β_3, GPIbα, and CD62P and exhibiting the apoptosis marker phosphatidylserine at the plasma membrane. Therefore, they can be identified via binding of annexin V. The second type of PMPs, corresponding to ectosomes, is smaller than 100 nm and expresses CD63, a membrane-spanning protein, present on α-granules which is translocated to the PM during PLT activation [106, 107]. They interact poorly only weakly with annexin V, do not bind prothrombin and factor X, and therefore have probably no coagulation function [108]. Among others [109], these authors separated PMPs by differential centrifugation in order to remove red and white blood cells as well as PLT followed by ultracentrifugation. PMPs, present in PLT-free plasma, were absorbed to filmed EM grids and investigated in the TEM after negative staining [108, 109]. Other groups investigated pellets of PMP, embedded in epoxy resin [106, 107].

In our own studies, pelleted PMPs were trapped in alginate beads, classically embedded, thin sectioned, and viewed under a TEM (Figure 7).

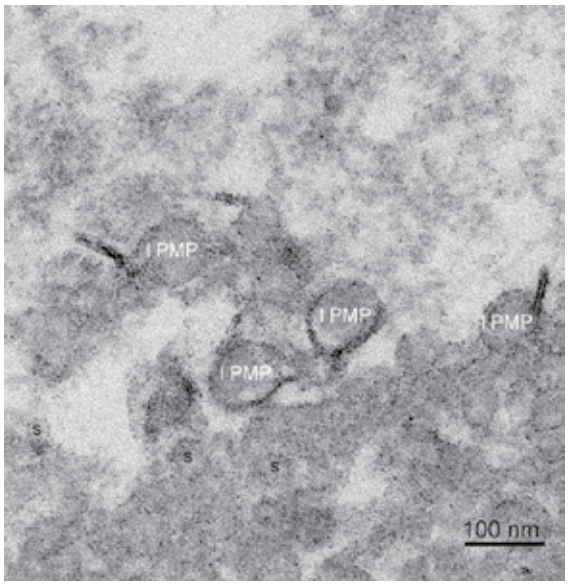

Figure 7. PMPs embedded in alginate beads. Larger PMPs (l PMP) ≥ 100 nm and aggregated small PMPs could be distinguished. Chemical fixation, dehydration, and embedding in Epon. 70 nm ultrathin sections were viewed under a Tecnai 20 electron microscope, and digital images were acquired using an Eagle 4k bottom-mount camera (FEI Co.).

We were able to visualize the formation of PMPs on glass-adherent PLTs. TEM images showed that small vesicular elements developed in a protrusion of a PLT. A close association of these

tightly packed vesicles with the DTS could be observed. The formation of such a multivesicular sphere and its delivery from the PLT is shown after using electron tomographic reconstruction. We suggest that microvesicles are delivered from this harboring ball-like structure (Figure 8).

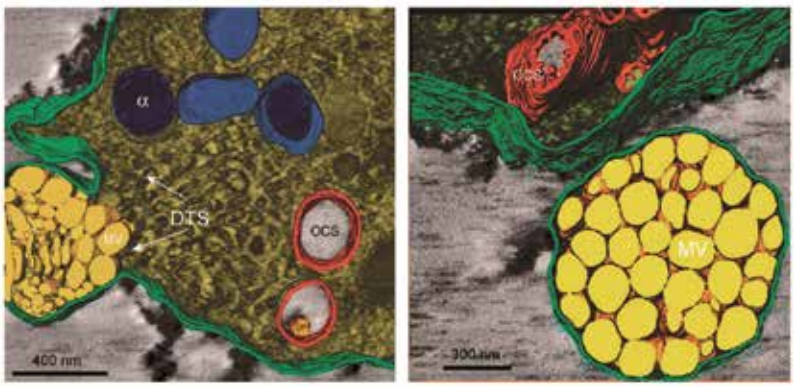

Figure 8. Formation of PLT protrusions containing microvesicles, demonstrated in an electron tomographic 3D model. Figure 8a shows the formation of a sac, filled with microvesicles; Figure 8b its delivery. Chemical fixation, dehydration, and embedding in Epon. 70 nm ultrathin sections were viewed under a Tecnai 20 electron microscope, and digital images were acquired using an Eagle 4k bottom-mount camera (FEI Co.).

3. Ultrastructural evaluation of PLT activation using TEM is suitable to monitor PC production

3.1. Production of PC

PCs can be produced by apheresis machines or by pooling of buffy coats obtained from whole blood donations. There is a long-lasting and long-winded discussion about the advantages and disadvantages of both methods [110]. To produce PC by apheresis, blood from a healthy donor is collected and subjected to centrifugation in an apheresis device, where blood cells are separated according to their density. Blood cells, with exception of PLTs, are reinfused. The technical features of the most common apheresis machines differ significantly with respect to stress on PLTs such as centrifugation and shear forces and their duration. In addition, the degree of contamination with residual leukocytes depends on the particular machine. Sometimes, apheresis machines produce higher leukocyte rates and have to be filtered using a leukocyte depletion filter to avoid side effects and complications in the recipient.

Buffy-coat-derived PCs are produced by two-step centrifugation method. Whole blood is collected into triple bags containing CPD in the primary bag and centrifuged at 4000 × *g* for 10 min at 22 °C within 12 h. Red blood cells and plasma are separated from the buffy coat fraction and transferred into satellite containers by using an automated separator. Subsequently, buffy coats from four different donors and one bag containing either 300 ml plasma from one of the four donors or PLT additive solution are connected by using a sterile connection device and

http://dx.doi.org/10.5772/60673

were pooled in one container. Subsequently a 1 l polyolefin bag and a leukocyte reduction filter are connected. This pool is then centrifuged at 500 × *g* for 8 min at 22 °C. The supernatant is squeezed out immediately into the storage bag by means of a plasma extractor [111].

PCs are stored in gas-permeable plastic bags for 5–7 days. In our experience, all manufacturing processes induce a slight PLT activation which might be also reversible. With lasting storage time, dead PLTs caused by necrosis but also by apoptosis [112–114] occur. Early stages of apoptosis can be detected by binding of annexin V to the exposed phosphatidylserine of the plasma membrane. At the ultrastructural level, this can be visualized by binding of a complex, consisting of annexin V, a specific antibody, and gold-labeled protein A to the PLT surface [115]. In late stages of apoptosis and necrosis, the PLT fine structure is then characterized by the loss in the integrity of membranes and by extraction of the cytoplasm that contains remnants of granules and cytoskeleton.

In a recent publication [111], we described a method to evaluate the alterations of PLTs at a single cell level. The method can be carried out easily in routine EM laboratories. A pre-fixation of PCs was done by mixing 9 ml PC with 1 ml of a 10 % buffered formaldehyde solution (BD CellFIX™, Becton Dickinson, Vienna, Austria) in order to avoid shape changes of PLT by the subsequent preparation steps. Immediately after pre-fixation, the samples were centrifuged at 800 x g for 10 min at 22 °C. After discarding the supernatant, the pellet was fixed with 10 ml of 2.5 % glutaraldehyde (Fluka, Vienna, Austria) in cacodylate buffer, pH 7.2, for 90 min at 4 °C. After fixation, the PLTs were washed twice by centrifugation at 800 x g for 10 min at 4 °C, transferred to 2 ml Eppendorf vials (Eppendorf AG, Hamburg, Germany), pelleted again, and fixed with 1 % O_sO_4 (Fluka) for 90 min, dehydrated in a graded series of ethanol (50, 70, 90, 96 and 100 %) and embedded in Epon (Serva, Heidelberg, Germany). Sections (70–80 nm) of Epon-embedded cells were cut with an UltraCut UCT ultramicrotome (Leica Inc., Vienna, Austria), transferred to copper grids, and routinely stained with uranyl acetate and lead citrate. The sections were viewed either under an EM900 transmission electron microscope (Carl Zeiss, Oberkochen, Germany), equipped with a 1k wide angle slow-scan CCD camera, allowing distortion-free images for photomontages (Tröndle, Munich, Germany) at 50 kV or under a Tecnai 20 transmission electron microscope (FEI Co., Eindhoven, The Netherlands) and a 1k slow-scan bottom-mount CCD camera (MSC 794, Gatan Inc., Pleasanton, CA, USA) at 80 kV. The panorama views consisting of eight single digital images at a magnification of 3000x providing a resolution of about 3700 x 1800 pixels.

- Score 0: unchanged discoid form showing the peripheral MTC in the equatorial plane (Figure 9a) or in the cross section (Figure 9 b)
- Score 1: formation of filopodia and dilatation of the OCS (Figure 9c)
- Score 2: pronounced shape alterations, centralization of the MTC and proceeding degranulation (white arrows; Figure 9d)
- Score 3: degeneration with alteration of the plasma membrane and necrosis (Figure 9e)
- In addition, also the formation of aggregates can be visualized (Figure 9f). Note that PLTs in the center of the aggregate are degranulated. All PLTs are connected among each other by interdigitating filopodia

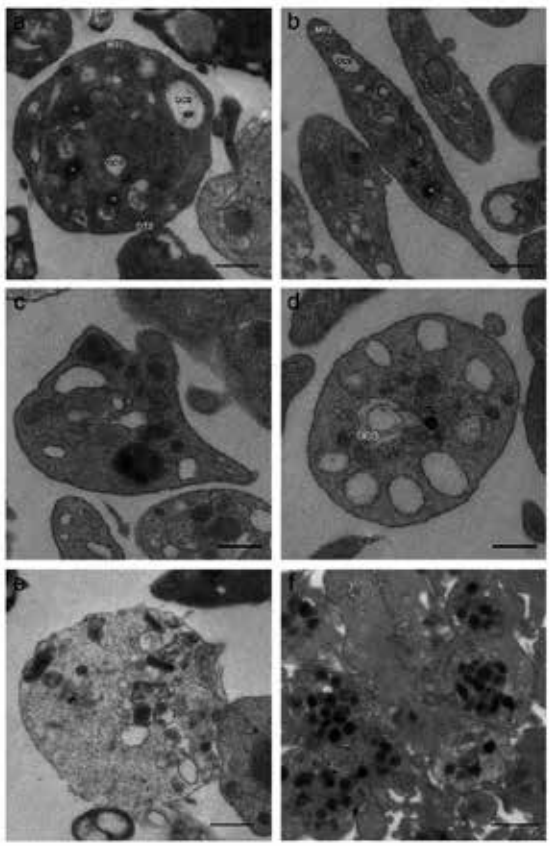

Figure 9. Stages of activation and degeneration of PLTs. The morphological evaluation of PLTs in TEM panorama views is based on a score classification of the individual PLT according to the following criteria:

Size bars: 500 nm in Figure 1a–e, 1 μm in Figure 1f. The samples were routinely prepared by chemical fixation, dehydration, and embedding in Epon, and 70 nm ultrathin sections were viewed under a Tecnai 20 (FEI Co.) at 80 KV acceleration voltage. Digital images were acquired using an Eagle 4k bottom-mount camera (FEI Co.).

PLTs representing a particular score value were counted using the analySIS® morphometry software (Soft Imaging System, Münster, Germany). The score values can be used for statistics comparing different processing methods using parameter-free rank tests.

The advantage of our score classification consists in the registration of alterations and different activation stages of PLT caused by the manipulations during production of PCs. It can distinguish between slight and advanced PLT activation. In addition, the presence of PLT aggregates is included in the evaluation. Nevertheless, one has to ignore PLTs that are only marginally sectioned, since in that case no appropriate evaluation is possible. The assembled images of the photomontages allow further zooming and a detailed analysis of subcellular features. The MTC and its centralization during PLT activation are only visible in equatorial

http://dx.doi.org/10.5772/60673

sections or in some cross sections. Early changes occur as strong dilatation of the OCS and formation of surface projections, while strongly activated PLTs show distinct signs of degranulation and frequently a budding of microparticles and ectosomes.

3.2. Examples on how EM can and has been applied for quality control of PC

EM can be used to examine PLT morphology in relation to different preparation and storage methods. Integrity as well as activation stages can be immediately monitored at single cell level. Further functional aspects can be investigated with automatized analytic systems such as flow cytometry, aggregometry turbometry, etc. The impact of the contribution of EM has already been pointed out by White and Krumwiede [116]. In this paper, the authors summarize the morphological features of PLTs and organelles such as MTC, α-granules, and the dense bodies in PLTs of healthy donors and patients suffering from the Hermansky–Pudlak syndrome and storage pool deficiency disorders as well as giant PLT diseases such as the white and the gray PLT syndrome. Another publication [117] describes the ultrastructural evaluation of PC function after intermittent-flow centrifugation apheresis collected from donors by combined platelet-leukapheresis with hydroxyethyl starch or by plateletpheresis without starch. The authors found that the PLT morphology was almost unchanged with the exception of glycogen granules being absent in PLTs isolated in presence of hydroxyethyl starch. They concluded that the starch did not significantly alter PLT morphology and PLT aggregation.

Forced by the occurrence of bovine spongiform encephalopathies (BSE), caused by prion infections in the United Kingdom and other countries in the 1990s of the last century, a better surveillance of blood donations and methods for the production of blood components has been introduced in most European countries [118]. In the course of these improvements, leucodepletion or better leukoreduction methods have been introduced as a new standard in blood banking. Even if it is unlikely that prions can be removed by leukoreduction, this procedure is able to prevent many side effects caused by unwanted cytokine release during storage. In this context some publications deal with the quality of PLTs after removal of white blood cells (WBCs). Using EM, no significant PLT alterations were found in surface modified polyester filters [119], in the filtration system (PL100) [120], as well as by using of the Sepacell PL system [121]. Similar results were obtained from prestorage WBC reduction filters designed for leukocyte depletion during the preparation of the pool PC from platelet-rich buffy coats [122]. Interestingly, in filters of WBC-depleted red blood cell concentrates, granulocyte depletion occurred also by indirect adhesion to activated and spread PLTs [123, 124].

Most of the authors, using EM to investigate PLT vitality, refer to the influence of storage conditions on the morphological appearance of PLTs [12, 68, 125–130]. Lactate accumulation may cause a pH fall in PC leading to a reduction of organelles and a progredient destruction of cell membranes [12, 126]. Storage of buffy-coat-derived PCs can be affected by the presence of residual WBCs [68] or due to additive solutions, partially replacing plasma. These solutions provoke increasing PLT activation and increasing chemokine release during storage [127]. Elias et al. described that a good maintenance of PLT ultrastructure could be achieved by adding a stable synthetic prostacyclin analogue (Iloprost) to the PC [128]. The chemical composition of storage bags can modify the adhesion of mononuclear cells to the plastic

substrate of the PLT storage bag and the release of cytokines. Bags composed of the polyolefin polymer induce a higher release of IL-1β, TNF-α, IL-6, and IL-8 compared to the single-donor apheresis polyvinyl chloride polymer platelet bags with the tri-(2-ethylhexyl) trimellitate (TEHTM) plasticizer. A similar study was carried out using polyvinyl chloride containers plasticized with tri(2-ethylhexyl) trimellitate (PL 1240 plastic) [129]. Even using the most advanced storage conditions, the quality of PLTs in PCs decreases significantly with storage time [127]. For this effect, the high storage temperature of 20 °C as well as a progressive loss of nutrients in the storage plasma or in the platelet additive solution as well as the accumulation of toxic metabolites can be taken into consideration. In our experience, the PLT activation is only slightly enhanced during storage time, while the percentage of necrotic PLTs increases significantly. In this respect, usually PCs are stored not longer than 5 days.

Ahnadi et al. [130] measured the ex vivo (basal) and in vitro (thrombin-induced) PLT activation in sodium citrate, ethylenediaminetetraacetic acid (EDTA), and citrate-theophylline-adenosine-dipyridamol (CTAD) in whole blood specimens. TEM studies verified shape modifications and simultaneous retention of granules at early post-venipuncture time periods in CTAD specimens.

Transfusion of washed PLTs is recommended for patients with history of allergic reactions. This procedure, commonly performed using neutral, calcium-free Ringer's acetate (NRA) can be performed before (prewash) or after storage of PC. Comparing the procedures, Kelley et al. [131] could not find any fine structural alterations even when the postwash procedure was carried out only after 6–7 days of storage. In addition, it could be demonstrated that the chemical structure of storage bags may induce cytokine release leading to alteration of PLT shape as demonstrated via SEM [132].

Some publications refer to the quality of chilled, frozen, or even lyophilized PLT. It has been demonstrated that long-term storage of fixed and lyophilized platelets that retain hemostatic properties after rehydration showed a rather normal ultrastructure [133]. Another option to increase the storage time is the cryopreservation of human PLTs. It has been shown that controlled-rate freezing procedure in combination with lower (6 %) Dimethylsulfoxide (DMSO) concentration resulted in less damage from freezing and higher recovered function of PLTs as revealed by light and electron microscopic parameters [134]. In contrast, Böck et al. observed clear signs of beginning cell necrosis after thawing and resuspension in autologous plasma [135].

An interesting field for EM investigations is the quality control of PC after pathogen inactivation and storage of pathogen-inactivated PCs. Advantages and controversies about this approach including the different techniques have been summarized in [136, 137]. Ultrastructural investigations are not available on this subject so far.

3.3. Interaction of PLTs with bacteria

PCs are stored at room temperature to avoid aggregation and injury of the plasma membrane. Therefore, problems of bacterial contamination and proliferation are increased. An estimation for bacterial contamination in the United States indicates that 1:1000–1:3000 of PCs leads to

http://dx.doi.org/10.5772/60673

severe life threatening complications in 1 out of 6 patients [138]. In contaminated PCs, the following kinds of bacteria could be detected: *Clostridium perfringens*, *Enterobacter cloacae*, *Escherichia coli*, *Flavobacterium* spp., *Klebsiella oxytoca*, *Propionibacterium acnes*, *Salmonella choleraesuis*, *Salmonella enterica* serotype enteritidis, *Salmonella enterica* serotype Heidelberg, *Serratia marcescens*, *Staphylococcus aureus*, *methicillin-resistant Staphylococcus aureus* (MRSA), *Staphylococcus carnosus*, *Staphylococcus epidermidis*, *Staphylococcus lugdunensis*, *Staphylococcus* spp. coagulase negative, *Streptococcus pneumoniae*, *Streptococcus pyogenes*, *Streptococcus viridans*, *Yersinia enterocolitica* serotype O:3. Bacterial contaminations can be caused by failures in blood drawing (mainly by insufficient disinfection of donor's skin), by leak plastic tubes, or the donor carries bacteria in his/her blood without clinical symptoms.

There exist different opinions about the ability of PLTs to kill bacteria. Even in some cases, PLTs exhibit adverse reactions for the host by transporting bacteria from the site of infection to another place in the circulation where they adhere and cause injury [139]. Nevertheless, as outlined in this review, PLTs are equipped with cell surface receptors reacting directly or indirectly with counter receptors and molecules at the bacterial wall. Among these PLT receptors, the fibrinogen receptor GPIIb/IIIa, the von Willebrand factor receptor GPIbα, the Fc receptor FcγRIIα, complement receptors, and toll-like receptors TLRs (belonging to the innate immune receptors) are functional. Indirect binding is mediated by fibrinogen, von Willebrand factor, complement, and IgG. PLTs can also produce bactericide agents such as β-lysins and PLT microbicidal proteins (PMPs) which do not induce lesions on the bacterial wall but interact with neutrophil granulocytes and lymphocytes, thrombin-induced PMPs (tPMPs), and their derivatives termed thrombocidins and kinocidins representing a subset of PMPs being classical chemokines that have direct microbicidal activity. They possess dual chemokine and microbicidal effector functions [140]. The host defense against bacteria induces an activated metabolic status, the change from discoid to ameboid shape with expression of receptors interacting with injured or infected tissues, the generation of oxygen radicals, as well as the extension of pseudopodia interacting with microbial pathogens. These changes are managed by the cytoskeleton which facilitates granule mobilization and degradation leading to the release of granule contents including host defense peptides.

In our own experiments, using electron tomography, we could impressively show that bacteria such *Escherichia coli* and *Streptococcus epidermidis* could cause their adhesion (Figure 10a), aggregation (Figure 10b), and engulfment (Figure 10a,c,d). Engulfment of bacteria is achieved by uptake into the OCS where they can be subsequently sequestered. The separation of parts of the OCS from the surrounding milieu was verified by the surface-coat-binding of the electron-dense dye ruthenium red. In sequestered areas of the OCS, both the membrane of the OCS and the bacterial wall remain unstained (Figure 10c), while in parts of the OCS that are in continuity with the environment, a distinct decoration of both structures could be found (Figure 10d). Preliminary studies with the pH-sensitive fluorescent dye pHrodo showed a decrease of pH in PLTs after engulfment of bacteria. In addition, killing of living bacteria could be demonstrated by fluorescence microscopy using the LIVE/DEAD® fixable dead cell stain kit (Life Technologies, Vienna, Austria).

There are different views concerning the phagocytic capacity of PLTs, one favoring the view of covercytes [141], others supporting the idea of phagocytosis. In this respect, Li et al. [142]

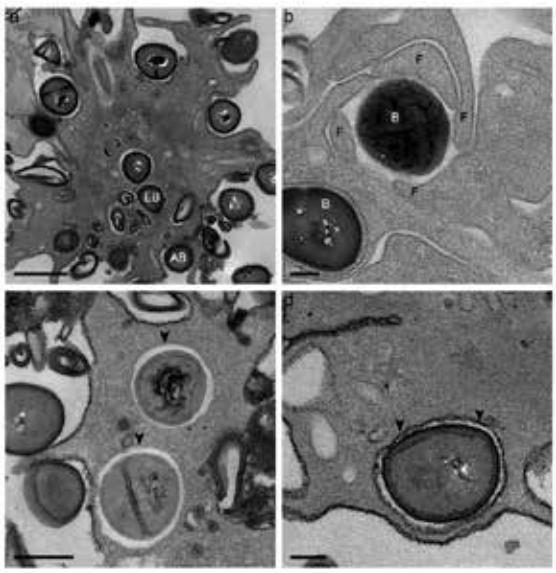

Figure 10. Adherent PLTs were stained with ruthenium red as tracer in order to show whether engulfed bacteria (*Staphylococcus epidermidis*) are still in contact with the extracellular milieu or separated from it. Figure 10a shows adhesion (AB) and engulfment of bacteria (EB). Figure 10b demonstrates the ability of PLTs to form aggregates by interdigitations of filopodia (F) in which bacteria (B) are sequestered. Figure 10c shows completely engulfed bacteria whereby both the membrane of the OCS (arrowheads) and the bacterial wall remain unstained. In contrast to this image, Figure 10d shows both parts decorated with ruthenium red, indicating that there exists still a communication with the surrounding milieu. Ultrathin sections were viewed under a Tecnai 20 electron microscope, and digital images were acquired using an Eagle 4k bottom-mount camera (FEI Co.).

reported the engulfment and phagocytosis of *Porphyromonas gingivalis* by ruthenium red staining. Using enzyme EM methods, as early as 1976, it could be demonstrated that phagocytosis of latex particles by PLTs leads to the formation of acid phosphatase-positive vesicles and to their killing and degradation [143].

In many countries, pathogen inactivation methods by cross linking of nucleic acids are used routinely (for reviews, see [144, 145]). There is much emphasis that transfusion-mediated infections can be avoided by these techniques. Nevertheless, several aspects concerning the function and recovery of pathogen-inactivated PCs in the recipient are still a matter of discussion.

4. Conclusion

PLTs are very dynamic cell fragments that display functions, widely exceeding those of blood coagulation [146]. Electron microscopy, implicating new techniques such as correlative microscopy, and the various variants of cryotechniques, combined with electron tomography, allow insights at high resolution, which cannot be achieved with other methods.

http://dx.doi.org/10.5772/60673

We would like to emphasize that EM analyses of PCs significantly supplement the routinely used quality assessment methods monitoring different manufacturing procedures. Methodical refinements, improving the preparation protocols of EM specimens, such as a wide range of cryomethods, stabilizing the samples close to the living state, together with electron tomography, 3D-reconstruction and modeling visualize structural details and dynamic processes at high resolution [99, 147, 148]. Thus new in vitro and in vivo tests of PLT function in transfused PCs can be efficiently controlled at the EM level. The technique is particularly helpful in the case a new apheresis system is introduced in a blood bank. EM evaluation of PLT qualities can significantly supplement the results obtained from commonly used laboratory methods.

Abbreviations

EM: electron microscopy; MK: megakaryocyte; PC: platelet concentrate; PLT: platelet, thrombocyte; PMPs: platelet membrane microparticles; PM: platelet membrane; TEM: transmission electron microscopy; OCS: open canalicular system; DTS: dense tubular system; DMS: demarcation membrane system; MTC: microtubular coil

Acknowledgements

The authors gratefully acknowledge the provision of apheresis PCs by Mrs. Renate Renz (Blood Donation Center of the Austrian Red Cross for Vienna, Lower Austria, and Burgenland), the skillful technical assistance of Mrs. Ivanna Federenko, Mrs. Beatrix Mallinger, and Mrs. Regina Wegscheider, and Mr. Ulrich Kaindl and Mr. Thomas Nardelli for their valuable help with the artwork and the 3D modeling (Center for Anatomy and Cell Biology, Department of Cell Biology and Ultrastructure Research, Medical University of Vienna).

Author details

Josef Neumüller[1], Adolf Ellinger[2] and Thomas Wagner[3*]

*Address all correspondence to: thomas.wagner@medunigraz.at

1 Blood Donation Center of the Austrian Red Cross for Vienna, Lower Austria, and Burgenland, Vienna, Austria

2 Medical University of Vienna, Center for Anatomy and Cell Biology, Department of Cell Biology and Ultrastructure Research, Vienna, Austria

3 Department of Blood Group Serology and Transfusion Medicine, Medical University of Graz, Graz, Austria

References

[1] Rebulla P. Revisitation of the clinical indications for the transfusion of platelet concentrates. Rev Clin Exp Hematol. 2001; 5(3): 288–310.

[2] Salama A, Kiesewetter H, Kalus U, Movassaghi K, Meyer O. Massive platelet transfusion is a rapidly effective emergency treatment in patients with refractory autoimmune thrombocytopenia. Thromb Haemost. 2008; 100(5): 762–765.

[3] Ali SF. Platelet activation of platelet concentrates derived from buffy coat and apheresis methods. Transfus Apher Sci. 2011; 44(1): 11–13.

[4] Altuntas F, Sari I, Kocyigit I, Kaynar L, Hacioglu S, Ozturk A, Oztekin M, Solmaz M, Eser B, Cetin M, Unal A. Comparison of plateletpheresis on the fenwal amicus and fresenius Com.Tec cell separators. Transfus Med Hemother. 2008; 35(5): 368–373.

[5] Bueno JL, Barea L, Garcia F, Castro E. A comparison of PLT collections from two apheresis devices. Transfusion. 2004; 44(1): 119–124.

[6] Burgstaler EA, Winters JL, Pineda AA. Paired comparison of Gambro Trima Accel versus Baxter Amicus single-needle plateletpheresis. Transfusion. 2004; 44(11): 1612–1620.

[7] Fontana S, Mordasini L, Keller P, Taleghani BM. Prospective, paired crossover comparison of multiple, single-needle plateletpheresis procedures with the Amicus and Trima Accel cell separators. Transfusion. 2006; 46(11): 2004–2010.

[8] Jilma-Stohlawetz P, Eichelberger B, Horvath M, Jilma B, Panzer S. In vitro platelet function of platelet concentrates prepared using three different apheresis devices determined by impedance and optical aggregometry. Transfusion. 2009; 49(8): 1564–1568.

[9] Perseghin P, Mascaretti L, Riva M, Sciorelli G. Comparison of plateletpheresis concentrates produced with Spectra LRS version 5.1 and LRS Turbo version 7.0 cell separators. Transfusion. 2000; 40(7): 789–793.

[10] Perseghin P, Mascaretti L, Speranza T, Belotti D, Baldini V, Dassi M, Riva M, Pogliani EM, Sciorelli G. Platelet activation during plasma-reduced multicomponent PLT collection: a comparison between COBE Trima and Spectra LRS turbo cell separators. Transfusion. 2004; 44(1): 125–130.

[11] Picker SM, Radojska SM, Gathof BS. Prospective comparison of high-dose plateletpheresis with the latest apheresis systems on the same donors. Transfusion. 2006; 46(9): 1601–1608.

[12] Ringwald J, Zingsem J, Zimmermann R, Strasser E, Antoon M, Eckstein R. First comparison of productivity and citrate donor load between the Trima version 4 (dual-

stage filler) and the Trima Accel (single-stage filler) in the same donors. Vox Sang. 2003; 85(4): 267–275.

[13] Seghatchian J, Krailadsiri P. The quality of MCS+ version C2 double dose platelet concentrate with leucodepletion through a continuous filtration process. Transfus Apher Sci. 2002; 26(1): 37–41.

[14] Zingsem J, Glaser A, Zimmermann R, Weisbach V, Kalb R, Ruf A, Eckstein R. Paired comparison of apheresis platelet function after storage in two containers. J Clin Apher. 2001; 16(1): 10–14.

[15] Zingsem J, Strasser E, Ringwald J, Zimmermann R, Weisbach V, Eckstein R. Evaluation of a new apheresis system for the collection of leukoreduced single-donor platelets. Transfusion. 2007; 47(6): 987–994.

[16] Picker SM. In-vitro assessment of platelet function. Transfus Apher Sci. 2011; 44(3): 305–319.

[17] Panzer S, Jilma P. Methods for testing platelet function for transfusion medicine. Vox Sang. 2011; 101(1): 1–9.

[18] Cognasse F, Hamzeh-Cognasse H, Lafarge S, Acquart S, Chavarin P, Courbil R, Fabrigli P, Garraud O. Donor platelets stored for at least 3 days can elicit activation marker expression by the recipient's blood mononuclear cells: an in vitro study. Transfusion. 2009; 49(1): 91–98.

[19] Spiess BD. Transfusion of blood products affects outcome in cardiac surgery. Semin Cardiothorac Vasc Anesth. 2004; 8(4): 267–281.

[20] Simak J, Gelderman MP. Cell membrane microparticles in blood and blood products: potentially pathogenic agents and diagnostic markers. Transfus Med Rev. 2006; 20(1): 1–26.

[21] Gilstad CW. Anaphylactic transfusion reactions. Curr Opin Hematol. 2003; 10(6): 419–423.

[22] White JG. The dense bodies of human platelets. Origin of serotonin storage particles from platelet granules. Am J Pathol. 1968; 53(5): 791–808.

[23] White JG. The submembrane filaments of blood platelets. Am J Pathol. 1969; 56(2): 267–277.

[24] White JG. Interaction of membrane systems in blood platelets. Am J Pathol. 1972; 66(2): 295–312.

[25] White JG. Identification of platelet secretion in the electron microscope. Ser Haematol. 1973; 6(3): 429–459.

[26] White JG. Morphological studies of platelets and platelet reactions. Vox Sang. 1981; 40(Suppl 1): 8–17.

[27] White JG. Cytoskeletal changes in aging platelets. Prog Clin Biol Res. 1985; 195: 49–77.

[28] White JG. An overview of platelet structural physiology. Scanning Microsc. 1987; 1(4): 1677–1700.

[29] White JG. Ultrastructural analysis of platelet contractile apparatus. Methods Enzymol. 1992; 215: 109–127.

[30] White JG. Platelet secretory granules and associated proteins. Lab Invest. 1993; 68(5): 497–498.

[31] White JG. Platelet secretory process. Blood. 1999; 93(7): 2422–2425.

[32] White JG. Electron microscopy methods for studying platelet structure and function. Methods Mol Biol. 2004; 272: 47–63.

[33] White JG. Electron opaque structures in human platelets: which are or are not dense bodies? Platelets. 2008; 19(6): 455–466.

[34] White JG, Escolar G. The blood platelet open canalicular system: a two-way street. Eur J Cell Biol. 1991; 56(2): 233–242.

[35] White JG, Estensen RD. Degranulation of discoid platelets. Am J Pathol. 1972; 68(2): 289–302.

[36] White JG, Gerrard JM. Ultrastructural features of abnormal blood platelets. A review. Am J Pathol. 1976; 83(3): 589–632.

[37] White JG, Gerrard JM. Platelet ultrastructure in relation to platelet function. Prog Clin Biol Res. 1978; 28: 5–23.

[38] White JG, Gerrard JM. Interaction of microtubules and microfilaments in platelet contractile physiology. Methods Achiev Exp Pathol. 1979; 9: 1–39.

[39] White JG, Krivit W. The ultrastructural localization and release of platelet lipids. Blood. 1966; 27(2): 167–186.

[40] White JG, Sauk JJ. Microtubule coils in spread blood platelets. Blood. 1984; 64(2) 470–478.

[41] White JG. Ultrastructural defects in congenital disorders of platelet function. Ann N Y Acad Sci. 1972; 201: 205–33.

[42] White JG. Platelet microtubules and giant granules in the Chediak-Higashi syndrome. Am J Med Technol. 1978; 44(4): 273–278.

[43] White JG. Ultrastructural studies of the gray platelet syndrome. Am J Pathol. 1979; 95(2): 445–462.

[44] White JG. Membrane defects in inherited disorders of platelet function. Am J Pediatr Hematol Oncol. 1982; 4(1): 83–94.

[45] White JG. Platelet granule disorders. Crit Rev Oncol Hematol. 1986; 4(4): 337–377.

[46] White JG. Use of the electron microscope for diagnosis of platelet disorders. Semin Thromb Hemost. 1998; 24(2): 163–168.

[47] White JG. Golgi complexes in hypogranular platelet syndromes. Platelets. 2005; 16(1): 51–60.

[48] White JG, de Alarcon PA. Platelet spherocytosis: a new bleeding disorder. Am J Hematol. 2002; 70(2): 158–166.

[49] White JG, Gerrard JM. The ultrastructure of defective human platelets. Mol Cell Biochem. 1978; 21(2): 109–128.

[50] Bessis M, Breton-Gorius J. Microtubules and fibrils in spread-out platelets. Nouv Rev Fr Hematol. 1965; 5(4): 657–662.

[51] Bessis M, Dreyfus B, Breton-Gorius J, Sultan C. Electron microscopic study of 11 cases of refractory anemias with multiple enzymopathies. Nouv Rev Fr Hematol. 1969; 9(1): 87–104.

[52] Berry S, Dawicki DD, Agarwal KC, Steiner M. The role of microtubules in platelet secretory release. Biochim Biophys Acta. 1989; 1012(1): 46–56.

[53] Escolar G, Sauk J, Bravo ML, Krumwiede M, White JG. Immunogold staining of microtubules in resting and activated platelets. Am J Hematol. 1987; 24(2): 177–188.

[54] Italiano JE, Jr., Bergmeier W, Tiwari S, Falet H, Hartwig JH, Hoffmeister KM, Andre P, Wagner DD, Shivdasani RA. Mechanisms and implications of platelet discoid shape. Blood. 2003; 101(12): 4789–4796.

[55] Lewis JC. Cytoskeleton in platelet function. Cell Muscle Motil. 1984; 5: 341–377.

[56] Radley JM, Hartshorn MA. Megakaryocyte fragments and the microtubule coil. Blood Cells. 1987; 12(3): 603–614.

[57] Spangenberg P. The cytoskeleton of platelets. Acta Histochem Suppl. 1990; 39: 385–395.

[58] White JG. Tubular elements in platelet granules. Blood. 1968; 32(1): 148–156.

[59] Xu Z, Afzelius BA. The substructure of marginal bundles in human blood platelets. J Ultrastruct Mol Struct Res. 1988; 99(3): 244–253.

[60] Xu Z, Afzelius BA. Early changes in the substructure of the marginal bundle in human blood platelets responding to adenosine diphosphate. J Ultrastruct Mol Struct Res. 1988; 99(3): 254–260.

[61] Canizares C, Vivar N, Tenesaca S. Analysis of the ultrastructure of the platelets during the process of aggregation, with emphasis in the cytoskeleton and membranous changes. Microsc Electron Biol Celular. 1988; 12(1): 1–15.

[62] White JG. Arrangements of actin filaments in the cytoskeleton of human platelets. Am J Pathol. 1984; 117(2): 207–217.

[63] Escolar G, White JG. The platelet open canalicular system: a final common pathway. Blood Cells. 1991; 17(3): 467–485; discussion 86–95.

[64] Escolar G, Leistikow E, White JG. The fate of the open canalicular system in surface and suspension-activated platelets. Blood. 1989; 74(6): 1983–1988.

[65] White JG. Platelets are covercytes, not phagocytes: uptake of bacteria involves channels of the open canalicular system. Platelets. 2005; 16(2): 121–131.

[66] Canizares C, Vivar N, Herdoiza M. Role of the microtubular system in platelet aggregation. Braz J Med Biol Res. 1994; 27: 1533–1551.

[67] Clawson CC, Rao GH, White JG. Platelet interaction with bacteria. IV. Stimulation of the release reaction. Am J Pathol. 1975; 81(2): 411–420.

[68] Daimon T, Gotoh Y, Kawai K, Uchida K. Ultrastructural distribution of peroxidase in thrombocytes of mammals and submammals. Histochemistry. 1985; 82(4): 345–350.

[69] Ebbeling L, Robertson C, McNicol A, Gerrard JM. Rapid ultrastructural changes in the dense tubular system following platelet activation. Blood. 1992; 80(3): 718–723.

[70] Gerrard JM, White JG, Peterson DA. The platelet dense tubular system: its relationship to prostaglandin synthesis and calcium flux. Thromb Haemost. 1978; 40(2): 224–231.

[71] Gerrard JM, White JG, Rao GH, Townsend D. Localization of platelet prostaglandin production in the platelet dense tubular system. Am J Pathol. 1976; 83(2): 283–298.

[72] Rendu F, Brohard-Bohn B. The platelet release reaction: granules' constituents, secretion and functions. Platelets. 2001; 12(5): 261–273.

[73] Saussy DL, Jr., Mais DE, Baron DA, Pepkowitz SH, Halushka PV. Subcellular localization of a thromboxane A2/prostaglandin H2 receptor antagonist binding site in human platelets. Biochem Pharmacol. 1988; 37(4): 647–654.

[74] van Nispen Tot Pannerden HE, van Dijk SM, Du V, Heijnen HF. Platelet protein disulfide isomerase is localized in the dense tubular system and does not become surface expressed after activation. Blood. 2009; 114(21): 4738–4740.

[75] White JG, Conard WJ. The fine structure of freeze-fractured blood platelets. Am J Pathol. 1973; 70(1): 45–56.

[76] Zhao B, Dierichs R, Liu JF, Zhu ZM, Berkes P, Frye S. Influence of low density lipoproteins on cytosolic free Ca^{2+} concentration and dense tubular system in human platelets. Thromb Res. 1993; 72(1): 33–37.

[77] Behnke O. Degrading and non-degrading pathways in fluid-phase (non-adsorptive) endocytosis in human blood platelets. J Submicrosc Cytol Pathol. 1992; 24(2): 169–178.

[78] Bentfeld-Barker ME, Bainton DF. Identification of primary lysosomes in human megakaryocytes and platelets. Blood. 1982; 59(3): 472–481.

[79] Stenberg PE, McEver RP, Shuman MA, Jacques YV, Bainton DF. A platelet alpha-granule membrane protein (GMP-140) is expressed on the plasma membrane after activation. J Cell Biol. 1985; 101(3): 880–886.

[80] Lewis JC, Hantgan RR, Stevenson SC, Thornburg T, Kieffer N, Guichard J, Breton-Gorius J. Fibrinogen and glycoprotein lib/Illa localization during platelet adhesion. Localization to the granulomere and at sites of platelet interaction. Am J Pathol. 1990; 136(1): 239–252.

[81] Machlus KR, Italiano JE Jr. The incredible journey: from megakaryocyte development to platelet formation. J Cell Biol. 2013; 201(6): 785–796.

[82] Bartley TD, Bogenberger J, Hunt P, Li YS, Lu HS, Martin F, Chang MS, Samal B, Nichol JL, Swift S, et al. Identification and cloning of a megakaryocyte growth and development factor that is a ligand for the cytokine receptor Mpl Cell. 1994; 77(1): 1117–1124.

[83] de Sauvage FJ, Hass PE, Spencer SD, Malloy BE, Gurney AL, Spencer SA, Darbonne WC, Henzel WJ, Wong SC, Kuang WJ, et al. Stimulation of megakaryocytopoiesis and thrombopoiesis by the c-Mpl ligand. Nature. 1994; 369(6481): 533–538.

[84] Kaushansky K. The mpl ligand: molecular and cellular biology of the critical regulator of megakaryocyte development. Stem Cells. 1994; 12(Suppl. 1): 91–96, discussion 96–97.

[85] Zimmet J, Ravid K. Polyploidy: occurrence in nature, mechanisms, and significance for the megakaryocyte-platelet system. Exp. Hematol. 2000; 28(1): 3–16.

[86] Eckly A, Heijnen H, Pertuy F, Geerts W, Proamer F, Rinckel JY, Léon C, Lanza F, Gachet C. Biogenesis of the demarcation membrane system (DMS) in megakaryocytes. Blood. 2014; 123(6): 921–930.

[87] Patel-Hett S, Wang H, Begonja AJ, Thon JN, Alden EC, Wandersee NJ, An X, Mohandas N, Hartwig JH, Italiano JE Jr. The spectrin based membrane skeleton stabilizes mouse megakaryocyte membrane systems and is essential for proplatelet and platelet formation. Blood. 2011; 118(6): 1641–1652.

[88] Thon JN, Montalvo A, Patel-Hett S, Devine MT, Richardson JL, Ehrlicher A, Larson MK, Hoffmeister K, Hartwig JH, Italiano JE Jr. Cytoskeletal mechanics of proplatelet maturation and platelet release. J Cell Biol. 2010; 191(4): 861–874.

[89] Thon JN, Macleod H, Begonja AJ, Zhu J, Lee KC, Mogilner A, Hartwig JH, Italiano JE Jr. Microtubule and cortical forces determine platelet size during vascular platelet production. Nat Commun. 2012; 3: 852.

[90] Schachtner H, Calaminus SD, Sinclair A, Monypenny J, Blundell MP, Leon C, Holyoake TL, Thrasher AJ, Michie AM, Vukovic M, Gachet C, Jones GE, Thomas SG, Watson SP, Machesky LM. Megakaryocytes assemble podosomes that degrade matrix and protrude through basement membrane. Blood. 2013; 121(13): 2542–2552.

[91] Meddens MB, van den Dries K, Cambi A. Podosomes revealed by advanced bioimaging: what did we learn? Eur J Cell Biol. 2014; 93(10–12): 380–387.

[92] Gavazzi I, Nermut M, Marchisio PCV. Ultrastructure and gold-immunolabelling of cell-substratum adhesions (podosomes) in RSV-transformed BHK cells. J Cell Sci. 1989; 94(Pt 1): 85–99.

[93] Nitsch L, Gionti E, Cancedda R, Marchisio PC. The podosomes of Rous sarcoma virus transformed chondrocytes show a peculiar ultrastructural organization. Cell Biol Int Rep. 1989; 13(11): 919–926.

[94] Tarone G, Cirillo D, Giancotti FG, Comoglio PM, Marchisio PC. Rous sarcoma virus-transformed fibroblasts adhere primarily at discrete protrusions of the ventral membrane called podosomes. Exp Cell Res. 1985; 159(1): 141–157.

[95] Carman CV, Sage PT, Sciuto TE, de la Fuente MA, Geha RS, Ochs HD, Dvorak HF, Dvorak AM, Springer TA. Transcellular diapedesis is initiated by invasive podosomes. Immunity. 2007; 26(6): 784–797.

[96] Cougoule C, Van Goethem E, Le Cabec V, Lafouresse F, Dupré L, Mehraj V, Mège J-L, Lastrucci C, Maridonneau-Parini I. Blood leukocytes and macrophages of various phenotypes have distinct abilities to form podosomes and to migrate in 3D environments. Eur J Cell Biol. 2012; 91(11–12): 938–949.

[97] Gawden-Bone C, Zhou Z, King E, Prescott A, Watts C, Lucocq J. Dendritic cell podosomes are protrusive and invade the extracellular matrix using metalloproteinase MMP-14. J Cell Sci. 2010; 123(Pt 9): 1427–1437.

[98] Van Goethem E, Guiet R, Balor S, Charrière GM, Poincloux R, Labrousse A,Maridonneau-Parini I, Le Cabec V. Macrophage podosomes go 3D. Eur J Cell Biol. 2013; 90(2–3): 224–236.

[99] van Nispen tot Pannerden H, de Haas F, Geerts W, Posthuma G, van Dijk S, Heijnen HF. the platelet interior revisited: electron tomography reveals tubular alpha-granule subtypes. Blood. 2010; 116: 1147–1156.

[100] Rivera J, Lozano ML, Navarro-Núñez L, Vicente V. Platelet receptors and signaling in the dynamics of thrombus formation. Haematologica. 2009; 94(5): 700–711.

[101] Ren Q, Ye S, Whiteheart SW. The platelet release reaction: just when you thought platelet secretion was simple. Curr Opin Hematol. 2008; 15(5): 537–541.

[102] Thushara RM, Hemshekhar M, Basappa, Kemparaju K, Rangappa KS, Girish KS. Biologicals, platelet apoptosis and human diseases: an outlook. Crit Rev Oncol Hematol. 2014; pii: S 1040-8428 (14)00186-3.

[103] Burnouf T, Goubran HA, Chou ML, Devos D, Radosevic M. Platelet microparticles: detection and assessment of their paradoxical functional roles in disease and regenerative medicine. Blood Rev. 2014; 28(4): 155–166.

[104] Wolf P. The nature and significance of platelet products in human plasma. Br J Haematol. 1967; 13(3): 269–288.

[105] Heijnen HF, Schiel AE, Fijnheer R, Geuze HJ, Sixma JJ. Activated platelets release two types of membrane vesicles: microvesicles by surface shedding and exosomes derived from exocytosis of multivesicular bodies and alpha-granules. Blood. 1999; 94(11): 3791–3799.

[106] Gambim MH, do Carmo Ade O, Marti L, Veríssimo-Filho S, Lopes LR, Janiszewski M. Platelet-derived exosomes induce endothelial cell apoptosis through peroxynitrite generation: experimental evidence for a novel mechanism of septic vascular dysfunction. Crit Care. 2007; 11(5): 1–12.

[107] Hughes M, Hayward CP, Warkentin TE, Horsewood P, Chorneyko KA, Kelton JG. Morphological analysis of microparticle generation in heparin-induced thrombocytopenia. Blood. 2000; 96(1): 188–194.

[108] Sadallah S, Eken C, Martin PJ, Schifferli JA. Microparticles (ectosomes) shed by stored human platelets downregulate macrophages and modify the development of dendritic cells. J Immunol. 2011; 186(11): 6543–6552.

[109] Aatonen MT, Öhman T, Nyman TA, Laitinen S, Grönholm M, Siljander PR. Isolation and characterization of platelet-derived extracellular vesicles. J Extracell Vesicles. 2014; 3: 24692.

[110] Schrezenmeier H, Seifried E. Buffy-coat-derived pooled platelet concentrates and apheresis platelet concentrates: which product type should be preferred? Vox Sang. 2010; 105(6): 783–791.

[111] Neumüller J, Meisslitzer-Ruppitsch C, Ellinger A, Pavelka M, Jungbauer C, Renz R, Leitner G, Wagner T. Monitoring of platelet activation in platelet concentrates using transmission electron microscopy. Transfus Med Hemother. 2013; 40(2): 101–107.

[112] Leytin V, Freedman J. Platelet apoptosis in stored platelet concentrates and other models. Transfus Apher Sci. 2003; 28(3): 285–295.

[113] Leytin V. Apoptosis in the anucleate platelet. Blood Rev. 2012; 26(2): 51–63.

[114] Ohto H, Nollet KE. Overview on platelet preservation: better controls over storage lesion. Transfus Apher Sci. 2011; 44(3): 321–325.

[115] Stuart MC, Bevers EM, Comfurius P, Zwaal RF, Reutelingsperger CP, Frederik PM. Ultrastructural detection of surface exposed phosphatidylserine on activated blood platelets. Thromb Haemost. 1995; 74(4): 1145–1151.

[116] White JG, Krumwiede M. Some contributions of electron microscopy to knowledge of human platelets. Thromb Haemost. 2007; 98(1): 69–72.

[117] Maguire LC, Henriksen RA, Strauss RG, Stein MN, Goedken MM, Echternacht B, Koepke JA, Thompson JS. Function and morphology of platelets produced for transfusion by intermittent-flow centrifugation plateletpheresis or combined platelet-leukapheresis. Transfusion. 1981; 21(1): 118–123.

[118] Foster PR. Prions and blood products. Ann Med. 2000; 32(7): 501–513.

[119] Böck M, Heim MU, Weindler R, Bilas A, Greither L, Salat C, Mempel W. White cell depletion of single-donor platelet preparations by a new adsorption filter. Transfusion. 1991; 31(4): 333–334.

[120] Böck M, Himmelsbach S, Gudden A, Greither L, Mempel W. Preparation of leukocyte-depleted thrombocyte concentrate: in-vitro testing of a new filtration system (PL 100). Infusionstherapie. 1991; 18(1): 30–32.

[121] Böck M, Salat C, Greither L, Heim MU, Weindler R, Bilas A, Mempel W. Production of leukocyte-poor thrombocyte concentrates: results with a new kind of filter system. Beitr Infusionsther. 1990; 26: 103–105.

[122] Christensen LD, Dickmeiss E. In vitro evaluation of a new filter for leucocyte depletion of platelet concentrate during component preparation. Vox Sang. 1994; 67(3): 267–271.

[123] Steneker I, Prins HK, Florie M, Loos JA, Biewenga J. Mechanisms of white cell reduction in red cell concentrates by filtration: the effect of the cellular composition of the red cell concentrates. Transfusion. 1993; 33(1): 42–50.

[124] Steneker I, van Luyn MJ, van Wachem PB, Biewenga J. Electron microscopic examination of white cell reduction by four white cell-reduction filters. Transfusion. 1992; 32(5): 450–457.

[125] Böck M, Greither L, Gudden A, Diehm H, Heim MU, Mempel W. Storage of thrombocyte concentrates: ultrastructural and functional changes. Infusionstherapie. 1991; 18(3): 137–138, 141–142.

[126] Bertolini F, Porretti L, Lauri E, Rebulla P, Sirchia G. Role of lactate in platelet storage lesion. Vox Sang. 1993; 65(3): 194–198.

[127] Wagner T, Vetter A, Dimovic N, Guber SE, Helmberg W, Kroll W, Lanzer G, Mayr WR, Neumüller J. Ultrastructural changes and activation differences in platelet concentrates stored in plasma and additive solution. Transfusion. 2002; 42(6): 719–727.

[128] Elias M, Heethuis A, Weggemans M, Bom V, Blom N, McShine RL, Halie MR, Smit Sibinga CT. Stabilization of standard platelet concentrates and minimization of the platelet storage lesion by a prostacyclin analogue. Ann Hematol. 1992; 64(6): 292–298.

[129] Grode G, Miripol J, Garber J, Barber T, Buchholz DH. Extended storage of platelets in a new plastic container. I. Biochemical and morphologic changes. Transfusion. 1985; 25(3): 204–208.

[130] Ahnadi CE, Sabrinah Chapman E, Lepine M, Okrongly D, Pujol-Moix N, Hernandez A, Boughrassa F, Grant AM. Assessment of platelet activation in several different anticoagulants by the Advia 120 hematology system, fluorescence flow cytometry, and electron microscopy. Thromb Haemost. 2003; 90(5): 940–948.

[131] Kelley WE, Edelman BB, Drachenberg CB, Hess JR. Washing platelets in neutral, calcium-free, Ringer's acetate. Transfusion. 2009; 49(9): 1917–1923.

[132] ElKattan I, Anderson J, Yun JK, Colton E, Yomtovian R. Correlation of cytokine elaboration with mononuclear cell adhesion to platelet storage bag plastic polymers: a pilot study. Clin Diagn Lab Immunol. 1999; 6(4): 509–513.

[133] Read MS, Reddick RL, Bode AP, Bellinger DA, Nichols TC, Taylor K, Smith SV, McMahon DK, Griggs TR, Brinkhous KM. Preservation of hemostatic and structural properties of rehydrated lyophilized platelets: potential for long-term storage of dried platelets for transfusion. Proc Natl Acad Sci USA. 1995; 92(2): 397–401.

[134] Balint B, Vucetic D, Trajkovic-Lakic Z, Petakov M, Bugarski D, Brajuskovic G, Taseski J. Quantitative, functional, morphological and ultrastructural recovery of platelets as predictor for cryopreservation. Haematologia (Budap) 2002; 32(4): 363–375.

[135] Böck M, Greither L, Heim MU. Morphologic and functional changes in thrombocytes after deep freezing with DMSO. Infusionsther Transfusionsmed. 1996; 23(2): 76–79.

[136] Lindholm PF, Annen K, Ramsey G. Approaches to minimize infection risk in blood banking and transfusion practice. Infect Disord Drug Targets. 2011; 11(1): 45–56.

[137] Marwaha N, Sharma RR. Consensus and controversies in platelet transfusion. Transfus Apher Sci. 2009; 41(2): 127–133.

[138] Burns KH, Werchs JB. Bacterial contamination of platelet units: a case report and literature survey with review of upcoming American association of blood banks requirements. Arch Pathol Lab Med. 2004; 128(3): 279–281.

[139] Cox D, Kerrigan SW, Watson SP. Platelets and the innate immune system: mechanisms of bacterial-induced platelet activation. J Thromb Haemost. 2011; 9(6): 1097–1107.

[140] Yeaman MR. Platelets in defense against bacterial pathogens. Cell Mol Life Sci. 2010; 67(4): 525–544.

[141] White JG. Platelets are covercytes, not phagocytes: uptake of bacteria involves channels of the open canalicular system. Platelets. 2005 16(2): 121–131.

[142] Li X, Iwai T, Nakamura H, Inoue Y, Chen Y, Umeda M, Suzuki H. An ultrastructural study of porphyromonas gingivalis-induced platelet aggregation. Thromb Res. 2008; 122(6): 810–819.

[143] Lewis JC, Maldonado JE, Mann KG. Phagocytosis in human platelets: localization of acid phosphatase-positive phagosomes following latex uptake. Blood. 1976; 47(5): 833–840.

[144] Kaiser-Guignard J, Canellini G, Lion N, Abonnenc M, Osselaer JC, Tissot JD. The clinical and biological impact of new pathogen inactivation technologies on platelet concentrates. Blood Rev. 2014; 28(6): 235–241.

[145] Lozano M, Cid J. Analysis of reasons for not implementing pathogen inactivation for platelet concentrates. Transfus Clin Biol. 2013; 20(2): 158–164.

[146] Leslie M. Cell biology. Beyond clotting: the powers of platelets. Science. 2010; 328(5978): 562–564.

[147] Ellinger A, Vetterlein M, Weiss C, Meisslitzer-Ruppitsch C, Neumüller J, Pavelka M. High-pressure freezing combined with in vivo-DAB-cytochemistry: a novel approach for studies of endocytic compartments. J Struct Biol. 2011; 169(3): 286–293.

[148] Meisslitzer-Ruppitsch C, Röhrl C, Ranftler C, Neumüller J, Vetterlein M, Ellinger A, Pavelka M. The ceramide-enriched trans-Golgi compartments reorganize together with other parts of the Golgi apparatus in response to ATP-depletion. Histochem Cell Biol. 2011; 135(2): 159–171.

Chapter 12

Ultrastructure and Topochemistry of Plant Cell Wall by Transmission Electron Microscopy

Xia Zhou, Dayong Ding, Jing Ma, Zhe Ji,
Xun Zhang and Feng Xu

Additional information is available at the end of the chapter

http://dx.doi.org/10.5772/60752

Abstract

Plant cell walls are typically described as complex macromolecular composites consisting of an ordered array of cellulose microfibrils embedded in a matrix of non-cellulosic polysaccharides and lignin. Generally, the plant cell wall can be divided into three major layers: middle lamella, primary cell wall, and secondary cell wall. Investigation of plant cell walls is complicated by the heterogeneous and complex hierarchical structure, as well as variable chemical composition between different sub-layers. Thus, a complete understanding of the ultrastructure of plant cell walls is necessary. Transmission electron microscopy (TEM) has proven to be a powerful tool in elucidating fine details of plant cell walls at nanoscale. The present chapter describes the layering structure and topochemistry of plant cell wall revealed by TEM.

Keywords: Plant cell wall, Transmission electron microscopy, Ultrastructure, Topochemistry

1. Introduction

Determining the ultrastructural organization of plant cell walls represents one of the most challenging problems in plant biology. Although considerable progress has been made in understanding the basic organization and functions of plant cell wall components, due to the highly complex and dynamic nature of the plant cell wall, the variation in cell wall architecture of wood and gramineous species remains poorly understood. These structural features are

INTECH
open science | open minds

© 2015 The Author(s). Licensee InTech. This chapter is distributed under the terms of the Creative Commons Attribution License (http://creativecommons.org/licenses/by/3.0), which permits unrestricted use, distribution, and reproduction in any medium, provided the original work is properly cited.

associated with cell growth and morphogenesis, which are also crucial in determining the mechanical properties of plant cell walls [1, 2]. Given that one of the critical processing steps in biomass conversion involves systematic deconstruction of cell walls, this structural information is also pivotal for developing novel approaches to convert biomass into liquid biofuels. Therefore, a comprehensive investigation of the architecture of the plant cell wall will not only help us to understand the assembly and biosynthesis of the plant cell wall, but will also contribute to improving the efficiency of biomass deconstruction [3].

The plant cell wall is a layered construction composed mainly of stiff crystalline cellulose microfibrils (Mfs) embedded in an amorphous matrix of non-crystalline cellulose, hemicelluloses and pectin, as well as various aromatic compounds and proteins [4]. Besides the varieties of chemical constituents, the ultrastructural organization of plant cell wall varies between species and cell types. Generally, the plant cell wall consists of three major layers: (i) the middle lamella (Ml), (ii) the primary wall (Pw), and (iii) the secondary wall (Sw). Due to the highest thickness, Sw accounts for the largest proportion of the plant cell wall. Sw in higher plants consists mainly of cellulose, lignin, and xylan and is the major component of biomass in many species. In hardwood fibers and softwood tracheids, the Sw is normally further differentiated into an outer layer (S1), a middle layer (S2), and an inner layer (S3), with the S2 having the largest thickness [5, 6]. By comparison, in gramineous species the lamellation of the Sw in fiber is generally described as alternating broad and narrow layers [7].

In the twentieth century, microscopic approaches began to offer high-resolution images to enhance our understanding of cell wall organization. Over the past few decades, atomic force microscopy (AFM) has been successfully applied to high-resolution architecture, assembly, and structure dynamic studies of a wide range of biological systems, which has enabled researchers to visualize the ultrastructure of the plant cell wall [8, 9]. More recently, confocal Raman microspectroscopy (CRM) has now also been successfully applied to acquire information on the preferential orientation of plant polymer functional groups and components distribution in situ [10, 11]. However, although these approaches have been comprehensively used to obtain new information on cell wall architecture, until now the highly complex and dynamic nature of the plant cell wall at nanoscale has limited our ability to generate detailed structural models.

By comparison, due to the higher spatial resolution (<1nm) and specificity when combined with chemical staining and immunolabeling approaches, transmission electron microscopy (TEM) can provide ultrastructural and topochemical information simultaneously and has been used to investigate plant cell wall [12-14]. In this chapter, we mainly discuss the application of TEM in detecting cell wall layering structure and cell wall topochemistry (lignin distribution and hemicelluloses distribution).

2. Cell wall layering structure

To get any information using transmitted electrons in the TEM, specimens have to be thin. “Thin” is a relative term, in this context it means electron transparent. For a specimen to be

http://dx.doi.org/10.5772/60752

transparent to electrons, it must be thin enough to transmit sufficient electrons such that enough intensity falls on the screen, charge coupled device (CCD), or photographic plate to give an interpretable image in a reasonable time. Generally this requirement is a function of the electron energy and the average atomic number (Z) of the specimen. It is almost an axiom in TEM that thinner is better and specimens <100 nm should be used wherever possible. However, a too thin section would produce low-contrast TEM image, which hides the subtle structure. For plant cell wall, specimens are generally cut to a thickness of ~80 nm when they are silvery gold in color under ultramicrotome. In extreme cases such as doing high-resolution TEM (HRTEM) or electron spectrometry, specimen thicknesses <50 nm (even <10 nm) are essential.

2.1. Cell wall layering structure in hardwoods and softwoods

TEM examination showed that *Cornus alba* L. fiber cell wall was composed of three major layers: the middle lamella (ML) and the primary wall (P), and the secondary wall layer (S1, S2, and S3), a typical layering structure of fiber cell walls in other wood species [13, 15, 16]. The boundary between primary wall and middle lamella was not clearly distinguishable due to its high density and extreme thinness. Therefore, both the middle lamella (ML) and the contiguous primary wall (P) were referred here as compound middle lamella (CML) (Fig. 1a). The CML was electron dense, but the density was not uniform and this cell wall region had a mottled appearance containing dense and less dense or lucent regions. Inhomogeneity in lignin distribution in CML has also been reported in a few other TEM studies of hardwood species [17, 18]. The secondary wall was divided into an outer layer (F-S1), a middle layer (F-S2), and an inner layer (F-S3). The F-S1 layer in *Cornus alba* L. fiber was well-defined and can be readily distinguished from the adjoining F-S2 layer because of its higher electron density compared to F-S2 layer. The F-S1 layer was variable in width within and among cells (0.22–0.32 μm) (Table 1). The widest F-S2 layer accounted for the largest proportion of the fiber wall. Measurements of the width of fiber radial wall showed that the average thickness of the F-S2 layer was 2.67 μm. Fiber cell walls also contained an F-S3 layer that was very thin and not well developed.

Cell wall regions	Average thickness (range)	Standard deviation
F-S1	0.30 (0.22–0.32)	0.06
F-S2	2.67 (1.20–4.07)	0.14
V-S1	0.21 (0.18–0.32)	0.05
V-S2	0.62 (0.55–0.67)	0.17
AP-S3	0.73 (0.60–1.67)	0.19
RP-S1	0.61 (0.24–0.82)	0.14
RP-S2	0.80 (0.32–0.91)	0.27

Table 1. The average thickness of cell wall layers in *Cornus alba L.*

In addition to fiber cell wall, the ultrastructural variation in vessel, axial parenchyma, and ray parenchyma was also investigated. As shown in Fig. 1b, the vessel wall was divided into three layers (V-S1, V-S2, and V-S3) of variable electron density. The width of V-S1 ranged from 0.18 μm to 0.32 μm, approximately equal to that of F-S1, while the V-S2 was much thinner, with width from 0.55 μm to 0.67 μm. For the axial parenchyma (AP), the secondary wall was clearly resolved into an outer layer (AP-S1), a middle layer (AP-S2), and an inner layer (AP-S3) (Fig. 1c). Unlike the widest F-S2 layer accounting for the largest proportion of the secondary wall, in axial parenchyma the AP-S3 was the major proportion of secondary wall with the thickness ranging from 0.60 μm to 1.67 μm. In ray parenchyma (RP), the secondary wall consisted of two well-defined layers (outer layer, RP-S1, and inner layer, RP-S2), which did not fit conventional S1, S2, and S3 classification (Fig. 1d). Measurements taken on TEM micrograph evidenced that the average width of the RP-S1 was 0.61 μm, while the average thickness of the RP-S2 was 0.80 μm.

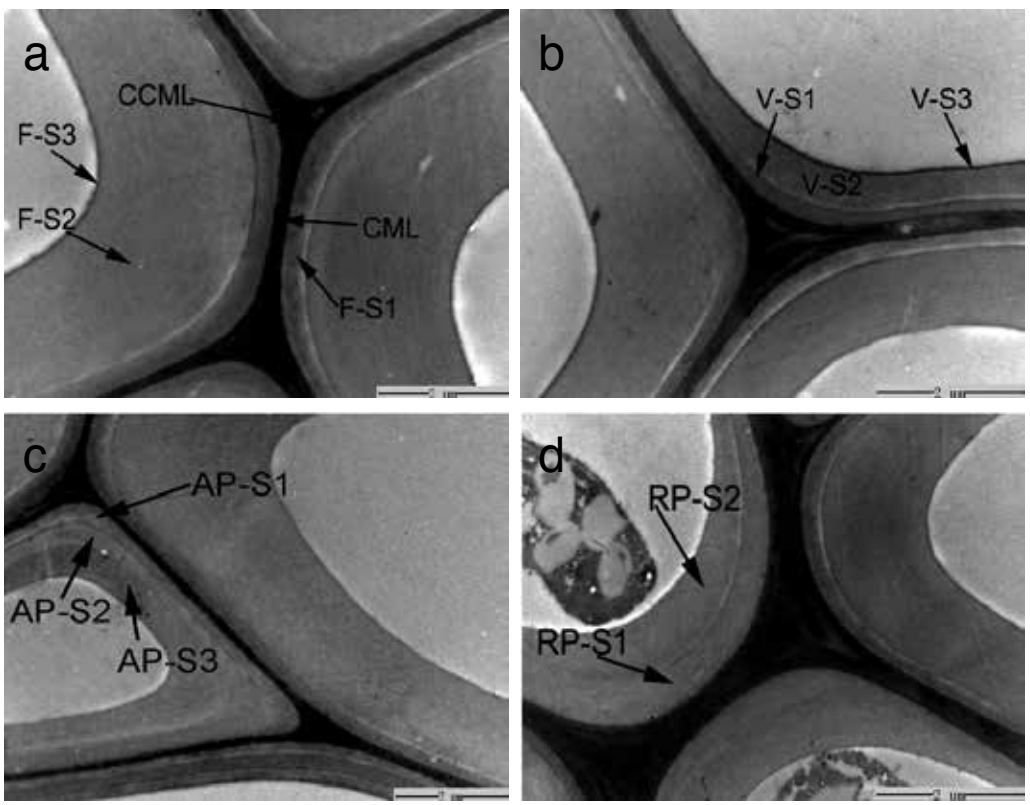

Figure 1. TEM micrographs of cross sections of *C. alba* L., taken at 80 kV. (a) CCML, cell corner middle lamella between adjoining fibers; CML, compound middle lamella between adjoining fibers; F-S1, outer secondary wall of fiber; F-S2, middle secondary wall of fiber; F-S3, inner secondary wall of fiber. (b) V-S1, outer secondary wall of vessel; V-S2, middle secondary wall of vessel; V-S3, inner secondary wall of vessel. (c) AP-S1, outer secondary wall of axial parenchyma; AP-S2, middle secondary wall of axial parenchyma; AP-S3, inner secondary wall of axial parenchyma. (d) RP-S1, outer secondary wall of ray parenchyma; RP-S2, inner secondary wall of ray parenchyma.

http://dx.doi.org/10.5772/60752

The ultrastructure of pit membrane (PM) among various wood elements (inter-fiber, fiber-vessel, fiber-axial parenchyma, and fiber-ray parenchyma) was also investigated. The thickness of PM varied considerably, with PM between fiber and ray parenchyma having a mean thickness of 500 nm, while PM between fiber and vessel had an average thickness of 220 nm. Thin PM with an average thickness of 230 nm was also found between parenchyma cells. PM varied also in their electron density, with inter-fiber PM (Fig. 2a) appearing distinctly denser than fiber-vessel (Fig. 2b) and fiber-parenchyma (axial and ray parenchyma) PM (Fig. 2c and 2d), which may reflect textural and/or compositional differences. The electron density variations originated from the deposition of lignin that is directly and linearly proportional to lignin concentration [13]. Thus, we can assume that the inter-fiber PMs have the highest lignin concentration, followed by fiber and parenchyma (axial and ray parenchyma) and fewest in the PM between fiber and vessel.

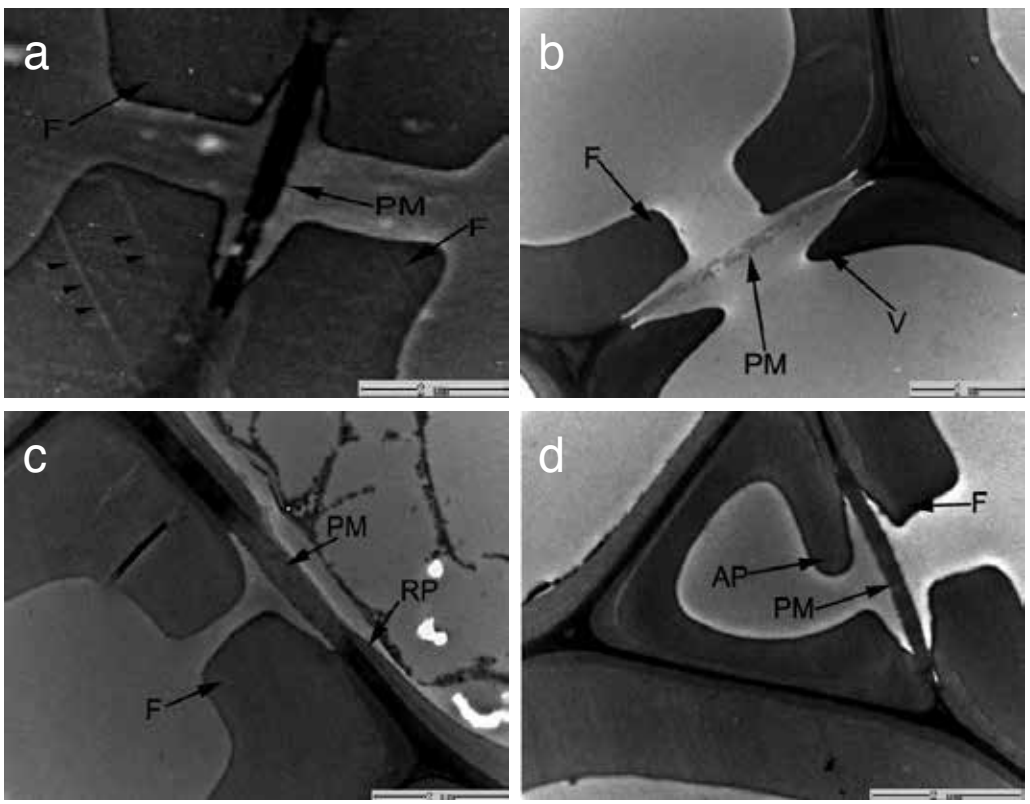

Figure 2. TEM micrographs of pit membrane among various cells in *C. alba* L., taken at 80 kV. (a) Pit membrane between fibers, (arrowheads: knife mark). (b) Pit membrane between fiber and vessel. (c) Pit membrane between fiber and ray parenchyma. (d) Pit membrane between fiber and axial parenchyma. F, fiber; V, vessel; RP, ray parenchyma; AP, axial parenchyma; PM, pit membrane.

Compared to hardwood, the cell type of softwood is uniform, mainly containing tracheids. In normal wood of *Pinus radiata* D. Don, the cell wall layering structure is similar to that of fiber

in hardwood, while the structure of tracheid cell walls in compression wood is quite different [19]. TEM observations revealed a highly lignified outer S2 layer (S2L) and the absence of an S3 layer in compression wood of *Pinus radiata* D. Don (Fig. 3) [20].

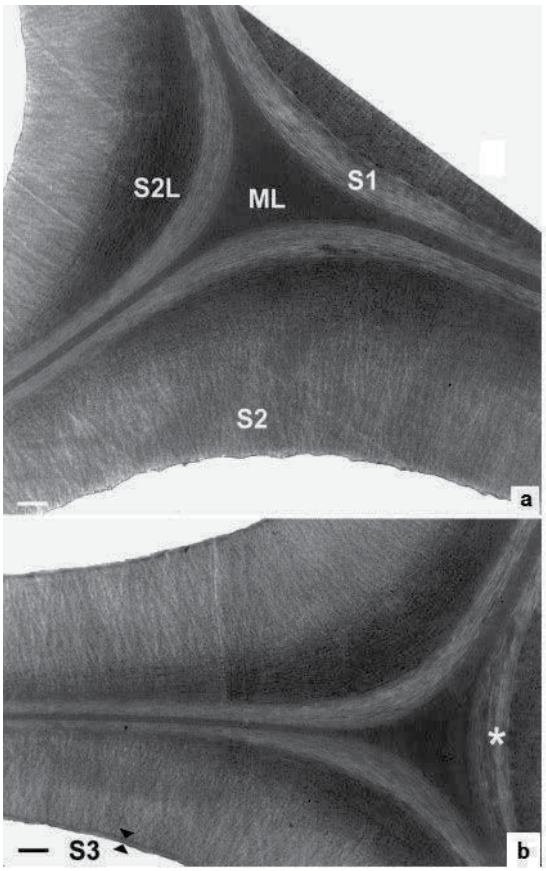

Figure 3. TEM micrographs of mild compression wood of *Pinus radiata* D. Don., taken at 80 kV. ML, middle lamella between adjoining tracheids; S1, outer secondary wall; S2, middle layer of secondary wall; S2L, outer S2 layer.

2.2. Cell wall layering structure in gramineous species

The investigation of the *Miscanthus sinensis* by TEM readily differentiated the sclerenchymatic fiber (Sf) into the middle lamella, the primary wall, and the secondary wall, a typical layering structure of fiber cell walls in wood and grass species (Fig. 4a) [13, 21, 22]. Interestingly, there was a greater degree of heterogeneity in the layering structure of Sf secondary wall (Fig. 4a and 4b), as represented by the fact that we were able to identify six main types (Type I-VI) depending on the number of alternating narrow and broad layers present. Narrow layers appeared as dark thin lines and had a more or less constant thickness. In order to establish the degree of variation in secondary wall patterning among

http://dx.doi.org/10.5772/60752

fiber, a classification system of frequently observed patterns was devised based on TEM observations in Sf adjacent to xylem and phloem (Fig. 5). For the outer Sf connected to the surrounding parenchymatic tissue, the distribution of types I to III (4–6 layers) were predominant, whereas Type IV-VI (7-9 layers) were discernible in individual Sf close to the xylem vessel and phloem cells. Much variation in cell wall layering structure has also been reported for other bamboo species, such as *Phyllostachys viridiglaucescens* and *Dendrocalamus asper*, in which the fibers are categorized into four and six major types according to their respective layering structure [21, 23]. Unlike the layering pattern of Sf adjacent to the xylem vessel in *Miscanthus sinensis*, *Dendrocalamus asper* fibers, which have the highest number of wall layers, were located at the periphery of the fiber bundles. Moreover, the poly-lamellated secondary wall is not an exclusive feature of herbaceous species and appears to have evolved in a variety of taxa. The sclerotic bark fibers of beech (*Fagus sylvatica*) have thick cell walls with numerous individual layers irregularly arranged [24]. Tension wood of *Laetia procera* (Poepp.) Eichl. (Flacourtiaceae) also shows a peculiar structure of secondary wall, which alters from thick to thin layers [25]. In the biomass conversion, the complex poly-lamellated structure acts like a barrier limiting the radial penetration of the chemicals and enzyme, which can be referred as the natural biomass recalcitrance.

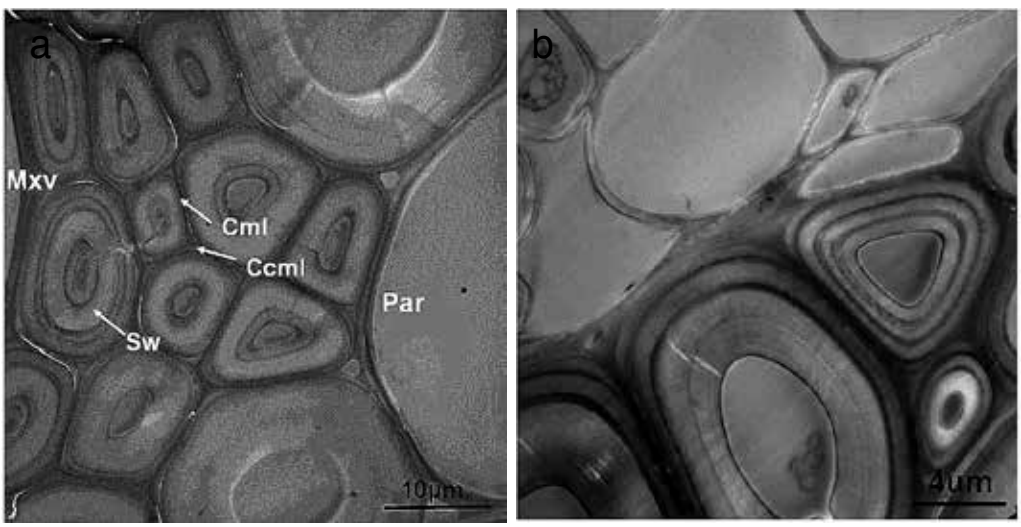

Figure 4. TEM images showing layering structure of Sf in *M. sinensis* cv. internode tissue, stained with 1% w/v $KMnO_4$. (a) Sf adjacent to xylem; (b) Sf adjacent to phloem. Sf, sclerenchymatic fiber; Ccml, cell corner middle lamella; Cml, compound middle lamella; Sw, secondary wall.

In addition to the layering features of Sf secondary wall, the ultrastructural variation in conductive tissue (xylem vessels) was also visualized using TEM images (Fig. 6a and 6b). The secondary wall of Mxv and Pxv could not be clearly divided into sub-layers. This is probably due to either the uniform electron density or the cellulose microfibrils (Mfs) orientation.

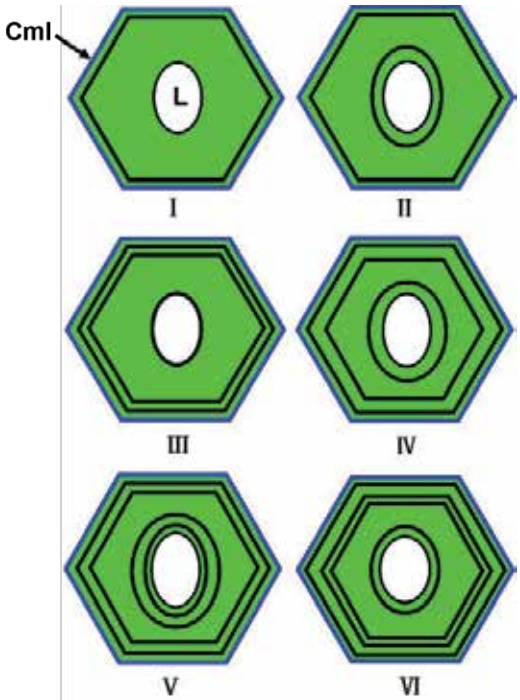

Figure 5. Schematic illustration of Sf layering pattern. "Thin" layers are depicted as black lines, whereas the "broad" layers are colored green. A number has been assigned to the different types of layering for convenience. L: Lumen.

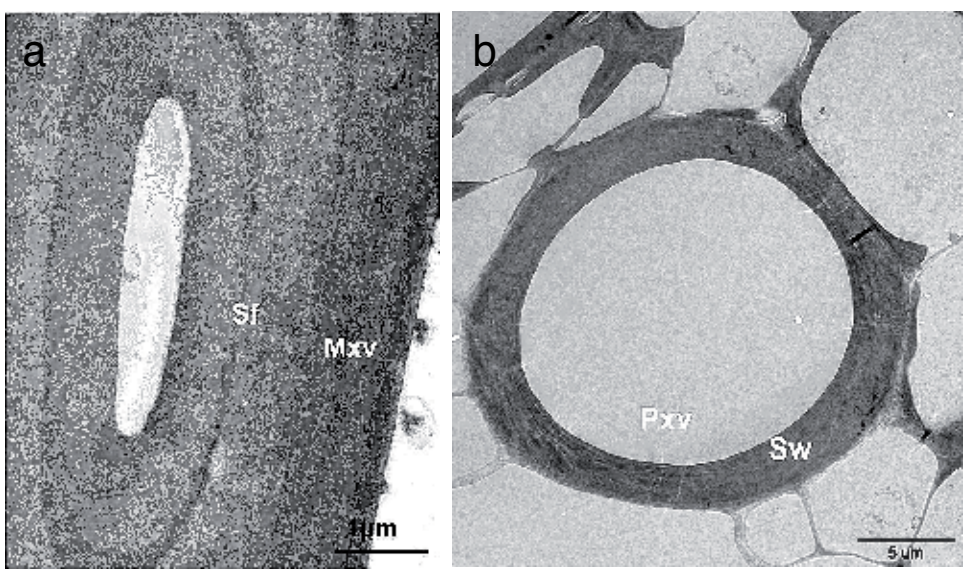

Figure 6. TEM images showing layering structure of *Miscanthus sinensis* internode tissue. (a) Metaxylem vessel (Mxv); (b) protoxylem vessel (Pxv).

http://dx.doi.org/10.5772/60752

3. Lignification and lignin distribution

Next to cellulose, lignin is the most abundant and important polymeric organic substance in plant cell wall. It is a complex phenolic polymer formed by radical coupling reactions of three main monolignols: *p*-coumaryl, coniferyl, and sinapyl alcohol [26, 27]. As a major component of the cell wall of higher plants, lignin plays a vital role in plant growth by enhancing the strength of plant tissues and sealing the wall from water leaks and pathogens invasion. During plant cell wall formation, lignification is generally regarded as the final stage of the differentiating process, where lignin is deposited within the polysaccharide cell wall framework by infilling interlamellar voids [28]. Studies of lignin distribution in plant cell walls are important because of the effect of uneven lignin distribution on wood properties, particularly pulping properties and resistance to decay. Until now, considerable effort has been applied to the investigation of lignin distribution in the cell wall. Since the early 1980s, advanced electron microscopic techniques were developed to obtain high-resolution information on the lignin distribution in plant cell walls. TEM coupled with potassium permanganate ($KMnO_4$) staining has proven to be effective in obtaining high-resolution information on the lignin deposition [13, 19, 29]. On the other hand, the bromination technique by combination of energy-dispersive X-ray analysis (EDXA) with TEM or scanning electron microscopy (SEM) has shown the potential of providing quantitative information on the distribution of lignin. A similar method was developed with the mercurization of specimen and subsequent SEM/TEM-EDXA analyses, which is also based on chemical reactions between lignin and inorganic compounds [16, 30, 31]. Moreover, using newly developed immunological labeling markers to probe lignin with respect to its monomeric composition and with respect to the nature of its structural internal linkages, immunogold TEM has proven to be powerful in distinguishing different lignin substructures on the ultrastructural level [32-35].

3.1. Lignification

The lignification of plant cell walls is generally known to last for a long period, from the S_1 stage to the F stage. After the enlargement of cell size, the secondary wall is thickened with the formation of the S1, S2, and S3 layers. The outermost region of the cell wall, including the intercellular layer, the cell comers, and the primary wall, is lignified during the S1 stage when the surface enlargement of the cell is completed, and just before the S1 starts thickening. This lignification, which will be called "intercellular layer (I)-lignification," may play an important role in stabilizing the cell size and adhering adjacent cells with one another. This I-lignification continues during the differentiation of the S1 and S2 layers, and even until the formation of the S3. On the other hand, the lignification of the secondary wall, which will be called "S-lignification", proceeds mainly after the development of a secondary wall framework, that is, in the final (F) stage of differentiation, although its initiation can be detected already during the S2 stage.

To obtain more detailed information, the immunogold-labeling technique has been applied to differentiate between macromolecular features of condensed (mainly C–C bonds) and non-condensed (*O*-4 aryl–alkyl bonds) lignin subunits during deposition. The results obtained with

a young poplar tree suggest that condensed G and GS types of lignin substructures are preferably formed in middle lamella and cell corners of the differentiating fibers, whereas the formation of non-condensed bonds is favorable in the incipient S1, just at the onset of secondarization [36]. Recently, a polyclonal antibody against a specific condensed lignin substructure, that is, the 8-ring dibenzodioxocin, has been raised for TEM-immunogold detection of the lignification process in cell walls of softwood xylem [33, 34, 37]. The results demonstrated the absence of the dibenzodioxocin structure in very young tracheids where secondary cell wall layers were not yet formed. Moreover, the dibenzodioxocin structure was more abundant in the secondary cell wall layers than in the middle lamella during secondary cell wall thickening. In contrast to the concept of late lignification, that is, in which wood tracheid cell walls undergo lignification only after deposition of polysaccharides, this is an indication that lignification possibly occurs parallel to polysaccharide deposition. In addition to direct lignin labeling, key enzymes involved in the lignification of plant cell walls were localized in developing walls with specific antibodies. In developing xylem cells of Populus, strong labeling of peroxidases in cell corner regions during early developing stages is probably confirming the onset of lignification in these wall portions [38].

3.2. Lignin distribution

3.2.1. Distribution of lignin in softwoods

A number of topochemical detections established that the compound middle lamella is more highly lignified than the secondary wall in typical softwood tracheids [15, 17, 19, 20, 39]. Moreover, the SEM-EDXA technique provided quantitative information of lignin distribution with relatively high accuracy. The distribution of lignin in loblolly pine (*Pinus taeda* L.) tracheids was determined by bromination coupled with SEM-EDXA. It is interesting to note that the lignin concentration in the S2 layer is lower than that in either the S1 or S3 layer [40]. Similar finding was also reported for tracheids of Japanese fir *(Abies suchalinensis* Fr. Schm.) [41].

3.2.2. Distribution of lignin in hardwoods

In contrast to the tracheid as the main cell in softwoods, hardwoods have a variety of cells, such as vessels, parenchyma, and fibers. The lignin distribution between secondary wall and middle lamella in hardwood fibers is similar to that in softwoods; however the secondary wall of hardwood fibers is often less lignified than the secondary wall of softwood tracheids. Figure 7 shows the distribution of lignin in *populous nigra* stem as determined by TEM with potassium permanganate staining [5]. The TEM image exhibits the inhomogeneous distribution of lignin.

3.2.3. Distribution of lignin in reaction woods

Reaction woods appear on leaning stems or branches by any force such as a landslide or snowfall. In softwoods, the reaction wood forms at the lower side of leaning stems or branches, where the compression stress reacts on the xylem. Therefore, this reaction wood is generally called compression wood. Compression wood differs from normal wood in its anatomical

http://dx.doi.org/10.5772/60752

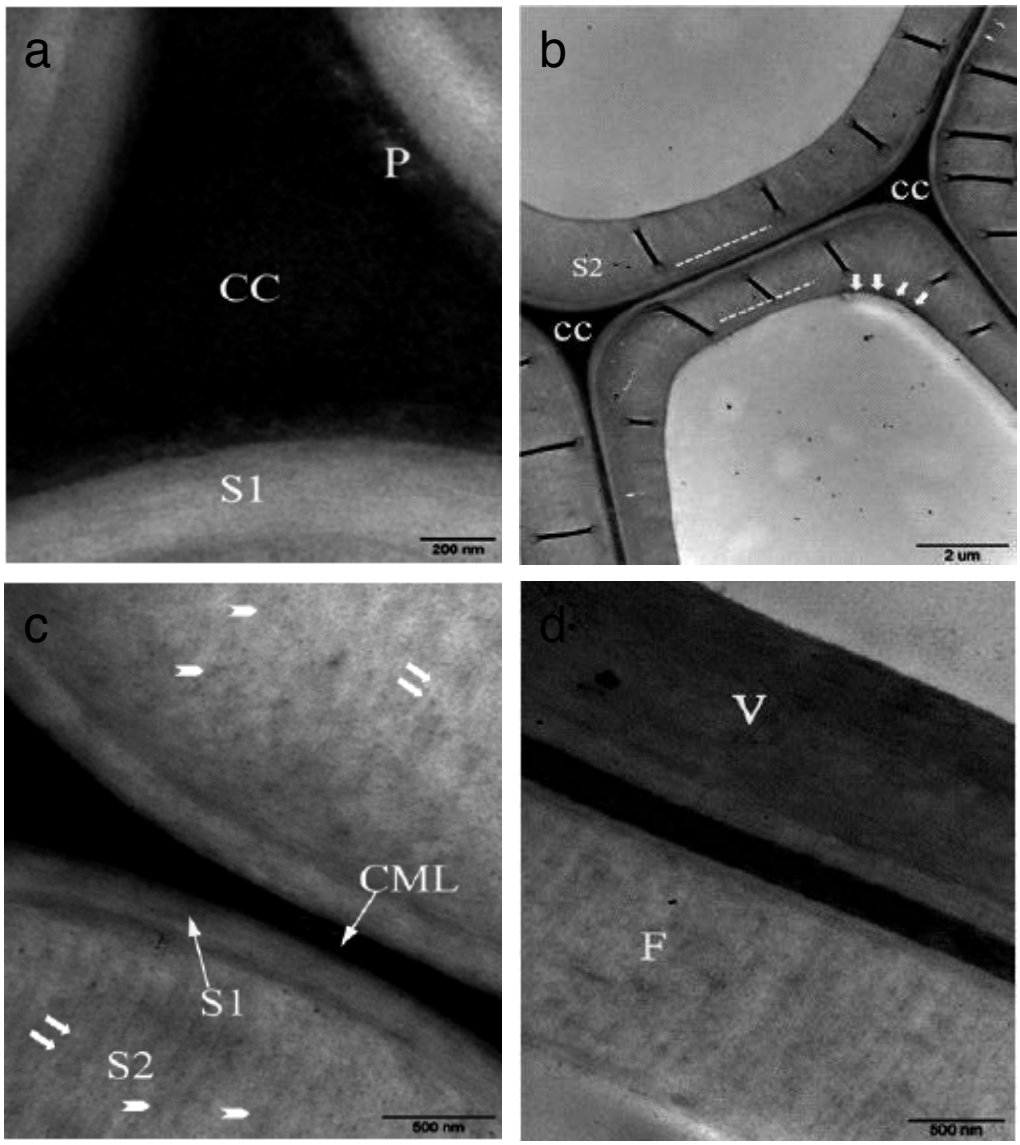

Figure 7. TEM images showing the inhomogeneous distribution of lignin, taken at 80 kV. (a) The CC and P showed higher electron density than the adjacent S1. (b) The outer and inner parts of the S2 layer appear more electron dense (stipplings) than the mid part, the density being particularly pronounced in the curved region of the wall (arrows). (c) The lignin distribution in the S2 layer is distinctly inhomogeneous, with the wall appearing to be a mosaic of electron-dense (arrowheads) and electron-lucent (arrows) regions. The lucent regions have a pattern of sinuous features along the radial directions. (d) The dark staining of the vessel indicated that it is highly lignified, V: vessel, F: fiber.

appearance. Differences include a more lignified secondary cell wall (S2L) layer, absence of an S3 layer, and the presence of intercellular spaces in the cell corner region [42, 43]. The distribution of lignin in compression wood has been extensively investigated. Compression wood shows marked changes in the distribution of lignin across the cell wall with reduced lignifi-

cation of the middle lamella and increased lignification of the S2L layer. In mild compression wood, the lignification of the CCML and the S2L regions is generally comparable, while the S1 and S2 layers were less lignified (Fig. 3) [20]. In severe compression wood, intercellular spaces reduce the contribution of middle lamella lignin to overall lignin content, which is nevertheless increased by the greater lignification of the S2L layer.

On the contrary, reaction wood named as tension wood is formed at the upper side of leaning stems or branches in hardwoods where the xylem loads the tensile stress. Tension wood is characterized by the presence of a cellulose abundant gelatinous layer (GL) forming part of the secondary wall in fibers [44-46]. In maple and oak TW fibers, the GL was divided into concentric sub-layers that appeared either as single rings or as several concentric zones of high and low contrast. Weak staining with potassium permanganate was also visualized at the interface of adjoining concentric layers in maple but was more widespread across the GL in oak, indicating the deposition of aromatic compounds within the cellulose structure of the GL [47].

4. Hemicelluloses deposition

Hemicelluloses are a heterogeneous group of polysaccharides, including xyloglucans, xylans, mannans, and glucomannans. They form physical and chemical bonds to cellulose and lignin and therefore have an important role in building the three-dimensional structures of plant cell walls [48]. The detailed structure of the hemicelluloses and their abundance vary widely among species and cell types. Combination of TEM and immunolabeling has provided detailed information about the deposition of main hemicelluloses related to tissue development and differentiation.

4.1. Hemicelluloses deposition in softwoods

Glucomannans (GMs) are the most abundant hemicelluloses found in softwoods. GMs are composed of a linear backbone of randomly β-(1,4)-linked D-glucosyl and D-mannosyl residues. The ratio of glucosyl and mannosyl units in softwood GMs is approximately 1:3, and D-galactosyl residues are occasionally attached to the backbone with α-(1,6)-glycosidic bonds. In addition to the galactosyl side chain of GMs, softwood GMs also contain partially substituted hydroxyl groups with *O*-acetyl groups at C-2 and C-3 of the mannosyl residues [49].

Many studies have reported the distribution of GMs in the softwood cell wall using various immunochemical probes specific to GMs in combination with TEM. Using the enzyme-gold complex method, Joseleau and Ruel (1984) have demonstrated that GMs of spruce (*Picea abies*) are present mainly in secondary walls but not in the compound middle lamella [50]. The distribution of GMs in the differentiating tracheid cell wall of *Chamaecyparis obtuse* was also investigated by immunogold labeling [51]. The electron microscopic observation showed that labeling of GMs was restricted to the secondary walls of the tracheids and the labeling density temporarily increased and then decreased in the outer and middle layers of the secondary wall during cell wall formation. Investigation of Lodgepole pine (*Pinus contorta var. latifolia*

http://dx.doi.org/10.5772/60752

Englem.) differentiating secondary xylem showed GM deposition not only in the secondary cell wall, but also in the Golgi apparatus, including vesicles [52]. Recently, the detailed spatial and temporal distribution of GMs in differentiating tracheid cell walls of *Cryptomeria japonica* was investigated using immunogold labeling in conjunction with TEM, and the influence of acetylation on immunolocalization of GMs was reported (Fig. 8) [53]. At the primary cell-wall formation stage in tracheids, GM labeling was absent in the cell wall. GMs began to deposit at the corner of the cell wall in the early S1 formation stage. Compared to the stronger GM labeling present in the innermost and outermost parts of the S1 layer, the middle of the S1 layer showed only minimal labeling, and then increased gradually during S1 formation. Thus, the authors speculate that some softwood GMs may show an intussusceptional deposition mode by penetrating into the intermicrofibrillar spaces during cell wall formation without binding to microfibrils. A clear uneven distribution of GMs in the S2 layer during S2 formation was also observed. GM labeling increased gradually in the S2 layer during S2 formation with the innermost part of the S2 layer showing the highest density of GM labeling. The deposition of GMs in S3 layer also showed a similar trend with weak labeling at the early stage of S3 formation, and then increased labeling during maturation. The increased GM labeling during cell wall maturation is not consistent with the previous study of the differentiating tracheid cell wall of *Chamaecyparis obtuse* suggesting that the density of GM labeling decreased gradually during cell wall formation because of lignin deposition during cell wall maturation. GM labeling in mature tracheids of *Cryptomeria japonica* showed higher concentration of GMs in the S1 layer than that in the S2 layer, which is in agreement with immunogold labeling study of *Chamaecyparis obtusa*. In addition, GM labeling was also observed in the CML of *Cryptomeria japonica* mature tracheids whereas GMs showing absence in the CML in either developing or mature tracheid cell walls of *Chamaecyparis obtuse* [51, 53]. To explore the influence of acetylation on immunolocalization of GMs, specimens treated with mild alkali solution were also investigated. Deacetylation of GMs with mild alkali treatment led to a significant increase in GM labeling, suggesting that some GM epitopes may be masked by acetylation. It is interesting to note that the changes in GM labeling after deacetylation were not very pronounced until the early stages of S2 formation, indicating that GMs deposited in the cell wall at early stages of cell wall formation may contain fewer acetyl groups than those deposited at later stages. Furthermore, the decreased GM labeling in mature tracheids suggests that some acetyl groups may be removed from GMs after cell wall formation [53].

In addition to GMs, the distribution of xylans in tracheid walls was also investigated. Xylans in wood cell walls are basically composed of a backbone of xylose units that are linked by β-(1-4)-glycosidic bonds. Softwood xylans that are called arabino-4-*O*-methylglucuronoxylans (AGXs) contain arabinofuranose units linked by α-(1-3)-glycosidic bonds to the xylan backbone [49]. The distribution of AGXs in differentiating earlywood tracheid cell walls of *Cryptomeria japonica* was systematically investigated using immune-TEM [54]. Xylans were found to first deposit in the corner of the S1 layer in the early stages of S1 formation in tracheids. In addition, large amount of xylans were also observed in CCML from the early stage of cell wall formation. During S1 formation, the innermost S1 layer showed weaker xylan labeling than did the rest of the cell wall. A similar pattern was observed during secondary cell wall formation, with the innermost layer and the boundary between the S1 and S2 layers showing

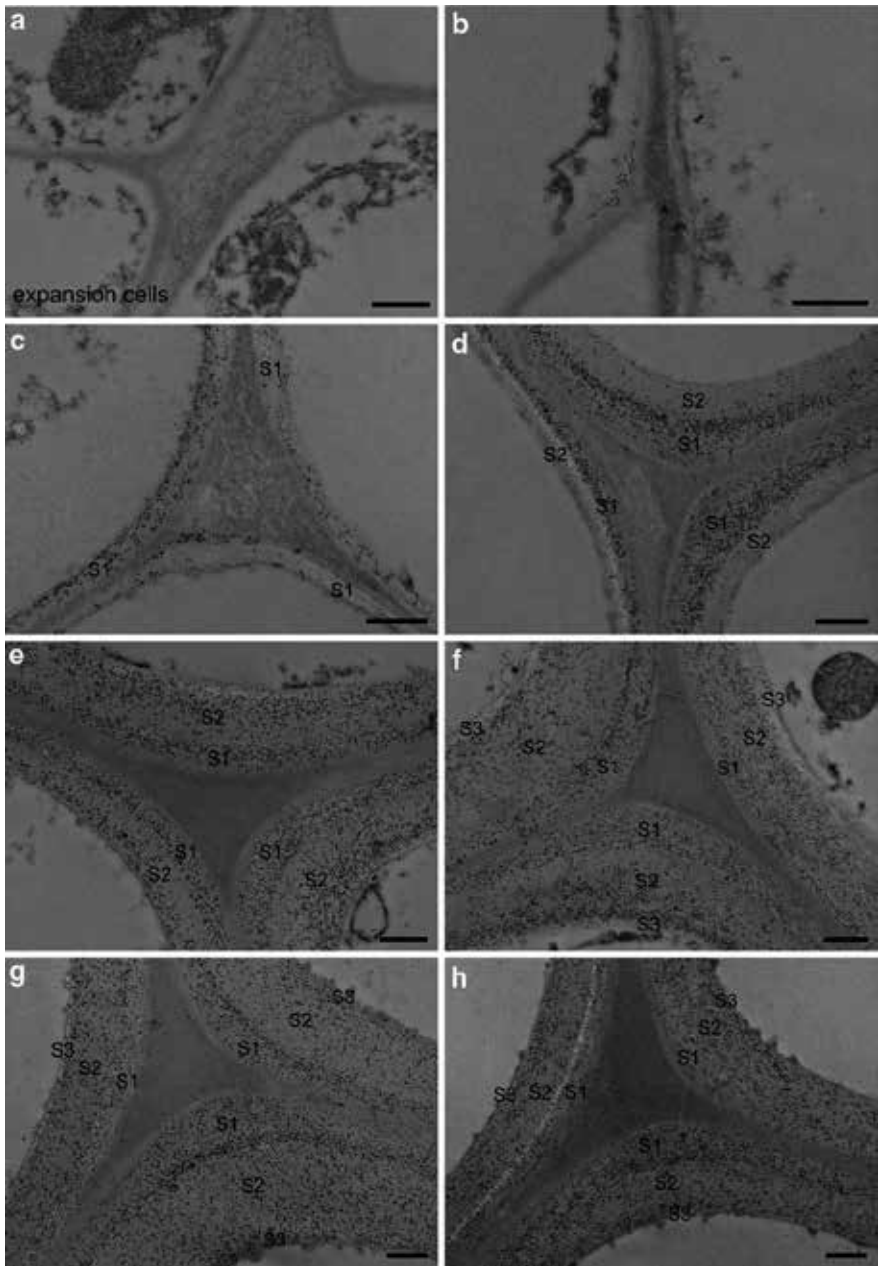

Figure 8. Immunogold localization of glucomannans (GMs) in differentiating and differentiated tracheids. (a) Expansion cells. (b) Tracheids at the early S1 formation stage. (c) Tracheids at the S1 layer formation stage. (d) Tracheids at the early S2 formation stage. (e) Tracheids at the formation of the S2 layer. (f) Tracheids at the formation of the S3 layer. (g, h) Mature tracheids.

weaker labeling than other parts of the cell wall. These results indicate the spatial consistency between xylan deposition and lignin deposition in the early stages of tracheid cell wall

http://dx.doi.org/10.5772/60752

formation [55]. However, an almost uniform distribution of xylans throughout the entire cell wall was observed in mature tracheids.

Furthermore, to extend the understanding of distributional diversities of hemicelluloses among cells, the deposition of GMs and AGXs in ray cells and pits was investigated by immunolabeling [56]. In comparison with tracheids, ray cells have different deposition processes of GMs and AGXs. GM labeling in ray cells began to be detected at the early stage of S1 formation in tracheids, whereas AGX labeling began to be detected in ray cells at the S2 formation stage in tracheids. In mature ray cells, GM labeling was absent in the innermost layer of ray cells, whereas AGXs were uniformly distributed in the entire ray cell walls. In pits, GM labeling was detected in pit membranes at an early stage of pit formation, but disappeared during pit maturation, indicating that enzymes capable of GM degradation may be involved in pit formation. In contrast to GM labeling, AGX labeling was not observed in pit membranes during the entire pit developmental process.

4.2. Hemicelluloses deposition in hardwoods

In hardwoods, *O*-acetyl-4-*O*-methylglucuronoxylans (AcGXs) are the main hemicellulose, occupying about 30% of total cell wall components. AcGXs consist of a β-(1,4)-xylan backbone, decorated with acetyl groups and side chains of 4-*O*-methyl-α-D glucuronic acid [49]. The localization of xylans has been studied by various in situ labeling methods, for example, the xylanase-gold method [57, 58], xylanase and anti-xylanase antibodies [59], and the immunogold method [60-62]. In differentiating xylem of Japanese beech, xylan deposition started in the middle of the S1 layer formation stage and labeling of GXs was seen only in the secondary walls of xylem cells, but not in the primary walls or the middle lamella. In addition, the increased labeling density during cell wall formation strongly suggested that the deposition of GXs may occur in a penetrative way [60]. The distribution of xylans in differentiating *Populus* xylem cells has been systematically investigated using immuno-microscopic methods in combination with monoclonal antibodies (LM10 and LM11) specific to β-(1-4)-linked xylopyranosyl residues [62]. LM10 antibody binds low-substituted xylans (lsAcGXs), whereas LM11 antibody binds high-substituted xylans (hsAcGXs) in addition to lsAcGXs [63]. Xylan deposition was detected earliest in fibers at the cell corner of the S1 layer, and then later in vessels and ray cells, respectively. During secondary cell wall development of fibers, xylan deposition began from the cell corner of the S1 layer after initiation of S1 formation and different labeling patterns of LM10 and LM11 antibodies were observed. LM10 showed stronger xylan localization in the outer secondary cell wall than inner layer, while LM11 showed uniform xylan labeling in the whole secondary cell wall. Differentiating vessels showed similar patterns of xylan labeling as fibers except that vessels showed more uniform labeling in the mature cell wall with stronger labeling of lsAcGXs than fibers. In ray cells, xylan labeling occurred at the S2 formation stage in fibers, which was much later than that in fibers and vessels, but was also detected at the beginning of secondary cell wall formation in ray cells. Unlike fibers and vessels, ray cells showed a more homogeneous composition and distribution of xylans than fibers and vessels. All of the three pit types in the secondary xylem of aspen (including fiber–fiber, vessel–vessel, and ray–vessel) showed strong labeling of hsAcGXs during differentiation, and yet gradually disappeared during pit maturation.

4.3. Hemicelluloses deposition in gramineous species

Most of the existing research about distribution of hemicelluloses in gramineous species concentrate on Arabidopsis, which is one of the most frequently used model plants in plant science. Several immunocytochemical studies have reported the distribution of xylans in Arabidopsis stem [64-66]. Xylan deposition in xylary fibers (fibers) was initiated at the cell corner of the S1 layer and the xylan labeling increased gradually during fiber maturation. Metaxylem vessels showed more developed stages of secondary cell wall formation than fibers, but revealed almost identical xylan labeling patterns to fibers during maturation. The consistency of the immunolabeling patterns between LM10 and LM11 in the cell wall of fibers, vessels, and protoxylem vessels indicated that vascular bundle cells may be chemically composed of a highly homogeneous xylan type. In contrast, interfascicular fibers showed different labeling patterns between the two antibodies and also between different developmental stages. Immunolocalization studies of mannans in Arabidopsis stems have shown that mannans are distributed in the various cell types with different concentrations [67-69]. Temporal and spatial variations in mannan labeling between cell types in the secondary xylem of Arabidopsis stems were examined using immunolocalization with mannan-specific monoclonal antibodies (LM21 and LM22). Mannan labeling in secondary xylem cells (except for protoxylem vessels) was initially detected in the cell wall during S2 formation and increased gradually during development. Labeling in metaxylem vessels (vessels) was detected earlier than that in xylary fibers (fibers), but was much weaker than fibers. The S1 layer of vessels and fibers showed much less labeling than the S2 layer. Some strong labeling was also detected in pit membranes of vessel pits.

5. Conclusions

The potential of TEM for investigation of plant cell walls has already been demonstrated on various plant tissues. The high spatial resolution allows detection of changes in the ultrastructure and cell wall polymer deposition on the cell and cell wall level. Nevertheless, complex sample preparation procedure will limit its extensive application, especially in living plant tissues. Thus, when combined with other in situ microscopic techniques (such as atom force microscopy, confocal laser microscopy, confocal Raman microscopy), much more information hidden in plant cell wall will be illustrated.

Author details

Xia Zhou, Dayong Ding, Jing Ma, Zhe Ji, Xun Zhang and Feng Xu*

*Address all correspondence to: xfx315@bjfu.edu.cn

Beijing Key Laboratory of Lignocellulosic Chemistry/MOE Key Laboratory of Wooden Material Science and Application, Beijing Forestry University, Beijing, China

http://dx.doi.org/10.5772/60752

References

[1] Rüggeberg M, Saxe F, Metzger TH, Sundberg B, Fratzl P, Burgert I. Enhanced cellulose orientation analysis in complex model plant tissues. Journal of Structural Biology 2013;183(3) 419-428.

[2] Mayo SC, Chen F, Evans R. Micron-scale 3D imaging of wood and plant microstructure using high-resolution X-ray phase-contrast microtomography. Journal of Structural Biology 2010;171(2) 182-188.

[3] Himmel ME, Ding SY, Johnson DK, Adney WS, Nimlos MR, Brady JW, Foust TD. Biomass recalcitrance: Engineering plants and enzymes for biofuels production. Science 2007;315(5813) 804-807.

[4] Cosgrove DJ. Growth of the plant cell wall. Nature Reviews Molecular Cell Biology 2005;6(11) 850-861.

[5] Ma J, Zhang Z, Yang G, Mao J, Xu F. Ultrastructural topochemistry of cell wall polymers in *Populus nigra* by transmission electron microscopy and Raman imaging. BioResources 2011;6(4) 3944-3959.

[6] Fangel JU, Ulvskov P, Knox JP, Mikkelsen MD, Harholt J, Popper ZA, Willats WG. Cell wall evolution and diversity. Frontiers in Plant Science 2012;3 152.

[7] Kim JS, Lee KH, Cho CH, Koch G, Kim YS. Micromorphological characteristics and lignin distribution in bamboo (*Phyllostachys pubescens*) degraded by the white rot fungus *Lentinus edodes*. Holzforschung 2008;62(4) 481.

[8] Yu H, Liu R, Shen D, Wu Z, Huang Y. Arrangement of cellulose microfibrils in the wheat straw cell wall. Carbohydrate Polymers 2008;72(1) 122-127.

[9] Hanley SJ, Giasson J, Revol J-F, Gray DG. Atomic force microscopy of cellulose microfibrils: comparison with transmission electron microscopy. Polymer 1992;33(21) 4639-4642.

[10] Gierlinger N, Schwanninger M. The potential of Raman microscopy and Raman imaging in plant research. Spectroscopy: An International Journal 2007; 21(2): 69-89.

[11] Agarwal UP, Atalla RH. In-situ Raman microprobe studies of plant cell walls: Macromolecular organization and compositional variability in the secondary wall of *Picea mariana* (Mill.) B.S.P. Planta 1986;169(3) 325-332.

[12] Singh AP, Donaldson LA. Ultrastructure of tracheid cell walls in radiata pine (*Pinus radiata*) mild compression wood. Canadian Journal of Botany 1999;77(1) 32-40.

[13] Singh A, Daniel G, Nilsson T. Ultrastructure of the S2 layer in relation to lignin distribution in *Pinus radiata* tracheids. Journal of Wood Science 2002;48(2) 95-98.

[14] Brandt B, Zollfrank C, Franke O, Fromm J, Göken M, Durst K. Micromechanics and ultrastructure of pyrolysed softwood cell walls. Acta Biomaterialia 2010;6(11) 4345-4351.

[15] Fromm J, Rockel B, Lautner S, Windeisen E, Wanner G. Lignin distribution in wood cell walls determined by TEM and backscattered SEM techniques. Journal of Structural Biology 2003;143(1) 77-84.

[16] Eriksson I, Lidbrandt O, Westermark U. Lignin distribution in birch (*Betula verrucosa*) as determined by mercurization with SEM- and TEM-EDXA. Wood Science and Technology 1988;22(3) 251-257.

[17] Tirumalai VC, Agarwal UP, Obst JR. Heterogeneity of lignin concentration in cell corner middle lamella of white birch and black spruce. Wood Science and Technology 1996;30(2) 99-104.

[18] Donaldson L, Hague J, Snell R. Lignin distribution in coppice poplar, linseed and wheat straw. Holzforschung 2001;55(4).

[19] Donaldson LA, Singh AP, Yoshinaga A, Takabe K. Lignin distribution in mild compression wood of *Pinus radiata*. Canadian Journal of Botany-Revue Canadienne De Botanique 1999;77(1) 41-50.

[20] Singh AP, Donaldson LA. Ultrastructure of tracheid cell walls in radiate pine (*Pinus radiata*) mild compression wood. Canadian Journal of Botany-Revue Canadienne De Botanique 1999;77(1) 32-40.

[21] Murphy RJ, Alvin KL. Variation in fibre wall structure in bamboo. IAWA Journal 1992;13(4) 403-410.

[22] Gritsch CS, Murphy RJ. Ultrastructure of fibre and parenchyma cell walls during early stages of culm development in *Dendrocalamus asper*. Annals of Botany 2005;95(4) 619-629.

[23] Gritsch CS, Kleist G, Murphy RJ. Developmental changes in cell wall structure of phloem fibres of the bamboo *Dendrocalamus asper*. Annals of Botany 2004;94(4) 497-505.

[24] Prislan P, Koch G, Schmitt U, Gričar J, Čufar K. Cellular and topochemical characteristics of secondary changes in bark tissues of beech (*Fagus sylvatica*). Holzforschung 2012;66(1) 131.

[25] Ruelle J, Yoshida M, Clair B, Thibaut B. Peculiar tension wood structure in *Laetia procera* (Poepp.) Eichl. (Flacourtiaceae). Trees 2007;21(3) 345-355.

[26] Nimz HH, Robert D, Faix O, Nemr M. Carbon-13 NMR spectra of lignins, 8. Structural differences between lignins of hardwoods, softwoods, grasses and compression wood. Holzforschung-International Journal of the Biology, Chemistry, Physics and Technology of Wood 1981;35(1) 16.

[27] Boerjan W, Ralph J, Baucher M. Lignin biosynthesis. Annual Review of Plant Biology 2003;54(1) 519-546.

[28] Donaldson LA. Lignification and lignin topochemistry-an ultrastructural view. Phytochemistry 2001;57(6) 859-873.

[29] Lee KH, Singh AP, Kim YS. Cellular characteristics of a traumatic frost ring in the secondary xylem of *Pinus radiata*. Trees 2007;21(4) 403-410.

[30] Saka S, Thomas RJ. Evaluation of the quantitative assay of lignin distribution by SEM-EDXA-technique. Wood Science and Technology 1982;16(1) 1-18.

[31] Donaldson LA, Ryan KG. A comparison of relative lignin concentration as determined by interference microscopy and bromination/EDXA. Wood Science and Technology 1987;21(4) 303-309.

[32] Kapat A, Dey S. An alternative approach to the detection of lignin: a note on the application of ELISA using polyclonal antibodies. Bioprocess Engineering 2000;22(1) 75-77.

[33] Kukkola E, Koutaniemi S, Gustafsson M, Karhunen P, Ruel K, Lundell T, Saranpää P, Brunow G, Teeri T, Fagerstedt K. Localization of dibenzodioxocin substructures in lignifying Norway spruce xylem by transmission electron microscopy-immunogold labeling. Planta 2003;217(2) 229-237.

[34] Kukkola E, Koutaniemi S, Pöllänen E, Gustafsson M, Karhunen P, Lundell T, Saranpää P, Kilpeläinen I, Teeri T, Fagerstedt K. The dibenzodioxocin lignin substructure is abundant in the inner part of the secondary wall in Norway spruce and silver birch xylem. Planta 2004;218(3) 497-500.

[35] Ligrone R, Carafa A, Duckett JG, Renzaglia KS, Ruel K. Immunocytochemical detection of lignin-related epitopes in cell walls in bryophytes and the charalean alga *Nitella*. Plant Systematics and Evolution 2008;270(3-4) 257-272.

[36] Ruel K, Montiel MD, Goujon T, Jouanin L, Burlat V, Joseleau JP. Interrelation between lignin deposition and polysaccharide matrices during the assembly of plant cell walls. Plant Biology 2002;4(1) 2-8.

[37] Kukkola E, Saranpää P, Fagerstedt K. Juvenile and compression wood cell wall layers differ in lignin structure in norway spruce and scots pine. IAWA Journal 2008;29(1) 47-57.

[38] Kim YS, Wi SG, Grünwald C, Schmitt U. Immuno electron microscopic localization of peroxidases in the differentiating xylem of populus spp. Holzforschung 2002;56(4) 355.

[39] Donaldson LA. Mechanical constraints on lignin deposition during lignification. Wood Science and Technology 1994;28(2) 111-118.

[40] Saka S, Thomas RJ. A study of lignification in loblolly pine tracheids by the SEM-EDXA technique. Wood Science and Technology 1982;16(3) 167-179.

[41] Fukazawa K, Imagawa H. Quantitative analysis of lignin using an UV microscopic image analyser. Variation within one growth increment. Wood Science and Technology 1981;15(1) 45-55.

[42] Timell TE. Recent progress in the chemistry and topochemistry of compression wood. Wood Science and Technology 1982;16(2) 83-122.

[43] Donaldson LA., Singh AP. Formation and structure of compression wood. In: Fromm J. (ed.), Cellular aspects of wood formation. Berlin Heidelberg: Springer; 2013. p225-256.

[44] Bowling AJ, Vaughn KC. Immunocytochemical characterization of tension wood: Gelatinous fibers contain more than just cellulose. American Journal of Botany 2008;95(6) 655-663.

[45] Mellerowicz EJ, Gorshkova TA. Tensional stress generation in gelatinous fibres: A review and possible mechanism based on cell-wall structure and composition. Journal of Experimental Botany 2012;63(2) 551-565.

[46] Yoshinaga A, Kusumoto H, Laurans F, Pilate G, Takabe K. Lignification in poplar tension wood lignified cell wall layers. Tree Physiology 2012;32(9) 1129-1136.

[47] Lehringer C, Daniel G, Schmitt U. TEM/FE-SEM studies on tension wood fibres of *Acer spp.*, *Fagus sylvatica* L. and *Quercus robur* L. Wood Science and Technology 2009;43(7-8) 691-702.

[48] Pauly M, Gille S, Liu L, Mansoori N, De Souza A, Schultink A, Xiong G. Hemicellulose biosynthesis. Planta 2013;238(4) 627-642.

[49] Fengel D, Wegener G. Wood: chemistry, ultrastructure, reactions. Berlin: De Gruyter; 1984.

[50] Ruel K, Joseleau JP. Use of enzyme-gold complexes for the ultrastructural localization of hemicelluloses in the plant cell wall. Histochemistry 1984;81(6) 573-580.

[51] Maeda Y, Awano T, Takabe K, Fujita M. Immunolocalization of glucomannans in the cell wall of differentiating tracheids in *Chamaecyparis obtusa*. Protoplasma 2000;213(3-4) 148-156.

[52] Samuels A, Rensing K, Douglas C, Mansfield S, Dharmawardhana D, Ellis B. Cellular machinery of wood production: differentiation of secondary xylem in *Pinus contorta var. latifolia*. Planta 2002;216(1) 72-82.

[53] Kim JS, Awano T, Yoshinaga A, Takabe K. Temporal and spatial immunolocalization of glucomannans in differentiating earlywood tracheid cell walls of *Cryptomeria japonica*. Planta 2010;232(2) 545-554.

[54] Kim JS, Awano T, Yoshinaga A, Takabe K. Immunolocalization and structural variations of xylan in differentiating earlywood tracheid cell walls of *Cryptomeria japonica*. Planta 2010;232(4) 817-824.

[55] Donaldson LA. Lignification and lignin topochemistry-an ultrastructural view. Phytochemistry 2001;57(6) 859-873.

[56] Kim JS, Awano T, Yoshinaga A, Takabe K. Temporal and spatial diversities of the immunolabeling of mannan and xylan polysaccharides in differentiating earlywood ray cells and pits of *Cryptomeria japonica*. Planta 2011;233(1) 109-122.

[57] Vian B, Reis D, Mosiniak M, Roland JC. The glucuronoxylans and the helicoidal shift in cellulose microfibrils in linden wood: *Cytochemistryin muro* and on isolated molecules. Protoplasma 1986;131(2) 185-199.

[58] Vian B, Roland J-C, Reis D, Mosiniak M. Distribution and possible morphogenetic role of the xylans within the secondary vessel wall of linden wood. IAWA Journal 1992;13(3) 269-282.

[59] Taylor JG, Haigler CH. Patterned secondary cell-wall assembly in tracheary elements occurs in a self-perpetuating cascade. Acta Botanica Neerlandica 1993;42(2) 153-163.

[60] Awano T, Takabe K, Fujita M. Localization of glucuronoxylans in Japanese beech visualized by immunogold labelling. Protoplasma 1998;202(3-4) 213-222.

[61] Awano T, Takabe K, Fujita M, Daniel G. Deposition of glucuronoxylans on the secondary cell wall of Japanese beech as observed by immuno-scanning electron microscopy. Protoplasma 2000;212(1-2) 72-79.

[62] Kim JS, Sandquist D, Sundberg B, Daniel G. Spatial and temporal variability of xylan distribution in differentiating secondary xylem of hybrid aspen. Planta 2012;235(6) 1315-1330.

[63] McCartney L, Marcus SE, Knox JP. Monoclonal antibodies to plant cell wall xylans and Arabinoxylans. Journal of Histochemistry & Cytochemistry 2005;53(4) 543-546.

[64] Brown DM, Zhang Z, Stephens E, Dupree P, Turner SR. Characterization of IRX10 and IRX10-like reveals an essential role in glucuronoxylan biosynthesis in Arabidopsis. The Plant Journal 2009;57(4) 732-746.

[65] Lee C, Teng Q, Huang W, Zhong R, Ye Z-H. The F8H glycosyltransferase is a functional paralog of FRA8 involved in glucuronoxylan biosynthesis in Arabidopsis. Plant and Cell Physiology 2009;50(4) 812-827.

[66] Wu A-M, Rihouey C, Seveno M, Hörnblad E, Singh SK, Matsunaga T, Ishii T, Lerouge P, Marchant A. The Arabidopsis IRX10 and IRX10-LIKE glycosyltransferases are critical for glucuronoxylan biosynthesis during secondary cell wall formation. The Plant Journal 2009;57(4) 718-731.

[67] Handford M, Baldwin T, Goubet F, Prime T, Miles J, Yu X, Dupree P. Localisation and characterisation of cell wall mannan polysaccharides in *Arabidopsis thaliana*. Planta 2003;218(1) 27-36.

[68] Goubet F, Barton CJ, Mortimer JC, Yu X, Zhang Z, Miles GP, Richens J, Liepman AH, Seffen K, Dupree P. Cell wall glucomannan in Arabidopsis is synthesised by CSLA glycosyltransferases, and influences the progression of embryogenesis. The Plant Journal 2009;60(3) 527-538.

[69] Marcus SE, Blake AW, Benians TAS, Lee KJD, Poyser C, Donaldson L, Leroux O, Rogowski A, Petersen HL, Boraston A, Gilbert HJ, Willats WGT, Paul Knox J. Restricted access of proteins to mannan polysaccharides in intact plant cell walls. The Plant Journal 2010;64(2) 191-203.

Chapter 13

Ultrastructural and Morphological Description of the Three Major Groups of Freshwater Zooplankton (Rotifera, Cladocera, and Copepoda) from the State of Aguascalientes, Mexico

Marcelo Silva-Briano, Araceli Adabache-Ortiz,
Gerardo Guerrero-Jiménez,
Roberto Rico-Martínez and
Guadalupe Zavala-Padilla

Additional information is available at the end of the chapter

http://dx.doi.org/10.5772/60659

Abstract

An ultrastructural and morphological description of the three major groups of freshwater zooplankton (Rotifera, Cladocera, and Copepoda) from the state of Aguascalientes using scanning electron microscopy (SEM) and transmission electron microscopy (TEM) was performed. The main characteristics used for identification keys for each group were particularly investigated and also the cellular morphology of rods and spermatozoids in males of the rotifer *Brachionus bidentatus* has also been investigated. It is noteworthy to mention that in the state of Aguascalientes, three endemic species of rotifers new to science have been described: *Keratella mexicana, Brachionus araceliae,* and *Brachionus josefinae*. Regarding the suborder Cladocera, the analysis of the first and second pair of antenna, rostrum, cephalic pores, postabdomen, and the five pairs of swimming legs has resulted in the description of seven species new to science from the state of Aguascalientes: four species of *Macrothrix,* two species of *Alona,* and one species of *Karualona*. Regarding the subclass Copepoda, four species of Cyclopoida group new to science have been described from Aguascalientes. The taxonomical description of these species included the morphological analysis of the buccal parts and the five pairs of swimming legs with emphasis on the fifth pair of

INTECH
open science | open minds

© 2015 The Author(s). Licensee InTech. This chapter is distributed under the terms of the Creative Commons Attribution License (http://creativecommons.org/licenses/by/3.0), which permits unrestricted use, distribution, and reproduction in any medium, provided the original work is properly cited.

legs. The ultrastructural and morphological analysis of each characteristic has been an exhaustive task. The use of SEM and TEM was crucial to identify all these new species. SEM has allowed focusing in the study of new micro-details that have been used for taxonomical clarity, while TEM allows for studies of cellular composition and the physiological functioning of these zooplankton species. The state of Aguascalientes inventory today comprehends more than 100 rotifer species and about 50 cladoceran and 30 copepod species (of which 14 were new to science in all three groups), leading us to believe that the number of species for this inventory could be increased, adding new species to science, in the process.

Keywords: Rotifera, Cladocera, Copepoda, Scanning electron microscopy (SEM), Taxonomy, Transmission electron microscopy (TEM)

1. Introduction

Electronic microscopy (EM) has different elements for its applications; all of them have produced important contributions to the different branches of science. While transmission electron microscopy (TEM) has produced an enormous advance in the study of the different cellular components as well as their function, the scanning electron microscopy (SEM) has helped in the recognition of surfaces of cells, tissues, and structures, developing a new way of more detailed study [1].

In the case of limnology, the use of SEM has been of great importance for taxonomists as a tool that allows for a more detailed study of the different planktonic organisms that are mainly microscopic, and thus optical microscopy might not allow for a clear distinction of structures of taxonomical importance. In the other hand, nuclear ultrastructure in animals, plants, fungi, and Protoctista was studied by TEM to consider variations of RNP particles that may be related to the initial evolution of posttranscriptional processing [2].

In the state of Aguascalientes, Mexico, with the help of SEM, the ultrastructural study of the taxonomic groups Rotifera, Cladocera, and Copepoda has led to the discovery of species new to science, as well as the observation of new structures previously unnoticed. Fourteen new species of these three taxonomic groups were described in Aguascalientes (Table 1). In spite of the discoveries obtained so far, there are still many water reservoirs that have not been analyzed before which opens the probability of increasing the number of new species records for the State or even species new to science.

1.1. Sample preparation

To prepare any organism for SEM is an art. To calculate the concentrations of each substance to apply, to measure the exposure time for each substance on the desired organism, and to know the order in which to proceed through this methodology is an alchemic process. For

http://dx.doi.org/10.5772/60659

Species new to science from Aguascalientes, México		
Rotifera	**Cladocera**	**Copepoda**
Brachionus araceliae	*Alona aguascalentensis*	*Acantocyclops caesariatus*
B. josefinae	*A. anamariae*	*A. dodsoni*
Keratella mexicana	*Karualona penuelasi*	*A. marceloi*
	Macrothrix agsensis	*Paracyclops hirsutus*
	M. mexicanus	
	M. sierrafriatensis	
	M. smirnovi	

Table 1. Fourteen species new to science described from Aguascalientes, México.

rotifers, cladocerans, and copepods, we have used methodologies previously designed. However, each organism requires slight adequations in this methodology to obtain better results for its observation. In these cases, we have used the next two methodologies.

1.1.1. Preparation of Samples for SEM

Specimens were fixed in 4 % formaldehyde, dehydrated in graded series of ethanol, taken to critical point, mounted in an aluminum stub (1 cm high and 1.2 cm in diameter) and covered with gold. To study the trophi in rotifers, organisms of every species were prepared according to the protocol of [3] with slight modifications. Briefly, this protocol consisted of isolating ten females of rotifers in a Petri dish and then adding a drop of sodium hypochlorite and waiting until the lorica was dissolved. Then the females were washed three times with distilled water and mounted in a SEM cylinder. The specimens were observed in a JEOL 5900 LV scanning electronic microscope.

1.1.2. Preparation of Male Specimens for TEM

We cultured rotifers until we obtained 500 males. They were fixed in 2 % glutaraldehyde (GTA) and 4 % paraformaldehyde (PFA) with 0.16 M phosphate buffer (PBS). Then, they were post-fixated with 1 % osmium tetroxide (OsO_4). Later, the males were embedded in epoxy resin (EPON) and observed in a JEOL 1010 transmission microscope operated at 80 kv.

2. Rotifera

2.1. General information

Rotifers are a primary group of small invertebrates ranging from 53 μm to 2 mm that play an important role in freshwater ecosystems; they can also colonize marine and terrestrial ecosystems; they can even be found in plants (Bromeliaceae), mosses, and lichens [4]. They are

recognized by three main characteristics: 1) the corona, which is a complex of cilia in the anterior part of the organism and allows the production of water currents that help the animal to capture food; 2) the trophi which is the chewing apparatus made of chitin [5], and its function is to grind food that has been captured; and 3) the foot which is found in the posterior part of the organism and its function is to secrete a sticky substance which allows the animal to adhere to a substratum. However, in some species, the foot can be absent, as in the case of the species of the genus *Asplanchna*.

This phylum is composed of three main classes: The Monogononta with 1,570 species, the Bdelloidea with 461 species, and the Seisonidae with a few marine species [6]. In Mexico, 300 species have been reported [7, 8], and for the state of Aguascalientes, there are 96 species belonging to 33 different genera (Biodiversidad de Aguascalientes 2009). In the state of Aguascalientes, the taxonomic studies so far has focused in the class Monogononta, specifically in the genera *Brachionus* and *Keratella*. These genera are very common and well represented in the state of Aguascalientes as well as worldwide; in both genera, cryptic species or species complexes have been described. Therefore, ultrastructural analysis represents an important tool to elucidate the relationship among species of these two genera. The emphasis in the use of Monogononta is related to the ease in its manipulation for ultrastructural analysis compared with Bdelloidea, where only a few specialists worldwide are able to correctly identify them. However, there are many other genera of rotifers that might be worth to study and to detail ultrastructural differences among cryptic species. That might be the case of the numerous genus *Lecane*.

2.2. Representative characteristics for identification

Rotifers are divided into loricated and illoricated, which means that the loricated rotifers possess a cover or carapace that protects them, while in the illoricated ones, the tegument is exposed to the medium. Due to this, the identification of rotifers is performed in two different ways:

1. For the study of illoricated organisms which is the case of the class Bdelloidea or the genus *Asplanchna*, it is necessary to locate the trophi (Figure 1) as it is the best structure to aid in the identification. However, we must record all the characteristics like body shape and count the number of ovaries, vitellarium, and other features in a live uncontracted animal previous to the fixation of the specimen.

2. For the loricated rotifers, it is necessary to fix them in 4 % formaldehyde. Identification is commonly based on the number and position of the spines as in the genus *Brachionus*; on the shape of the dorsal and ventral valves of the lorica, the different folds, and the shape and structure of the foot and the presence or absence of claws as in the genus *Lecane*; and on the structure and number of the facets of the lorica and the number and disposition of spines in the genus *Keratella* (Figure 1).

However, for a complete analysis in certain species, it is necessary to observe the male and the ornamentation of the cysts; and in cryptic species (like the *Brachionus calyciflorus*, *Brachionus plicatilis*, and *Keratella cochlearis* species complexes), a genetic analysis of coxI sequences [10] or data on cross-mating behavior tests [11] is necessary.

http://dx.doi.org/10.5772/60659

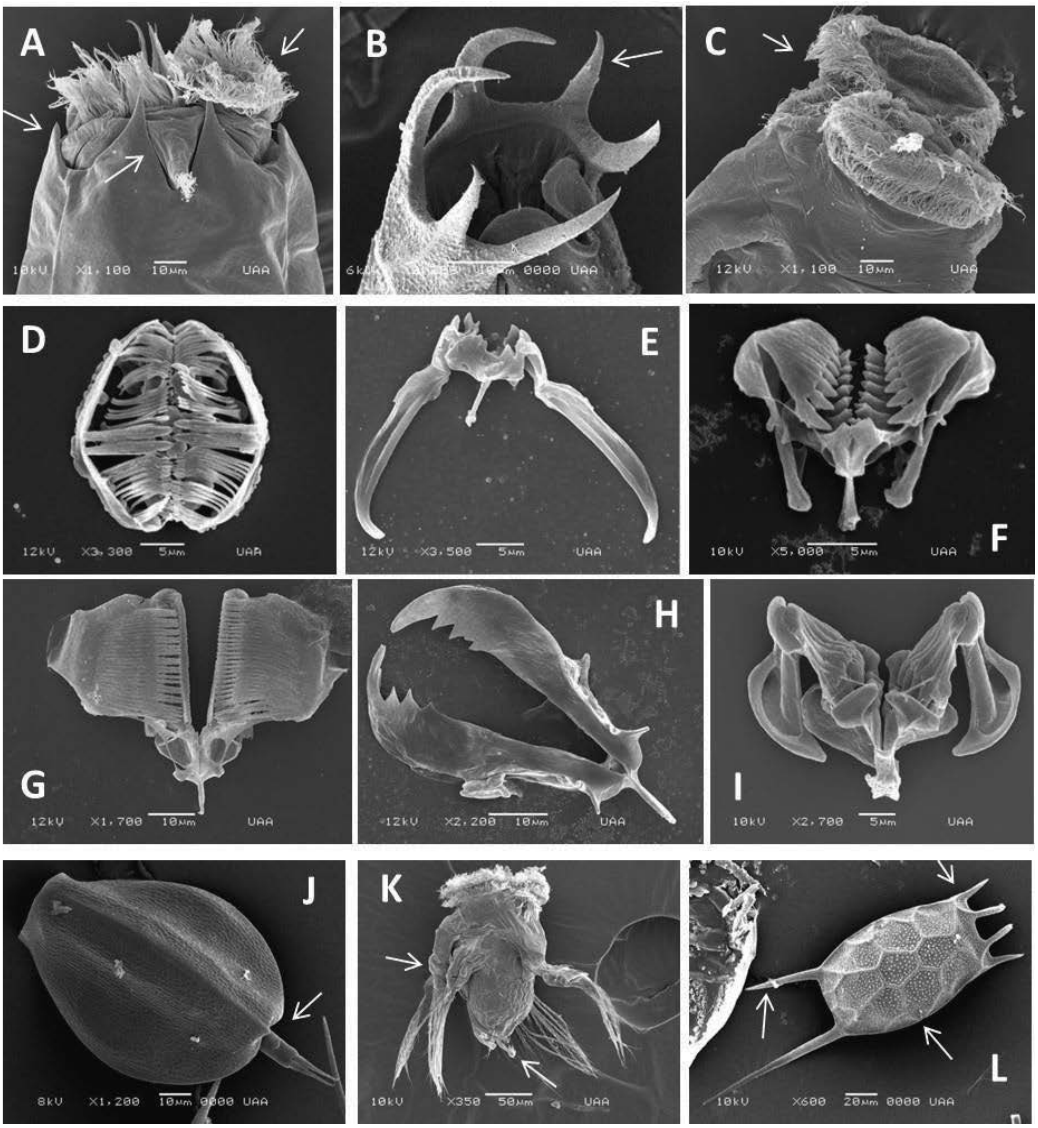

Figure 1. Several characteristics used for rotifer identification. The corona and anterior spines of *Brachionus* (A), anterior spines of *Keratella* (B), corona of *Hexarthra* (C), ramate trophi of a Bdelloid (D), malleate trophi of *Lecane* (E), malleate trophi of *Keratella* (F); malleoramate trophi of *Filinia* (G), incudate trophi of *Asplanchna* (H), malleate trophi of *Brachionus* (I), the loricated rotifer *Lepadella* with arrow showing pseudosegments of the foot (J), the illoricated rotifer *Hexarthra* showing the arms and setae needed for identification (K), and the loricated rotifer *Keratella* with arrows pointing to the facets of the lorica and anterior and posterior spines needed for identification (L).

2.3. Sexual behavior and morphology of germ line of cells in rotifers

The variations in the taxonomic characteristics, as well as the peculiar way in which mating behavior occurs in the different genera, have aroused great interest about the knowledge of sexual reproductive behavior in rotifers. Usually class Monogononta reproduces mostly via

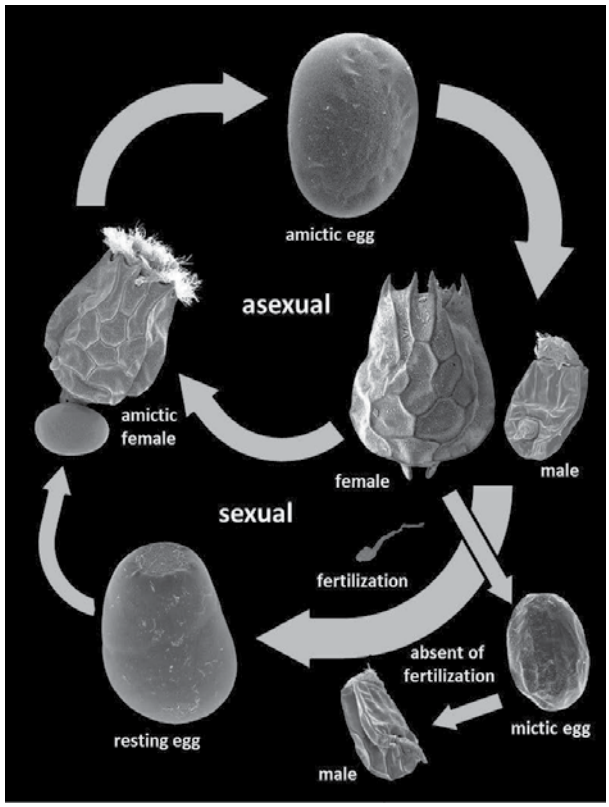

Figure 2. Monogononta life cycle: When the female produces an amictic egg, then an amictic (parthenogenetic) female is born and this asexual reproduction goes on until some environmental factors trigger sexual reproduction. However, when a mictic (sexual) female is born, it produces a mictic egg that can be fertilized to produce a resting egg (cyst), or if the egg is not fertilized, this unfertilized mictic egg produces a male. The presence of males in the environment allows cross-mating that results in production of sexual eggs or cysts (that are still known as resting eggs). Cysts represent a strategy to overcome harsh environmental conditions.

parthenogenesis, but during environmental conditions that still remain controversial, males appear in the environment and sexual reproduction takes place (Figure 2). However, the class Bdelloidea lacks sex completely [12].

The study of sexual reproductive behavior of rotifers has helped taxonomy to clarify the position of some species thought to be cryptic as is the case of *B. araceliae* which some authors suggested that it might belong to *B. bidentatus* [13]. However, it was recognized as a new species after cultivation in the laboratory for several generations showed that it was not a morphotype of *B. bidentatus*, but rather a new species [14]. Later, significant differences between the male of both species were noted [15].

Similar studies on cross-mating tests of species within the same family but belonging to different genera have been reported [11]. Unusual sexual reproductive behaviors and the peculiar life of male rotifers led to the study of the two types of sexual cells present in males (spermatozoa and rods) (Figure 3).

http://dx.doi.org/10.5772/60659

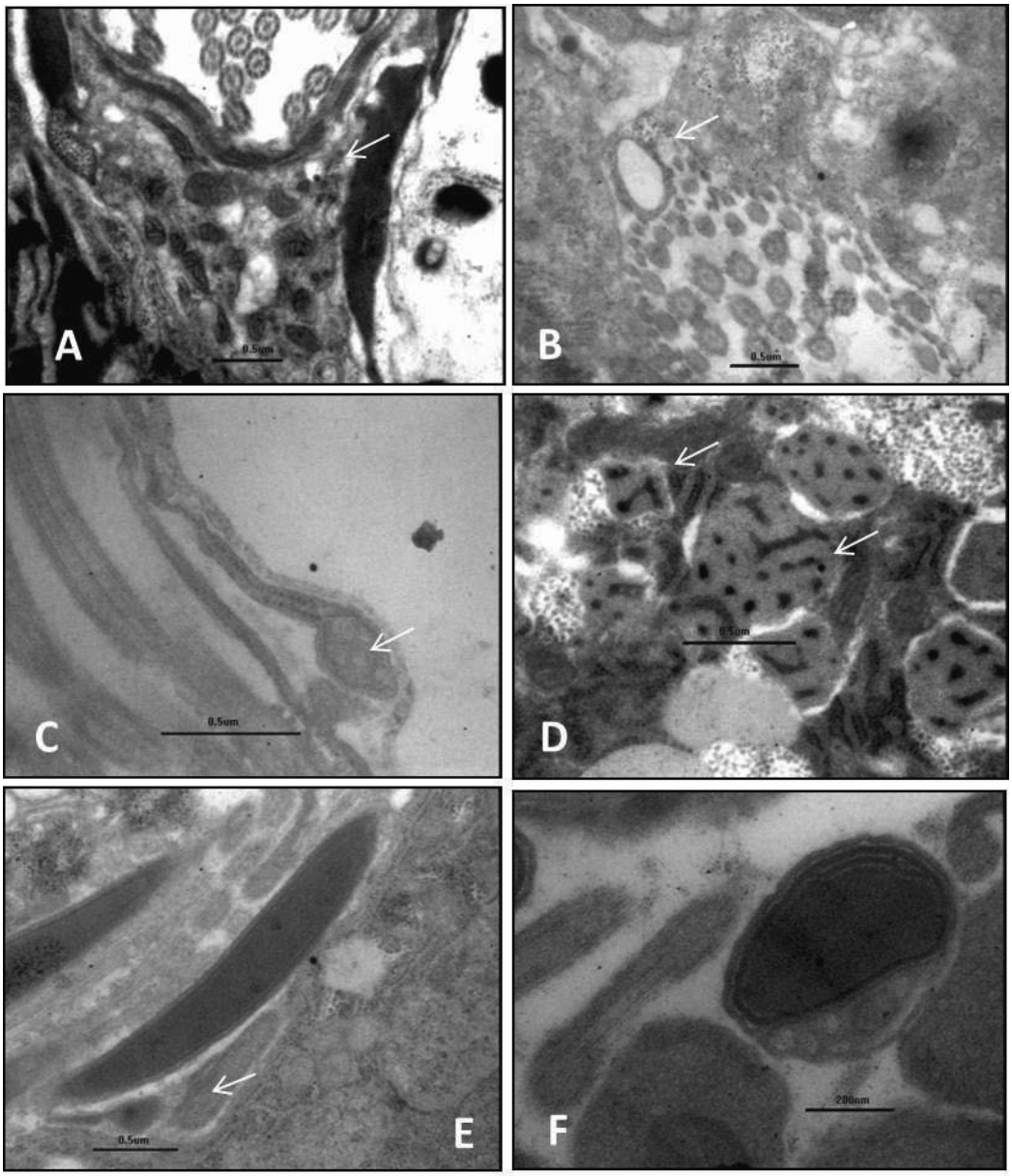

Figure 3. Cavity of the cilia in the male of *B. bidentatus* surrounded by cytoplasmatic material produced by rods (A) and (B), spermatozoon (C), different views of transversal cuts of spermatozoa (D), rod segregating cytoplasmatic material (E), and transversal cut of a rod (F).

It has been observed that these two cells are intimately related with the fertilization process. Some photographs have evidenced that the cytoplasmic substance that secretes the rods adheres to the necks of the spermatozoa. These results are still not clear, but apparently the chamber in which the spermatozoa are found is surrounded by rods waiting for the sperma-

tozoa to appear. According to [16], rods assist in the sperm delivery during fecundation and are the first element that is introduced in the female. We are working to determine the role of rods in the reproductive mechanism of rotifers using ultrastructural studies. However, we do not have a very conclusive result yet, but it would be an important contribution to the knowledge of sexual reproductive embryology for invertebrates.

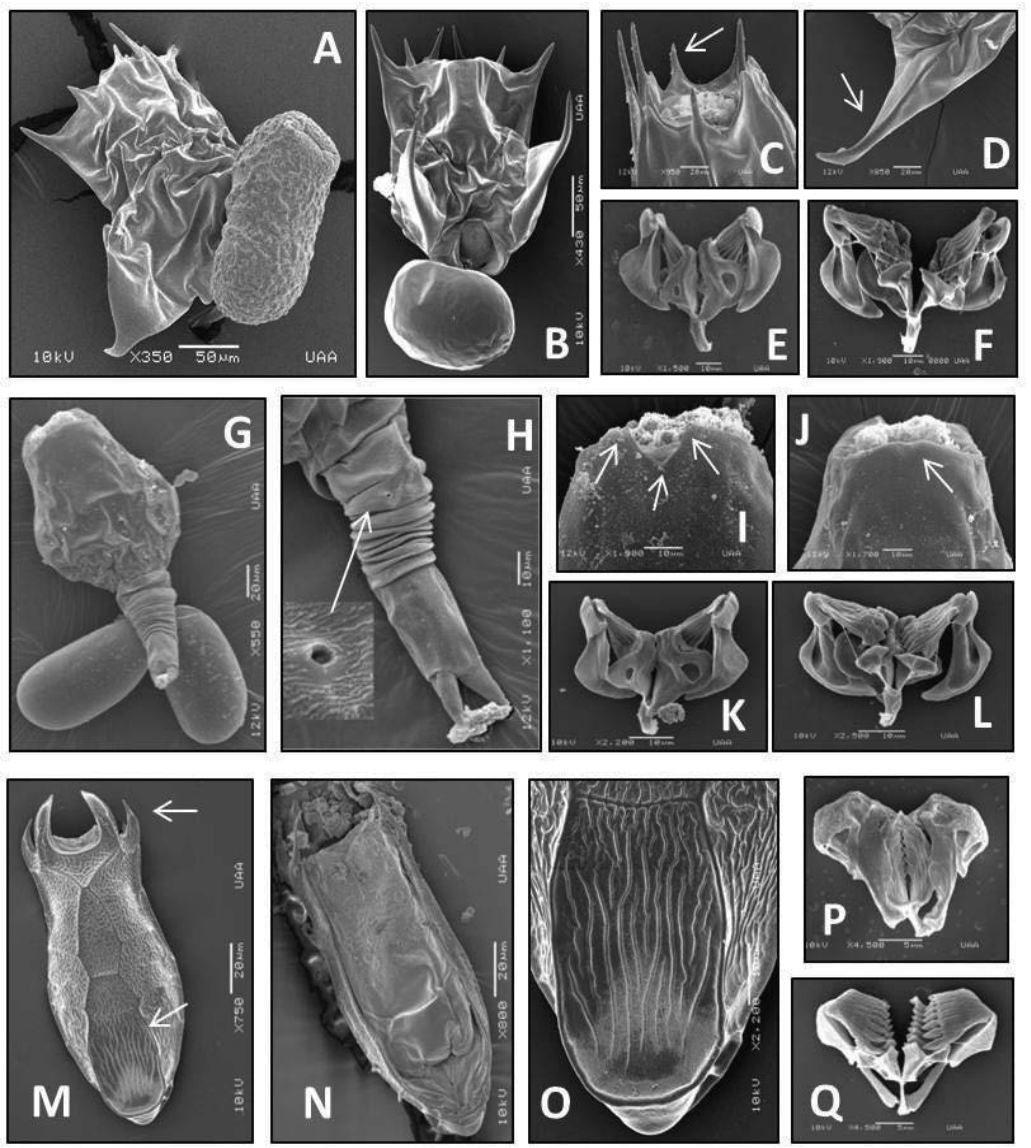

Figure 4. Three new species of rotifers recorded in Aguascalientes, Mexico. *Brachionus araceliae* dorsal view A, ventral view B, anterior spines C, posterior wing D, trophi dorsal view E, ventral view F [14]); *B. josefinae* ventral view G, foot H, dorsal spines I, ventral spines J, trophi dorsal view K, ventral view L [18, 19]; *Keratella mexicana* dorsal view M, ventral view N, plaque O, trophi dorsal view P, and ventral view Q [20, 21].

http://dx.doi.org/10.5772/60659

2.4. New species of rotifers from Aguascalientes, Mexico

The study of morphology and ultrastructure of rotifers along with studies of sexual reproductive behavior has led to the description of males new to science as in *Platyias quadricornis* [17] and more importantly, to the description of three species new to science. That is the case of *Brachionus araceliae* [14], *Brachionus josefinae* [18, 19], and *Keratella mexicana* [20, 21] (Figure 4).

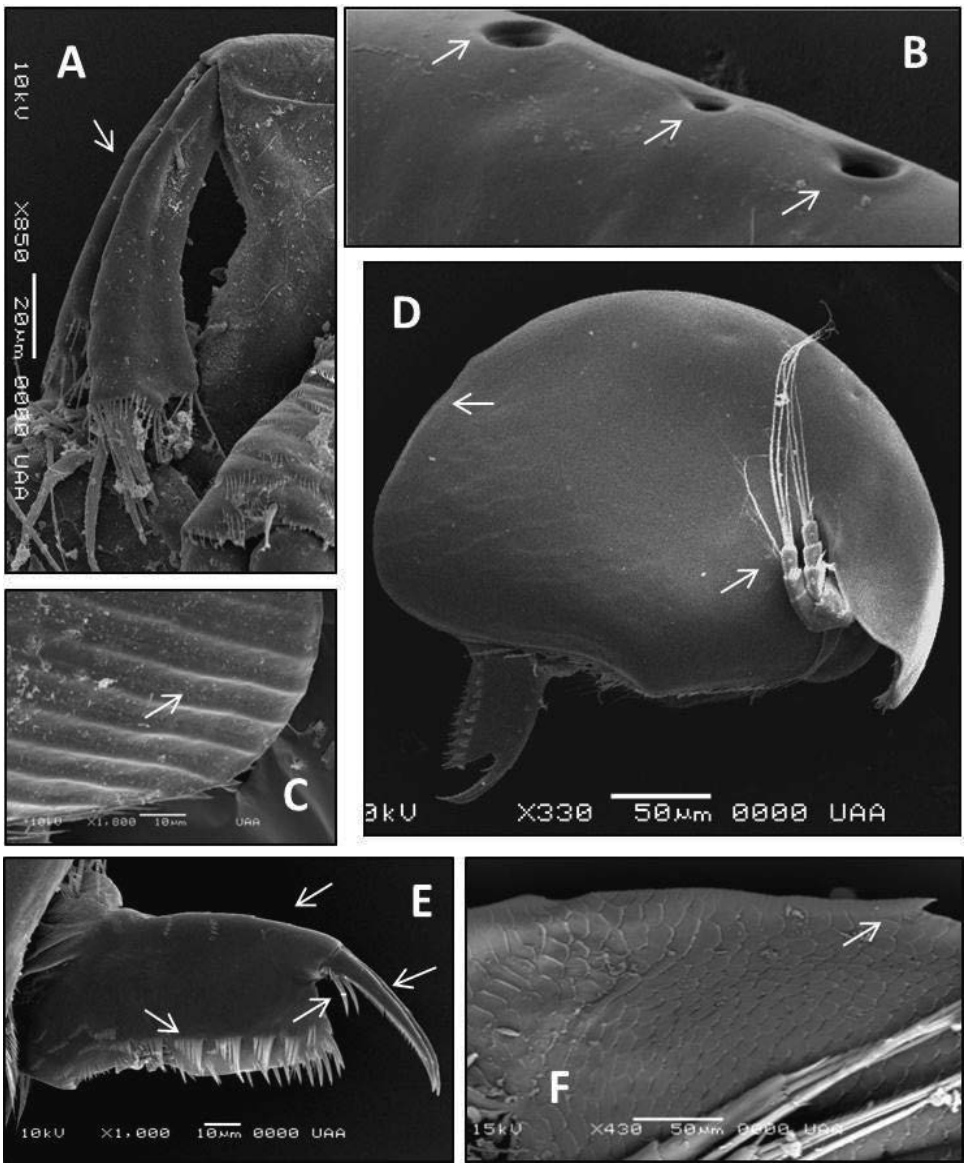

Figure 5. Several characteristics important for cladoceran identification. The first pair of antennas (A); cephalic pores (B); caudal ornamentation of carapace (C); second pair of antennas and shape of carapace (D); postabdomen, endclaw, basal spine, and lateral fasciculla of setae (E); and dorsal keel (F).

3. Cladocera

3.1. General information

Cladocerans are small-size crustaceans ranging from 0.2 to 18.0 mm in length. Most species are characterized for having a carapace that covers the entire body except for the head [22]. A clearer and more general description of cladocerans is achieved by taking the water flea (genus *Daphnia*) as a model: an organism of this genus has a body not clearly segmented; it has a head and trunk, but the latest one is covered by the carapace in the anterior part. The first part of antennas is small and the second part is big and visible; in the head, there is a compound eye. Cladocerans have 5 to 6 pairs of swimming appendages; the postabdomen is quite characteristic of these crustaceans; in the dorsal part, there is an incubation chamber where eggs are deposited.

There are 600 species of cladocerans worldwide [23]. In Mexico, some authors have estimated 150 species [24], and for the state of Aguascalientes, there are 45 species recorded which are distributed in six families [9]. Cladocerans can be found in lakes, ponds, small rivers, and streams, among others. However, some genera are found in musks, lichens, soil, and saline reservoirs.

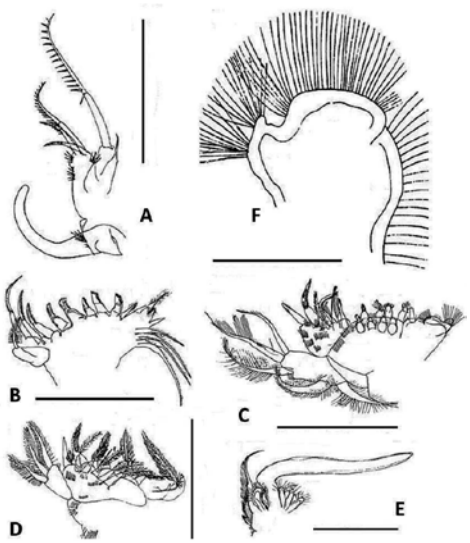

Figure 6. Typical swimming appendages of a cladoceran. First pair (A), second pair (B), third pair (C), fourth pair (D), fifth pair (E), and sixth pair (F). Scale bar equals 100 μm.

3.2. Representative characteristics for identification

The basic characteristics used for cladoceran identification are a) head with or without a compound eye, b) ocellus, c) cephalic pores, d) the first and second pair of antennas, e) shape and ornamentation of the carapace, f) postabdomen including the endclaw and a number of

http://dx.doi.org/10.5772/60659

natatory setae, and g) the five or six pairs of swimming appendages. There are some extra characteristics that might be important tools to help with species identification, but sometimes to observe these peculiar features, it is necessary to dissect the organism. These peculiar features are many times crucial to achieve the species level. Such are the cases of a) the cephalic pores of *Alona anamariae* (Figure 5B), b) the absent or very rudimentary eyes of the genus *Spinoalona* [25], and c) the keel in the dorsal part of the carapace of *Macrothrix mexicanus* (Figure 5 F), just to mention a few cases. However, it is always necessary to support the identification with the analysis of all structures including the five or six swimming appendages (see Figure 6).

3.3. New species of cladocera from Aguascalientes, Mexico

Nearly 500 water reservoirs have been examined in the state of Aguascalientes, mainly to determine the biodiversity of zooplanktonic groups with special emphasis in rotifers, cladocerans, and copepods. The study of cladocerans in the state of Aguascalientes has led to the discovery of seven species new to science. The genus *Macrothrix* is especially well represented with four species new to science: *Macrothrix agsensis* [26], *M. mexicanus* [27], *M. sierrafriatensis* [28], and *M. smirnovi* [29] (Figure 7A, D, E, F, & G). The genus *Alona* contributed with two species new to science: *Alona aguascalentensis* (Figure 7C) and *A. anamariae* [30] (Figure 7B). The genus *Karualona* contributed with one species: *K. penuelasi* [13] (Figure 7C), which is truly endemic and only found in a small part of the state. Besides the description of new species, these studies have provided information about the distribution, endemism, and morphological variation of the different morphotypes that a particular species might show. These ultrastructure studies with SEM and TEM have strengthened the identification of certain taxa and provided criteria that can be used in the future to resolve taxonomic disputes within the Cladocera group.

4. Copepoda

4.1. General information

Copepods have several characteristics by which they can be recognized from other invertebrates. They have a cylindrical shape and a segmented body. In the anterior part, there is a pair of antennules and in the ventral part of the body, there are five pairs of swimming appendages; in the posterior part of the body, there is an abdomen or urosome containing caudal branches. These organisms are very diverse, and there are more than 11,500 species worldwide [31]. In Mexico, 100 species have been described in epicontinental waters from the three main orders: Cyclopoidea, Calanoidea, and Harpaticoidea [24]. In the state of Aguascalientes, 47 species have been recorded; however, only the orders Calanoidea and Cyclopoida have been studied (Dodson & Silva Briano 1996; [33]; CONABIO-IMAE-UAA, 2008; [35]. Copepods are located in oceans, lakes, and ponds, but they have also been found in musks, lichens, dry leaves, and bromeliads [39]; a few species have been recognized as parasites [22]. In Mexico, the species of Calanoidea and in a lesser proportion Cyclopoida have shown high endemic rates [36]. Therefore, ultrastructural studies can be important to describe new species, separate cryptic species within a species complex, and elucidate restricted distribution patterns.

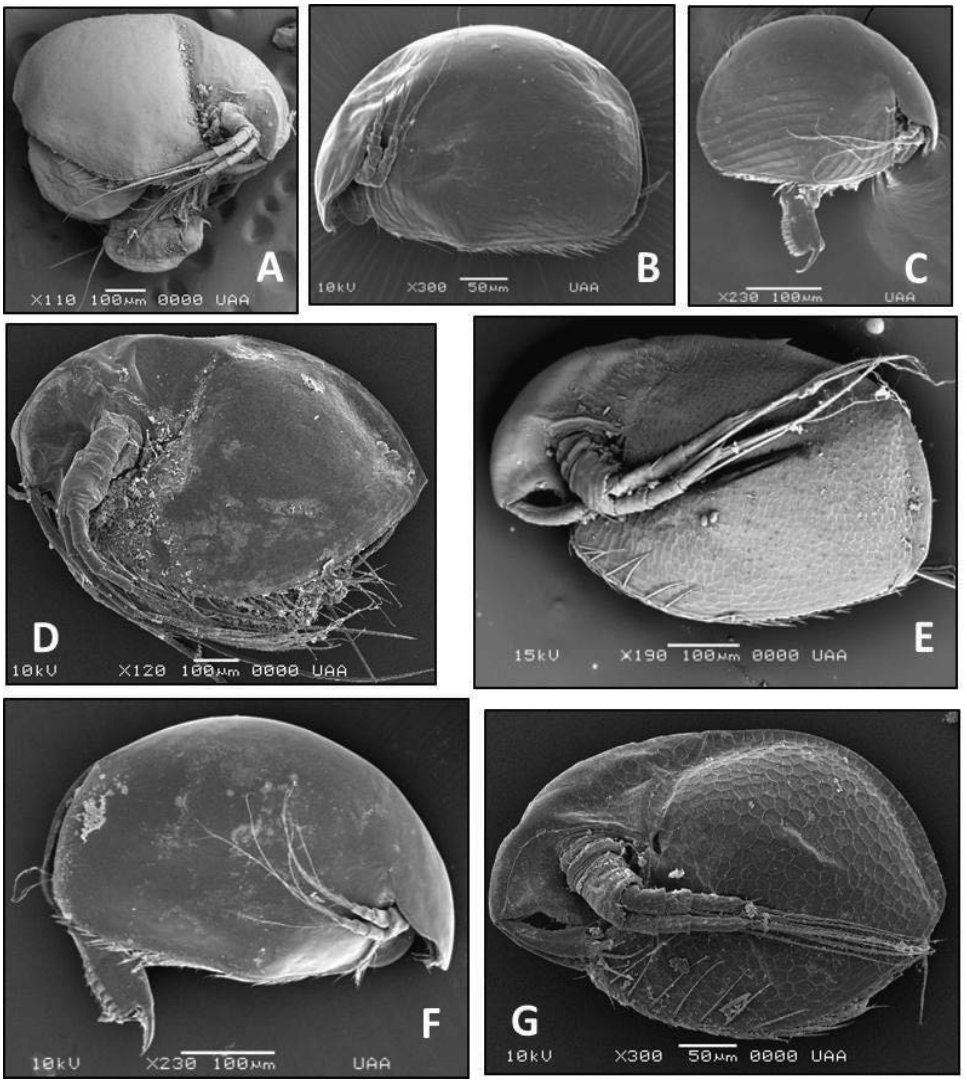

Figure 7. Seven species new to science of cladocerans found in Aguascalientes, Mexico. *Macrothrix agsensis* (A) [26], *Alona anamariae* (B) [30], *Karualona penuelasi* (C) [13], *M. smirnovi* (D) [29], *Macrothrix mexicanus* (E) [27], *A. aguascalentensis* (F) [30], and *M. sierrafriatensis* (G) [28].

4.2. Representative characteristics for identification

Identifying a copepod requires closed examination of the fifth swimming appendages of the female for cyclopoids and of the male for calanoids. For harpacticoids, it is required to closely examine the maxillipeda for the initial identification. However, the fifth pair of swimming appendages and the maxillipeda are just two of the many features that have to be analyzed. For the populations of calanoids and cyclopoids, we require to analyze a) the first two pairs of antennas, b) the buccal apparatus (mandible, maxilula, maxillae, and the maxillipeda), and

http://dx.doi.org/10.5772/60659

c) the urosome (Figure 8). For calanoids, it is necessary to observe the growth in some appendages in the last segments of the thorax. Other morphological variations that might be important for taxonomic identification include a) pores in the swimming appendages, b) different patterns of setae, and c) modifications in the second pair of antennas in some parasite copepods.

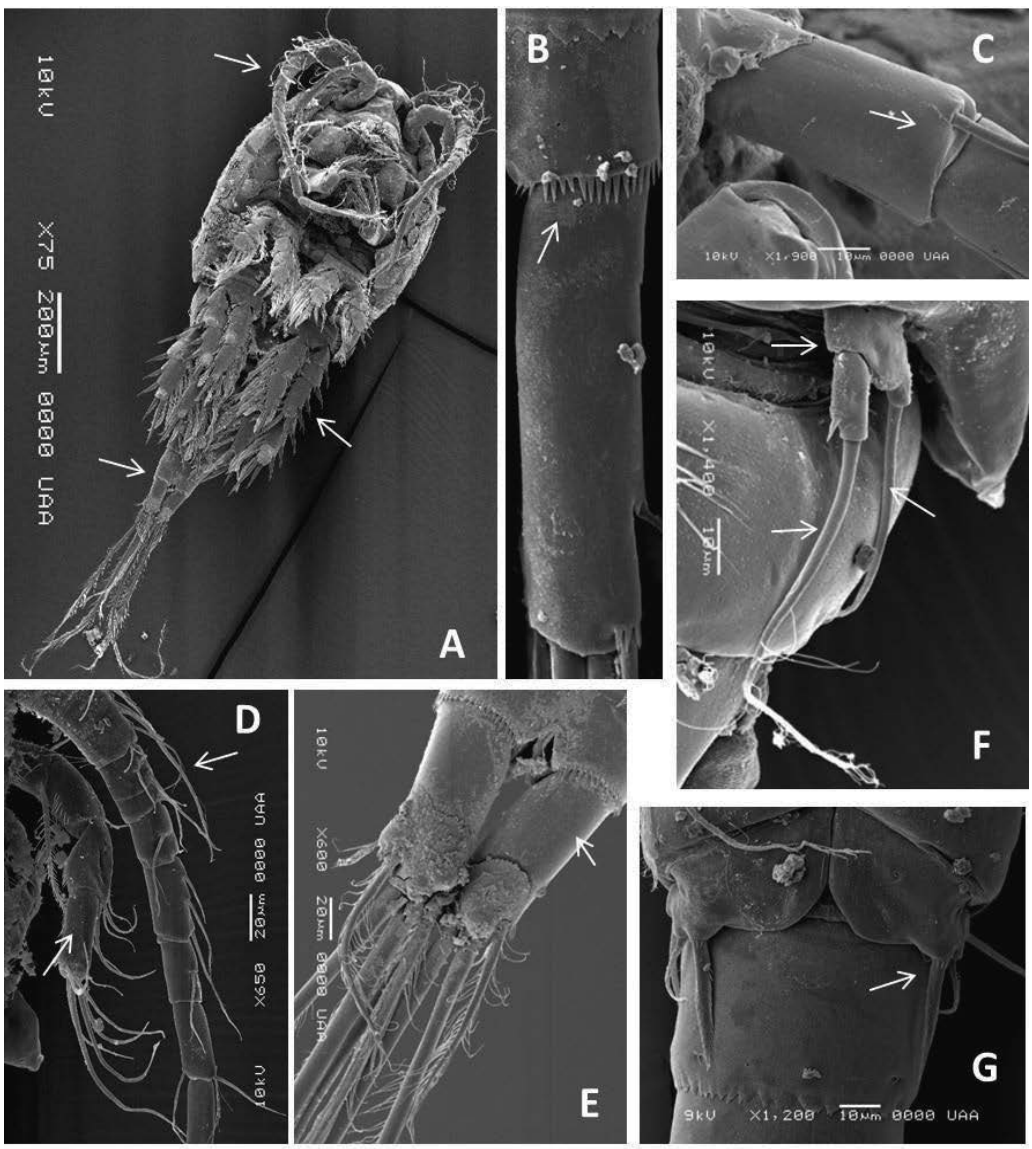

Figure 8. Habitus with arrows pointing to the second pair of antennas, a pair of swimming appendages, and urosome (A), caudal part of the urosome (B), segment of the second pair of antennas (C), the first and second pair of antennas (D), caudal part of the urosome (E), fifth pair of swimming appendages (F), and urosome showing the sixth pair of swimming appendages (G).

4.3. New species of copepods from Aguascalientes, Mexico

The study of copepods in the state of Aguascalientes has been less intense than that of cladocerans and rotifers. This is because the state lacks an established researcher with a permanent position in the main academic and research facilities, a condition that exists for the other two taxonomic groups. In spite of that, four species new to science have been found in Aguascalientes. That is the case of *Acanthocyclops dodsoni* [33] (Figure 9), *A. marceloi* [38] (Figure 9), *A. caesariatus* [37] (Figure 9), and *Paracyclops hirsutus* [38].

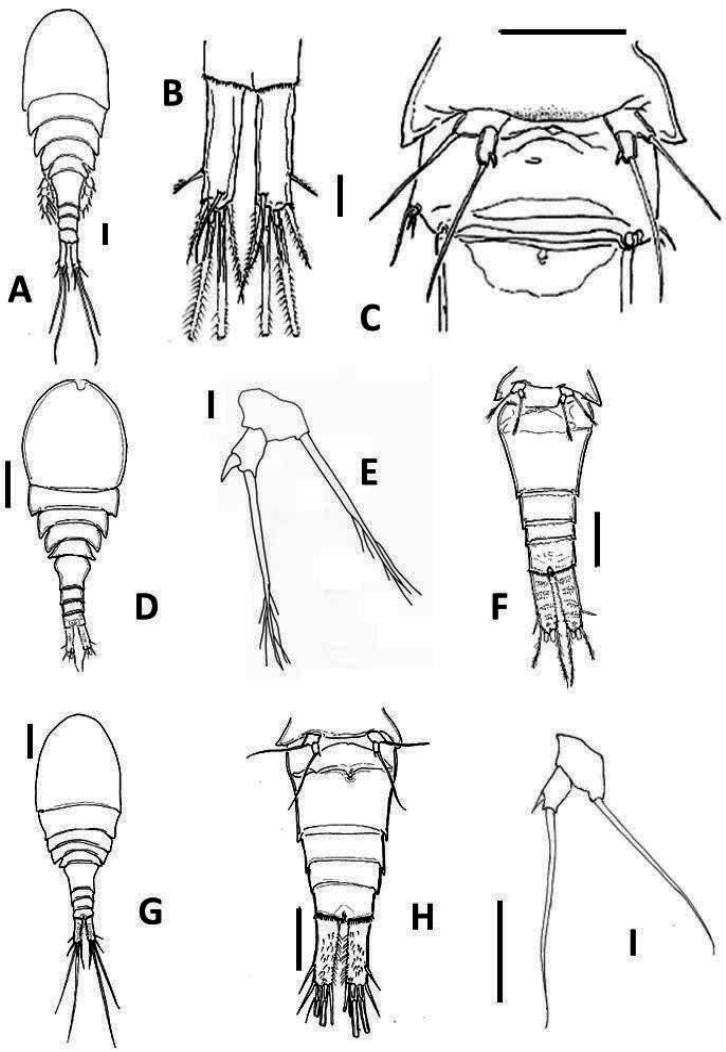

Figure 9. Three new species of copepod recorded in Aguascalientes, Mexico. *Acanthocyclops dodsoni*, dorsal view (A); caudal rami, dorsal view (B); fifth pedigerous and genital doble-somites, ventral view (C) (Mercado- Salas et al. 2006); *A. marceloi*, dorsal view (D); fifth pedigerous, ventral view (E), and urosome, ventral view (F) [37]; *A. cesariatus*, dorsal view (G); fifth pedigerous, ventral view (H); and urosome, ventral view (I) [38]. Scale bar: A, C=250 μm; G=200 μm; B, D, F, H=100 μm; I=50 μm; and E=10 μm.

http://dx.doi.org/10.5772/60659

5. Importance of the taxonomic study of rotifers, cladocerans, and copepods

The primary goal of the taxonomical study of rotifers, cladocerans, and copepods is to know the morphology and to carry on an inventory of all species located in a particular geographic area. The second goal is achieved once species are compared regarding morphological similarities and differences which allows for a better system to identify and classify them correctly. However, all these comparisons at the end allow clarification of questions related to evolution and adaptation when we combine ultrastructural morphological, physiological, and genetic studies.

The observation of small modifications among species of these three taxonomic groups only evidences the specificity that exists between the external environment and the internal function of the organism. The perfect design of each species defines the specific niche of each species in an ecosystem. Each slight modification like apparition of small setae in the fifth leg of a copepod, the changes in the structure of a trophi in rotifers, or the presence of a slightly more elongated endclaw in cladocerans is of the greatest importance since such tiny change can be the difference between a species able to perpetuate itself and the others that go extinct. These observations only corroborate the philosophy started by Darwin in his famous book *On the Origin of the Species*. With this philosophy in mind, then we can estimate the socioeconomic importance that each species implies. The precise knowledge of the species distribution, the kind of ecosystems and niches where we found each species, and the way in which each species interact are a necessity to the economical and sustainable use of each species. For example, if one wishes to use copepods as food for fishes, it would be convenient to know which species grow easily in the region. This knowledge would help to curve maintenance costs and to attain a maximal production of the cultured organisms, in the meantime avoiding producing an ecological misbalance. Another clear example is the use of the cladoceran *Daphnia magna* as model organism for acute toxicological test according to the Mexican Norm NMX-AA087-SCFI-2010, in which sometimes we exposed neonates of this organism in situ to determine the survival rate. However, this species is native of Europe and it is adapted to reservoirs with conditions quite different to the Europeans (like Mexico). The use of nonnative species to evaluate the health of Mexican ecosystems only introduces a bias into the experimental results. If instead we are able to identify and culture native species for each region and use it as a model organisms, we would obtain high-quality results and be more prepared to preserve the environmental health of our reservoirs.

Some other questions of even greater transcendence, as well as improvement in experimental and industrial designs, are the results of basic research as it is the case of the taxonomy aided by ultrastructural studies.

Acknowledgements

We are thankful to M. Sc. Reyna Lara Martinez who helped us in the management of the TEM JEOL 1010 at the Faculty of Sciences of the Universidad Nacional Autónoma de México.

Author details

Marcelo Silva-Briano[1*], Araceli Adabache-Ortiz[1], Gerardo Guerrero-Jiménez[1], Roberto Rico-Martínez[2] and Guadalupe Zavala-Padilla[3]

*Address all correspondence to: msilva@correo.uaa.mx

1 Universidad Autónoma de Aguascalientes Laboratorio de Ecología, Depto. Biología, Avenida Universidad, Aguascalientes,

2 Universidad Autónoma de Aguascalientes, Laboratorio de Toxicología Acuática, Depto. Química, Avenida Universidad, Aguascalientes, México

3 Unidad de Microscopía Electrónica. Instituto de Biotecnología, Universidad Nacional Autónoma de México, Av. Universidad, Cuernavaca, México

References

[1] Vázquez-Nin G. & Echeverría O. (2000) Introducción a la Microscopía Electrónica Aplicada a las Ciencias Biológicas. Fondo de Cultura Económica. México, 168 pp.

[2] Jiménez-García L. F., Elizundia J. M., López-Zamorano B., Maciel A., Zavala G., Echeverría O. M. & Vázquez-Nin G. H. (1989)Implications for evolution of nuclear structures of animals, plants, fungi and protoctists. *Biosystems*, 22: 103-16.

[3] Segers H., Murugan G. & Dumont H. (1993) On the taxonomy of the Brachionidae: description of *Plationus* n. gen. (Rotifera, Monogononta). *Hydrobiology*, 268, 1- 8.

[4] Wallace R., Snell T., Ricci C. & Nogrady T. (2006) Rotifera Part 1: Biology, Ecology and Systematics. 2da Ed. Kenobi Production. 229 pp.

[5] Klusemann J., Kleinow W. & Peters W. (1990). The hard parts (trophi) of the rotifer mastax to contain chitin: evidence from studies on *Brachionus plicatilis*. *Histochem,* 94, 277-283.

[6] Segers H. (2007) Global diversity of rotifers (Rotifera) in freshwater. *Hydrobiology*, 595, 49-59.

[7] Sarma S. S. S. (1999) Checklist of Rotifera (rotifers) from Mexico. *Environment and Ecology*, 17, 978-983.

[8] García-Morales A. & Elías-Gutiérrez M. (2004) Rotifera from southeastern Mexico, new records and comments on zoogeography. *Anales del Instituto de Biología*, 75, 99-120.

[9] La Biodiversidad en Aguascalientes: Estudio de Estado. (2008) Comisión Nacional para el Conocimiento y Uso de la Biodiversidad (CONABIO), Instituto del Medio

http://dx.doi.org/10.5772/60659

Ambiente del Estado de Aguascalientes (IMAE), Universidad Autónoma de Aguascalientes (UAA). México. 26-27 pp.

[10] Rico-Martínez R., Snell T.W. & Shearer T. (2013) Synergistic toxicity of Macondo crude oil and dispersant Corexit 9500A® to the *Brachionus plicatilis* species complex (Rotifera). *Environmental Pollution*, 173, 5-10.

[11] Rico-Martínez R. & Snell T. W. (1998). Mating behavior in eight rotifer species: Using cross-mating tests to study species boundaries. *Hydrobiologia*, 356, 165-173.

[12] Melone G. & Ferraguti M. (1993). The Spermatozoon of *Brachionus plicatilis* (Rotifera, Monogononta), with some notes on sperm ultraestructure in Rotifera. *Acta Zoologica, 75*(2), 81-88.

[13] Silva-Briano M. & Adabache-Ortiz A. (2000) *Brachionus* species in Aguascalientes State, México. *Aquatic Ecosystems of México*, 203- 211.

[14] Silva-Briano M., Galván-de la Rosa R., Pérez-Legaspi A. & Rico-Martínez R. (2007) On the description of *Brachionus araceliae* sp.nov. A new species of freshwater rotifer from Mexico. *Hidrobiológica*, *17* (2), 179-183.

[15] https://youtu.be/iV5VKdcQOJE

[16] Koehler J. K. (1965) An electron microscope study of the dimorphic spermatozoa of *Asplanchna* (Rotifera). I. *The adult tesis. Z. Zellforsh,* 67, 57-76.

[17] Velázquez-Rojas C. A., Santos-Medrano, G. E. & Rico-Martínez R. (2002) Sexual reproductive biology of *Platyias quadricornis* (Rotifera: Monogononta). *International Review of Hydrobiology* 87(1), 97-105.

[18] Silva–Briano M. & Segers H. (1992) *Brachionus josefinae* n. esp. *Hydrobiology,* 25, 283-285.

[19] https://youtu.be/iV5VKdcQOJE

[20] Kutikova L. A. & Silva-Briano M. (1995) *Keratella mexicana* sp. nov., a new planktonic rotifer from Aguascalientes, Mexico. *Hydrobiology*, 310, 119-122.

[21] https://www.youtube.com/watch?v=iV5VKdcQOJE&feature=youtu.be

[22] Thorp J. H. & Covich A. (2010) Ecology and Classification of North American Freshwater Invertebrates. E.U.A. 3rd Ed. Academic Press. 967 pp.

[23] Forro L., Korovchinsky N. M., Kotov A. A. & Petrusek A. (2008) Global diversity of cladocerans (Cladocera; Crustacea) in freshwater. *Hydrobiology,* 595, 177-184.

[24] Elías-Gutiérrez M., Suárez-Morales E., Gutiérrez-Aguirre M. A., Silva-Briano M., Granados-Ramírez J. G. & Garfias-Espejo T. (2008) Cladocera y Copepoda de las Aguas Continentales de Mexico. Guía ilustrada. México, 322 pp.

[25] Kotov A. A. & Elías-Gutiérrez M. (2002) Analysis of the morphology of *Spinalona anophtalma* Ciros-Pérez & Elías-Gutiérrez, 1997 (Aloninae, Anomopoda, Cladocera). *Hydrobiology*, 468, 185-192.

[26] Dumont H. J., Silva-Briano M. & Subhash-Babu J. J. (2002). A re-evaluation of the *Macrothrix rosea-triserialis* group, with the description of two new species (Crustacea Anomopoda: Macrothricidae). *Hydrobiology*, 467, 1-44.

[27] Ciros-Pérez J., Silva-Briano M. & Elías Gutiérrez M. (1996) A new species of *Macrothrix* (Anomopoda: Macrothricidae) from Central Mexico. *Hydrobiology*, 319, 159-166.

[28] Silva-Briano M., Quang Dieu N. & Dumont H. J. (1999) Redescription of *Macrothrix laticornis* (Jurine, 1820), and description of two new species of the *M. laticornis*-group. *Hydrobiology*, 403, 39-61.

[29] Ciros-Pérez J. & Elías-Gutierrez M. (1997) *Macrothrix smirnovi,* a new species (Crustacea: Anomopoda: Macrothricidae) from Mexico, a member of the *M. triseriales*-group. *Proccedings of the Biological Society of Washington*, 110 (1), 115-127.

[30] https://www.youtube.com/watch?v=iV5VKdcQOJE&feature=youtu.be

[31] Humes A. G. (1994) How many copepods? *Hydrobiology*, 292/293, 1-7.

[32] Dumont H. J. & Silva-Briano M. (2000) *Karualona* n.gen. (Anomopoda: Chydoridae), with a description of two new species, and a key to all known species. *Hydrobiology*, 435, 61-82.

[33] https://www.youtube.com/watch?v=iV5VKdcQOJE&feature=youtu.be

[34] Comisión Nacional para el Conocimiento y Uso de la Biodiversidad (CONABIO), Instituto del Medio Ambiente del Estado de Aguascalientes (IMAE), Universidad Autónoma de Aguascalientes (UAA). La Biodiversidad en Aguascalientes: Estudio de Estado. 2008. México.

[35] Mercado-Salas N. F., Suárez-Morales E. (2012) Morfología, diversidad y distribución de los Cyclopoida (Copepoda) de zonas áridas del centro-norte de México. II. Eucyclopinae y análisis biogeográfico. *Hidrobiológica* 22 (2), 99-124.

[36] Elías-Gutiérrez M., Suárez-Morales E. &Romano-Márquez B. (1999) A new species of *Leptodiaptomus* (Copepoda, Diaptomidae) from Northwestern Mexico with comments on the distribution of the genus. *Journal of Plankton Research*, 21, 603-614.

[37] Mercado-Salas N. F., Suárez-Morales E. & Silva-Briano M. (2009) Two new species of *Acanthocyclops* Kiefer, 1927 (Copepoda: Cyclopoida: Cyclopinae) with Pilose Caudal Rami from semiarid areas of Mexico. *Zological Studies*, 48, 380-393.

[38] Mercado-Salas N. F. & Suárez-Morales E. (2009) A new species and illustrated records of *Paracyclops* Claus, 1893 (Copepoda: Cyclopoida: Cyclopinae) from Mexico. *Journal of Natural History*. 43 (45–46), 2789-2808.

http://dx.doi.org/10.5772/60659

[39] Suárez-Morales E. (2000) Copépodos, seres ubicuos y poco conocidos. CONABIO. *Biodiversitas,* 29, 7-11.

[40] NMX-AA-087-SCFI. (1995) Norma Mexicana que establece el método de prueba de toxicidad aguda con *Daphnia magna* Straus (Crustacea-Cladocera).

Chapter 14

Veterinary Diagnostic using Transmission Electron Microscopy

M.H.B. Catroxo and A.M.C.R.P.F. Martins

Additional information is available at the end of the chapter

http://dx.doi.org/10.5772/61125

Abstract

Transmission electron microscopy has been an excellent tool, essential for the diagnosis of bacterial and viral animal diseases. Four basic techniques have been widely used: negative staining (rapid preparation), immunoelectron microscopy, immunolabeling with colloidal gold particles and resin embedding. The negative staining technique (rapid preparation) is the most applied, due to its speed, simplicity and specificity and can be used in various clinical specimens – such as feces, semen, urine, serum, organ fragments, crusts, body fluids, cell culture suspension, oral, ocular and fecal swabs, among others –, in which the agents can be directly viewed in large numbers in the samples. The immunoelectron microscopy technique using a specific primary antibody promotes the clumping of particles, also allowing the serotyping of the agents. In the immunolabeling with colloidal gold technique antigen-antibody reaction is enhanced by marking the antigen colloidal gold particles associated with protein A. The method of resin embedding, followed by ultrathin sections of cells or infected tissues can monitor the different stages of maturation viruses or bacteria and their behavior inside of host cells by determining not only the infection, but also the course of the disease in farms. The techniques can be applied to all animal species, either large or small, including aquatic and wild animals. Its implementation allows rapid diagnosis, providing subsidies for the immediate institution of prophylactic measures, and control and prevention of bacterial and viral animal diseases.

Keywords: Veterinary diagnostic, Negative staining, Immunoelectron microscopy, Immunolabeling with colloidal gold particles, Resin embedding, Transmission electron microscopy

INTECH
open science | open minds

© 2015 The Author(s). Licensee InTech. This chapter is distributed under the terms of the Creative Commons Attribution License (http://creativecommons.org/licenses/by/3.0), which permits unrestricted use, distribution, and reproduction in any medium, provided the original work is properly cited.

1. Introduction

In recent decades there has been a major advance in the diagnosis field, allowing the development mainly of sophisticated techniques at the molecular level, facilitating increasingly improved detection of diseases of viral and bacterial origin.

Despite this progress, electron microscopy remains an excellent and sensitive tool in the application of such techniques, and they are essential for the rapid diagnosis of these agents [1,2,3].

Four basic techniques have been widely used: negatively stained (rapid preparation), immunoelectron microscopy, immunolabeling with colloidal gold particles and resin embedding [4].

2. Negative staining (Rapid preparation)

The negative staining technique is the main method of electron microscopy, as well as the most used, due to its ease in preparation and speed in obtaining results, which are achieved in 5-10 min [1,5,6]. It was developed by Brenner & Horne in 1959 [7], when the viral particles could be viewed at the ultrastructural level [8].

The technique utilizes an electron opaque substance to surround the virus or another biological structure, showing contrast between the electron lucent biological material and the background against which it is viewed. The image formation is the result of electron being absorbed or deflected by the stain [9,10].

To develop the samples, copper or nickel grids measuring from 200-400 meshs are used and require plastic film pretreatment before being covered with carbon. Several types of plastic films are used for this purpose, with Formvar, Parlodion and Pioloform being the most common ones [11,12]. In our laboratory we use the Parlodium 0.5% in amyl acetate, followed by deposition of thin carbon under a metallizer.

Various types of contrasting (heavy metals salts) are used to provide better contrast to agents. The most used are the phosphotunstic acid (PTA), uranyl acetate, sodium silicotungstate, methylamine tungstate and ammonium molybdate 11,12].

We chose the 2% ammonium molybdate and pH5.0 as standard contrasting in our laboratory, in fact, in order to provide a soft contrast in all types of samples, clearly showing ultrastructural detail, such as the envelope covered with spikes and tape nucleocapsid shaped "Hering-bone", found in paramyxovirus [4,13,14].

This heavy metal has been used to contrast negatively many virus species [15].

The technique can be applied in various types of samples, such as feces; urine; serum; organ fragments; crusts; vesicular and peritoneal fluid; semen; ocular; nasal and fecal swabs; epithelium; cell culture supernatant; and others [16,17,1,18,19,20,21,22,6].

http://dx.doi.org/10.5772/61125

Small amounts of samples (1 drop of 40 μl) are necessary for the technical processing [6].

Samples must be collected and maintained immediately under refrigeration (4º C) before being transported and sent to the electron microscopy laboratory to ensure preservation of the morphology of viral particles [19].

In this technique the samples are suspended and drops collected from the surface of the suspension are transferred to metallic grids, which are then negatively contrasted [7,23,24,25, 26,27,28,29,20,15,30,19,6].

The rapid diagnosis of viral agents is accomplished through the comparison between the dimensions and specific morphology of the visualized particles and the other taxonomically combined viral families. The viruses can be morphologically classified according to their symmetry, which can be helical, cubic, icosahedral or complex [31]. The more commonly used criteria for the taxonomic classification are the following: dimension, shape and structure; shape of the viral capsid; presence or absence of the envelope; and surface projections. Complete and incomplete particles, as well as empty capsids, can also be distinguished [4,2].

The most commonly found viruses in cases of diarrhea outbreaks in several animal species are the coronavirus (fig. 1), rotavirus (fig. 2), adenovirus (fig. 3), astrovirus, and parvovirus, which can be seen in large numbers in feces, fecal swabs or intestine fragments [1,4,13,6].

Viruses that cause respiratory diseases such as influenza virus (fig. 4), coronavirus, and paramyxovirus (fig. 5), can also be easily detected in lung fragments, lung washes and nasal discharge [1,13].

Other viruses responsible for important reproductive diseases such as herpesvirus (infectious bovine rhinotracheitis), flavivirus (bovine viral diarrhea virus) (fig. 6), parvovirus (porcine parvovirus), herpesvirus (Aujeszky's disease), and circovirus (circovirosis swine) can be widely found in organ fragments [13].

Negative staining also plays an important role in the rapid investigation of viral diseases that cause skin lesions caused by herpes virus (fig. 7), poxvirus (figs. 8, 9) and papillomavirus (fig. 10) in fragments of lesions, crusts, epithelium and vesicular fluid [1,19,6,12,20,32,33,34].

The large brick-shaped orthopoxvirus can readily be distinguished from the parapoxvirus and the smaller icosahedral herpesvirus [35], being one of the most recommended techniques by the OIE for the accomplishment of the laboratorial diagnosis of the virus in skin lesion [36].

This technique also allows the detection of different viral particles in the same sample [13,6], especially in cases of diarrhea caused by the simultaneous presence of rotavirus and coronavirus (fig.11).

The negative staining can also be applied to identify the presence of a few types of bacteria of easy morphological identification, such as Leptospira (fig. 12), mycoplasma (fig. 13) and other bacteria types found in specific cell cultures.

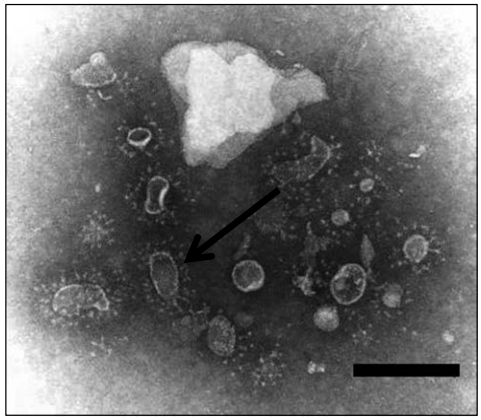

Figure 1. Negatively stained coronavirus particles showing characteristic radial projections forming a corona, in feces of *Mazama gouazoubira* (arrow). Bar: 200 nm.

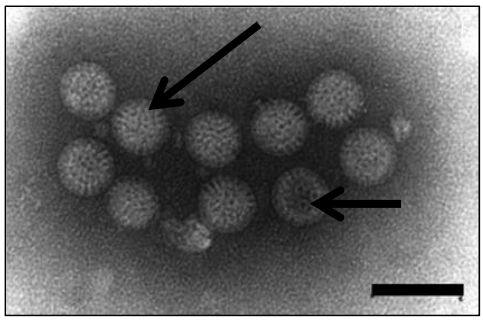

Figure 2. Negatively stained rotavirus, showing complete" (big arrow) and "empty" (minor arrow) particles in feces of swine. Bar: 110 nm.

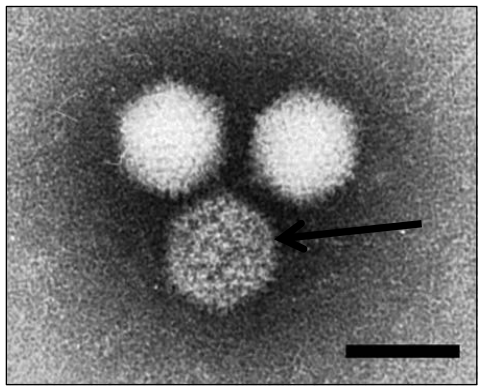

Figure 3. Negatively stained adenovirus particles, exhibiting the hexagonal outline formed by the distinct capsomers (arrow) in feces of pigeon. Bar: 70 nm.

http://dx.doi.org/10.5772/61125

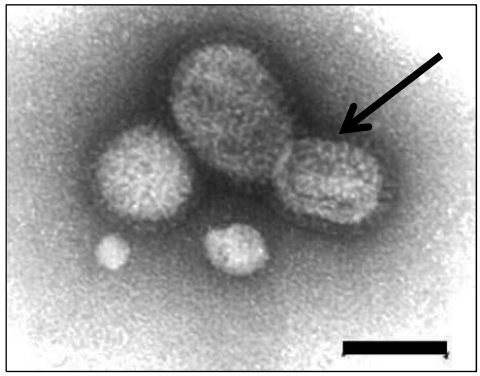

Figure 4. Influenza virus in feces of ferret, showing well defined spikes (arrow). Bar: 80 nm.

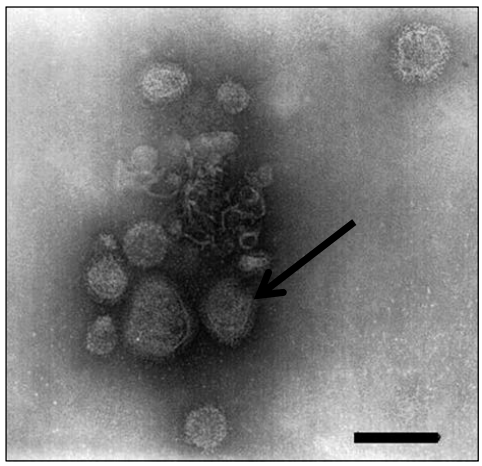

Figure 5. Negatively stained paramyxovirus particles, pleomorphic,roughly spherical, containing an envelope covered by spikes (arrow) in feces of parrot. Bar: 140 nm.

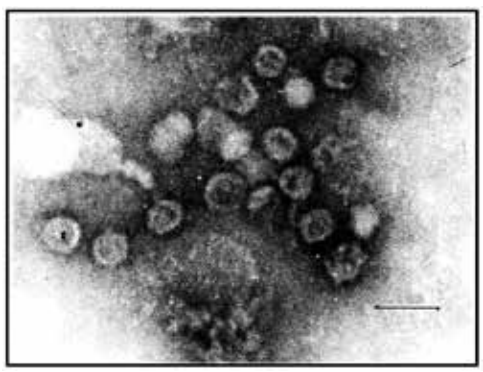

Figure 6. Flavivirus isometric particles in bovine intestine. Bar: 70 nm.

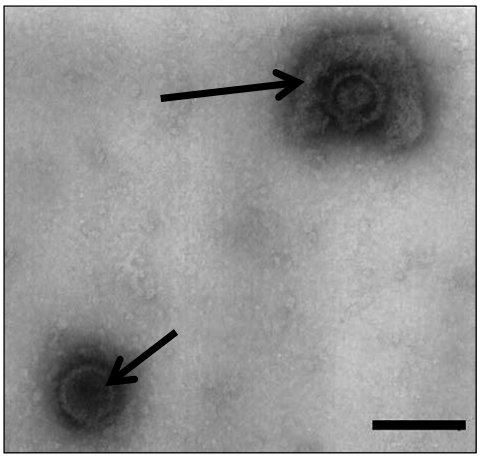

Figure 7. Herpesvirus in skin lesion of parrot, showing enveloped (big arrow) and non-enveloped particles (minor arrow). Bar: 100 nm.

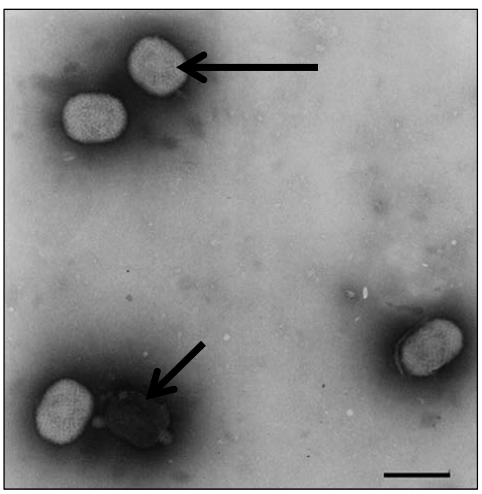

Figure 8. Negatively stained poxvirus showing regular spaced thread-like ridges comprising the exposed surface (big arrow) and enveloped particle (minor arrow). Bar: 320 nm.

http://dx.doi.org/10.5772/61125

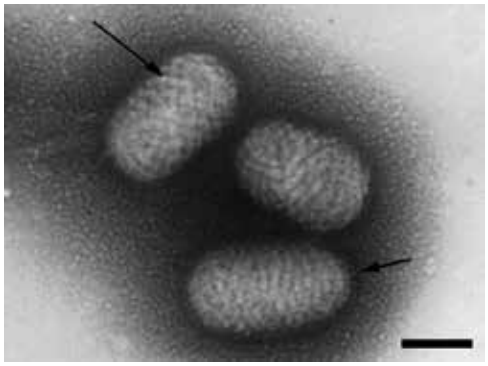

Figure 9. Parapoxvirus particles with a distinctive criss-cross filament pattern derived from the superimposition of upper and lower virion surfaces (big arrow) and projections surface (minor arrow). Bar: 110 nm.

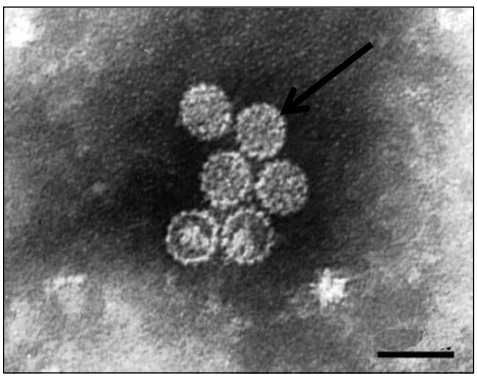

Figure 10. Negatively stained papillomavirus particles exhibit distinct, isolated capsomers (arrow). Bar: 70 nm.

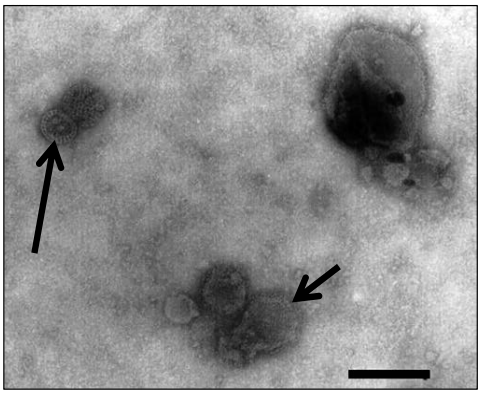

Figure 11. Simultaneous presence of particles of rotavirus (big arrow) and coronavirus (minor arrow) in feces of cattle. Bar: 150 nm.

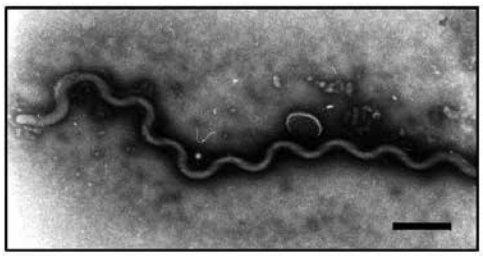

Figure 12. Negatively stained *Leptospira interrogans*. Bar: 1000 nm.

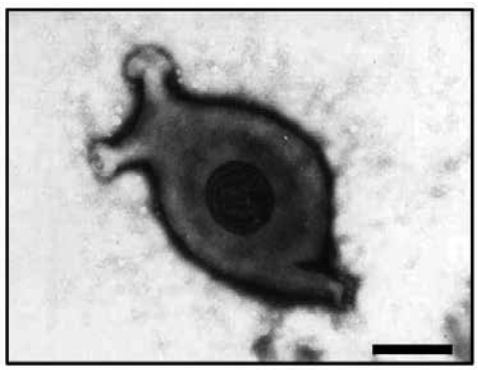

Figure 13. Negatively stained *Mycoplasma gallisepticum*. Bar: 140 nm.

2.1. Immunoelectron microscopy technique

The immunoelectron microscopy technique is an antigen-antibody reaction which promotes increased sensitivity in 100-fold when using a specific antibody connected to a known antigen [35,37,11].

It was first developed for quantifying plant virus by Derrick (19730 [38] being subsequently used in various types of clinical specimens [39,40,41,42].

Used when the number of agent particles in a sample is very low, it allows identification of the agent for specific antigen-antibody reaction - such identification can be achieved by its morphology.

The technique does not require purification of antibodies and detects contaminating antigens and/or antibodies [37]. It is also used to serotype morphologically similar (but antigenically distinct) particles [43,9].

Three variations of the method have been described, immune clumping or direct immunoelectron microscopy [4,44,45] solid phase immune electron microscopy (SPIEM) [38], and decoration [46].

http://dx.doi.org/10.5772/61125

In the immune clumping method, an antigen suspension is blended with an equal volume of specific antibody against the said antigen; the suspension is incubated for 1 h at 37º C and negatively contrasted to allow the execution of the antigen-antibody reaction. The particles of the agent create aggregation through the reaction with its homologous antibody [4,9].

This procedure has been used to facilitate the detection and distinction of small viral particles from the background debris present in clinical specimens [47].

The sensitivity of immunoelectron microscopy can be increased by applying the most used SPIEM method in our laboratory.

In this technique, a grid is previously prepared with colodium film and sensitized with the antibody, cleaned with PBS, incubated with the antigen and negatively contrasted. As a result of the antigen-antibody reaction, the particles of the agent are agglutinated, creating groups on the grid surface (fig. 14) [4,9].

Several types of viruses can be added by this technique, such as flaviviruses, rotavirus, poxvirus, paramyxovirus, and parvovirus, among others.

Immunoelectron microscopy was used to trap particles of equine herpesvirus in organ fragments in cases of abortion [48].

The technique can also be applied to trap some types of bacteria and mycoplasma.

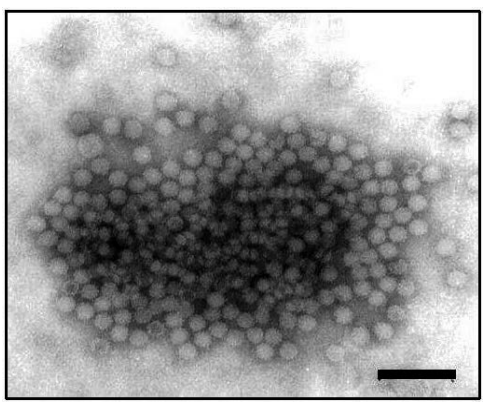

Figure 14. Immunoelectron microscopy of parvovirus particles aggregated by antigen-antibody interaction in suspension of swine liver. Bar: 120 nm.

2.2. Decoration technique

In the decoration or antigen-coated grid technique, the antibodies are used to "decorate" or coat viruses [37,46].

Carbon-coated electron microscope grids are incubated with a specific antibody that is used to trap antigen particles found in a suspension. After the trapping, the treated grids are washed and negatively stained. The antigen particles covered in a dense and relatively continuous

antibody coat, which bypasses the said particles, result in a “decoration”. Such a feature indicates a positive reaction [49,50].

This technique can be used to detect very small viruses or to serotype virus [15].

Some types of bacteria such as Leptospira can be perfectly "decorated" by this technique (fig. 15).

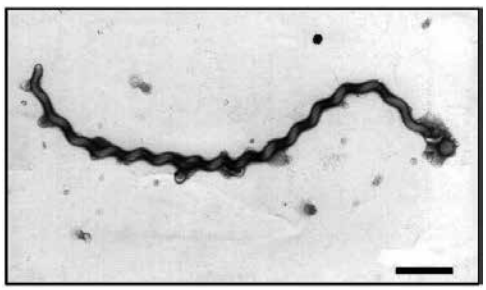

Figure 15. *Leptospira interrogans* “decorated” by decoration technique. Bar: 1000 nm.

2.3. Immunolabeling with colloidal gold particles by negative staining technique

Immunocytochemical techniques are powerful tools for the localization of special antigens utilizing a specific marker 51].

Tracers or markers are exogenously administered substances that, when visualized in electron microscopy preparations, provide valuable information about cell compartments, junctional elements, and cells surfaces [24].

The antigen marking plays a fundamental role in the identification of difficult viruses to be visualized or those with a low titer [23].

Two types of markers have been used to detect virus and virus-antibody interaction in liquid preparations, ferritin and colloidal gold. Ferritin is a protein enclosing an iron core and colloidal gold is formed by the reduction of chloroauric acid with sodium citrate [9].

Ferritin conjugated to antibody combined with negative staining methods has been utilized to show the attachment of IgG on influenza virus and on hepatitis B core antigen. The method has also been used to detect rotavirus, adenovirus, and enterovirus [52,53,54,55,56].

The colloidal gold has been the most widely used marker in liquid preparations.

This gold-labeled antibody decoration technique antigen differs by the amount of gold label attached to the antigens [9].

The advantage of colloidal gold compared to other markers can be attributed to the particulate nature of the probe and the availability of different sizes and densities of the electron beam [1,57].

http://dx.doi.org/10.5772/61125

In this technique the antigen-antibody reaction is enhanced by determining the protein-A associated antigen through colloidal gold particles which, when linked to the antigen, allow the latter to be easily visualized through an electron microscope [11].

In our laboratory, we use a method originally developed by Knutton (1995) [51] to identify and characterize proteinaceous filamentous bacterial surface structures, such as fimbriae or pili, which function as adhesins and can also be applied to mark viral particles.

In this method, the grids are treated with drops of viral or bacterial suspension, incubated with the primary antibody diluted to 1/80, post-incubated in protein A drops in association with gold particles (secondary antibody) and negatively stained. The antigen-antibody interaction is strongly enhanced by the dense colloidal gold particles on viruses, indicating a positive reaction (fig. 16).

The method also allows detection and identification of antigen structures induced by the virus and its localization in infected cells, serotype viral strains [58], and determines antigenic variants in isolated strains [59].

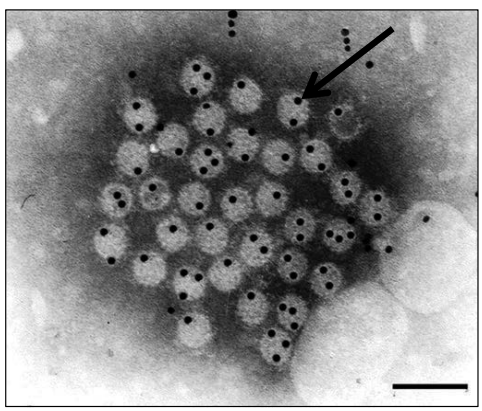

Figure 16. Bovine papillomavirus marked by the particles of colloidal gold (arrow). Bar 100 nm.

2.4. Immunolabeling in ultrathin sections technique

The immunoelectron microscopy is one of the best methods for detecting and localizing proteins in cells and tissues and to detect virus or viral antigen on the surface of or within ultrathin sections of the cells [9,60,61].

The type of marker used depends on the type, location, and stability of the antigen under study [9].

Various types of markers have been used in ultrathin sections. The best known are the red ruthenium, lanthanum nitrate, horseradish peroxidase, ferritin, colloidal thorium dioxide (thorotrast) and colloidal gold [24].

The ruthenium red has been applied to study ultrastructural aspects of retroviruses, such as details of the structure of peplomers, fusion or entry, assembly, release, and budding in infected cells [62,63,64].

Ruthenium red staining also promotes the ultrastructural visualization of glycoprotein layer surrounding the spore of *Bacillus anthracis* and *Bacillus subtilis* [65].

Applications of immunolabeling with ferritin allowed investigation of the complex antigenic interactions induced in cells by infection with herpesvirus [66] and by influenza and vaccinia viruses [67], as well as aspects of maturation and budding of African swine fever virus [68].

This marker facilitated electron microscopic study on the penetration of Newcastle disease virus into cells leading to the formation of polykaryocytes [69]. However, the immunolabeling antibody against the surface hemagglutinin spike on the viral surface of Newcastle disease virus showed that the size of the ferritin particles resulted in confusion with natural ferritin in the cell cytoplasm [57].

Electron microscopic observations of bacteria and Mycoplasma ultrastructure has been made by immunolabeling with ferritin [70,71].

Horseradish peroxidase-labeled antibody was used for localization of viral precursor antigens of reovirus [72], herpes simplex and vaccinia viruses [73], and rotavirus [74] and to study the organization of the endosome compartment of Semliki Forest virus [75].

There has been a recent report on the development of "Apex" (monomeric 28-kDa peroxidase), a genetically encodable EM tag that is active in all cellular compartments that withstands strong EM fixation to give excellent ultrastructural preservation [76].

The application of lanthanum in culture of *Scherichia coli*, allowed the study of the components of the cell envelope, the periplasm, and the energized inner membrane [77].

Ultrastructural aspects of the attachment and penetration of herpesvirus in BHK21 cells [78] and loci of viral ribonucleic acid synthesis of arbovirus [79] were described by immunolabeling with colloidal thorium dioxide.

Combined methods of ferritin tracing, lanthanum staining, and acid phosphatase localization was employed to demonstrate active process of retrovirus phagocytosis [80].

The association of tracers, ruthenium red with lanthanum nitrate was utilized as a marker for scrapie particles [81].

The gold particle labeling technique was first described by Faulk & Taylor in 1971 [82], when they were able to tag gold particles to anti-salmonella rabbit gamma globulins in one step in order to identify the location of the antigens of salmonella.

The use of primary antibodies conjugated with gold particles allows high resolution detection and localization of a multiplicity of antigens, both on and within the cells, revealing the distribution of molecular components at various structural levels [60,83].

This technique allows immunolocalization of viral proteins and their association with cell membranes of infected cells [84].

http://dx.doi.org/10.5772/61125

Two methods of immunolabeling were developed, the pre-embedding method and the post-embedding method. The pre-embedding method primarily detects determinants exposed at the surface of infected cells such as virus receptors or envelope glycoproteins of budding viruses that are freely accessible to antibodies and reagents. The post-embedding labeling of thin sections allows access to determinants present in the different compartments of the cell and to internal viral structures since they become exposed at the surface of the section [85].

The major advantage offered by the post-embedding method is that each antigen molecule at the surface of the section should stand the same chance of being immunodetected, regardless of its cellular or sub-cellular localization of bacterial cells proteins [86].

In post-embedding methods of immunogold staining, the cells or tissues are fixed chemically or cryo-immobilized, dehyidrated, and embedded in epoxy or acrylic resins. The sections are then immunochemically stained with primary antibodies raised against antigens exposed on the surface of the sections. The primary antibodies are visualized by staining immunochemically with secondary antibodies raised against the species and isotype of the primary antibodies, conjugated to colloidal gold particles. The ultrathin sections are stained with uranyl acetate and lead citrate [9,60,87].

This technique was used to label glycoproteins GP1 and GP4 of the bovine herpesvirus type 1 epitopes exposed at the surface of the cytoplasmic membrane or the envelope of the budding viral particles [85].

Immunolabeling using VP8-specific antiserum and colloidal gold labeled protein A as the electron-dense marker was applied to identify tegument protein VP8 of bovine herpesvirus-1 [88].

Salanueva et al. [89] showed that the two types of particles of the porcine transmissible gastroenteritis virus, large annular virus and small dense viruses are closely related, since both large and small particles reacted equally with polyclonal and monoclonal antibodies specific for TGEV proteins.

Another application of this technique showed that the collapse of the endoplasmic reticulum cisternae observed during African swine fever virus infection is dependent on viral envelope protein, J13Lp [90].

2.5. Resin embedding technique

The introduction of the epoxy resins for electron microscopy in the 1950s was a major step in the development of thin section electron microscopy for ultrastructural analysis [91].

The resin embedding technique consists of glutaraldehyde or paraformaldehyde fixation (2,5%), osmic acid post-fixation (1%), uranyl acetate en bloc staining, dehiydration with acetone, embedding in epoxy resin, thin sectioning and staining [92,93,94].

Ultrathin sections is an important tool to reveal fine details of the ultrastructure of all types of cells and tissues [95]. In an infectious process, it allows observing pathogenesis of infection and the identification of the agent [43].

The thin sectioning technique has the advantage of allowing the observation of virus cell interaction, which reveals the site of virus replication and maturation in the host cells, a pertinent information in the identification of unknown viruses [96].

Many ultrastructural aspects of this interaction can be observed in infections by several genera of poxviruses and papillomavirus. Amorphous, fibrillar, homogeneous, crystalline and A-B types inclusion bodies (fig. 17), nuclei with aspect dentate, membrane-bound vacuoles and mature and immature particles budding from cellular membranes, can be distinctly visualized in ultrathin sections after the resin inclusion of lesion or crust fragments in cases of ecthyma contagious, myxomatosis, swinepox, and avianpox, among others [32,33,34,97,98].

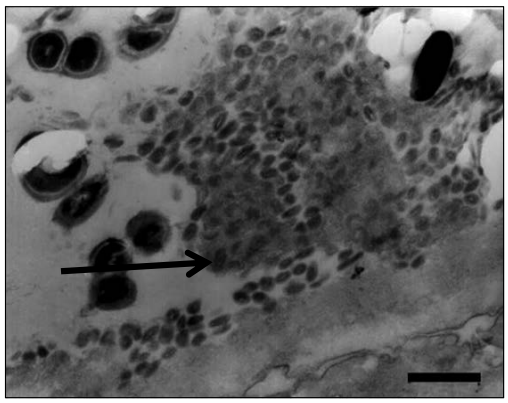

Figure 17. Ultrathin section of the scabs fragments infected by Avian pox. Type A or Bollinger intracytoplasmic inclusion bodies, containing in its Interior mature particles (arrow). Bar: 800 nm.

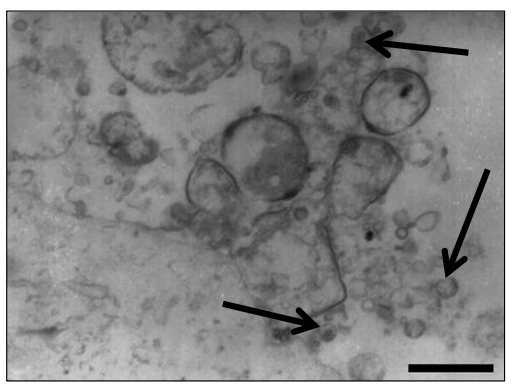

Figure 18. herpesvirus particles in various stages of development (arrow) in cells inoculated with brain suspension of monkeys infected with herpesvirus type 1. Bar: 660 nm.

Several aspects of morphogenesis herpesvirus were seen in Vero cell monolayers inoculated with brain suspension of monkeys infected with herpesvirus type 1 (fig. 18).

These ultrastructural details not only determine the infection, but also the course of the disease in the creations.

The embedding technique was used to describe a new *Rickettsia* species isolated from the tick *Amblyomma incisum* from the Southeast of Brazil, the *R. monteiroi*, showing characteristic Gram-negative morphology, with a cell wall and a cytoplasmic membrane separated from the cell wall by the periplasmic space [99].

Different methods for thin section electron microscopy have been developed for detection of mycobacteria [100].

3. Discussion

Electron microscopy is undoubtedly an indispensable tool in the diagnosis of animal infectious diseases and to investigate the structural analysis of cells and tissues at various levels of resolution [1, 101].

The negative staining is a traditional technique that allows a quick, efficient, simple and conclusive diagnosis. The "open view" of the direct electron microscopy can visualize all agents on the specimen grid, also unknown microbes as well as unsuspected ones [6].

No simple method for an unequivocal and rapid diagnosis of infectious disease is available [19].

The success of the diagnosis depends on the quality of the sample taken, preparation and experience of the ultramicroscopist [102].

A positive detection requires of 10^5 particles per ml in the diagnostic suspension [4,6].

In the feces, however, the viral particles are present in high concentrations and are easily visualized [35].

One of the main applications of negative staining is the investigation of outbreaks of viral gastroenteritis [11] that cause high mortality in the creations.

This technique has also been used to detect the presence of enteric viruses such as poult enteritis complex (PEC), a disease economically important in poultry, characterized by enteritis, diarrhea, poor weight, and high mortality [103].

The technique also allows the identification of multiple agents in a same sample [19].

Herpesvirus, poxvirus, and papillomavirus particles are also found in large numbers in crusting, blistering, vesicular fluid or epithelium [4,6].

Some viruses may have low viral titer; however, this problem can be circumvented by applying the techniques of immunoelectron microscopy and immunolabeling with colloidal gold.

The electron microscopy has been utilized as a front-line method in emergency infectious diseases and/or in suspect cases of bioterrorism [19, 104].

The sudden appearance of vesicular lesions or respiratory illness in farm animals may be evidence of an emerging disease, a possible zoonosis or an agriterrorist act [19].

Exotic infections in several animal species have also been identified by electron microscopy [20]. Coronavirus particles were detected in ferrets with clinical status of diarrhea [105].

Several outbreaks of viral diseases were detected in wild animals using electron microscopy techniques. An enteric coronavirus was detected in capybaras [106] and the presence of poxvirus and paramyxovirus was confirmed in wild birds [32, 98].

Electron microscopy plays a fundamental role in assisting veterinary clinics and hospitals, Ecological Parks, Zoos, and breeding farms.

The immediate results of examinations of electron microscopy allows the rapid introduction of therapeutic, preventive and control measures in breeding sites and plan strategies for fighting infection, avoiding unnecessary loss of animals and economic damages.

The gain in time is an important factor in the control of infections [1,107].

In the event of new outbreaks caused by infectious agents, electron microscopy allows to assess the possibility of developing specific vaccine for the protection of the creations.

The introduction of electron microscopy techniques in diagnostic routine during outbreaks in farm animals allows to helping determine the risk areas at the site to be studied, collaborating in this way with the National Agribusiness, giving a base for health programs.

Another important use of electron microscopy is the identification of an unknown virus that has been isolated in tissue culture [20] or those viral agents particularly difficult to cultivate [3] and when alternative standard diagnostic methods fail to produce reasonable results [26].

The obtained electron micrographs are widely used to illustrate practically any text scientific papers, monographs, atlases and books in cell biology, anatomy, and pathology [95].

Future applications in this area include negative staining and cryo-negative staining, cryo-preparation methods of vitreous sections (CEMOVIS) and digital images for transmission electron microscopy that can be processed by software programs may contribute to the improvement of veterinary diagnostic by electron microscopy [57,101,108,109].

The electron microscope is an expensive (costs about 600,000 euros), sophisticated, and extremely efficient equipment for rapid veterinary diagnosis, the annual cost spent on maintenance, should not be considered a disadvantage.

The main requirement of an Electron Microscopy Laboratory, however, is the need for highly trained operators with knowledge and skills to handle the equipment, prepare the sample, and realize the diagnosis accurately [6,12,26,43,110].

The preparation of a negative staining sample amounts to less than 0.5 euros, which is much less than the costs for alternative molecular tests [6].

The cost to the user is around $ 16.50 per sample processed by this technique in our laboratory.

Considering the importance of electron microscopy in the diagnosis and research preparation is key to the new generation of ultramicroscopists with the appropriate technical skills [11].

Author details

M.H.B. Catroxo* and A.M.C.R.P.F. Martins

*Address all correspondence to: catroxo@biologico.sp.gov.br

Electron Microscopy Laboratory - Research and Development Center in Animal Health - Biological Institute of São Paulo, São Paulo,SP, Brazil

References

[1] Hyatt HD. The application of electron microscopy to veterinary virus diagnostic. Aust. Vet. J. 1989; 66(12):445-449.

[2] Gelderblom HR, Mãnnel A. Diagnostic electron microscopy in infectious diseases: up date. Microsc. Microanal. 2003; 9 (suppl.3):432-433.

[3] Arcangeletti MC, De Conto F, Pinardi F, Medici MC, Valcavi P, Ferraglia F, Motta F, Covan S, Calderaro A, Chezzi C, Dettori G. Electron microscopy as a reliable tool for rapid and convenional detection of enteric viral agents. A five-year experience report. Acta Biomed. 2005; 761:65-70.

[4] Doane FW. Immunoelectron microscopy in diagnostic virology. Ultrastruct. Pathol. 1987; 11:681-685.

[5] Gelderblom HR, Hazelton PR. Specimen collection for electron microscopy. Emerg. Infect. Dis.2000; 6:433–434.

[6] Gentile M, Gelderblom HR. Electron microscopy in rapid viral diagnosis: an update. New Microbiol. 2014; 37:403-422.

[7] Brenner S, Horne RW. A negative staining method for high resolution electron microscopy of viruses. Biochem. Biophys.Acta.1959; 34:103.

[8] Johnsen CK, Böttiger B, Blom J. Confirmation of electron microscopic results by direct testing of viruses adhered to grids using nucleic acid amplification techniques. J. Virol. Meth.2006; 134(1-2):92-98.

[9] Palmer E L, Martin M. L. Electron Microscopy in Viral Diagnosis. 2_{nd} ed. Boca Raton, FL: CRC; 2000. 194p.

[10] Harris KM, Perry E, Bourne J, Feinberg M, Ostroff L, Hurlburt J. Uniform serial sectioning for transmission electron microscopy. J.Neurosci. 2006; 26:12101–12103.

[11] Curry A, Appleton H, Dowsett B. Application of transmission electron microscopy to the clinical study of viral and bacterial infections: present and future. Micron. 2006; 37: 91–106.

[12] Schramlova J, Arientova, S Hulinska, D. The role of electron microscopy in the rapid diagnosis of viral infections – review. Folia Microbiol. 2010; 55(1):88-101.

[13] Fenner F, Bachmann, P A. Gibbs, E. P. J.; Murphy, F.A.; Studdert, M. J. & White, D. O. Virologia Veterinária. Acribia: Zaragoza, 1992, 691p.

[14] Fields BN, Knipe DM, Howley PM, editors. Fields virology. 3rd ed. Lippincott-Raven: Philadelphia, 1996.

[15] Hayat M A, Miller S E. Negative staining. Mc. Graw-Hill Publ. Company: New York, 1990, 253 p.

[16] Kapikian AZ, Wyatt RG, Dolin R. Visualization by immune electron microscopy of a 27 nm particle associated with acute infectious non-bacterial gastroenteritis. J. Virol. 1972; 10:1075-1081.

[17] Plummer FA, Hammond GW, Forward K, Sekla L, Thompson RN, Jones B, Kidd IM, Anderson MJ. An erythema infectiosum-like illness caused by human parvovirus. N. Engl. J. Med.1985; 313:74-79.

[18] Hazelton PR, Aoki FY, Hammond GW, Coombs KM, Dawood M. Identification of a proposed novel agent of viral gastroenteritis. 18th Annual Meeting of the American Society for Virology, Amherst, MA. American Society for Microbiology: Washington, 1999, pp.10-14.

[19] Hazelton PR, Gelderblom HR. Electron microscopy for rapid diagnosis of infectious agents in emergent situations. Emerg. Infect. Dis. 2003; 9:294-303.

[20] Goldsmith CS, Miller SE. Modern uses of electron microscopy for detection of viruses. Clin. Microbiol. Rev. 2009; 22:552-563.

[21] Goldsmith CS, Tatti KM, Ksiazek TG, Rollin PE, Comer JA, Lee WW, Rota PA, Bankamp B, Bellini WJ, Zaki SR. Ultrastructural characterization of SARS coronavirus. Emerg. Infect. Dis. 2004; 10:320-326.

[22] Goldsmith CS, Ksiazek TG, Rollin PE, Comer JA, Nicholson WL, Teresa CT, Erdman P DD, Bellini WJ, Harcourt BH, Rota PA, Bhatnagar J, Bowen MD, Erickson BR, McMullan LK, Nichol ST, Shieh W-J, Paddock CD, Zaki SR. Cell culture and electron microscopy for identifying viruses in diseases of unknown cause. Emerg. Infect. Dis. 2013; 19:864-869.

[23] Madeley C R. Electron microscopy and virus diagnosis. J. Clin.Pathol. 1997; 50:454-456.

[24] Bozzola JJ, Russel LD. Electron microscopy: principles and techniques for biologists. 2nd ed. Jones & Bartlett: Boston, 1999, 670p.

[25] De Carlo S, Harris JR. Negative staining and cryo-negative staining of macromolecules and viruses for TEM. Micron. 2011; 421:17-131.

[26] Biel SS, Gelderblom HR. Electron microscopy of viruses*:* Virus cell culture - a practical approach. Cann, AJ (Ed.). Oxford University Press: EUA, 1999, pp. 111-147.

[27] Gelderblom HR, Renz H, Ozel M. Negative staining in diagnostic virology. Micr. Microsc. Acta.1991; 22:435-447.

[28] Gelderblom HR. Elektronenmikroskopie im Methodenspektrum der Bioterrorismus-Diagnostik. Bundesgesundheitsbl., Gesundheitsforsch. Gesundheitsschutz. 2003; 46: 984-988.

[29] Gentile M, Gelderblom HR. Rapid viral diagnosis: role of electron microscopy. New Microbiol. 2005; 28:1-12.

[30] Harris JR. Negative staining and cryo-electron microscopy: the thin film techniques. Edition 35 of Microscopy Handbooks. Bios Scientific Publishers: Oxford England, 1997; 208p.

[31] Madeley CR, Field AM. Virus morphology. Churchill Livingstone: Edinburgh London, 1988.

[32] Catroxo MHB, Bersano JG, Martins AMCPF, Petrella S, Portugal MASC, Souza OS. Ultrastructural study of poxvirus causing myxomatosis in rabbits, in São Paulo and Santa Catarina, Brazil. Int. J. Morphol. 2009a; 27(2):543-552.

[33] Catroxo MHB, Pongiluppi T, Melo NA, Milanelo L, Petrella S, Martins AMCPF, Rebouças MM. Identification of poxvirus under transmission electron microscopy during outbreak period in wild birds in São Paulo, Brazil. Int. J. Morphol. 2009b; 27(2): 577-585.

[34] Catroxo MHB, Martins AMCRPF, Petrella S, Souza F, Nastari BDB. Ultrastructural study of bovine papillomavirus during outbreaks in Brazil. Int. J. Morphol. 2013; 31(2):777-784.

[35] Doane FW. Virus morphology as an aid for rapid diagnosis. Yale J. Biol. Med. 1980; 53:19-25.

[36] OIE. Manual of diagnostic tests & vaccines for terrestrial animal. In: Fowlpox. 6 th ed., França: Paris, 2008. pp. 531-7.

[37] Katz D, Kohn A. Immunosorbent electron microscopy for detection of viruses. Adv. Virus Res.1984; 29:169-194.

[38] Derrick KS. Quantitative assay for plant viruses using serologically specific electron microscopy. Virol.1973; 56:652-653.

[39] Gerna G, Passarini N, Sarasini A, Battaglia M. Characterization of human rotavirus strains by solid-phase immune electron microscopy. J. Infect. Dis.1985; 152:1143-1151.

[40] Gerna G, Sarasini A, Passarini N, Torsellini M, Parea M, Battaglia M. Comparative evaluation of a commercial enzyme-linked immunoassay and solid-phase immune electron microscopy for rotavirus in stool specimens. J. Clin. Microbiol. 1987; 25:1137-1139.

[41] Humphrey CD, Cook EH Jr, Bradley DW. Identification of enterically transmitted virus particles by solid phase immune electron microscopy. J. Virol. Meth. 1990; 29:177-188.

[42] Lewis DC. Three serotypes of Norwalk-like virus demonstrated by solidphase immune electron microscopy. J. Med. Virol.1990; 30:77-81.

[43] Field AM. Diagnostic virology using electron microscopic techniques. Advan. Virus Res.1982; 27:2-69.

[44] Almeida JD, Waterson AP. Immune complexes in hepatitis. Lancet, 1969; 2:983-986.

[45] Anderson N, Doane FW. Specific identification of enteroviruses by immuno-electron microscopy using a serum-in-agar diffusion method. Can. J. Microbiol. 1973;19:585-589.

[46] Milne RG, Luisoni E. Rapid high-resolution immune electron microscopy of plant viruses. Virol.1975; 68:270-274.

[47] Lee TW, Megson B, Kurtz J B. Enterovirus typing by immune electron microscopy. J. Med. Microbiol.1996; 44:151-153.

[48] Chenchev I, Kazachka D, Martinov S. Using the immunoelectron microscope methods for diagnosing the herpesvirus infection in horses. Biotechnol. & Biotechnol. Equip. 1997; 11(1-2):65-68.

[49] Milne RG. Immunoelectron-microscopy for virus identification. In: Electron microscopy of plant pathogens. Mendgen K, Lesemann (Eds.). Springer-Verlag: New York, 1990.

[50] Wright DM. Immunoelectron microscope techniques in plant virus diagnosis. Meth. Mol. Biol. 2005; 295:193-206.

[51] Knutton S. Electron microscopical methods in adhesion. Methods Enzymol.1995; 253:145-158.

[52] Almeida JD, Skelly J, Howard CR, Zuckerman S. The use of markers in immune electron microscopy. J. Virol. Methods. 1981; 2(3):169-174.

[53] Berthiaume L, Alain R, McLaughlin B, Payment P, Trepanier P. Rapid detection of human viruses by a simple indirect immune electron microscopy technique using ferritin-labelled antibodies. J. Virol. Methods. 1981; 2(6):367-373.

[54] Morgan C, Rifkind RA, Hsu KC, Holden M, Seegal BC, Rose HM. Electron microscopic localization of intracellular viral antigen by the use of ferritin-conjugated antibody. Virol. 1961; 14(2):292-296.

[55] Patterson S. Detection of antibody in virus-antibody complexes by immunoferritin labelling and subsequent negative staining. J. Immunol. Methods. 1975; 9(2):115-122.

[56] Huang SN, Neurat AR. Immunohistologic demonstration of hepatitis B viral antigen in liver injury. Lab. Invest. 1979; 40(1):1-17.

[57] Cheville NF, Stasko J. Techniques in electron microscopy of animal tissue. Vet. Pathol. 2013; 10:1-14.

[58] Kjeldsberg E. Use of gold IgG complexes and human antisera for electron microscopy identification of hepatitis A virus and polioviruses. J. Virol. Meth.1986; 13:207.

[59] Patterson S, Oxford JS. Analysis of antigenic determinants on internal and external proteins of influenza virus and identification of antigenic subpopulations of virion in recent field isolates using monoclonal antibodies and immunogold labeling. Arch. Virol. 1986; 88:189-202.

[60] De Paul AL, Mukdsi JH, Petiti JP, Gutiérrez S, Quintar A A, Maldonado CA, Alicia I, Torres AI. Immunoelectron Microscopy: A Reliable Tool for the Analysis of Cellular Processes, Applications of Immunocytochemistry, Dr. Hesam Dehghani (Ed.). InTech: Rijeka, 2012, pp.65-96.

[61] Rosso F, Papale F, Barbarisi A. Environmental scanning electron microscopy gold immunolabeling in cell biology. Meth. Mol. Boil. (Clifton, N.J.). 2013; 931:517-523.

[62] Fassel TA, Raisch KP, Chetty N, Grossberg SE, Kushnaryov VM. Ruthenium red preserves glycoprotein peplomers of C-type retroviruses for transmission electron microscopy. Biotech. Histochem.1998; 73(4):222-227.

[63] Marechal V, Prevost M-C, Petit C, Perret E, Heard J-M, Schwartz O. Human immunodeficiency virus type 1 entry into macrophages mediated by macropinocytosis. J. Virol. 2001; 75(22):11166-11177.

[64] Welsch S, Keppler OT, Habermann A, Allespach I, Krijnse-Locker J, Kräusslicht H-G. HIV-1 buds predominantly at the plasma membrane of primary human macrophages. PLoS Pathog. 2007; 3(3):e36.

[65] Waller LN, Fox N, Fox KF, Fox A, Price RL. Ruthenium red staining for ultrastructural visualization of a glycoprotein layer surrounding the spore of *Bacillus anthracis* and *Bacillus subtilis.* J. Microbiol. Methods. 2004; 58(1):23-30.

[66] Nii S, Morgan C, Rose HM, Hsu KC. Electron microscopy of herpes simplex virus. IV studies with ferritin-conjugated antibodies. J. Virol.1968; 2(10):1172-1184.

[67] Morgan C, Rifkind RA, Rose HM. The use of ferritin-conjugated antibodies in electron microscopic studies of influenza and vaccinia viruses. Cold Spring Harb Symp. Quant Biol.1962; 27:57-65.

[68] Breese SS Jr, Stone SS, De Boer CJ Hess WR. Electron microscopy of the interaction of African swine fever virus with ferritin-conjugated antibody. Virol.1967; 31(3): 508-513.

[69] Meiselman N, Kohn A, Danon DJ. Electron microscopic study of penetration of Newcastle disease virus into cells leading to formation of polykaryocytes. J. Cell. Sci. 1967; 2:71-76.

[70] Anderson KL. Cationized ferritin as a stain for electron microscopic observation ob bacterial ultrastructure. Biotech. Histochem. 1998; 73(5):278-288.

[71] Neyrolles O, Brenner C, Prevost MC, Fontaine T, Montagnier L, Blanchard A. Identification of two glycosylated components of *Mycoplasma penetrans*: a surface-exposed capsular polysaccharide and a glycolipid fraction. Microbiol. 1998; 144(5):1247-1255.

[72] Ubertini T, Wilkie BN, Noronha F. Use of horseradish peroxidase-labeled antibody for light and electron microscope localization of reovirus antigen. Appl. Microbiol. 1971; 21(3):534-538.

[73] Shabo AL, Vetricciani JC, Kirschstein RL. Identification of herpes simplex and vaccinia viruses in corneal cell cultures with immunoperoxidase: a light and electron microscopic study. Invest. Ophthalmol. 1973; 12(11):839-847.

[74] Chasey D. Investigation of immunoperoxidase-labelled rotavirus in tissue culture by light and electron microscopy. J. Gen. Virol.1980; 50(1):195-200.

[75] Marsh M, Griffiths G, Dean GE, Mellman I, Helenius A. Three-dimensional structure of endosomes in BHK-21 cells. Proc. Natl. Acad. Sci. 1986; 83:2899-2903.

[76] Martell D, Deerinck TJ. Sancak Y, Poulos TL, Mootha VK, Sosinsky GE, Ellisman MH, Ting AY. Engineered ascorbate peroxidase as a genetically encoded reporter for electron microscopy. Nat. Biotechnol. 2012; 30:1143-148.

[77] Bayer ME, Bayer MH. Lanthanide accumulation in the periplasmic space of Escherichia coli B. J. Bacteriol. 1991; 173(1):141-149.

[78] Holmes IH, Watson DH. An electron microscope study of the attachment and penetration of herpes virus in BHK21 cells. Virol. 1963; 21(1):112-123.

[79] Grimley PM, Berezesky IK, Friedman RM. Cytoplasmic structures associated with an arbovirus infection: loci of viral ribonucleic acid synthesis. J. Virol. 1968; 2(11): 1326-1338.

[80] Lambertenghi G, Harven E, Sato T, Tennant JR. Electron microscope study of a BALB/c leukemia virus in cell culture systems. Cancer Res.1972; 32:1108-1116.

[81] Narang HK. Ruthenium red and lanthanum nitrate a possible tracer and negative stain for scrapie "particles"? Acta Neuropath. (Berl.). 1974; 29:37-43.

[82] Faulk WP, Taylor GM. An immunocolloid method for electron microscope. Immunochem. 1971; 8 (11):1081–1083.

[83] Foissner I, Hoeftberger M. Immunogold labeling of resin-embedded electron microscopical sections. Methods Mol. Biol. 2014; 1080:183-193.

[84] Briquet S, Vaquero C. Immunolocalization studies of an antisense protein in HIV-1-infected cells and viral particles. Virol.2002; 292:177-184.

[85] Hyatt AD, Eaton B. Immuno-Gold Electron Microscopy in Virus Diagnosis and Research. CRC Press: USA, 2000.

[86] Smit J, Todd WJ. Colloidal gold labels for immunocytochemical analysis of microbes. In: Ultrastructure techniques for microorganisms, Aldrich HC, Todd WJ, Eds. Plenum Press: New York, 1986.

[87] Skepper JN, Powell JM. Immunogold staining of London resin (LR) white sections for transmission electron microscopy (TEM). CSH Protocols. 2008; 3(6):1-5.

[88] Van Den Hurk SVDL, Garzon S, Van Den Hurk JV, Babiuk LA, Tijssen P. The role of the major tegument protein VP8 of bovine herpesvirus-1 in infection and immunity. Virol. 1995; 206:413-425.

[89] Salanueva IJ, Carrascosa JL, Risco C. Structural maturation of the transmissible gastroenteritis coronavirus. J. Virol. 1999; 73(10):7952-7964.

[90] Windsor M, Hawes P, Monaghan P, Snapp E, Salas ML, Rodriguez JM, Wileman T. Mechanism of collapse of endoplasmic reticulum cisternae during African Swine Fever virus infection. Traffic. 2012; 13(1):30-42.

[91] Finck H. Epoxy resins in electron microscopy. J. Biophyc. Biochem. Cytol. 1960; 7:27.

[92] Luft JA. Improvements in an epoxy resin embedding methods. J. Biophys. Biochem. Cytol. 1961; 9:409-414.

[93] Gonzales-Santander R. Técnicas de microscopia eletrônica en biología. Aguilar: Madrid, 1969. 666p.

[94] Newman GR, Hobot JA. Resins for combined light and electron microscopy: a half century of development. Histochem. J.1999; 31(8):495-505.

[95] Glauert AM, Lewis PR. An introduction to fixation and embedding procedures and their safe use in the laboratory: Biological specimen preparation for transmission electron microscopy. Portland Press Ltd: London, 1998, 319p.

[96] Fong CKY. Electron microscopy for the rapid detection and identification of viruses from clinical specimens. Yale J. Biol. Med. 1989; 62:115-130.

[97] Bersano JG, Catroxo MHB, Villalobos EMC, Leme MCM, Martins AMCRPF, Peixoto Z MP, Portugal MASC, Monteiro RM, Ogata RA, Curi NA. Varíola suína: Estudo sobre a ocorrência de surtos nos Estados de São Paulo e Tocantins, Brasil. Arq. Inst. Biol. 2003; 70(3):269-278.

[98] Catroxo MHB, Martins AMCPF, Petrella S, Milanelo L, Aschar M, Souza F, Nastari BDB, Souza RB. Avian paramyxoviruses. Detection by transmission electron microscopy techniques. Int. J. Morphol. 2012; 30(2):723-730.

[99] Pacheco RC, Moraes-Filho J, Marcili A, Richtzenhain LJ, Matias P J, Szabo MP, Catroxo MHB, Bouyer DH, Labruna MB. *Rickettsia monteiroi* sp. nov., Infecting the Tick *Amblyomma incisum* in Brazil. Appl. Environ. Microbiol. Appl. 2011; 77(15):5207-5211.

[100] Bleck CKE, Merz A, Gutierrez MG. Comparison of different methods for thin section EM analysis of *Mycobacterium smegmatis*. J. Microsc. 2010; 237(pt 1):23-38.

[101] Mielanczyk L, Matysiak N, Michalski M, Buldak R, Wojnicz R. Closer to the native state. Critical evaluation of cryo-techniques for Transmission Electron Microscopy: preparation of biological samples. Folia Histochem. Cytobiol. 2014; 52(1):1-17.

[102] Marshall JA, Catton MG. Specimen collection for electron microscopy. Emerg. Infect. Dis. 1999; 5:842.

[103] Jindal N, Mor SK, Goyal SM. Enteric viruses in turkey enteritis. Virus Dis. 2014; 25(2): 173-185.

[104] Madeley CR. Diagnosing smallpox in possible bioterrorist attack. Lancet. 2003; 361:97-98.

[105] Gregori F, Catroxo MHB, Lopes VS, Ruiz VLA, Brandão PE. Occurrence of ferret enteric coronavirus in Brazil (preliminary report). Braz. J. Vet. Res. Anim. Sci. 2010; 47(2):156-158.

[106] Catroxo MHB, Miranda LB, Lavorenti A, Petrella S, Melo N A, Martins AMCPRF. Detection of coronavirus in capybaras (*Hydrochoeris hydrochaeris*) by transmission electron microscopy in São Paulo, Brazil. Int. J. Morphol. 2010; 28(2):549-555.

[107] Gelderblom HR. Electron microscopy in diagnostic virology. BIOforum Int. 2001; 5:64-67.

[108] Hurbain I, Sachset M. The future is cold: cryo-preparation methods for transmission electron microscopy of cells. Biol. Cell. 2011; 103:405-420.

[109] Harris JR, De Carlo S. Negative staining and cryo-negative staining: applications in biology and medicine. Methods Mol. Biol. 2014; 1117:215-258.

[110] Vale FF, Correia AC, Matos B, Nunes JFM, Matos APA. Applications of transmission electron microscopy to virus detection and identification. Formatex. 2010;128-136.

Edited by Khan Maaz

This book The Transmission Electron Microscope abundantly illustrates necessary insight and guidance of this powerful and versatile material characterization technique with complete figures and thorough explanations. The second edition of the book presents deep understanding of new techniques from introduction to advance levels, covering in-situ transmission electron microscopy, electron and focused ion beam microscopy, and biological diagnostic through TEM. The chapters cover all major aspects of transmission electron microscopy and their uses in material characterization with special emphasis on both the theoretical and experimental aspects of modern electron microscopy techniques. It is believed that this book will provide a solid foundation of electron microscopy to the students, scientists, and engineers working in the field of material science and condensed matter physics.

ISBN 978-953-51-6384-8

Photo by ffly / DollarPhoto

IntechOpen